BONE MARROW ADIPOSITY: ESTABLISHING HARMONIZED, MECHANISTIC AND MULTIDISCIPLINARY APPROACHES TO REACH CLINICAL TRANSLATION

EDITED BY: Nathalie Bravenboer, Stephanie Lucas and Clifford James Rosen
PUBLISHED IN: Frontiers in Endocrinology

frontiers Research Topics

ISSN 1664-8714
ISBN 978-2-88966-283-8
DOI 10.3389/978-2-88966-283-8

About Frontiers

Frontiers is more than just an open-access publisher of scholarly articles: it is a pioneering approach to the world of academia, radically improving the way scholarly research is managed. The grand vision of Frontiers is a world where all people have an equal opportunity to seek, share and generate knowledge. Frontiers provides immediate and permanent online open access to all its publications, but this alone is not enough to realize our grand goals.

Frontiers Journal Series

The Frontiers Journal Series is a multi-tier and interdisciplinary set of open-access, online journals, promising a paradigm shift from the current review, selection and dissemination processes in academic publishing. All Frontiers journals are driven by researchers for researchers; therefore, they constitute a service to the scholarly community. At the same time, the Frontiers Journal Series operates on a revolutionary invention, the tiered publishing system, initially addressing specific communities of scholars, and gradually climbing up to broader public understanding, thus serving the interests of the lay society, too.

Dedication to Quality

Each Frontiers article is a landmark of the highest quality, thanks to genuinely collaborative interactions between authors and review editors, who include some of the world's best academicians. Research must be certified by peers before entering a stream of knowledge that may eventually reach the public - and shape society; therefore, Frontiers only applies the most rigorous and unbiased reviews.
Frontiers revolutionizes research publishing by freely delivering the most outstanding research, evaluated with no bias from both the academic and social point of view. By applying the most advanced information technologies, Frontiers is catapulting scholarly publishing into a new generation.

What are Frontiers Research Topics?

Frontiers Research Topics are very popular trademarks of the Frontiers Journals Series: they are collections of at least ten articles, all centered on a particular subject. With their unique mix of varied contributions from Original Research to Review Articles, Frontiers Research Topics unify the most influential researchers, the latest key findings and historical advances in a hot research area! Find out more on how to host your own Frontiers Research Topic or contribute to one as an author by contacting the Frontiers Editorial Office: researchtopics@frontiersin.org

BONE MARROW ADIPOSITY: ESTABLISHING HARMONIZED, MECHANISTIC AND MULTIDISCIPLINARY APPROACHES TO REACH CLINICAL TRANSLATION

Topic Editors:
Nathalie Bravenboer, VU University Medical Center, Netherlands
Stephanie Lucas, Université du Littoral Côte d'Opale, France
Clifford James Rosen, Maine Media College, United States

Citation: Bravenboer, N., Lucas, S., Rosen, C. J., eds. (2020). Bone Marrow Adiposity: Establishing Harmonized, Mechanistic and Multidisciplinary Approaches to Reach Clinical Translation. Lausanne: Frontiers Media SA.
doi: 10.3389/978-2-88966-283-8

Table of Contents

frontiers in Endocrinology

EDITORIAL
published: 27 October 2020
doi: 10.3389/fendo.2020.604110

Editorial: Bone Marrow Adiposity: Establishing Harmonized, Mechanistic, and Multidisciplinary Approaches to Reach Clinical Translation

Stephanie Lucas[1], *Clifford James Rosen*[2] *and Nathalie Bravenboer*[3]*

[1] Marrow Adiposity and Bone Lab-MABLab ULR4490, Univ. Littoral Côte d'Opale, Boulogne-sur-Mer, Univ. Lille, CHU Lille, Lille, France, [2] Center for Clinical & Translational Research, Maine Medical Center Research Institute, Scarborough, ME, United States, [3] Department Clinical Chemistry, Amsterdam Movement Sciences, Amsterdam University Medical Center, Amsterdam, Netherlands

Keywords: Bone Marrow Adiposity Society, bone marrow adipocytes, special issue, methodology, nomenclature

OPEN ACCESS

Edited and reviewed by:
Jonathan H. Tobias,
University of Bristol, United Kingdom

***Correspondence:**
Nathalie Bravenboer
n.bravenboer@amsterdamumc.nl

Specialty section:
This article was submitted to Bone Research, a section of the journal Frontiers in Endocrinology

Received: *08 September 2020*
Accepted: *05 October 2020*
Published: *27 October 2020*

Citation:
Lucas S, Rosen CJ and Bravenboer N (2020) Editorial: Bone Marrow Adiposity: Establishing Harmonized, Mechanistic, and Multidisciplinary Approaches to Reach Clinical Translation. Front. Endocrinol. 11:604110. doi: 10.3389/fendo.2020.604110

Editorial on the Research Topic

Bone Marrow Adiposity: Establishing Harmonized, Mechanistic, and Multidisciplinary Approaches to Reach Clinical Translation

This Research Topic comprises ten articles describing different approaches to study the regulation or maturation of bone marrow adiposity. The conversion of the "red" hematopoietic bone marrow to a "yellow" fatty one is a long-known phenomenon that has been referred to by many names. Bone Marrow Adipocytes (BMAds) have also been revealed as puzzling yet intriguing cells, which could provide exciting novel insights into the pathophysiology and treatment of aging, osteoporosis, anorexia nervosa, obesity and diabetes, aplastic anemia, multiple myeloma, leukemia, bone metastases, and many other clinical conditions. Thus, it is no wonder that enthusiasm surrounding Bone Marrow Adiposity (BMA) research has accelerated in recent years, especially since techniques for the isolation and study of BMAds have become increasingly refined and established (**Figure 1**). However, literature on the role of BMAds shows considerable variation and inconsistencies so far. The need for consensus and uniformity in this growing field of research is therefore a major issue that has been highlighted by the International Bone Marrow Adiposity Society (BMAS).

BMAS was founded in 2017 to consolidate the growing scientific community interested in BMA, after the success of meetings organized since 2015. This young society brings together physicians and scientists working on rheumatology and bone biology, oncology, hematology, medical imaging, endocrinology, and metabolic perturbations, for which BMA research provides a new scientific direction. So far there have been five meetings with an excellent standard of keynote lectures and research presentations, in combination with interactive discussions in working groups. Reports from the third and the fourth meetings are presented in this Research Topic (Corsi et al.; Penel

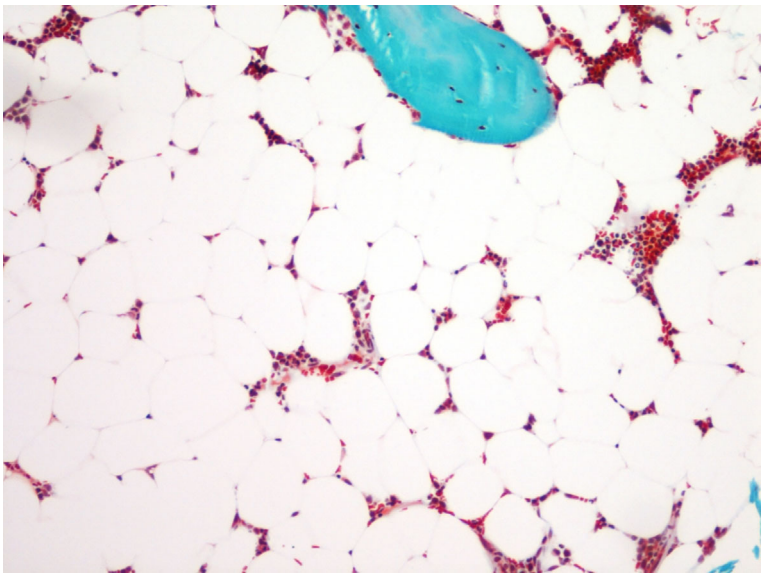

FIGURE 1 | Bone marrow adiposity in a human transiliac bone biopsy. Bone marrow adipocytes appear as "gost" cells in a Goldner's stained section. Magnification 10 × 10.

et al.). BMAS is an open society with many investigators from diverse fields who have been gathering in working groups to share protocols and experience. Two of those working groups have important publications in this Research Topic (Bravenboer et al.; Tratwal et al.), which are sure to provide a foundation with a high impact on BMA research in the future. Other BMAS working groups are now finalizing additional position papers (*e.g.* for Biobanking), which will provide further important resources for future BMA research.

One position paper addresses the nomenclature challenge regarding the diverse terminology used so far to describe the fat depot, the adipose cells, their subtypes or their stem and progenitor cells within the bone marrow, as well as the methods used for their study (Bravenboer et al.). Indeed, BMA can be measured through histomorphometry, computed tomography (CT), and Magnetic Resonance Imaging (MRI), a diversity of techniques that has also led to a confusing heterogeneity. Recommendations of specific terms, abbreviations, and units have thus been discussed and compiled to propose a standardized nomenclature to be adopted by the BMA research community. As observed in the field of bone histomorphometry following the first consensus publication in 1987 (1) such terminological harmonization is expected to improve the consistency between studies and to facilitate collaborations and inputs from the diverse fields.

Another critical need related to methodological standards has also led to a second position paper (Tratwal et al.). This paper already has received many readings and downloads online, demonstrating that uniformity in methods has become indispensable to boost BMA research not only in quantity but also in quality. Based on the review of the literature and on expert opinions, specific gold-standard methodologies are discussed regarding 1) histomorphometry of BMAds, 2) *ex vivo* BMA imaging using μCT following the staining with osmium tetroxide or other contrast-enhancing agents, 3) *in vivo* BMA imaging using MRI techniques in clinical studies, 4) cell isolation, culture, differentiation, and *in vitro* modulation of primary BMAd and BM stromal cell precursors, 5) lineage tracing and *in vivo* BMA modulation, and 6) BMA biobanking. Importantly, this second publication highlights the requirements for consensual annotations and standardization in techniques (choice of referent and condition) and provides guidelines for a detailed description of critical experimental parameters to minimize variability and to improve the comparability between studies. Emerging techniques are also described, which may soon come to complement or substitute the gold standards. One of these techniques is histomorphometry by unbiased semi-automatic image analysis; this is thoroughly described in this Research Topic by Tratwal et al. in an original research paper on MarrowQuant, a new image analysis plug-in. Other relevant technical strategies have also been developed and are described in the other associated articles.

Many scientists aimed to answer the urgent questions on how BMA is regulated. Several papers in this Research Topic address this subject. A well-known stimulus for BMA accretion is irradiation. It is therefore highly relevant that Costa and Reagan put into perspectives the consequences of therapeutic irradiation on Skeletal Stem Cell (SSC) properties and BMAT development in rodents and patients with skeletal complications (Costa and Reagan). In doing so, they propose new strategies in conjunction with radiotherapy. The central nervous system is a key mediator of adipose tissue function through sympathetic

adrenergic neurons. Wee et al. investigate whether central autonomic pathways are also involved in BMAT regulation using viral transneuronal tract tracing in two mouse strains (Wee et al.). After quantifying the local sympathetic adrenergic innervation, they establish that BMAT shares common central neuroanatomic pathways, notably with peripheral adipose tissue, which paves the way for future studies on BMAT functional regulation. An interesting additional hypothesis is that temperature also regulates BMAT through the sympathetic nervous system. Turner et al. report the effects of propranolol in mice housed at 22°C or thermoneutrality to highlight that β-adrenergic receptor signaling contributes to regulating BMAT levels and metabolism without critically impacting on the premature cancellous bone loss observed at room temperature (Turner et al.). Chronic hyperglycemia has also been revealed as a promoting factor for adipogenesis within the bone marrow. Rharass and Lucas further investigate the impact of low and high glucose levels on human SSC-derived BMAds and their non-lipid-laden-cell counterparts (Rharass and Lucas). They demonstrate that high glucose concentrations drive only mature BMAds toward an altered phenotype through a rise in reactive oxygen species (ROS) generation. Finally, Dalla Valle et al. evaluate in this Research Topic the handling of free fatty acid (FFA) desaturation in human SSCs to prevent saturated FFA-induced lipotoxicity (Dalla Valle et al.). Using pharmacological agents to modulate LXR activity, they provide evidence for a protective role of the desaturase enzyme Stearoyl-CoA 9-Desaturase (SCD)1 in human SSC viability during saturated FFA exposure.

Most of the research in this Research Topic focuses on the regulation of BMAT and the differentiation routes of SSCs. Elucidation of these entangled pathways is crucial for targeting SSCs or BMAds for the treatment of osteoporosis or other metabolic (bone) diseases. For this ambition, we also need to clarify how BMAds regulate bone cells such as osteoblasts and osteoclasts. Unravelling the cross talk between BMAds and bone cells is crucial not only to target BMAds for improved bone health, but also if we are to uncover other mechanisms important in local and systemic metabolism.

AUTHOR CONTRIBUTIONS

NB and SL wrote the manuscript. CR corrected and approved the final manuscript. All authors contributed to the article and approved the submitted version.

REFERENCE

1. Parfitt AM, Drezner MK, Glorieux FH, Kanis JA, Malluche H, Meunier PJ, et al. Bone histomorphometry: standardization of nomenclature, symbols, and units. Report of the ASBMR Histomorphometry Nomenclature Committee. *J Bone Miner Res* (1987) 2(6):595–610. doi: 10.1002/jbmr.5650020617

Conflict of Interest: The authors declare that the research was conducted in the absence of any commercial or financial relationships that could be construed as a potential conflict of interest.

frontiers in Endocrinology

PERSPECTIVE
published: 28 May 2019
doi: 10.3389/fendo.2019.00336

Brief Report From the 3rd International Meeting on Bone Marrow Adiposity (BMA 2017)

Alessandro Corsi[1], *Biagio Palmisano*[1], *Josefine Tratwal*[2], *Mara Riminucci*[1]* and *Olaia Naveiras*[2,3]*

[1] Department of Molecular Medicine, Sapienza University of Rome, Rome, Italy, [2] Institute of Bioengineering (IBI) and Swiss Institute for Experimental Cancer Research (ISREC), École Polytechnique Fédérale de Lausanne (EPFL), Lausanne, Switzerland, [3] Hematology Service, Departments of Oncology and Laboratory Medicine, Centre Hospitalier Universitaire Vaudois (CHUV), Lausanne, Switzerland

The 3rd International Meeting on Bone Marrow Adiposity (BMA) was held at the Olympic Museum in Lausanne, Switzerland, on August 31st and September 1st, 2017. This brief monograph summarizes the scientific contents of the meeting and highlights the birth of the International Bone Marrow Adiposity Society (BMAS).

Keywords: bone marrow adiposity, bone marrow adipocytes, bone marrow, bone marrow adiposity society (BMAS), bone, bone marrow fat, bone metabolism, yellow marrow

OPEN ACCESS

Edited by:
Nathalie Bravenboer, VU University Medical Center, Netherlands

Reviewed by:
Beata Lecka-Czernik, University of Toledo, United States
Jawed Akhtar Siddiqui, University of Nebraska Medical Center, United States

***Correspondence:**
Mara Riminucci
mara.riminucci@uniroma1.it
Olaia Naveiras
olaia.naveiras@epfl.ch

Specialty section:
This article was submitted to Bone Research, a section of the journal Frontiers in Endocrinology

Received: *21 December 2018*
Accepted: *09 May 2019*
Published: *28 May 2019*

Citation:
Corsi A, Palmisano B, Tratwal J, Riminucci M and Naveiras O (2019) Brief Report From the 3rd International Meeting on Bone Marrow Adiposity (BMA 2017). Front. Endocrinol. 10:336. doi: 10.3389/fendo.2019.00336

INTRODUCTION

A two-day meeting on Bone Marrow Adiposity (BMA) was held at the Olympic Museum in Lausanne, Switzerland, on August 31st and September 1st, 2017 (https://bma2017.sciencesconf.org). The meeting was co-organized by Olaia Naveiras, Alessandro Corsi, and Mara Riminucci with the active collaboration of Biagio Palmisano and Josefine Tratwal, as a joint effort between their laboratories at the Ecole Polytechnique Federale de Lausanne (EPFL) and the Sapienza University of Rome. This meeting was dedicated to the memory of the excellent scientist and expert in bone and bone marrow (BM) physiopathology, Paolo Bianco, anatomical pathologist at the Sapienza University of Rome who passed away in 2015 (1, 2).

In continuity with the first two meetings held in Lille, France [https://bma2015.sciencesconf.org; (3)], and in Rotterdam, the Netherlands [https://adiposity.sciencesconf.org/; (4)], the 3rd International Meeting on BMA was organized to provide physicians and scientists worldwide with different backgrounds -including bone biology, metabolism, oncology, endocrinology, hematology, and rheumatology- the opportunity to share novel results and exchange views on the emerging field of BMA (5–17). Reflecting the focus of the hosting laboratories, emphasis was placed on the bioengineering aspects and stem cell biology perspectives in BMA.

Through recent years, the increasing focus of sessions and symposia on BMA together with the invitation of BMA experts to congresses organized by international societies across different fields (endocrinology, hematology, bone, imaging) underlines the important implications of BMA in metabolic homeostasis, pathologic conditions (osteoporosis, diabetes, obesity, anorexia nervosa, blood diseases, cancer), and aging. Based on this broad and impactful relevance, documented also by the growing number of scientific articles published on this topic in recent years (**Figure 1**), the need to potentiate basic, translational, and clinical research on BMA was reflected at the constitutive assembly of the BMA meeting in Lausanne, where attendees voted to approve the creation of the International BMA Society (BMAS; http://bma-society.org/) as detailed below.

OVERVIEW OF THE SCIENTIFIC SESSIONS

The meeting focused on varying aspects of BMA, from the developmental origin, functional properties, and endocrine and paracrine regulation of BM adipocytes to the relationship between BM adipocytes in hematopoiesis and with bone tissue. It also included novel technologies and engineering approaches for assessing BMA and the role of BMA in disease. Sixty-six delegates from 14 different countries traveled from as far as China, South Africa, the USA, and across Europe to attend the two-day meeting. The seven invited speakers came from France, Denmark, the USA, and China, bringing fresh aspects of their research fields to the multidisciplinary BMA community.

Twenty-four abstracts were received and ranked by an external committee, resulting in 17 oral presentations and seven poster presentations with a dedicated poster pitching session. Prizes for best oral presentations were awarded to the top scoring abstract, "Regulation of bone marrow adipocytes by the sympathetic nervous system: from bone to brain" by *EL Scheller*, and the top junior presentation, "Biomimetic engineering of a functional *ex vivo* human hematopoietic niche" by *T Klein*. Further echoing the high scientific content of BMA 2017, the contents of many of the oral and poster presentations have been published immediately before or after the meeting (18–35). Even though this long list of published papers unequivocally attests the recent advances in understanding the development, properties and (endocrine and paracrine) regulation of BMA, in clarifying the strong relationship between BMA and haematopoiesis/skeletal tissue and the role of BMA in disease as also the improvement of the technological approaches for assessing BMA, the need for more in-depth research emerged in all scientific sessions. Challenges associated to the lack of uniform nomenclature and lack of standardization of the methodologies specific to BMA and research were recurrent comments during the discussions, reason why the first tasks assigned to the newly created working groups were the preparation of consensus documents in Nomenclature and BMA methodologies, which were discussed in the subsequent meetings among the members of each of the two groups and whose final form accompanies this Frontiers in Endocrinology Bone Research Section issue.

A debate session on the origin of BM adipocytes among three community leaders (*MC Horowitz, T Schulz,* and *BO Zhou*) with an equally prominent moderator (*M Kassem*) was also organized. The heterogeneity of BM adipocytes and the methodological difficulties in tracing their origin were uncovered through the distinct perspectives that emerged during the discussion. A consensus was reached at the meeting that BMA is indeed heterogeneous depending on skeletal location, with regionalization based on genetic tracers pinpointing to specific differences in limbs and tail BM adipocytes as compared to the axial skeleton, and that different stimuli induce apparent variations in BMA, though the progenitor/BM adipocyte hierarchy and the relationship to skeletal stem cells remains to be illuminated.

The complete list of scientific sessions and contributors in each session is presented in **Appendix A**.

INVITED SPEAKERS

Using diverse mouse models of marrow aplasia, *Bo Zhou* and *K Liu* focused on the role of BM adipocytes in hematopoietic regeneration. *Bo Zhou* showed that, in response to irradiation and BM transplantation, the cellular composition of the BM hematopoietic stem cell (HSC) niche changes since HSC maintenance and hematopoietic regeneration are promoted by BM adipocytes at different stages of commitment and BM stromal cells (BMSCs) (24). *K Liu* showed that adiponectin is one of the main molecules involved in the regulation of delayed hematopoietic recovery after chemotherapy or BM transplantation (36). *AJ van Wijnen* (23, 32) and *M Kassem* (21, 25) explored the molecular mechanisms involved in the lineage-specific commitment (adipocyte vs. osteoblast) of BMSCs, the understanding of which can provide significant insights into the process of age- and osteoporosis-related impaired osteogenesis. *MC Horowitz* and *DB Chou* presented data on novel technological tools to investigate BM adipogenesis. *MC Horowitz* presented details of a technique that couples histochemical staining of cell-bound lipids using osmium tetroxide with micro-Computerized Tomography (microCT) to visualize and quantify mouse BMA and underlined the importance of linear tracing experiments to assess the ontogeny of BM adipocytes (20). *DB Chou* discussed the ongoing development of human BM on a chip, a microfluidic device able to reproduce important aspects of the *in vivo* microenvironment, detailing its performance in recapitulating radiation-induced acute myelosuppression. *F Pflumio* focused on the role of different BM sites in orchestrating human and mouse T-cell acute lymphoblastic leukemia to convincingly demonstrate that adipocyte-rich sites contribute to drug-resistant leukemic cells escaping treatment (19).

SELECTED SPEAKERS

A substantial part of the selected presentations used different mouse models to focus on the ontogeny of BMA; the relationship between hematopoiesis, bone tissue, and BMA; the endocrine and paracrine regulation of BM adipocytes; the role of BMA in diseases. *CS Craft,* using adiponectin-Cre$^{DTA+/-}$ and Uncoupling-Protein-1(UCP1)-Cre$^{DTA+/-}$, provided critical insights into the region-specific properties of BM adipocytes, particularly regarding the expression of adiponectin and the capacity of some BMAT depots to induce beiging. Data on Tyrosine Kinase Substrate with four SH3 domains (Tks4), inorganic Phosphate Transporter-2 (PiT2), and adiponectin receptor-1 (AR-1) deficient mice were the subjects of the presentations by *V Vas*, *S Beck-Cormier,* and *A Sowman,* respectively. Tks4, a scaffold protein involved in podosome formation, *Epithelial Growth Factor Receptor* (EGFR) signaling, and *Reactive Oxygen Species* (ROS) production, was shown to be necessary for both the adipogenic and osteogenic differentiation of BMSCs (37). The phenotypic characterization of PiT2 (reduced bone volume, impaired mineralization, altered biomechanical parameters, increased circulating alkaline phosphatase, and an increase in BMA in the absence of significant changes of the plasma levels of adiponectin) and AR-1 (low bone

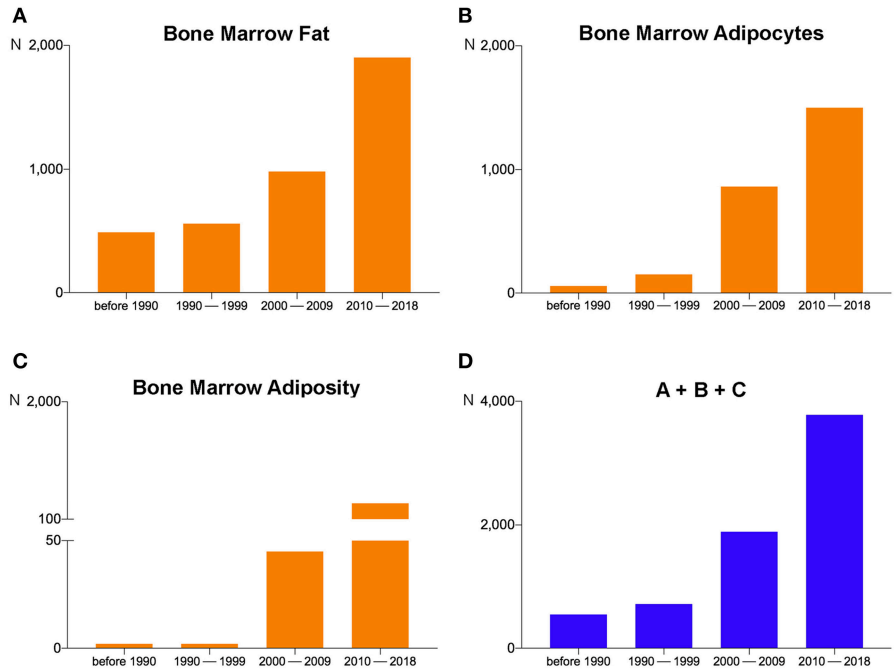

FIGURE 1 | Pubmed search results on September 10, 2018 for **(A)** "Bone Marrow Fat," **(B)** "Bone Marrow Adipocytes," and **(C)** "Bone Marrow Adiposity" revealed 3,929, 2,571, and 428 items, respectively. For each search, the period from 2010–2018 contains the largest number of items. **(D)** The sum of the items obtained by the three different searches (A + B + C). The number of the total items in 2010–2018 has grown by about 100%, 500%, and 700%, respectively, compared to 2000–2009, 1990–1999, and before 1990.

mass due to decreased osteoblast formation and increased BMA) knockout mice also supported a role for both molecules in the modulation of BMSC lineage commitment and differentiation toward adipocyte or osteogenic lineages. *TH Ambrosi* delineated the ontology of BM adipose tissue and the molecular identity of bone-resident adipocytes, establishing their involvement in age-dependent dysfunction of bone and hematopoietic regeneration (18). *A Wilson* explored hematopoiesis within the BM of lipodystrophic mouse models entirely lacking adipocytes, including the epiblast-specific PPAR-γ deletion, and reported that the lack of BM adipocytes alters the HSC niche and contributes to the onset of severe extramedullary hematopoiesis (34). Mattiucci et al. explored the role of BM adipocytes isolated from hip surgery patients in supporting HSC survival (22). He showed that short-term hematopoietic progenitors would not proliferate in the presence of primary human BM adipocytes as compared to undifferentiated BMSC controls, but HSCs survived and could form colonies after 5 weeks of co-culture with primary BM adipocytes, thus supporting the role of BM adipocytes in the hematopoietic niche. *E Douni* described two transgenic RANKL mouse lines wherein the number of copies of the transgene correlates with the severity of the osteoporotic phenotype, emphasizing their suitability as models for investigating the pathogenetic mechanisms that regulate the development and expansion of BMA in osteoporosis. *EL Scheller* focused on the regulation of BM adipose tissue by peripheral sympathetic nerves (29, 31); in this context, she identified regulatory pathways and sites within the brain with the potential to coordinate BMA in concert with peripheral adipose depots. Based on *in vitro* and *in vivo* data, *A Perino* showed that the bile acid-responsive membrane receptor TGR5 promotes mitochondrial fission through the ERK/DRP1 pathway and demonstrated beige remodeling of subcutaneous white adipose tissue under multiple environmental cues, including cold exposure and prolonged high-fat diet feeding (33).

Three of the selected presentations focused on technologies and engineering approaches for assessing BMAs. A novel microCT contrast agent for the three-dimensional simultaneous visualization of mineralized and soft skeletal tissue, the Hafnium-substituted polyoxotungstate, was presented by Kerckhofs et al. (30). Bourgine et al. (26) presented a three-dimensional *in vitro* biomimetic engineered human BM analog that exhibited compositional and structural features of human BM while supporting the maintenance of HSCs and progenitors. The metabolic functions of the BM adipose tissue in mice and humans, as revealed by [^{18}F]-FDG-PET/CT imaging, were illustrated by *K Suchacki*.

Other selected presentations explored the relationship between BMA and diverse pathologic conditions. *N Al Rassy* showed that moderate physical activity does not prevent BMA accumulation in a mouse model of chronic food restriction. Using the separation-based anorexia (SBA) mouse model, *C Chauveau* suggested that corticosterone is involved in the BMA regulation of SBA mice and demonstrated the impact of the differentiation of BMSCs toward the adipocyte lineages as well as of the stimulated bone resorption on the reduced bone

mass. Data on the potential role of the Methyl-CpG binding protein-2 (MeCP-2) and its related microRNAs in BMSC-derived adipogenesis were presented by *MR Rippo*. Finally, with her study on BMSCs isolated from BM aspirates obtained from lean, overweight, and obese men, *M Tencerova*, reported that BMSCs from obese men maintained insulin responsiveness and suggested that the enhanced adipogenic differentiation potential of BMSCs may lead to their exhaustion, contributing to the impaired bone formation and bone fragility observed in obesity.

POSTERS

The seven posters covered different aspects of BMA, including the lack of involvement of the Peroxisome Proliferator-Activated Receptor-γ (PPAR-γ) pathway in the accumulation of BMA in an ovariectomy mouse model (*K Beekman*); the use of digital holographic microscopy for quantifying lipid content during adipocyte differentiation *in vitro* in a non-perturbing manner (*V Campos*; 25); the long-term effect of ovariectomy on mandibular bone microarchitecture and BMA in a comparison of the tibia of adult rats (28); the expression of brown fat genes during adipocytic differentiation and its modulation by glucorticoid in rat proximal femur-derived BMSCs (*WF Ferris*); the phenotypic characterization of mice with targeted expression of $G\alpha s^{R201C}$ in mature adipocytes (*R Labella*); the molecular characterization of new potential markers of BM adipocytes (*G Maurizi*); and the association of increased BMA with chronic kidney disease (35).

CREATION OF THE INTERNATIONAL BMAS

The creation of a scientific society dedicated to BMA was envisioned as early as 2015 when a first group of physicians and scientists was formed (the BoneAHeaD group, BONE Adiposity in HEAlth and Diseases) with a shared need for an international society that focused on BMA. This group was funded by the French Research Agency with the goal of building a European network and applying to international funding calls. The need for the creation of a society was repeatedly posed during the 1st [BMA 2015, https://bma2015.sciencesconf.org: (3)] and 2nd BMA meetings [BMA 2016, https://adiposity.sciencesconf.org/; (4)] and in the last meeting of the BoneAHeaD group that took place in Boulogne-sur-Mer, France, in March 2017. At the BMA 2017, a preparatory meeting was organized on August 30th, 2017 (15:30–20:00) at EPFL in which members of the BoneAHead group invited speakers from the three BMA meetings (BMA 2015, BMA 2016, and BMA 2017) and other researchers who expressed an interest in the creation of an international society dedicated to BMA. The purpose of this preparatory meeting was to elaborate a consensus proposal regarding the name, aims, statutes, and general organization of the society that were to be presented and voted on at the constitutive assembly (CA) that was held during the BMA 2017 (September 1st, 2017, 12:15–13:00). All participants of BMA 2017 were invited to the CA and also constituted the general assembly (GA). The name and aims of the society and the criteria for the composition and missions of the GA, executive board (EB), and scientific board (SB) were proposed, voted on, and unanimously approved by the CA. The interim (founding) EB and SB, the procedures to elect the definitive EB and SB, and the locations of upcoming meetings were also proposed, voted on, and unanimously approved. For the composition of the definitive EB and SB, priority was given to an appropriate gender, geographical, and scientific background balance. The aims of the International BMAS are the organization of BMA meetings, the research and training of young researchers in the BMA field, data sharing, establishing common research standards, fostering collaborations, and public engagement. In the statutes of the BMAS, the founding executive and scientific boards reflect the importance of maintaining rigorous research and guidelines within the society and BMA community at large. Consequently, to work toward the missions of the society, three working groups were created (nomenclature, methodologies, and biobanking) and three (public engagement, data repositories, and sponsorship) planned and definitely established soon after. Finally, the legal status and organization of the society was proposed, voted on, and unanimously approved. Statutes of the society were documented in French and English following the meeting and signed by members of the first EB on February 2nd, 2018. In the meantime, a society website (http://bma-society.org/) has also been created. From its beginning on September 1st, 2017 in Lausanne, where the BMAS headquarters are located, the society seeks to advance the knowledge of BMA by facilitating interdisciplinary exchanges, developing research strategies, and promoting the emergence of new ideas and concepts eventually aimed to improve understanding and treatment of the numerous diseases in which BMA is involved.

CONCLUDING REMARKS AND PERSPECTIVE ON THE INTERNATIONAL BMAS

Over the past 5–10 years, new research has massively advanced our understanding of BMA development and functions. BMA has been recognized as an active tissue involved in diverse biological processes (i.e., skeletal remodeling, hematopoietic and metabolic regulation), clinical conditions (i.e., caloric restriction, anorexia nervosa, osteoporosis, leukemia, multiple myeloma, cancer induced bone disease), and in aging. However, many biological and physiopathological questions regarding BMA remain unaddressed. For example: Which is the true identity of BM Adipocyte progenitors? Is there only one BM Adipocyte progenitor? How do different BM adipocyte progenitor change upon skeletal maturation and aging? What is the role of BMA in BM homeostasis? How do BM Adipocytes metabolically interact with their neighboring cells? How do BM Adipocytes and their immediate progenitors contribute to regulation of hematopoiesis and the HSC niche? How is BMA involved in osteoblastogenesis and osteoclastogenesis? Which factors (i.e., metabolites and hormones) do BM Adipocytes produce? Can we develop tools to address clear cause-effect relationships between BMA and disease beyond the now abundant correlative studies? Can BM adipocytes serve as an energy source for HSCs and BMSCs? Why (and how)

BMA volume changes do occur in different clinical conditions (i.e., diabetes, obesity, anorexia nervosa)? What is the role of BM Adipocytes in the context of whole-body energy balance? What is the role of BM Adipocytes in the development of BM metastasis?

BMA 2017 has been a success both for the fruitful discussions resulting from the scientific program and collaborative spirit of the attendees, and for the creation of an international scientific society, the International Bone Marrow Adiposity Society (BMAS). In the short term, BMAS has set itself the ambitious task of establishing a common, consensual nomenclature, of identifying the technical challenges specific to the study of BMA and of working toward the harmonization of methodologies and biobanking approaches to encourage data sharing and collaboration. The Authors' perspective is that the BMAS will hold the community together, ensuring its continuity, and will inevitably contribute to the in-depth biological and functional characterization of BMAT, also catching the interest of young physicians, scientists, engineers and the public at large.

AUTHOR CONTRIBUTIONS

All authors listed have made a substantial, direct and intellectual contribution to the work, and approved it for publication.

ACKNOWLEDGMENTS

We wish to thank the Swiss National Science Foundation (FNS) as the Premium sponsor (grants SNF 31CO30_173949 and PP00P3_144857); Frontiers (Journal) and CELLnTEC as Gold sponsors; Avanti Polar Lipids, Sysmex Suiss AG, Lyncee Tec, and STEMCELL Technologies as Bronze sponsors; Adipocyte (Journal) as a partner; and the Sapienza University of Rome, Rome, Italy (https://bma2017.sciencesconf.org/; https://www.uniroma1.it/it/node/37881) as supporter. We also wish to thank Aurelien Oggier, Laura Bischoff, Naveed Tavakol, Yannick Yersin, Shanti Rojas-Sutterlin, and Vasco Campos (FNS-funded members of the Laboratory of Regenerative Hematopoiesis, EPFL, Switzerland) and Rossella Labella (Sapienza-funded Member, Department of Molecular Medicine, Sapienza University of Rome, Italy) who actively participated in the organization of the meeting; and Professor Moustapha Kassem (University Hospital of Odense, Odense, Denmark) for the critical reading of the manuscript.

SUPPLEMENTARY MATERIAL

The Supplementary Material for this article can be found online at: https://www.frontiersin.org/articles/10.3389/fendo.2019.00336/full#supplementary-material

REFERENCES

1. Kassem M, Jacob F. Paolo Bianco (1955-2015). *Stem Cell Res*. (2015) 15:342. doi: 10.1016/j.scr.2015.12.004
2. Robey PG, Riminucci M, Boyde A, Sipp D. Paolo Bianco (1955-2015). *Cell Stem Cell*. (2015) 17:649–50. doi: 10.1016/j.stem.2015.11.013
3. Hardouin P, Marie PJ, Rosen CJ. New insights into bone marrow adipocytes: report from the First European Meeting on *Bone* Marrow Adiposity (BMA 2015). *Bone*. (2016) 93:212–5. doi: 10.1016/j.bone.2015.11.013
4. van der Eerden B, van Wijnen A. Meeting report of the 2016 bone marrow adiposity meeting. *Adipocyte*. (2017) 6:304–13. doi: 10.1080/21623945.2017.1313374
5. Naveiras O, Nardi V, Wenzel PL, Hauschka PV, Fahey F, Daley GQ. Bone-marrow adipocytes as negative regulators of the haematopoietic microenvironment. *Nature*. (2009) 460:259–63. doi: 10.1038/nature08099
6. Scheller EL, Troiano N, Vanhoutan JN, Bouxsein MA, Fretz JA, Xi Y, et al. Use of osmium tetroxide staining with microcomputerized tomography to visualize and quantify bone marrow adipose tissue *in vivo*. *Methods Enzymol*. (2014) 537:123–39. doi: 10.1016/B978-0-12-411619-1.00007-0
7. Scheller EL, Doucette CR, Learman BS, Cawthorn WP, Khandaker S, Schell B, et al. Region-specific variation in the properties of skeletal adipocytes reveals regulated and constitutive marrow adipose tissues. *Nat. Commun*. (2015) 6:7808. doi: 10.1038/ncomms8808
8. Scheller EL, Cawthorn WP, Burr AA, Horowitz MC, MacDougald OA. Marrow adipose tissue: trimming the fat. *Trends Endocrinol. Metab*. (2016) 27:392–403. doi: 10.1016/j.tem.2016.03.016
9. Suchacki KJ, Cawthorn WP, Rosen CJ. Bone marrow adipose tissue: formation, function and regulation. *Curr. Opin. Pharmacol*. (2016) 28:50–56. doi: 10.1016/j.coph.2016.03.001
10. Ambrosi TH, Schulz TJ. The emerging role of bone marrow adipose tissue in bone health and dysfunction. *J Mol Med*. (2017) 95:1291–301. doi: 10.1007/s00109-017-1604-7
11. Cawthorn WP, Scheller EL. Editorial: Bone Marrow Adipose Tissue: formation, function, and impact on health and disease. *Front Endocrinol*. (2017) 8:112. doi: 10.3389/fendo.2017.00112
12. Hawkes CP, Mostoufi-Moab S. Fat-bone interaction within the bone marrow milieu: impact on hematopoiesis and systemic energy metabolism. *Bone*. (2019) 119:57–64. doi: 10.1016/j.bone.2018.03.012
13. Paccou J, Penel G, Chauveau C, Cortet B, Hardouin P. Marrow adiposity and bone: review of clinical implications. *Bone*. (2019) 118:8–15. doi: 10.1016/j.bone.2018.02.008
14. Pierce JL, Begun DL, Westendorf JJ, McGee-Lawrence ME. Defining osteoblast and adipocyte lineages in the bone marrow. *Bone*. (2019) 118:2–7. doi: 10.1016/j.bone.2018.05.019
15. Singhal V, Bredella MA. Marrow adipose tissue imaging in humans. *Bone*. (2019) 118:69–76. doi: 10.1016/j.bone.2018.01.009
16. Suchacki KJ, Cawthorn WP. Molecular interaction of bone marrow adipose tissue with energy metabolism. *Curr. Mol. Biol. Rep*. (2018) 4:41–49. doi: 10.1007/s40610-018-0096-8
17. Veldhuis-Vlug AG, Rosen CJ. Clinical implications of bone marrow adiposity. *J Intern Med*. (2018) 283:121–39. doi: 10.1111/joim.12718
18. Ambrosi TH, Scialdone A, Graja A, Gohlke S, Jank AM, Bocian C, et al. Adipocyte accumulation in the bone marrow during obesity and aging impairs stem cell-based hematopoietic and bone regeneration. *Cell Stem Cell*. (2017) 20:771–784. doi: 10.1016/j.stem.2017.02.009
19. Cahu X, Calvo J, Poglio S, Prade N, Colsch B, Arcangeli ML, et al. Bone marrow sites differently imprint dormancy and chemoresistance to T-cell acute lymphoblastic leukemia. *Blood Adv*. (2017) 1:1760–72. doi: 10.1182/bloodadvances.2017004960
20. Horowitz MC, Berry R, Holtrup B, Sebo Z, Nelson T, Fretz JA, et al. Bone marrow adipocytes. *Adipocyte*. (2017) 6:193–204. doi: 10.1080/21623945.2017.1367881
21. Jafari A, Qanie D, Andersen TL, Zhang Y, Chen L, Postert B, et al. Legumain regulates differentiation fate of human bone marrow stromal cells

and is altered in postmenopausal osteoporosis. *Stem Cell Rep.* (2017) 8:373–86. doi: 10.1016/j.stemcr.2017.01.003
22. Mattiucci D, Maurizi G, Izzi V, Cenci L, Ciarlantini, M, Mancini S, et al. Bone marrow adipocytes support hematopoietic stem cell survival. *J. Cell. Physiol.* (2017) 233:1500–1511. doi: 10.1002/jcp.26037
23. Sen B, Uzer G, Samsonraj RM, Xie Z, McGrath C, Styner M, et al. Intranuclear actin structure modulates mesenchymal stem cell differentiation. *Stem Cells.* (2017) 35:1624–35. doi: 10.1002/stem.2617
24. Zhou BO, Yu H, Yue R, Zhao Z, Rios JJ, Naveiras O, et al. Bone marrow adipocytes promote the regeneration of stem cells and haematopoiesis by secreting SCF. *Nat. Cell Biol.* (2017) 19:891–903. doi: 10.1038/ncb3570
25. Abdallah BM, Alzahrani AM, Kassem M. Secreted Clusterin protein inhibits osteoblast differentiation of bone marrow mesenchymal stem cells by suppressing ERK1/2 signaling pathway. *Bone.* (2018) 110:221–9. doi: 10.1016/j.bone.2018.02.018
26. Bourgine PE, Klein T, Paczulla AM, Shimizu T, Kunz L, Kokkaliaris KD, et al. In vitro biomimetic engineering of a human hematopoietic niche with functional properties. *Proc Natl Acad Sci USA*. (2018) 115:E5688–E5695. doi: 10.1073/pnas.1805440115
27. Campos V, Rappaz B, Kuttler F, Turcatti G, Naveiras O. High-throughput, nonperturbing quantification of lipid droplets with digital holographic microscopy. *J Lipid Res*. (2018) 59:1301–10. doi: 10.1194/jlr.D085217
28. Coutel X, Olejnik C, Marchandise P, Delattre J, Béhal H, Kerckhofs G, et al. A novel microCT method for bone and marrow adipose tissue alignment identifies key differences between mandible and tibia in rats. *Calcif Tissue Int*. (2018) 103:189–97. doi: 10.1007/s00223-018-0397-1
29. Craft CS, Li Z, MacDougald OA, Scheller EL. Molecular differences between subtypes of bone marrow adipocytes. *Curr Mol Biol Rep*. (2018) 4:16–23. doi: 10.1007/s40610-018-0087-9
30. Kerckhofs G, Stegen S, van Gastel N, Sap A, Falgayrac G, Penel G, et al. Simultaneous three-dimensional visualization of mineralized and soft skeletal tissues by a novel microCT contrast agent with polyoxometalate structure. *Biomaterials*. (2018) 159:1–12. doi: 10.1016/j.biomaterials.2017.12.016
31. Robles H, Park S, Joens MS, Fitzpatrick JAJ, Craft CS, Scheller EL. Characterization of the bone marrow adipocyte niche with three-dimensional electron microscopy. *Bone*. (2019) 118:89–98. doi: 10.1016/j.bone.2018.01.020
32. Samsonraj RM, Paradise CR, Dudakovic A, Sen B, Nair AA, Dietz AB, et al. Validation of osteogenic properties of Cytochalasin D by high-resolution RNA-sequencing in Mesenchymal Stem Cells derived from bone marrow and adipose tissues. *Stem Cells Dev*. (2018) 27:1136–45. doi: 10.1089/scd.2018.0037
33. Velazquez-Villegas LA, Perino A, Lemos V, Zietak M, Nomura M, Pols TWH, et al. TGR5 signalling promotes mitochondrial fission and beige remodelling of white adipose tissue. *Nat. Commun.* (2018) 9:245. doi: 10.1038/s41467-017-02068-0
34. Wilson A, Fu H, Schiffrin M, Winkler C, Koufany M, Jouzeau JY, et al. Lack of adipocytes alters hematopoiesis in lipodystrophic mice. *Front Immunol.* (2018) 9:2573. doi: 10.3389/fimmu.2018.02573
35. Woods GN, Ewing SK, Sigurdsson S, Kado DM, Ix JH, Hue TF, et al. Chronic kidney disease is associated with greater bone marrow adiposity. *J Bone Miner Res.* (2018) 33:2158–64. doi: 10.1002/jbmr.3562
36. Lu W, Wang W, Wang S, Feng Y, Liu K. Rosiglitazone promotes bone marrow adipogenesis to impair myelopoiesis under stress. *PLoS ONE.* (2016) 11:e0149543. doi: 10.1371/journal.pone.0149543
37. Dülk M, Kudlik G, Fekete A, Ernszt D, Kvell K, Pongrácz JE, et al. The scaffold protein Tks4 is required for the differentiation of mesenchymal stromal cells (MSCs) into adipogenic and osteogenic lineages. *Sci Rep*. (2016) 6:34280. doi: 10.1038/srep34280

Conflict of Interest Statement: The authors declare that the research was conducted in the absence of any commercial or financial relationships that could be construed as a potential conflict of interest.

frontiers in Endocrinology

MINI REVIEW
published: 29 August 2019
doi: 10.3389/fendo.2019.00587

Therapeutic Irradiation: Consequences for Bone and Bone Marrow Adipose Tissue

Samantha Costa[1,2,3] *and Michaela R. Reagan*[1,2,3]*

[1] Center for Clinical and Translational Research, Maine Medical Center Research Institute, Scarborough, ME, United States, [2] University of Maine Graduate School of Biomedical Science and Engineering, Orono, ME, United States, [3] Tufts University School of Medicine, Boston, MA, United States

Radiotherapy continues to be one of the most accepted medical treatments for cancer. Localized irradiation is the most common treatment for prostate, pancreatic, rectal, cervical and endometrial malignancies. Conventional localized fractions are total doses of 30-62Gy at 1.8-2Gy per fraction, with administration of ∼60Gy often used for tumor ablation. However, even the lowest dose of localized irradiation exposure can result in adverse complications to adjacent organs, tissues, and vessels, which absorb a portion of the treatment. Skeletal complications are common amongst cancer patients undergoing these localized treatments. Irradiation exposure causes deterioration to the overall quantity and quality of bone by interfering with the trabecular architecture through increased osteoclast activity and decreased osteoblast activity. Irradiation-induced bone damage parallels adipocyte infiltration of the bone marrow (BM) resulting in compositional alterations of the microenvironment that may further affect bone quality and disease state. There may also be direct effects of irradiation on the BM adipocyte/pre-adipocyte, although *in vitro* findings do not always agree and cellular response is dependent on irradiation dosage. Hematopoietic cells also become apoptotic upon irradiation, which causes a range of skeletal effects. Bone loss leaves patients at a greater risk for osteopenia, osteoporosis, osteonecrosis, and skeletal fractures that drastically reduce quality of life. Osteoanabolic agents stimulate bone formation and reduce fracture risk in patients with low bone density; thus, osteoanabolic or anti-resorptive agents may be useful co-treatments with irradiation. This review discusses these topics and proposes further research directions using novel or combination therapies to enhance bone health during irradiation.

Keywords: irradiation, bone marrow microenvironment, bone marrow adipose tissue, osteoblast, adipocyte

OPEN ACCESS

Edited by:
Nathalie Bravenboer, VU University Medical Center, Netherlands

Reviewed by:
Eleni Douni, Agricultural University of Athens, Greece
Monica De Mattei, University of Ferrara, Italy

***Correspondence:**
Michaela R. Reagan
mreagan@mmc.org

Specialty section:
This article was submitted to Bone Research, a section of the journal Frontiers in Endocrinology

Received: *13 May 2019*
Accepted: *09 August 2019*
Published: *29 August 2019*

Citation:
Costa S and Reagan MR (2019) Therapeutic Irradiation: Consequences for Bone and Bone Marrow Adipose Tissue. Front. Endocrinol. 10:587. doi: 10.3389/fendo.2019.00587

INTRODUCTION

Since the discovery of the X-ray in 1895, irradiation science has offered advanced developments in techniques, multidisciplinary approaches, and research (1). Radiation therapy continues to be a widely accepted treatment for malignant cancers through its effective manner of killing cancer cells and reducing tumor size (1, 2). Irradiation induces free radicals in the form of reactive oxygen species (ROS) that leads to DNA damage (2). With improved treatment regiments, there have been improvements in disease outcomes and reductions in the adverse side effects of

irradiation therapy (1, 2). The effectiveness of irradiation therapies, in combination with advances in pharmaceutical treatments, early detection, prevention, and cancer awareness, has drastically improved patient quality of life and decreased mortality rates; in some cases, these advancements have changed cancer from being an acute disease to a treatable chronic disease (1). The American Cancer Society projected there were over 2.6 million fewer cancer-related deaths from 1991 to 2016 (3).

Despite the advancements in irradiation therapies, there is still an unmet concern surrounding the systemic and localized effects of irradiation on adjacent tissues, vessels, and bone (4–6). Patients undergoing irradiation therapy have the potential to experience increased irradiation toxicity, even with fractionation of treatments, and adjacent soft tissue and bone damage as an adverse side effect due to limited tumor uptake and retention of irradiation doses (6). Tumor microenvironments promote tumor growth and angiogenesis through paracrine stimulatory factors and immune-mediated interactions (7). There are many cytokines released by the immune system that are considered "pro-tumor" or "anti-tumor" that alter the tumor microenvironment (7). After irradiation exposure, there are increased inflammatory cytokines, IL-1α/β, IL-6, IL-17, TNF-α, and VEGF, and evidence of increased cellular senescence, demonstrated through increased senescence-associated secretory phenotype (SASP) proteins (2, 7, 8). This change to the tumor microenvironment and increased immune activity is thought to explain the abscopal effect, in which localized irradiation results in regression of metastatic cancer that are distant from the initial irradiation site (7).

Due to the high calcium content, bone absorb 30-40% more irradiation than the surrounding tissues; thus, the absorption of any given irradiation dose is considerably higher in bone than the surrounding tissues, making bone a common site for irradiation-induced damage (9). As previously discussed, irradiation exposure releases cytokines as an injury response that triggers acute inflammation (9, 10). This acute inflammation is characterized by increased vascular permeability with localized edema, destruction of endothelial cells, and an association with vascular thrombosis (9). Irradiation exposure also induces late stage fibroatrophy that results in poorly vascularized tissue which does not allow for proper healing, ultimately increasing tissue fragility and the recurrence of inflammation upon local injury (9, 10).

The damage observed within the bone and bone marrow (BM) after irradiation therapy is similar to the pathological conditions seen with osteoporosis (2). There is a decrease in trabecular bone volume, an increase in bone marrow adiposity (BMA), increased CTX/TRAP5 levels in the serum, and prolonged fracture healing times (2). Irradiation also depletes hematopoietic and skeletal stem cell populations within the BM (11–13). Bone marrow transplants allow for trabecular recovery, reduced BMA, and increased cell number within the BM microenvironment (12). Skeletal stem cells (SSCs), previously referred to as mesenchymal stem cells, appear to be effected by the irradiation source (photon irradiation vs. ionizing irradiation) and dose resulting in the varying differentiation potential observed in different *in vitro* studies (**Figure 1**) (11, 14–16). In murine models, the balance favors adipogenesis at the expense of osteogenesis, as a result of irradiation-induced bone loss. This bone loss is in part due to the increased osteoclast activity immediately following irradiation exposure and then the latent decrease in osteoblast activity in the sequential weeks (4, 5, 12, 17).

Studies have shown that osteoanabolic agents stimulate bone formation and reduce fracture risk in patients with low bone density (18–20). Since an adverse side effect of irradiation is decreased bone density and increased bone fragility, combination therapies of osteoanabolic, or anti-resorptive agents may be useful for patients receiving irradiation therapies. This review will discuss these topics and propose further research directions including *in vitro* and *in vivo* studies using novel or combination therapies to enhance bone strength in patients after irradiation (18).

IN VITRO IRRADIATION OF SKELETAL STEM CELLS ALTERS DIFFERENTIATION POTENTIAL

The regenerative capabilities of SSCs *in vitro* have been shown in a multitude of tissue damage models (14). Human bone marrow skeletal stem cells (hSSCs) have been shown to be resistant to the effects of low-dose irradiation (2.5Gy) with no apparent changes to morphology or immunophenotype (11). Preciado et al. have shown irradiated and non-irradiated hSSCs still expressed CD73, CD90, CD105, CD44, and CD166 and are negative for CD34, CD45, CD14, CD19, and HLA-DR, which are definitive markers of a typical SSC immunophenotypic profile (11). Irradiated hSSCs also had no significant changes to cell viability 1 or 72 h after exposure compared to non-irradiated hSSC controls (11). However, low-dose irradiation exposure affected hSSC behavior and differentiation potential *in vitro* (11). Irradiated hSSCs were capable of differentiation, but had significantly less adipocytes, evident through decreased Oil-Red-O staining and significantly less mRNA expression of adipogenic differentiation markers, *CEBPα* and *PPARγ*, when compared to the non-irradiated cells (11). On the other hand, low level irradiation exposure stimulated hSSCs osteogeneic differentiation apparent through increased mineralization expression of *SPP1* and Alizarin Red staining, despite having reduced *RUNX2* expression, an early osteogenesis marker (11).

The observed *in vitro* results in the Preciado study are likely because the exposure was a single, low-dose compared to other studies that use a single high-dose or fractionized doses that are needed therapeutically (4, 5, 17, 21, 22). Other studies suggest SSC retention of stem cell characteristics is dose-dependent and can be altered with a single high-dose exceeding 10Gy (22–24). Schönmeyr et al. demonstrated the effects of high-dose irradiation (7 and 12Gy) on rat SSCs (rSSCs) resulted in a dose dependent response compared to non-irradiated cells (22). After high-dose irradiation exposure rSSCs had a higher percentage of apoptotic cells and more cells in the G_2 cellular arrest phase (22). The irradiated cells also had reduced expression of osteogeneic markers, *ALP* and osteocalcin, as well as reduced expression of adipogenic markers, *LPL*, *CEBPβ*, and Leptin

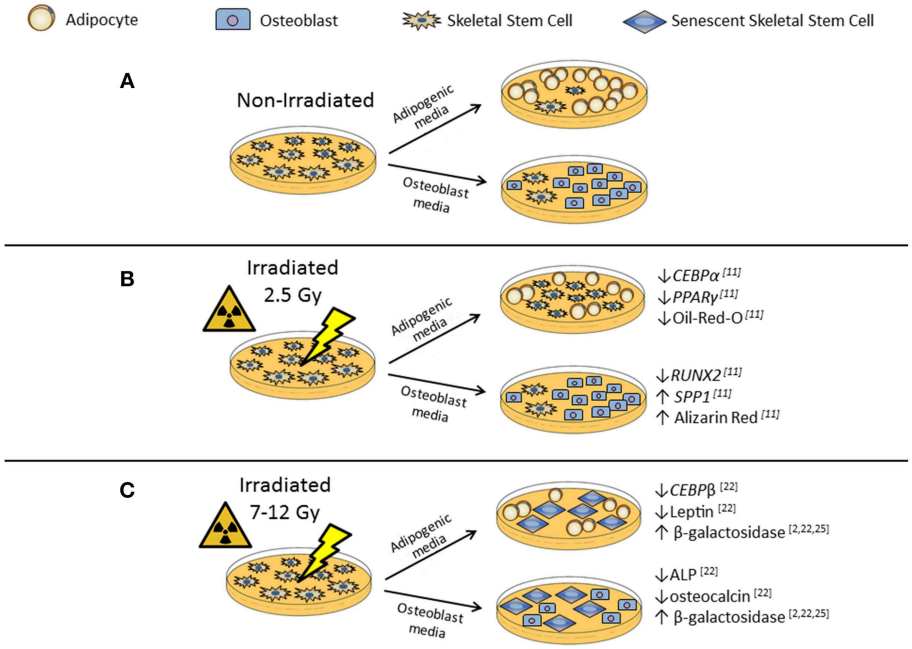

FIGURE 1 | *In vitro* irradiation affects adipogenic and osteogenic differentiation potential of skeletal stem cells (SSCs). **(A)** Non-irradiated SSCs, represent control differentiation. **(B)** Low-dose (2.5Gy) irradiated SSCs in adipogenic or osteogenic differentiation media have differing differentiation potentials. Low-dose irradiation caused reduced adipocyte differentiation with decreased adipocyte markers, such as *CEBPα* and *PPARγ*, and decreased Oil-Red-O staining when compared to the control. Osteoblast differentiation showed decreased *RUNX2* expression, but increased mineralization markers *SPP1* and Alizarin Red staining after low-dose exposure when compared to the control. There was no significant difference in osteoblast differentiation when compared to the controls. **(C)** High-dose (7-12Gy) irradiated SSCs have reduced adipocyte and osteoblast differentiation potential and evidence of increased β-galactosidase activity, a marker for cellular senescence.

(22). The reduced differentiation potential seen *in vitro* could be evidence of irradiation-induced cellular senescence (2, 11). A marker for senescence, β-galactosidase, has been used *in vitro* to show irradiation-induced senescence in a time and dose dependent manner (2, 22, 25). The level of differentiation potential down the osteogenic and adipogenic lineages of SSCs has been shown to be more sensitive or more resistant based on the dosage of ionizing radiation (11, 22, 26, 27). The altered SSC differentiation capacity impacts the hematopoietic niche and enhances engraftment of BM derived stem cell transplantations to the BM microenvironment (12).

Interestingly, irradiation induced by radionucleotides, such as Strontium-90, can also induce similar effects on SSCs (15). After 7 days of exposure *in vitro*, a pre-osteoblast cell line showed a decreased ability to proliferate, changes in cytokine expression, and changes in their ability to support hematopoietic progenitor proliferation and differentiation (15). Exposure to Strontium-90 also showed evidence of increased senescence through increased β-galactosidase as well as senescent morphology with enlarged cytoplasm and nucleus (15). Despite these intriguing findings *in vitro, in vivo* studies are necessary to determine if the same *in vitro* phenomena are observed.

In vivo Irradiation in Rodents (Mouse and Rat) Cause Bone Loss and Increased BMAT

In contrast to the decreased adipogenesis induced by irradiation observed in *in vitro* studies, *in vivo* models demonstrated that irradiation increases BMA and deteriorates trabecular bone at both high and low irradiation doses. For example, Willey et al. showed that as early as 3 days post low-dose (2Gy) whole-body irradiation of thirteen-week-old C57BL/6 mice there was a significant increase in osteoclast activity through significantly increased TRAP-5b serum levels and significantly increased osteoclast numbers per bone surface, although BMA analysis was not done (21). Ten days post low-dose (5Gy) whole-body irradiation exposure of C57BL/6 mice resulted in rapid infiltration of BM adipocytes within the BM (5). This significant increase in BMA was coupled with a significant decrease in trabecular bone volume/total volume (BV/TV), which has been observed in 8 and 16-week-old C57BL/6 mice (5, 17). This irradiation-induced bone damage was not recovered 8 weeks post exposure (5, 17). BM recovery of 8 and 16-week-old mice has been shown to be age and time dependent (17). Two and ten-days post irradiation exposure, the total number of BM cells in 8 and 16-week-old mice were significantly decreased by more than 60% (17). By 8 weeks, only 8-week-old mice showed recovery to their BM cells (17). In sum, *in vivo* models using a wide range of irradiation doses have consistently shown that irradiation decreases trabecular bone volume and increases BMA compared to non-irradiated controls (**Figure 2**). This finding is likely due to a shift in SSC lineage differentiation (i.e., favoring adipogenesis over osteogenesis) that appears to be in response to irradiation-induced BM microenvironment alternations, rather than SSC autonomous responses to irradiation, because these same shifts are not observed in SSCs *in vitro*.

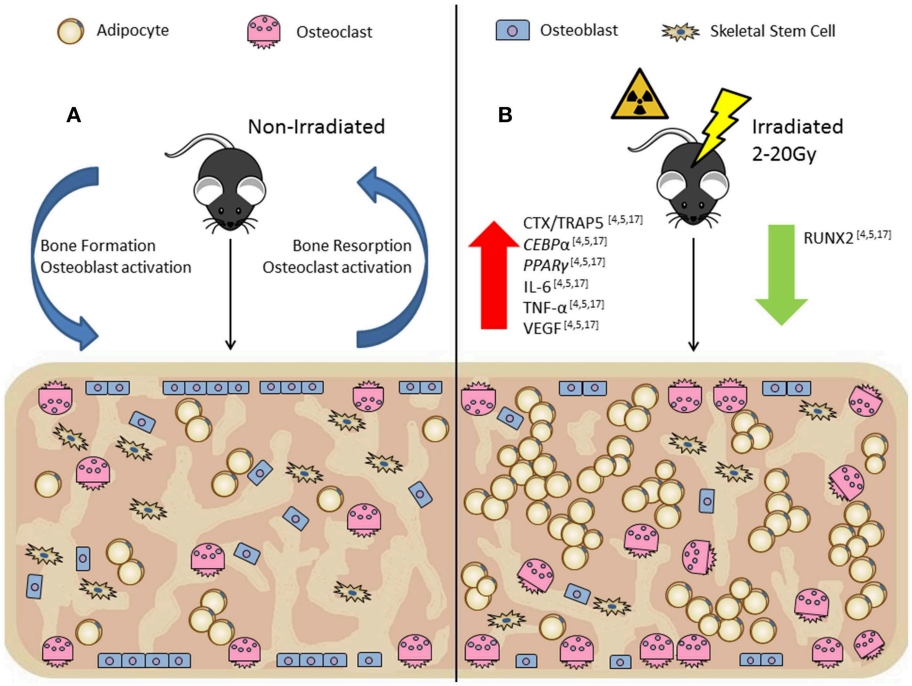

FIGURE 2 | *In vivo* rodent models show irradiation alters the bone marrow microenvironment by increasing osteoclast numbers per bone surface (Oc.S/BS) and decreasing osteoblast numbers per bone surface (Ob.S/BS) resulting in decreased trabecular bone volume with a rapid influx of bone marrow adipocytes. **(A)** Non-irradiated control, demonstrates normal bone turnover processes. **(B)** Irradiated (2-20Gy), demonstrates the uncoupling of the bone formation/resorption ratio through increased CTX/TRAP5 (osteoclast activity) and decreased *RUNX2* (osteoblast activity) expression. *In vivo* irradiation exposure also has increased *CEBPα* and *PPARγ* (adipogenesis markers), and IL-6, TNF-α, and VEGF (inflammatory and senescent markers).

Localized irradiation has been shown to affect healthy tissue adjacent to the irradiation site, with about half of the localized dose being absorbed by healthy tissue and bone (4). In 4 month old male Sprague-Dawley rats, localized exposure of 20Gy to the right hind-limb, spanning the proximal tibia to the distal femur, revealed significant reductions in trabecular bone mineral density (tBMD) and trabecular BV/TV of the irradiated femur and also in the contralateral femur compared to the sham irradiated controls (4). Cortical thickness was not affected by irradiation, but cortical porosity was increased in the irradiated and contralateral femur (4). BMAT increased at 2 weeks and 12 weeks post-irradiation in the irradiated and contralateral tibias. These alterations in trabecular bone were due to a decrease in osteoblast surface per bone surface at 2 and 12 weeks post-irradiation in the irradiated and contralateral tibias (4). Within the BM, expression of *RUNX2* and *PPARγ* of osteoblast and adipocyte progenitor cells were determined using reverse transcriptase-PCR (RT-qPCR) (4). At 2 weeks, *RUNX2* and *PPARγ* expression were significantly decreased in both the irradiated and contralateral (4). By 12 weeks, the mRNA expression of *RUNX2* continued to be downregulated by 94.5% in the irradiated and 44.1% in the contralateral, yet the expression of *PPARγ* was upregulated by 13-fold in the irradiated and 9-fold in the contralateral relative to the control (4). This study demonstrated how irradiation-induced bone damage does not require direct exposure to result in impairment, referred to as the bystander effect (4, 28).

There is also a rapid increase in osteoclast activity after irradiation exposure, seen with an increase in osteocalcin and TRAP5 levels in rat serum (4). However, 2 weeks post-irradiation there were no significant effects on bone suggesting irradiation did not compromise or uncouple the bone formation/resorption ratio immediately after exposure (4). These results differ from the observed changes seen in many irradiation mouse models. By 12 weeks post-exposure, there were significant decreases in trabecular bone volume, yet osteoclastogenesis was now comparable to the controls while osteoblastogenesis was significantly decreased, resulting in an altered formation/resorption ratio within the BM microenvironment that affected bone quality (4).

Clinical Trials Mirror *in vivo* Animal Model Findings

Irradiation-induced bone loss has been reported to cause more than insufficiency fractures; other complications from irradiation therapy include osteitis and osteolysis (29). A patient study of 510 patients (ages 40–84 years) analyzed pelvic bone related complications after irradiation therapy for uterine cervical cancer. Osteolysis was detected in 4 patients and avascular necrosis of the femoral head was diagnosed in 2 patients post irradiation therapy (29). One-hundred patients were diagnosed with insufficiency fractures a median of ∼16.9 months (range 1–87 months) after pelvic irradiation therapy (29). Of the patients diagnosed with insufficiency fractures, 85% had sacral involvement and 61% developed multiple pelvic insufficiency

fractures; 40% of those patients had symmetric bilateral lesions of the sacral alae (29).

Patients can experience late stage complications from irradiation exposure as part of an advanced treatment for head and neck tumors (9). Osteoradionecrosis (ORN) of the jaw bones (and surrounding soft tissue) is the most severe last stage complication (9). ORN illustrates increased inflammation and the development of hypovascular, hypocellular, and hypoxic tissues, which causes increased cell death and collagen breakdown that exceeds the normal cell repair and collagen synthesis homeostasis (9, 30). ORN diagnostic criteria is a slow healing (failure to recover over a 3 month period) irradiation-induced necrosis of the bone, associated with surrounding tissue necrosis in the absence of local tumor necrosis, recurrence, or metastatic disease (9). Irradiated specimens were obtained from 40 patients treated for ORN (control specimens were obtained from non-irradiated patients treated from head and neck tumors) (9). The total irradiation dosage of these specimen ranged from 50.4 to 70.4Gy (9). A histopathology examination on the bone and soft tissue samples revealed hyperemia and endarteritis as early effects of irradiation that were prolonged for up to 6 months post exposure (9). Signs of increased hypocellularity occurred rapidly after irradiation exposure; the irradiated bone samples showed greater cell loss than the soft tissue samples (9, 31). Evidence of thrombosis was apparent through densely fibrous material seen years post irradiation exposure (9, 31). There was a loss in vascular content, increase in BMAT, and fibrosis that showed a linear correlation to the time post exposure that were considered end stage markers of the irradiation-induced injury (9, 31). This current study suggested the increase in BMAT in the irradiated bone samples was due to the stunted bone turnover processes (9, 32).

Another clinical study showed 13 female patients, ages 35–63 years old, with gynecological malignancies that received irradiation or chemotherapy treatments had increased BMAT 6 and 12 months after initiating therapy treatments through repeated MRI scan (baseline, 6 months, and 12 months post therapy initiation) (33). Sagittal images of signal fat fraction (SFF) were taken in patients receiving focal irradiation therapy with the pelvic region as the target field (33). Approximately half of the irradiation therapy dose was absorbed by the sacrum and adjacent tissues and bones, such as the L4 vertebral body (33). At the baseline MRI scan, the SFF of the BMAT in the L4 and S1 were similar, however, by the 6-month scan the increase in the SFF in the S1 was marginally higher than in L4 (33). The increased SFF seen in S1 compared to L4 correlated to the higher irradiation absorption at S1 resulting in more BMAT accumulation (33). It is believed there is a progressive conversion of the hematopoietic marrow to the more adipocyte rich, yellow marrow observed throughout these regions as a response to irradiation treatment (33). The SFF of the L4 and femoral neck increased at the 6-month post-treatment scan (irradiation and chemotherapy treatments combined in this analysis) (33). These significant increases of SFF in the L4 and femoral neck were compared to skeletal muscle and subcutaneous white adipose tissue as controls, demonstrating the effects of irradiation on localized tissues and more specifically on the BM microenvironment (33).

Bisphosphonates and Osteoanabolic Agents Have Potential Restorative Effects on Irradiation-Induced Bone Damage

Anti-resorptive agents, such as bisphosphonates (BPs), and osteoanabolic agents are commonly used as osteoporosis treatments. BPs mediate bone resorption through osteoclast apoptosis (19, 20, 34). BPs can also reduce osteoblast and osteocyte apoptosis, but do not actively result in bone accrual (34). In rodent models, the administration of BPs following irradiation therapy can improve bone quality, bone strength, and BMD (19, 35, 36). However, there are conflicting data across patient trials regarding bone quality and pain management with BPs alone, in respect to cancer and irradiation therapies, suggesting combination treatments of BPs, and osteoanabolic agents may be needed to combat irradiation-induced bone damage (20, 35, 37–39).

Well-studied osteoanabolic treatments are human parathyroid hormone (hPTH) and sclerostin antibody (Scl-Ab). Both of these agents stimulate bone formation, but through different modes of action (40, 41). Scl-Ab increases bone formation by inhibiting sclerostin binding to lipoprotein receptor protein (LRP) 5/6 that inhibits canonical WNT signaling and subsequently activating SSC differentiation into osteoblasts (40, 41). Scl-Ab also suppresses bone resorption through inhibitory effects on osteoclastogenesis regulators (41–43). hPTH stimulates both anabolic and catabolic activities with a net gain in favor of the former, but there is evidence that hPTH anabolic capabilities are dependent on its ability to stimulate osteoclastogenesis (41, 44). Not only do these osteoanabolic agents increase bone accrual, but they also decrease BMA (41). Scl-Ab results in increased trabecular bone and decreased BMA, but hPTH has a direct effect on BMA reductions despite bone accrual (41). Since irradiation causes bone deterioration and adipocyte infiltration, which in combination may exacerbate bone related complications, administration of osteoanabolic agents in conjunction with irradiation therapy may prevent excessive bone loss and adipocyte infiltration (16).

CONCLUSION

Clinical studies and *in vivo* rodent models have shown high-dose and sub-lethal dose irradiation causes rapid bone loss due to increased osteoclast activity and decreased osteoblast activity, which results in increased BMA and secondary late stage bone complications that are believed to be from continued irradiation damage (16). Through *in vitro* experiments, it has been shown that SSCs are capable of maintaining their proliferation, differentiation, and regenerative properties at low-dose irradiation exposure, but at a lower capacity than non-irradiated SSCs (11). However, after high-dose exposure SSCs lose their stem cell characteristics or experience cell death (22–24, 26, 27). Currently, irradiation therapy is provided to patients in fractionized doses, but even low-doses over the course of several weeks show signs of decreased BMD and increased BMA (16). With decreased BMD, patients are at a greater risk for skeletal fractures and other bone related diseases and complications. A patient's quality of life is

severely affected by these irradiation-induced bone incidences. Future directions point to more investigative research (and potential clinical practices) into the benefits of combination therapies to reverse the adverse side effects of irradiation-induced bone loss and adipocyte infiltration. Osteoanabolic agents, such as Scl-Ab or hPTH, and BPs may be needed in conjunction or following irradiation therapy treatments to combat the bone, tissue, and cell damages currently being observed.

AUTHOR CONTRIBUTIONS

SC wrote the manuscript. MR advised and edited the manuscript. MR and SC approved the final version of the manuscript.

FUNDING

Funding was supplied by the NIH/NIGMS (P20GM121301). The authors' work was also supported by start-up funds from the Maine Medical Center Research Institute and the American Cancer Society (Research Grants #IRG-16-191-33 and #133077-RSG-19-037-01-LIB). This research utilized services of the U54GM115516 Core, which was supported by NIH/NIGMS P20GM121301 (L. Liaw, PI), U54GM115516 (C. Rosen, PI), and P30GM106391 (R. Friesel, PI). Funding/research grants were provided by Amgen Inc. and UCB Inc. Amgen Inc. and UCB Inc. had no role in the study design, data collection/analysis, decision to publish, or preparation of the manuscript.

REFERENCES

1. Bernier J, Hall EJ, Giaccia A. Radiation oncology: a century of achievements. *Nat Rev Cancer*. (2004) 4:737–47. doi: 10.1038/nrc1451
2. Chandra A, Park SS, Pignolo RJ. Potential role of senescence in radiation-induced damage of the aged skeleton. *Bone*. (2019) 120:423–31. doi: 10.1016/j.bone.2018.12.006
3. Siegel RL, Miller KD, Jemal A. Cancer statistics, 2019., CA. *Cancer J Clin*. (2019) 69:7–34. doi: 10.3322/caac.21551
4. Zou Q, Hong W, Zhou Y, Ding Q, Wang J, Jin W, et al. Bone marrow stem cell dysfunction in radiation-induced abscopal bone loss. *J Orthop Surg Res*. (2016) 11:3. doi: 10.1186/s13018-015-0339-9
5. Green DE, Adler BJ, Chan ME, Lennon JJ, Acerbo AS, Miller LM, et al Altered composition of bone as triggered by irradiation facilitates the rapid erosion of the matrix by both cellular and physicochemical processes. *PLoS ONE*. (2013) 8:e64952. doi: 10.1371/journal.pone.0064952
6. Sparks RB, Crowe EA, Wong FC, Toohey RE, Siegel JA. Radiation dose distributions in normal tissue adjacent to tumors containing (131)I or (90)Y: the potential for toxicity. *J Nucl Med*. (2002) 43:1110–4.
7. Elgström E, Ohlsson TG, Eriksson SE. Cytokine evaluation in untreated and radioimmunotherapy-treated tumors in an immunocompetent rat model. *Tumor Biol*. (2017) 39:101042831769755. doi: 10.1177/1010428317697550
8. Linard C, Marquette C, Mathieu J, Pennequin A, Clarençon D, Mathé D. Acute induction of inflammatory cytokine expression after gamma-irradiation in the rat: effect of an NF-kappaB inhibitor. *Int J Radiat Oncol Biol Phys*. (2004) 58:427–34. doi: 10.1016/j.ijrobp.2003.09.039
9. Curi MM, Cardoso CL, de Lima HG, Kowalski LP, Martins MD. Histopathologic and histomorphometric analysis of irradiation injury in bone and the surrounding soft tissues of the jaws. *J Oral Maxillofac Surg*. (2016) 74:190–9. doi: 10.1016/j.joms.2015.07.009
10. Delanian S, Lefaix JL. The radiation-induced fibroatrophic process: therapeutic perspective via the antioxidant pathway. *Radiother Oncol*. (2004) 73:119–131. doi: 10.1016/j.radonc.2004.08.021
11. Preciado S, Muntión S, Rico A, Pérez-Romasanta LA, Ramos TL, Ortega R, Borrajo J, et al. Mesenchymal stromal cell irradiation interferes with the adipogenic/osteogenic differentiation balance and improves their hematopoietic-supporting ability. *Biol Blood Marrow Transplant*. (2018) 24:443–51. doi: 10.1016/j.bbmt.2017.11.007
12. Herberg S, Kondrikova G, Hussein KA, Periyasamy-Thandavan S, Johnson MH, Elsalanty ME, et al. Total body irradiation is permissive for mesenchymal stem cell-mediated new bone formation following local transplantation. *Tissue Eng Part A*. (2014) 20:3212–27. doi: 10.1089/ten.tea.2013.0663
13. Higashi T, Fisher SJ, Brown RS, Nakada K, Walter GL, Wahl RL. Evaluation of the early effect of local irradiation on normal rodent bone marrow metabolism using FDG: preclinical PET studies. *J Nucl Med*. (2000) 41:2026–35.
14. Nicolay NH, Lopez Perez R, Saffrich R, Huber PE. Radio-resistant mesenchymal stem cells: mechanisms of resistance and potential implications for the clinic. *Oncotarget*. (2015) 6:19366–80. doi: 10.18632/oncotarget.4358
15. Musilli S, Nicolas N, El Ali Z, Orellana-Moreno P, Grand C, Tack K, et al. DNA damage induced by Strontium-90 exposure at low concentrations in mesenchymal stromal cells: the functional consequences. *Sci Rep*. (2017) 7:41580. doi: 10.1038/srep41580
16. Sun R, Zhu G, Wang J, Tong L, Zhai J. Indirect effects of X-irradiation on proliferation and osteogenic potential of bone marrow mesenchymal stem cells in a local irradiated rat model. *Mol Med Rep*. (2017) 15:3706–14. doi: 10.3892/mmr.2017.6464
17. Green DE, Adler BJ, Chan ME, Rubin CT. Devastation of adult stem cell pools by irradiation precedes collapse of trabecular bone quality and quantity. *J Bone Miner Res*. (2012) 27:749–59. doi: 10.1002/jbmr.1505
18. Ramchand SK, Seeman E. Advances and unmet needs in the therapeutics of bone fragility. *Front Endocrinol*. (2018) 9:505. doi: 10.3389/fendo.2018.00505
19. Krempien R, Huber PE, Harms W, Treiber M, Wannenmacher M, Krempien B. Combination of early bisphosphonate administration and irradiation leads to improved remineralization and restabilization of osteolytic bone metastases in an animal tumor model. *Cancer*. (2003) 98:1318–24. doi: 10.1002/cncr.11646
20. Arrington SA, Fisher ER, Willick GE, Mann KA, Allen MJ. Anabolic and antiresorptive drugs improve trabecular microarchitecture and reduce fracture risk following radiation therapy. *Calcif Tissue Int*. (2010) 87:263–72. doi: 10.1007/s00223-010-9390-z
21. Willey JS, Lloyd SAJ, Robbins ME, Bourland JD, Smith-Sielicki H, Bowman LC, et al. Early increase in osteoclast number in mice after whole-body irradiation with 2 Gy X rays. *Radiat Res*. (2008) 170:388–92. doi: 10.1667/RR1388.1
22. Schönmeyr BH, Wong AK, Soares M, Fernandez J, Clavin N, Mehrara BJ. Ionizing radiation of mesenchymal stem cells results in diminution of the precursor pool and limits potential for multilineage differentiation. *Plast Reconstr Surg*. (2008) 122:64–76. doi: 10.1097/PRS.0b013e31817743cd
23. Nicolay NH, Sommer E, Lopez R, Wirkner U, Trinh T, Sisombath S, et al. Mesenchymal stem cells retain their defining stem cell characteristics after exposure to ionizing radiation. *Int J Radiat Oncol*. (2013) 87:1171–8. doi: 10.1016/j.ijrobp.2013.09.003
24. Li J, Kwong DLW, Chan GCF. The effects of various irradiation doses on the growth and differentiation of marrow-derived human mesenchymal stromal cells. *Pediatr Transplant*. (2007) 11:379–87. doi: 10.1111/j.1399-3046.2006.00663.x
25. Hong EH, Lee SJ, Kim JS, Lee KH, Um HD, Kim JH, et al. Ionizing radiation induces cellular senescence of articular chondrocytes via negative regulation of SIRT1 by p38 kinase. *J Biol Chem*. (2010) 285:1283–95. doi: 10.1074/jbc.M109.058628

26. Mussano F, Lee KJ, Zuk P, Tran L, Cacalano NA, Jewett A, et al. Differential effect of ionizing radiation exposure on multipotent and differentiation-restricted bone marrow mesenchymal stem cells. *J Cell Biochem.* (2010) 111:322–32. doi: 10.1002/jcb.22699
27. Oliver L, Hue E, Séry Q, Lafargue A, Pecqueur C, Paris F, et al. Differentiation-related response to DNA breaks in human mesenchymal stem cells. *Stem Cells.* (2013) 31:800–7. doi: 10.1002/stem.1336
28. Marín A, Martín M, Liñán O, Alvarenga F, López M, Fernández L, et al. Bystander effects and radiotherapy. *Reports Pract Oncol Radiother.* (2015) 20:12. doi: 10.1016/j.rpor.2014.08.004
29. Kwon JW, Huh SJ, Yoon YC, Choi SH, Jung JY, Oh D, et al. Pelvic bone complications after radiation therapy of uterine cervical cancer: evaluation with MRI. *Am J Roentgenol.* (2008) 191:987–94. doi: 10.2214/AJR.07.3634
30. Marx RE. Osteoradionecrosis: a new concept of its pathophysiology. *J Oral Maxillofac Surg.* (1983) 41:283–8. doi: 10.1016/0278-2391(83)90294-X
31. Marx RE, Johnson RP. Studies in the radiobiology of osteoradionecrosis and their clinical significance. *Oral Surgery Oral Med Oral Pathol.* (1987) 64:379–90. doi: 10.1016/0030-4220(87)90136-8
32. Marx RE, Tursun R. Suppurative osteomyelitis, bisphosphonate induced osteonecrosis, osteoradionecrosis: a blinded histopathologic comparison and its implications for the mechanism of each disease. *Int J Oral Maxillofac Surg.* (2012) 41:283–9. doi: 10.1016/j.ijom.2011.12.016
33. Bolan PJ, Arentsen L, Sueblinvong T, Zhang Y, Moeller S, Carter JS, et al.Water-fat MRI for assessing changes in bone marrow composition due to radiation and chemotherapy in gynecologic cancer patients. *J Magn Reson Imaging.* (2013) 38:1578–84. doi: 10.1002/jmri.24071
34. Drake MT, Clarke BL, Khosla S. Bisphosphonates: mechanism of action and role in clinical practice. *Mayo Clin Proc.* (2008) 83:1032–45. doi: 10.4065/83.9.1032
35. Groenen KH, Pouw MH, Hannink G, Hosman AJ, van der Linden YM, Verdonschot N, et al. The effect of radiotherapy, and radiotherapy combined with bisphosphonates or RANK ligand inhibitors on bone quality in bone metastases. A systematic review. *Radiother Oncol.* (2016) 119:194–201. doi: 10.1016/j.radonc.2016.03.001
36. Arrington SA, Damron TA, Mann KA, Allen MJ. Concurrent administration of zoledronic acid and irradiation leads to improved bone density, biomechanical strength, and microarchitecture in a mouse model of tumor-induced osteolysis. *J Surg Oncol.* (2008) 97:284–90. doi: 10.1002/jso.20949
37. Atahan L, Yildiz F, Cengiz M, Kaplan B, Özkan M, Yazici G, et al. Zoledronic acid concurrent with either high- or reduced-dose palliative radiotherapyin the management of the breast cancer patients with bone metastases: a phase IV randomized clinical study. *Support Care Cancer.* (2010) 18:691–8. doi: 10.1007/s00520-009-0663-x
38. Rasmusson B, Vejborg I, Jensen AB, Andersson M, Banning AM, Hoffmann T, et al. Irradiation of bone metastases in breast cancer patients: a randomized study with 1 year follow-up. *Radiother Oncol.* (1995) 34:179–84. doi: 10.1016/0167-8140(95)01520-Q
39. Vassiliou V, Kalogeropoulou C, Christopoulos C, Solomou E, Leotsinides M, Kardamakis D. Combination ibandronate and radiotherapy for the treatment of bone metastases: clinical evaluation and radiologic assessment. *Int J Radiat Oncol Biol Phys.* (2007) 67:264–72. doi: 10.1016/j.ijrobp.2006.08.022
40. Ominsky MS, Brown DL, Van G, Cordover D, Pacheco E, Frazier E, et al. Differential temporal effects of sclerostin antibody and parathyroid hormone on cancellous and cortical bone and quantitative differences in effects on the osteoblast lineage in young intact rats. *Bone.* (2015) 81:380–91. doi: 10.1016/j.bone.2015.08.007
41. Costa S, Fairfield H, Reagan MR. Inverse correlation between trabecular bone volume and bone marrow adipose tissue in rats treated with osteoanabolic agents. *Bone.* (2019) 123:211–23. doi: 10.1016/j.bone.2019.03.038
42. Ominsky MS, Boyce RW, Li X, Ke HZ. Effects of sclerostin antibodies in animal models of osteoporosis. *Bone.* (2017) 96:63–75. doi: 10.1016/j.bone.2016.10.019
43. Spencer GJ. Wnt signalling in osteoblasts regulates expression of the receptor activator of NF B ligand and inhibits osteoclastogenesis *in vitro*. *J Cell Sci.* (2006) 119:1283–96. doi: 10.1242/jcs.02883
44. Sims NA, Vrahnas C. Regulation of cortical and trabecular bone mass by communication between osteoblasts, osteocytes and osteoclasts. *Arch Biochem Biophys.* (2014) 561:22–8. doi: 10.1016/j.abb.2014.5.015

Conflict of Interest Statement: The authors declare that the research was conducted in the absence of any commercial or financial relationships that could be construed as a potential conflict of interest.

frontiers in Endocrinology

ORIGINAL RESEARCH
published: 10 September 2019
doi: 10.3389/fendo.2019.00607

High Glucose Level Impairs Human Mature Bone Marrow Adipocyte Function Through Increased ROS Production

*Tareck Rharass and Stéphanie Lucas**

University of Littoral Côte d'Opale, University of Lille, CHU Lille, EA4490-PMOI-Physiopathologie des Maladies Osseuses Inflammatoires, Boulogne-sur-Mer, France

Bone marrow adipocytes (BMAds) accumulate in aging, menopause, and metabolic diseases such as Type 2 diabetes. These osteoporotic conditions are associated with oxidative stress and hyperglycemia which are both considered as critical factors underlying bone fragility. Glucose excess and reactive oxygen species (ROS) are known to favor adipogenesis over osteoblastogenesis. In this study, we investigated whether high glucose exposure could determine dysfunction of mature BMAds, specifically through ROS production. The effects of low (LG, 5 mM) or high glucose (HG, 25 mM) concentrations were examined using human bone mesenchymal stromal cells (hBMSCs) in the time course of differentiation, and, up to 21 days once adipocytes were mature. HG did not alter the adipocyte differentiation process of hBMSCs. Yet, after 21 days under HG exposure, *PPARG*, *CEBPA,* and adiponectin mRNA expressions were decreased. These alterations were also observed following adipogenic inducer withdrawal as well as in adipocytes fully differentiated in LG then cultured in HG for the last 11 days. Without inducers, HG condition also led to decreased leptin mRNA level. Importantly, intracellular and extracellular ROS concentrations measured using Amplex Red were significantly raised by 50% under HG exposure. This rise was observed once adipocytes ended differentiation and was reproduced within the different cell culture settings without any cytotoxicity. Among genes involved in ROS metabolism, the mRNA level of the H_2O_2 generating enzyme NOX4 was found upregulated in the presence of HG. Following cell separation, mature BMAds were shown to overproduce ROS and to display the gene alterations in contrast to non-lipid-laden cells. Finally, a non-lethal treatment with a pro-oxidant agent under LG condition reduces the mRNA levels of *PPARG*, adiponectin, and leptin as the HG condition does in the absence of inducers, and amplifies the effect of glucose excess on gene expression. HG concentration drives mature BMAds toward altered expression of the main adipokines and transcriptional factors. These perturbations are associated with a rise in ROS generation likely mediated through enhanced expression of *NOX4*. Mature BMAds are thus responsive to changes in glucose and ROS concentrations, which is relevant regarding with their phenotype and function in age- or metabolic disease-related osteoporosis.

Keywords: adipocyte, bone marrow, mesenchymal skeletal stem cells, glucose, hyperglycemia, reactive oxygen species, oxidative stress, osteoporosis

OPEN ACCESS

Edited by:
Basem M. Abdallah, University of Southern Denmark, Denmark

Reviewed by:
Maria Felicia Faienza, University of Bari Aldo Moro, Italy
Jan Josef Stepan, Charles University, Czechia

****Correspondence:***
Stéphanie Lucas
stephanie.lucas@univ-littoral.fr

Specialty section:
This article was submitted to Bone Research, a section of the journal Frontiers in Endocrinology

Received: *14 June 2019*
Accepted: *21 August 2019*
Published: *10 September 2019*

Citation:
Rharass T and Lucas S (2019) High Glucose Level Impairs Human Mature Bone Marrow Adipocyte Function Through Increased ROS Production. Front. Endocrinol. 10:607. doi: 10.3389/fendo.2019.00607

INTRODUCTION

Over these last decades, Bone Marrow Adipocytes (BMAds) have been revealed as a new component interfering with bone homeostasis and the hematopoiesis function. The fat fraction within the bone marrow is well-known to accrue and to negatively correlate with bone density in aging (1) and postmenopausal (2) subjects. Moreover, the bone marrow fat fraction can increase in Type 2 diabetic patients (3–5) and is found closely associated with a poor glycemic control (5–9) which broadens its involvement in the compromised bone quality reported in such metabolic pathologies. Several *in vitro* studies and first *ex vivo* characterization of BMAds have emphasized how these specific adipocytes diverge from typical extramedullary adipocytes and release various products—adipokines, growth factors, inflammatory mediators, fatty acids—which can affect the differentiation, function, or survival of the bone-forming osteoblasts and/or the bone-resorbing osteoclasts (10). Furthermore, many local and systemic factors reciprocally regulate the commitment and differentiation of the bone marrow mesenchymal stem cells also referred to as Bone Mesenchymal Stromal Cells (BMSCs) toward either osteoblastogenesis or adipogenesis (11). Beyond these established characterizations, factors that regulate BMAd functions are barely studied.

Chronic hyperglycemia defines diabetes while severe delayed blood glucose clearance takes hold in aging and menopause. Over time, high glucose levels damage bone through biochemical modifications of protein matrix with accumulation of advanced glycosylation end-products (AGEs) (12) and cellular dysregulations such as reduced BMSC proliferation (13, 14). Besides, osteoblastogenesis has been shown to be diverted toward adipogenesis in human BMSCs (13–15), rodent bone marrow stromal cells (16, 17), osteoblast precursor (18), and osteoblast-cell lines (19, 20) upon high glucose concentration exposure. In this context, a higher production of Reactive Oxygen Species (ROS) has been reported (18) in line with ROS involvement in suppressing osteogenic signaling pathways while triggering those of adipogenesis (21). Moreover, hyperglycemia condition also interferes with mature osteoblast biomineralization (22) and with functions of fully differentiated extramedullary adipocytes. Indeed, for the 3T3-L1 adipocytes, the prototypical cell line to model adipogenesis and white adipocyte functions, differentiation, and maturation in high glucose concentrations attenuate the insulin-stimulated signaling pathway (23), increase the expression of several inflammatory and chemotactic mediators (23, 24), and elevate levels of mitochondrial and endoplasmic reticulum stress (25). Importantly, a significant rise in intracellular ROS production is induced in the presence of high glucose concentrations both in 3T3-L1 adipocytes (23, 26) and mature adipocytes isolated from visceral fat pads (27) and has been associated with adipocyte dysregulations in metabolic diseases. Glucose excess and ROS generation are thus closely intertwined in both adipogenesis and adipocyte dysfunction.

Finely-tuned and moderate ROS levels are required as messengers of redox-sensitive signaling pathways during adipocyte differentiation as evidenced for extramedullary adipocytes [reviewed in (28)] and BMAds (18, 29–31). Yet, a persistent and high production of ROS leads to oxidative stress with molecule oxidation contributing to insulin-resistance and altered adipokine secretion in white adipocytes (32). The ROS rate results from the combination of various generating enzymes and scavenging defense systems which are differently expressed in the course of stem cell commitment, differentiation, and maturation of adipocytes. ROS sources mainly include the mitochondrial respiratory chain and the Nicotinamide Adenine Dinucleotide Phosphate (NADPH) oxidases (28, 32). ROS levels are enhanced in extramedullary adipose tissues in both fat-depot- and age-related fashions (33) and in metabolic disorders (34). Remarkably, oxidative stress in bone stimulates resorption (35) while represses formation (36) and is considered as one of the key processes in the loss of bone integrity in aging (37) and post-menopausal state (38). Yet ROS production in BMAds has only been studied in differentiating BMSCs within the first 12 days (21, 29–31, 39) and the contribution and sensitivity of mature (fully differentiated) BMAds to a high oxidative status has never been assessed.

As exemplified (29–31, 39), BMAds derived from human BMSCs or rodent bone marrow stromal cells are commonly studied in DMEM containing a high glucose concentration (i.e., 4.5 g/L or 25 mM glucose). In this study, we thus addressed whether such high glucose (HG) condition may affect the function and ROS generation of human BMSC-derived BMAds once they have reached their mature state. Indeed, the impact of glucose excess in comparison to the normoglycemic or low glucose concentration (i.e., 1 g/L or 5.5 mM glucose) was reappraised during the first 10 days of differentiation and followed up to 21 days of culture. Moreover, the influence of a pro-oxidant agent was analyzed to determine if ROS generation is involved in HG-induced BMAd deregulation. Using various cell culture set-ups, gene expression analyses and direct H_2O_2 measurements in intracellular and extracellular compartments, our results sustain that HG concentration leads to a ROS overproduction that perturbs notably adipokine synthesis.

Abbreviations: AmR, Amplex Red; ADIPOQ, Adiponectin; BMAds, Bone marrow adipocytes; CAT, Catalase; CEBPA, CCAAT/enhancer binding protein alpha; Dexa, Dexamethasone; DGAT2, Diacylglycerol O-acyltransferase 2; GLUT4, Glucose transporter type 4; GPX4, Glutathione peroxidase 4; H_2O_2, Hydrogen peroxide; HG, High glucose; hBMSCs, Human bone mesenchymal stromal cells; HRP, Horseradish peroxidase; IBMX, 3-isobutyl-1-methylxanthine; ind, Adipogenic inducers; Indo, Indomethacin; KRPG, Krebs-Ringer phosphate buffer; LEP, Leptin; LG, Low glucose; NAC, *N*-acetyl-*L*-cysteine; NOX4, NADPH oxidase 4; PPARG, Peroxisome proliferator activated receptor gamma; PLIN2, Perilipin 2; ROS, Reactive oxygen species; RPL13A, Ribosomal protein L13a; SOD2, Superoxide dismutase 2; TBHP, Tert-butyl hydroperoxide.

MATERIALS AND METHODS

Cell Culture and Adipocyte Differentiation

Pre-screened human bone marrow mesenchymal stem cells now referred to as Bone Mesenchymal Stromal Cells (hBMSCs) were classically proliferated in high glucose (25 mM) DMEM medium, 10% fetal bovine serum (FBS), 1% L-glutamine and 1% penicillin/streptomycin (all from PanBiotech), up to 80% cell confluence to proceed with subsequent passages or adipocyte

differentiation. All the experiments were performed between passages 7–9 for two donors (from Lonza; 19 year male, lot n°6F4393, and, 23 year female, lot n°423370).

hBMSC differentiation into BMAds was induced either in a low glucose (LG; 5 mM, to represent normal glycemia) or a high glucose (HG; 25 mM, to imitate severe diabetes) concentration. The two corresponding DMEM media (with FBS, L-glutamine, and penicillin/streptomycin) were supplemented with 1 μM insulin (PanBiotech), and other adipogenic inducers i.e., 0.5 μM dexamethasone (Dexa), 0.5 mM 3-isobutyl-1-methylxanthine (IBMX), and 50 μM indomethacin (Indo; all from Sigma). Adipogenic media were replaced every 3–4 days with fresh media up to 21 days of culture. Besides, in a third condition referred to as LG/HG, hBMSCs were differentiated in LG for the first 10 days (i.e., during the differentiation process) and in HG the following 11 days (i.e., once adipocytes are mature). Furthermore, to address the impact of adipogenic inducers [condition referred to as (+ind)], Dexa, IBMX and Indo were removed from media 2 days before the final analyzed time points (i.e., at day 12 or 19) and referred to as (–ind).

The cell differentiation and maturation were monitored using bright field microscopy up to 21 days; microscopic images were acquired and brightness/contrast adjustments were applied equally to every pixel in the images using Fiji/ImageJ (NIH).

BMAd Treatments With Pro- and Antioxidant Reagents

Stock solutions of 10 mM tert-butyl hydroperoxide (TBHP) and 400 mM *N*-acetyl-*L*-cysteine (NAC) (all from Sigma-Aldrich) were freshly prepared in sterile distilled water and PBS, respectively. Fully differentiated BMAds (at day 13 or 20) were treated for 1 day with either 10 to 200 μM TBHP (pro-oxidant) or with 1–10 mM NAC (antioxidant).

Separation of Non-lipid-laden and Lipid-Laden Cells

The procedure for separating lipid-laden and non-lipid-laden cell subpopulations was modified from Holt et al. (40). Differentiated cells were trypsinized on day 14 or 21 for a short duration (3–5 min) to allow detachment of non-lipid-laden cells only. The supernatant containing a majority of non-lipid-laden cells was collected and further processed with four centrifugation steps at room temperature (first, at 1,000 rpm for 5 min; second, at 2,000 rpm for 5 min; finally, two steps at 300 rpm for 10 min). At each step, the supernatant containing residual lipid-laden cells was carefully discarded, and the cell pellet corresponding to non-lipid-laden cells was resuspended in fresh media and vigorously mixed. Pelleted cells were either plated in the corresponding media for cell observation or used for subsequent analysis. After trypsin treatment, the remaining adherent cells, which mostly consist in lipid-laden cells i.e., BMAds, were washed twice with PBS and replenished with the corresponding media for 1 h before further processing.

The two cell subpopulations were lysed either in Extract-All (Eurobio) for mRNA expression analysis or lysis reagent (Life technologies) for ROS assays.

Quantitative Real-Time Polymerase Chain Reaction

Total RNAs were extracted using Extract-All following the manufacturer's instructions. Residual contaminating genomic DNA was digested by 2.5 unit/μl of DNase I recombinant (Roche). Reverse transcription was performed from 1 μg to 100 ng (for separated cell subpopulations) RNA using Maxima first strand cDNA synthesis kit (Thermo Scientific).

Real-time PCR analysis was carried out with FastStart Essential DNA Green SYBR master mix using the LightCycler Nano Instrument (Roche). Primers were designed with OLIGO Primer Analysis Software 6 (Molecular Biology Insights) and used when efficiency was >1.8 as for the following gene sequences: *ADIPOQ* (Fwd 5′-AGC TCT GCC CGG TCA-3′, Rev 5′-GAT CTT GGT AAA GCG AAT GG-3′), *CAT* (Fwd 5′-AAA CCG CAC GCT ATG GCT G-3′, Rev 5′-TGG AGA ACC GAA CTG CGA TG-3′); *CEBPA* (Fwd 5′-ACT GGG ACC CTC AGC CTT G-3′, Rev 5′-TGG ACT GAT CGT GCT TCG TG-3′); *DGAT2* (Fwd 5′-GCC TCT TCT CCT CCG ACA C-3′, Rev 5′-CCG AAC TTG GTC TTG TGC TT-3′); *GLUT4* (Fwd 5′-ATG CTG CTG CCT CCT ATG AA-3′, Rev 5′-CAG TTG GTT GAG CGT CCC-3′); *GPX4* (Fwd 5′-GCC TTC CCG TGT AAC CAG T-3′, Rev 5′-GCG AAC TCT TTG ATC TCT TCG T-3′) (41); *LEP* (Fwd 5′-ATT TCA CAC ACG CAG TCA GT-3′, Rev 5′-GAA GAA GAT CCC GGA GGT-3′); *NOX4* (Fwd 5′-AGG ATC ACA GAA GGT TCC AAG C-3′, Rev 5′-TCC TCA TCT CGG TAT CTT GCT G-3′) (42); *PLIN2* (Fwd 5′-CAG AAG CTA GAG CCG CAA AT-3′, Rev 5′-ACG CCA CTG CTC ACG AG-3′); *PPARG* (Fwd 5′-GCT TCT GGA TTT CAC TAT GG-3′, Rev 5′-AAA CCT GAT GGC ATT ATG AG-3′); *RPL13A* (Fwd 5′-GCG GAT GAA CAC CAA CCC TT-3′, Rev 5′-GCA GCA TAC CTC GCA CGG-3′); *SOD2* (Fwd 5′-ACC TGC CCT ACG ACT ACG G-3′, Rev 5′-GGT ACT TCT CCT CGG TGA CG-3′). Amplifications were performed as follows: 10 min at 95°C for polymerase activation; 40 repeats of three-step cycling (20 s denaturation at 95°C, 10 s annealing at 54–61°C, 10–36 s elongation at 72°C) for amplification. A melting curve analysis confirmed product specificity. The relative mRNA expression of tested genes was calculated according to Ct values and primer efficiencies (E), then normalized to the ones calculated for the ribosomal protein L13a (*RPL13A*) housekeeping gene according to $E_{gene}^{-Ctgene}/E_{ref}^{-Ctref}$. As mentioned, relative mRNA expression were appropriately expressed as fold level according to LG condition either at day 3 (d3) or d21 for each donor and data are presented as average values ± SEM.

Cell Viability Assay

Cytotoxicity was assessed using CyQuant cell proliferation assay kit according to the manufacturer's instructions (Life technologies). hBMSCs were seeded on Corning Costar 96 well plates (Sigma-Aldrich), then differentiated and treated as aforementioned. The DNA-bound fluorescence was measured using Xenius XMA fluorescence microplate reader (Safas) at ∼500 nm excitation and ∼530 nm emission maxima in each lysed sample. The parameter settings (photomultiplier voltage of ∼800–1,000 V; excitation duration of ∼0.5 s; shaking duration of

∼10 s prior measurement) were kept constant for all comparative set of experiments. Results were obtained from one single excitation in each sample well; yet, no photobleaching was detected after several repeated excitation steps on the same sample. A reference standard curve was created for converting sample fluorescence values into cell numbers. Each condition was assessed at least in triplicate. Data are presented as average values of cell amount ± SEM and expressed in % of cell viability compared to the initial cell number (i.e., at day 0).

Reactive Oxygen Species Assay

Amplex Red hydrogen peroxide/peroxidase assay kit (Life technologies) was used to measure intracellular and extracellular reactive oxygen species (ROS) (29, 43, 44) following a procedure previously reported (45, 46). Cells seeded in Corning Costar 96 well plates were rinsed twice with PBS, then lysed with 50 µl/well of microplate lysis reagent (Life technologies) diluted to 4X in Krebs-Ringer phosphate buffer (KRPG, containing 145 mM NaCl, 5.7 mM Na_3PO_4, 4.86 mM KCl, 0.54 mM $CaCl_2$, 1.22 mM $MgSO_4$), during 10 min at 37°C, and mixed vigorously. Then, each cell lysate was mixed with a KRPG solution containing Amplex Red (AmR) dye (final concentration: 50 µM; DMSO < 0.1%) and horseradish peroxidase (HRP) enzyme (final concentration: 0.1 unit/ml), to a final volume of 200 µl/well, mixed thoroughly and incubated at room temperature for 10 min, in the dark. As for extracellular ROS levels, a volume of 50 µl of cell media (i.e., conditioning media, CM) was collected from each well, from an initial volume of 200 µl/well. Each CM sample were placed in new 96 well plates and thoroughly mixed with AmR/HRP solution as previously mentioned, to a final volume of 100 µl/well. Sample fluorescence was measured using Safas Xenius XMA spectrofluorimeter at maxima excitation and emission wavelengths of 570 and 585 nm, respectively. The parameter settings (photomultiplier voltage between 600 and 1,000 V; excitation duration of ∼0.2 s; shaking duration of ∼5 s prior measurement) were kept constant for all comparative set of experiments. Results were averaged from four excitations in each sample well, and excitations were performed at equal distance (0.5 mm distance deviation from the first excitation) in each well; neither photobleaching nor photo-induction (47) were induced after three repeated excitation steps on the same sample following our experimental procedure. A hydrogen peroxide (H_2O_2) standard curve was generated for converting sample fluorescence values into H_2O_2 concentrations. A stock solution of 20 µM H_2O_2 was freshly prepared in KRPG from 3% H_2O_2 solution (Sigma-Aldrich) to produce H_2O_2 concentrations ranging from 0 to 2 µM. Solutions were loaded with AmR/HRP mix and fluorescence intensities were measured as abovementioned. Each condition was examined at least in triplicate (i.e., 3–4 wells/condition). Data were calculated as average values of ROS concentrations in function of the cell number in the wells ± SEM and expressed either in nM/cell or in fold change compared to control.

Statistical Analysis

Statistical analyses were performed using two-way Anova for kinetics or two-tailed unpaired Student's *t*-test with Prism 5 (GraphPad). $p < 0.05$ was considered significant. Data are presented as means ± standard error of the mean (i.e., SEM) from at least three independent experiments and two distinct donors.

RESULTS

HG Level Does Not Modify hBMSC Differentiation Into Adipocytes but Alters BMAds Once Mature

We investigated whether glucose levels affect adipogenesis and/or maintenance of the functions of BMAds by cultivating hBMSCs in pro-adipogenic media [i.e., (+ind) with insulin] up to 21 days in the presence of either low glucose (LG, 5 mM) or high glucose (HG, 25 mM) concentration. As shown by light microscopy (**Figure S1**), hBMSC phenotype changes along the differentiation: cells slowly accumulate lipids up to 7 days of differentiation, and mainly display typical BMAd phenotype (i.e., cells rich in lipid droplets) from 14 days. In fact, the differentiated population does not only contain typical BMAds, but also a significant part of cells exhibiting a fibroblast-like phenotype i.e., non-lipid-laden cells as referred in Holt et al. (40). Of note, no major difference regarding cell morphology and proportions in any subpopulation is observed between the two glucose levels (**Figure S1**).

Following the mesenchymal stem cell commitment, the early differentiation step of adipogenesis is dependent on the expression of the two main transcriptional factors PPARG (peroxisome proliferator activated receptor gamma) and CEBPA (CCAAT/enhancer binding protein alpha) and requires around 7 to 10 days of stimulation by adipogenic inducers (15, 39, 40). The terminal differentiation step encompasses acquisition of typical adipocyte genes such as lipogenic factors (e.g., the main glucose transporter *GLUT4,* the diacylglycerol O-acyltransferase 2 enzyme *DGAT2* involved in fatty acid esterification into triglycerides) and adipokines (48), which leads to mature functional cells with larger lipid accumulation (39, 40, 48). To address if adipocyte differentiation was enhanced in HG conditions as previously reported (13–15), mRNA expression was analyzed at different days for the two donors (**Figure 1A**). As expected, the expression level of *PPARG* and *CEBPA* are significantly induced from day 3 (d3) to d14 in adipogenic media. Markers of the terminal differentiation such as the adipokines *ADIPOQ* (adiponectin; **Figure 1A**) and *LEP* (leptin; **Figure S2A**), *GLUT4* (**Figure 1A**) and *DGAT2* (**Figure S2A**) are expressed from d7 and markedly upregulated at d14. Yet, in line with microscopic observation, no modification can be observed between the LG and HG conditions supporting that in our settings, adipocyte differentiation is not modified in the presence of 25 mM glucose [**Figure 1A** and **Figure S2A**, compare (+ind)]. Finally from d14 to d21, the mRNA expression of the different markers was analyzed in several independent replicates for the two donors and appeared overall stabilized in the LG condition: *PPARG*, *CEBPA* (**Figure 1B**), and *LEP* (**Figure S2A**) are unchanged, though *ADIPOQ, GLUT4,* and *DGAT2* are significantly modified by −25, +36, and +61%, respectively;

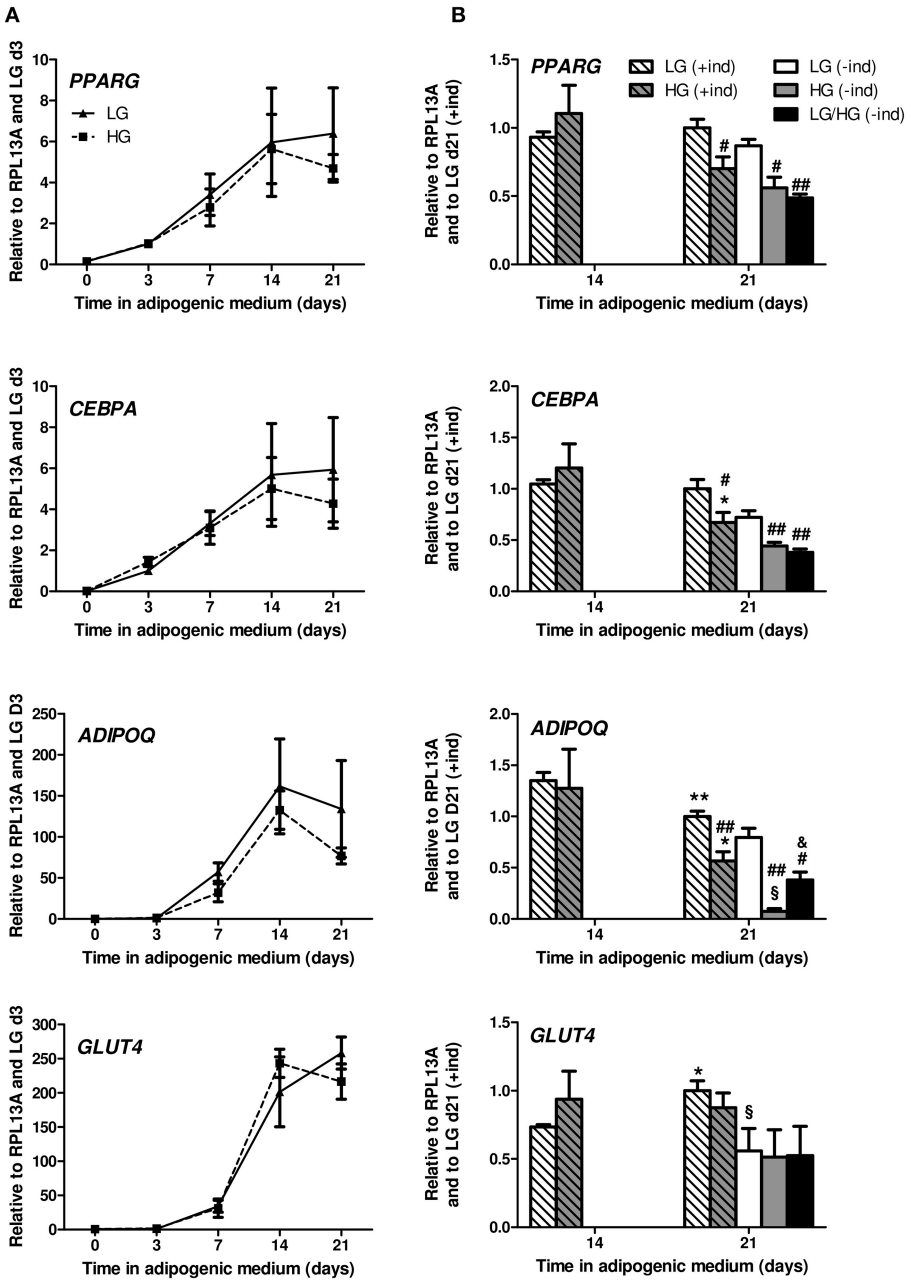

FIGURE 1 | HG level does not impact adipocyte differentiation potential of hBMSCs but alters mature BMAds. **(A)** Kinetics of the expression of *PPARG*, *CEBPA*, *ADIPOQ,* and *GLUT4* genes observed after 0, 3, 7, 14, and 21 days in adipogenic differentiation medium under LG or HG concentrations. Data were obtained from one kinetic experiment performed in two donors and are expressed as relative mRNA fold changes according to values obtained at day 3 for each donor; data are presented as mean ± SEM. Using two-way ANOVA tests, the effect of time within adipogenic medium was found significant for all genes with $p < 0.01$. **(B)** Comparison of the mRNA levels measured after 14 and 21 days in differentiation media in the presence (+ind) or after the removal of the inducers 2 days prior to measurements (–ind), under LG and HG concentrations for 21 days or under HG condition for the last 11 days (LG/HG). Data were obtained from three independent experiments at day 14 and from six to seven independent experiments at day 21 with the two donors. Data are expressed as relative mRNA fold changes according to values obtained at day 21 in LG condition. Data are shown as mean ± SEM. $^{*}p < 0.05$, $^{**}p < 0.01$ compared to values obtained at day 14 for each glucose concentration; $^{\#}p < 0.05$, $^{\#\#}p < 0.01$ compared to values obtained in the respective LG condition. $^{\S}p < 0.05$ compared to values obtained in the respective (+ind) condition. $^{\&}p < 0.05$ compared to values obtained in the respective HG condition (using unpaired *t*-tests).

however such variations are clearly inferior to that observed from d7 to d14. Altogether, these data infer that at d21, culture-derived BMAds can be considered as mature.

While adipocyte differentiation was unaltered, some genes were significantly down-regulated in BMAds cultured in HG by d21 [**Figure 1B**, compare (+ind)]. Indeed, compared to d14,

one supplementary week in HG leads to a decline in *PPARG* ($p = 0.06$), *CEBPA* and *ADIPOQ* mRNA levels. The expression level of these genes is also significantly decreased compared to LG at d21. As for *GLUT4*, *DGAT2,* and *LEP* (**Figure 1B** and **Figure S2B**) expression is not modified at d21 whatever the glucose concentration.

Adipogenic inducers (Dexa, Indo, IBMX) can be suspected to stimulate ROS production in adipocytes (49, 50). Consequently, we examined the impact of the removal of inducers (–ind) for the last 2 days [**Figure 1B**, see (+ind) vs. (–ind)]. The expression levels of *PPARG* and *CEBPA* tend to diminish; *ADIPOQ* mRNA level is affected in LG (−20%, $p = 0.06$) and more reduced in HG (−87%) upon inducer withdrawal. Such changes have already been observed in hBMSC-derived BMAds (40). Yet, the impact of glucose excess on the perturbed gene expression of *PPARG*, *CEBPA,* and *ADIPOQ* is preserved [**Figure 1B**, see LG (–ind) vs. HG (–ind)]. Of note, *LEP* mRNA (**Figure S2B**) is unchanged when inducers are removed in LG condition, but significantly decreased in HG condition.

One could argue that chronic exposure to HG level from the differentiation process has determined such alterations. We thus analyzed BMAds which were first differentiated in LG condition for 10 days, and, by then switched to the HG condition for the following 11 days [**Figure 1B**, see LG/HG (–ind) condition]. Strikingly, changes observed between LG and LG/HG conditions are similar to those reported above between LG and HG conditions, with reduced levels for *PPARG*, *CEBPA*, *ADIPOQ,* and *LEP*. The genes involved in lipogenesis such as *GLUT4* and *DGAT2* do not vary according to glucose concentration.

Our settings thus indicate that, upon a condition mimicking hyperglycemia, hBMSC-derived adipocytes functions are rapidly dysregulated with perturbed adipogenic transcriptional factors and adipokine levels.

HG Level Enhances ROS Production Both Intracellularly and Extracellularly in BMAds Once Mature

Next, we addressed whether reactive oxygen species (ROS) metabolism is altered and involved in the impairment of BMAd functions by HG. Intracellular ROS levels were measured during the differentiation process (from d0 to d14) and the maturation phase (i.e., at d21) in hBMSC-derived BMAds using the Amplex Red (AmR) method (45–47). Intracellular ROS production doubles along the different time points up to d14 in adipogenic LG medium and accelerates while reaching the maturation step between d14 and d21 (**Figure 2A**). Importantly, ROS levels are similar whatever the glucose concentration up to d7 of differentiation, while they markedly rise in the presence of HG concentration from d14 (3-fold increase vs. HG d7) to d21. Consequently, and as also shown in **Figure 2B**, HG exposure raises up to 46% the ROS rate compared to LG at both days 14 and 21. To verify whether adipogenic inducers contribute in regulating ROS metabolism as suspected (49, 50), ROS levels were also measured at d14 and d21 after the removal of the inducers 2 days prior to measurements (**Figure 2B**). Interestingly, withdrawing inducers (–ind) did not affect the ROS production since levels remained comparable to those obtained following permanent inducer stimulation (+ind), under either LG or HG conditions. To emphasize that BMAds are able to produce more ROS in the presence of HG concentration once mature, we compared intracellular ROS levels in cells fully cultured in LG or HG conditions for 21 days with cells exposed to LG condition the first 10 days followed by 11 days under HG, i.e., LG/HG condition. BMAds derived from the LG/HG condition display a 52% higher ROS production than those under LG, and at a similar rate than BMAds generated in HG condition (**Figure 2C**).

Additionally, as adipocytes also produce extracellular ROS (51), we measured ROS levels 21 days after the induction of differentiation within conditioned media (**Figure 2D**). BMAds are found to profusely produce extracellular ROS as their levels exceed by 1.5- to 3-fold the intracellular ones for both glucose conditions (**Figure 2B** vs. **Figure 2D**). Yet, results recapitulate the aforementioned changes in intracellular ROS metabolism. First, BMAds exposed to HG condition release higher ROS levels (by ∼55%) than cells under LG, which is in line with the stronger level of intracellular ROS metabolism found under the higher glucose concentration. Next, removing the inducers 2 days prior to measurements (–ind) do not influence on the extracellular ROS levels which remain similar to the ones measured under continuous stimulation by inducers (+ind). Finally, elevated extracellular ROS levels observed under HG do not result from any perturbations of the differentiation process since comparable results are found for BMAds under LG/HG condition (**Figure 2D**).

One could argue that the aforementioned changes in ROS levels may result from variations in cell amounts in response to ROS-mediated oxidative stress and underlying cell damages. We therefore measured the cell amounts by means of a fluorimetric assay based on cellular DNA content. We found that cell amounts are unmodified along the cell differentiation upon the different glucose conditions (**Figure S3**) confirming that ROS changes are independent from any alteration of cell viability. Additionally, since it has been reported that the use of fluorescent ROS sensors can have several pitfalls (45–47), we verified the specificity of the AmR probe for both intracellular and extracellular ROS levels as well as its sensitivity for ROS detection by spectrofluorimetry (**Figure S4**). Results show that the AmR method is reliable for detecting intracellular H_2O_2 following cell lysis (**Figure S4A**) and for measuring extracellularly released H_2O_2 levels without any reaction from medium compounds (**Figure S4B)** or photo-induction of the probe (**Figure S4C**). Taken together, these data substantiate that changes in ROS levels found in **Figure 2** do not result from any artifact but rather depend on glucose conditions.

Glucose Modulates ROS Metabolism of Mature BMAds in a NOX4-Dependent Manner

We then aimed to identify which intracellular enzymatic system mediates the rise in ROS metabolism under HG condition. Among multiple enzymatic systems, mitochondria are well-known for being the main source for intracellular ROS

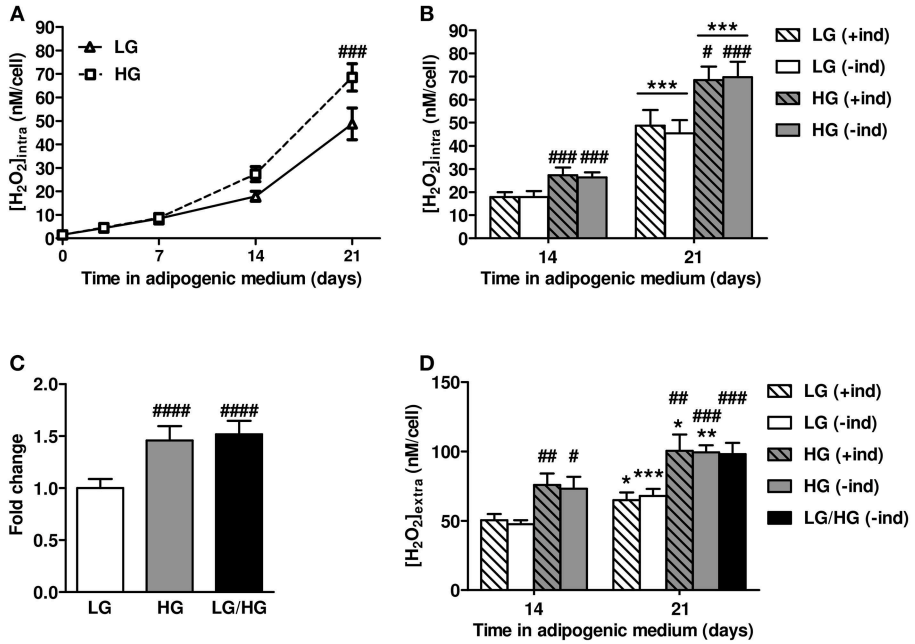

FIGURE 2 | HG level stimulates intracellular and extracellular ROS production by mature BMAds. **(A)** Kinetics of intracellular reactive oxygen species (ROS) levels examined up to 21 days of BMAd differentiation and maturation under LG or HG concentrations in presence of adipogenic inducers (+ind). Data were obtained from six to nine independents measurements (at least three technical replicates for the two donors) and are expressed as intracellular H_2O_2 concentration in nM per cell, mean ± SEM. Using two-way ANOVA tests, the effect of time within adipogenic medium was found significant for both glucose concentrations with $p < 0.0001$; the effect of HG was found significant with $p = 0.013$ and Bonferroni post-test $^{\#\#\#}p < 0.001$. **(B)** Comparison of intracellular ROS levels measured at days 14 and 21, under LG or HG conditions, and under continuous stimulation by inducers (+ind) or after their removal 2 days prior to measurements (–ind). Data were obtained from six to nine independents measurements and are expressed as abovementioned with mean ± SEM. $^{***}p < 0.001$ compared to values obtained at day 14 for the respective medium composition; $^{\#}p < 0.05$, $^{\#\#\#}p < 0.001$ compared to values obtained in the respective LG condition (using unpaired *t*-tests). **(C)** Intracellular ROS levels measured after 21 days in LG or HG concentrations or after 11 days in HG (LG/HG) following adipogenic inducer removal 2 days prior measurements (–ind). Data were obtained from eight to fourteen independents measurements, expressed as fold change compared to the LG condition, and are mean ± SEM. $^{\#\#\#\#}p < 0.0001$ compared to LG condition (using unpaired *t*-tests). (**D**) Extracellular ROS levels assessed at days 14 and 21 in adipogenic medium, under LG, HG, or LG/HG conditions, with continuous stimulation by inducers (+ind) or after their removal 2 days before measurements (–ind). Data were obtained from four independents measurements from the two donors and are expressed as extracellular H_2O_2 concentration in nM per cell, mean ± SEM. $^{*}p < 0.05$, $^{**}p < 0.01$, $^{***}p < 0.001$ compared to values obtained at day 14 for the respective medium composition; $^{\#}p < 0.05$, $^{\#\#}p < 0.01$, $^{\#\#\#}$p < 0.001 compared to values obtained in the respective LG condition (using unpaired *t*-tests).

production. We thus evaluated the mRNA expression levels of *SOD2* (superoxide dismutase 2), a mitochondrial enzyme converting the superoxide anion into H_2O_2 and whose activity is tightly associated with the function of the mitochondrial electron transport chain that leaks the superoxide anion (52). As for the antioxidant defense system, we focused on the expression of *CAT* (catalase) and *GPX4* (glutathione peroxidase 4) which both scavenge excessive amounts of H_2O_2 and have already been found to be well-expressed in hBMSC-derived adipocytes (39) and BMAds from aging mice (53), respectively.

Regardless of the glucose level, *SOD2* and *CAT* mRNA levels rapidly increase during adipocyte differentiation (**Figure 3A**) as already reported (39). The expression level of *GPX4* is stable during the first week of differentiation and slightly progresses from d7 to d14. In LG condition, all genes reach their maximal expression by d14 (**Figure 3B**). Yet HG exposure for 21 days leads to a decrease in *GPX4* and *CAT* ($p = 0.06$) levels compared to LG condition, with no change for *SOD2* (**Figure 3B**). The removal of inducers does not disrupt the expression of these genes for BMAds in LG or HG medium [**Figure 3B**, see (+ind) vs. (–ind)]. Nevertheless, the absence of inducers reveals better the impact of HG concentration on the expression of *CAT*, *GPX4,* and *SOD2* which are down-regulated compared to LG condition. Surprisingly, a 11 day exposure to HG concentration (LG/HG condition) does not totally reproduce the impact of cell exposure in the high glucose concentration from the differentiation process: indeed, *SOD2* and *GPX4* levels are unchanged compared to LG and increased compared to HG condition. Of note, the expression of *CAT* mRNA remains significantly diminished in LG/HG compared to LG (**Figure 3B**). Altogether, these data do not support any primary involvement of these systems in the rise of ROS generation under HG exposure (either HG or LG/HG) as observed (**Figures 2B,D**): discrepancies are obvious between the gene expression pattern of the H_2O_2 generating enzyme *SOD2* and ROS amounts in our different conditions. As for the *CAT* and *GPX4* gene expression, the HG-induced decrease could be suspected to contribute to ROS accumulation after 21 days but not from 14 days as observed (**Figure 2B**).

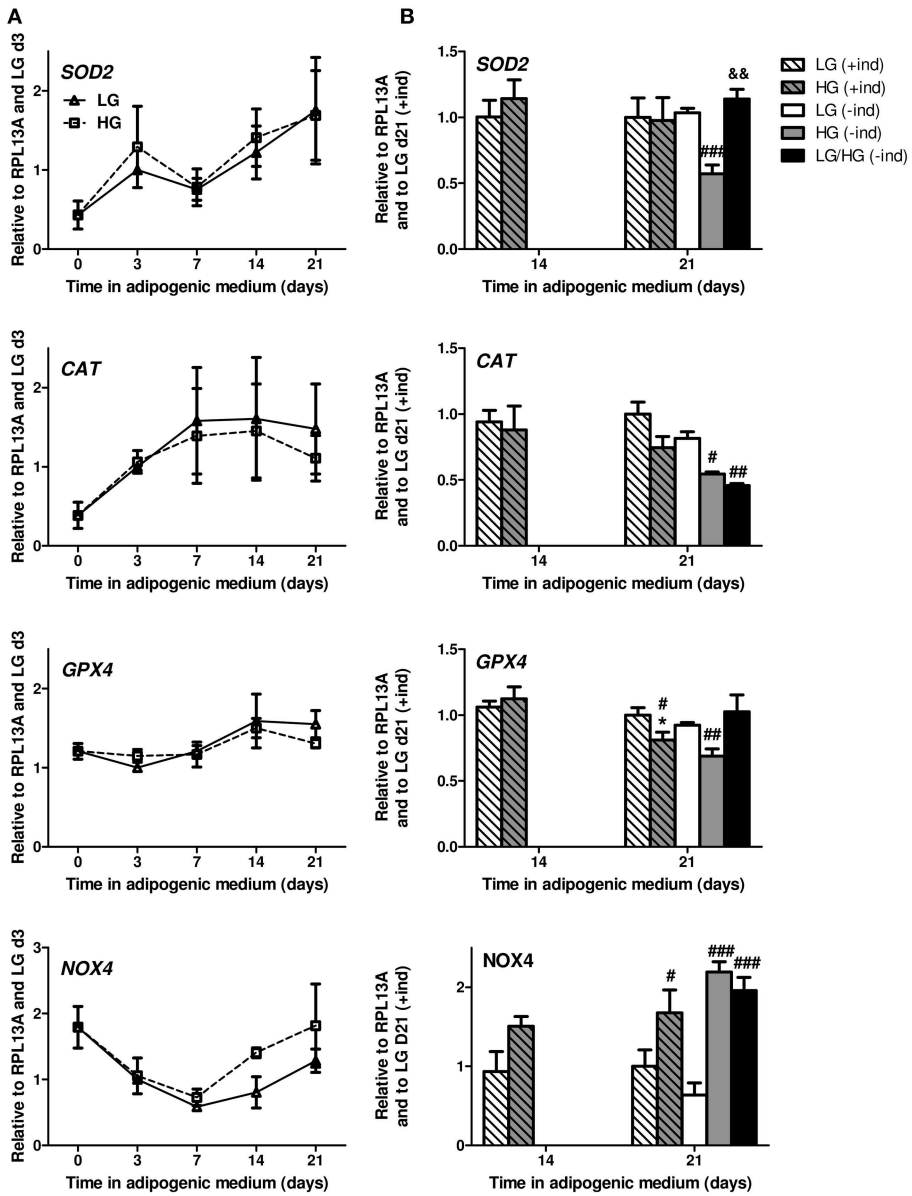

FIGURE 3 | ROS are mainly produced in a NOX4-dependent manner in mature BMAds. **(A)** Kinetics of *SOD2*, *CAT*, *GPX4,* and *NOX4* mRNA levels observed after 0, 3, 7, 14, and 21 days in adipogenic differentiation medium under LG or HG concentrations. Data were obtained from one kinetic experiment performed in two donors and are expressed as relative mRNA fold changes according to values obtained at day 3 for each donor; data are presented as mean ± SEM. Using two-way ANOVA tests, the effect of time within adipogenic medium was found significant for all genes with $p < 0.02$. **(B)** Comparison of the mRNA levels measured after 14 and 21 days in differentiation media in the presence (+ind) or after the removal of the inducers 2 days prior to measurements (–ind), under LG and HG concentrations for 21 days or under HG condition for the last 10 days (LG/HG). Data were obtained from three independent experiments at day 14 and from six to seven independent experiments at day 21 with the two donors. Data are expressed as relative mRNA fold changes according to values obtained at day 21 in LG condition. Data are shown as mean ± SEM. $^{*}p < 0.05$, compared to values obtained at day 14 for each glucose concentration; $^{\#}p < 0.05$, $^{\#\#}p < 0.01$, $^{\#\#\#}p < 0.001$ compared to values obtained in the respective LG condition. $^{\&\&}p < 0.01$ compared to values obtained in the respective HG condition (using unpaired *t*-tests).

Consequently, we investigated whether HG-mediated ROS metabolism involves NADPH oxidases (NOX). These membrane-bound enzyme complexes lead to both intracellular and extracellular ROS (i.e., H_2O_2) production (51, 54). NOX4 is reported to be the major isoform in extramedullary adipocytes and to be critically regulated during both the differentiation process (21, 51) and the exposure to nutrients excess (55) of 3T3-L1 adipocytes. *NOX4* mRNA expression drastically decreases during the early differentiation stage (up to d7, −67% compared to d0) in a comparable manner between LG and HG

levels (**Figure 3A**), which reproduces previous results for the differentiating 3T3-L1 cell line (51). Since ROS levels increase during such time period (**Figure 2A**), it is therefore unlikely that NOX4 constitutes the main source for ROS production during the differentiation process. Interestingly, from d7 to d21, *NOX4* mRNA levels increase with LG and HG exposure, respectively, leading to 72 to 100% of the expression level at d0 (**Figure 3A**). Indeed, compared to LG, *NOX4* mRNA level is up-regulated in the HG condition by 61% ($p = 0.11$) and 68% at d14 and d21, respectively (**Figure 3B**). Besides, the absence of inducers does not significantly affect *NOX4* expression; yet, the impact of glucose concentration is more emphasized with a ∼3-fold increase of *NOX4* levels in HG and LG/HG conditions compared to the LG one [**Figure 3B**, see (+ind) vs. (–ind)]. From d14 to d21 and in the different culture conditions, ROS generation and *NOX4* expression evolve according to a comparable pattern, which supports the central involvement of the enzyme in the glucose-induced ROS production of mature BMAds.

Glucose-Induced Stimulation of ROS Metabolism Is Restricted to Mature Lipid-Laden BMAds

As shown in **Figure 3A** and in previous works (21), NOX4 is highly expressed in adipocyte precursors. Yet, as commonly observed, the hBMSC-derived fully differentiated cell population displays both lipid-laden (i.e., mature BMAds) and non-lipid-laden cells which are barely studied (**Figure S1**). To characterize how each subpopulation contributes to the ROS production, we thus performed an isolation procedure to get enriched fractions in lipid-laden and non-lipid-laden cells after 21 days in LG or HG adipogenic media. As shown in **Figures 4A,B**, each cell fraction is remarkably enriched in each specific cell type. Gene expression analysis demonstrates that the lipid-laden cells considerably express higher *PPARG* (>6-fold), *CEBPA* [(>19-fold), not shown] and *ADIPOQ* (>21-fold) mRNA levels than non-lipid-laden cells (**Figure 4C**). Besides HG exposure results in decreased expression levels of *PPARG* ($p = 0.15$), *CEBPA* ($p = 0.07$), and *ADIPOQ* ($p = 0.06$) in the lipid-laden subpopulation, as shown for the whole cell populations in **Figure 1B**. Of note non-lipid-laden cells express *PLIN2* (perilipin2) which encodes for proteins recovering nascent lipid droplets during adipocyte differentiation (56). Yet, *PLIN2* mRNA level remains 2.6-fold lower expressed in non-lipid-laden cells than in lipid-laden cells. *PLIN1* (perilipin 1), the most specific and abundant protein covering mature triglyceride droplets in adipocytes (56), is drastically reduced by 50-fold in the non-lipid-laden subpopulation compared to the lipid-laden one (data not shown). Interestingly, *GLUT4* mRNA expression was found similarly expressed in the two cell subpopulations. These data thus confirm the cell separation efficiency and suggest that non-lipid-laden cells can be considered as immature cells committed in the adipocyte lineage that, yet, already rely on glucose metabolism.

We then quantified intracellular ROS concentrations in each subpopulation (**Figure 4D**). Regardless of glucose level, lipid-laden cells produce much higher ROS levels that non-lipid-laden cells, confirming that BMAds constitute the main cell source for ROS production in our model. Interestingly, changes in glucose levels did not affect the ROS levels in non-lipid-laden cells. In contrast, HG condition enhances ROS generation in the fully functional lipid-laden cells by about 50% compared with LG, both at d14 and d21, as found for the whole cell populations (**Figure 2B**). These findings support that the up-regulation of ROS metabolism by increased glucose level is connected to a molecular machinery which takes place only once cells were fully differentiated.

Expressions of genes controlling the ROS rate were also studied within each cell fraction (**Figure 4E**). The H_2O_2 generating enzyme *SOD2* is found 3-fold better expressed in BMAds than in non-lipid-laden cells and is down-regulated by 23% upon HG exposure, in a similar way to the whole cell population (**Figure 3B**). Importantly, BMAd subpopulation displays the highest levels of the other H_2O_2 generating enzyme *NOX4* which, furthermore, is up-regulated by 65% in the presence of HG concentration (**Figure 4E**), confirming that the increased expression induced by HG exposure is due to mature BMAds within the whole cell population. Regarding the antioxidant enzymes, *CAT* and *GPX4* mRNA levels are ∼2-fold less abundant within non-lipid-laden cells compared to BMAds, yet without any significant impact of the glucose concentration. Altogether, our data support that the glucose-induced enhancement of ROS generation is restricted to mature BMAds and most likely relies on the activity of NOX4.

Impairment of BMAd Function Under HG Level Is Mediated Through Enhanced ROS Metabolism

Next, we investigated whether the ROS excess produced during the HG concentration exposure could mediate the variations in the expression of the key adipogenic transcriptional factors and adipokines of BMAds observed at d21. We first assessed the responsiveness of the cells to treatments that artificially modulate intracellular ROS levels. BMAds were treated with different doses of pro- or antioxidant reagents, i.e., TBHP or NAC, respectively, for 1 day in the absence of inducers, under either LG of HG concentrations, prior to measurements of ROS levels, and cell viability (**Figure 5**). At both d14 and d21, exposing BMAds in LG to 50 μM TBHP increases the ROS levels to the ones observed for cells under HG alone, while 5 mM NAC in HG decreases the ROS rate to that of LG alone (**Figure 5A**). Besides, more ROS amount can be accumulated in BMAds treated with 50 μM TBHP and without any change in cell viability (**Figure 5B**). In contrast, the highest dose of TBHP (200 μM) triggers oxidative stress since the further rise in ROS levels is associated with a 60% loss of cells. Using NAC at either 5 or 10 mM lowers at a rather similar degree the intracellular ROS concentration at d21. Yet treatment with the highest NAC concentration results in cytotoxicity. Furthermore, in contrast to TBHP treatment, one has to point out that analyses of gene expression following NAC treatment do not appear advisable since either 5 or 10 mM of the reagent lead to a marked remodeling of lipid droplets (not shown) as already reported for adipocytes differentiated from

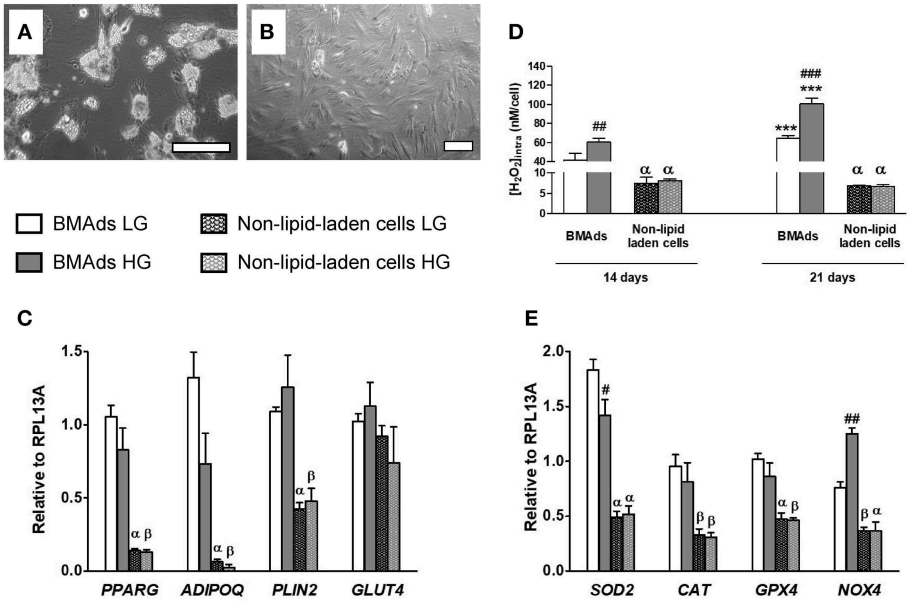

FIGURE 4 | HG level stimulates ROS production specifically in the lipid-laden BMAds subpopulation. **(A,B)** Microscopic images showing the two different cell populations which were separated as described in Materials and Methods. Adherent cells remaining after trypsin treatment are mostly lipid-laden BMAds as shown in **(A)** after 1 h of recovery in the corresponding adipogenic medium. The detached cell subpopulation was also seeded in the corresponding adipogenic medium to assess cell purity; as shown in **(B)**, most cells are non-lipid-laden cells. Scale, 50 μm. **(C)** The mRNA expression level of adipocyte genes (*PPARG*, *ADIPOQ*, *PLIN2*, *GLUT4*) were measured in the lipid-laden BMAd-enriched subpopulation and in the non-lipid-laden cell-enriched subpopulation to prove cell separation efficiency. Gene expression analysis was performed after 21 days in LG or HG conditions; inducers were removed 2 days before cell separation. Results are Mean ± SEM from four independent experiments (two technical replicates with the two donors). **(D)** Intracellular ROS levels were measured in both cell subpopulations following their separation. Measurements were performed after 14 or 21 days in LG or HG conditions and after removal of the inducers for the last 2 days. Intracellular H_2O_2 concentration data (expressed in nM per cell) are Mean ± SEM from three independent experiments (technical replicates with the two donors). **(E)** The mRNA expression level of several genes involved in ROS metabolism (*SOD2*, *CAT*, *GPX4,* and *NOX4*) were measured in the lipid-laden BMAd-enriched subpopulation and in the non-lipid-laden cell-enriched subpopulation to analyse their respective contribution. Results are Mean ± SEM from four independent experiments [as described in **(C)**]. $^{***}p < 0.001$ vs. lipid-laden BMAds after 14 days in adipogenic medium at the corresponding glucose concentration; $^{\beta}p < 0.05$, $^{\alpha}p < 0.001$ vs. lipid-laden BMAds at the corresponding glucose concentration and time analysis; $^{\#\#}p < 0.01$, $^{\#\#\#}p < 0.001$ between the two glucose concentrations (using unpaired *t*-tests).

a bone marrow stromal cell line (57), suggesting side effects in addition to the antioxidant activities. Overall, these data indicate that mature BMAds are well-responsive to any modulation of the redox state and handle higher ROS levels whatever the glucose concentration.

We therefore examined gene expression in mature BMAds under LG or HG conditions in the presence of a non-lethal dose of the pro-oxidant TBHP (50 μM; **Figure 5C**). Interestingly, TBHP treatment in LG condition results in similar decreases of *PPARG* and *ADIPOQ* mRNA levels than those observed in the HG condition alone. While *LEP* mRNA level tends to be lower in HG condition compared to the LG one, its expression is remarkably reduced in the LG TBHP condition compared to LG alone. Indeed, the transcriptional regulation of *ADIPOQ* and *LEP* genes display a high sensitivity to an increase in ROS amounts since both mRNA levels are further decreased in HG TBHP condition compared to HG alone (−40%, $p = 0.06$ and −60%, respectively). Of note, *CEBPA* expression levels tend to be reduced in HG condition ($p = 0.09$) but are unmodified in the presence of TBHP whatever the glucose concentrations, which suggests that the HG-mediated down-regulation in *CEBPA* mRNA level most likely relies on ROS-independent mechanisms. Altogether, the TBHP-induced increase in ROS levels mimics the down-regulation in the gene expression of *PPARG* and *ADIPOQ* observed in the HG condition (**Figure 1B**) and exacerbates the reported effect of HG on *LEP* expression (**Figure S2**), sustaining that HG-induced mature BMAd dysfunction is mediated by augmented intracellular ROS formation.

DISCUSSION

The involvement of various signaling pathways and mediators such as ROS has been substantially investigated in the BMAd differentiation process (11, 21). Yet, factors which regulate mature BMAd function are still poorly characterized while these specific adipocytes are considered as active cells interacting within the bone and bone marrow microenvironment (10, 11). Our study reports for the first time that mature BMAds exposed to a HG concentration display several alterations in the expression of the main adipokines and transcriptional factors involved in the maintenance of adipocyte function. These perturbations are associated with a rise in ROS generation likely mediated through the enhanced expression of *NOX4*.

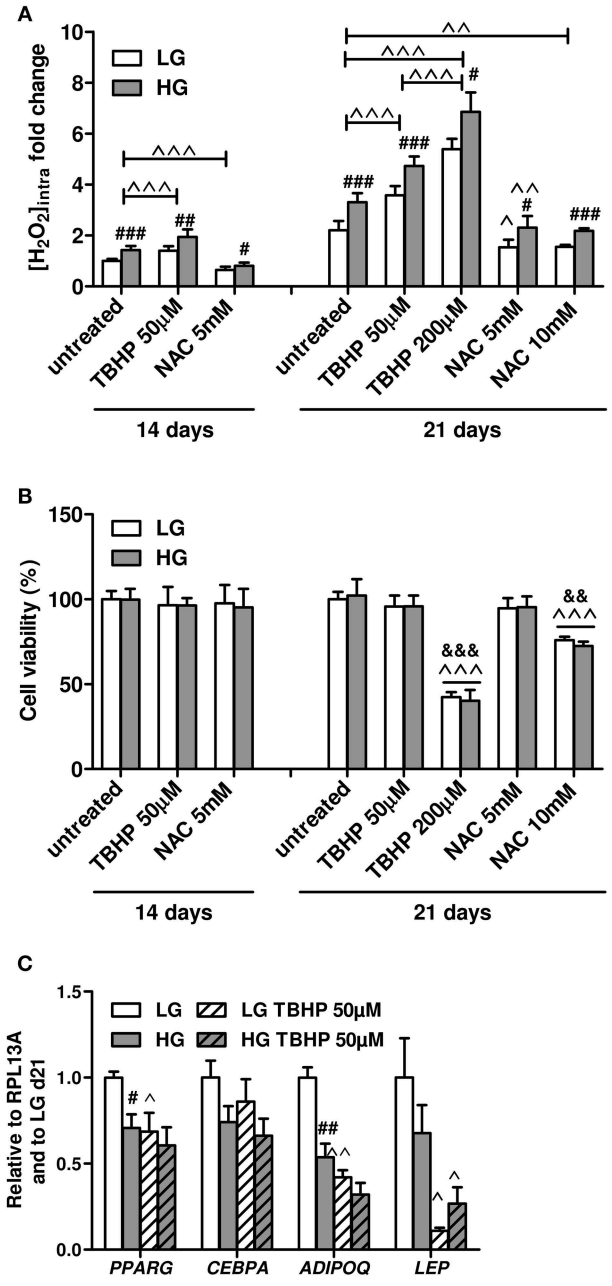

FIGURE 5 | Low doses of TBHP enhance ROS production in mature BMAds in a non-lethal manner and impair the gene expression of typical adipocyte genes. **(A)** Effects of 1 day treatment of mature BMAds after 14 or 21 days in LG or HG conditions with TBHP (50 and 200 µM) or NAC (5 or 10 mM) on intracellular ROS levels. Inducers have been removed from cell culture media 2 days prior to measurements. Data were obtained from six to ten independent experiments (at least three technical replicates with the two donors) and expressed as relative fold changes of measured H_2O_2 concentration according to values obtained at d14 in LG condition. Data are shown as mean ± SEM. Significant elevations of ROS levels between d14 and d21 were found but are not indicated. $^{\#\#\#}p < 0.001$, $^{\#\#}p < 0.01$, $^{\#}p < 0.05$ between the two glucose concentrations for the respective treatment. $^{\wedge\wedge\wedge}p < 0.001$, $^{\wedge\wedge}p < 0.01$, $^{\wedge}p < 0.05$ compared to untreated conditions for the respective glucose concentration (using unpaired *t*-tests). **(B)** Cell viability measured at

(Continued)

FIGURE 5 | d14 and d21 in untreated BMAds and following treatments with different doses of TBHP or NAC, under LG or HG conditions after removal of the inducers. Data were obtained from four independent experiments (two technical replicates with the two donors) and are presented as percentage of cell viability ± SEM compared to the cell amount at d0. $^{\wedge\wedge\wedge}p < 0.001$ compared to untreated conditions for the respective glucose concentration; $^{\&\&\&}p < 0.001$, $^{\&\&}p < 0.01$ compared to the lowest dose for the respective pharmacological agent (using unpaired *t*-tests). **(C)** Effects of a 1 day treatment with TBHP (50 µM) of mature BMAds at d21, in LG or HG conditions, on the expression levels of *PPARG*, *CEBPA*, *ADIPOQ,* and *LEP.* Inducers have been removed 2 days prior to measurements. Data were obtained from three to six independent experiments including the two donors. Data are expressed as relative mRNA fold changes according to values obtained at d21 in LG condition, and are mean ± SEM. $^{\#}p < 0.05$, $^{\#\#}p < 0.01$ compared to values obtained in the respective LG condition; $^{\wedge\wedge}p < 0.01$, $^{\wedge}p < 0.05$ compared to untreated conditions for the respective glucose concentration (using unpaired *t*-tests).

Actually, a non-lethal treatment with a pro-oxidant agent under LG condition reduces the mRNA levels of *PPARG* and *ADIPOQ* as the HG condition does, and amplifies the effect of glucose excess on *LEP* expression. Using various cell culture set-ups, several findings sustain that HG can regulate mature BMAd function. Firstly, examinations of gene expression, cell amount and ROS metabolism in the time course of adipocyte differentiation did not reveal any impact of glucose concentration. Secondly, any potential conditioning from the differentiation step has been analyzed and then discarded by using BMAds once fully differentiated under LG concentration. Indeed, an 11 day exposure to HG of these BMAds (LG/HG condition) recapitulates the modifications observed when cells were cultivated from differentiation in HG medium. Besides, removing adipogenic inducers once cells are differentiated does not suppress the ROS production and the gene expression profile induced by glucose. Finally, mature BMAds isolated from non-lipid-laden cells were found being the main cell source responsible of ROS production as well as being modulated by glucose with regard to gene expression alterations and ROS metabolism.

Mature BMAds are thus responsive to changes in glucose and ROS concentrations which is highly relevant regarding their phenotype and functionality in age- or metabolic disease-related bone disorders. Compared to extramedullary adipocytes, mature BMAds are characterized by low expression levels of *Pparg*, *Adipoq,* and *Lep* which are further reduced with the aging of mice (53). BMAds from Type 2 diabetic patients display a marked decrease in ADIPOQ expression and secretion with unchanged *PPARG* expression, and higher LEP mRNA and protein levels compared to BMAds from non-diabetic patients (4). Here we demonstrated that either HG-triggered ROS generation or artificially-induced ROS excess can alter *PPARG* and *ADIPOQ* expression without inducing any cytotoxicity. Interestingly, *PPARG* and *ADIPOQ* mRNA expressions have been shown to be suppressed by H_2O_2 in a dose-dependent manner in 3T3-L1 adipocytes (34). PPARG expression level and activity in mature extramedullary adipocytes is considered crucial to maintain adiponectin and other lipogenic enzymes expression level (58) and to repress inflammation (59) resulting

in insulin-sensibility preservation (58). In our study, TBHP treatment in LG concentration reproduced the diminished expression levels of *PPARG* and *ADIPOQ* observed in HG condition (**Figure 5C**), supporting that the glucose-induced elevation in ROS production contributes to the regulation of their expression. Besides, in contrast to *PPARG*, *ADIPOQ* expression—whose mRNA level is further reduced in the presence of the pro-oxidant agent in HG condition—appears highly sensitive to the ROS rate in mature BMAds. This is a reminiscent feature of white adipocytes as reported through previous relationships between oxidative stress and ADIPOQ level in the 3T3-L1 model, in the visceral fat pads of mouse models and in human plasmas (34). Regarding the regulation of *LEP* expression in BMAds, several factors are likely involved. The impact of HG concentration and ROS metabolism is only revealed once inducers are removed from media (**Figure S2** and **Figure 5C**). Actually, Dexa—one of the adipogenic inducers—has already been shown to stimulate the expression and release of LEP in hBMSC-derived adipocytes (60) and human primary cultivated BMAds (61). It is thus likely that, in our context, the impact of Dexa outcompetes the glucose-triggered effect when inducers are present. Interestingly, in the absence of Dexa, a pro-oxidant environment results in a tremendous decrease in *LEP* mRNA levels both in LG and HG conditions (**Figure 5C**). Altogether our data highlight that in a context of increased oxidative stress, such as the one triggered in aging (37), BMAds display an altered phenotype with a compromised capacity to synthetize ADIPOQ and LEP as already reported for mice (53) and humans (62). Such pro-oxidant status could also underlie the defect in *ADIPOQ* expression observed in the BMAds from Type 2 diabetic patients (4) while other factors predominate in the control of *LEP* expression.

Our study also provides evidence that the negative impact of hyperglycemia on bone is connected to an enhanced extracellular ROS production by mature BMAds, as supported with extracellular ROS concentrations higher than intracellular ones (**Figure 2**). Comparable amounts of H_2O_2 severely decrease viability of human osteoblast-like cells (63, 64). An excessive oxidative stress also promotes osteocyte apoptosis which, given the critical role of these main bone cells in bone remodeling, results in an increased and unbalanced bone resorption (65, 66). Conversely, counteracting oxidative stress improves osteocyte viability and cytokine expression (67), and prevents osteoblast apoptosis in aged (68) or gonadectomized (37) mice. Besides, differentiating osteoblasts from hBMSCs express less antioxidant enzymes than differentiating adipocytes (39). As previously emphasized, increased ROS metabolism also represses osteoblastogenesis (17, 69) and promotes adipogenesis (21, 31). Beyond these cell processes, oxidative stress combined with hyperglycemia accelerate AGEs formation and accumulation, such as pentosidine which is more and more considered as a critical determinant in the BMD-independent bone frailty of metabolic diseases (70–72). Our findings thus expand the deleterious roles of BMAds in Type 2 diabetes skeletal defects: besides compromising osteoblastogenesis, BMAds could further damage bone quality and properties by releasing more ROS in the context of uncontrolled hyperglycemia leading altogether to an exacerbation in AGEs formation.

HG-triggered ROS elevation in mature BMAds is likely associated with an increased NOX4 activity. The transcriptional regulation of *NOX4* has been shown to give account on its enzymatic activity in cell culture (51, 73). Among the different NOX isoforms, NOX4 directly and constitutively produces H_2O_2 (54), and, has been reported to be the main isoform expressed in adipose tissues (51). In our study, both a rise in ROS amounts and *NOX4* expression levels are observed in BMAds exposed to HG concentration, either from the maturation step (i.e., from d14, **Figures 2A**, **3A**), in the presence or absence of adipogenic inducers or after a shorter exposure time to HG (LG/HG condition) (**Figures 2B**, **3B**). In contrast, *SOD2* mRNA levels are found either unchanged or even decreased upon inducer withdrawal when BMAds are cultured in HG concentration (**Figure 3B**). The expression levels of enzymes involved in ROS detoxification—such as CAT and GPX4—are also down-regulated in HG condition, which could contribute to a higher ROS rate. Yet, such regulation is at most observed while adipogenic inducers are absent and within a moderate range [e.g., −34% for *CAT*, LG (–ind) vs. HG (–ind)] compared to the one observed for NOX4 (+245%, LG (–ind) vs. HG (–ind), **Figure 3B**). Moreover, the gene expression pattern of *NOX4* in our experiments is consistent with data from the 3T3-L1 preadipocyte cell line: while adipocyte differentiation is associated with decreased expression of NOX4 (51), fully differentiated adipocytes cultured in the presence of 25 mM glucose display a higher ROS generation which is concomitant with increased NOX4 activity (55). Indeed in that model, glucose excess was shown to be metabolized through the pentose phosphate pathway to provide larger amounts of NADPH which are cofactors of NOX enzymes. Besides, HG condition stimulates NOX4 translocation to lipid rafts of the plasma membrane (55). Though these findings have not been confirmed in hBMSC-derived adipocytes, it has to be pointed out that NOX4 activity is considered to provide continuously and independently of any activator H_2O_2 which is a membrane-diffusible and stable ROS (54). The HG-induced elevation in ROS levels observed both extracellularly and intracellularly is therefore likely ascribed to the increased *NOX4* expression in mature BMAds.

Finally, hBMSCs or rodent bone marrow stromal cells are usually grown, differentiated and matured into different cell lineages in DMEM containing a HG concentration, i.e., with 25 mM glucose (29–31, 39). Such cell culture practice is also used for the 3T3-L1 cell line despite the induction of several adipocyte alterations (24, 26, 55) as emphasized above. The requirement of such HG concentration has been recently reappraised in the different handling steps of the 3T3-L1 cell line: a 3 day pulse with 25 mM glucose was demonstrated to be needed during the differentiation process and not the proliferation, nor the maturation of the cells (74). Here, our study provides evidence that hBMSC differentiation into adipocytes is unaltered when using a LG concentration. Besides, maturing adipocytes in the presence of HG concentration results in several functional alterations with decreased *PPARG* and *ADIPOQ* levels, and increased ROS metabolism. With an increasing interest for BMAds in energy and nutrient metabolism perturbations, a particular attention regarding glucose

concentration in culture conditions should thus be brought to better decipher BMAd involvement and regulation using *in vitro* models.

In conclusion, beyond being accrued in Type 2 diabetes (3–5), mature BMAds release higher ROS levels in their microenvironment in response to HG concentration exposure. This ROS overproduction induces in mature BMAds defects in *PPARG* and *ADIPOQ* expressions without any cytotoxicity. Considering that excessive ROS production is closely associated with an inflammatory response and impaired insulin signaling in extramedullary adipocytes, further dysfunctions in BMAds in the settings of hyperglycemia could be expected and are worth investigating.

DATA AVAILABILITY

The datasets generated for this study are available on request to the corresponding author.

AUTHOR CONTRIBUTIONS

TR and SL designed the study, performed cell culture, qPCR and microscopy, analyzed the data, and wrote the manuscript. TR carried out microfluorimetry experiments. SL supervised the study. All authors read, critically reviewed, and approved the final manuscript.

FUNDING

This work was supported by MSD AVENIR Foundation [ADIMETABONE project] to SL. This work was also supported by the University of Littoral Côte d'Opale (ULCO) through a post-doctoral fellowship to TR and an equipment grant [BQR R/0902017].

ACKNOWLEDGMENTS

The authors thank Anne Résonet (University of Littoral Côte d'Opale, Boulogne sur Mer, France) for technical assistance with qPCR experiments. We thank Dr. Guillaume Duflos (ANSES, Boulogne sur Mer, France) for providing spectrofluorimeter facility.

SUPPLEMENTARY MATERIAL

The Supplementary Material for this article can be found online at: https://www.frontiersin.org/articles/10.3389/fendo.2019.00607/full#supplementary-material

REFERENCES

1. Justesen J, Stenderup K, Ebbesen EN, Mosekilde L, Steiniche T, Kassem M. Adipocyte tissue volume in bone marrow is increased with aging and in patients with osteoporosis. *Biogerontology*. (2001) 2:165–71. doi: 10.1023/A:1011513223894
2. Schwartz AV, Sigurdsson S, Hue TF, Lang TF, Harris TB, Rosen CJ, et al. Vertebral bone marrow fat associated with lower trabecular BMD and prevalent vertebral fracture in older adults. *J Clin Endocrinol Metab*. (2013) 98:2294–300. doi: 10.1210/jc.2012-3949
3. Sheu Y, Amati F, Schwartz AV, Danielson ME, Li X, Boudreau R, et al. Osteoporotic Fractures in Men (MrOS) Research Group. Vertebral bone marrow fat, bone mineral density and diabetes: the Osteoporotic Fractures in Men (MrOS) study. *Bone*. (2017) 97:299–305. doi: 10.1016/j.bone.2017.02.001
4. Ferland-McCollough D, Masseli D, Spinetti G, Sambataro M, Sullivan N, Blom A, et al. MCP-1 feedback loop between adipocytes and mesenchymal stromal cells causes fat accumulation and contributes to hematopoietic stem cell rarefaction in the bone marrow of diabetic patients. *Diabetes*. (2018) 67:1380–94. doi: 10.2337/db18-0044
5. Zhu L, Xu Z, Li G, Wang Y, Li X, Shi X, et al. Marrow adiposity as an indicator for insulin resistance in postmenopausal women with newly diagnosed type 2 diabetes - an investigation by chemical shift-encoded water-fat MRI. *Eur J Radiol*. (2019) 113:158–64. doi: 10.1016/j.ejrad.2019.02.020
6. Baum T, Yap SP, Karampinos DC, Nardo L, Kuo D, Burghardt AJ, et al. Does vertebral bone marrow fat content correlate with abdominal adipose tissue, lumbar spine bone mineral density, and blood biomarkers in women with type 2 diabetes mellitus? *J Magn Reson Imaging*. (2012) 35:117–24. doi: 10.1002/jmri.22757
7. de Paula FJA, de Araújo IM, Carvalho AL, Elias J, Salmon CEG, Nogueira-Barbosa MH. The relationship of fat distribution and insulin resistance with lumbar spine bone mass in women. *PLoS ONE*. (2015) 10:e0129764. doi: 10.1371/journal.pone.0129764
8. de Araújo IM, Salmon CEG, Nahas AK, Nogueira-Barbosa MH, Elias J, de Paula FJA. Marrow adipose tissue spectrum in obesity and type 2 diabetes mellitus. *Eur J Endocrinol*. (2017) 176:21–30. doi: 10.1530/EJE-16-0448
9. Yu EW, Greenblatt L, Eajazi A, Torriani M, Bredella MA. Marrow adipose tissue composition in adults with morbid obesity. *Bone*. (2017) 97:38–42. doi: 10.1016/j.bone.2016.12.018
10. Hardouin P, Rharass T, Lucas S. Bone marrow adipose tissue: to be or not to be a typical adipose tissue? *Front Endocrinol*. (2016) 7:85. doi: 10.3389/fendo.2016.00085
11. Rharass T, Lucas S. Mechanisms in endocrinology: bone marrow adiposity and bone, a bad romance? *Eur J Endocrinol*. (2018) 179:R165–82 doi: 10.1530/EJE-18-0182
12. Yamamoto M, Sugimoto T. Advanced glycation end products, diabetes, and bone strength. *Curr Osteoporos Rep*. (2016) 14:320–6. doi: 10.1007/s11914-016-0332-1
13. Keats E, Khan ZA. Unique responses of stem cell-derived vascular endothelial and mesenchymal cells to high levels of glucose. *PLoS ONE*. (2012) 7:e38752. doi: 10.1371/journal.pone.0038752
14. Hankamolsiri W, Manochantr S, Tantrawatpan C, Tantikanlayaporn D, Tapanadechopone P, Kheolamai P. The effects of high glucose on adipogenic and osteogenic differentiation of gestational tissue-derived MSCs. *Stem Cells Int*. (2016) 2016:9674614. doi: 10.1155/2016/9674614
15. Keats EC, Dominguez JM, Grant MB, Khan ZA. Switch from canonical to noncanonical Wnt signaling mediates high glucose-induced adipogenesis. *Stem Cells*. (2014) 32:1649–60. doi: 10.1002/stem.1659
16. Chuang CC, Yang RS, Tsai KS, Ho FM, Liu SH. Hyperglycemia enhances adipogenic induction of lipid accumulation: involvement of extracellular signal-regulated protein kinase 1/2, phosphoinositide 3-kinase/Akt, and peroxisome proliferator-activated receptor gamma signaling. *Endocrinology*. (2007) 148:4267–75. doi: 10.1210/en.2007-0179
17. Wang A, Midura RJ, Vasanji A, Wang AJ, Hascall VC. Hyperglycemia diverts dividing osteoblastic precursor cells to an adipogenic pathway and induces synthesis of a hyaluronan matrix that is adhesive for monocytes. *J Biol Chem*. (2014) 289:11410–20. doi: 10.1074/jbc.M113.541458
18. Zhang Y, Yang J-H. Activation of the PI3K/Akt pathway by oxidative stress mediates high glucose-induced increase of adipogenic differentiation

in primary rat osteoblasts. *J Cell Biochem*. (2013) 114:2595–602. doi: 10.1002/jcb.24607
19. Botolin S, McCabe LR. Chronic hyperglycemia modulates osteoblast gene expression through osmotic and non-osmotic pathways. *J Cell Biochem*. (2006) 99:411–24. doi: 10.1002/jcb.20842
20. Wang W, Zhang X, Zheng J, Yang J. High glucose stimulates adipogenic and inhibits osteogenic differentiation in MG-63 cells through cAMP/protein kinase A/extracellular signal-regulated kinase pathway. *Mol Cell Biochem*. (2010) 338:115–22. doi: 10.1007/s11010-009-0344-6
21. Atashi F, Modarressi A, Pepper MS. The role of reactive oxygen species in mesenchymal stem cell adipogenic and osteogenic differentiation: a review. *Stem Cells Dev*. (2015) 24:1150–63. doi: 10.1089/scd.2014.0484
22. García-Hernández A, Arzate H, Gil-Chavarría I, Rojo R, Moreno-Fierros L. High glucose concentrations alter the biomineralization process in human osteoblastic cells. *Bone*. (2012) 50:276–88. doi: 10.1016/j.bone.2011.10.032
23. Lin Y, Berg AH, Iyengar P, Lam TKT, Giacca A, Combs TP, et al. The hyperglycemia-induced inflammatory response in adipocytes: the role of reactive oxygen species. *J Biol Chem*. (2005) 280:4617–26. doi: 10.1074/jbc.M411863200
24. Han CY, Subramanian S, Chan CK, Omer M, Chiba T, Wight TN, et al. Adipocyte-derived serum amyloid A3 and hyaluronan play a role in monocyte recruitment and adhesion. *Diabetes*. (2007) 56:2260–73. doi: 10.2337/db07-0218
25. Tanis RM, Piroli GG, Day SD, Frizzell N. The effect of glucose concentration and sodium phenylbutyrate treatment on mitochondrial bioenergetics and ER stress in 3T3-L1 adipocytes. *Biochim Biophys Acta*. (2015) 1853:213–21. doi: 10.1016/j.bbamcr.2014.10.012
26. Yeop Han C, Kargi AY, Omer M, Chan CK, Wabitsch M, O'Brien KD, et al. Differential effect of saturated and unsaturated free fatty acids on the generation of monocyte adhesion and chemotactic factors by adipocytes: dissociation of adipocyte hypertrophy from inflammation. *Diabetes*. (2010) 59:386–96. doi: 10.2337/db09-0925
27. Talior I, Yarkoni M, Bashan N, Eldar-Finkelman H. Increased glucose uptake promotes oxidative stress and PKC-delta activation in adipocytes of obese, insulin-resistant mice. *Am J Physiol Endocrinol Metab*. (2003) 285:E295–302. doi: 10.1152/ajpendo.00044.2003
28. Wang X, Hai C. Redox modulation of adipocyte differentiation: hypothesis of "Redox Chain" and novel insights into intervention of adipogenesis and obesity. *Free Radic Biol Med*. (2015) 89:99–125. doi: 10.1016/j.freeradbiomed.2015.07.012
29. Tormos KV, Anso E, Hamanaka RB, Eisenbart J, Joseph J, Kalyanaraman B, et al. Mitochondrial complex III ROS regulate adipocyte differentiation. *Cell Metab*. (2011) 14:537–44. doi: 10.1016/j.cmet.2011.08.007
30. Kanda Y, Hinata T, Kang SW, Watanabe Y. Reactive oxygen species mediate adipocyte differentiation in mesenchymal stem cells. *Life Sci*. (2011) 89:250–8. doi: 10.1016/j.lfs.2011.06.007
31. Wang W, Zhang Y, Lu W, Liu K. Mitochondrial reactive oxygen species regulate adipocyte differentiation of mesenchymal stem cells in hematopoietic stress induced by arabinosylcytosine. *PLoS ONE*. (2015) 10:e0120629. doi: 10.1371/journal.pone.0120629
32. Han CY. Roles of reactive oxygen species on insulin resistance in adipose tissue. *Diabetes Metab J*. (2016) 40:272–9. doi: 10.4093/dmj.2016.40.4.272
33. Hauck AK, Huang Y, Hertzel AV, Bernlohr DA. Adipose oxidative stress and protein carbonylation. *J Biol Chem*. (2019) 294:1083–8. doi: 10.1074/jbc.R118.003214
34. Furukawa S, Fujita T, Shimabukuro M, Iwaki M, Yamada Y, Nakajima Y, et al. Increased oxidative stress in obesity and its impact on metabolic syndrome. *J Clin Invest*. (2004) 114:1752–61. doi: 10.1172/JCI21625
35. Bartell SM, Kim H-N, Ambrogini E, Han L, Iyer S, Serra Ucer S, et al. FoxO proteins restrain osteoclastogenesis and bone resorption by attenuating H2O2 accumulation. *Nat Commun*. (2014) 5:3773. doi: 10.1038/ncomms4773
36. Ambrogini E, Almeida M, Martin-Millan M, Paik J-H, Depinho RA, Han L, et al. FoxO-mediated defense against oxidative stress in osteoblasts is indispensable for skeletal homeostasis in mice. *Cell Metab*. (2010) 11:136–46. doi: 10.1016/j.cmet.2009.12.009
37. Almeida M, Han L, Martin-Millan M, Plotkin LI, Stewart SA, Roberson PK, et al. Skeletal involution by age-associated oxidative stress and its acceleration by loss of sex steroids. *J Biol Chem*. (2007) 282:27285–97. doi: 10.1074/jbc.M702810200
38. Lean JM, Davies JT, Fuller K, Jagger CJ, Kirstein B, Partington GA, et al. A crucial role for thiol antioxidants in estrogen-deficiency bone loss. *J Clin Invest*. (2003) 112:915–23. doi: 10.1172/JCI200318859
39. Bruedigam C, Eijken M, Koedam M, van de Peppel J, Drabek K, Chiba H, et al. A new concept underlying stem cell lineage skewing that explains the detrimental effects of thiazolidinediones on bone. *Stem Cells*. (2010) 28:916–27. doi: 10.1002/stem.405
40. Holt V, Caplan AI, Haynesworth SE. Identification of a subpopulation of marrow MSC-derived medullary adipocytes that express osteoclast-regulating molecules: marrow adipocytes express osteoclast mediators. *PLoS ONE*. (2014) 9:e108920. doi: 10.1371/journal.pone.0108920
41. Speckmann B, Bidmon H-J, Pinto A, Anlauf M, Sies H, Steinbrenner H. Induction of glutathione peroxidase 4 expression during enterocytic cell differentiation. *J Biol Chem*. (2011) 286:10764–72. doi: 10.1074/jbc.M110.216028
42. Tyurin-Kuzmin PA, Zhdanovskaya ND, Sukhova AA, Sagaradze GD, Albert EA, Ageeva LV, et al. Nox4 and Duox1/2 mediate redox activation of mesenchymal cell migration by PDGF. *PLoS ONE*. (2016) 11:e0154157. doi: 10.1371/journal.pone.0154157
43. Kalyanaraman B, Darley-Usmar V, Davies KJA, Dennery PA, Forman HJ, Grisham MB, et al. Measuring reactive oxygen and nitrogen species with fluorescent probes: challenges and limitations. *Free Radic Biol Med*. (2012) 52:1–6. doi: 10.1016/j.freeradbiomed.2011.09.030
44. Bell EL, Klimova TA, Eisenbart J, Moraes CT, Murphy MP, Budinger GRS, et al. The Qo site of the mitochondrial complex III is required for the transduction of hypoxic signaling via reactive oxygen species production. *J Cell Biol*. (2007) 177:1029–36. doi: 10.1083/jcb.200609074
45. Rharass T, Gbankoto A, Canal C, Kurşunluoglu G, Bijoux A, Panáková D, et al. Oxidative stress does not play a primary role in the toxicity induced with clinical doses of doxorubicin in myocardial H9c2 cells. *Mol Cell Biochem*. (2016) 413:199–215. doi: 10.1007/s11010-016-2653-x
46. Ribou A-C. Synthetic sensors for reactive oxygen species detection and quantification: a critical review of current methods. *Antioxid Redox Signal*. (2016) 25:520–33. doi: 10.1089/ars.2016.6741
47. Zhao B, Summers FA, Mason RP. Photooxidation of Amplex Red to resorufin: implications of exposing the Amplex Red assay to light. *Free Radic Biol Med*. (2012) 53:1080–7. doi: 10.1016/j.freeradbiomed.2012.06.034
48. Gregoire FM, Smas CM, Sul HS. Understanding adipocyte differentiation. *Physiol Rev*. (1998) 78:783–809. doi: 10.1152/physrev.1998.78.3.783
49. Higuchi M, Dusting GJ, Peshavariya H, Jiang F, Hsiao ST-F, Chan EC, et al. Differentiation of human adipose-derived stem cells into fat involves reactive oxygen species and forkhead box O1 mediated upregulation of antioxidant enzymes. *Stem Cells Dev*. (2013) 22:878–88. doi: 10.1089/scd.2012.0306
50. Dong X, Bi L, He S, Meng G, Wei B, Jia S, et al. FFAs-ROS-ERK/P38 pathway plays a key role in adipocyte lipotoxicity on osteoblasts in co-culture. *Biochimie*. (2014) 101:123–31. doi: 10.1016/j.biochi.2014.01.002
51. Mouche S, Mkaddem SB, Wang W, Katic M, Tseng Y-H, Carnesecchi S, et al. Reduced expression of the NADPH oxidase NOX4 is a hallmark of adipocyte differentiation. *Biochim Biophys Acta*. (2007) 1773:1015–27. doi: 10.1016/j.bbamcr.2007.03.003
52. Zou X, Ratti BA, O'Brien JG, Lautenschlager SO, Gius DR, Bonini MG, et al. Manganese superoxide dismutase. (SOD2): is there a center in the universe of mitochondrial redox signaling? *J Bioenerg Biomembr*. (2017) 49:325–33. doi: 10.1007/s10863-017-9718-8
53. Liu L-F, Shen W-J, Ueno M, Patel S, Kraemer FB. Characterization of age-related gene expression profiling in bone marrow and epididymal adipocytes. *BMC Genomics*. (2011) 12:212. doi: 10.1186/1471-2164-12-212
54. Schröder K. NADPH oxidases in bone homeostasis and osteoporosis. *Free Radic Biol Med*. (2019) 132:67–72. doi: 10.1016/j.freeradbiomed.2018.08.036
55. Han CY, Umemoto T, Omer M, Den Hartigh LJ, Chiba T, LeBoeuf R, et al. NADPH oxidase-derived reactive oxygen species increases expression of monocyte chemotactic factor genes in cultured adipocytes. *J Biol Chem*. (2012) 287:10379–93. doi: 10.1074/jbc.M111.304998

56. Barneda D, Christian M. Lipid droplet growth: regulation of a dynamic organelle. *Curr Opin Cell Biol*. (2017) 47:9–15. doi: 10.1016/j.ceb.2017.02.002
57. Raffaele M, Barbagallo I, Licari M, Carota G, Sferrazzo G, Spampinato M, et al. N-Acetylcysteine (NAC) ameliorates lipid-related metabolic dysfunction in bone marrow stromal cells-derived adipocytes. *Evid Based Complement Altern Med*. (2018) 2018:5310961. doi: 10.1155/2018/5310961
58. Anghel SI, Wahli W. Fat poetry: a kingdom for PPAR gamma. *Cell Res*. (2007) 17:486–511. doi: 10.1038/cr.2007.48
59. Pascual G, Fong AL, Ogawa S, Gamliel A, Li AC, Perissi V, et al. A sumoylation-dependent pathway mediating transrepression of inflammatory response genes by PPARγ. *Nature*. (2005) 437:759–63. doi: 10.1038/nature03988
60. Wang D, Haile A, Jones LC. Dexamethasone-induced lipolysis increases the adverse effect of adipocytes on osteoblasts using cells derived from human mesenchymal stem cells. *Bone*. (2013) 53:520–30. doi: 10.1016/j.bone.2013.01.009
61. Uchihashi K, Aoki S, Shigematsu M, Kamochi N, Sonoda E, Soejima H, et al. Organotypic culture of human bone marrow adipose tissue. *Pathol Int*. (2010) 60:259–67. doi: 10.1111/j.1440-1827.2010.02511.x
62. Poloni A, Maurizi G, Serrani F, Mancini S, Zingaretti MC, Frontini A, et al. Molecular and functional characterization of human bone marrow adipocytes. *Exp Hematol*. (2013) 41:558–66.e2. doi: 10.1016/j.exphem.2013.02.005
63. She F, Wang W, Wang Y, Tang P, Wei J, Chen H, et al. Melatonin protects MG63 osteoblast-like cells from hydrogen peroxide-induced cytotoxicity by maintaining mitochondrial function. *Mol Med Rep*. (2014) 9:493–8. doi: 10.3892/mmr.2013.1832
64. Dai P, Mao Y, Sun X, Li X, Muhammad I, Gu W, et al. Attenuation of oxidative stress-induced osteoblast apoptosis by curcumin is associated with preservation of mitochondrial functions and increased Akt-GSK3β signaling. *Cell Physiol Biochem*. (2017) 41:661–77. doi: 10.1159/000457945
65. Manolagas SC, Parfitt AM. What old means to bone. *Trends Endocrinol Metab*. (2010) 21:369–74. doi: 10.1016/j.tem.2010.01.010
66. Domazetovic V, Marcucci G, Iantomasi T, Brandi ML, Vincenzini MT. Oxidative stress in bone remodeling: role of antioxidants. *Clin Cases Miner Bone Metab*. (2017) 14:209–216. doi: 10.11138/ccmbm/2017.14.1.209
67. Fontani F, Marcucci G, Iantomasi T, Brandi ML, Vincenzini MT. Glutathione, N-acetylcysteine and lipoic acid down-regulate starvation-induced apoptosis, RANKL/OPG ratio and sclerostin in osteocytes: involvement of JNK and ERK1/2 signalling. *Calcif Tissue Int*. (2015) 96:335–46. doi: 10.1007/s00223-015-9961-0
68. Jilka RL, Almeida M, Ambrogini E, Han L, Roberson PK, Weinstein RS, et al. Decreased oxidative stress and greater bone anabolism in the aged, when compared to the young, murine skeleton with parathyroid hormone administration. *Aging Cell*. (2010) 9:851–67. doi: 10.1111/j.1474-9726.2010.00616.x
69. Iyer S, Ambrogini E, Bartell SM, Han L, Roberson PK, de Cabo R, et al. FOXOs attenuate bone formation by suppressing Wnt signaling. *J Clin Invest*. (2013) 123:3409–19. doi: 10.1172/JCI68049
70. Napoli N, Chandran M, Pierroz DD, Abrahamsen B, Schwartz AV, Ferrari SL, et al. Mechanisms of diabetes mellitus-induced bone fragility. *Nat Rev Endocrinol*. (2017) 13:208–19. doi: 10.1038/nrendo.2016.153
71. Saito M, Fujii K, Mori Y, Marumo K. Role of collagen enzymatic and glycation induced cross-links as a determinant of bone quality in spontaneously diabetic WBN/Kob rats. *Osteoporos Int*. (2006) 17:1514–23. doi: 10.1007/s00198-006-0155-5
72. Marin C, Papantonakis G, Sels K, van Lenthe GH, Falgayrac G, Vangoitsenhoven R, et al. Unraveling the compromised biomechanical performance of type 2 diabetes- and Roux-en-Y gastric bypass bone by linking mechanical-structural and physico-chemical properties. *Sci Rep*. (2018) 8:5881. doi: 10.1038/s41598-018-24229-x
73. Serrander L, Cartier L, Bedard K, Banfi B, Lardy B, Plastre O, et al. NOX4 activity is determined by mRNA levels and reveals a unique pattern of ROS generation. *Biochem J*. (2007) 406:105–14. doi: 10.1042/BJ20061903
74. Jackson RM, Griesel BA, Gurley JM, Szweda LI, Olson AL. Glucose availability controls adipogenesis in mouse 3T3-L1 adipocytes via up-regulation of nicotinamide metabolism. *J Biol Chem*. (2017) 292:18556–64. doi: 10.1074/jbc.M117.791970

Conflict of Interest Statement: The authors declare that the research was conducted in the absence of any commercial or financial relationships that could be construed as a potential conflict of interest.

frontiers in Endocrinology

ORIGINAL RESEARCH
published: 27 September 2019
doi: 10.3389/fendo.2019.00668

Shared Autonomic Pathways Connect Bone Marrow and Peripheral Adipose Tissues Across the Central Neuraxis

Natalie K. Y. Wee[1,2], *Madelyn R. Lorenz*[1], *Yusuf Bekirov*[1], *Mark F. Jacquin*[3] *and Erica L. Scheller*[1,4]*

[1] Division of Bone and Mineral Diseases, Department of Medicine, Washington University School of Medicine, St. Louis, MO, United States, [2] Department of Reconstructive Sciences, UConn Health, Farmington, CT, United States, [3] Department of Neurology, Washington University School of Medicine, St. Louis, MO, United States, [4] Department of Cell Biology and Physiology, Washington University School of Medicine, St. Louis, MO, United States

Bone marrow adipose tissue (BMAT) is increased in both obesity and anorexia. This is unique relative to white adipose tissue (WAT), which is generally more attuned to metabolic demand. It suggests that there may be regulatory pathways that are common to both BMAT and WAT and also those that are specific to BMAT alone. The central nervous system (CNS) is a key mediator of adipose tissue function through sympathetic adrenergic neurons. Thus, we hypothesized that central autonomic pathways may be involved in BMAT regulation. To test this, we first quantified the innervation of BMAT by tyrosine hydroxylase (TH) positive nerves within the metaphysis and diaphysis of the tibia of B6 and C3H mice. We found that many of the TH+ axons were concentrated around central blood vessels in the bone marrow. However, there were also areas of free nerve endings which terminated in regions of BMAT adipocytes. Overall, the proportion of nerve-associated BMAT adipocytes increased from proximal to distal along the length of the tibia (from ∼3–5 to ∼14–24%), regardless of mouse strain. To identify the central pathways involved in BMAT innervation and compare to peripheral WAT, we then performed retrograde viral tract tracing with an attenuated pseudorabies virus (PRV) to infect efferent nerves from the tibial metaphysis (inclusive of BMAT) and inguinal WAT (iWAT) of C3H mice. PRV positive neurons were identified consistently from both injection sites in the intermediolateral horn of the spinal cord, reticular formation, rostroventral medulla, solitary tract, periaqueductal gray, locus coeruleus, subcoeruleus, Barrington's nucleus, and hypothalamus. We also observed dual-PRV infected neurons within the majority of these regions. Similar tracings were observed in pons, midbrain, and hypothalamic regions from B6 femur and tibia, demonstrating that these results persist across mouse strains and between skeletal sites. Altogether, this is the first quantitative report of BMAT autonomic innervation and reveals common central neuroanatomic pathways, including putative "command" neurons, involved in coordinating multiple aspects of sympathetic output and facilitation of parallel processing between bone marrow/BMAT and peripheral adipose tissue.

Keywords: bone marrow adipose tissue, fat, brain-bone interactions, pseudorabies virus, viral tract tracing, energy metabolism, sympathetic nerve, autonomic nervous system

OPEN ACCESS

Edited by:
Stephanie Lucas, Université du Littoral Côte d'Opale, France

Reviewed by:
Christopher J. Madden, Oregon Health & Science University, United States
Kristy Townsend, University of Maine, United States

***Correspondence:**
Erica L. Scheller
scheller@wustl.edu

Specialty section:
This article was submitted to Bone Research, a section of the journal Frontiers in Endocrinology

Received: *26 April 2019*
Accepted: *16 September 2019*
Published: *27 September 2019*

Citation:
Wee NKY, Lorenz MR, Bekirov Y, Jacquin MF and Scheller EL (2019) Shared Autonomic Pathways Connect Bone Marrow and Peripheral Adipose Tissues Across the Central Neuraxis. Front. Endocrinol. 10:668. doi: 10.3389/fendo.2019.00668

INTRODUCTION

Within the peripheral nervous system, sympathetic adrenergic signals are transmitted by several distinct sets of ganglia, which regulate regions in the head, trunk, viscera, and limbs. Common higher order processing centers are needed to ensure rapid, precise coordination of whole-body responses such as changes in vascular tone and energy metabolism. Consistent with this, the central nervous system (CNS) is recognized as a key mediator of peripheral adipose tissue function (1–7). The bone marrow is also an important site of peripheral adiposity with evidence for unique regulation and function [reviewed in (8)]. However, to date, very little is known about the neural control of bone marrow adipose tissue (BMAT) or its relationship to other adipose tissue depots across the central neuraxis.

The existence and prevalence of sympathetic neurons within the skeleton and bone marrow is well established (9–12). Ducy et al. first functionally demonstrated that central leptin administration reduced bone mass (13). This was later followed by other studies demonstrating that this effect was mediated via sympathetic nerves and modulation of β-adrenergic signaling (14, 15). Centrally, key neuropeptides associated primarily with the hypothalamus (e.g., NPY, CART, AgRP, POMC) have also been implicated in regulating bone homeostasis [reviewed in (16)]. Despite current work linking both the hypothalamus and sympathetic nerves to modulation of the bone microenvironment, the central regulatory regions influencing the skeleton are still relatively undefined.

We hypothesized that shared central neural pathways, relative to white adipose tissue (WAT), may be involved in BMAT regulation. To test this hypothesis, we performed viral transneuronal tract tracing from bone marrow and inguinal WAT. Viral tract tracing is a tool used to identify neural circuits. In particular, attenuated pseudorabies virus (PRV) recombinants such as the PRV-Bartha strain are well-established tracers that can be used for multi-synaptic directional tracing (17–19). After local PRV injection, all exposed viral axons within the site are infected. The virus then traffics to the cell body, replicates, and spreads across retrograde efferent synapses. This facilitates multi-synaptic tracing through the spinal cord and CNS. Whilst sensory cell bodies can be infected with PRV, they will not sort viral particles into central axons across afferent synapses and thus, viral transmission terminates in these cells. These properties make PRV tracers ideal for identifying and mapping efferent pathways from peripheral tissues, inclusive of those within the sympathetic nervous system (SNS).

Several previous reports have used tracing techniques to begin to map the higher order autonomic networks that regulate bone, adipose tissues, and other organs (4, 5, 20–27). However, shared regulatory regions between bone marrow/BMAT and peripheral WAT have not been identified. Thus, in this study, we first determined the proportion of BMAT adipocytes that are innervated by the SNS in C3H/HeJ (C3H) and C57BL/6J (B6) mice. Then, we used PRV to trace efferent neuroanatomical circuits from both tibial bone marrow (inclusive of BMAT) and inguinal WAT of C3H animals. Tracing from B6 femur/tibia was used as a control to examine strain- and skeletal site-specificity. To accomplish this, we used replication competent, isogenic, attenuated strains of the PRV virus (PRV-Bartha) in which the gG locus had been replaced with a fluorescent reporter (28).

METHODS

Mice

The Institutional Animal Care and Use Committee (IACUC) at Washington University in St. Louis approved all procedures, and these experiments were performed in AAALAC accredited facilities. For all experiments, C3H/HeJ (C3H, Stock:000659) and C57BL/6J (B6, Stock:000664) mice were obtained from Jackson Labs; mice were acclimatized for 1 week prior to experiments. Mice were housed on a 12-h light/dark cycle at 70 ± 2 degrees Fahrenheit and fed standard chow (LabDiet® 5053). Relative to B6 mice, C3H mice are known to have a significant expansion of BMAT in the proximal tibia by 12-weeks of age (29).

Retrograde Viral Tract Tracing

Mice at 12-weeks of age underwent surgery and were euthanized for analysis 5–6 days after viral infection. This timing is sufficient to allow for retrograde transsynaptic transport of virus through 3 synaptic relays, up to 4 orders of neurons (1). Two isogenic pseudorabies retrograde tracing viruses were obtained from the NIH Center for Neuroanatomy with Neurotropic Viruses (CNNV): PRV-152 (30, 31) and PRV-614 (28). The PRV-152 virus has EGFP as the reporter, while mRFP is the reporter for PRV-614. C3H: Half the mice received PRV-152 into the tibia and PRV-614 into iWAT; whilst the other half received PRV-614 into the tibia and PRV-152 into iWAT. B6: Half the mice received PRV-152 into the proximal tibia and PRV-614 into distal femur; whilst the other half received PRV-614 into tibia and PRV-152 into femur. **Figure 1A** lists the viral loads injected at each site (fat vs. bone). A drilled bone defect model was used to place virus directly in bone using a pulled glass needle, microinjector, and stereotaxic apparatus to deliver 0.10 μL (PRV-152) or 0.15 μL (PRV-614) of viral solution at depths of 2.5, 3, and 3.5 mm from the top of the bone including the cartilage (**Figures 1B–D**). The injection site was sealed with bone wax to prevent leakage of the virus. For iWAT injections, 0.15 μL (PRV-152) or 0.20 μL (PRV-614) of virus was injected using a pulled glass needle at each of four sites along the length of the iWAT. All mice were given Buprenorphine SR (ZooPharm, 1.0 mg/kg) and monitored daily post-surgery until euthanasia. In our hands, 25% of injected C3H mice and 36% of injected B6 mice did not display evidence of infection in the brain. This could be due to failed ejection of the viral solution from the microinjector tip, failed viral infection, replication and/or spread, or mis-injection into the circulation. Previous work has shown that IV injection of PRV does not cause central neuronal infection (32).

Tissue Collection

Mice were sedated with Ketamine/Xylazine and perfused through the left ventricle with 25 mL of phosphate buffered solution (PBS) followed by 25 mL 4% paraformaldehyde (PFA) at a rate of 5.0 mL per minute using a peristaltic pump. Tissues were post-fixed

A

PRV-152 (GFP)			
Titer: 1.30E+09 pfu/ml		Total volume (nl)	Total PFU injected
Bone injection	3 x 100nl	300	3.90E+05
Fat injection	4 x 150nl	450	5.85E+05
PRV-614 (RFP)			
Titer: 9.05E+08 pfu/ml		Total volume (nl)	Total PFU injected
Bone injection	3 x 150nl	450	4.07E+05
Fat injection	4 x 200nl	800	7.24E+05

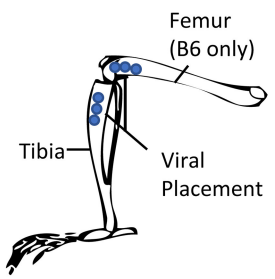

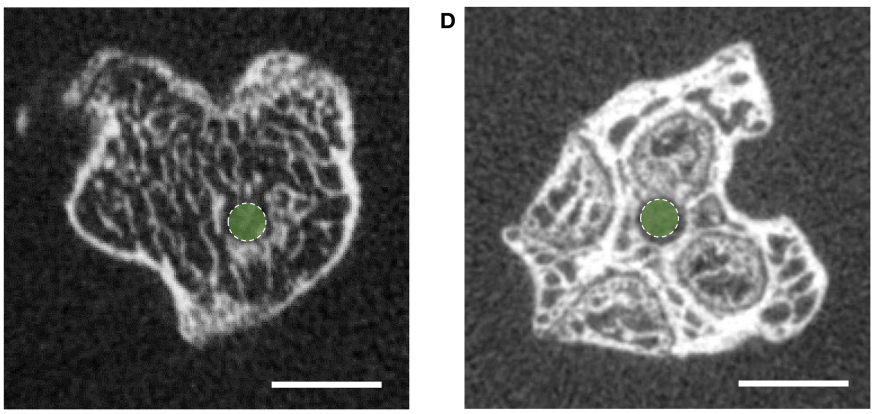

FIGURE 1 | Virus placement and weight loss. **(A)** Viral titers and injection volumes. **(B)** Virus placement in the tibia at depths of 2.5, 3.0, and 3.5 mm from the top of the tibia or femur. Access to the tibial bone marrow was gained at the knee between the medial and lateral tibial condyles (B6 and C3H mice). Access to the femoral bone marrow was also via the joint surface (B6 mice only). **(C)** Representative computed tomography image of the needle tract into the tibial metaphysis (green dot). A pulled glass microinjector was used to minimize any disturbance to the surrounding bone and marrow. **(D)** Representative computed tomography of the needle tract into the femur (green dot).

overnight in 4% PFA and then placed in PBS for storage or processed and analyzed as described below.

MicroCT

Post-fixation, bones were embedded in 2% agarose gel. The proximal ends of the tibiae were scanned at 20 μm voxel resolution using a Scanco μCT 40 (Scanco Medical AG) calibrated using a hydroxyapatite phantom. Scans were used to verify placement of the needle into the bone (**Figures 1C,D**).

Immunostaining and Analysis

Tibia

To assess skeletal innervation, whole tibiae from 13-week old C3H and B6 male mice were sectioned transversely at 50 μm along the length of the bone. Tissues were processed in 30% sucrose and embedded in Tissue-Plus OCT compound (Fisher Scientific, Hampton, New Hampshire, USA, 23-730-571) prior to cutting. Sections were blocked in 10% normal donkey serum (Sigma, St. Louis, MO, USA, D9663) in TNT buffer (0.1M Tris-HCl pH 7.4; 0.15 NaCl; 0.05% Tween-20). The sections were then incubated for 48-h with primary antibodies to tyrosine hydroxylase (TH) and perilipin (**Supplemental Table 1**). Following three rinses in TNT buffer, primary antibody staining was visualized using fluorescently-tagged secondary antibodies. The sections were rinsed again with TNT buffer and incubated in DAPI (1:1,000 dilution; Sigma, St. Louis, MO, USA, D9542) for 5-min before mounting with Fluoromount-G (ThermoFisher Scientific, Waltham, Massachusetts, USA, 00-4958-02). Tiled sections were imaged at 10X on a Nikon spinning disk confocal microscope. Images were reconstructed and analyzed in ImageJ/FIJI (33). The number of perilipin positive adipocytes was counted manually in each section and the proportion adjacent to a TH+ axon was recorded (<5 μm spacing). It is important to note that only TH+ structures the bone marrow with a size and morphology that was consistent with an autonomic axon fiber were considered in our analysis (size ∼1 μm in diameter, fibrous/branching, no nuclei—see **Figure 2A** as an example).

Spinal Cord

After perfusion, processing in 30% sucrose, and embedding in Tissue-Plus OCT compound, whole embedded spines were stored at −80°C until sectioning. The entire spinal cord was sectioned at 50 μm on a cryostat (Leica CM1850) and then collected onto Superfrost charged slides (Fisher Scientific, Hampton, New Hampshire, USA, 12-550-15). Every 8th section was stained. The sections were thawed at room temperature for 10-min, prior to immunostaining. Sections were first blocked in 10% normal donkey in TNT buffer. The sections were then incubated for 48-h in primary antibodies against RFP and GFP (**Supplemental Table 1**).

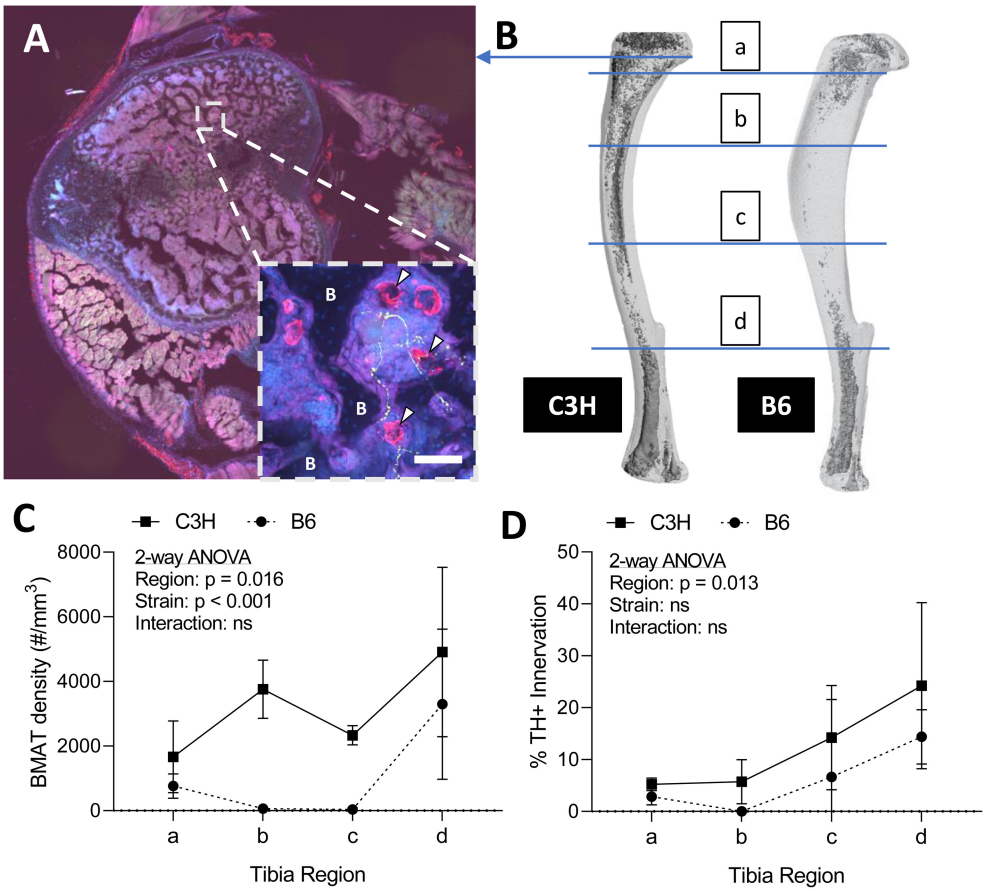

FIGURE 2 | Innervation of BMAT adipocytes by sympathetic autonomic nerves. **(A)** Cross-section of the proximal tibial metaphysis with immunohistochemical stains for adipocytes (perilipin, red) and sympathetic adrenergic nerves (tyrosine hydroxylase, green) overlaid with dapi (blue). In some regions, perilipin+ adipocytes are observed immediately adjacent to TH+ axons (~1 μm in diameter, fibrous/branching, representative inset, white arrowheads). B, bone. Scale bar = 50 μm. **(B)** Representative distribution of bone marrow adipose tissue (BMAT) in a C3H and B6 male, 13-week old tibiae. Osmium stain and CT reconstruction. Immunohistochemical sections along the length of the tibia were analyzed for adiposity and TH+ innervation as indicated. **(C)** The number of perilipin positive adipocytes in a full tibial cross-section (see example in **A**) was counted in each region as indicated in **B** and normalized to the volume of the bone marrow. As previously reported Scheller et al. (29), C3H mice had increased density of BMAT adipocytes along the length of the tibia relative to B6 animals (2-way ANOVA). **(D)** In the same regions, the number of adipocytes <5 μm from a TH+ nerve were counted and expressed relative to the total number of adipocytes within the section ["% BMAT Innervation (TH+)"]. Despite differences in adipocyte density, the proportion of BMAT adipocytes that were adjacent to a TH+ axon remained relatively consistent between strains. In addition, the % of innervated BMAT adipocytes was highest in distal regions of the tibia of both B6 and C3H mice. *N* = 3, C3H; *N* = 5, B6. 2-way repeated measures ANOVA. Graphed as mean ± SD.

Following three rinses in TNT buffer, primary antibody staining was visualized using fluorescently-tagged secondary antibodies. The sections were rinsed again with TNT buffer and incubated in DAPI for 5 min before mounting with Fluoromount-G. The sections were imaged with a Hamamatsu 2.0-HT NanoZoomer at 20x magnification. Spinal cord sections were analyzed using the Allen Spinal Cord Atlas as a reference database (34).

Brain

Dry ice (solid CO_2) was crushed to make a powder; each brain was rolled in the CO_2 and then left to freeze solid on dry ice. Each sample was mounted using Tissue-Plus OCT compound to a H/I Cryo-Histomat MK-3 (Hacker Instruments, Winnsboro, South Carolina, USA) and cut into slices of 30 μm thickness. Sections were split into six series and stored in cryoprotectant solution (0.2M phosphate buffer pH 7.4, ethylene glycol, sucrose) until stained. Sections were washed in TNT buffer and blocked in 0.1M PBS with 0.05% Tween 20 and 5% normal donkey serum. Primary antibodies to GFP, RFP, and/or TH were diluted in 0.1M PBS with 0.05% Tween 20 and 1% normal donkey serum and were incubated overnight at 4°C (**Supplemental Table 1**). Following rinsing in TNT buffer, sections were incubated with secondary antibody for 1-h at room temperature (**Supplemental Table 1**). Sections were then incubated with DAPI (1:1,000) and then arranged onto slides and coverslipped with Fluoromount-G. Imaging was performed with a Hamamatsu 2.0-HT NanoZoomer at 20x magnification. Sections spanning the entire brain were matched to images in The Mouse Brain in Stereotaxic Coordinates Brain by Paxinos and

Franklin (35) in order to identify traced central sites. For figure generation, a subset of sections were imaged at 10X magnification on a Leica confocal microscope.

Statistics

Statistics were performed in GraphPad Prism®. Statistical tests are indicated in the figure legends.

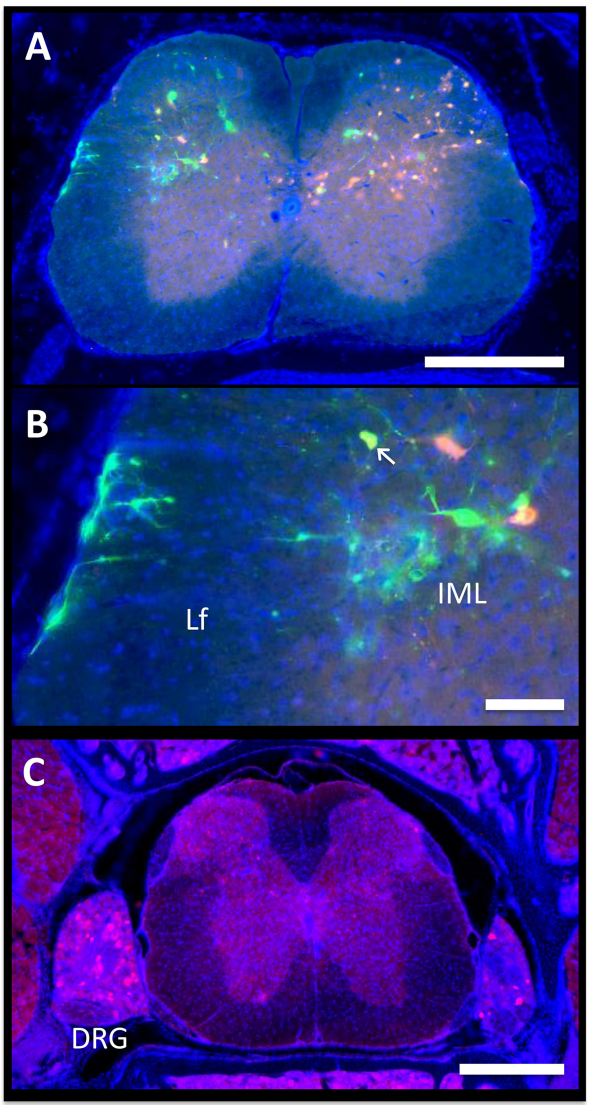

FIGURE 3 | Spinal cord. The axon of the most distal neuron within bone or fat, also known as the postganglionic autonomic neuron, connects to its cell body in the sympathetic chain ganglia. Within the ganglion, this cell body synapses with a new neuron, the sympathetic preganglionic neuron (SPN). The cell bodies of the SPNs are located in the spinal cord in the intermediolateral (IML) nuclei. Spinal cord neurons are then controlled by supraspinal circuits from the brain, which send target axons to synapse on SPNs through descending pathways. These are ultimately responsible for the coordinated regulation of neuro-skeletal and neuro-adipose tissue interactions. **(A,B)** In the presented case, PRV-614 (RFP) was injected into the tibia, whilst PRV-152 (GFP) was injected into iWAT. Yellow neurons are neurons that have become infected with both viruses (arrow). Scale bar = 500 μm **(A)** and 100 μm **(B)**. Lf, lateral funiculus. **(C)** We observed positive cells within dorsal root ganglia (DRG) ipsilateral to the site of infection. In some cases, we also observed positive DRG cells on the contralateral side. However, spread to the brain through ascending spinal cord pathways was not noted. Representative image, PRV-614 (RFP) into iWAT. Scale bar = 500 μm.

TABLE 1 | Traced brain regions from C3H tibial bone marrow [tibia, inclusive of bone marrow adipose tissue (BMAT)] and inguinal white adipose tissue (iWAT).

Region of the brain	Abbreviation	Tibia (*N* = 5)	iWAT (*N* = 5)	Dual labeled neurons
MEDULLA AND RETICULAR FORMATION				
Raphe obscurus nucleus	ROb	4	4	Yes
Raphe magnus nucleus	RMg	5	3	Yes
Raphe pallidus nucleus	RPa	5	4	Yes
Gigantocellular reticular nucleus	GRN	5	4	Yes
Lateral paragigantocellular nucleus	LPGi	4	4	Yes
Rostroventral medulla	RVLM	3	2	–
Nucleus of the solitary tract	NTS	5	4	Yes
Area postrema	AP	4	2	–
PONS				
Barrington's Nucleus	BN	5	5	Yes
Locus coeruleus	LC	5	5	Yes
Subcoeruleus nucleus	SLC	5	5	Yes
MIDBRAIN				
Dorsomedial periaqueductal gray	DMPAG	5	3	Yes
Lateral periaqueductal gray	LPAG	5	3	Yes
Ventrolateral periaqueductal gray	VLPAG	4	3	Yes
HYPOTHALAMUS				
Paraventricular hypothalamic nucleus, dorsal cap	PaDC	4	4	Yes
Paraventricular hypothalamic nucleus, lateral magnocellular part	PaLM	5	4	Yes
Paraventricular hypothalamic nucleus, medial magnocellular part	PaMM	5	3	Yes
Paraventricular hypothalamic nucleus, posterior part	PaMP	5	4	
Paraventricular hypothalamic nucleus, medial parvicellular part	PaPo	4	4	Yes
Lateral hypothalamus	LH	5	2	Yes
Posterior hypothalamic area	PH	4	1	–
Arcuate nucleus	Arc	3	1	–
Dorsomedial hypothalamus	DMH	2	2	Yes
Ventromedial hypothalamus	VMH	2	0	–
Suprachiasmatic nucleus	SCN	2	0	–
OTHERS				
Amygdala	Me	3	2	–
Pyriform cortex	Pir	2	2	–

An unpaired *t*-test was used to assess differences in body mass.

RESULTS

Sympathetic Adrenergic Innervation of Tibial BMAT Adipocytes in C3H and B6 Mice

Sympathetic adrenergic axons in bone and adipose tissues are rich in TH+ varicosities and terminate as free nerve endings (9, 36, 37). The proximity of the axon facilitates diffusion of neurotransmitters and subsequent actions on surrounding target cells, such as adipocytes. Thus, we performed immunohistochemical analysis of TH+ adrenergic nerve fibers and quantified their relationship to perilipin positive BMAT adipocytes at four sites along the length of the tibia. Consistent with previous reports (9, 38), we found that many of the TH+ axons were concentrated around central blood vessels in the bone marrow. However, there were also sparse areas of free nerve endings, particularly in the proximal metaphysis, which terminated in regions of BMAT adipocytes (**Figure 2A**). The relationship of BMAT adipocytes with TH+ axons was further explored by quantifying the percent of BMAT adipocytes that were directly adjacent to an axon (<5 μm away) along the length of the tibia in both C3H and B6 mice (**Figures 2B–D**). These included all adipocytes along the length of the neuron, not just at the axon terminal. As expected, the tibial adipocyte density was significantly greater in C3H mice relative to B6, particularly within the diaphysis (**Figure 2C**). However,

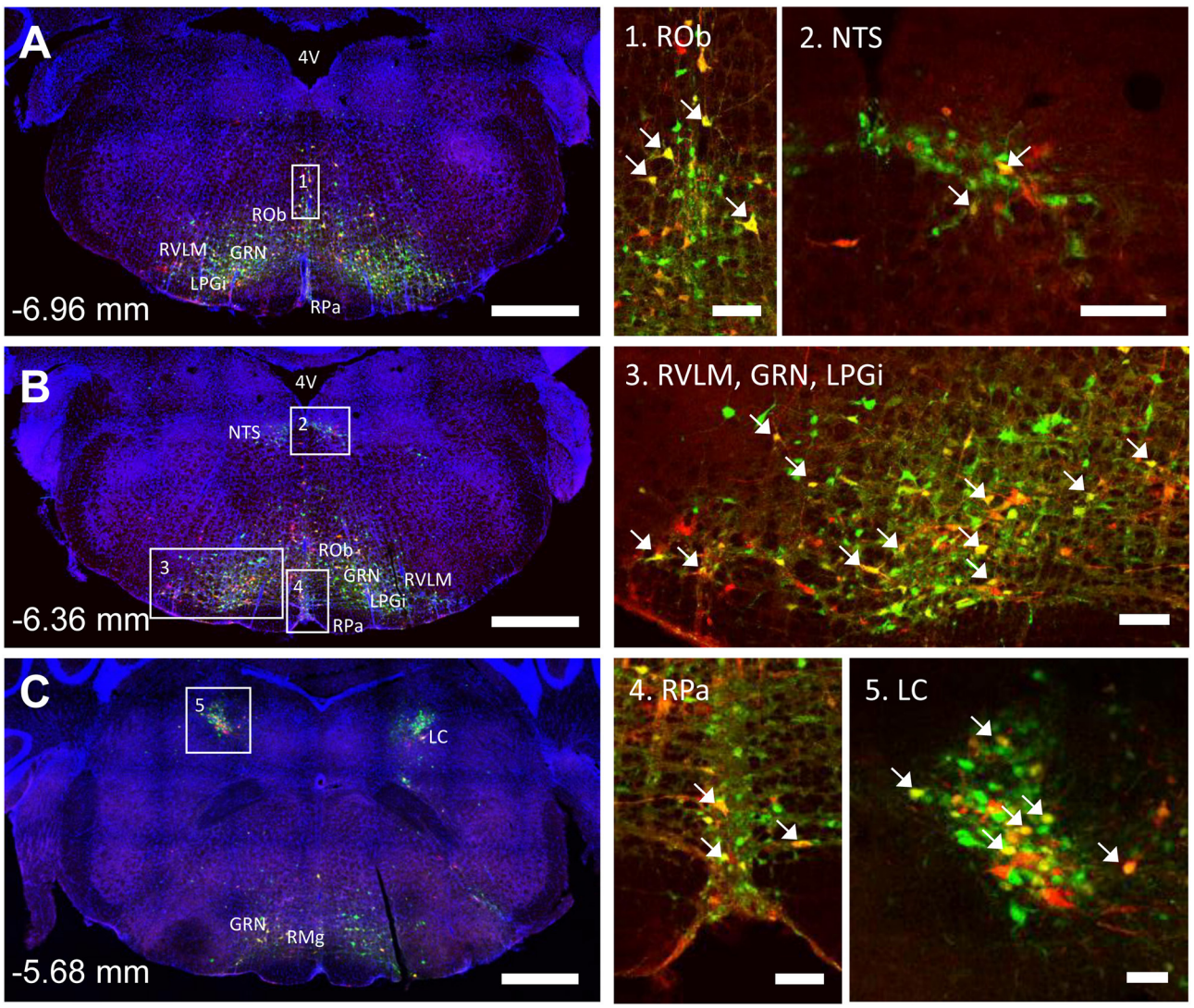

FIGURE 4 | Co-infection of neurons from bone marrow/BMAT and iWAT in the medulla and pons. In the presented case, green neurons are traced from the tibia, whilst red neurons are from iWAT. Yellow neurons are those that have become infected with both viruses (white arrows). **(A,B)** Brainstem medulla, scale bar = 1 mm. **(C)** Pons, scale bar = 1 mm. Insets, scale = 100 μm: (1) Raphe obscurus (ROb), (2) nucleus of the solitary tract (NTS), (3) gigantocellular reticular nucleus (GRN), lateral paragigantocellular nucleus (LPGi) and rostral ventrolateral medulla (RVLM), (4) raphe pallidus (RPa), and (5) locus coeruleus (LC). RMg, raphe magnus.

despite this difference in density, the proportion of innervated BMAT adipocytes was comparable between strains and increased gradually from proximal to distal along the length of the tibia (**Figure 2D**). Specifically, from the proximal metaphysis to the region of the tibia/fibula junction, innervation increased from 5.2±1.2% to 24.2±16.0% in the C3H mice and 2.9±1.4% to 14.4±4.5% in B6 (**Figure 2D**).

PRV Tracing Identifies Central Pathways Mediating Efferent Innervation of Bone Marrow (Inclusive of BMAT) and iWAT

Infection Rate and Viral Characteristics

Male C3H mice at 12-weeks of age were injected with isogenic PRV viruses as detailed in **Figures 1A,B**. Half received PRV-152 (EGFP) into tibia and PRV-614 (mRFP) into iWAT, and the other half had PRV-614 (mRFP) into tibia and PRV-152 (EGFP) into iWAT. Though not uniformly reported or discussed in previous publications, PRV infection causes weight loss, lethargy, and eventually death in experimental animals (5, 19). C3H animals that were positively infected with one or both viruses demonstrated weight loss of 15±1.6%, whilst mice negative for viral infection lost $<3.9 \pm 0.6\%$ body weight ($p = 0.003$). At the end of the experiment, 75% of mice demonstrated positive infection with at least one virus that had progressed to the brain. Upon μCT verification of needle placement, one mouse was excluded due to needle perforation through the tibial cortical bone. The results from the remaining animals are described below.

Spinal Cord

Autonomic pathways consist of a two-neuron relay, which connects the tissue of interest to the spinal cord. In our experiments, the spinal cord was examined using serial thick frozen sections from the upper thoracic to the lower sacral regions. Labeling was observed to some extent at all levels of the thoracic, lumbar, and sacral spinal cord, except for the lowest sacral portions. Though a unilateral predominance was generally noted, the majority of the cases had progressed to a point where bilateral spread was evident. In all cases, cellular staining was notable in the sympathetic preganglionic neurons (SPNs) of the intermediolateral (IML) nuclei (**Figure 3A**). Connections from the IML were commonly present across the intercalated nucleus and labeling was also prominent within the central autonomic nucleus (lamina X). In the surrounding white matter, positive axons were noted to be crossing the lateral funiculus from the surface of the spinal cord (**Figure 3B**).

Positive axons were also observed in the lateral reticulospinal tract just outside of the IML, in laminae II, V, and VII, and occasionally in the ventral horn. In mice where dual labeling was present in the brain, the staining pattern was the same as described above. In addition, though the majority of labeled neurons in the spinal cord were of a single color/origin, a small subset of dual-labeled neurons was present.

Lastly, given our cross-sectional analysis paradigm, we were able to observe several of the dorsal root ganglia. Though the PRV virus used is only capable of crossing between neurons at retrograde synapses of efferent axons, it initially infects all axons within the target tissue, including sensory afferent neurons. Consistent with this, we observed positive staining in a subset of the dorsal root ganglia; infection within contralateral ganglia was also present in some cases (**Figure 3C**). However, further spread from these neurons through anterograde spinal cord pathways was not noted.

Medulla, Pons, and Midbrain

The spinal cord connects to the brainstem at the base of the skull, transitioning into the medulla. Consistent with previous studies (4, 5, 20–27), PRV infection occurred bilaterally within the brain, even though only the right tibia and right iWAT were injected. A summary of traced brain regions and their incidence is presented in **Table 1**. Within the medulla, we observed pronounced positive staining in the area postrema (AP), the nucleus of the solitary tract (NTS), including the medial and ventrolateral parts, and the reticular formation of the medulla, originating from both regions of BMAT and iWAT (**Figures 4A,B**; **Table 1**). Within the median reticular formation, the nucleus raphe obscurus (ROb), the raphe pallidus (RPa) and nucleus raphe magnus (RMg) were consistently traced with PRV (**Figures 4A–C**). Moderate staining was also consistently observed between samples in the gigantocellular reticular nucleus (GRN) and the lateral paragigantocellular nucleus (LPGi) (**Figures 4A,B**). Adjacent to the reticular formation, staining from bone marrow/BMAT and iWAT was notable in the rostroventral medulla (RVLM) (**Figure 4B**). In the pons, located between the medulla and the midbrain, tracing was prominent from both injection sites within the locus coeruleus (LC), subcoeruleus (SLC), and Barrington's nucleus (BN) (**Figures 4C, 5A,B**). As performed previously (22, 39), co-stains with TH were used to distinguish these three regions (**Figure 5**). In the midbrain, positive infection from bone marrow and iWAT was detected in the periaqueductal gray (PAG) (**Figures 6A–C**). Staining within the PAG was predominantly identified in the dorsomedial, lateral, and the ventrolateral areas.

In multi-labeled samples, dual infected neurons from both injection sites were present in the medullary reticular formation (ROb, RMg, RPa, GRN, LPGi) and NTS (**Figure 4**). We similarly observed a subset of pontine LC, SLC, and BN neurons that were co-infected with viruses originating from bone marrow and iWAT (**Figure 5**). Lastly, several dual traced neurons were present in the PAG (**Figure 6**).

Hypothalamus and Forebrain

PRV infection was prominent within the hypothalamus, most notably within the paraventricular hypothalamus (PVH) (**Figure 7**; **Supplemental Figures 1, 2**). Infection of the PVH was bilateral from both bone marrow and iWAT; however, there was typically a discernable difference with a greater number of neurons stained on one side than the other (**Supplemental Figure 1**). This may be due to the virus crossing the midline via interneurons and then proceeding up into the brain, thus viral infection may lag on contralateral side, leading to the observed difference. In dual positive-infected mice, we observed a substantial number of neurons arising

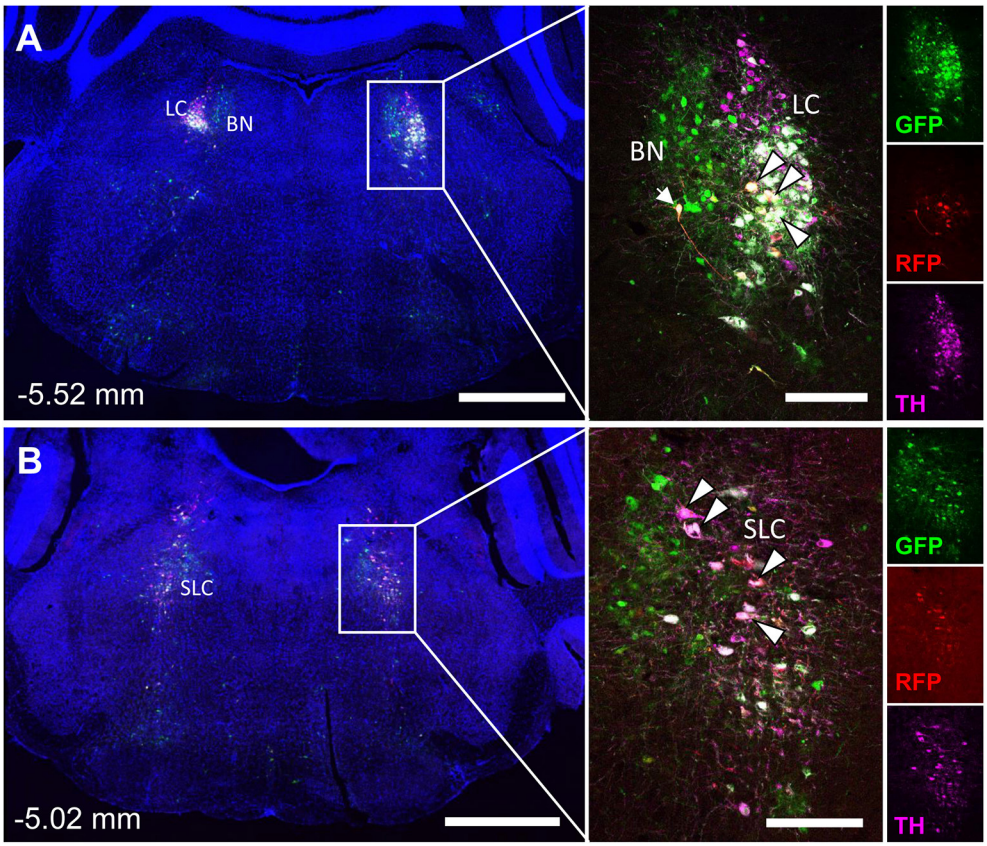

FIGURE 5 | Tyrosine hydroxylase staining identifies co-infected 'command neurons' in the locus coeruleus (LC), subcoeruleus (SLC), and Barrington's nucleus (BN). In the presented case, green neurons are traced from the tibia, whilst red neurons are from iWAT. A co-stain for tyrosine hydroxylase (TH) was used to define the boundaries of the locus coeruleus and subcoeruleus (LC and SLC, TH+) relative to Barrington's nucleus (BN, TH–). Yellow neurons are those that have become infected with both viruses without co-staining for tyrosine hydroxylase (TH) (white arrow). White neurons are those that are triple positive for GFP, RFP, and TH—indicating co-infection of a TH+ neuron within the LC or SLC as indicated (white arrowheads with black borders). **(A)** Overview of pons including the locus coeruleus (LC) and Barringtons nucleus (BN) at −5.52 mm from bregma. Scale bars: 1 mm and 200 μm (inset). **(B)** Overview of pons including the subcoeruleus (SLC) at −5.02 mm from bregma. Scale bars: 1 mm and 200 μm (inset). Individual channels for GFP (green), RFP (red), and TH (magenta) are shown for reference.

from the tibial injection and a number of neurons arising from iWAT in both posterior and medial parts of the PVH (**Figures 7A–C**). Again, similar to regions of the medulla and pons, we also identified neurons that were co-infected with both viruses (**Figure 7**; **Table 1**). Other regions of the hypothalamus with positive PRV infection include the lateral hypothalamus (LH), posterior hypothalamic area (PH), arcuate nucleus (ARC), dorsomedial hypothalamus (DMH), ventromedial hypothalamus (VMH), and suprachiasmatic nucleus (SCN) (**Figure 7**; **Table 1**). Lastly, we found robust labeling of neurons in the amygdala in a subset of animals (**Figure 7B**; **Supplemental Figure 3**). In close proximity to the amygdala, PRV-infected neurons were also present in the pyriform cortex in a 2/5 tracings from bone marrow/BMAT and iWAT (**Table 1**; **Supplemental Figure 3**).

PRV Tracing From B6 Femur and Tibia Mimics That Observed From C3H Mice

To examine the strain- and skeletal site-specificity of PRV, we traced to the brain from the proximal tibia and distal femur of a matched set of male 12-week-old, B6 mice. As above, some mice received PRV-152 (EGFP) into tibia and PRV-614 (mRFP) into femur while in others this was reversed. At the end of the experiment, needle placement was confirmed with μCT. Due to minor issues with tissue processing, the medulla and reticular formation could not be included in these analyses. However, in the pons, infection from the tibia and femur was observed in the BN, LC, and SLC (**Table 2**). Staining from both sites was also identified in the midbrain, specifically within the PAG (**Table 2**). As in C3H mice, the hypothalamus contained positive PRV infection predominantly in the PVH (**Table 2**; **Supplemental Figure 4**). Additional traced neurons were identified in the LH, PH, DMH, and SCN from a subset of animals (**Table 2**). Lastly, one of four cases from the tibia and two of three from the femur resulted in PRV infection in the amygdala (**Table 2**).

DISCUSSION

Shared innervation has been established between peripheral WAT and BAT adipose tissues (1–7). However, to date, our

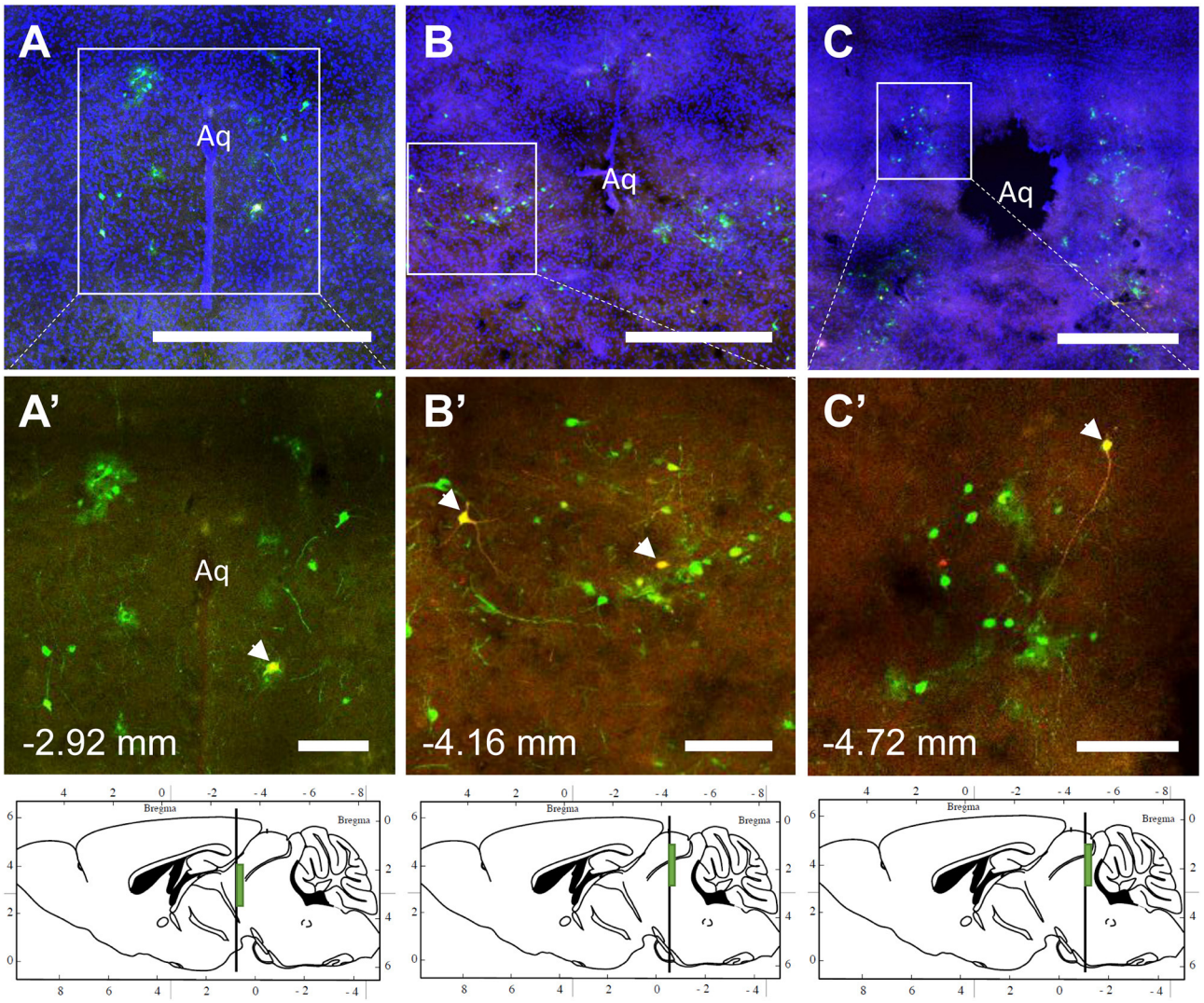

FIGURE 6 | Co-infection of neurons from bone marrow/BMAT and iWAT in the periaqueductal gray (PAG). In the presented case, green neurons are traced from the tibia, whilst red neurons are from iWAT. Yellow neurons are those that have become infected with both viruses (white arrows). **(A–C)** Overview of tracing around the central aqueduct (Aq) at three regions including −2.92, −4.16, and −4.72 mm from bregma. Scale bar = 1 mm. **(A'–C')** Magnified insets showing individually traced neurons and those with co-infection from both sites (arrowheads). Scale bar = 200 μm. Green boxes on the sagittal sections denote the relative location of the displayed regions.

understanding of neural interactions with bone marrow/BMAT has been limited. We have previously demonstrated that cold exposure, a model of elevated sympathetic tone and catecholamine release, depleted BMAT from the proximal end of the tibia (29). More recently, it was shown that bone marrow adipocytes respond to isoproterenol (pan-adrenergic agonist—β1, β2, and β3) by increased phospho-hormone sensitive lipase, whilst the response following treatment with a β3 agonist, a major regulator of lipolysis in other adipose tissues, was present at a lower level (40). Together, this information suggests that there is likely some shared regulation of adipose tissues within the body but also that there may be subtle differences between BMAT and other adipose depots. Building on previous work, this study has been able to establish the presence of shared autonomic pathways between BMAT and iWAT. Dual labeled "command" neurons were noted regions such as the reticular formation, NTS, LC, PBN, SLC, BN, and hypothalamus—indicating that common neurons may be involved in the central regulation of both sites. Though the prevalence of dual infection reflects a wide range of variables including initial infection and viral trafficking, the overlap in our current study appears to range from 7 to 18% depending on the region (**Figures 4–7**). This is consistent with previous work on dual injections of PRV into different adipose depots which identified an incidence of 5–55% of dual-infected neurons, indicative of shared innervation between fat depots (41). The results provide the foundation for future studies to

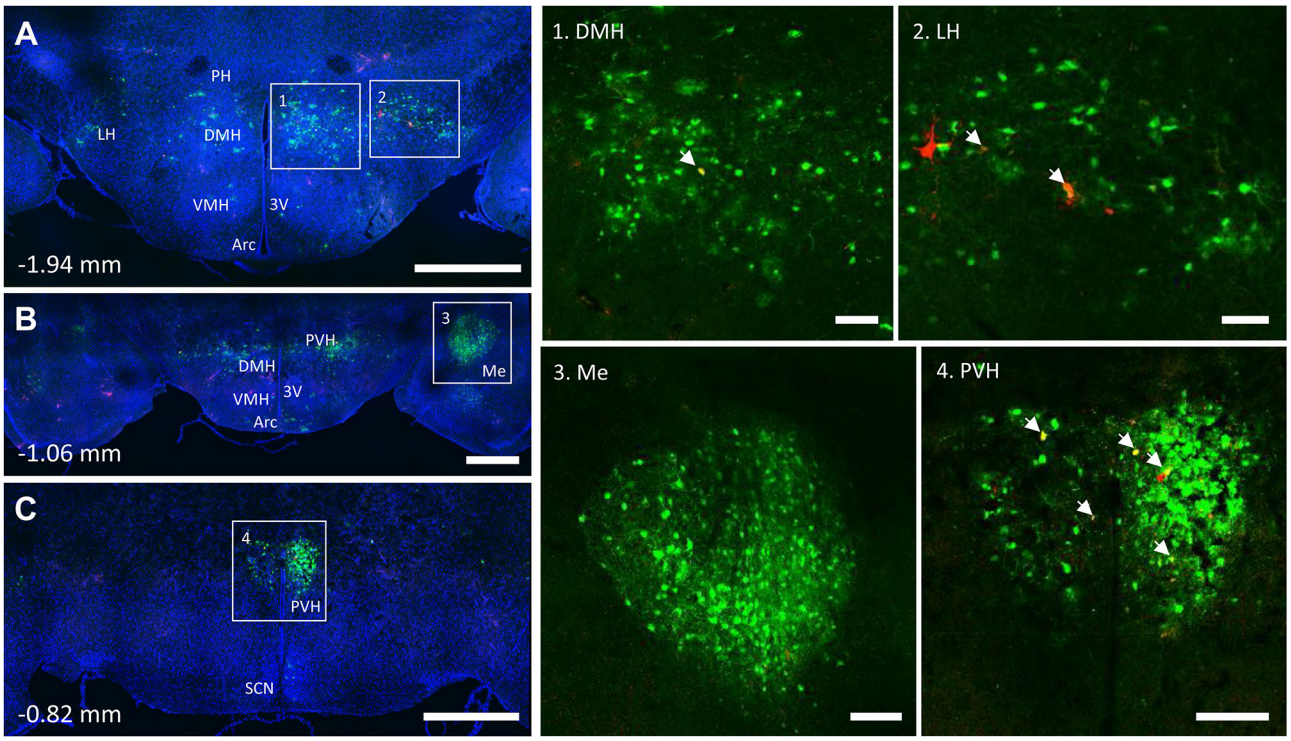

FIGURE 7 | Co-infection of neurons from bone marrow/BMAT and iWAT in the hypothalamus. In the presented case, green neurons are traced from the tibia, whilst red neurons are from iWAT. Yellow neurons are those that have become infected with both viruses (white arrows). **(A)** Overview of hypothalamic tracing at −1.94 mm from bregma. Scale bar = 1 mm. **(B)** Overview of hypothalamic tracing, including amygdala, at −1.06 mm from bregma. Scale bar = 1 mm. **(C)** Medial portion of the paraventricular hypothalamus and suprachiasmatic nucleus at −0.82 mm from bregma. Scale bar = 1 mm. Insets: (1) dorsomedial hypothalamus (DMH), scale = 100 μm, (2) lateral hypothalamus (LH), scale = 100 μm, (3) amygdala (Me), scale = 200 μm and (4) paraventricular hypothalamus (PVH), scale = 200 μm. Regions identified include: third ventricle (3V), arcuate nucleus (Arc), dorsomedial hypothalamus (DMH), lateral hypothalamus (LH), amygdala (Me), posterior hypothalamus (PH), paraventricular hypothalamus (PVH), and suprachiasmatic nucleus (SCN).

evaluate the functional roles of the identified central regulatory regions on BMAT, particularly within the contexts of shared regulation of WAT, bone, and bone marrow.

Innervation of BMAT

The presence of sympathetic neurons in the skeleton is well established (9–12). Similarly, the innervation of WAT adipocytes is well-documented (42, 43). In WAT, EM studies demonstrate that ∼5% of WAT adipocytes are immediately adjacent to a sympathetic nerve axon (43). By contrast, beige or brown adipocytes have an innervation rate that approaches 100%, often with multiple nerve fibers per cell (43, 44). Our results suggest that TH+ innervation of BMAT is more similar to what has been documented for WAT, with ∼5–25% of the BMAT adipocytes located immediately adjacent to a TH+ axon (**Figure 2**). This helps to define when and where locally-released neurotransmitters have the potential to act directly on the cells. Conversely, it suggests that upwards of 70% of BMAT adipocytes are relatively disconnected from the local adrenergic nerve supply (though regulatory impulses could be communicated indirectly or by diffusion). In the metaphysis, TH+ axons were occasionally observed to branch and terminate in regions of BMAT. In the diaphysis, the trajectory of the axons was generally restricted to the arterial vasculature, with less branching. It is unknown whether positioning of a BMAT adipocyte near an axon along its length vs. at the termini impacts the ability of the neuron to act on the cell. In other organ systems, axons have been shown to release neurotransmitters along their entire length (45). More work is needed, however, based on this data it is clear that TH+ neurons are well-positioned to signal to a subset of BMAT cells.

Shared Pathways—Vasoregulatory Responses

A key strength of these experiments is our ability to examine the results within the context of the extensive range of previously published PRV tracing studies across most major organ systems. Upon doing so, several patterns emerge. First, there are multiple regions that have been traced in nearly all studies to date. This includes early infection in areas of the pontine and medullary reticular formation, RVLM, raphe nuclei, and PVH from organs including spleen (21, 22), kidney (23, 24), adrenal gland (25), BAT (5, 27), sympathetic ganglia (25), pancreas (26), lumbar muscle (46), and iWAT/eWAT (4). These structures represent a common neural circuit controlling sympathetic autonomic outflow to a diverse set of organs (**Figure 8**). One likely explanation for this is the need for coordinated, whole-body regulation of vascular tone

TABLE 2 | Traced brain regions—B6 tibia and femur bone marrow (inclusive of BMAT).

Region of the brain (from B6 mice)	Abbreviation	Tibia (*N* = 4)	Femur (*N* = 3)
PONS			
Barrington's Nucleus	BN	4	2
Locus coeruleus	LC	4	3
Subcoeruleus nucleus	SLC	3	3
MIDBRAIN			
Dorsomedial periaqueductal gray	DMPAG	0	1
Lateral periaqueductal gray	LPAG	1	2
Ventrolateral periaqueductal gray	VLPAG	3	2
HYPOTHALAMUS			
Paraventricular hypothalamic nucleus, dorsal cap	PaDC	4	3
Paraventricular hypothalamic nucleus, lateral magnocellular part	PaLM	3	3
Paraventricular hypothalamic nucleus, medial magnocellular part	PaMM	3	3
Paraventricular hypothalamic nucleus, posterior part	PaMP	4	3
Paraventricular hypothalamic nucleus, medial parvicellular part	PaPo	4	3
Lateral hypothalamus	LH	2	2
Posterior hypothalamic area	PH	2	2
Arcuate nucleus	Arc	0	2
Dorsomedial hypothalamus	DMH	2	2
Ventromedial hypothalamus	VMH	0	2
Suprachiasmatic nucleus	SCN	2	2
OTHERS			
Amygdala	Me	1	2
Pyriform cortex	Pir	0	2

by the autonomic nervous system (47). For example, functional studies in cats and primates demonstrate that stimulation of the PVH causes systemic vasopressor responses that are mediated by the descending autonomic vasomotor fibers on the surface of the spinal cord, which synapse on SPNs in the IML to signal to peripheral tissues (48). In our study, this is consistent with prominent labeling in regions including the PVH (**Figure 7**), the surface of the lateral funiculus of the spinal cord, the SPNs of the IML nucleus and the medially associated cord/SPN regions such as the intercalated nucleus and central autonomic area (lamina X) (**Figure 3**) (49). Similarly, the pre-sympathetic neurons of the RVLM, traced from both sites in this study, are a key source of excitatory inputs to the SPNs in the spinal cord that help to maintain baseline arterial pressure (**Figure 4**) (50).

Many of these areas have also been implicated in reflex autonomic control of vascular tone, a collection of diverse mechanisms by which the body integrates information from peripheral sensory inputs to subsequently coordinate autonomic responses. Within the spinal cord, for example, stimulation of sensory roots can influence the activity of autonomic SPNs (48). Locally, this may be explained by modulation of SPNs by autonomic interneurons within the dorsal horn (**Figure 3**) [discussed in (51, 52)]. To date, pre-sympathetic interneurons have been identified in laminae V, VII, and X. In our study, we also observed tracing in these laminae (**Figure 3**), emphasizing the potential for integration and modulation of sensory and sympathetic signals to iWAT/BMAT within the spinal cord (48). Integration also occurs within the brain. From this study, labeled central sites including the LC, NTS, RVLM, and medullary raphae (ROb, RMg, RPa) have the potential to integrate peripheral sensory inputs (e.g., somatosensory stimuli, peripheral chemoreceptors, arterial baroreceptors) with subsequent regulation of autonomic responses, including vascular tone (47, 50, 53–55). Thus, our work puts bone marrow/BMAT and iWAT into the same vasoregulatory network as organs including the spleen, kidney, adrenal gland, BAT, muscle and pancreas; however, future functional studies are needed to explore differences, if any, in the magnitude and timing of centrally-evoked responses.

Shared Pathways—Energy Utilization and Lipolysis

Nerve endings in both WAT and bone marrow exist as free terminals and lack conventional synapses with surrounding cells [reviewed in (56)]. Thus, peripheral neurotransmission is mediated by bulk release and diffusion of signaling factors. The catecholamine norepinephrine has a well-established role in mediating SNS activity to peripheral tissues. Norepinephrine controls local SNS-mediated vasoregulation (57), SNS-mediated lipolysis (56, 58), and SNS-mediated thermogenesis/beiging (59). Though its expression is not restricted to neurons, there is also evidence that neuropeptide Y (NPY), another sympathetic neurotransmitter, can regulate peripheral adipose tissues both *via* central circuits and locally through direct actions on adipocytes and surrounding cells (60, 61). This emphasizes that those central pathways which cause bulk peripheral neurotransmitter release, as described above for vasoregulation, may also promote lipolysis and/or adipose tissue thermogenesis. Few studies have examined the effect of sympathetic neurotransmitters on BMAT directly and this is an area that could be the further explored in the future.

Central integration of peripheral inputs is similarly critical to ensure optimal autonomic contributions to energy partitioning. A key mediator of this relationship is the adipocyte-secreted hormone leptin. Our viral tracing demonstrated prominent labeling from iWAT and bone marrow/BMAT in leptin-responsive regions such as the PVH, ARC, DMH, VMH, and AP. In addition to known actions on food intake, leptin has been implicated in the central regulation of bone marrow and peripheral adipocytes. Studies examining leptin deficient models (*ob/ob*) have found increased BMAT (62, 63). Leptin treatment of *ob/ob* mice reduces BMAT number and size due to lipid mobilization and apoptosis whilst simultaneously increasing bone formation (63, 64). In addition, leptin delivery to the VMH of healthy rats for 5 days induces a significant depletion of peripheral fat pads and also BMAT (65); this functionally demonstrates that central regulatory regions such as the VMH, also identified in our study, can simultaneously influence both BMAT and peripheral adipose tissues.

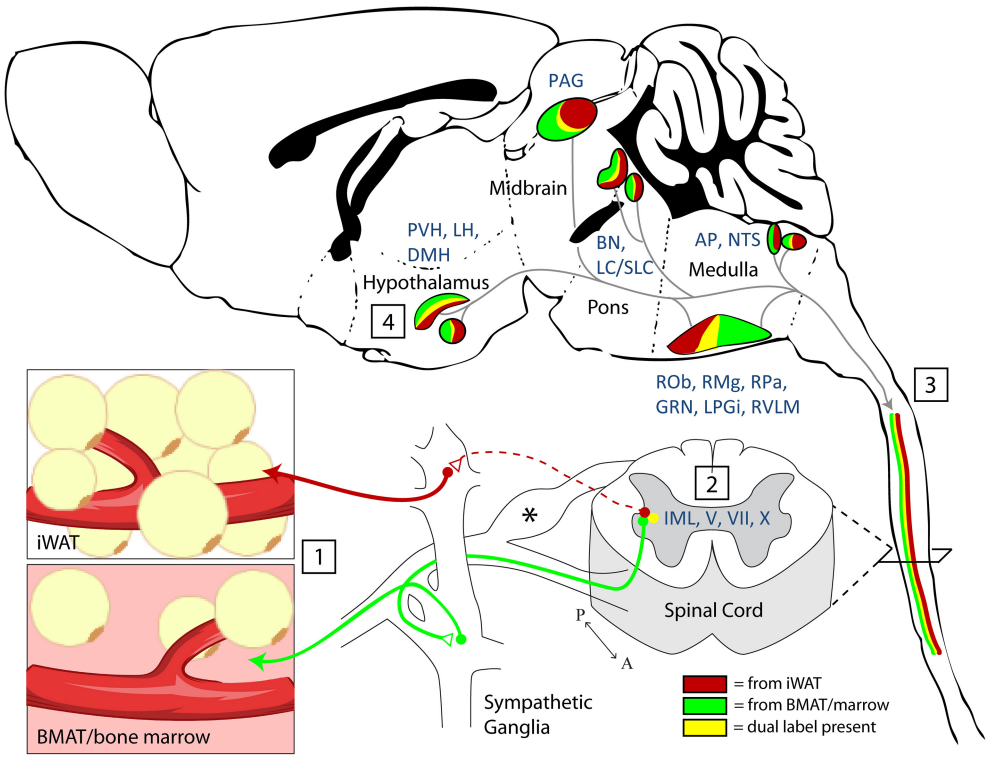

FIGURE 8 | Summary and model. (1) Nerve endings were infected by PRV-bartha virus after local injection into inguinal white adipose tissue (iWAT) or regions of BMAT in the proximal tibia. (2) Infection of sympathetic post-ganglionic axons and their ganglionic cell bodies progressed to infect the sympathetic preganglionic neurons (SPNs) within the intermediolateral nucleus (IML) of the spinal cord. Infection within the spinal cord was also noted across the intercalated nucleus and in laminae V, VII, and X. *Infection was also present in the dorsal root ganglia. This is due to the ability of PRV-Bartha to infect free endings of afferent neurons. However, after this, it is not able to traffic across afferent synapses toward the brain. (3) Viral tracing ascended through efferent pathways to central brain regions (4). The full list of traced regions is available in **Tables 1**, **2**. Functionally, traced central regions are capable of coordinating autonomic signals through shared pathways, which descend to the target tissues. These regions have previously been implicated in regulation of vascular tone, lipolysis, and bone turnover.

Regulation of Skeletal Homeostasis

While our focus is on adipose tissue comparisons, it should be noted that the bone injections would label nerves that interact with a heterogeneous population of cells: bone cells, bone marrow, and BMAT. Signaling in the VMH, for example, may link bone marrow with splenic innervation. Functionally, the VMH has been shown to suppress splenic lymphocyte activity (66) and natural killer cell cytotoxicity (67) demonstrating a clear role for sympathetic regulation of hematopoietic cells in spleen that may mirror what has been described for bone marrow (68).

In addition to hematopoiesis, for the past two decades, there have been numerous studies demonstrating the effects of central regulation on bone mass; interactions between the brain and bone mass have primarily focused on the hypothalamus (13, 14, 69). Consistent with this, we observed robust staining from bone to hypothalamic regions: LH, PH, ARC, DMH, VMH, and SCN. To date, the arcuate nucleus has a well-established role in regulating bone mass through AgRP/NPY neurons (70, 71) and more recently Kiss neurons (72). Interestingly, deletion of the estrogen receptor from Kiss1 neurons had sex-specific effects on bone mass with females having a striking 500% increase in cancellous bone mass in the distal femur, whilst males had normal bone mass in comparison to control WT mice (72). These studies, while focused on a single regulatory center of the brain, the arcuate nucleus, demonstrate the potential impact of modulating neuronal activity on the bone microenvironment. This same region is strongly linked to the regulation of energy homeostasis and the modulation of BAT and WAT, thus is a good candidate to further study to elucidate the effect of arcuate neurons on BMAT.

Similar to other adipose tissues, the bone microenvironment is also influenced by circulating cues such as leptin, which can influence sympathetic tone and also act directly on progenitor cells within the skeleton [reviewed in (73)]. Early work by Karsenty et al. demonstrated that leptin could inhibit bone formation via a central hypothalamic relay (13); this work predominantly examined the effects on vertebral bone mass, a site in the mouse that does not typically have many bone marrow adipocytes. The effects of leptin on bone have been complicated and been much debated; in *ob/ob* mice restoration of peripheral leptin signaling has an anabolic effect on bone mass (74), which opposes the central effects. This was also demonstrated when Prrx1-cre or Col3.6-cre was used to remove the leptin receptor; these mice had a significant increase in bone mass (75, 76).

In addition to the hypothalamus, the area postrema (AP) is another region that can respond to physiological factors

as they enter the CNS and can influence autonomic control (77). The subpostrema, a V-shaped area, is located adjacent to the AP and on the upper limit of the commissural part of the NTS; it too is involved in autonomic regulation and provides bidirectional connections between area postrema and the NTS (78). Recently, Zhang et al. determined that Neuropeptide FF receptor 2 (Npffr2) signaling regulated NPY neuron activity in the arcuate nucleus and influenced BAT activity via the PVH (79). In addition to Npffr2 expression in the ARC, retrograde tracing from the ARC demonstrated that brainstem regions such as the area postrema, subpostrema, and NTS could provide input and regulate ARC neurons (79). Npffr2 deficient mice on a high fat diet show increased adiposity, reduced whole body energy expenditure, reduced UCP-1 protein in BAT and increases in cancellous bone mass (79). This study shows that brainstem neurons are able to influence the hypothalamus and regulate the bone microenvironment.

Other factors also implicated in energy homeostasis have been shown to influence the bone microenvironment *via* central signaling. Kajimura et al. (80) showed that adiponectin could influence sympathetic tone by regulating neurons within the locus coeruleus; leading to an inhibition of bone formation and increased bone resorption through RANKL (80). Notably, the central actions of adiponectin were apparent in older adiponectin deficient mice and differed from younger mice. Young adiponectin deficient mice had reduced bone mass, consistent with the direct effects of adiponectin to inhibit proliferation and induce apoptosis in osteoblasts (80). Similarly, hypocretin (also known as orexin) has been reported to reduce serum leptin levels *via* central signaling and reduce cancellous bone mass (81). Although sympathetic tone was not evaluated in that study, the changes in central orexin signaling were abolished in leptin deficient (*ob/ob*) mice suggesting that changes in leptin levels are affecting sympathetic tone (81). These studies highlight the notion that peptides can act through multiple pathways and thus, our study is a good tool for identifying potential regulatory regions that influence BMAT to assist with examining and targeting these central effects.

LIMITATIONS

While we hypothesize that there may be unique sites that signal to the BMAT environment in a context-specific manner, our viral tract tracing is limited as it is only able to establish the presence of infection and co-infection *vs.* iWAT. For example, we identified infected neurons from bone marrow/BMAT in only 2 out of 5 cases of positive PRV infection in the VMH, but not when traced from iWAT (**Table 1**). However, previous work has shown that stimulation of the leptin-responsive neurons in the VMH significantly affects both WAT and BMAT adipose tissue depots (65). Thus, the absence of infection in neuronal tracing studies does not mean that a region is functionally unimportant. In addition, while we can focus and integrate information known about single neural sites, it is also important to consider that these central regulatory regions are connected and interact with each other, i.e., the arcuate nucleus sends projections to other regions within the hypothalamus (82), that subsequently project to other parts such as the locus coeruleus, solitary tract, and reticular formation. Thus, several regions may actually work together to regulate bone, bone marrow and BMAT. Lastly, though expression of TH has been widely used to characterize peripheral nerves within bone, bone marrow, and the periosteum (9, 11, 83, 84), it has the potential to be upregulated with nerve stimulation (85). Thus, it is possible that the proportion of TH+ nerve-associated BMAT adipocytes may be higher in settings of increased sympathetic tone.

PROSPECTUS AND CONCLUSION

A large proportion of work into understanding the neural regulation of adipose tissue was originally performed in Siberian hamsters. Siberian hamsters (*Phodopus sungorus*) display large variations in body composition depending on the photoperiod they are exposed to: hamsters exposed to long days can have around 50% adiposity whilst exposure to shorter days leads to around 20% adiposity (86, 87). This connection between circadian rhythm and adiposity suggested a potential role for the CNS in regulating adipose tissue. While there are distinctive roles of the SNS in regulating brown adipose tissue (BAT) function in comparison to WAT, PRV retrograde tracing reveals that the central regulatory regions are similar between these peripheral adipose depots (5, 27). Consistent with this, we demonstrate that PRV tracing from bone marrow/BMAT identifies many of the same regions. In addition, we define a novel population of dual PRV-infected "command" neurons that are connected to both bone marrow/BMAT and iWAT. These neurons may coordinate multiple aspects of sympathetic output and facilitate parallel processing for local effects such as lipolysis, thermogenesis and vasoregulation (88–92). Moving forward, more work is needed, both at the level of the brain and locally within the bone marrow, to understand how and in what contexts neural impulses are necessary regulators of BMAT function.

DATA AVAILABILITY STATEMENT

The datasets generated for this study are available on request to the corresponding author.

ETHICS STATEMENT

The Institutional Animal Care and Use Committee (IACUC) at Washington University in St. Louis approved all procedures, and these experiments were performed in AAALAC accredited facilities.

AUTHOR CONTRIBUTIONS

NW and ES conception of the work. NW, ML, YB, MJ, and ES acquisition and analysis of data, approved final copy of manuscript. NW, MJ, and ES interpretation of the data and drafting of the manuscript.

FUNDING

This work was funded by grants from the National Institutes of Health including R01NS091439, P40-RR018604, R00-DE024178, U01-DK116317, and P30-AR057235.

ACKNOWLEDGMENTS

We would like to thank Ron Perez and the Hope Center Neurosurgical Core at Washington University in St. Louis for assistance with the viral injections. Thank you to Zhaohua Wang for technical assistance with the dissections. We would like to thank the Hope Center Alafi Neuroimaging Core for access to the Nanozoomer. Viruses were obtained from the CNNV and we appreciate the feedback received from Dr. Lynn Enquist (cnnv.pitt.edu, funded by P40-RR018604).

SUPPLEMENTARY MATERIAL

The Supplementary Material for this article can be found online at: https://www.frontiersin.org/articles/10.3389/fendo.2019.00668/full#supplementary-material

Supplemental Figure 1 | Paraventricular hypothalamus from all C3H mice injected with PRV into the tibia or iWAT. Medial portion of the paraventricular hypothalamus from each mouse injected with either PRV-152 (GFP) or PRV-614 (RFP) and the site of injection, tibia or iWAT. Scale bar: 1 mm.

Supplemental Figure 2 | PRV infection from bone marrow/BMAT traces to various parts within paraventricular hypothalamus. PRV-152 (GFP) was injected into the tibia and the following sites showed PRV infection: **(A)** Suprachiasmatic nucleus (SCN) and paraventricular hypothalamic nuclei: dorsal cap (PaDC), lateral magnocellular part (PaLM), and medial magnocellular part (PaMM); **(B)** Posterior paraventricular hypothalamic nuclei: posterior part (PaMP) and medial parvicellular part (PaPo).

Supplemental Figure 3 | Amygdala and pyriform cortex traced from tibia. **(A)** Overview of brain slice. **(B)** Amygdala. **(C)** Overview of pyriform cortex relative to amygdala. **(D)** Pyriform cortex.

Supplemental Figure 4 | Paraventricular hypothalamus from all B6 mice injected with PRV into the tibia or iWAT. Medial portion of the paraventricular hypothalamus from each mouse injected with either PRV-152 (GFP) or PRV-614 (RFP) and the site of injection, tibia or iWAT. Scale bar: 1 mm.

Supplemental Table 1 | Antibodies used for immunostaining.

REFERENCES

1. Wiedmann NM, Stefanidis A, Oldfield BJ. Characterization of the central neural projections to brown, white, and beige adipose tissue. *FASEB J*. (2017) 31:4879–90. doi: 10.1096/fj.201700433R
2. Ryu V, Watts AG, Xue B, Bartness TJ. Bidirectional crosstalk between the sensory and sympathetic motor systems innervating brown and white adipose tissue in male Siberian hamsters. *Am J Physiol Regul Integr Comp Physiol*. (2017) 312:R324–37. doi: 10.1152/ajpregu.00456.2015
3. Ryu V, Bartness TJ. Short and long sympathetic-sensory feedback loops in white fat. *Am J Physiol Regul Integr Comp Physiol*. (2014) 306:R886–900. doi: 10.1152/ajpregu.00060.2014
4. Bamshad M, Aoki VT, Adkison MG, Warren WS, Bartness TJ. Central nervous system origins of the sympathetic nervous system outflow to white adipose tissue. *Am J Physiol*. (1998) 275:R291–9. doi: 10.1152/ajpregu.1998.275.1.R291
5. Bamshad M, Song CK, Bartness TJ. CNS origins of the sympathetic nervous system outflow to brown adipose tissue. *Am J Physiol*. (1999) 276:R1569–78. doi: 10.1152/ajpregu.1999.276.6.R1569
6. Bartness TJ, Ryu V. Neural control of white, beige and brown adipocytes. *Int J Obesity Suppl*. (2015) 5:S35–9. doi: 10.1038/ijosup.2015.9
7. Bartness TJ, Shrestha YB, Vaughan CH, Schwartz GJ, Song CK. Sensory and sympathetic nervous system control of white adipose tissue lipolysis. *Mol Cell Endocrinol*. (2010) 318:34–43. doi: 10.1016/j.mce.2009.08.031
8. Scheller EL, Cawthorn WP, Burr AA, Horowitz MC, MacDougald OA. Marrow adipose tissue: trimming the fat. *Trends Endocrinol Metab*. (2016) 27:392–403. doi: 10.1016/j.tem.2016.03.016
9. Mach DB, Rogers SD, Sabino MC, Luger NM, Schwei MJ, Pomonis JD, et al. Origins of skeletal pain: sensory and sympathetic innervation of the mouse femur. *Neuroscience*. (2002) 113:155–66. doi: 10.1016/S0306-4522(02)00165-3
10. Zhu Y, Ma Y, Elefteriou F. Cortical bone is an extraneuronal site of norepinephrine uptake in adult mice. *Bone Rep*. (2018) 9:188–98. doi: 10.1016/j.bonr.2018.11.002
11. Chartier SR, Mitchell SAT, Majuta LA, Mantyh PW. The changing sensory and sympathetic innervation of the young, adult and aging mouse femur. *Neuroscience*. (2018) 387:178–90. doi: 10.1016/j.neuroscience.2018.01.047
12. Robles H, Park S, Joens MS, Fitzpatrick JAJ, Craft CS, Scheller EL. Characterization of the bone marrow adipocyte niche with three-dimensional electron microscopy. *Bone*. (2019) 118:89–98. doi: 10.1016/j.bone.2018.01.020
13. Ducy P, Amling M, Takeda S, Priemel M, Schilling AF, Beil FT, et al. Leptin inhibits bone formation through a hypothalamic relay: a central control of bone mass. *Cell*. (2000) 100:197–207. doi: 10.1016/S0092-8674(00)81558-5
14. Takeda S, Elefteriou F, Levasseur R, Liu X, Zhao L, Parker KL, et al. Leptin regulates bone formation via the sympathetic nervous system. *Cell*. (2002) 111:305–17. doi: 10.1016/S0092-8674(02)01049-8
15. Elefteriou F, Ahn JD, Takeda S, Starbuck M, Yang X, Liu X, et al. Leptin regulation of bone resorption by the sympathetic nervous system and CART. *Nature*. (2005) 434:514–20. doi: 10.1038/nature03398
16. Wee NK, Kulkarni RN, Horsnell H, Baldock PA. The brain in bone and fuel metabolism. *Bone*. (2016) 82:56–63. doi: 10.1016/j.bone.2015.10.020
17. Card JP, Enquist LW. Transneuronal circuit analysis with pseudorabies viruses. *Curr Protoc Neurosci*. (2001) Chapter 1:Unit1.5. doi: 10.1002/0471142301.ns0105s09
18. Card JP, Enquist LW. Use and Visualization of Neuroanatomical Viral Transneuronal Tracers. In: Badoer E, editor. *Visualization Techniques*. Totowa, NJ: Humana Press (2012). p. 225–68.
19. Card JP, Enquist LW. Transneuronal circuit analysis with pseudorabies viruses. *Curr Protoc Neurosci*. (2014) 68:1.5.1–39. doi: 10.1002/0471142301.ns0105s68
20. Dénes A, Boldogkoi Z, Uhereczky G, Hornyák A, Rusvai M, Palkovits M, et al. Central autonomic control of the bone marrow: multisynaptic tract tracing by recombinant pseudorabies virus. *Neuroscience*. (2005) 134:947–63. doi: 10.1016/j.neuroscience.2005.03.060
21. Cano G, Sved AF, Rinaman L, Rabin BS, Card JP. Characterization of the central nervous system innervation of the rat spleen using viral transneuronal tracing. *J Comp Neurol*. (2001) 439:1–18. doi: 10.1002/cne.1331
22. Cano G, Card JP, Rinaman L, Sved AF. Connections of Barrington's nucleus to the sympathetic nervous system in rats. *J Auton Nerv Syst*. (2000) 79:117–28. doi: 10.1016/S0165-1838(99)00101-0
23. Schramm LP, Strack AM, Platt KB, Loewy AD. Peripheral and central pathways regulating the kidney: a study using pseudorabies virus. *Brain Res*. (1993) 616:251–62. doi: 10.1016/0006-8993(93)90216-A

24. Weiss ML, Chowdhury SI. The renal afferent pathways in the rat: a pseudorabies virus study. *Brain Res*. (1998) 812:227–41. doi: 10.1016/S0006-8993(98)00950-0
25. Strack AM, Sawyer WB, Hughes JH, Platt KB, Loewy AD. A general pattern of CNS innervation of the sympathetic outflow demonstrated by transneuronal pseudorabies viral infections. *Brain Res*. (1989) 491:156–62. doi: 10.1016/0006-8993(89)90098-X
26. Jansen AS, Hoffman JL, Loewy AD. CNS sites involved in sympathetic and parasympathetic control of the pancreas: a viral tracing study. *Brain Res*. (1997) 766:29–38. doi: 10.1016/S0006-8993(97)00532-5
27. Zhang Y, Kerman IA, Laque A, Nguyen P, Faouzi M, Louis GW, et al. Leptin-receptor-expressing neurons in the dorsomedial hypothalamus and median preoptic area regulate sympathetic brown adipose tissue circuits. *J Neurosci*. (2011) 31:1873–84. doi: 10.1523/JNEUROSCI.3223-10.2011
28. Banfield BW, Kaufman JD, Randall JA, Pickard GE. Development of pseudorabies virus strains expressing red fluorescent proteins: new tools for multisynaptic labeling applications. *J Virol*. (2003) 77:10106–12. doi: 10.1128/JVI.77.18.10106-10112.2003
29. Scheller EL, Doucette CR, Learman BS, Cawthorn WP, Khandaker S, Schell B, et al. Region-specific variation in the properties of skeletal adipocytes reveals regulated and constitutive marrow adipose tissues. *Nat Commun*. (2015) 6:7808. doi: 10.1038/ncomms8808
30. Demmin GL, Clase AC, Randall JA, Enquist LW, Banfield BW. Insertions in the gG gene of pseudorabies virus reduce expression of the upstream Us3 protein and inhibit cell-to-cell spread of virus infection. *J Virol*. (2001) 75:10856–69. doi: 10.1128/JVI.75.22.10856-10869.2001
31. Smith BN, Banfield BW, Smeraski CA, Wilcox CL, Dudek FE, Enquist LW, et al. Pseudorabies virus expressing enhanced green fluorescent protein: A tool for in vitro electrophysiological analysis of transsynaptically labeled neurons in identified central nervous system circuits. *Proc Natl Acad Sci USA*. (2000) 97:9264–9. doi: 10.1073/pnas.97.16.9264
32. Larsen PJ, Enquist LW, Card JP. Characterization of the multisynaptic neuronal control of the rat pineal gland using viral transneuronal tracing. *Eur J Neurosci*. (1998) 10:128–45. doi: 10.1046/j.1460-9568.1998.00003.x
33. Schindelin J, Arganda-Carreras I, Frise E, Kaynig V, Longair M, Pietzsch T, et al. Fiji: an open-source platform for biological-image analysis. *Nat Methods*. (2012) 9:676–82. doi: 10.1038/nmeth.2019
34. Allen Institute for Cell Science. Allen Spinal Atlas. *Allen Brain Atlas*. (2008) Available online at: http://mousespinal.brain-map.org/ (accessed March 31, 2019).
35. *Paxinos and Franklin's the Mouse Brain in Stereotaxic Coordinates*. 4th Edn. Available online at: https://www.elsevier.com/books/paxinos-and-franklins-the-mouse-brain-in-stereotaxic-coordinates/paxinos/978-0-12-391057-8 (accessed April 1, 2019).
36. Imai S, Tokunaga Y, Maeda T, Kikkawa M, Hukuda S. Calcitonin gene-related peptide, substance P, and tyrosine hydroxylase-immunoreactive innervation of rat bone marrows: an immunohistochemical and ultrastructural investigation on possible efferent and afferent mechanisms. *J Orthop Res*. (1997) 15:133–40. doi: 10.1002/jor.1100150120
37. Brazill JM, Beeve AT, Craft CS, Ivanusic JJ, Scheller EL. Nerves in bone: evolving concepts in pain and anabolism. *J Bone Miner Res*. (2019) 34:1393–406. doi: 10.1002/jbmr.3822
38. Martin CD, Jimenez-Andrade JM, Ghilardi JR, Mantyh PW. Organization of a unique net-like meshwork of CGRP+ sensory fibers in the mouse periosteum: implications for the generation and maintenance of bone fracture pain. *Neurosci Lett*. (2007) 427:148–52. doi: 10.1016/j.neulet.2007.08.055
39. Plummer NW, Scappini EL, Smith KG, Tucker CJ, Jensen P. Two subpopulations of noradrenergic neurons in the locus coeruleus complex distinguished by expression of the dorsal neural tube marker pax7. *Front Neuroanat*. (2017) 11:60. doi: 10.3389/fnana.2017.00060
40. Scheller EL, Khandaker S, Learman BS, Cawthorn WP, Anderson LM, Pham HA, et al. Bone marrow adipocytes resist lipolysis and remodeling in response to β-adrenergic stimulation. *Bone*. (2019) 118:32–41. doi: 10.1016/j.bone.2018.01.016
41. Nguyen NL, Randall J, Banfield BW, Bartness TJ. Central sympathetic innervations to visceral and subcutaneous white adipose tissue. *Am J Physiol Regul Integr Comp Physiol*. (2014) 306:R375–86. doi: 10.1152/ajpregu.00552.2013
42. Zeng W, Pirzgalska RM, Pereira MM, Kubasova N, Barateiro A, Seixas E, et al. Sympathetic neuro-adipose connections mediate leptin-driven lipolysis. *Cell*. (2015) 163:84–94. doi: 10.1016/j.cell.2015.08.055
43. Loncar D, Afzelius BA, Cannon B. Epididymal white adipose tissue after cold stress in rats. I. Nonmitochondrial changes. *J Ultrastruct Mol Struct Res*. (1988) 101:109–22. doi: 10.1016/0889-1605(88)90001-8
44. Lončar D, Bedrica L, Mayer J, Cannon B, Nedergaard J, Afzelius BA, et al. The effect of intermittent cold treatment on the adipose tissue of the cat. *J Ultrastruct Mol Struct Res*. (1986) 97:119–29. doi: 10.1016/S0889-1605(86)80012-X
45. Thyssen A, Hirnet D, Wolburg H, Schmalzing G, Deitmer JW, Lohr C. Ectopic vesicular neurotransmitter release along sensory axons mediates neurovascular coupling via glial calcium signaling. *Proc Natl Acad Sci USA*. (2010) 107:15258–63. doi: 10.1073/pnas.1003501107
46. Xiang HB, Liu C, Liu TT, Xiong J. Central circuits regulating the sympathetic outflow to lumbar muscles in spinally transected mice by retrograde transsynaptic transport. *Int J Clin Exp Pathol*. (2014) 7:2987–97.
47. Morrison SF. Medullary raphe neurons in autonomic regulation. In: NJ Dun, BH Machado, PM. Pilowsky, editors. *Neural Mechanisms of Cardiovascular Regulation*. Boston, MA: Springer (2004). p. 245–64. doi: 10.1007/978-1-4419-9054-9_11
48. Kerr FWL, Alexander S. Descending autonomic pathways in the spinal cord. *Arch Neurol*. (1964) 10:249–61. doi: 10.1001/archneur.1964.00460150019002
49. Vera PL, Ellenberger HH, Haselton JR, Haselton CL, Schneiderman N. The intermediolateral nucleus: an "open" or "closed" nucleus? *Brain Res*. (1986) 386:84–92. doi: 10.1016/0006-8993(86)90144-7
50. Zoccal DB, Furuya WI, Bassi M, Colombari DS, Colombari E. The nucleus of the solitary tract and the coordination of respiratory and sympathetic activities. *Front Physiol*. (2014) 5:238. doi: 10.3389/fphys.2014.00238
51. Deuchars SA. Multi-tasking in the spinal cord–do "sympathetic" interneurones work harder than we give them credit for? *J Physiol*. (2007) 580:723–9. doi: 10.1113/jphysiol.2007.129429
52. Deuchars SA. How sympathetic are your spinal cord circuits? *Exp Physiol*. (2015) 100:365–71. doi: 10.1113/EP085031
53. Elam M, Svensson TH, Thorén P. Locus coeruleus neurons and sympathetic nerves: activation by cutaneous sensory afferents. *Brain Res*. (1986) 366:254–61. doi: 10.1016/0006-8993(86)91302-8
54. Ruggiero DA, Underwood MD, Mann JJ, Anwar M, Arango V. The human nucleus of the solitary tract: visceral pathways revealed with an "in vitro" postmortem tracing method. *J Auton Nerv Syst*. (2000) 79:181–90. doi: 10.1016/S0165-1838(99)00097-1
55. McCulloch PF, Panneton WM, Guyenet PG. The rostral ventrolateral medulla mediates the sympathoactivation produced by chemical stimulation of the rat nasal mucosa. *J Physiol*. (1999) 516 (Pt 2):471–84. doi: 10.1111/j.1469-7793.1999.0471v.x
56. Bartness TJ, Liu Y, Shrestha YB, Ryu V. Neural innervation of white adipose tissue and the control of lipolysis. *Front Neuroendocrinol*. (2014) 35:473–93. doi: 10.1016/j.yfrne.2014.04.001
57. Kvietys PR. *Extrinsic Vasoregulation: Neural and Humoral*. (2010) Available online at: https://www.ncbi.nlm.nih.gov/books/NBK53091/
58. Brito NA, Brito MN, Bartness TJ. Differential sympathetic drive to adipose tissues after food deprivation, cold exposure or glucoprivation. *Am J Physiol Regul Integr Comp Physiol*. (2008) 294:R1445–52. doi: 10.1152/ajpregu.00068.2008
59. Cannon B, Nedergaard J. Nonshivering thermogenesis and its adequate measurement in metabolic studies. *J Exp Biol*. (2011) 214:242–53. doi: 10.1242/jeb.050989
60. Kuo LE, Kitlinska JB, Tilan JU, Li L, Baker SB, Johnson MD, et al. Neuropeptide Y acts directly in the periphery on fat tissue and mediates stress-induced obesity and metabolic syndrome. *Nat Med*. (2007) 13:803–11. doi: 10.1038/nm1611
61. Zhang L, Lee IC, Enriquez RF, Lau J, Vähätalo LH, Baldock PA, et al. Stress- and diet-induced fat gain is controlled by NPY in catecholaminergic neurons. *Mol Metabol*. (2014) 3:581–91. doi: 10.1016/j.molmet.2014.05.001
62. Hamrick MW, Pennington C, Newton D, Xie D, Isales C. Leptin deficiency produces contrasting phenotypes in bones of the limb and spine. *Bone*. (2004) 34:376–83. doi: 10.1016/j.bone.2003.11.020

63. Hamrick MW, Della-Fera MA, Choi YH, Pennington C, Hartzell D, Baile CA. Leptin treatment induces loss of bone marrow adipocytes and increases bone formation in leptin-deficient ob/ob mice. *J Bone Miner Res*. (2005) 20:994–1001. doi: 10.1359/JBMR.050103
64. Lindenmaier LB, Philbrick KA, Branscum AJ, Kalra SP, Turner RT, Iwaniec UT. Hypothalamic leptin gene therapy reduces bone marrow adiposity in ob/ob mice fed regular and high-fat diets. *Front Endocrinol.* (2016) 7:110. doi: 10.3389/fendo.2016.00110
65. Hamrick MW, Della Fera MA, Choi YH, Hartzell D, Pennington C, Baile CA. Injections of leptin into rat ventromedial hypothalamus increase adipocyte apoptosis in peripheral fat and in bone marrow. *Cell Tissue Res*. (2007) 327:133–41. doi: 10.1007/s00441-006-0312-3
66. Okamoto S, Ibaraki K, Hayashi S, Saito M. Ventromedial hypothalamus suppresses splenic lymphocyte activity through sympathetic innervation. *Brain Res*. (1996) 739:308–13. doi: 10.1016/S0006-8993(96)00840-2
67. Wrona D, Trojniar W. Suppression of natural killer cell cytotoxicity following chronic electrical stimulation of the ventromedial hypothalamic nucleus in rats. *J Neuroimmunol*. (2005) 163:40–52. doi: 10.1016/j.jneuroim.2005.02.017
68. Katayama Y, Battista M, Kao WM, Hidalgo A, Peired AJ, Thomas SA, et al. Signals from the sympathetic nervous system regulate hematopoietic stem cell egress from bone marrow. *Cell*. (2006) 124:407–21. doi: 10.1016/j.cell.2005.10.041
69. Rowe GC, Vialou V, Sato K, Saito H, Yin M, Green TA, et al. Energy expenditure and bone formation share a common sensitivity to AP-1 transcription in the hypothalamus. *J Bone Miner Res*. (2012) 27:1649–58. doi: 10.1002/jbmr.1618
70. Kim JG, Sun BH, Dietrich MO, Koch M, Yao GQ, Diano S, et al. Agrp neurons regulate bone mass. *Cell Rep*. (2015) 13:8–14. doi: 10.1016/j.celrep.2015.08.070
71. Baldock PA, Sainsbury A, Couzens M, Enriquez RF, Thomas GP, Gardiner EM, et al. Hypothalamic Y2 receptors regulate bone formation. *J Clin Invest*. (2002) 109:915–21. doi: 10.1172/JCI0214588
72. Herber CB, Krause WC, Wang L, Bayrer JR, Li A, Schmitz M, et al. Estrogen signaling in arcuate Kiss1 neurons suppresses a sex-dependent female circuit promoting dense strong bones. *Nat Commun*. (2019) 10:163. doi: 10.1038/s41467-018-08046-4
73. Wee NK, Baldock PA. The Skeletal Effects of Leptin. In: Blum EL, editor. *Leptin: Biosynthesis, Functions and Clinical Significance. Endocrinology Research and Clinical Developments*. Hauppauge, NY: Nova Science Publishers (2014). p. 129–40.
74. Iwaniec UT, Boghossian S, Lapke PD, Turner RT, Kalra SP. Central leptin gene therapy corrects skeletal abnormalities in leptin-deficient ob/ob mice. *Peptides*. (2007) 28:1012–9. doi: 10.1016/j.peptides.2007.02.001
75. Yue R, Zhou BO, Shimada IS, Zhao Z, Morrison SJ. Leptin receptor promotes adipogenesis and reduces osteogenesis by regulating mesenchymal stromal cells in adult bone marrow. *Cell Stem Cell*. (2016) 18:782–96. doi: 10.1016/j.stem.2016.02.015
76. Scheller EL, Song J, Dishowitz MI, Soki FN, Hankenson KD, Krebsbach PH. Leptin functions peripherally to regulate differentiation of mesenchymal progenitor cells. *Stem Cells*. (2010) 28:1071–80. doi: 10.1002/stem.432
77. Smith PM, Brzezinska P, Hubert F, Mimee A, Maurice DH, Ferguson AV. Leptin influences the excitability of area postrema neurons. *Am J Physiol Regul Integr Comp Physiol*. (2016) 310:R440–8. doi: 10.1152/ajpregu.00326.2015
78. Fodor M, Palkovits M, Gallatz K. Fine structure of the area subpostrema in rat. Open gate for the medullary autonomic centers. *Ideggyogy Sz*. (2007) 60:83–8.
79. Zhang L, Ip CK, Lee ICJ, Qi Y, Reed F, Karl T, et al. Diet-induced adaptive thermogenesis requires neuropeptide FF receptor-2 signalling. *Nat Commun*. (2018) 9:4722. doi: 10.1038/s41467-018-06462-0
80. Kajimura D, Lee HW, Riley KJ, Arteaga-Solis E, Ferron M, Zhou B, et al. Adiponectin regulates bone mass via opposite central and peripheral mechanisms through FoxO1. *Cell Metab*. (2013) 17:901–15. doi: 10.1016/j.cmet.2013.04.009
81. Wei W, Motoike T, Krzeszinski JY, Jin Z, Xie XJ, Dechow PC, et al. Orexin regulates bone remodeling via a dominant positive central action and a subordinate negative peripheral action. *Cell Metab*. (2014) 19:927–40. doi: 10.1016/j.cmet.2014.03.016
82. Bouret SG, Draper SJ, Simerly RB. Formation of projection pathways from the arcuate nucleus of the hypothalamus to hypothalamic regions implicated in the neural control of feeding behavior in mice. *J Neurosci*. (2004) 24:2797–805. doi: 10.1523/JNEUROSCI.5369-03.2004
83. Hill EL, Elde R. Distribution of CGRP-, VIP-, D beta H-, SP-, and NPY-immunoreactive nerves in the periosteum of the rat. *Cell Tissue Res*. (1991) 264:469–80. doi: 10.1007/BF00319037
84. Cherruau M, Morvan FO, Schirar A, Saffar JL. Chemical sympathectomy-induced changes in TH-, VIP-, and CGRP-immunoreactive fibers in the rat mandible periosteum: influence on bone resorption. *J Cell Physiol*. (2003) 194:341–8. doi: 10.1002/jcp.10209
85. Chevalier J, Derkinderen P, Gomes P, Thinard R, Naveilhan P, Vanden Berghe P, et al. Activity-dependent regulation of tyrosine hydroxylase expression in the enteric nervous system. *J Physiol.* (2008) 586:1963–75. doi: 10.1113/jphysiol.2007.149815
86. Wade GN, Bartness TJ. Effects of photoperiod and gonadectomy on food intake, body weight, and body composition in Siberian hamsters. *Am J Physiol*. (1984) 246:R26–30. doi: 10.1152/ajpregu.1984.246.1.R26
87. Bartness TJ, Hamilton JM, Wade GN, Goldman BD. Regional differences in fat pad responses to short days in Siberian hamsters. *Am J Physiol*. (1989) 257:R1533–40. doi: 10.1152/ajpregu.1989.257.6.R1533
88. Jansen AS, Nguyen XV, Karpitskiy V, Mettenleiter TC, Loewy AD. Central command neurons of the sympathetic nervous system: basis of the fight-or-flight response. *Science*. (1995) 270:644–6. doi: 10.1126/science.270.5236.644
89. Stefanidis A, Wiedmann NM, Adler ES, Oldfield BJ. Hypothalamic control of adipose tissue. *Best Pract Res Clin Endocrinol Metab*. (2014) 28:685–701. doi: 10.1016/j.beem.2014.08.001
90. Oldfield BJ, Allen AM, Davern P, Giles ME, Owens NC. Lateral hypothalamic "command neurons" with axonal projections to regions involved in both feeding and thermogenesis. *Eur J Neurosci*. (2007) 25:2404–12. doi: 10.1111/j.1460-9568.2007.05429.x
91. Krout KE, Mettenleiter TC, Loewy AD. Single CNS neurons link both central motor and cardiosympathetic systems: a double-virus tracing study. *Neuroscience*. (2003) 118:853–66. doi: 10.1016/S0306-4522(02)00997-1
92. Kerman IA, Enquist LW, Watson SJ, Yates BJ. Brainstem substrates of sympatho-motor circuitry identified using trans-synaptic tracing with pseudorabies virus recombinants. *J Neurosci*. (2003) 23:4657–66. doi: 10.1523/JNEUROSCI.23-11-04657.2003

Conflict of Interest: The authors declare that the research was conducted in the absence of any commercial or financial relationships that could be construed as a potential conflict of interest.

frontiers in Endocrinology

CORRECTION
published: 22 January 2020
doi: 10.3389/fendo.2019.00904

Corrigendum: Shared Autonomic Pathways Connect Bone Marrow and Peripheral Adipose Tissues Across the Central Neuraxis

Natalie K. Y. Wee[1,2], *Madelyn R. Lorenz*[1], *Yusuf Bekirov*[1], *Mark F. Jacquin*[3] and *Erica L. Scheller*[1,4]*

[1] Division of Bone and Mineral Diseases, Department of Medicine, Washington University School of Medicine, St. Louis, MO, United States, [2] Department of Reconstructive Sciences, UConn Health, Farmington, CT, United States, [3] Department of Neurology, Washington University School of Medicine, St. Louis, MO, United States, [4] Department of Cell Biology and Physiology, Washington University School of Medicine, St. Louis, MO, United States

Keywords: bone marrow adipose tissue, fat, brain-bone interactions, pseudorabies virus, viral tract tracing, energy metabolism, sympathetic nerve, autonomic nervous system

OPEN ACCESS

Approved by:
Frontiers Editorial Office, Frontiers Media SA, Switzerland

***Correspondence:**
Erica L. Scheller
scheller@wustl.edu

Specialty section:
This article was submitted to Bone Research, a section of the journal Frontiers in Endocrinology

Received: *10 December 2019*
Accepted: *11 December 2019*
Published: *22 January 2020*

Citation:
Wee NKY, Lorenz MR, Bekirov Y, Jacquin MF and Scheller EL (2020) Corrigendum: Shared Autonomic Pathways Connect Bone Marrow and Peripheral Adipose Tissues Across the Central Neuraxis. Front. Endocrinol. 10:904. doi: 10.3389/fendo.2019.00904

A Corrigendum on

Shared Autonomic Pathways Connect Bone Marrow and Peripheral Adipose Tissues Across the Central Neuraxis

by Wee, N. K. Y., Lorenz, M. R., Bekirov, Y., Jacquin, M. F., and Scheller, E. L. (2019). Front. Endocrinol. 10:668. doi: 10.3389/fendo.2019.00668

There is an error in the **Funding** statement. The correct number for "U01-DR116317" is "U01-DK116317."

The authors apologize for this error and state that this does not change the scientific conclusions of the article in any way. The original article has been updated.

frontiers in Endocrinology

PERSPECTIVE
published: 18 October 2019
doi: 10.3389/fendo.2019.00691

Brief Report From the 4th International Meeting on Bone Marrow Adiposity (BMA2018)

Guillaume Penel[1], *Greet Kerckhofs*[2,3] *and Christophe Chauveau*[1]*

[1] *Inflammatory Bone Diseases Lab, Univ. Littoral Côte d'Opale, Boulogne-Sur-Mer, and Univ. Lille, Lille, and CHU Lille, Lille, France,* [2] *Biomechanics Lab, Institute of Mechanics, Materials and Civil Engineering, UCLouvain, Louvain-la-Neuve, Belgium,* [3] *Department Materials Engineering, KU Leuven, Leuven, Belgium*

The 4th International Meeting on Bone Marrow Adiposity (BMA2018) was hosted at the premises of the Regional Government of *Hauts de France* in Lille, from August 29th to August 31st 2018. This congress brought together physicians and scientists working on rheumatology and bone biology, oncology, hematology, endocrinology, and metabolic diseases, all interested in bone marrow adiposity. They shared their opinions, hypothesis, and original results. Six invited keynotes were given by S. Badr, B.C.J. van der Eerden, M.J. Moreno Aliaga, O. Naveiras, C.J. Rosen, and A.V. Schwartz. Twenty-one short talks were also given. This report briefly summarizes the scientific content of the meeting and the progress of the working groups of the BMA Society (http://bma-society.org/).

Keywords: bone marrow adiposity, bone marrow adipocytes, bone marrow fat, yellow marrow, bone metabolism, bone marrow adiposity society (BMAS)

OPEN ACCESS

Edited by:
Nathalie Bravenboer, VU University Medical Center, Netherlands

Reviewed by:
Beata Lecka-Czernik, University of Toledo, United States
Reinhold Gottfried Erben, University of Veterinary Medicine Vienna, Austria

***Correspondence:**
Christophe Chauveau
chauveau@univ-littoral.fr

Specialty section:
This article was submitted to Bone Research, a section of the journal Frontiers in Endocrinology

Received: *21 June 2019*
Accepted: *23 September 2019*
Published: *18 October 2019*

Citation:
Penel G, Kerckhofs G and Chauveau C (2019) Brief Report From the 4th International Meeting on Bone Marrow Adiposity (BMA2018). Front. Endocrinol. 10:691. doi: 10.3389/fendo.2019.00691

INTRODUCTION

The 4th International congress on Bone Marrow Adiposity (BMA) was hosted at the premises of the Regional Government of *Hauts de France* in Lille, From August 29th to August 31st 2018 (https://bma2018.sciencesconf.org). The meeting was organized by C. Chauveau and G. Penel from the laboratory *Pathophysiology of Inflammatory Bone Diseases* EA4490 (currently becoming *Marrow Adiposity and Bone Lab*) located in Lille (University of Lille) and Boulogne sur Mer (Littoral Côte d'Opale University), with the collaboration of G. Kerckhofs from the Skeletal Biology and Engineering Research Center, KU Leuven, and the Institute of Mechanics Materials and Civil Engineering, UCLouvain, Belgium. Attendees were coming from 13 European countries, Canada and USA.

Three annual meetings were previously organized in Lille, France (https://bma2015.sciencesconf.org) (1); in Rotterdam, the Netherlands (https://adiposity.sciencesconf.org/) (2); and in Lausanne, Switzerland (https://bma2017.sciencesconf.org) (3). The fourth annual meeting, once again organized in Lille, France, brought together physicians and scientists working on rheumatology and bone biology, oncology, hematology, endocrinology, and metabolic diseases, all interested in BMA. The meeting was organized in the continuity of the previous ones, with the same purpose of facilitating exchanges between members of the emerging scientific community interested in BMA. To reflect the diversity of the attendees, oral communications were organized in five sessions: bone marrow adipocyte (BMAd) biology, BMA and clinical translation, BMA imaging, BMA in hematology and cancer, and finally BMA and metabolism. Details on the sessions and the contributors are given in **Appendix A** (Supplementary Material).

For the first time, *Meet the Professor* sessions were organized with the precious involvement of C.J. Rosen and A.V. Schwartz. Finally, each working group, dedicated to *nomenclature*, *methodologies*, *biobank, public engagement, data repositories,* and *sponsorship* met to start or continue its work.

The submitted abstracts were ranked by all members of the Scientific Board of the BMA Society (BMAS), leading to 21 oral presentations and eight poster presentations. Two junior presentations (by M. Tencerova and A. Lovdel) were awarded by the Scientific Board of the BMAS by a free registration for the next BMA congress in Odense, Denmark.

In the present report, data unpublished at the time of the congress were highlighted by the symbol §.

SCIENTIFIC COMMUNICATIONS AND DEBATES

Bone Marrow Adipocyte Biology

Data on the biology of BMAds remain rare and far between. Moreover, some of these data appear to be contradictory. This situation justified a session dedicated to the biology of BMAds including two invited talks given by Prof. C.J. Rosen and Prof. B.C.J. van der Eerden. Based on relevant and remarkable data from the literature and their own work, speakers highlighted the specificity of BMAds related to their location in the skeleton and the hematopoietic niche, their endocrine, paracrine and autocrine functions, and the unique regulation of BMA. The main points presented by C.J. Rosen were: (i) links between PGC1α expression and BMA in mice depending on the bone analyzed (4), (ii) the effect of PTH on BMAd size, perhaps through stimulation of lipolysis (5), (iii) the hypothetic involvement of differentiation and dedifferentiation processes allowing changes between adipocyte and pre-adipocyte states (6), and (iv) links between mitophagy in stromal cell differentiation and their activity or ability to differentiate §. B.C.J. van der Eerden introduced the use of bioinformatics to study skeletal stem cell adipogenesis pathway. His study of the changes that occur in gene expression during the very early moments after induction revealed the first temporality of the processes that lead to adipocyte differentiation. This wide approach allowed the use of Connectivity Map (CMap) leading to the identification of new factors like parbendazole that are highly involved in adipocyte or osteoblast differentiation (7).

Other presented data gave more information on the nature of BMAds. In their study, E.L. Scheller and C.S. Craft used 3D electron microscopy to show that these cells have an extensive mitochondrial network (8). They are capable of adrenergic-induced lipid droplet remodeling but neither of UCP1 expression nor thermogenesis *in vivo* (9).

Relationships between BMAds and RANKL were also discussed in two studies. Indeed, N. Bravenboer showed that BMAds display changing activities like expression of RANKL after ovariectomy §. E. Douni revealed that transgenic overexpression of RANKL is associated in mice with high BMA and high bone resorption. Moreover, the same study showed that the inhibition of osteoclastogenesis is associated with low BMA §. R. Labella demonstrated high bone resorption and high osteoclastogenesis in female mice with a gain of function mutation of Gsα expressed under the control of an AdipoQ promoter, suggesting that BMAds may affect the bone/bone marrow microenvironment through the Gsα/cAMP signaling pathway §. Finally, G. Frangi pointed out links between the inactivation of the sodium-phosphate co-transporter, recently shown to be deleterious for ossification and bone quality (10), and BMA. Interestingly, the induced BMA increase is not associated with changes in plasma levels of adiponectin §.

BMA and Clinical Translation

Prof. A.V. Schwartz gave an invited lecture on the clinical determinants of BMA. While it was shown that BMA is under the control of gonadal and pituitary hormones in rodents, conclusive studies on the changes and differences in BMA that occur between men and women, during life and during menstrual cycle, remain scarce (11). Clinical and translational studies suggest that, depending on the situation or protocol, estradiol and testosterone plasma levels, or treatments with these hormones could be associated with a slightly low vertebral BMA in men and women for both kind of hormone (12, 13).

Data from two observational studies on several hundreds of subjects from the AGES—Reykjavik cohort were presented. The first one, presented by G. Woods, identified high vertebral BMA as a predictor of greater reductions in bone quality in spine, hip and femoral neck of older women §. The second one, presented by A. Veldhuis-Vlug, demonstrated an association between FSH and greater vertebral BMA in older women. Interestingly, for both studies no association was found in older men §.

Data from two interventional studies were also presented. A. Velduis-Vlug, starting from the positive effects of PTH treatment on bone from mice associated with decreased BMA, showed a trend toward lower BMA after treatment with Abaloparatide or Teriparatide in postmenopausal women (Abaloparatide-SC Comparator Trial In Vertebral Endpoints -*Active*- trial) with osteoporosis with beneficial effects on bone §. P.H. Bisschop pointed out the bariatric surgery (Roux-en-Y gastric bypass)-induced decrease in vertebral BMA of non-diabetic post-menopausal women. Compared with other studies, these data lead to suppose different effects of RYGB on BMA and bone depending on menopausal and diabetic statuses §.

BMA Imaging

Exploring *in vivo* bone marrow adiposity (BMA) using clinical imaging tools remains challenging. It is also of crucial interest to bring clinical and basic research closer together, as this could lead to relevant therapeutic solutions. In his invited lecture, S. Badr proposed magnetic resonance imaging (MRI) as the current best available technique to qualitatively and quantitatively assess BMA, especially through single-voxel proton spectroscopy and chemical shift encoding-based water fat imaging. However, interfaces between trabecular bone and BMA foster a local magnetic inhomogeneity that must be taken into consideration to provide accurate measurements (14). He proposed that future works might aim to extend the two main clinically available quantitative parameters—the proton-density fat fraction and

lipid unsaturation level—to other imaging features to best depict BMA.

Additionally, two studies that illustrated what could be expected of MRI tools were presented. N. Sollmann investigated the relationship between vertebral BMA and paraspinal muscle fat composition, two parameters shown to be altered in various diseases. Interestingly, postmenopausal but not premenopausal women display high and correlated levels of fat in the two tissues (15). E. Burian presented a second study designed to better characterize BMA, and particularly its spatial heterogeneity. This feasibility study was driven on healthy pre- and postmenopausal women, using chemical shift encoding-based water-fat magnetic resonance imaging. Data from this study led to the validation of the approach and allowed to conclude to an increased bone marrow heterogeneity in lumbar spine of postmenopausal women (16).

BMA in Hematology and Cancer

The close location of BMAds and hematopoietic stem cells (HSCs) in the bone marrow, as well as results from *in vitro* experiments, support the hypothesis of direct interactions between these two cell types (17). During her invited lecture, Prof. O. Naveiras highlighted the rapid transition from red to yellow marrow within 1–3 weeks after chemotherapy, radiotherapy, or even food restriction and in some situations the fast reversion to red marrow. Also, the differences between environments of endosteal and perivascular HSC were taken into account, and the relationships between BMAds and HSCs seem to be complex because BMAds appear to compromise HSC-derived progenitors but not primitive HSC functions. Moreover, BMAds and preadipocytes seem to act differently on hematopoiesis.

Several studies highlighting these relationships were presented. With the ambition to accelerate the red-to yellow-to red transition after irradiation-induced bone marrow aplasia, S. Rojas-Sutterlin presented a first study that characterized changes of the stromal cell compartment in this situation, and identified phenotypic populations with differential kinetics. The adipocyte differentiation axis was particularly studied and associated with hematopoietic recovery §.

D. Mattiucci showed the results of a second study, also dealing with this relationship but in a caloric restriction situation. He concluded that adiponectin is mainly produced by BMAds in this situation and is not directly acting on bone marrow HSCs, but it contributes to the immunomodulatory effects of caloric restriction §.

M. Reagan studied the involvement of BMAds in the efficacy of antimyeloma treatments with dexamethasone. She showed that BMAds or their conditioned media support MM1S myeloma cells drug resistance, possibly through the action of IL-6. Moreover, treatment with anti-sclerostin antibody to decrease BMA *in vivo* lowers the resistance properties of myeloma cells §.

BMA and Metabolism

It is well-known that obesity and associated disorders are related with dysfunctional white adipose tissue (WAT) metabolism and a secretory pattern. During her invited lecture, Prof. M.J. Moreno Aliaga wondered whether brown adipose tissue (BAT) could be an anti-obesity and anti-diabetic tissue. She highlighted the therapeutical potential of some of the specialized pro-resolving lipid mediators (SPMs) such as maresin1, on dysfunctional adipose tissues (18). In ob/ob and diet-induced obesity mice, this SPM induces beneficial effects on WAT, activates BAT, and decreases insulinemia (19).

Six studies were presented during this session. K. Suchacki showed that adipocytes from the bone marrow and the WAT in human but also from rabbits are molecularly and functionally distinct. She demonstrated that insulin does not induce an increase in glucose uptake in most of the bone marrow cavities, but interestingly this result is depending on anatomic localization §.

M. Tencerova showed results on high fat diet mice suggesting that the diet induces insulin resistance in mesenchymal stem cells from subcutaneous adipose tissue but not in skeletal stem cells from bone marrow (20). This study also showed an increased insulin signaling in BMSCs from obese patients compared to those from lean subjects, hypothesizing that these data reflect an evolutionary conserved mechanism for bone as energy storage organ §.

Interestingly, in the postmenopausal state, also associated with metabolic alterations, S. Lucas demonstrated that BMAds show an evolving phenotype. In this context, or under high glucose exposure, BMAds express pro-osteoclastic, and/or anti-osteoblastic factors suggesting that they could contribute to the bone loss of postmenopausal osteoporosis §.

C.S. Craft enlarged the field of thinking by including the nervous system as a possible regulator of BMA. Indeed, her study showed that neuropathy-resistant mice are protected against type-1diabetes-induced neuropathy, bone marrow fat expansion, and bone alterations §.

P. Boroumand's study focused on the relationship between obesity-induced inflammation and bone marrow. Notably, she wondered whether increased BMA favors the development of inflammatory monocytes in this context. *In vivo* and *in vitro* results suggest that the high fat diet-induced changes in BMAd functions could be directly responsible for the activation of monocytes in the bone marrow §.

A last study from A. Lodvel on the involvement of glucocorticoids on caloric restriction-induced BMA increase revealed that in this context BMAT expansion is not sufficient for trabecular bone loss and that caloric restriction-induced alterations of bone and bone marrow are sex-dependent in mice. Moreover, the knockout of 11b-hydroxysteroid dehydrogenase type 1 protects male mice but not female mice from caloric restriction-induced increase in BMA §.

WORKING GROUPS

Nomenclature

Among the most developed groups, the working group for *Nomenclature* (Chairman: W.P. Cawthorn) has been working for almost 1 year to identify the terminology that has been used in the BMA field, and to propose a unified nomenclature system that will provide clarity and consensus as research into BMA

continues to increase. The *Nomenclature* working group has pursued this work on the basis of the literature and the wide expertise of its members. During its meeting session at BMA2018, this working group validated propositions on 28 terms that have been used in the BMA research field, deciding which of these terms to use, and which to stop using. For those terms recommend to use, an exact meaning was also proposed. Finally, the group agreed to start the writing of a white paper on this subject. These recommendations are proposed as a review article in the present issue on BMA.

Methodologies

The working group *Methodologies* (Chairwomen: O. Naveiras and A. Veldhuis-Vlug) is preparing a review paper on the existing methodologies to characterize BMA. The working group members are all active researchers in the field of BMA, both clinical and preclinical. The working group members searched the literature for articles describing the investigation of BMA and discussed the results during personal and telephone conferences. The consensus opinion, both based on the review of the literature and on expert opinion, will be discussed in the review. The following topics will be tackled: (1) cell isolation, culture, differentiation and *in vitro* modulation of primary bone marrow adipocytes and adipocytic precursors, (2) histomorphometry of bone marrow adipocytes in 2D and 3D, (3) imaging of BMA *in vivo* with magnetic resonance imaging, (4) imaging of BMA *ex vivo* with contrast enhanced computed tomography, (5) *in vitro* microscopy, and (6) modulation of BMA in animal models.

Biobank

The BMAS working group on *Biobank* (Chairman: B.J.C. van der Eerden) has discussed how to proceed with its ambition to generate standardized approaches toward isolation, characterization and long-term storage of tissues/cells and data related to BMA. Additional aspects of biobanking that the working group will scrutinize are privacy regulations regarding participants/patients, data protection, and ethical guidelines. Obviously, within an international community focusing on BMA with a desire to unify methodologies and guidelines, challenges will emerge, and which will be the focus of the working group.

Public Engagement

Chair position for the working group *Public engagement* was transferred from E.L. Scheller to C.S. Craft. This working group proposed to assist E.L. Scheller in planning 2020 Seattle BMAS meeting. Members of this group would like to set up a LinkedIn account for BMAS similar to ASBMR's page. We also suggest adding a lab website link to each BMAS member name on the BMAS website.

Data Repositories

A first meeting of the working group *Data repositories* (Chairman: A. van Wijnen) allowed discussions on the objective of sharing data and on how to obtain omics data suitable for later comparisons.

Sponsorship

Chair position for the working group *Sponsorship* was transferred from G. Penel to P.H. Bisschop. Among the items discussed during this first meeting of the working group a standardization of the contracts with the sponsors of the congresses was proposed on the basis of those used for the current meeting. The presentation of the sponsors on the websites (congress and society) was identified as a crucial point.

CONCLUDING REMARKS AND PERSPECTIVES

This congress confirmed the dynamism of this young field of research. Indeed, numerous investigators showed their results related to all the fields of research interested in BMA (rheumatology and bone biology, oncology, hematology, endocrinology, and metabolic diseases). Moreover, several of the presented studies have been published since the congress (5, 8–10, 14, 15) or just before (4, 6, 13, 16–18, 20).

For the first time, each working group within the BMA Society (BMAS) met to work on its specific topic, resulting in the submission of two white papers. A long term work was initiated by the other working groups.

Also, the organization of the 2020 Seattle BMA congress was strengthened. Indeed, the young and dynamic BMAS discussed the organization of future BMA congresses. BMA 2019 will be organized in Odense (Denmark), whereas BMA2020 will be affiliated to the annual congress of the American Society for Bone and Mineral Research (ASBMR) in Seattle (USA).

As future perspective, the authors believe that the BMAS has to play a crucial role in holding this multidisciplinary community together, and in stimulating close interactions between the players in this field of research. Indeed, it is research at the forefront of scientific and technological development and knowledge, as confirmed by the presentations given during BMA 2018 congress, which brought a large overview on this tissue and demonstrated its involvement in numerous physiological functions and pathologies. One of the most interesting points was that BMAds seem to be adaptive and their activities depend on the context. Thus, a multidisciplinary approach seems essential to allow a rapid and certain progression of knowledge of this tissue and the use of this knowledge for therapeutic purposes. Additionally, we are convinced that the development of clinical imaging tools for routine assessment of BMA will be a challenging but decisive step.

AUTHOR CONTRIBUTIONS

All authors listed have made a substantial, direct and intellectual contribution to the writing of the congress report and approved it for publication.

ACKNOWLEDGMENTS

Authors wish to thank Lilly, Linsey Tec, UCB and Dutscher as sponsor companies. We also wish to thank the regional government *Hauts-de-France* and its Vice-president in charge of higher education, research, Europe and territorial planning, Nicolas Lebas, for supporting this event and generously sharing the premises of the Regional Government in Lille. We also acknowledge our Universities, *Université du Littoral Côte d'Opale* and *Université de Lille*, for their financial and technical supports. We wish to thank the chairmen of the working groups, for reporting on their respective session. Finally, we wish to thank Aline Clabaut, Alexandrine During, Guillaume Falgayrac, Anne Galet, Damien Leterme, Marie-France Louchet, and Cécile Olejnik (Pathophysiology of Inflammatory Bone Diseases Lab, EA4490) for their precious contribution in the organization of the meeting.

SUPPLEMENTARY MATERIAL

The Supplementary Material for this article can be found online at: https://www.frontiersin.org/articles/10.3389/fendo.2019.00691/full#supplementary-material

REFERENCES

1. Hardouin P, Marie PJ, Rosen CJ. New insights into bone marrow adipocytes: report from the First European Meeting on Bone Marrow Adiposity (BMA 2015). *Bone.* (2016) 93:212–5. doi: 10.1016/j.bone.2015.11.013
2. van der Eerden B, van Wijnen A. Meeting report of the 2016 bone marrow adiposity meeting. *Adipocyte.* (2017) 6:304–13. doi: 10.1080/21623945.2017.1313374
3. Corsi A, Palmisano B, Tratwal J, Riminucci M, Naveiras. Brief report from the 3rd international meeting on bone marrow adiposity (BMA 2017). *Front Endocrinol.* (2019) 10:336. doi: 10.3389/fendo.2019.00336
4. Horowitz MC, Tommasini SM. Fat and bone: PGC-1α regulates mesenchymal cell fate during aging and osteoporosis. *Cell Stem Cell.* (2018) 23:151–3. doi: 10.1016/j.stem.2018.07.010
5. Maridas DE, Rendina-Ruedy E, Helderman RC, DeMambro VE, Brooks D, Guntur AR, et al. Progenitor recruitment and adipogenic lipolysis contribute to the anabolic actions of parathyroid hormone on the skeleton. *FASEB J.* (2019) 33:2885–98. doi: 10.1096/fj.201800948RR
6. Wang QA, Song A, Chen W, Schwalie PC, Zhang F, Vishvanath L, et al. Reversible de-differentiation of mature white adipocytes into preadipocyte-like precursors during lactation. *Cell Metab.* (2018) 28:282–8.e3. doi: 10.1016/j.cmet.2018.05.022
7. Brum AM, van de Peppel J, van der Leije CS, Schreuders-Koedam M, Eijken M, van der Eerden B, et al. Connectivity Map-based discovery of parbendazole reveals targetable human osteogenic pathway. *PNAS.* (2015) 112:12711–6. doi: 10.1073/pnas.1501597112
8. Robles H, Park S, Joens MS, Fitzpatrick JAJ, Craft CS, Scheller EL. Characterization of the bone marrow adipocyte niche with three-dimensional electron microscopy. *Bone.* (2019) 118:89–98. doi: 10.1016/j.bone.2018.01.020
9. Scheller EL, Khandaker S, Learman BS, Cawthorn WP, Anderson LM, Pham HA, et al. Bone marrow adipocytes resist lipolysis and remodeling in response to β-adrenergic stimulation. *Bone.* (2019) 118:32–41. doi: 10.1016/j.bone.2018.01.016
10. Beck-Cormier S, Lelliott CJ, Logan JG, Lafont DT, Merametdjian L, Leitch VD, et al. Slc20a2, encoding the phosphate transporter PiT2, is an important genetic determinant of bone quality and strength. *J Bone Miner Res.* (2019) 34:e3691. doi: 10.1002/jbmr.3691
11. Limonard EJ, Veldhuis-Vlug AG, van Dussen L, Runge JH, Tanck MW, Endert E, et al. Short-term effect of estrogen on human bone marrow fat. *J Bone Miner Res.* (2015) 30:2058–66. doi: 10.1002/jbmr.2557
12. Syed FA, Oursler MJ, Hefferanm TE, Peterson JM, Riggs BL, Khosla S. Effects of estrogen therapy on bone marrow adipocytes in postmenopausal osteoporotic women. *Osteoporos Int.* (2008) 19:1323–30. doi: 10.1007/s00198-008-0574-6
13. Mistry SD, Woods GN, Sigurdsson S, Ewing SK, Hue TF, Eiriksdottir G, et al. Sex hormones are negatively associated with vertebral bone marrow fat. *Bone.* (2018) 108:20–4. doi: 10.1016/j.bone.2017.12.009
14. Badr S, Legroux-Gérot I, Vignau J, Chauveau C, Ruschke S, Karampinos DC, et al. Comparison of regional bone marrow adiposity characteristics at the hip of underweight and weight-recovered women with anorexia nervosa using magnetic resonance spectroscopy. *Bone.* (2019) 127:135–45. doi: 10.1016/j.bone.2019.05.033
15. Sollmann N, Dieckmeyer M, Schlaeger S, Rohrmeier A, Syvaeri J, Diefenbach MN, et al. Associations between lumbar vertebral bone marrow and paraspinal muscle fat compositions—an investigation by chemical shift encoding-based water-fat MRI. *Front Endocrinol.* (2018) 9:563. doi: 10.3389/fendo.2018.00563
16. Baum T, Rohrmeier A, Syväri J, Diefenbach MN, Franz D, Dieckmeyer M, et al. Anatomical variation of age-related changes in vertebral bone marrow composition using chemical shift encoding-based water-fat magnetic resonance imaging. *Front Endocrinol.* (2018) 9:141. doi: 10.3389/fendo.2018.00141
17. Mattiucci D, Maurizi G, Izzi V, Cenci L, Ciarlantini M, Mancini S, et al. Bone marrow adipocytes support hematopoietic stem cell survival. *J Cell Physiol.* (2018) 233:1500–11. doi: 10.1002/jcp.26037
18. Laiglesia LM, Lorente-Cebrián S, López-Yoldi M, Lanas R, Sáinz N, Martínez JA, et al. Maresin 1 inhibits TNF-alpha-induced lipolysis and autophagy in 3T3-L1 adipocytes. *J Cell Physiol.* (2018) 233:2238–46. doi: 10.1002/jcp.26096
19. Martínez-Fernández L, González-Muniesa P, Laiglesia LM, Sáinz N, Prieto-Hontoria PL, Escoté X, et al. Maresin 1 improves insulin sensitivity and attenuates adipose tissue inflammation in ob/ob and diet-induced obese mice. *FASEB J.* (2017) 31:2135–45. doi: 10.1096/fj.201600859R
20. Tencerova M, Figeac F, Ditzel N, Taipaleenmäki H, Nielsen TK, Kassem M. High-fat diet-induced obesity promotes expansion of bone marrow adipose tissue and impairs skeletal stem cell functions in mice. *J Bone Miner Res.* (2018) 33:1154–65. doi: 10.1002/jbmr.3408

Conflict of Interest: Authors wish to thank Lilly, Linsey Tec, UCB and Dutscher as sponsor companies who supported the organization of the congress. The funders had no role in study design, data collection and analysis, decision to publish, or preparation of the manuscript.

frontiers in Endocrinology

ORIGINAL RESEARCH
published: 24 October 2019
doi: 10.3389/fendo.2019.00726

Induction of Stearoyl-CoA 9-Desaturase 1 Protects Human Mesenchymal Stromal Cells Against Palmitic Acid-Induced Lipotoxicity and Inflammation

*Antoine Dalla Valle[1], Pascale Vertongen[1], Delphine Spruyt[1], Jessica Lechanteur[1], Valérie Suain[2], Nathalie Gaspard[1], Jean-Pierre Brion[2], Valérie Gangji[1,3] and Joanne Rasschaert[1]**

[1] Laboratory of Bone and Metabolic Biochemistry, Faculty of Medicine, Université libre de Bruxelles, Brussels, Belgium, [2] Laboratory of Histology, Neuroanatomy and Neuropathology, Faculty of Medicine, ULB Neuroscience Institute (UNI), Université libre de Bruxelles, Brussels, Belgium, [3] Department of Rheumatology and Physical Medicine, Erasme Hospital, Université libre de Bruxelles, Brussels, Belgium

OPEN ACCESS

Edited by:
Clifford James Rosen, Maine Media College, United States

Reviewed by:
Marco Bugliani, University of Pisa, Italy
Melissa Orlandin Premaor, Federal University of Minas Gerais, Brazil

***Correspondence:**
Joanne Rasschaert
jrasscha@ulb.ac.be

Specialty section:
This article was submitted to Bone Research, a section of the journal Frontiers in Endocrinology

Received: *09 May 2019*
Accepted: *09 October 2019*
Published: *24 October 2019*

Citation:
Dalla Valle A, Vertongen P, Spruyt D, Lechanteur J, Suain V, Gaspard N, Brion J-P, Gangji V and Rasschaert J (2019) Induction of Stearoyl-CoA 9-Desaturase 1 Protects Human Mesenchymal Stromal Cells Against Palmitic Acid-Induced Lipotoxicity and Inflammation. Front. Endocrinol. 10:726. doi: 10.3389/fendo.2019.00726

In bone diseases such as osteonecrosis and osteoporosis, a shift toward a preferential differentiation of mesenchymal stromal cells (MSC) into adipocytes at the expense of the osteoblastic lineage is described, leading to excessive accumulation of adipocytes in the bone marrow of the patients. The influence of cytokines and adipokines secreted by adipocytes on skeletal health is already well-documented but the impact of free fatty acids release on bone cell biology and viability is an emerging concept. We have previously demonstrated that the saturated fatty acid (SFA) palmitate (Palm) is cytotoxic for human MSC (hMSC) and osteoblasts whereas oleate (Ole), a monounsaturated fatty acid (MUFA), has no toxic effect. Moreover, Ole protects cells against lipotoxicity. Our observations led us to propose that the toxicity of the SFA is not correlated to its intracellular accumulation but could rather be related to the intracellular SFA/MUFA ratio, which finally determines the toxic effect of SFA. Therefore, in the present study, we have investigated the potential protective role of the enzyme stearoyl-CoA 9-desaturase 1 (SCD1) against the deleterious effects of Palm. SCD1 is an enzyme responsible for desaturation of SFA to MUFA; its activation could therefore lead to modifications of the intracellular SFA/MUFA ratio. In the present study, we showed that hMSC express SCD1 and liver X receptors (LXRs), transcription factors regulating SCD1 expression. Human MSC treatment with a LXRs agonist triggered SCD1 expression and drastically reduced Palm-induced cell mortality, caspases 3/7 activation, endoplasmic reticulum stress and inflammation. We also observed that, in the presence of Palm, the LXRs agonist provoked lipid droplets formation, augmented the total cellular neutral lipid content but decreased the SFA/MUFA ratio when compared to Palm treatment alone. Addition of an inhibitor of SCD1 activity abrogated the positive effects of the LXRs agonist, suggesting that SCD1 could play a key role in protecting hMSC against lipotoxicity.

Keywords: human mesenchymal stromal cells (hMSC), fatty acids, lipotoxicity, endoplasmic reticulum stress (ER stress), inflammation, liver X receptor activator, stearoyl-CoA 9-desaturase 1 (SCD1), bone diseases

INTRODUCTION

Osteoporosis (OP) and non-traumatic osteonecrosis (ON) are bone diseases affecting the quality of life. They are associated with low bone mass and increased fracture risk (1, 2). The prevalence of OP and ON is growing (3) and, although both diseases share some common risk factors (i.e., alcohol abuse and glucocorticoid treatment), their etiology is still not well-understood. It is now established that OP and ON are characterized by a decreased number of bone marrow mesenchymal stromal cells (MSC) and adipocyte accumulation in the bone marrow niche (4–6). Adipocytes release adipokines, cytokines and free fatty acids (FFA) that might influence skeletal cell survival and function and, hence, affect bone remodeling (2, 7–9).

FFA are an essential energy source for various cell types but it is recognized that a chronic exposure to high concentrations of those nutrients may be deleterious for cell function and survival in a process called lipotoxicity. The cellular and molecular mechanisms involved in lipotoxicity are still not completely understood although different processes have been described, including reactive oxygen species production (10), ceramide synthesis (11), and endoplasmic reticulum (ER) stress initiation (12). Lipotoxicity has been widely studied in different cell types including hepatocytes (13), pancreatic β cells (14), podocytes (15), and artery endothelial cells (16) but was poorly investigated in human MSC (hMSC). The role of lipotoxicity in the pathogenesis of bone diseases associated with lipid metabolism abnormalities such as OP and ON is now the subject of growing interest.

In a previous work, we showed that palmitic acid (Palm; C16:0), a saturated fatty acid (SFA), induced apoptosis of hMSC and osteoblasts. Cell death was preceded by activation of endoplasmic reticulum (ER) stress, pro-apoptotic pathways and by induction of a pro-inflammatory state. Addition of oleic acid (Ole; C18:1), a mono-unsaturated fatty acid (MUFA), prevented the deleterious effects of Palm by favoring its channeling and esterification in lipid droplets (LD) (17). We further demonstrated that SaOS-2 cells, a human osteoblastic cell line (18), co-treated with Palm and Ole accumulated higher intracellular amounts of Palm than SaOS-2 cells exposed to Palm alone (17). These observations led us to propose that the toxicity of the SFA is not correlated to its intracellular accumulation but, rather, could be related to the intracellular SFA/MUFA ratio (17).

In order to validate this hypothesis, we have now evaluated the implication of stearoyl-CoA 9-desaturase (SCD1) in hMSC protection against lipotoxicity. SCD1 catalyzes the desaturation of Palm and stearic acid (C18:0) in their monounsaturated counterparts, Cis-9-palmitoleic acid (C16:1) and Ole. Insulin, carbohydrates, SFA, MUFA, polyunsaturated fatty acids (PUFA) and cholesterol (19, 20) modulate expression of SCD1 by activation of different transcription factors such as liver X receptors (LXRs), peroxisome proliferator-activated receptors α, sterol regulatory element-binding proteins and CCAAT-enhancer-binding proteins (C/EBP)α.

LXRs are members of the nuclear hormone receptors superfamily of ligand-activated transcription factors inducing the expression of target genes after ligand binding. Oxysterol, oxidized cholesterol, cholesterol biosynthesis intermediates and glucose are natural ligands of LXRs and synthetic agonists of LXRs like T0901317 and GW3965 are routinely used for *in vitro* experiments (16, 21). LXR has two isoforms: LXRα that is mainly expressed in metabolically active tissues such as liver, intestine, macrophages, and adipose tissue and LXRβ which is ubiquitously expressed (21, 22).

In the present study, we postulate that LXRs activation could protect hMSC from lipotoxicity by modulating SCD1 expression and, consequently, inducing modifications of the intracellular SFA/MUFA ratio. Therefore, we examined the expression and regulation of the two isoforms of LXR in hMSC and we investigated the effect of a synthetic LXRs agonist, T0901317, on gene and protein expression as well as on cell function and survival.

Abbreviations: CAY, CAY 10566; C/EBPα, CCAAT-enhancer-binding proteins; EM, electronic microscopy; ER, endoplasmic reticulum; FA, fatty acids; hMSC, human mesenchymal stromal cells; HV_{MSC}, hMSC obtained from healthy volunteers; LD, lipid droplet; LXRs, liver X receptors; MCP1, monocyte chemoattractant protein-1; MSC, mesenchymal stromal cells; MUFA, monounsaturated fatty acid; NL, neutral lipids; Ole, oleic acid; ON, non-traumatic osteonecrosis; ON_{MSC}, hMSC isolated from ON patients; OP, osteoporosis; Palm, palmitic acid; PL, phospholipids; PUFA, polyunsaturated fatty acids; RANKL, nuclear factor kappa-B ligand; SFA, saturated fatty acid; SCD1, stearoyl-CoA 9-desaturase 1; TLR4, toll-like receptor 4; UPR, unfolded protein response.

MATERIALS AND METHODS

Isolation, Culture, and Characterization of hMSC

hMSC were obtained from bone marrow aspirated from the posterior iliac crest of healthy volunteers and patient affected by osteonecrosis (all donors were aged ≥18 years). The study was approved by our local institutional ethical committee, Comité d'Ethique hospitalo-facultaire Erasme-ULB (021/406), agreation number by "Ordre des Médecins" OM021. All participants gave their written consent. Bone marrow was diluted 1:0.5 with PBS and overlaid on Ficoll-Paque PREMIUM (GE Healthcare, Diegem, Belgium). Mononuclear cells were isolated after centrifugation and seeded at a density of 5.7×10^4 cells/cm^2 in DMEM low glucose (1 g/l; Invitrogen, Gent, Belgium) supplemented with 10% FBS (Sigma-Aldrich, Diegem, Belgium), 100 U/ml penicillin and 100 µg/ml streptomycin (Invitrogen, Gent, Belgium). The culture medium was renewed after 4 days of culture and then every 2–3 days until cells reached confluence. hMSC were detached by enzymatic treatment (Trypsin-EDTA; Invitrogen, Gent, Belgium) every week and seeded at a density of 5.7×10^3 cells/cm^2 until passage 8. In order to confirm the mesenchymal nature of the isolated cells, phenotyping by FACS flow cytometer and differentiation assays were performed (17). SaOS-2 cells, a human osteoblastic cell line (a kind gift from Bone Therapeutics, Gosselies, Belgium) were grown in McCoy's 5A medium (Invitrogen, Gent, Belgium) supplemented with 10% FBS, 100 U/ml penicillin and 100 µg/ml streptomycin. Culture conditions were the same as with hMSC.

Free Fatty Acid Treatment

Sodium oleate and sodium palmitate (Sigma-Aldrich Diegem, Belgium) were weighted and then solubilized in 90%/10% ethanol/water at 70°C to prepare 50 mM stock solutions. Before use, Palm and Ole were diluted in the appropriate culture medium (see below) containing 1% fatty acid free bovine serum albumin (BSA; Sigma-Aldrich, Diegem, Belgium). Taking into account the stepwise equilibrium model and the respective binding affinities of Palm and Ole for BSA (23) the free concentrations of palm and Ole used in our study are close to the physiological ones (24): it is estimated that in the presence of 0.5 mM total FA and 1% BSA, the free (i.e., unbound to BSA) Palm and Ole concentrations are, respectively, 27 nM and 47 nM (25). For FFA supplementation experiments, cells were cultured for the indicated times in a FA-specific medium composed of DMEM low glucose (hMSC) or McCoy's 5A (SaOS-2 cells) medium supplemented with 1% FBS, 100 U/ml penicillin, 100 µg/ml streptomycin, 1% FFA free BSA (Sigma-Aldrich, Diegem, Belgium) and, when required, diluted Palm and/or Ole (0.25–0.50 mM). As Palm and Ole were solved in ethanol, a similar dilution of the alcohol was added in the control culture condition (e.g., absence of FA).

T0901317 (N-(2,2,2-trifluoro-ethyl)-N-[4-(2,2,2-tri-fluoro-1-hydroxy-1-trifluoromethyl-ethyl)-phenyl]benzene-sulfonamide, Sigma-Aldrich Diegem, Belgium), the LXRs agonist, was solubilized in DMSO and used in pretreatment during 16 or 24 h and for treatment during 16, 24, or 48 h at 1–10,000 nM. CAY 10566 (CAY), the SCD1 inhibitor (3-[4-(2-chloro-5-fluorophenoxy)-1-piperidinyl]-6-(5-methyl-1,3,4-oxadiazol-2-yl)-pyridazine, Santa Cruz Biotechnology, Heidelberg, Germany) was dissolved in DMSO and used at 25 µM during 16, 24, or 48 h of treatment. Diluted DMSO was added in the control condition.

Determination of Cell Viability

Cells were seeded in 96-well plates at a density of 14.7×10^3 cells/cm^2 for hMSC, and 20.6×10^3 cells/cm^2 for SaOS-2 cells. After 3 days, culture media were replaced by the FA-specific medium containing or not increasing concentrations of Palm and/or Ole for the indicated times and concentrations. At the end of the treatment period, the cells were washed and incubated for 15 min with the nuclear binding dyes propidium iodide 10 µg/ml (Sigma-Aldrich Diegem, Belgium) and Hoechst 33342 10 µg/ml (Sigma-Aldrich Diegem, Belgium). Cell viability was examined by inverted microscopy (Axiovision Zeiss, Zaventem, Belgium) with UV excitation (λ excitation/emission: 365/397 nm). Living cells were characterized by their intact nuclei with blue fluorescence, whereas dead cells were depicted by yellow-red fluorescence. In each experimental condition, a minimum of 500 cells were counted.

Measurement of Caspases-3/7 Activity

Caspases-3/7 activity was determined using the Caspase-Glo® 3/7 assay (Promega, Leiden, The Netherlands). 29.4×10^3 cells/cm^2 were seeded in 96-well white plates. After 3 days, culture media were replaced by FA-specific medium supplemented with increasing concentrations of Palm, complemented or not with Ole, for the indicated times. At the end of the incubation period, 100 µl of culture medium were replaced by 100 µl of Caspase-Glo reagent resulting in cell lysis and cleavage of the Caspase-Glo® 3/7 substrate by the activated caspases. The luminescent signal generated was detected after 1 h using a Victor2 (PerkinElmer, Zaventem, Belgium).

TABLE 1 | Primer sequences for real-time PCR.

	Sequence	Product size (bp)
BiP (HSPA5)-For	5′-ACCAATTATCAGCAAACTCTATGGAA-3′	74
BiP (HSPA5)-Rev	5′-CATCTTTTTCTGCTGTATCCTCTTCA-3′	
CHOP (DDIT3)-For	5′-TGGAAGCCTGGTATGAGGAC-3′	123
CHOP (DDIT3)-Rev	5′-AAGCAGGGTCAAGAGTGGTG-3′	
HPRT1-For	5′-GGCGTCGTGATTAGTGATGAT-3′	189
HPRT1-Rev	5′-CTTGAGCACACAGAGGGCTAC-3′	
IL6-For	5′-AGCCACTCACCTCTTCAGAACGAA-3′	122
IL6-Rev	5′-CAGTGCCTCTTTGCTGCTTTCACA-3′	
IL8 (CXCL8)-For	5′-GGACCACACTGCGCCAACACAG-3′	88
IL8 (CXCL8)-Rev	5′-TCCACAACCCTCTGCACCCAGTT-3′	
LXRα (NR1H3)-For	5′-CGCACTACATCTGCCACAGT-3′	141
LXRα (NR1H3)-Rev	5′-TCAGGCGGATCTGTTCTTCT-3′	
LXRβ (NR1H2)-For	5′-CCTCCTGAAGGCATCCACTA-3′	163
LXRβ (NR1H2)-Rev	5′-GAACTCGAAGATGGGGTTGA-3′	
SCD1 (SCD)-For	5′-TGTTCGTTGCCACTTTCTTG-3′	163
SCD1 (SCD)-Rev	5′-TAGTTGTGGAAGCCCTCACC-3′	

Quantification of mRNA Expression by Quantitative Polymerase Chain Reaction (qPCR)

Total RNA was isolated from cells seeded 3 days before treatment in 6-well plates at a density of 10.4×10^3 cells/cm^2, using AURUM™ kit (Bio-Rad, Nazareth Eke, Belgium) according to the manufacturer's protocol. Total RNA (100 ng) was reverse transcribed in 20 µl using iScript cDNA synthesis kit (Bio-Rad, Nazareth Eke, Belgium). qPCR reactions were performed using a CFX96 thermal system (Bio-Rad, Nazareth Eke, Belgium) in a total reaction volume of 20 µl containing 3 mM $MgCl_2$, 0.3 µM (each) forward and reverse primers (**Table 1**) (Eurogentec, Seraing, Belgium), 10 µl SYBR Green mix (Bio-Rad, Nazareth Eke, Belgium), and 2 µL cDNA. The cycling program was as follow: 95°C for 3 min followed by 40 cycles at 95°C for 30 s and 60°C for 30 sec. Hypoxanthine phosphoribosyltransferase 1 (*HPRT1*) was used as housekeeping gene.

Western Blotting

hMSC (10.4×10^3 cells/cm^2 in 6-well plates) were treated with FFA and then lyzed with Laemmli buffer (10% glycerol, 0.5 mM DTT, 63 mM Tris-HCl, 1% SDS, pH 6.8) containing a cocktail of proteases and phosphatases inhibitors (Roche Diagnostics, Vilvoorde, Belgium). Proteins were quantified by a paper dye binding assay. Equal protein amounts were separated by SDS-PAGE using 10% polyacrylamide gels. Proteins were transferred on polyvinylidene difluoride (PVDF) membranes Immobilion-P (Millipore, Overijse, Belgium) and immunolabeled overnight at

4°C using SCD1 antibody (rabbit, #2438, lot 2, Cell Signaling Technology, Leiden, The Netherlands). Membranes were then incubated for 1 h at room temperature with the secondary antibody peroxidase-conjugated ECL™ (GE healthcare, Diegem, Belgium). The immune complexes were detected by using the enhanced chemiluminescence method (Western Lightning® *Plus*-ECL, PerkinElmer Inc, Zaventem, Belgium). Band densities were quantified by ImageJ program (NIH, Bethesda, USA). Results were expressed as relative ratio between the protein of interest and β-actine (rabbit, #4967, lot 7, Cell Signaling Technology, Leiden, The Netherlands).

Detection of Intracellular Lipid Droplets

SaOS-2 cells were seeded in 6 well plates at 20.6×10^3 cells/cm^2. When required, cells were pretreated with T0901317 (10 μM) during 16 h. After 24 h incubation in the presence or absence of Palm (0.25 mM), T0901317 (10 μM) and/or CAY (25 μM), SaOS-2 cells were washed twice with PBS and fixed with 4% paraformaldehyde for 15 min. The neutral lipids accumulated in intracellular LD were stained by BODIPY™ 493/503 (D3922, Thermofisher, Alost, Belgium) 1 μg/ml for 1 h. Nuclei were stained by Hoechst 33342 10 μg/ml (Sigma-Aldrich, Diegem, Belgium) for 10 min. After coloration, cells were rinsed twice with PBS before microscopic observation, in DMEM without FBS at room temperature using an Axiovert 200M fluorescence microscope and Axiocam MRm (Axiovision Zeiss, Zaventem, Belgium). The images have been merged with Axiovision software and scales have been added with ImageJ program (NIH, Bethesda, USA).

Ultrastructural Analysis by Electron Microscopy (EM)

SaOS-2 cells were seeded in flask of 75 cm^2 at a density of 20.6 $\times 10^3$ cells/cm^2. Cells were pretreated with or without T0901317 (10 μM) during 16 h and further cultured in control conditions or treated for 24 h with Palm (0.25 mM), T0901317 (10 μM) and/or CAY 10566 (CAY) (25 μM). Cells were then collected and centrifuged at 320 g and the pellets were fixed with 4% (v/v) glutaraldehyde in 0.1 mol/L phosphate buffer (Millonig's buffer) at pH 7.4 for 1 h at RT. After 24 h washing in Millonig's buffer containing 0.5% sucrose (w/v), cells were post-fixed in 2% (w/v) OsO4 for 45 min, dehydrated, and embedded in Epon. Ultrathin sections were counterstained with lead citrate and uranyl acetate and observed with a Zeiss EM 109 at 50 kV (26). Scales have been added on images with ImageJ program (NIH, Bethesda, USA).

Gas Chromatography Analysis

SaOS-2 cells were seeded in flasks of 75 cm^2 at a density of 20.6×10^3 cells/cm^2,and pretreated with or without T0901317 (10 μM) during 16 h. To evaluate the cellular content of FA after 24 h of treatment in the presence or absence of Palm (0.25 mM), T0901317 (10 μM), and/or CAY (25 μM), cells were washed with PBS, scrapped and collected in 1 ml lysis buffer (1% SDS, 60 mM Tris-HCl and 10 mM EDTA). Total lipids were extracted with chloroform/methanol/water (2:2:1) and separated on a solid phase extraction -columns (Bond Elut-NH2, 200 mg, 3 ml, Agilent, Diegem, Belgium) in 3 fractions: free FA, neutral lipids (e.g., mono-, di- and triglycerides and cholesterol esters) and phospholipids. Quantification and characterization of the FA profile of the 3 lipidic fractions were then performed according to Louis et al. (27) on a Agilent 6890 series gas chromatography with a Supelco 24019 column (Sigma-Aldrich, Diegem, Belgium).

Statistical Analysis

Data are presented as means ± SEM. Values were determined from at least three independent experiments. Statistical analysis was performed by SPSS using Student's *t*-test or one-way ANOVA followed by *t*-test with the Fisher LSD correction for triple comparisons. Differences between groups were considered as statistically significant at $p < 0.05$.

RESULTS

LXRs Activation Triggers LXRα Expression in hMSC

T0901317 is a non-steroidal agonist of both isoforms of the transcription factor LXR, inducing the expression of genes under

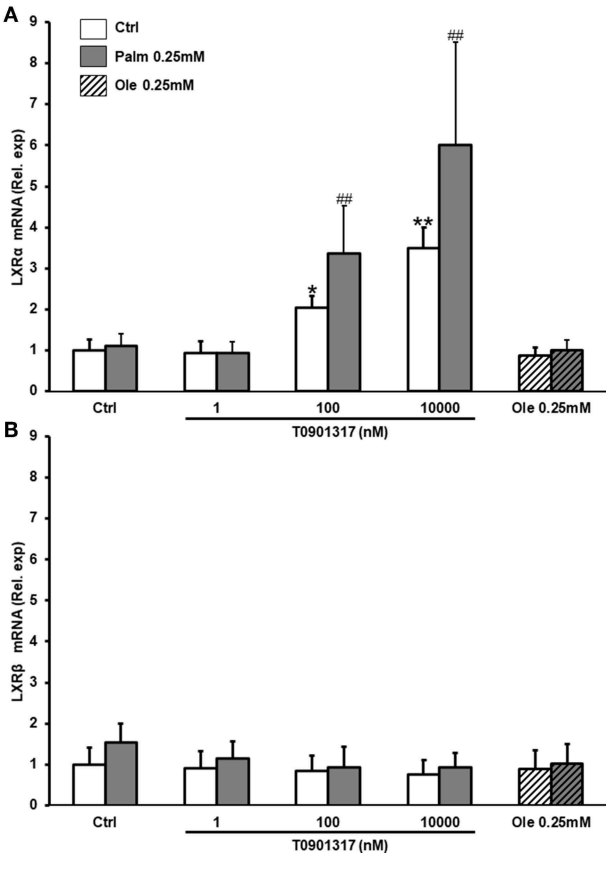

FIGURE 1 | T0901317 increases the expression of LXRα. hMSC were pretreated during 16 h with T0901317 and treated for 24 h with T0901317 in the absence of Palm (white column) or in the presence of Palm 0.25 mM (gray column), Ole 0.25 mM (shaded column). LXRα **(A)**, LXRβ **(B)**, expression were quantified by qPCR using the ΔΔCT method. Values were normalized for HPRT1 expression and are expressed as the ΔΔCT relative to control (Ctrl). Results are mean ± SEM of 9-12 individual experiments. *$p < 0.01$; **$p < 0.001$ vs. Ctrl; ##$p < 0.001$ vs. Palm 0.25 mM.

their control (28). To study the effect of LXRs activation, hMSC were pretreated during 16 h with T0901317 (1 nM to 10 μM) before a further 24 h culture period in the absence or presence of 0,25 mM of Palm or Ole.

As previously described in other cell types, T0901317 increased *LXRα* mRNA in a dose-dependent manner in hMSC but neither Palm, nor Ole significantly affected *LXRα* expression (**Figure 1A**). Neither T0901317, nor Ole (0.25 mM), nor Palm (0.25 mM) modulated the expression of LXRβ, the FFA being tested individually or in combination (**Figure 1B**).

LXRs Activation Protects hMSC From Palm Cytotoxicity and Represses Palm-Induced ER Stress and Inflammation

As shown before (17), treatment of hMSC with Palm (0.25 mM or 0.50 mM) induced cell death and activated caspases 3/7 (**Figures 2A,B**). We now demonstrated that addition of T0901317 decreased Palm-triggered cell mortality in a dose-dependent manner. At the highest concentration tested (100 nM), T0901317 abolished cell death and caspases 3/7 activation (**Figures 2A,B**). T0901317 did not significantly affect cell viability and caspase 3/7 activation (**Supplementary Figure 1A**).

Ig heavy-chain binding protein (BiP) and C/EBP homologous protein (CHOP) are usually used as ER stress markers. We confirmed that cell treatment with Palm increased *BiP* and *CHOP* mRNA (**Figures 3A,B**) as well as the expression of the pro-inflammatory cytokines *IL6* and *IL8* (**Figures 3C,D**). Furthermore, our results revealed that LXRs activation by T0901317 decreased Palm-induced gene expression related to ER stress and cytokines in a dose-dependent manner in hMSC.

LXRs Activation Increases SCD1 Expression in hMSC

SCD1 is an enzyme implicated in FFA metabolism by converting SFA into MUFA. Its expression is under the control of several factors including LXRs (20). We observed that T0901317, a LXRs agonist, significantly increased SCD1 expression in a dose-dependent manner at both mRNA and protein levels in hMSC (**Figures 4A,B**). Palm used alone or in combination with T0901317, did not significantly regulate SCD1 protein expression. Of interest, we observed that Ole, tested alone or in combination with Palm, significantly decreased *SCD1* mRNA (**Figure 4A**).

Inhibition of SCD1 Activity Abolishes the Protective Action of the LXRs Agonist in hMSC

CAY 10566 (CAY) is a potent and selective inhibitor of SCD1 activity, thus preventing the conversion of SFA into MUFA (29). CAY did not significantly affected cell death or caspase activity (**Supplementary Figure 1B**). In the presence of Palm 0.25 mM, inhibition of SCD1 by CAY significantly magnified the toxicity of the SFA, increasing both cell death and caspases 3/7 activation. Furthermore, our results demonstrated that inhibition of SCD1 activity abolished the protective action of the LXRs agonist T0901317 on Palm-triggered cell death and caspases 3/7 activation (**Figure 5**).

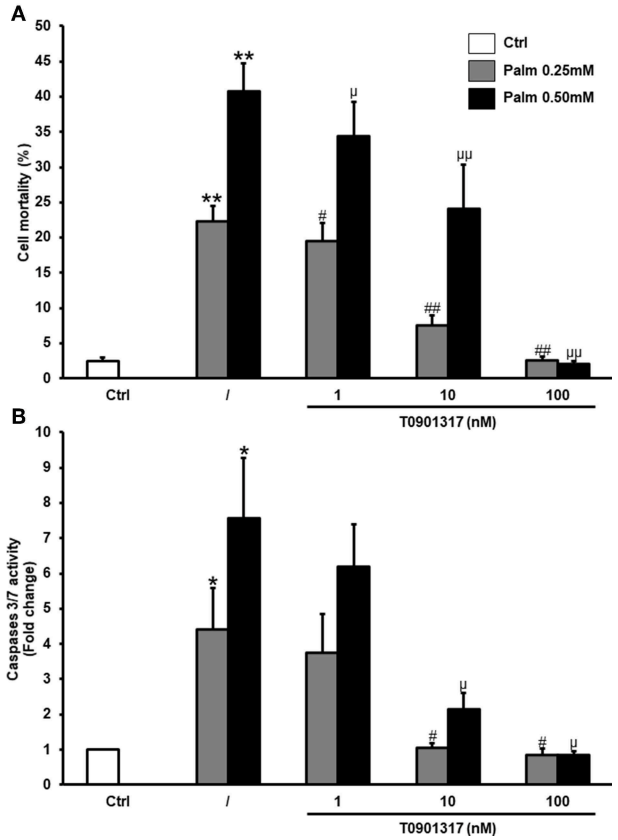

FIGURE 2 | T0901317 decreases Palm-induced cell death. hMSC were pretreated during 16 h with T0901317 and treated 24 h with T0901317 in the absence of Palm (white column) or in the presence of Palm 0.25 mM (gray column) or 0.50 mM (black column). Cell death **(A)** was quantified by nuclear staining with Hoechst and propidium iodide. Values are mean ± SEM of 12–17 individual experiments. Caspases-3/7 activity **(B)** was measured using the Caspases-3/7 Glo assay. Values are expressed relative to Ctrl and are mean ± SEM of 3 individual experiments. $^{*}p < 0.05$; vs. Ctrl; $^{**}p < 0.001$; $^{\#}p < 0.05$; $^{\#\#} < 0.001$ vs. Palm 0.25 mM; $^{\mu}p < 0.05$; $^{\mu\mu} < 0.001$ vs. Palm 0.50 mM.

Activation of LXRs Increases FFA Incorporation in Lipid Droplets in SaOS-2 Cells

We further evaluated the impact of LXRs activation and SCD1 inhibition on ER morphology in Palm-treated cells. Cell imaging by EM and FA quantification and analysis require large amounts of biological material. As hMSC are a rare and precious resource, SaOS-2 cells, a human osteoblastic cell line, were used to perform EM as we previously demonstrated that those cells are highly sensitive to lipotoxicity, showing a greater decrease of cell viability and a stronger activation of caspases 3/7 and ER stress in response to Palm than hMSC and hMSC-derived osteoblasts (17). The present results documented that LXRs activation increased SCD1 expression and viability

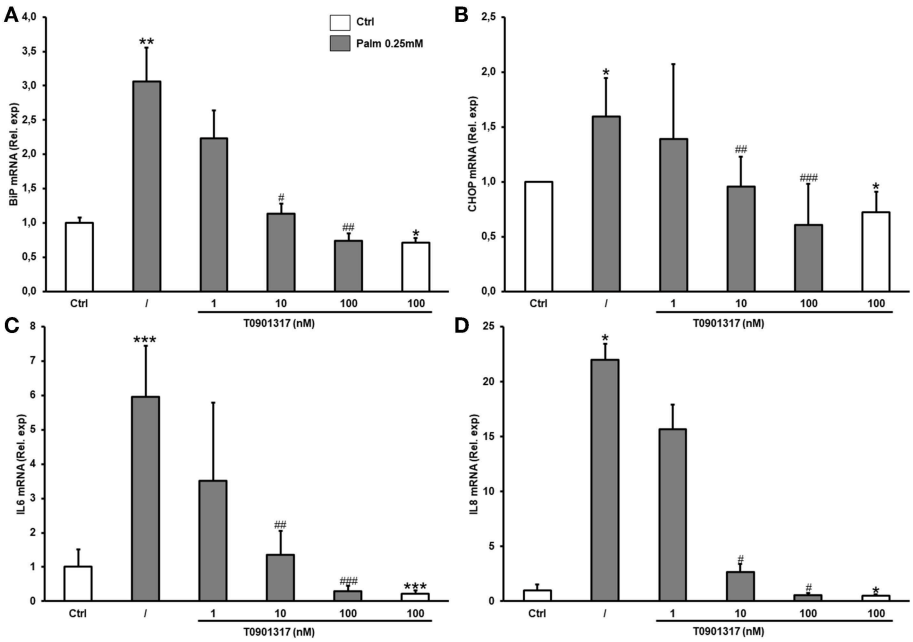

FIGURE 3 | T0901317 counteracts Palm-induced ER stress and inflammation in a dose dependent manner. hMSC were pretreated during 16 h with T0901317 and treated for 24 h with T0901317 in the absence (white column), or in the presence of Palm 0.25 mM (gray column). BiP **(A)** and CHOP **(C)** was used as marker of ER stress. IL6 **(B)**, IL8 **(D)** was used to showed inflammation. Gene expression was quantified by qPCR using the ΔΔCT method. Values were normalized for HPRT1 expression and are expressed as the ΔΔCT compared to control (Ctrl). Results are mean ± SEM of 12 individual experiments. $^{*}p < 0.05$; $^{**}p < 0.01$; $^{***}p < 0.001$ vs. Ctrl; $^{\#}p < 0.05$; $^{\#\#}p < 0.01$ $^{\#\#\#}p < 0.001$ vs. Palm 0.25 mM.

in SaOS-2 cells (**Supplementary Figures 2A,B**), as observed in hMSC (**Figures 2A**, **4A**).

Lipid droplets (LD) were not detected in SaOS-2 cells cultured in control condition (**Figures 6A,E**), whereas, as shown in **Figure 6B**, Palm-treated SaOS-2 cells displayed bodipy signal and we observed by EM that the ER was disrupted and inflated or angular (**Figure 6F**). Bodipy fluorescence markedly increased in SaOS-2 cells co-treated with Palm and T0901317 (10 μM) (**Figure 6C**). Moreover, we noticed the presence of numerous large LD surrounding the nucleus and often located in contact with, or close to, mitochondria (**Figure 6G**); the ER structure appeared unaltered in most of the cells. Addition of CAY, the SCD1 inhibitor, to Palm and T0901317 suppressed LD formation, severely damaged the ER (**Figures 6D–H**) and induced cell death (**Supplementaury Figure 2B**).

LXRs Activation Abolishes Palm-Induced Modifications of the SFA/MUFA Ratio in SaOS-2 Cells

We further characterized and quantified the fatty acids (FA) present in the FFA, neutral lipids (NL) and phospholipids (PL) fractions obtained from SaOS-2 cell lysates cultured in control conditions or in the presence of Palm, Palm and T0901317, and/or CAY. The FA profile (i.e., SFA, MUFA, and PUFA contents) of the FFA fraction was unaffected by the different culture conditions (data not shown).

When cells were exposed to Palm, we observed an important accumulation of SFA in the NL fraction whereas the MUFA content was slightly decreased (**Figure 7A**). Of note, myristic acid (C14:0) augmented but its total amount remained smaller than Palm (**Table 2**). Taken together, these modifications led to an increase of the SFA/MUFA ratio from 4 to 11 in SaOS-2 cells exposed to Palm.

As shown in **Table 2**, activation of LXRs by T0901317 in the presence of Palm induced a massive cellular accumulation of NL (10 times the amount measured in the control condition). As both SFA (from 9 to 86 ng/μg cell protein) and MUFA (from 2 to 19 ng/μg cell protein) increased, LXRs activation restored the SFA/MUFA ratio close to its control value (**Figure 7A**). Of note, Palm represented 65% of the total SFA.

In Palm + T0901317 treated cells, inhibition of SCD1 by CAY decreased twice the NL fraction, as compared to Palm + T0901317 treated cells. As total SFA and MUFA were decreased by 40 and 85%, respectively, the SFA/MUFA ratio increased to 17.3, principally due to modifications of Palm and of Cis-9-palmitoleic acid, Ole and Cis-11-vaccenic acid contents (**Table 2**).

In the PL fraction (**Figure 7B**), Palm or Palm + T0901317 treatments did not significantly affect SFA and MUFA content. However, addition of CAY to Palm and T0901317 doubled the SFA content while decreasing 4 times the quantity of MUFA. The SFA/MUFA ratio was thus only significantly affected by the concomitant presence of Palm, T0901317 and CAY in the PL fraction. Of note, despite the fact that we observed that the

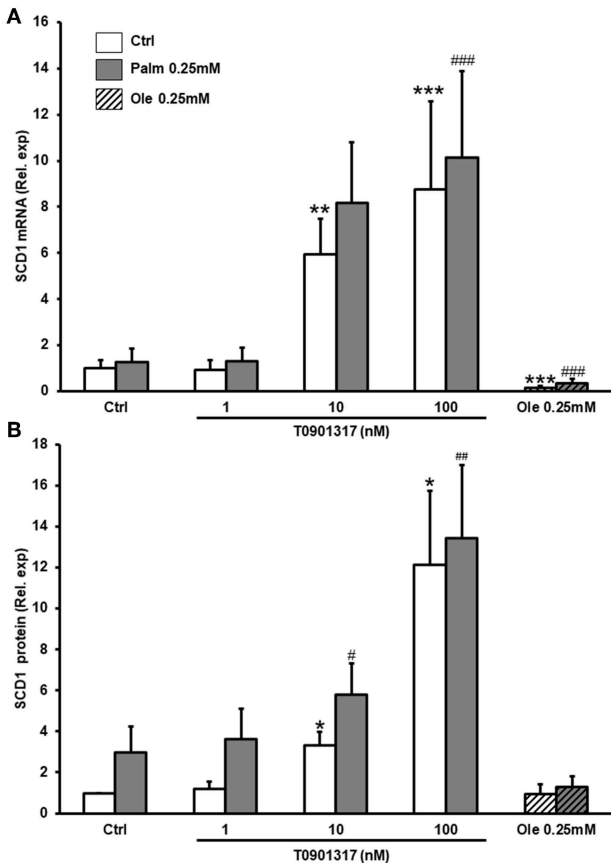

FIGURE 4 | T0901317 increases SCD1 mRNA and protein expression. hMSC were pretreated during 16 h with T0901317 and treated for 24 h with T0901317 in the absence (white column), or presence of Palm 0.25 mM (gray column), Ole 0.25 mM (shaded column). SCD1 mRNA expression **(A)**, was quantified by qPCR using the ΔΔCT method. Values were normalized for HPRT1 expression and are expressed as the ΔΔCT compared to control (Ctrl). Values are mean ± SEM of 12 individual experiments SCD1 protein level **(B)**, was evaluated by Western blotting and normalized for β actine and Ctrl. Values are mean ± SEM of 7 individual experiments. $^{*}p < 0.05$; $^{**}p < 0.01$; $^{***}p < 0.001$ vs. Ctrl; $^{\#}p < 0.05$; $^{\#\#}p < 0.01$ $^{\#\#\#}p < 0.001$ vs. Palm 0.25 mM.

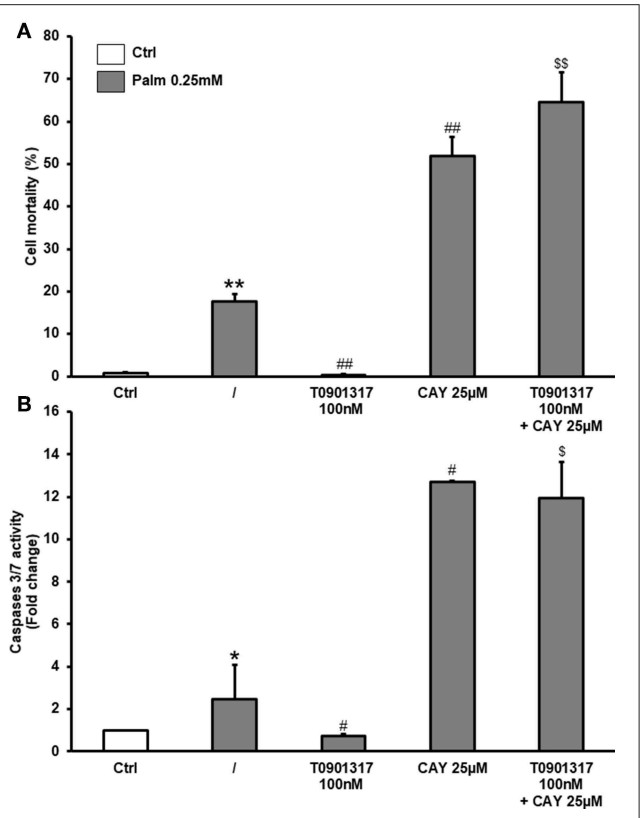

FIGURE 5 | CAY suppresses T0901317 effect on cell viability and caspases 3/7 activation. hMSC were pretreated during 16 h with T0901317 and treated 48 h with T0901317, CAY 25 μM in the absence (white column) or presence of Palm 0.25 mM (gray column). Cell death **(A)** was quantified by nuclear staining with Hoechst and propidium iodide. Values are mean ± SEM of 4 individual experiments. Caspases-3/7 activity **(B)** was measured using the Caspases-3/7 Glo assay. Values are expressed relative to Ctrl and are mean ± SEM of 3 individual experiments. $^{*}p < 0.05$; $^{**}p < 0.01$ vs. Ctrl; $^{\#}p < 0.05$; $^{\#\#}p < 0.01$ vs. Palm 0.25 mM; $^{\$}p < 0.05$; $^{\$\$}p < 0.01$ vs. Palm 0.25 mM + T0901317 100 nM.

total lipid content was not significantly modified by Palm, the SFA/MUFA ratio was enhanced by around 50% as Palm content increased while Ole and Cis-11-vaccenic acid amounts decreased (**Figure 7B**, **Table 2**). Conversely, addition of T0901317 to Palm reduced the SFA/MUFA ratio, although in a non-significant manner, compared to Palm alone treatment (**Figure 7B**).

Of note, as expected, in both the NL and PL fractions, Palm slightly raised the quantity of Cis-9-palmitoleic acid whereas addition of T0901317 largely increased it (**Table 2**).

The objective of the present work is to evaluate the hypothesis that Palm lipotoxicity is prevented by decreasing the SFA/MUFA ratio in hMSC. To reach this purpose, cells were treated with a LXRs agonist in order to trigger SCD1 expression. SCD1 is an enzyme located in the ER membrane where it catalyzes the desaturation of SFA in their monounsaturated counterparts; its expression is upregulated by nutrients such as glucose, fructose, SFA and by LXR activation (30). Due to the very short half-life (3–4 h) of SCD1 protein, the activity of the enzyme is easily controlled via regulation of its expression (31).

DISCUSSION

LXRs are mainly known for their regulatory function on lipid and carbohydrate metabolism by oxysterols, the main natural LXRs ligands (32, 33). Indeed, LXRs regulate expression of genes involved in cholesterol metabolism and efflux. In the liver, LXRs induce the expression of several enzymes, including SCD1 (34). Oxysterols were implicated in osteoblastic and adipogenic differentiation of murine MSC, although their influence is still under debate. In mouse bone marrow-derived MSC, it was reported that activation of LXRs inhibits sonic hedgehog-induced osteoblastic differentiation (35). At the opposite, oxysterols were shown to promote osteoblastic differentiation by activation of both the hedgehog (36) and the LXRs signaling pathways

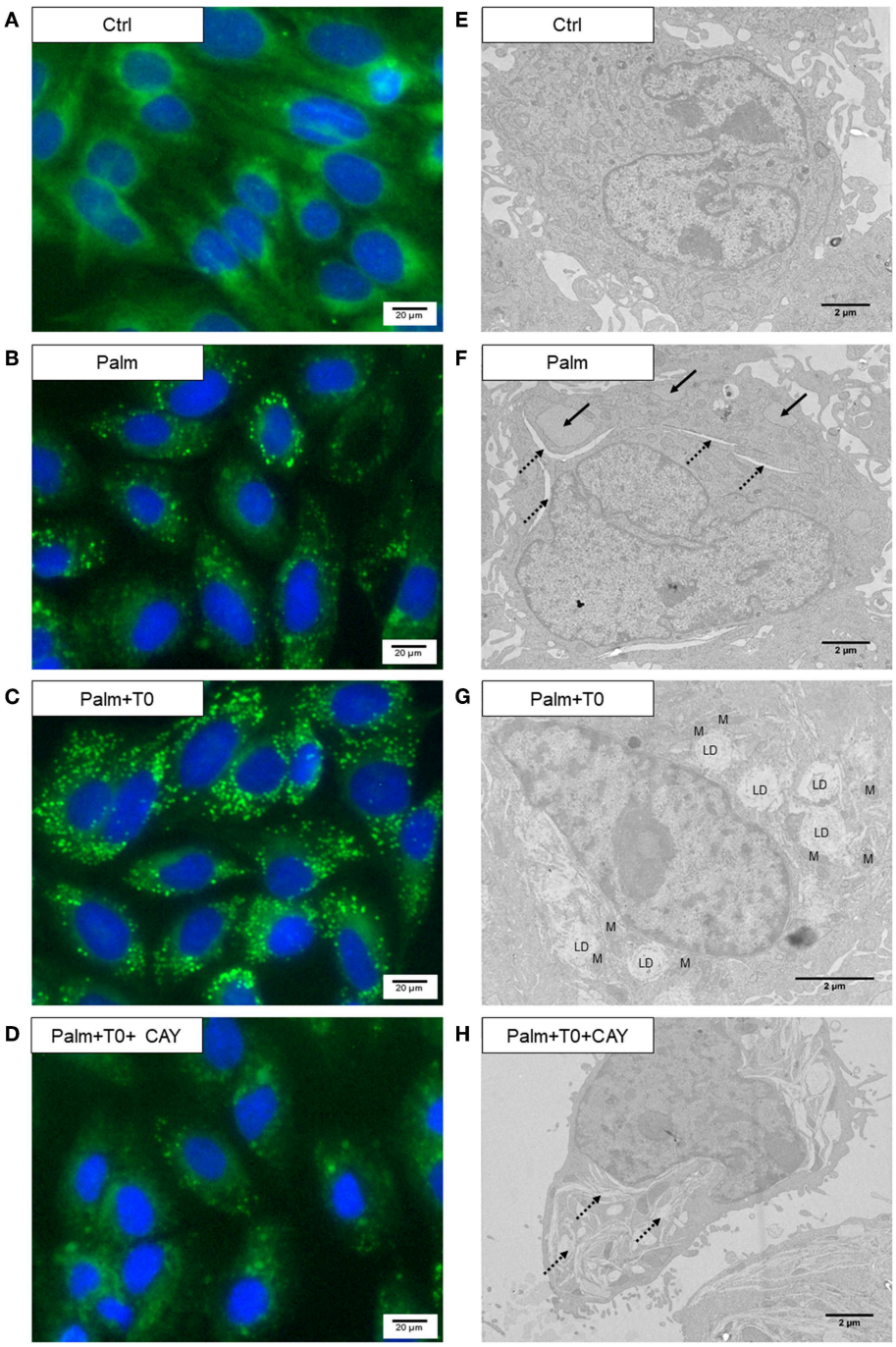

FIGURE 6 | T0901317 induces LD formation in the presence of Palm and counteracts Palm-induced ER disturbance. SaOS-2 cells were pretreated during 24 h with 10 µM T0901317 (T0) and treated for 16 h with T0901317 10 µM, CAY 25 µM in absence, or in the presence of Palm 0.25 mM. Bodipy staining of lipidic vacuoles, microscopic observations were performed with a 20 fold magnification lenses **(A–D)**. Electron micrographs **(E–H)**. Arrow, inflated ER; discontinued arrow, angular ER; LD, lipid droplet; M, mitochondria.

(37) while they reduce adipogenic differentiation in a mouse multipotent bone marrow stromal cell line (36). Moreover, it was documented that oxysterol 20(S)-Hydroxycholesterol stimulates osteogenic differentiation by inducing notch target gene expression (37). Interestingly the overexpression of LXRα has an inhibitory effect on adipocyte differentiation (38), and LXRs activation was shown to decrease osteoclastogenesis and to trigger osteoclast apoptosis (39), thus reducing *in vitro* bone resorption (40). In a co-culture osteoporosis model of mouse osteoblasts and osteoclasts, LXRs activation counteracts

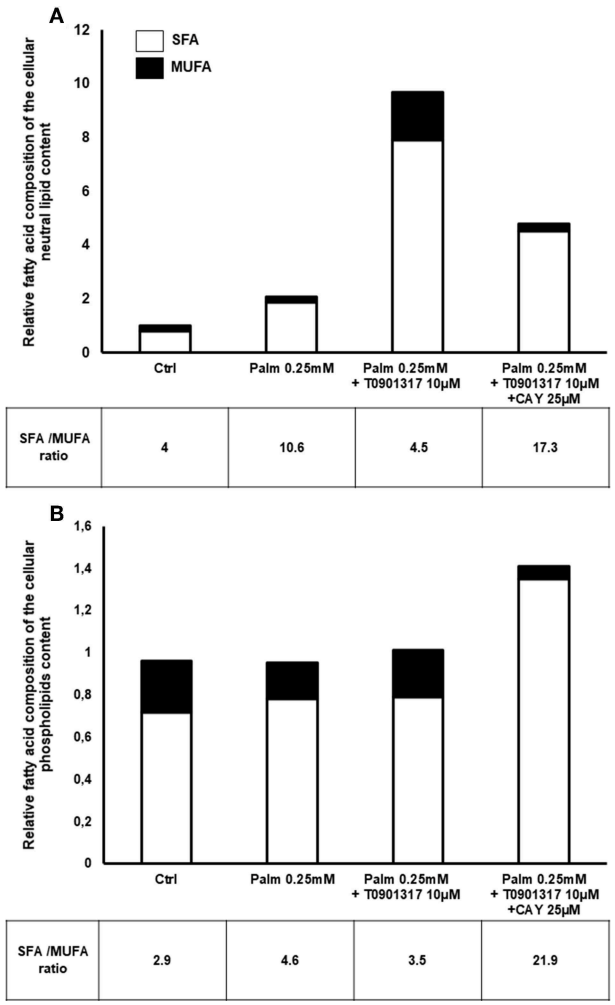

FIGURE 7 | Relative FA content in SFA and MUFA. Normalized FA composition of SaOS-2 cells extract regroup in 2 classes: SFA and MUFA. Values are expressed relative to Ctrl. SaOS-2 cells were pretreated during 24 h with T0901317 and treated 16 h with T0901317 10 μM, CAY 25 μM in absence, or in the presence of Palm 0.25 mM. The fat extract is separated in 3 fractions: NL **(A)**, PL **(B)** and FFA (data not shown). Values are mean ± SEM from 4 to 7 individual experiments.

osteoclastogenesis via inhibition of receptor activator of nuclear factor kappa-B ligand (RANKL) production by osteoblasts. In this model, activation of LXRs restores a physiological RANKL/osteoprotegerin ratio, promoting bone homeostasis (41). Up to now, the impact of LXRs activation on the biology of human MSC has been poorly investigated. In a particular cell sub-population, the multilineage-differentiating stress enduring (Muse) cells, LXRs activation has been linked to stem cell self-renewal and immunomodulation (42). The presence of LXRs-responsive elements in the LXRα promoter was previously documented, allowing regulation of LXRα expression by its own ligand in different cell types (43). In the present study, we confirm that hMSC expressed both LXR isoforms and we demonstrate that LXRs activation increases LXRα expression [the isoform particularly implicated in the control of lipid biosynthesis (22)] without affecting LXRβ expression. We further reveal for the first time that LXRs activation totally counteracts the deleterious effects of Palm in hMSC. LXRs were recently described as a connection between lipid metabolism and immune response (44). Indeed, in macrophages, LXRs activation counteracts the effects of LPS on expression of cytokines such as IL6 and IL1β and of the chemokine monocyte chemoattractant protein-1 (MCP-1), probably through modulation of NF-kB activity (45). In hMSC, our results show that LXRs activation decreases the inflammatory process triggered by Palm as IL6 and IL8 expression are significantly reduced. These observations are in line with the results of Wang et al. who demonstrated that activation of LXRs by artificial ligand decreases inflammation via toll-like receptor 4 (TLR4)/NF-κB and Keap-1/Nrf-2 pathways in adipose-derived mouse MSC (46). In macrophages, TLR4 activation reduces LXRs activation and decreases LXRs target gene expression after bacterial infection (47), suggesting a crosstalk between the two signaling pathways. Of interest, SFA are endogenous ligands of TLR4 and we have previously showed that Palm activates NF-kB and increases TLR4 expression as well as IL6 and IL8 secretion in hMSC, suggesting that TLR pathway might be embroiled in Palm-induced lipotoxicity in hMSC (17).

LXRs agonists such as SFA are known to upregulate SCD1 expression while MUFA and PUFA decrease SCD1 transcription in human aortic smooth muscle cells and mouse hepatocytes (30, 31). In the present work, we demonstrate for the first time a dose dependent effect of T0901317, the LXRs agonist on both SCD1 mRNA and protein expression in hMSC. As expected, Ole decreases SCD1 transcription. However, we could not show a significant effect of Palm on SCD1 mRNA and protein expression but this could be related to the high variability of SCD1 expression between subjects (**Supplementary Figure 3**), as previously documented (48). Our observations are in fair agreement with the literature as Karaskov et al., showed that medium-chain SFA, and particularly lauric acid (C12:0), bind and activate LXRα whereas long-chain SFA have no effect (49). Moreover, Bedi et al. observed that Palm binds to but does not activate LXRα in LXRα-transfected COS-7 cells (50).

The molecular mechanisms involved in SFA-induced lipotoxicity are still not fully understood. Various mechanisms were described (10–12), some are common to all cell types while others are specific of the cell type examined. SFA may provoke cell death by induction of an ER stress as Palm accumulation in the ER induces its engorgement, leading to disruption of the ER homeostasis and activation of the unfolded protein response (UPR) (51). UPR initially acts as a pro-survival response by triggering distinct mechanisms to overcome the ER overload: decreased protein translation, increased ER chaperone synthesis and misfolded protein clearance. If UPR does not successfully manage the ER engorgement, the response switches to activation of a pro-apoptotic pathway and, finally, leads to cell death (13, 41). In hMSC, we previously demonstrated that Palm treatment activates UPR by increasing expression of BiP, an ER chaperone and CHOP, an UPR-related protein inducing cell death. Activation of UPR is concomitant with caspases 3/7 activation and cell death (17). We now demonstrate that the

TABLE 2 | Modifications of SFA and MUFA content in SaOs-2 cells treated with Palm, an agonist of LXRs and/or a SCD1 inhibitor.

Fatty acid	Ctrl	Palm 0.25 mM	Palm 0.25 mM + T0901317 10 μM	Palm 0.25 mM + T0901317 10 μM + CAY 25 μM
NEUTRAL LIPIDS				
C14:0	0.05 ± 0.03	0.30 ± 0.12	1.89 ± 0.31$^{\#\#}$	0.85 ± 0.20$^{\$\$\$}$
C16:0	3.59 ± 0.11	14.66 ± 0.61**	76.13 ± 9.95$^{\#\#\#}$	39.87 ± 5.91$^{\$\$\$}$
C18:0	5.04 ± 0.30	5.63 ± 0.38	7.69 ± 0.62	8.36 ± 0.89
Total SFA	**8.67 ± 0.38**	**20.58 ± 0.58*** **	**85.99 ± 10.83$^{\#\#\#}$**	**49.08 ± 6.51$^{\$\$\$}$**
C16:1cis9	ND	0.30 ± 0.11*	7.81 ± 1.07$^{\#\#\#}$	0.28 ± 0.11$^{\$\$\$}$
C18:1cis9	1.08 ± 0.27	1.18 ± 0.07	5.30 ± 0.85$^{\#\#}$	1.58 ± 0.22$^{\$\$}$
C18:1cis11	1.09 ± 0.41	0.44 ± 0.28	5.67 ± 0.83$^{\#\#\#}$	0.95 ± 0.48$^{\$\$\$}$
Total MUFA	**2.17 ± 0.61**	**1.93 ± 0.37**	**19.09 ± 2.75$^{\#\#\#}$**	**2.84 ± 0.72$^{\$\$\$}$**
PHOSPHOLIPIDS				
C14:0	0.91 ± 0.21	0.56 ± 0.18*	0.40 ± 0.16#	1.07 ± 0.32$^{\$}$
C16:0	17.04 ± 2.55	20.08 ± 4.01	19.85 ± 3.90	36.11 ± 7.89$^{\$}$
C18:0	5.90 ± 0.77	5.38 ± 0.71	5.99 ± 0.88	7.68 ± 1.56
Total SFA	**23.85 ± 3.37**	**26.02 ± 4.86**	**26.24 ± 4.85$^{\#}$**	**44.86 ± 9.67$^{\$}$**
C16:1cis9	0.71 ± 0.09	1.10 ± 0.19	2.06 ± 0.46#	0.12 ± 0.12$^{\$}$
C18:1cis9	4.86 ± 0.66	3.06 ± 0.47*	3.42 ± 0.62	1.29 ± 0.66^{S}
C18:1cis11	2.52 ± 0.30	1.42 ± 0.19*	1.85 ± 0.30	0.62 ± 0.38$^{\$}$
Total MUFA	**8.20 ± 1.07**	**5.66 ± 0.88**	**7.40 ± 1.41$^{\#}$**	**2.05 ± 1.13$^{\$}$**

*Main FA extracted in SaOS-2 cells. SaOS-2 cells were pretreated during 24 h with T0901317 and treated 16 h with Palm 0.25 mM in the presence or absence of T0901317 10 μM and CAY 25 μM. Values are mean ± SEM of 4–7 individual experiments and are expressed in ng of fatty acid per μg of cell protein. *$p < 0.05$; **$p < 0.01$ vs. Ctrl; ***$p < 0.001$; $^{\#}p < 0.05$; $^{\#\#}p < 0.01$; $^{\#\#\#}p < 0.001$ vs. Palm 0.25 mM; $^{\$}p < 0.05$; $^{\$\$}p < 0.01$; $^{\$\$\$}p < 0.001$ vs. Palm 0.25 mM + T0901317 100 nM.*

LXRs agonist T090137 counteracts Palm activation of the UPR pathway and of caspases 3/7, thus promoting hMSC survival. All these effects are likely mediated by activation of SCD1 expression since inhibition of SCD1 activity abrogates the beneficial impacts of T090137.

In INS-1E cells, a rat pancreatic β cell line, downregulation of SCD1 expression enhances ER stress and apoptosis (52) whereas increasing SCD1 expression prevents lipotoxicity by favoring the incorporation of Palm in LD (53) These observations are in line with the present work, as we showed that the LXRs agonist T0901317 triggers SCD1 expression, LD formation and protects hMSC from Palm-induced toxicity. To further characterize the effects of Palm on cell organelles by EM, we used SaOS-2 cells, a human osteoblastic cell line, as susceptible to lipotoxicity than hMSC and hMSC-derived osteoblasts (17). Our results establish that Palm treatment distends the ER and induces ER membrane rupture. SaOS-2 cells co-treated with Palm and the LXRs agonist display LD formation and present less ER abnormalities such as inflated, angular or disrupted ER and cell viability is preserved. Lastly, we show that addition of an inhibitor of SCD1 activity to Palm and T0901317 suppress LD formation, provokes substantial damage to the whole cytoplasm and magnifies cell death, demonstrating the key role of SCD1 in the anti-lipotoxicity action of the LXRs agonist.

To further characterize the molecular mechanisms involved in the beneficial action of LXRs activation, we used gas chromatography to determinate the changes in nature and amount of the FA constituting LD and membrane in cells cultured in our different experimental conditions. Cell lipid extracts were separated into three fractions: (1) neutral lipids (NL) that are essentially composed of triglycerides, (2) phospholipids (PL), containing the membrane phospholipids, and (3) FFA, the non-esterified fatty acids. We observed that the lipid composition of this last fraction is unaffected by the different treatments tested (data not shown), as previously stated by Ariyama et al. in Hela cells (54).

In the NL fraction, Palm treatment increases the total lipid amount as well as the SFA/MUFA ratio, which is linked to enhanced cell death. Addition of the LXRs agonist to Palm drastically augments the total amount of NL, particularly the MUFA part, resulting in a decreased SFA/MUFA ratio that is associated with enhanced LD formation, as identified by EM. Upregulation of SCD1 protein synthesis by LXRs activation protects cells from lipotoxicity probably by promoting conversion of Palm to palmitoleic acid and, therefore, favoring its further integration in triglycerides and storage in LD. Indeed, it is known that MUFA are more easily added to diacylglycerol than SFA by the triglyceride-forming enzyme diacylglycerol O-acyltransferase (55). Inhibition of SCD1 activity drastically decreases the MUFA content, leading to a rise of the SFA/MUFA ratio and increased cell mortality. Altogether, these results corroborate the hypothesis that the beneficial action of the LXRs agonist is mediated by SCD1 increased expression and activity. As ER stress is also induced by alteration of the ER membrane fluidity (14, 54, 56), we hypothesized that in Palm-treated hMSC, an increase of saturated PL content could favor stiffening of the membranes and, therefore,

participate to ER stress and cell mortality. Indeed, Chamulitrat et al. observed a 2.12 fold increase of the SFA/MUFA ratio in PL concomitant to caspases 3/7 activation when mouse hepatocytes are treated with Palm (56). In our work, even if Palm treatment has no significant effect on the SFA/MUFA ratio in the PL fraction, we observe nevertheless a 1.59 fold increase. Such a rise is weak but was reproducible; improving the experimental protocol by purification of ER membranes could probably permit to reach significant statistical results but this would require a huge number of cells to be performed. Furthermore, our results are concordant with literature and with our EM observations, supporting the idea that the degree of saturation of PL is embroiled in ER stress and cell death (14, 56).

Modifications of the PL membrane SFA/MUFA ratio affects membrane properties by several mechanisms and a membrane enriched in saturated PL shows perturbation of protein activity. Li et al. demonstrated on RAW 264.7 macrophages that saturated PL inhibit the activity of the sarco(endo)plasmic reticulum calcium ATPase-2b (SERCA2b), a calcium pump (57), leading to ER Ca^{2+} depletion and ER stress. In addition, increasing PL membrane saturation triggers the recruitment of cellular Src kinase to the membrane, activates c-Jun N-terminal kinases (JNK) signaling pathway and so, potentially induces inflammation (58). In hMSC, Palm causes inflammation but we have not observed modifications of JNK phosphorylation (data not shown). Palm may also affect membrane properties simply by modifying its hydrophobic nature as Palm aggregates within the membranes and thus increases membrane permeability (59). While addition of the LXRs agonist to Palm abolishes cell death, we have only observed a weak decrease of the SFA/MUFA ratio in the PL fraction (**Figure 7B**), mainly due to a significant rise (>25 fold) of Cis-9-palmitoleic acid (**Table 2**). In hMSC, such an increase could indeed partially restore membrane fluidity and thus contributes to preservation of cell viability, as mentioned in the literature (60).

Taken as a whole, our results suggest that lipotoxicity is not related to the accumulation of intracellular Palm but rather to the SFA/MUFA ratio in NL and PL fractions. Indeed, hMSC co-treated with Palm and the LXRs agonist have the largest amount of Palm in the NL fraction, a SFA/MUFA ratio similar to the control condition and do not suffer from lipotoxicity. In contrast, cells treated with Palm alone or in combination with the LXR agonist and the inhibitor of SCD1 contain less Palm in the NL fraction, present a high SFA/MUFA ratio and increased cell death.

ON and OP are bone diseases sharing common similarities such as bone marrow adipocyte accumulation as well as blood increase in triglycerides, high density lipoprotein (HDL) and cholesterol concentrations (61, 62). In a previous work, we have demonstrated that the bone marrow microenvironment of ON patients is enriched in SFA when compared to healthy subjects (9). Moreover, hMSC isolated from ON patients (ON_{MSC}) are more sensitive to lipotoxicity than hMSC obtained from healthy volunteers (HV_{MSC}). These observations were associated with an inverse regulation of SCD1 expression by Palm: Palm triggered SCD1 expression in HV_{MSC} whereas it reduced it in ON_{MSC} (9). Moreover, the basal expression level of carnitine palmitoyltransferase I, the limiting enzyme of FA β-oxidation, was 2 fold lower in ON_{MSC} than in HV_{MSC}, indicating that lipid degradation is also affected in ON_{MSC} (9). Of note, dysfunctions of the NF-kB, TLR and TNF pathways implicating LXRs were recently highlighted in ON and OP patients (44, 63, 64). Altogether our observations suggest an important role for SCD1 in the prevention of lipotoxicity in hMSC.

Of note, dysfunctions of the NF-kB, TLR and TNF pathways implicating LXRs were recently highlighted in ON and OP patients (44, 63, 64).

In animal models, LXRs agonists are tested to treat hyperlipidemia (65) and atherosclerosis (66). Activation of LXRs has also been studied to treat diabetes. In an *in vitro* human hyperinsulinemia-induced insulin resistance model, activation of LXRs restores insulin sensitivity and decreases inflammatory phenotype. In such a model, addition of T0901317 restores insulin-stimulated glucose up-take, fatty acid synthase expression and counteracts metabolic disorder by decreasing secretion of the pro-inflammatory cytokine IL6 (67). Due to their ability to counteract lipotoxicity and their putative positive action on bone formation via decreased adipocyte/osteoclast differentiation and favoring osteoblast differentiation (36–38), LXRs agonists appear to be hopeful treatments for bone diseases associated with lipid metabolic disorders like ON and OP. Unfortunately artificial LXRs ligands like T0901317 or GW3965 increase serum triglyceride levels and exacerbate steatosis (68). Use of a selective LXRβ agonist could eventually maintain the beneficial effects as the triggering of SCD1 expression and the anti-inflammatory effect and suppress the impact on hepatic lipogenesis [for review (69)]. Another strategy proposed to avoid deleterious effects on liver is the use of tissue-selective drugs carrier (69). Instead of increasing SCD1 expression via LXRs activation, it would also be conceivable to increase lifespan of the protein by inhibiting the proteasome or by stabilizing the protein through phosphorylation of Y55 (70, 71).

In conclusion, our work demonstrates the essential role of SCD1 as a protective agent against lipotoxicity in bone marrow hMSC. Of interest, a recent study shows modification of SCD1 methylation at the menopausal age (72). Hypermethylation may impact enzyme expression and therefore, activity, and it is well-known that menopausal women are frequently affected by osteoporosis.

Our work also highlights the importance of maintaining a low intracellular SFA/MUFA ratio to preserve cell viability and validates our hypothesis that the SFA/MUFA ratio rather than Palm accumulation is responsible for cell death. This proposal is further supported by the work of Li et al., showing by NMR spectroscopy studies that bone marrow adipose tissue of ON patients is enriched in SFA and depleted of MUFA, leading to an increase of the SFA/MUFA ratio, when compared to controls subjects. Moreover, they correlated a high SFA/MUFA ratio with a lowest bone mineral density (73). In this work we performed *in vitro* studies on primary cultures of hMSC. Further *in vivo* studies, using animal models of OP and ON, are needed to better understand the physiological roles of SCD1 and LXRs activation in bone remodeling.

Altogether, our observations support future investigations for the use of LXRs agonists as potential therapeutic tools for bone diseases associated with lipid metabolism dysfunction.

DATA AVAILABILITY STATEMENT

The datasets generated for this study are available on request to the corresponding author.

AUTHOR CONTRIBUTIONS

AD conceived and designed the study. AD, PV, and JR analyzed the data and wrote the paper. PV, DS, J-PB, VG, and JR critically reviewed the results. JL, NG, and VS made substantial contributions to acquisition of data. All authors contributed to revise the manuscript.

FUNDING

This work was supported by the Fonds National de la Recherche Scientifique (Convention J.0188.16), the Fonds J.-P. Naets, and the Fonds David et Alice Van Buuren.

ACKNOWLEDGMENTS

We thank Vincent Van Hée for paper preparation, Gillet Céline for technical advices and Johannes Cnudde for technical support.

SUPPLEMENTARY MATERIAL

The Supplementary Material for this article can be found online at: https://www.frontiersin.org/articles/10.3389/fendo.2019.00726/full#supplementary-material

REFERENCES

1. Motyl KJ, Guntur AR, Carvalho AL, Rosen CJ. Energy metabolism of bone. *Toxicol Pathol*. (2017) 45:887–93. doi: 10.1177/0192623317737065
2. Gangji V, Soyfoo MS, Heuschling A, Afzali V, Moreno-Reyes R, Rasschaert J, et al. Non traumatic osteonecrosis of the femoral head is associated with low bone mass. *Bone*. (2018) 107:88–92. doi: 10.1016/j.bone.2017.11.005
3. Mont MA, Cherian JJ, Sierra RJ, Jones LC, Lieberman JR. Nontraumatic osteonecrosis of the femoral head: where do we stand today? A ten-year update. *J Bone Joint Surg Am*. (2015) 97:1604–27. doi: 10.2106/JBJS.O.00071
4. Hernigou P, Beaujean F, Lambotte JC. Decrease in the mesenchymal stem-cell pool in the proximal femur in corticosteroid-induced osteonecrosis. *J Bone Joint Surg Br*. (1999) 81:349–55. doi: 10.1302/0301-620X.81B2.8818
5. Sheng H, Sheng CJ, Cheng XY, Zhan G, Lee KM, Leung KS, et al. Pathomorphological changes of bone marrow adipocytes in process of steroid-associated osteonecrosis. *Int J Clin Exp Pathol*. (2013) 6:1046–50.
6. Hardouin P, Rharass T, Lucas S. Bone marrow adipose tissue: to be or not to be a typical adipose tissue? *Front Endocrinol*. (2016) 7:85. doi: 10.3389/fendo.2016.00085
7. Rosen CJ, Bouxsein ML. Mechanisms of disease: is osteoporosis the obesity of bone? *Nat Clin Pract Rheumatol*. (2006) 2:35–43. doi: 10.1038/ncprheum0070
8. Drosatos-Tampakaki Z, Drosatos K, Siegelin Y, Gong S, Khan S, Van Dyke T, et al. Palmitic acid and DGAT1 deficiency enhance osteoclastogenesis, while oleic acid-induced triglyceride formation prevents it. *J Bone Miner Res*. (2014) 29:1183–95. doi: 10.1002/jbmr.2150
9. Gillet C, Dalla Valle A, Gaspard N, Spruyt D, Vertongen P, Lechanteur J, et al. Osteonecrosis of the femoral head: lipotoxicity exacerbation in msc and modifications of the bone marrow fluid. *EndocrinologyJN*. (2017) 158:490–502. doi: 10.1210/en.2016-1687
10. Listenberger LL, Ory DS, Schaffer J. E. Palmitate-induced apoptosis can occur through a ceramide-independent pathway*. *J Biol Chem*. (2001) 276:14890–5. doi: 10.1074/jbc.M010286200
11. Kolesnick RN, Krönke M. Regulation of ceramide production and apoptosis. *Annu Rev Physiol*. (1998) 60:643–65. doi: 10.1146/annurev.physiol.60.1.643
12. Boslem E, Weir JM, MacIntosh G, Sue N, Cantley J, Meikle PJ, et al. Alteration of endoplasmic reticulum lipid rafts contributes to lipotoxicity in pancreatic β-cells. *J Biol Chem*. (2013) 288:26569–82. doi: 10.1074/jbc.M113.489310
13. Zámbó V, Simon-Szabó L, Szelényi P, Kereszturi E, Bánhegyi G, Csala M. Lipotoxicity in the liver. *World J Hepatol*. (2013) 5:550–7. doi: 10.4254/wjh.v5.i10.550
14. Moffitt JH, Fielding BA, Evershed R, Berstan R, Currie JM, Clark A. Adverse physicochemical properties of tripalmitin in beta cells lead to morphological changes and lipotoxicity *in vitro*. *Diabetologia*. (2005) 48:1819–29. doi: 10.1007/s00125-005-1861-9
15. Sieber J, Weins A, Kampe K, Gruber S, Lindenmeyer MT, Cohen CD, et al. Susceptibility of podocytes to palmitic acid is regulated by stearoyl-CoA desaturases 1 and 2. *Am J Pathol*. (2013) 183:735–44. doi: 10.1016/j.ajpath.2013.05.023
16. Peter A, Weigert C, Staiger H, Rittig K, Cegan A, Lutz P, et al. Induction of stearoyl-CoA desaturase protects human arterial endothelial cells against lipotoxicity. *Am. J Physiol*. (2008) 339–49. doi: 10.1152/ajpendo.00022.2008
17. Gillet C, Spruyt D, Rigutto S, Dalla Valle A, Berlier J, Louis C, et al. Oleate abrogates palmitate-induced lipotoxicity and proinflammatory response in human bone marrow-derived mesenchymal stem cells and osteoblastic cells. *Endocrinology*. (2015) 156:4081–93. doi: 10.1210/en.2015-1303
18. Murray E, Provvedini D, Curran D, Catherwood B, Sussman H, Manolagas S. Characterization of a human osteoblastic osteosarcoma cell line (SAOS-2) with high bone alkaline phosphatase activity. *J Bone Miner Res*. (2009) 2:231–8. doi: 10.1002/jbmr.5650020310
19. Waters KM, Miller CW, Ntambi JM. Localization of a polyunsaturated fatty acid response region in stearoyl-CoA desaturase gene 1. *Biochim Biophys Acta*. (1997) 1349:33–42. doi: 10.1016/S0005-2760(97)00069-6
20. Koeberle A, Löser K, Thürmer M. Biochimica et biophysica acta Stearoyl-CoA desaturase-1 and adaptive stress signaling. *BBA Mol Cell Biol Lipids*. (2016) 1861:1719–26. doi: 10.1016/j.bbalip.2016.08.009
21. Gabbi C, Warner M, Gustafsson JÅ. Action mechanisms of liver X receptors. *Biochem Biophys Res Commun*. (2014) 446:647–50. doi: 10.1016/j.bbrc.2013.11.077
22. Huang C. Natural modulators of liver X receptors. *J Integr Med*. (2014) 12:76–85. doi: 10.1016/S2095-4964(14)60013-3
23. Oliveira AF, Cunha DA, Ladriere L, Igoillo-Esteve M, Bugliani M, Marchetti P, et al. *In vitro* use of free fatty acids bound to albumin: a comparison of protocols. *Biotechniques*. (2015) 58:228–33. doi: 10.2144/000114285
24. Baylin A, Kabagambe EK, Siles X, Campos H. Adipose tissue biomarkers of fatty acid intake. *Am J Clin Nutr*. (2002) 76:750–7. doi: 10.1093/ajcn/76.4.750
25. Cnop M, Hannaert JC, Hoorens A, Eizirik DL, Pipeleers DG. Inverse relationship between cytotoxicity of free fatty acids in pancreatic islet cells and cellular triglyceride accumulation. *Diabetes*. (2001) 50:1771–7. doi: 10.2337/diabetes.50.8.1771
26. Audouard E, Houben S, Masaracchia C, Yilmaz Z, Suain V, Authelet M, et al. High-molecular-weight paired helical filaments from alzheimer brain induces seeding of wild-type mouse tau into an argyrophilic 4R tau pathology *in vivo*. *Am J Pathol*. (2016) 186:2709–22. doi: 10.1016/j.ajpath.2016.06.008
27. Louis C, Van den Daelen C, Tinant G, Bourez S, Thomé J-P, Donnay I, et al. Efficient *in vitro* adipocyte model of long-term lipolysis: a tool to study the behavior of lipophilic compounds. *In Vitro Cell Dev Biol Anim*. (2014) 50:507–18. doi: 10.1007/s11626-014-9733-6

28. Jamroz-wiśniewska A, Wójcicka G., Horoszewicz K. Liver X receptors (LXRs). Part I: Structure, function, regulation of activity, and role in lipid metabolism. Cześć II: Działania niezwiazane z gospodarka lipidowa, znaczenie w patologii i implikacje terapeutyczne. *Postep Hig Med Dosw Online*. (2007) 61:760–85. Available online at: https://www.google.com/url?sa=t&rct=j&q=&esrc=s&source=web&cd=7&ved=2ahUKEwiA0PvD-57lAhVKKlAKHaMbDcEQFjAGegQIARAC&url=https%3A%2F%2Fpdfs.semanticscholar.org%2Fd83f%2Fc6d7c612f0caba07fe36ac15280edf4dc6c6.pdf&usg=AOvVaw288uMAVMxbvbsTFm0Uk3NC
29. Liu G, Lynch JK, Freeman J, Liu B, Xin Z, Zhao H, et al. Discovery of potent, selective, orally bioavailable stearoyl-CoA desaturase 1 inhibitors. *J Med Chem*. (2007) 50:3086–100. doi: 10.1021/jm070219p
30. Minville-Walz M, Gresti J, Pichon L, Bellenger S, Bellenger J, Narce M, et al. Distinct regulation of stearoyl-CoA desaturase 1 gene expression by cis and trans C18:1 fatty acids in human aortic smooth muscle cells. *Genes Nutr*. (2012) 7:209–16. doi: 10.1007/s12263-011-0258-2
31. Sampath H, Ntambi JM. The role of stearoyl-CoA desaturase in obesity, insulin resistance, and inflammation. *Ann N Y Acad Sci*. (2011) 1243:47–53. doi: 10.1111/j.1749-6632.2011.06303.x
32. Laffitte BA, Chao LC, Li J, Walczak R, Hummasti S, Joseph SB, et al. Activation of liver X receptor improves glucose tolerance through coordinate regulation of glucose metabolism in liver and adipose tissue. *Proc Natl Acad Sci USA*. (2003) 100:5419–24. doi: 10.1073/pnas.0830671100
33. Dalen KT, Ulven SM, Bamberg K, Gustafsson J-Å, Nebb HI. Expression of the insulin-responsive glucose transporter GLUT4 in adipocytes is dependent on liver X receptor α. *J Biol Chem*. (2003) 278:48283–91. doi: 10.1074/jbc.M302287200
34. Zelcer N, Tontonoz P. Liver X receptors as integrators of metabolic and inflammatory signaling. *J Clin Invest*. (2006) 116:607–14. doi: 10.1172/JCI27883
35. Kim W-K, Meliton V, Park KW, Hong C, Tontonoz P, Niewiadomski P, et al. Negative regulation of Hedgehog signaling by liver X receptors. *Mol Endocrinol*. (2009) 23:1532–43. doi: 10.1210/me.2008-0453
36. Johnson JS, Meliton V, Kim WK, Lee K-B, Wang JC, Nguyen K, et al. Novel oxysterols have pro-osteogenic and anti-adipogenic effects *in vitro* and induce spinal fusion *in vivo*. *J Cell Biochem*. (2011) 112:1673–84. doi: 10.1002/jcb.23082
37. Kim W-K, Meliton V, Tetradis S, Weinmaster G, Hahn TJ, Carlson M, et al. Osteogenic oxysterol, 20(S)-hydroxycholesterol, induces notch target gene expression in bone marrow stromal cells. *J Bone Miner Res*. (2010) 25:782–95. doi: 10.1359/jbmr.091024
38. Matsushita K, Morello F, Zhang Z, Masuda T, Iwanaga S, Steffensen KR, et al. Nuclear hormone receptor LXRα inhibits adipocyte differentiation of mesenchymal stem cells with Wntbeta-catenin signaling. *Lab Investig*. (2016) 96:230–8. doi: 10.1038/labinvest.2015.141
39. Kim H-J, Yoon K-A, Yoon H-J, Hong JM, Lee M-J, Lee I-K, et al. Liver X receptor activation inhibits osteoclastogenesis by suppressing NF-κB activity and c-Fos induction and prevents inflammatory bone loss in mice. *J Leukoc Biol*. (2013) 94:99–107. doi: 10.1189/jlb.1112601
40. Remen KMR, Henning P, Lerner UH, Gustafsson J-Å, Andersson G. Activation of liver X receptor (LXR) inhibits receptor activator of nuclear factor κB ligand (RANKL)-induced osteoclast differentiation in an LXRβ-dependent mechanism. *J Biol Chem*. (2011) 286:33084–94. doi: 10.1074/jbc.M111.235937
41. Kleyer A, Scholtysek C, Bottesch E, Hillienhof U, Beyer C, Distler JH, et al. Liver X receptors orchestrate osteoblast/osteoclast crosstalk and counteract pathologic bone loss. *J Bone Miner Res*. (2012) 27:2442–51. doi: 10.1002/jbmr.1702
42. Alessio N, Özcan S, Tatsumi K, Murat AAA, Peluso G, Dezawa M, et al. The secretome of MUSE cells contains factors that may play a role in regulation of stemness, apoptosis and immunomodulation. *Cell Cycle*. (2017) 16:33–44. doi: 10.1080/15384101.2016.1211215
43. Kohro T, Nakajima T, Wada Y, Sugiyama A, Ishii M, Tsutsumi S, et al. Genomic structure and mapping of human orphan receptor LXR alpha: upregulation of LXRa mRNA during monocyte to macrophage differentiation. *J Atheroscler Thromb*. (2000) 7:145–51. doi: 10.5551/jat1994.7.145
44. Schulman IG. Liver X receptors link lipid metabolism and inflammation. *FEBS Lett*. (2017) 591:2955–7. doi: 10.1002/1873-3468.12702
45. Joseph SB, Castrillo A, Laffitte BA, Mangelsdorf DJ, Tontonoz P. Reciprocal regulation of inflammation and lipid metabolism by liver X receptors. *Nat Med*. (2003) 9:213–9. doi: 10.1038/nm820
46. Wang Y, Li CC, Cheng K, Zhang RR, Narsinh K, Li S, et al. Activation of liver X receptor improves viability of adipose-derived mesenchymal stem cells to attenuate myocardial ischemia injury through TLR4/NF-κB and Keap-1/Nrf-2 signaling pathways. *Antioxid Redox Signal*. (2014) 21:2543–57. doi: 10.1089/ars.2013.5683
47. Castrillo A, Joseph SB, Vaidya SA, Haberland M, Fogelman AM, Cheng G, et al. Crosstalk between LXR and toll-like receptor signaling mediates bacterial and viral antagonism of cholesterol metabolism. *Mol Cell*. (2003) 12:805–16. doi: 10.1016/S1097-2765(03)00384-8
48. Peter A, Weigert C, Staiger H, Machicao F, Schick F, Machann J, et al. Individual stearoyl-CoA desaturase 1 expression modulates endoplasmic reticulum stress and inflammation in human myotubes and is associated with skeletal muscle lipid storage and insulin sensitivity *in vivo*. *Diabetes*. (2009) 58:1757–65. doi: 10.2337/db09-0188
49. Matsui H, Yokoyama T, Sekiguchi K, Iijima D, Sunaga H, Maniwa M, et al. Stearoyl-Coa desaturase-1 (SCD1) augments saturated fatty acid-induced lipid accumulation and inhibits apoptosis in cardiac myocytes. *PLoS ONE*. (2012) 7:e33283. doi: 10.1371/journal.pone.0033283
50. Bedi S, Hines GV, Lozada-Fernandez V V, de Jesus Piva C, Kaliappan A, Rider SD, et al. Fatty acid binding profile of the liver X receptor α. *J Lipid Res*. (2017) 58:393–402. doi: 10.1194/jlr.M072447
51. Karaskov E, Scott C, Zhang L, Teodoro T, Ravazzola M, Volchuk A. Chronic palmitate but not oleate exposure induces endoplasmic reticulum stress, which may contribute to INS-1 pancreatic beta-cell apoptosis. *Endocrinology*. (2006) 147:3398–407. doi: 10.1210/en.2005-1494
52. Thörn K, Hovsepyan M, Bergsten P. Reduced levels of SCD1 accentuate palmitate-induced stress in insulin-producing β-cells. *Lipids Health Dis*. (2010) 9:108. doi: 10.1186/1476-511X-9-108
53. Busch AK, Gurisik E, Cordery DV, Sudlow M, Denyer GS, Ross Laybutt D, et al. Increased fatty acid desaturation and enhanced expression of stearoyl coenzyme A desaturase protects pancreatic β-cells from lipoapoptosis. *Diabetes*. (2005) 54:2917–24. doi: 10.2337/diabetes.54.10.2917
54. Ariyama H, Kono N, Matsuda S, Inoue T, Arai H. Decrease in membrane phospholipid unsaturation induces unfolded protein response. *J Biol Chem*. (2010) 285:22027–35. doi: 10.1074/jbc.M110.126870
55. Yen C-LE, Stone SJ, Koliwad S, Harris C, Farese RV. Thematic review series: glycerolipids. DGAT enzymes and triacylglycerol biosynthesis. *J Lipid Res*. (2008) 49:2283–301. doi: 10.1194/jlr.R800018-JLR200
56. Chamulitrat W, Liebisch G, Xu W, Gan-Schreier H, Pathil A, Schmitz G, et al. Ursodeoxycholyl lysophosphatidylethanolamide inhibits lipoapoptosis by shifting fatty acid pools toward monosaturated and polyunsaturated fatty acids in mouse hepatocytes. *Mol Pharmacol*. (2013) 84:696–709. doi: 10.1124/mol.113.088039
57. Li Y, Ge M, Ciani L, Kuriakose G, Westover EJ, Dura M, et al. Enrichment of endoplasmic reticulum with cholesterol inhibits sarcoplasmic-endoplasmic reticulum calcium ATPase-2b activity in parallel with increased order of membrane lipids: implications for depletion of endoplasmic reticulum calcium stores and apoptos. *J Biol Chem*. (2004) 279:37030–9. doi: 10.1074/jbc.M405195200
58. Holzer RG, Park E-J, Li N, Tran H, Chen M, Choi C, et al. Saturated fatty acids induce c-Src clustering within membrane subdomains, leading to JNK activation. *Cell*. (2011) 147:173–84. doi: 10.1016/j.cell.2011.08.034
59. Knecht V, Mark AE, Marrink S-J. Phase behavior of a phospholipid/fatty acid/water mixture studied in atomic detail. *J Am Chem Soc*. (2006) 128:2030–4. doi: 10.1021/ja056619o
60. Leekumjorn S, Cho HJ, Wu Y, Wright NT, Sum AK, Chan C. The role of fatty acid unsaturation in minimizing biophysical changes on the structure and local effects of bilayer membranes. *Biochim Biophys Acta Biomembr*. (2009) 1788:1508–16. doi: 10.1016/j.bbamem.2009.04.002
61. Bijelic R, Balaban J, Milicevic S. Correlation of the lipid profile, BMI and bone mineral density in postmenopausal women. *Mater Socio Medica*. (2016) 28:412. doi: 10.5455/msm.2016.28.412-415
62. Liu F, Wang W, Yang L, Wang B, Wang J, Chai W, et al. An epidemiological study of etiology and clinical characteristics in patients with

nontraumatic osteonecrosis of the femoral head. *J Res Med Sci*. (2017) 22:15. doi: 10.4103/1735-1995.200273
63. Okazaki S, Nagoya S, Matsumoto H, Mizuo K, Sasaki M, Watanabe S, et al. Development of non-traumatic osteonecrosis of the femoral head requires toll-like receptor 7 and 9 stimulations and is boosted by repression on nuclear factor kappa B in rats. *Lab Investig*. (2015) 95:92–9. doi: 10.1038/labinvest.2014.134
64. Han Y, Si M, Zhao Y, Liu Y, Cheng K, Zhang Y, et al. Progranulin protects against osteonecrosis of the femoral head by activating ERK1/2 pathway. *Inflammation*. (2017) 40:946–55. doi: 10.1007/s10753-017-0539-z
65. Rong X, Albert CJ, Hong C, Duerr MA, Chamberlain BT, Tarling EJ, et al. LXRs regulate ER stress and inflammation through dynamic modulation of membrane phospholipid composition. *Cell Metab*. (2013) 18:685–97. doi: 10.1016/j.cmet.2013.10.002
66. Tangirala RK, Bischoff ED, Joseph SB, Wagner BL, Walczak R, Laffitte BA, et al. Identification of macrophage liver X receptors as inhibitors of atherosclerosis. *Proc Natl Acad Sci*. (2002) 99:11896–901. doi: 10.1073/pnas.182199799
67. Fernández-Veledo S, Nieto-Vazquez I, de Castro J, Ramos MP, Brüderlein S, Möller P, et al. Hyperinsulinemia induces insulin resistance on glucose and lipid metabolism in a human adipocytic cell line: paracrine interaction with myocytes. *J Clin Endocrinol Metab*. (2008) 93:2866–76. doi: 10.1210/jc.2007-2472
68. Gao M, Bu L, Ma Y, Liu D. Concurrent activation of liver X receptor and peroxisome proliferator-activated receptor alpha exacerbates hepatic steatosis in high fat diet-induced obese mice. *PLoS ONE*. (2013) 8:e65641. doi: 10.1371/journal.pone.0065641
69. Maqdasy S, Trousson A, Tauveron I, Volle DH, Baron S, Lobaccaro J-MA. Once and for all, LXRα and LXRβ are gatekeepers of the endocrine system. *Mol Aspects Med*. (2016) 49:31–46. doi: 10.1016/j.mam.2016.04.001
70. Liang W, Wu X, Fang W, Zhao Y, Yang Y, Hu Z, et al. Network meta-analysis of erlotinib, gefitinib, afatinib and icotinib in patients with advanced non-small-cell lung cancer harboring EGFR mutations. *PLoS ONE*. (2014) 9:e85245. doi: 10.1371/journal.pone.0085245
71. Zhang J, Song F, Zhao X, Jiang H, Wu X, Wang B, et al. EGFR modulates monounsaturated fatty acid synthesis through phosphorylation of SCD1 in lung cancer. *Mol Cancer*. (2017) 16:127. doi: 10.1186/s12943-017-0704-x
72. Lu S, Xu F, Hu W, Niu Z, Cai H, Chen Y, et al. SCD1 methylation in subcutaneous adipose tissue associated with menopausal age. *Climacteric*. (2019) 22:395–402. doi: 10.1080/13697137.2019.1571028
73. Li X, Shet K, Xu K, Rodríguez JP, Pino AM, Kurhanewicz J, et al. Unsaturation level decreased in bone marrow fat of postmenopausal women with low bone density using high resolution magic angle spinning (HRMAS) 1H NMR spectroscopy. *Bone*. (2017) 105:87–92. doi: 10.1016/j.bone.2017.08.014

Conflict of Interest: The authors declare that the research was conducted in the absence of any commercial or financial relationships that could be construed as a potential conflict of interest.

frontiers in Endocrinology

REVIEW
published: 24 January 2020
doi: 10.3389/fendo.2019.00923

Standardised Nomenclature, Abbreviations, and Units for the Study of Bone Marrow Adiposity: Report of the Nomenclature Working Group of the International Bone Marrow Adiposity Society

Nathalie Bravenboer[1], Miriam A. Bredella[2], Christophe Chauveau[3,4,5,6], Alessandro Corsi[7], Eleni Douni[8,9], William F. Ferris[10], Mara Riminucci[7], Pamela G. Robey[11], Shanti Rojas-Sutterlin[12], Clifford Rosen[13], Tim J. Schulz[14,15] and William P. Cawthorn[16] on behalf of the Nomenclature Working Group of the International Bone Marrow Adiposity Society (BMAS)[†]*

[1] Department of Clinical Chemistry, Amsterdam Movement Sciences, Amsterdam University Medical Center, Vrije Universiteit, Amsterdam, Netherlands, [2] Department of Radiology, Massachusetts General Hospital and Harvard Medical School, Boston, MA, United States, [3] Univ. Littoral Côte d'Opale, Boulogne-sur-Mer, France, [4] Univ. Lille, Lille, France, [5] CHU Lille, Lille, France, [6] Physiopathologie des Maladies Osseuses Inflammatoires, Boulogne-sur-Mer, France, [7] Department of Molecular Medicine, Sapienza University of Rome, Rome, Italy, [8] Biological Sciences Research Center "Alexander Fleming", Athens, Greece, [9] Department of Biotechnology, Agricultural University of Athens, Athens, Greece, [10] Division of Endocrinology, Department of Medicine, Faculty of Medicine and Health Sciences, Stellenbosch University, Cape Town, South Africa, [11] Skeletal Biology Section, NIDCR, NIH, DHHS, Bethesda, MD, United States, [12] Institute for Research in Immunology and Cancer, Université de Montréal, Montreal, QC, Canada, [13] Maine Medical Research Center Institute, Scarborough, ME, United States, [14] German Institute of Human Nutrition Potsdam-Rehbrücke, Nuthetal, Germany, [15] German Center for Diabetes Research (DZD), München, Germany, [16] BHF Centre for Cardiovascular Science, The Queen's Medical Research Institute, University of Edinburgh, Edinburgh, United Kingdom

Research into bone marrow adiposity (BMA) has expanded greatly since the late 1990s, leading to development of new methods for the study of bone marrow adipocytes. Simultaneously, research fields interested in BMA have diversified substantially. This increasing interest is revealing fundamental new knowledge of BMA; however, it has also led to a highly variable nomenclature that makes it difficult to interpret and compare results from different studies. A consensus on BMA nomenclature has therefore become indispensable. This article addresses this critical need for standardised terminology and consistent reporting of parameters related to BMA research. The International Bone Marrow Adiposity Society (BMAS) was formed in 2017 to consolidate the growing scientific community interested in BMA. To address the BMA nomenclature challenge, BMAS members from diverse fields established a working group (WG). Based on their broad expertise, the WG first reviewed the existing, unsystematic nomenclature and identified terms, and concepts requiring further discussion. They thereby identified and defined 8 broad concepts and methods central to BMA research. Notably, these had been described using 519 unique combinations of term, abbreviation and unit, many of which were overlapping or redundant. On this foundation a second consensus was reached, with each term classified as "*to use*" or "*not to use.*" As a result, the WG reached

OPEN ACCESS

Edited by:
Guillaume Mabilleau, Université d'Angers, France

Reviewed by:
Stéphane Blouin, Ludwig Boltzmann Institute of Osteology (LBIO), Austria
Beata Lecka-Czernik, University of Toledo, United States
Natalie A. Sims, St Vincents Institute of Medical Research, Australia

***Correspondence:**
William P. Cawthorn
W.Cawthorn@ed.ac.uk

[†]Authors are ordered alphabetically by surname, except for the corresponding author

Specialty section:
This article was submitted to Bone Research, a section of the journal Frontiers in Endocrinology

Received: *11 September 2019*
Accepted: *18 December 2019*
Published: *24 January 2020*

Citation:
Bravenboer N, Bredella MA, Chauveau C, Corsi A, Douni E, Ferris WF, Riminucci M, Robey PG, Rojas-Sutterlin S, Rosen C, Schulz TJ and Cawthorn WP (2020) Standardised Nomenclature, Abbreviations, and Units for the Study of Bone Marrow Adiposity: Report of the Nomenclature Working Group of the International Bone Marrow Adiposity Society. Front. Endocrinol. 10:923. doi: 10.3389/fendo.2019.00923

a consensus to craft recommendations for 26 terms related to concepts and methods in BMA research. This was approved by the Scientific Board and Executive Board of BMAS and is the basis for the present recommendations for a formal BMA nomenclature. As an example, several terms or abbreviations have been used to represent "bone marrow adipocytes," including *BMAds*, *BM-As*, and *BMAs*. The WG decided that *BMA* should refer to "bone marrow adiposity"; that *BM-A* is too similar to *BMA*; and noted that "Ad" has previously been recommended to refer to adipocytes. Thus, it was recommended to use *BMAds* to represent *bone marrow adipocytes.* In conclusion, the standard nomenclature proposed in this article should be followed for all communications of results related to BMA. This will allow for better interactions both inside and outside of this emerging scientific community.

Keywords: nomenclature, bone marrow adiposity, bone marrow adipose tissue, bone marrow adipocyte, skeletal stem cells, histomorphometry, MRI, computed tomography

INTRODUCTION

Bone marrow adiposity (BMA) is the phenomenon of fat storage within the bone marrow (BM). Several different cell types within the skeleton are capable of lipid uptake, including haematopoietic stem cells and osteoblasts (1–3). However, BM adipocytes are the principal cell type responsible for this BM fat storage. Studies relating to BMA have been published since at least the mid-nineteenth century, yet for much of the twentieth century there was relatively little research in this field. However, the past 20 years have seen a resurgence of interest in this topic: even as publication rates have grown across all fields, publications relating to BMA are increasing at an even greater rate (**Figure 1**). While the earliest studies of BM adipocytes focused on their roles in haematopoiesis, the field has since expanded to include many other disciplines, including skeletal biology, endocrinology and metabolism, stem cells, cancer biology, ageing, biomedical imaging, and beyond. This multidisciplinary nature is one of the strengths of the burgeoning BMA research community; however, it has also contributed to increasing variability in the terminology used in the BMA literature (**Figure 1**). This is leading to confusion and risks hindering progress in this field. Therefore, there is a need for a standardised nomenclature to facilitate communication between researchers from different fields, and to provide a foundation and consensus for future research relating to BMA.

The challenges for BMA nomenclature were first discussed in 2017 at the Third International Meeting on Bone Marrow Adiposity in Lausanne, Switzerland (4). To address this challenge, members of the International Bone Marrow Adiposity Society (BMAS), representing diverse fields, established a Nomenclature Working Group (WG). The authors of this manuscript represent the Nomenclature WG of BMAS. Our WG has since met several times, including via teleconference and in person, to identify the present state of nomenclature relevant to BMA research and to identify recommended terms, abbreviations and units for a standardised nomenclature. As stated in a previous nomenclature

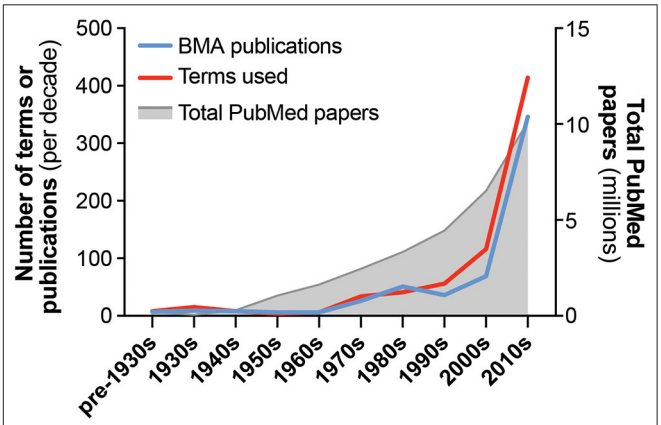

FIGURE 1 | Growth in publications and terminology related to bone marrow adiposity. The number of publications and unique terms relevant to the study of bone marrow adiposity (BMA) are shown, arranged by decade of publication. Also shown is the total number of papers indexed in PubMed for each time period. Publications relevant to BMA were identified through a systematic search of PubMed using the following terms: "marrow[Title] AND (fat[Title/Abstract] OR adipose[Title/Abstract] OR adipocyte[Title/Abstract] OR adiposity[Title/Abstract])"; publication dates up to 31/07/2019 were included. Because earlier studies (e.g., pre-1950) are often not indexed in PubMed, many of these papers were added manually based on our existing knowledge of the literature. Search results were then manually assessed to identify publications relevant to the study of BMA and to exclude results that were not directly relevant. This was necessary because many results related to other subjects, such as fat embolisms of bone marrow or, from 2000 onwards, adipose tissue stem cells. This approach identified 568 papers relevant to BMA nomenclature. By reading these papers, we distinguished the full range of terms that have been used to report concepts and/or measurements related to BMA research. If terms were associated with an abbreviation and/or unit of measurement, these were also recorded. Together, this generated a list of 519 unique combinations of term, abbreviation and unit; if two papers used the same term (e.g., bone marrow adipocyte) but with different abbreviations or units (e.g., BMAd vs. BM-AD), then these were counted as two unique terms. The number of papers and unique terms used per decade are shown. Key concepts and methods are described in **Table 1**, and terms related to these are presented in **Tables 2**–**9**. Further details are provided in **Supplementary Tables 1–8**.

position paper for bone histomorphometry (5), "*Our purpose is not to encourage or discourage the use of abbreviations and symbols but to ensure that the same ones are used by everybody*."

PUBLICATIONS AND TERMINOLOGY FOR THE STUDY OF BONE MARROW ADIPOSITY: HISTORICAL PERSPECTIVES

The existence of adipocytes as a major component of the BM has been noted since at least the 1860s, when Bizozzero and Neumann independently identified BM as the site of blood production (6, 7). In his seminal 1875 book on histology, Ranvier noted that caudal vertebrae of tailed animals are full of fat (8), further confirming that fat is a constituent of normal BM anatomy. Thereafter, references to fat cells, "yellow marrow" and "yellow adipose tissue" within the BM can be found not only in the writings of Neumann (9), but also in contemporary English-language works on pathology and BM anatomy (10, 11). Indeed, Coats noted that the BM is a place "*where normally adipose tissue exists*" (10). Use of the term "yellow marrow" underscored its distinction from the "red marrow" in which haematopoiesis occurs.

Piney's excellent 1922 paper summarised these earlier studies of BM anatomy but used the term "fatty marrow" instead of "yellow marrow" or "yellow adipose tissue" (12). Both "fatty marrow," "yellow marrow," and "yellow bone marrow" continued to be used interchangeably in the 1930s, sometimes being combined into the term "yellow fatty marrow" (13–19) or "yellow fat" (15). These and other contemporaneous studies continued to highlight the existence of "fat cells" in histological BM sections (15, 16, 18–21) but the term "adipocyte" is rarely used, and some papers ignore this cellular nature by instead referring to "fat spaces," (22). Still other studies mention BM fat cells without referring to "fatty marrow" or "yellow marrow" (20, 21), and vice versa (17). Thus, in the 1930s it seems that BM adipocytes were not yet considered as an integrated adipose tissue.

In the latter half of the 1930s and the early 1940s, the term "bone marrow fat" begins to appear, often used alongside "fatty marrow" and "yellow marrow" (19, 23). The term "red marrow fat" was also used in contrast to "yellow marrow fat" (23); this demonstrates recognition that adipocytes also exist in the red marrow, and that these may have different properties to those within the yellow marrow. Hilditch and Murti further noted that the "bone marrow fat" of oxen shares properties of perinephric adipose tissue (23), presaging later suggestions that adipocytes within BM might constitute a *bona fide* adipose tissue (24). Nevertheless, the notion of marrow fat as an adipose tissue was not reiterated until the mid-1950s when Evans et al. suggested that marrow fat is essentially a fat depot, based on its similar lipid composition to perinephric adipose tissue (24). This period also sees the first use of more-quantitative histomorphometric analyses (25, 26), although it is not until the late 1980s that this would become widespread.

From the mid-1950s to mid-1960s the use of "marrow fat" became far more prevalent (24, 27–30), largely replacing "yellow marrow" as the term of choice. One notable exception is the 1967 study by Zakaria and Shafrir (31), who introduced the acronym "YBM" to refer to yellow bone marrow. They showed that, like white adipose tissue (WAT), YBM is capable of uptake and esterification of glucose and free fatty acids, as well as lipolysis for fatty acid release. Based on this, they concluded that YBM could be considered an adipose tissue. This period also includes one of the earliest uses of "marrow adiposity" (32), a term that has become increasingly prevalent in the past two decades (**Table 2**).

The 1970s saw increased interest in BMA, with notable growth in both the number of publications and the range of terms used therein (**Figure 1**). The terms "bone marrow adipose tissue" and "bone marrow adipocyte" first appear in the mid-1970s (33, 34), with another obvious shift being the increasing use of "marrow adipose cells," "marrow adipocytes," "marrow adipose tissue," or "bone marrow adipose tissue" (33–45). This may reflect the growing recognition of BM adipocytes, collectively, as an integrated adipose tissue. However, many contemporary papers continued using "fatty marrow," "yellow marrow," and "marrow fat" (46–51), and in some cases a mixture of all of these terms can be found within a single paper (52). Thus, the increased study of BMA did not coincide with any consensus or standardisation of the nomenclature used. The late 1970s also saw the use of terms to specify anatomical location, such as "femoral" or "vertebral adipose cell" (40), or "proximal" and "distal" to describe marrow fat and red marrow (51). As we discuss herein in the section on Subtypes of Bone Marrow Adipocytes, terms addressing the site-specific properties of BM adipocytes are an important aspect of the standardised nomenclature for BMA research (**Tables 1**, **6**).

The number of BMA-related publications and terms continued to increase in the 1980s (**Figure 1**), with one notable development being the emergence of new methods for quantitative assessment of BMA. These include magnetic resonance imaging (MRI) (53–57), computed tomography (CT) and dual-energy CT (58–61), and advances in histomorphometric analysis (62–64). Typically, these methods provide readouts of the fraction of BM consisting of fat or adipocytes, as reflected by use of terms such as "fat fraction" (56), "fat content" (57–59, 61, 65), and "adipose tissue fraction" (63). These method-related terms often are associated with units of measurement, although the units used frequently vary between studies. This theme has persisted in more-recent BMA research, with numerous combinations of terms, abbreviations, and units applied to the same measurement (**Tables 7–9**). Thus, an important goal of our proposed nomenclature is to standardise the terminology used in reporting common measurements in the BMA field.

In the 1990s there was further growth in the number of terms used, despite a slight decrease in publications (**Figure 1**). This suggests an increasing diversity and continued lack of consensus for BMA nomenclature. Studies using histomorphometry or MRI became increasingly prevalent, with proton magnetic resonance spectroscopy (1H-MRS) also emerging as a powerful tool for BMA quantification (**Tables 7**, **8**). The 1990s also saw an increased focus on progenitors for BM adipocytes, exemplified by references to "bone marrow stromal cells" (**Table 6**).

TABLE 1 | Key concepts and methods in the field of bone marrow adiposity.

Concept or method	Definition	Recommended terms and abbreviations	Further details
Bone marrow adiposity	The phenomenon of fat storage within the bone marrow (BM), primarily within BM adipocytes.	• Bone marrow adiposity (BM adiposity; BMA) • Yellow marrow; red marrow; fatty marrow (*Not abbreviated*)	**Table 2**
Bone marrow adipocytes	The cells within the BM whose primary function is lipid storage.	• Bone marrow adipocyte (BM adipocyte; BMAd)	**Table 3**
Bone marrow adipose tissue	The functionally integrated tissue formed collectively by BM adipocytes	• Bone marrow adipose tissue (BMAT) • Bone marrow fat (BM fat)	**Table 4**
Site-specific differences (BMAd subtypes)	The concept that BM adipocytes have distinct morphological, molecular and functional characteristics, depending on their skeletal location. This may also apply to BMAd progenitors.	• Constitutive or Regulated BMAT or BMAd (cBMAT, cBMAd; rBMAT, rBMAd) • *Use "distal" or "proximal" to denote BMAT or BMAd location within long bones; and bone-specific terms to denote skeletal site (e.g., femoral, tibial, vertebral, etc…)*	**Table 5**
Stem and progenitor cells	The self-renewing, multipotent progenitor cells within the BM that give rise to adipocytes, osteoblasts, chondrocytes, and fibroblasts.	• Skeletal stem cell (SSC) • Bone marrow stromal cell (BMSC) • *Do not refer to bone marrow/mesenchymal "stem" cells (this is a misnomer)*	**Table 6**
Histo-morphometry	Use of histomorphometry to quantify bone marrow adiposity, either on a per-adipocyte level (e.g., *Ad.Ar, Ad.Dm, Ad.Pm*)* or a whole-tissue level *(e.g., adipocyte density, adipose area, adipose volume).*	• Adipocyte area (Ad.Ar, μm^2) • Adipocyte diameter (Ad.Dm, μm) • Adipocyte perimeter (Ad.Pm, μm) • Adipocyte density *or* Adipocyte Number* (N.Ad relative to Ma.Ar, Ma.V, T.Ar or TV) • Adipose area* (Ad.Ar relative to Ma.Ar, T.Ar; report as %) • Adipose volume* (Ad.V relative to Ma.V or TV; report as %)	**Table 7**
Magnetic resonance imaging or spectroscopy (MRI/MRS)	Use of proton-based MRI/MRS to quantify the proportion or absolute amount of fat within the BM. Typically *in vivo,* volumetric measurements.	• Fat fraction (FF, %) • Bone marrow fat fraction (BMFF, %) • Proton density fat fraction (PDFF, %)	**Table 8**
Computed tomography	Use of CT to estimate BM fat fraction, or μCT to measure BMAT volume or BMAd density. Typically done *ex vivo* using contrast agents but can also be done *in vivo*.	• FF (%) or BMFF (%) • Adipose area per marrow area*(Ad.Ar/Ma.Ar, %) • Adipose volume per marrow volume* (Ad.V/Ma.V, %) • Adipocyte density* (N.Ad/Ma.V or N.Ad/M.Ar)	**Table 9**

These concepts and methods were identified through a systematic literature search, as described in the legend to ***Figure 1****. The recommendations include 26 unique terms and 35 abbreviations. Abbreviations used in this table (*) are defined as follows: N.Ad, adipocyte number; Ad.Ar, total adipocyte area; Ad.V, total adipocyte volume; Ma.Ar, marrow area; Ma.V, marrow volume; T.Ar, tissue area; TV, tissue volume. Further details for each concept/method are provided in the indicated tables and in the main text.*

The numbers of BMA-related papers and terminology further increased in the 2000s, and since 2010 this growth has been even more substantial (**Figure 1**). The abbreviation BMAT, for "bone marrow adipose tissue," first appears in 2007 (66), preceding the first use of MAT ("marrow adipose tissue") in 2012 (67); each of these abbreviations is now widespread in the BMA literature (**Table 3**). Similarly, "bone marrow adiposity" first appears in 2002 but has become increasingly prevalent ever since (68) (**Table 2**). The past two decades have also witnessed the development of new methods for BMA analysis, including μCT of osmium tetroxide-stained bones (69, 70) and advances in MRI/MRS-based quantitation (71). These developments therefore have led to the introduction of additional new terms related to such methods (**Tables 7–9**). Many other notable terms have also emerged in the BMA literature during this period, such as SSC (for "skeletal stem cell") (72) (**Table 6**), and use of "regulated" and "constitutive" to distinguish distinct BMAT subtypes (73) (**Table 5**). Given the vast number of terms used since 2000, it is not possible to succinctly summarise all of the key developments in these paragraphs. Therefore, readers should consult **Tables 1–9**, and further data in the Supplement, for a full overview of the nomenclature used in the BMA literature to date.

KEY CONCEPTS AND GOALS FOR A STANDARDISED NOMENCLATURE

This historical overview is based on our systematic search of PubMed (**Figure 1**) and our knowledge of other less-accessible papers. Thus, references to the "first use" of a term apply only to this extensive body of BMA-related literature; because some relevant publications may have been missed, some terms may have even earlier uses. Nevertheless, these historical perspectives

TABLE 2 | Summary of terms and abbreviations that have been used to refer to bone marrow adiposity, yellow marrow, fatty marrow, or red marrow.

Term	Abbreviation	Year first used*	No. of papers using this term*	Recommended term(s) and abbreviation(s)
BONE MARROW ADIPOSITY				
Marrow adiposity	–	1967	119	Bone marrow adiposity (BM adiposity, BMA)
Bone marrow adiposity	–	2002	78	
	BM adiposity	2011	12	
	BMA	2013	9	
	BMAT	2017	1	
Bone adiposity	–	2009	4	
YELLOW MARROW				
Yellow marrow	–	1883	109	Yellow marrow (*No abbreviation)*
	YM	2010	1	
Yellow bone marrow	–	1936	23	
	YBM	1967	2	
	Yellow BM	1996	2	
	YM	2019	1	
Yellow fatty marrow; yellow fatty bone marrow; yellow fat marrow	–	1933	7	
FATTY MARROW				
Fatty marrow	–	1922	82	Fatty marrow (*No abbreviation*)
Fatty bone marrow	–	1990	7	
	Fatty BM	2008	1	
Fatty yellow marrow	–	2013	7	
RED MARROW				
Red marrow	–	1883	122	Red marrow *(No abbreviation)*
	RM	2010	2	
Red marrow (active marrow)	–	2003	1	
Red bone marrow	–	1922	21	
	Red BM	1996	2	
	RM	2019	1	
	RBM	2015	2	
h(a)em(at)opoietic marrow	–	1936	24	
OTHER TERMS (SEE SUPPLEMENTARY TABLE 1)				

Relevant terms and abbreviations were identified through a systematic search of the literature relating to bone marrow adiposity. Within these search results, the total number of papers using each term/abbreviation combination is indicated, along with the year that these were first used; asterisks (*) are shown to emphasise that other uses may exist. For most terms, no abbreviation is used (–). Based on this and other considerations (described in the main text), we recommend use of the term bone marrow adiposity (abbreviated as "BM adiposity" or "BMA"). Use of the terms "yellow marrow," "fatty marrow" or "red marrow" is also acceptable, given the long-term use of these terms in the BMA literature. Red marrow is in some cases described as hematopoietic marrow, hemopoietic marrow, haematopoietic marrow or haemopoietic marrow; for simplicity, we have grouped together papers using these spelling variants. Terms specific to measurements of bone marrow adiposity, such as "fat fraction" or "fat content," have not been included and are shown instead in ***Tables 6–8****. Additional terms and abbreviations, as well as references for papers using each combination, are provided in* ***Supplementary Table 1****.*

on the BMA literature provide an essential foundation on which to establish a standardised nomenclature for studies relevant to BMA. The two major benefits of this literature review are as follows.

Firstly, we show that the existing BMA literature uses a highly diverse, heterogeneous terminology to report concepts and measurements relevant to BMA. As shown in **Figure 1**, the rate of publications within the BMA literature has increased dramatically in the past decade, reflecting the growing interest in this topic; however, the number of unique terms is growing even more quickly (**Figure 1**). Thus, since the 1990s, there has been an increasing diversity and lack of consensus for nomenclature relating to BMA research. Indeed, new terms continue to be proposed to this day (74). It is likely that research into BMA will continue expanding, and therefore it is essential to adopt a standardised nomenclature to provide a foundation and consensus for this growing field.

Secondly, reviewing the history of BMA research has identified key concepts and methods relevant to studies of BMA (**Table 1**). A standardised nomenclature must therefore incorporate terms, abbreviations and units related to these concepts and methods.

The following sections provide further discussion of the nomenclature for each of these, concluding with recommendations for the terms, abbreviations and units to be used in future reports of BMA research.

TABLE 3 | Summary of terms and abbreviations used to refer to bone marrow adipocytes.

Term	Abbreviation	Year first used*	No. of papers using this term*	Recommended term(s) and abbreviation(s)
BONE MARROW ADIPOCYTE				
Adipocyte	–	1981	39	Bone marrow adipocyte (BM adipocyte, BMAd)
	AC	2018	1	
Adipose cell	–	1971	16	
	Adip	2005	1	
Bone adipocyte	–	1981	6	
Marrow adipocyte	–	1978	105	
Marrow adipose cell	–	1971	8	
Bone marrow adipocyte	–	1976	100	
	BM adipocyte	1995	30	
	BMA	2016	17	
	BMAd	2019	2	
	MAT adipocyte	2015	6	
	BMAT adipocyte	2018	3	
	BM-A	2013	2	
	BM-AD	2018	2	
	Marrow AC	2016	1	
Bone marrow adipose cell	–	1974	3	
Marrow-associated adipose cell	–	1974	1	
Medullary adipocyte	–	2010	1	
Skeletal adipocyte	–	2015	1	
Yellow adipocyte	–	2019	1	
BONE MARROW FAT CELL				
Fat cell	–	1893	48	Don't use
	FC	1935	1	
Fatty cell	–	1985	3	
Marrow fat cell	–	1931	14	
Bone marrow fat cell	–	1966	10	
	BM fat cell	1998	1	
Fat-containing cell	–	1980	2	
	FCC	1983	1	
OTHER TERMS (SEE SUPPLEMENTARY TABLE 2)				

*Data are presented as described for **Table 2**; asterisks (*) are shown in the column headers to emphasise that other uses may exist.*
*Based on this and other considerations (described in the main text), we recommend use of the term bone marrow adipocyte, abbreviated as BM adipocyte or BMAd. Terms related to measurements of bone marrow adipocytes, such as "adipocyte density," have not been included and are shown instead in **Tables 6**–**8**. Additional terms and abbreviations, as well as references for papers using each combination, are provided in **Supplementary Table 2**.*

NOMENCLATURE RECOMMENDATIONS

Bone Marrow Adiposity

We define bone marrow adiposity as "The phenomenon of fat storage within the BM, primarily within BM adipocytes." This can be considered an overarching concept for the field: it is the central theme that links several diverse disciplines, including haematology, bone biology, metabolism, endocrinology, stem cells, developmental biology, oncology, gerontology, and beyond. Given the centrality of this concept, we think it is important to provide both a clear definition and a standardised abbreviation for use in future studies. The abbreviation "BM adiposity" is recommended because "BM" is already used across the biomedical literature to refer to bone marrow, and therefore "BM adiposity" should be widely understandable. However, we also recommend the abbreviation "BMA" for two reasons: firstly, this abbreviation for "bone marrow adiposity" has become increasingly common in the literature since its first use in 2013 (**Table 2**); and, secondly, "BMA" is now recognised for this meaning through its use in the name BMAS (the International Bone Marrow Adiposity Society) and in the names of the five international meetings devoted to this topic (BMA2015–BMA2019) (4, 75, 76). It is important to note that BMA has also been used as an acronym for "bone marrow aspiration" (77) and "bone marrow aspirate" (78); however, the increasing use and recognition of BMA to refer to bone marrow adiposity should minimise any confusion with these other uses.

In considering the concept of BMA, it is essential to also highlight the terms "yellow marrow," "fatty marrow," and "red marrow." Each of these refers to concepts intimately

TABLE 4 | Summary of terms and abbreviations used to refer to bone marrow adipose tissue, yellow adipose tissue, or marrow fat.

Term	Abbreviation	Year first used*	No. of papers using this term*	Recommended term(s) and abbreviation(s)
BONE MARROW ADIPOSE TISSUE				
Adipose tissue	–	1883	17	Bone marrow adipose tissue (BMAT)
Adipose tissue from bone marrow	–	1999	1	
Adipose marrow	–	1991	4	
Adipose marrow tissue	–	2017	1	
Marrow adipose	–	1971	2	
Marrow adipose tissue	–	1971	31	
	MAT	2012	56	
Marrow-associated adipose tissue	–	1974	1	
Bone marrow adipose	–	1979	5	
bone marrow adipose tissue	–	1974	34	
	BMAT	2007	49	
	BM adipose tissue	1988	6	
	MAT	2014	15	
	BM-AT	2019	1	
MARROW FAT				
Marrow fat	–	1954	101	Marrow fat or Bone marrow fat (BM fat)
	MF	2008	3	
Bone marrow fat	–	1936	80	
	BM fat	2002	3	
	BMF	2007	11	
	MF	2014	1	
Medullary fat	–	1994	2	
Bone fat	–	2010	1	
YELLOW ADIPOSE TISSUE				
Yellow adipose tissue	–	1883	2	Don't use
	YAT	2011	4	
Yellow adipose	–	2016	1	
Yellow fat	–	1933	2	
Yellow adipose marrow	–	2018	1	
Fatty tissue	–	1922	1	
Fatty yellow adipose tissue	–	2019	1	
Bone marrow fatty tissue	–	1993	1	

*Data are presented as described for **Table 2**; asterisks (*) are shown in the column headers to emphasise that other uses may exist. Based on this and other considerations (described in the main text), we recommend use of the term bone marrow adipose tissue, abbreviated as BMAT. Use of "marrow fat" or "bone marrow fat (BM fat)" is also acceptable, given the long-standing use of these terms in the BMA literature. References for papers using each combination of term and abbreviation are provided in **Supplementary Table 3**.*

related to BMA and has longstanding and widespread use in the field (**Table 2**). Thus, "yellow marrow" and "fatty marrow" are used to refer to more-lipid-laden regions of BM whereas "red marrow" refers to those regions of the BM where adiposity is less prominent and haematopoiesis predominates; each of these terms is also used for macroscopic descriptions of different regions of BM, often in clinical contexts. Although numerous variations of these three terms have been used, "yellow marrow," "fatty marrow," and "red marrow" are by far the most common (**Table 2** and **Supplementary Table 1**). Thus, given their widespread use, historical significance and clinical recognition, we recommend continued use of these terms in future studies relevant to BMA.

Further details of these four recommended terms, and the many terms that we recommend to avoid using, are provided in **Table 2** and **Supplementary Table 1**.

Bone Marrow Adipocytes

A defining feature of BMA is the storage of lipid within bone marrow adipocytes. We define these cells as a population of *bona fide* adipocytes, that is, a cell type whose main functional and morphological characteristic is the storage and metabolism of lipids in a single large or several smaller triglyceride-filled vacuoles. This distinguishes adipocytes from other cell types, such as hepatocytes and myofibers, that in principle are also able to store triglycerides ectopically. In these latter cells, lipid accumulation is thought of as predominantly

TABLE 5 | Summary of terms and abbreviations used to refer to different subtypes of BMAT and BMAds.

Term used	Abbreviation	Year first used*	No. of papers using this term*	Recommended term(s) and abbreviation(s)
CONSTITUTIVE OR REGULATED BMAT AND BMAds				
Constitutive marrow adipose tissue	cMAT	2014	26	**Use of cBMAT, cBMAd, rBMAT, and rBMAd is acceptable** *(But when discussing subtypes, it is preferable to refer to skeletal location of the BMAT and BMAds)*
	Constitutive MAT	2017	1	
Constitutive bone marrow adipose tissue	cBMAT	2017	7	
	Constitutive BMAT	2017	2	
Constitutive bone marrow adipocyte	cMAT adipocyte	2015	6	
	cBMA	2016	7	
Regulated marrow adipose tissue	rMAT adipocyte	2014	26	
	Regulated MAT	2017	1	
Regulated bone marrow adipose tissue	rBMAT	2017	7	
	Regulated BMAT	2017	2	
Regulated bone marrow adipocyte	rMAT adipocyte	2015	6	
	rBMA	2016	8	
	–	2017	1	
DISTAL OR PROXIMAL BMAT AND BMAds				
Distal marrow adipose tissue	distal MAT	2016	1	**Use "distal" or "proximal" to refer to BMAT/BMAd location within long bones**
Distal marrow fat	–	1979	1	
Distal tibia marrow adipose tissue	dMAT	2017	1	
Proximal marrow adipose tissue	Proximal MAT	2016	1	
Proximal marrow fat	–	1979	1	
Proximal tibia marrow adipose tissue	pMAT	2017	1	
BONE-SPECIFIC TERMS				
Femoral adipose cell	–	1977	1	**When required, use bone-specific terms to indicate location of BMAT or BMAds** *(see text for further details)*
Femur marrow fat	FMF	1984	1	
Tibial adipose bone marrow	–	1985	1	
Vertebrae adipose cell	–	1977	1	
Vertebral fat	–	1989	1	
Intravertebral bone marrow fat	–	2002	1	
Vertebral bone marrow fat	–	2012	1	
	VMB fat	2017	1	
Vertebral BMAT	vBMAT	2018	1	
Vertebral marrow fat	–	2012	1	
Vertebral MAT	vMAT	2018	1	
BMAT WITHIN RED OR YELLOW MARROW				
Red marrow fat	–	1940	2	**Don't use**
Red bone marrow fat	–	2001	2	
	RBM fat	2019	1	
Red marrow adipose tissue	rMAT	2018	2	
Yellow marrow adipose tissue	yMAT	2018	2	

*Data are presented as described for **Table 2**; asterisks (*) are shown in the column headers to emphasise that other uses may exist. When necessary, we recommend indicating site-specific differences in BMAT/BMAd subtypes by referring to the skeletal site (e.g., "femoral," "tibial," "vertebral") and the location within these bones (e.g., "proximal" or "distal"). Use of "constitutive" or "regulated" is also acceptable, with the recommended acronyms being cBMAT, cBMAd, rBMAT, and rBMAd, consistent with the recommended nomenclature for bone marrow adipocytes (BMAd) and bone marrow adipose tissue (BMAT). Further considerations are provided in the main text. References for papers using each combination of term and abbreviation are provided in **Supplementary Table 4**.*

TABLE 6 | Summary of terms and abbreviations used to refer to progenitors for BMAds.

Abbreviation	Term used	Year first used*	No. of papers using this term*	Recommended term(s) and abbreviation(s)
SSC	Skeletal stem cell (SSC)	2004	12	**Skeletal stem cell (SSC)**
	Skeletal stem cell (*no abbreviation)*	2004	11	
	Mouse skeletal stem cell (mSSC)	2015	1	
	human skeletal stem cell (hSSC)	2018	1	
BMSC	Bone marrow stromal cell	2004	20	**Use BMSC to refer to bone marrow stromal cells** *(see text for further considerations)*
	Bone marrow mesenchymal stem cell	2013	5	
	Bone marrow mesenchymal stem cell	2012	1	
	Bone marrow stromal cell (mBMSC)**	2015	1	
	Bone mesenchymal stem cell	2016	1	
	Bone-derived marrow mesenchymal stem cell	2017	1	
	Bone marrow stromal cell (BM stromal cell)	2017	1	
	Bone marrow mesenchymal cell	2018	1	
	Bone marrow mesenchymal stromal cell	2018	1	
	Not defined	2018	1	
	Bone marrow mesenchymal stem/stromal cell	2019	1	
MSC	Mesenchymal stem cell	2003	59	**Don't use**
	Mesenchymal stromal cell	2012	10	
	Abbreviation not defined	2015	5	
	Human mesenchymal stem cell (hMSC)	2004	4	
	Bone marrow mesenchymal stromal cell	2014	4	
	Mesenchymal stem/stromal cell	2016	4	
	Marrow stromal cell	2003	3	
	Bone marrow mesenchymal stem cell	2015	3	
	Bone marrow stromal cell	2004	2	
	Human bone marrow stromal cell (hMSC)	2004	1	
	Bone marrow mesenchymal stem cell	2012	1	
	Mesenchymal progenitor	2016	1	
	Bone marrow-derived mesenchymal stem cell	2018	1	
	Bone mesenchymal stem cell	2018	1	
BM-MSC	Bone marrow mesenchymal stem cell	2013	5	**Don't use**
	Bone marrow mesenchymal stromal cell	2018	2	
	Bone marrow MSC	2017	1	
	Bone marrow skeletal stem cell‡	2018	1	
	Bone marrow stromal stem cell‡	2019	1	

*No abbreviation used (see **Supplementary Table 5**)*

*Data are presented as described for **Table 2**; asterisks (*) are shown in the column headers to emphasise that other uses may exist. Terms are organised by abbreviation used, and then by frequency and date of use. Further considerations are provided in the main text. Terms used without an abbreviation, and references for papers using each combination of term and abbreviation, are presented in **Supplementary Table 5**.*

***mBMSC, mouse bone marrow stromal cell.*

‡Although we recommend using "skeletal stem cell" and "bone marrow stromal cell," the former should be abbreviated as "SSC" rather than "BM-MSC"; and the latter should be described as a "stromal cell," not a "stem cell," and should be abbreviated as "BMSC," not as "BM-MSC".

pathological, presumably due to lipotoxic reactions. In addition, haematopoietic stem cells and osteoblasts are also capable of lipid uptake (1–3). However, unlike these other cell types, mature adipocytes are uniquely equipped for metabolising and storing triglycerides and intermediates of lipid metabolism and feature a higher level of resistance to lipotoxicity. We would therefore also recommend against use of less-specific or even colloquial terms, including "fatty cell" or "fat cell" in a combination with the bone marrow, as these may refer to any type of lipid-containing cell (**Table 3** and **Supplementary Table 2**).

A number of abbreviations to specifically define bone marrow-resident adipocytes have been used in the recent literature

TABLE 7 | Summary of terms, abbreviations, and units that have been used to report histomorphometric measurements of bone marrow adiposity.

Measurement type	Year first reported*	No. of papers*	Recommended term(s)	Recommended abbreviation(s) and unit(s)
Adipocyte area (per cell; mean or median)	2002	28	**Adipocyte area** (mean or median)	Ad.Ar, μm2 *(Showing the frequency distribution of Ad.Ar is recommended)*
Adipocyte area (total)	2015	1	**Don't use** *(instead report as % Ma.Ar or % T.Ar)*	
Adipocyte diameter (per cell; mean or median)	1989	25	**Adipocyte diameter** (mean or median)	Ad.Dm, μm *(Showing the frequency distribution of Ad.Dm is recommended)*
Adipocyte perimeter (per cell; mean or median)	2002	5	**Adipocyte perimeter** (mean or median)	Ad.Pm, μm *(Showing the frequency distribution of Ad.Pm is recommended)*
Adipocyte perimeter (total; mean or median)	2015	1	**Don't use** *(instead report average Ad.Pm per cell, as above)*	
Adipocyte density (cells per field, area, or volume)	1990	70	**Adipocyte density** or **Adipocyte number**	N.Ad/Ma.Ar, N.Ad/Ma.V, N.Ad /T.Ar, N.Ad /TV. *Units should be clearly stated (e.g., cells/mm2, cells/μm2, etc …)*
Adipocyte number (absolute N.Ad without clearly defined referent)	1993	10	**Don't use** *(instead report Adipocyte density or Adipocyte number as N.Ad per referent area or volume, as above)*	
Adipose area (per field, marrow area or tissue area)	1950	39	**Adipose area** or **Adipose tissue area**	**Report as adipose area (Ad.Ar) relative to marrow area (Ma.Ar) or tissue area (T.Ar).** *This must be presented as %*
Adipose tissue area (absolute)	2017	1	**Don't use** *(instead report as % Ma.Ar or % T.Ar, as above)*	
Adipose volume (per field, marrow volume or tissue volume)	1991	29	**Adipose volume** or **Adipose tissue volume**	**Report as adipose volume (Ad.V) relative to marrow volume (MA.V) or tissue volume (TV).** *This must be presented as %.*
Adipose volume (absolute)	1983	1	**Don't use** *(instead report as % Ma.V or % TV, as above)*	
Other Measurements (**Supplementary Table 6**)			**Don't use**	

Terms are grouped based on the type of measurement reported. For each type of measurement, several different terms, abbreviations and units have been used in the literature; these variants are shown in ***Supplementary Table 6****. For the Year first reported and the Number of papers, asterisks (*) are shown to emphasise that other uses may exist. We recommend that measurements of BMAd density are presented as cell number relative to the area or volume of the marrow or total tissue, and that these are reported as "Adipocyte density"; however for consistency with the published guidelines for bone histomorphometry (5), it is also acceptable to describe this measurement as "Adipocyte number," provided that a suitable referent region is used. Adipocyte area (Ad.Ar; μm^2) or volume (Ad.V; μm^3) can be reported either for individual adipocytes or for the sum of all adipocytes within the regions analysed. The former should be reported as the mean or median per adipocyte or as a distribution of adipocyte areas or volumes per sample. The latter should be reported as "Adipose area" and presented as % relative to the area or volume of the marrow (Ma) or total tissue (T). This is consistent with the standardised nomenclature for bone histomorphometry (5), and with our recommendations for BMA measurements based on MRI/MRS or CT (****Tables 8****, ****9****). In some instances, it may be necessary to use "Extravascular marrow" area or volume (ExVa.Ma.Ar or ExVa.Ma.V). This and further considerations are discussed in the main text. References for papers using each combination of term, abbreviation and unit are provided in* ***Supplementary Table 6****.*

on BMA. Our recommendation is to maintain consistency with the broader context of adipocyte biology and bone histomorphometry, where adipocytes are commonly abbreviated with "Ad" (5). We therefore propose the consistent use of the terms "BMAd" or "BM adipocyte" to designate mature adipocytes within the bone marrow (**Table 3** and **Supplementary Table 2**).

In addition to their ability to store lipids, another important property of BMAds is secretion of bioactive factors. This is reminiscent of both white and brown adipocytes, which release hormones, lipid species, cytokines, and other factors to exert local and systemic effects (79). Collectively, such adipocyte-derived secreted factors are known as "adipokines" and these contribute extensively to the physiological and pathological functions of adipose tissue (79). BMAds are also becoming increasingly recognised for their ability to secrete adipokines and thereby exert paracrine and endocrine functions (80). The two most prominent adipokines are the hormones leptin and adiponectin, which regulate energy homeostasis and have other diverse effects (79). BMAds express and secrete leptin both in primary culture and after *in vitro* differentiation from human bone marrow stromal cells (BMSCs) (81–83). BMAds also express and secrete adiponectin and might influence circulating concentrations of this adipokine (80, 84, 85). This suggests that BMAds might have endocrine functions.

BMAds also secrete many other endocrine and paracrine factors, including RANKL (86–88), DPP-4 (89), and stem cell factor (SCF) (90); cytokines such as interleukin-6 (IL-6), IL-3, IL-8, tumor necrosis factor-α (TNF-α), CXCL1, CXCL2, CXCL12,

TABLE 8 | Summary of the most common terms, abbreviations, and units that have been used to report MRI/1H-MRS-based measurements of bone marrow adiposity.

Term	Abbreviations used	Units used	Year first used*	No. of papers using this term*	Recommendations for MRI/MRS measurements
FAT FRACTION					
Fat fraction	*None;* FF	*n.s.;* %; Lipid/water ratio	1999	27	**Fat fraction (FF), Bone marrow fat fraction (BMFF), proton density fat fraction (PDFF)**. *Values should be reported as %.*
Marrow fat fraction	*None;* FF; MFF	*n.s.;* %; Lipid/water ratio	1992	27	
Bone marrow fat fraction	*None;* BM fat fraction; BMF; BMFF; FF	*n.s.;* %; Lipid/water ratio	1995	23	
Proton density fat fraction	*None;* proton density FF; PDFF; bone marrow PDFF	*n.s.;* %	2014	21	
Signal fat fraction; fat signal fraction	*None;* sFF	*n.s.;* %	2012	7	
Lipid fraction; bone marrow lipid fraction	*None;* LF	%; Lipid/water ratio	1985	4	
FAT CONTENT					
Fat content	*None;* FC	*n.s.;* %	1987	15	**Don't use for reporting MR-based measurements of fat fraction.**
Bone marrow fat content	*None;* BMF content; bone marrow FC; FC	*n.s.;* %; Lipid/water ratio	2009	11	
Marrow fat content	*None*	%; % Fat fraction; L	2005	9	
Bone marrow adipose tissue content	MAT content; BMAT content	*n.s.;* %; Lipid/water ratio	2016	3	
RATIO (FAT/WATER OR LIPID/WATER)					
Lipid/water ratio	*None;* l/w; LWR	%; Lipid/water ratio	2004	13	**Don't use**
Fat/water ratio; bone marrow fat/water ratio	*None*	%; Lipid/water ratio	2014	1	
Bone marrow fat/water %	*None*	%	2011	1	
AREA					
Bone marrow adipose tissue area	BMA	cm^2	2015	1	**Don't use.** *Instead present relative to marrow area*
Bone marrow adiposity cross-sectional area	CSA	cm^2	2017	1	
Yellow bone marrow cross-sectional area	CSA	mm^2	2013	1	
OTHER TERMS (SEE SUPPLEMENTARY TABLE 7)					

*Terms are grouped into subcategories (bold, capitalised text) based on the wording used. Other data are presented as described for **Tables 2–7**; for the Year first reported and the Number of papers, asterisks (*) are shown to emphasise that other uses may exist. We recommend that MRI/MRS-based readouts be reported as fat fraction, because this is the approach used most commonly in the existing literature. For consistency, fat fraction measurements should be reported as %, rather than as lipid/water ratios. Measurements of BMAT area (Ad.Ar) should be reported as % of marrow area (M.Ar), i.e., Ad.Ar/M.Ar, as recommended for histological or CT-based measurements (**Tables 7**, **9**). Further considerations are discussed in the main text. Additional terms/abbreviations/units, as well as references for papers using each combination, are provided in **Supplementary Table 7**.*

and MCP-1 (91–95); lipid species, such as free fatty acids (96–98); and RNA molecules within extracellular vesicles (80). Through these factors BMAds are reported to modulate haematopoiesis and skeletal remodelling. A full discussion of these functions is beyond the scope of this position paper, but more details are available in several recent reviews (80, 99, 100).

Relating to lipid storage, an unresolved question concerns BM adipocytes' unilocular vs. multilocular nature. These properties are traditionally linked to white and brown adipocyte identity, respectively (79, 101). Some studies suggest that BMAds with a brown adipocyte-like phenotype can occur in the bone marrow cavity (102), and brown adipocyte-like phenotypes can be induced *in vitro* using cell culture models of BMAds, for example after overexpression of FoxC2 (103) or SIRT1 (103). However, recent data indicate that *in vitro* cell models do not reliably recapitulate the properties of BMAds *in vivo* (74). Indeed, microarrays show that UCP1 transcripts are not enriched in whole BM of mice or humans (104, 105), nor is *Ucp1* expression greater in BMAds vs. white adipocytes of mice (106). Recent work using lineage tracing and genetic models has also demonstrated that BMAds do not express *Ucp1* during development or after adrenergic stimulation in mice (107). Similarly, primary BMAd progenitors have very limited, if any, brown adipogenic potential (89), and BMAds *in vivo*

TABLE 9 | Summary of terms, abbreviations, and units that have been used to report CT-based measurements of bone marrow adiposity.

Imaging method	Measurement type	Year first reported*	No. of papers*	Recommended term(s)	Recommended abbreviation and unit
SECT, DECT *or* ***μCT*** *(Without contrast agent)*	**Fat fraction** (% or fraction)	1987	8	**Fat fraction; Bone marrow fat fraction**	**FF** (%), **BMFF** (%)
	Adipose volume (per marrow volume)	2019	2	**Adipose volume**	**Ad.V/Ma.V** (%)
	BM density	1986	6	**Don't use** *(Report as Adipose volume, FF or BMFF, as above)*	
	Adipose volume (per tissue volume)	2011	2	**Don't use** *(Report as % Ma.V, as above)*	
μCT *(Samples stained with osmium tetroxide or other contrast agents)*	**Adipose volume** (per marrow volume)	2012	11	**Adipose volume**	Ad.V/Ma.V (%)
	Adipocyte density (per marrow volume)	2014	2	**Adipocyte density** or **Adipocyte number**	N.Ad/Ma.V *(Cell number/unit volume)*
	Adipocyte area (Distribution of individual adipocyte areas)	2015	1	**Adipocyte area** (mean or median)	**Ad.Ar, μm²** *(Show frequency distribution)*m
	Total adipocyte area *(per Slice)*	na	na	**Adipose area**	**Ad.Ar/Ma.Ar** (%)
	Adipocyte volume *(per slice)*	na	na	**Adipocyte volume** (mean or median)	Ad.V, μm^3 *(show frequency distribution)*
	Adipose volume *(per tissue or total volume)*	2014	12	**Don't use** *(Report as % Ma.V, as above)*	
	Adipose volume *(Unclear if per tissue volume or per marrow volume)*	2015	4		
	Adipose volume (absolute)	2015	10		

Data are presented as described for ***Table 7****, except that imaging method is also indicated. For the Year first reported and the Number of papers, asterisks (*) are shown to emphasise that other uses may exist. For each type of measurement, several different terms, abbreviations, and units have been used in the literature; these variants are presented in* ***Supplementary Table 8****. Most in vivo studies using SECT or DECT report measurements of fat fraction or relative adipose volume, and therefore we recommend reporting these as indicated in the table. Most ex vivo μCT studies assess adipose volume normalised to marrow volume or total tissue volume, although in some cases it is unclear which of these is used for normalisation. Other studies present absolute adipose volume or assess adipocyte density or area. We recommend that μCT-based readouts of adipose volume or area be reported relative to marrow volume (Ma.V) or marrow area (Ma.Ar), and that individual adipocyte areas be reported as the mean or median, or as a frequency distribution. This is consistent with our recommendations for histology-based measurements (****Table 7****). Further considerations are discussed in the main text. References for papers using each combination of term, abbreviation and unit are provided in* ***Supplementary Table 8****.*

do not undergo cold-induced glucose uptake (108). However, multilocular BMAds do exist and account for around 5% of all BMAds in the long bones of mice (107). Thus, while it seems that BM adipocytes are distinct from brown adipocytes, it is unlikely that this multilocularity is indeed equated to brown adipocyte-like functions of BMAds. This also pertains to BMAd-intrinsic ability for rapid lipid mobilization in response to adrenergic stimulation or other physiological stimuli known to recruit brown adipocytes for their main function, which is thermogenesis. These remain open issues to be assessed in greater detail. Future authors may therefore opt to add further attributes to the term "bone marrow adipocyte" to better define parameters such as number of vacuoles (locularity), and also to reference anatomical localisation or metabolic characteristics. This relates to the recent discussion on distinct types of BMAds, regulated and constitutive, which will be discussed in the section on Subtypes of Bone Marrow Adipocytes.

Bone Marrow Adipose Tissue

One area of debate is whether BMAds are simply a subpopulation of BM cells that constitute a part of BM as a tissue, or whether, collectively, BMAds act as an integrated adipose tissue. References to "adipose tissue" within the BM can be found as early as 1883 (10), and studies from the 1940s and 1950s also proposed "yellow marrow" or "marrow fat" to be an adipose tissue, based on its similar lipid composition with WAT depots (23, 24). In 1967, Zakaria and Shafrir studied explants of "yellow bone marrow" (YBM), concluding: *"The experiments demonstrate the capacity of YBM to synthesize fatty acids and glycerol from glucose, to take up and esterify long-chain FFA (free fatty acids) from an external medium and to release FFA under hormonal stimulation. All these activities are typical of adipose tissue function. Thus, the YBM seems to represent a metabolically active variety of fat store, similar to depots in other anatomical sites, but presumably with a specialized local importance"* (31). These studies support the concept that BMAds, collectively, form an integrated adipose tissue.

One caveat, discussed further in the section on Subtypes of Bone Marrow Adipocytes, is that BMAd characteristics vary depending on skeletal site. The studies described above focussed on the yellow marrow, in which BMAds form a contiguous unit that is morphologically similar to white adipose tissue (109). However, BMAds also exist interspersed among the red marrow,

where they do not form a spatially contiguous grouping; it is less clear whether these cells, designated "regulated" BMAds, can be considered as an adipose tissue.

This issue was debated extensively among the members of the Nomenclature WG. After much discussion, we concluded that it is appropriate to refer to BMAds as an adipose tissue, even for those adipocytes interspersed among the red marrow. This decision is based on two key points. Firstly, even in white adipose tissue, adipocytes comprise <25% of the total cell population (110). Thus, the fact that BMAds do not predominate in the red marrow does not preclude these from being considered as an adipose tissue. Secondly, "tissue" has been defined as *"an aggregation of similarly specialized cells united in the performance of a particular function"* (5); hence, possessing a common function is more important than the physical grouping of the cells. Although the roles of BMAds are still being elucidated, it is clear that these cells work together to perform common functions (109), and therefore they can be considered as an integrated adipose tissue.

A second point of debate regards how to abbreviate "bone marrow adipose tissue." By far the most common abbreviations for this are "MAT" and "BMAT" (**Table 4**). One benefit of "MAT" is that this is more consistent with other abbreviations in the adipose field, such as "WAT" and "BAT." One downside to "BMAT" is that this also been used to refer to a "bone marrow aspirate and trephine" biopsy (111); however, there are several benefits to the use of "BMAT" to abbreviate "bone marrow adipose tissue." Firstly, by using "BM," "BMAT" refers unambiguously to the BM and is consistent with other abbreviations recommended in this standardised nomenclature (e.g., BMA, BMAd, BMSC, BMFF). Secondly, in the BMA literature the use of "BMAT" precedes use of "MAT" by 5 years, and therefore there is a historical priority for "BMAT" (**Table 4**). Finally, use of "BMAT" has been recommended in a previous editorial (112), which provides further rationale for its continued use. In summary, we recommend the term "bone marrow adipose tissue" and the abbreviation "BMAT." This can be defined as a collection of BMAds, which may be clustered together or interspersed among the haematopoietic marrow, that work together to perform common functions.

Two other terms are also recommended. Despite the longstanding references to adipose tissue within the BM, it has historically been more common to refer to "marrow fat" or "bone marrow fat" (**Table 4**). These terms continue to be used to this day, often in clinical reports and/or to reflect gross measurements of BMA (**Supplementary Table 3**). Considering the historical prominence and continued use of these terms, we have included "marrow fat" and "bone marrow fat (BM fat)" in the standardised BMA nomenclature. However, when discussing the formation and function of BMAds as a collective, integrated tissue, use of "bone marrow adipose tissue (BMAT)" should be given preference.

Further details of these recommendations, and the many terms that we recommend to avoid using, are provided in **Table 4** and **Supplementary Table 3**.

Subtypes of Bone Marrow Adipocytes

One important concept in BMA research is that BMAds and BMAT display distinct characteristics depending on skeletal location. This was first shown in 1965 by Cohen and Gardiner, who found that during starvation in rabbits, lipid is mobilised from BMAds within the proximal red marrow but not from BMAds in the distal yellow marrow (28). Subsequent work in the 1970s extended these observations, including the demonstration of distinct lipid composition in proximal vs. distal BMAds [reviewed in (113)]. This concept was relatively overlooked until the mid 2010s, when Scheller et al. proposed the existence of "regulated" and "constitutive" subtypes of BMAds (73, 114). Further details, including the evidence supporting these two subtypes, are provided in an excellent recent review (113). Therein, regulated BMAds are "*defined histologically as single adipocytes interspersed within the haematopoietic BM. They form gradually throughout life and accumulate with aging*." In contrast, constitutive BMAds *"form early in development, are larger in size, and appear histologically as densely packed groups of adipocytes with little intervening haematopoiesis"* (113).

The terms regulated and "constitutive" have since gained traction in the field, as evident through the increasing use of the abbreviations "rMAT" or "rBMAT" and "cMAT" or "cBMAT" to refer to these subtypes (**Table 5**). However, this classification raises an important question: are there only two general classes, or is the heterogeneity less binary than this? For example, in the mouse tibia, proximal ("regulated"), and distal ("constitutive") BMAds display different properties, in particular in terms of fatty acid saturation, but, like their "regulated" counterparts, the "constitutive" BMAds can also be altered in certain contexts (115, 116). Moreover, in some models of lipodystrophy there is a loss of cBMAT at the distal tibia, whereas cBMAT in caudal vertebrae is maintained (117). Thus, like rBMAT, cBMAT can also display plasticity in response to environmental cues, and cBMAT properties vary depending on skeletal site. Finally, most studies of cBMAT and rBMAT are based in animal models; hence, it remains unclear to what extent these exist as distinct subtypes in humans.

Because of these complexities, as a priority we recommend referring to BMAT and BMAd subtypes based on their anatomical location, in preference to using the "constitutive" and "regulated" terminology. This approach, which already is common in the literature (**Table 5**), provides a definitive, unambiguous description that addresses the issue of site-specific characteristics. However, given the increasing use of "constitutive" and "regulated," and the evidence supporting existence of these two broad subtypes (113), we accept that there is still value in continued use of these terms. Therefore, if authors do wish to use these terms, we recommend using rBMAT and cBMAT to refer to the regulated and constitutive subtypes of BMAT, and rBMAd and cBMAd when referring to these subtypes of BM adipocytes.

Further details of these recommendations, and the many terms that we recommend to avoid using, are provided in **Table 5** and **Supplementary Table 4**.

Progenitors for Bone Marrow Adipocytes

BMAds originate from marrow-derived skeletal stem cells (SSCs) (72, 118). These cells go by different names, based on two different concepts regarding their differentiation properties and their tissue of origin. The first concept emanates from *in vivo* transplantation studies. These studies confirm the existence of multipotent progenitors present in BM stroma that can generate heterotopic bone/marrow organs (ossicles) with donor-derived skeletal cell phenotypes (chondrocytes, osteoblasts, stromal cells), including BMAds [reviewed in (119)]. The term Bone Marrow Stromal Cell (BMSC) is a time-honoured term used to indicate the population of non-hematopoietic, non-endothelial, rapidly adherent cells isolated from BM; adherence in culture is one characteristic property of these stromal cells. Clonal analysis of BMSCs coupled with *in vivo* transplantation revealed the presence of a *subset* of multipotent cells (120, 121). Later, these multipotent cells were found to be sinusoidal pericytes, cells that wrap around blood vessels providing them with stability. Furthermore, they were found to restore the perivascular compartment from which they originate (the ability to self-renew), making these cells bona fide SSCs (122). Thus, SSCs are a multipotent, self-renewing subset of BMSCs: all SSCs are BMSCs, but not all BMSCs are SSCs. It is essential to emphasise this because these terms have been used inconsistently in the literature, causing confusion about the relationship between SSCs and BMSCs.

Notably, the term "skeletal stem cell" currently describes a biological activity rather than a well-defined cell phenotype, since the specific identity of multipotent and self-renewing SSCs is not yet clear. As discussed in the accompanying BMAS Methodologies position paper by Tratwal et al., agreement on how to purify SSCs has not yet been reached: even populations highly enriched by using certain cell surface markers are still not homogeneous. Nonetheless, the use of the term "SSC" is appropriate based on the retrospective evidence of stemness demonstrated by the generation of ossicles by clonal populations of BMSCs. However, it is important to note that other populations of SSCs have recently been identified in the growth plate and in the periosteum in both mice and humans, but it does not appear that SSCs from these origins contribute to BMA [reviewed in (123)] (104, 123–126). Similarly, stromal cells capable of adipogenesis *ex vivo* have been isolated from cortical bone of the femoral diaphysis and cancellous/cortical bone of the proximal epiphysis of rats (127, 128). Although it remains to be confirmed if these cells can generate BMAds *in vivo,* their *ex vivo* adipogenic capacity differs depending on skeletal site. This echoes the site-specific differences in BMAd subtypes discussed in the previous section. Thus, the tissue origin of SSCs must always be identified. Indeed, not all populations of SSCs give rise to adipocytes, as determined by *in vivo* transplantation or lineage tracing in mice. Of note, "*in vivo*" is the operative term here, as it is known that the *in vitro* assay for adipogenesis is prone to artefact. In many fibroblastic populations, a few cells accumulate fat from serum in the medium, but do not synthesize triglycerides or hydrolyse them to the same extent as *bona fide* adipocytes.

According to the second concept, the term "Mesenchymal Stem Cell (MSC)" was introduced, based on the ability of BMSCs/SSCs to make cells and tissues of *mesodermal* origin. These include not only skeletal cell types (chondrocytes, osteoblasts and BMAds) but also non-skeletal phenotypes such as myoblasts, tenocytes, fibrocytes (ligament), white adipocytes, and others (124). However, as defined by developmental biologists, mesenchyme is an embryonic connective tissue that makes connective tissue, blood, and blood vessels during foetal development, and is not found in post-natal tissue (129). In spite of this, it was proposed that "MSCs" reside in all post-natal tissues, based on non-specific cell surface markers shared by virtually all fibroblastic cells (130), and that all "MSCs" are pericytes (125), able to give rise to osteoblasts, chondrocytes and adipocytes, making them equivalent to SSCs within the BM. However, during embryonic development, none of the non-skeletal cell types, including pericytes, have a common embryonic origin (118). Lastly, the "MSC" term emerged from less-than-rigorous *in vitro* studies; more-recent *in vivo* work has confirmed that the progenitor activity of different populations of perivascular stromal cells (if any) is always restricted to that of the tissue of origin (126).

For these reasons, the use of the term "Mesenchymal Stem Cell" and any other definition including the word "Mesenchymal," especially the use of the acronym "BMSC" to indicate bone marrow *mesenchymal stem* cells rather than bone *marrow stromal* cells, is not scientifically accurate and is not recommended. Thus, we recommend using "SSCs" to refer to "Skeletal Stem Cells" and "BMSCs" to refer to "Bone Marrow Stromal Cells." Describing the anatomical location from which these cells are isolated, as well as the species of origin, is also important when reporting studies of SSCs and BMSCs.

Further details of these recommendations, and the terms and abbreviations that we recommend to avoid using, are provided in **Table 6** and **Supplementary Table 5.**

BMAT Morphometric Analyses

The elaboration of an appropriate nomenclature for BMAT morphometry cannot be conceived without considering the guidelines for bone histomorphometry that have been established for more than 25 years (5, 131). Indeed, many of the terms usable for BMAT morphometry are well-defined and properly abbreviated in the first Standardized Nomenclature, Symbols, and Units for Bone Histomorphometry (131) and in its revision (5).

As for bone, BMAT morphometry can be based on two- or three-dimensions (2D or 3D) and applied to many types of biological material, most commonly iliac crest bone/BM biopsies obtained from human subjects, and bones from experimental animals. Recent studies have also analysed BMAds within BM plugs of transgenic mice, allowing study of BMAd development by lineage tracing (132). A mixture of terminology for 2D and 3D techniques of analysis should not be used in the same article, unless different methods of analysis (i.e., histology vs. micro-CT) are used (5).

Both primary measurements and referents (i.e., some clearly defined area or volume within the sample) must be considered. The former include Adipocyte Area (Ad.Ar), Volume (Ad.V), Perimeter (Ad.Pm), Diameter (Ad.Dm), and Number (N.Ad);

each of these abbreviations is consistent with the guidelines for bone histomorphometry (5). In addition to adipocyte number, measurements of the size of individual adipocytes (Ad.Ar, Ad.V, Ad.Pm, Ad.Dm) are important in the physiology and pathology of BMAT. Indeed, changes in total BMAT may be the result of mechanisms that lead to the increase or decrease of either BMAd size (lipid storage/lipolytic activity) or number (adipogenic differentiation, or BMAd apoptosis and clearance). Size-related measurements may have meaning *per se* and not require a referent. For example, they can be used for the calculation of mean (and median) of BMAds and to construct distribution curves; the latter provide a more accurate representation of BMAd sizes across the sample and therefore are the recommended method of presenting such data (**Table 7**).

In contrast to these measurements of BMAd size, for N.Ad, total adipose tissue area and total adipose volume, referents are needed, and must be properly defined. Since BM is distributed throughout the cavities of the skeleton and includes distinct kinds of tissues/cells (haematopoietic cells, BMAds, and BMSCs) and is highly vascularised, the referents may be different. Some of them (i.e., Tissue Area in 2D and Tissue Volume in 3D) have been already defined and abbreviated (T.Ar and TV, respectively) in the Standardized Nomenclature, Symbols, and Units for Bone Histomorphometry (5). For studies of BMA, additional referents to be considered include Marrow Area (Ma.Ar, in 2D) and Marrow Volume (Ma.V, in 3D), which coincide with the spaces of the skeleton delimited by endosteal surfaces (cancellous bone surfaces and endocortical surfaces).

The choice between T.Ar (or TV) or Ma.Ar (or Ma.V) as referents is important for the accurate interpretation of the data. For example, when osteopenia does occur, the Ma.Ar (or Ma.V) increases while T.Ar (or TV) does not. In addition, since haematopoietic cells and adipocytes are located in the Extra-Vascular compartment of the BM, the use of this region (Area: ExVa.Ma.Ar, i.e., Marrow Area *minus* Vascular Area; Volume: ExVa.Ma.V, i.e., Marrow Volume *minus* Vascular Volume) as referent could be more appropriate and, in principle, to be preferred in respect to Ma.Ar and Ma.V. Indeed, this Extra-Vascular compartment can be used as a referent not only for assessments of BMA (i.e., with total Ad.Ar, total Ad.V, or N.Ad as the numerator), but also for measuring the percentage of haematopoietic marrow. The latter is calculated by expressing the haematopoietic area (Hm.Ar) or haematopoietic volume (Hm.V) relative to ExVa.Ma.Ar or ExVa.Ma.V, respectively. As discussed in the accompanying BMAS Methodologies paper, the ratio of haematopoietic to adipose area (Hm.Ar./Ad.Ar.) may also be of interest in some instances but should not be confounded with measures of adiposity (e.g., Ad.Ar/Ma.Ar) or hematopoietic cellularity (e.g., Hm.Ar/Ma.Ar).

One challenge is that measurement of the Extra-Vascular Marrow compartment can be highly time-consuming. Thus, we suggest to use the area (or volume) of the Extra-Vascular Marrow compartment as referent in specific conditions only, for example in mouse long bone whole-mount sections in which the vascular spaces (sinusoids and central vein) may constitute a very significant and dynamic area or volume (133); and, in humans, in those haematological diseases in which BM vascularity is known to be altered (134). Use of the Extra-Vascular Marrow referent is, however, still limited by technological challenges, which may resolve as whole-mount 3D microscopy and high-resolution contrast-enhanced μCT become more widely available to reconstruct, and subtract, the vascular network within the BM space (135, 136). Subtraction of the central vein from the Marrow Area is, however, common in whole-bone histology of murine long bones due to the dilated lumen often associated with retraction artefacts upon fixation (reviewed in the accompanying BMAS Methodologies position paper by Tratwal et al.).

A final consideration, debated extensively among WG members, is whether to use the term "Adipocyte density" or "Adipocyte number" when describing measurements of N.Ad relative to a referent region (i.e., Ma.Ar, Ma.V, T.Ar, TV, ExVa.Ma.Ar, or ExVa.Ma.V). Such measurements report the population density of BMAds within the region of interest, and therefore we recommend that these are reported as "Adipocyte density" (**Table 7**). However, one concern with the term 'density' is that readers may confuse this with a measurement of the actual physical density of BMAds (i.e., mass per unit volume of the cells); this concern was raised in the published guidelines for bone histomorphometry (5), which therefore prioritises the term "number" over "density" when reporting relative cell numbers. Thus, to be consistent with these previous guidelines, we agree that use of "Adipocyte number" is also acceptable when describing measurements of N.Ad relative to a referent region. What is essential is that studies should never report measurements of N.Ad alone: a suitable referent must always be used.

Details of the proposed nomenclature regarding BMAT morphometry are presented in **Table 7**, with further information in **Supplementary Table 6**.

MRI- and/or MRS-Based Analyses

MRI analysis of BMA was first reported in the mid-1980s (53–57), but the past 20 years have seen a notable increase in publications using MRI and/or 1H-MRS for assessment of BMA (**Table 8** and **Supplementary Table 7**). Most studies report the fat fraction (FF) or lipid:water ratio, calculated from the lipid and water peaks in MR spectra (71); however, there is much inconsistency in how these measurements are reported. As shown in **Table 8**, measurements described by the term "fat fraction (FF)," or the related terms "marrow fat fraction" or "bone marrow fat fraction (BMFF)," typically are reported as a %, but in some cases the actual measurement reported is the lipid/water ratio and not the % fat fraction. Conversely, sometimes measurements described as a "ratio" are actually reported as % fat fraction. Confusing issues further, some studies have used the term "fat content" when reporting measurements of % fat fraction, whilst others have used this term when reporting the lipid/water ratio. In other cases, the terms "fat fraction" or "fat content" are used, but the units of measurement are not stated; this may cause confusion about whether the measurement is a fraction or a ratio. Finally, MRI has been used to report the volume or area of BMA from 3D or 2D images, respectively (**Table 8**).

This variability underscores the need for standardisation. To date, most studies use the term "fat fraction," "marrow fat

fraction," or "bone marrow fat fraction" to report the % fat fraction of the BM (**Table 8**). These measurements typically are based on dual-echo MRI or MRS data, which can be subject to confounding factors (e.g., attenuation of the T2* signal) (71). In contrast, measurement of the proton density fat fraction (PDFF), based on multi-echo data, removes the effect of these confounding factors and thereby represents a truly standardised BMA measurement (71). Thus, in addition to 1H-MRS, PDFF is emerging as another gold-standard for BMA quantification. Nevertheless, many studies report dual-echo fat fraction measurements. We recommend reporting MRI and 1H-MRS-based measurements as fat fraction (FF) or bone marrow fat fraction (BMFF) when based on dual-echo data, and as PDFF when based on appropriate multi-echo sequences. These measurements should be reported as %, rather than the lipid/water ratio.

A final issue is the ability of MR to measure the degree of lipid saturation. Terms such as "unsaturation index" (UI) and "unsaturated lipid fraction" (ULF) have been used (137–141), and this capacity to assess not just BMAT quantity, but also BMAT quality, may reveal further insights about the clinical implications of altered BMA (71, 99). However, compared to reports of FF, BMFF or PDFF, there are far fewer papers reporting BMAT saturation, and therefore we feel it is too early to recommend terms, abbreviations or units for describing such measurements.

Further details of these recommendations, and the terms that we recommend to avoid using, are provided in **Table 8** and **Supplementary Table 7**.

CT-Based Analyses

As for MRI, CT-based BMA analysis was first reported in the mid-1980s (58, 59, 61). However, the application of these two approaches has since diverged: MRI has found widespread use for clinical BMA assessment *in vivo* but remains relatively under used in preclinical animal studies. In contrast, only a handful of studies have used CT to measure BMA *in vivo,* whereas its preclinical use has flourished in recent years, particularly for μCT (**Table 9**). The latter is primarily a result of the development of contrast agents, such as osmium tetroxide, that allow μCT-based visualisation and quantification of BMA *ex vivo*.

Clinically, both single-energy CT (SECT) and dual-energy CT (DECT) have been used to assess BMA *in vivo* and *ex vivo*. SECT-based measurements of BM density, expressed in Hounsfield Units, correlate inversely with BMA; however, these measurements include the density of yellow and red marrow as well as trabecular bone, and therefore do not allow for direct quantification of BMA (142). Nevertheless, several recent studies have used SECT to estimate relative adipose volume within the BM based on HU thresholds indicative of adipose tissue (108, 143). In contrast to SECT, DECT is able to separate BMA from the other tissue components, allowing true quantification of BMA. Such DECT-based measurements, reported as fat fraction (**Table 9**), show good agreement with MRI/MRS-based assessment of BMA (142, 144, 145). Thus, for consistency with nomenclature for histomorphometry and MRI/MRS-based measurements (**Tables 7**, **8**), we recommend that CT-based assessment of BMA should be reported as fat fraction (FF, %), bone marrow fat fraction (BMFF, %), or adipose volume (Ad.V/Ma.V, %).

Ex vivo, staining of tissue samples with contrast agents allows direct measurement of adipose volume by μCT. Most such studies report Ad.V as the % or fraction relative to Ma.V or TV, although a sizeable minority have reported absolute Ad.V; in some cases, it is not clear if absolute or relative adipose volume is being reported (**Table 9**). Consistent with our proposals for BMAT histomorphometry (**Table 7**), we recommend that μCT-based readouts of adipose volume should be reported relative to Ma.V (i.e., as Ad.V/Ma.V, %). For the referent, Ma.V should be prioritised over TV because the latter can include bone and other tissues that necessarily exclude BMAds; the size of these tissues may also vary based on the physiological or pathological context, confounding analysis of BMA. Thus, presenting Ad.V/Ma.V provides a more accurate assessment of BMA.

An emerging application of μCT is the ability to measure the number and size of individual BMAds. Adipocyte density (i.e., N.Ad/Ma.V) has been reported for samples stained with osmium tetroxide (146) or with a Hafnium-based polyoxometalate contrast agent (135). Similarly, nano-CT has been used to quantify the area of individual BMAds in 2D image slices of osmium tetroxide-stained samples, allowing the distribution of individual BMAd areas to be determined (147). As for BMAT histomorphometry, we recommend reporting these readouts as "Adipocyte density" (N.Ad/Ma.V) and the frequency distribution of "Adipocyte area" (Ad.Ar, μm^2), respectively; "Adipocyte number" may also be used in place of "Adipocyte density," as discussed in the section BMAT Morphometric Analyses. An obvious extension of these methods would be the measurement of total adipocyte area in 2D slices of CT scans, and of individual adipocyte volume in 3D scans. While such readouts have not yet been published (**Table 8**), for the sake of foresight we recommend that these should be reported, respectively, as "Adipose area" (Ad.Ar/Ma.Ar, %) or frequency distributions of "Adipocyte volume" (Ad.V, μm^3).

Further details of these recommendations, and the terms that we recommend to avoid using, are provided in **Table 9** and **Supplementary Table 8**.

CONCLUDING REMARKS

The study of BMA is a dynamic, vibrant, and expanding field of research. As populations and sub-populations of cells are more accurately defined, it may be necessary to reappraise the nomenclature to accommodate subtle nuances found between cells that may influence function. Similarly, it is likely that the BMA nomenclature will have to be updated to reflect advances in methodologies relevant to BMA research. The Nomenclature Working Group of the International Bone Marrow Adiposity Society will therefore endeavour to regularly reassess the field

and make practical recommendations on nomenclature to help define and characterise the cells and environment that initiate, propagate and maintain BMA, and the methods used to assess these. Such future updates will depend on the continued growth and development of the BMA field. For now, we hope that the nomenclature guidelines herein will provide a foundation to support this growth; to promote collaboration; and to provide a consensus for the diverse fields of study related to BMA.

AUTHOR CONTRIBUTIONS

WC conceptualized the manuscript and coordinated the literature review, tables, figure, and assembly of the different sections written by the other authors. WC led the writing for the sections on Bone Marrow Adiposity, Bone Marrow Adipose Tissue, Subtypes of Bone Marrow Adipocytes, and CT-based analyses. CC led the writing for the Abstract. TS led the writing for the section on Bone Marrow Adipocytes. MR, PR, and AC wrote the section on Progenitors for Bone Marrow Adipocytes. AC wrote the section on BMAT Morphometric Analyses, with MR providing additional input. MB and WC wrote the section on MRI- and/or MRS-Based Analyses. WF led the writing of the Concluding Remarks. All authors, including NB, SR-S, ED, and CR discussed the terminology identified and, through several meetings, agreed on the nomenclature recommendations. All authors edited and approved the final version of the manuscript.

FUNDING

The BMA2017 annual meeting to constitute BMAS and its Working Groups was funded by Swiss National Science Foundation (SNSF) grant 31CO30_173949. A Nomenclature WG meeting was organised during the BMA2018 annual meeting, which was funded by Région Hauts-de-France and Université du Littoral Côte d'Opale. MB was supported by grants from the US National Institutes of Health (NIDDK 1K24DK109940 and NIDDK R24DK084970). WC was supported by grants from the UK Medical Research Council (MR/M021394/1 and MR/S010505/1). AC has received funding from Sapienza University (Nos. RM118164289636F0). WF was supported by the National Research Foundation of South Africa (Grant Nos. 118565 and 118990), the South African Sugar Association (Project 257) and The Harry Crossley Foundation. MR acknowledges support from the Fondazione Cenci Bolognetti. PR was supported by the DIR, NIDCR, NIH, DHHS (ZIA DE000380). TS was supported by the German Research Foundation (DFG; SCHU 2445/5-1 and SCHU 2445/6-2), the German Ministry of Education and Research (BMBF) and the State of Brandenburg (DZD grant 82DZD00302 and FKZ 82DZD0038G).

ACKNOWLEDGMENTS

A special thank you to Olaia Naveiras, Ecole Polytechnique Fédérale de Lausanne, for help on aligning this manuscript with the accompanying BMAS methodologies position paper, and to all members of the BMAS Scientific Board for providing feedback on these nomenclature recommendations. Finally, in our systematic review of the BMA literature we have strived to include all relevant publications; however, given the scope of this effort, we may have missed some papers relevant to this field. We apologise to any authors whose work we have inadvertently overlooked.

SUPPLEMENTARY MATERIAL

The Supplementary Material for this article can be found online at: https://www.frontiersin.org/articles/10.3389/fendo.2019.00923/full#supplementary-material

REFERENCES

1. Yusuf RZ, Scadden DT. Fate through fat:lipid metabolism determines stem cell division outcome. *Cell Metab.* (2012) 16:411–3. doi: 10.1016/j.cmet.2012.09.011
2. Frey JL, Li Z, Ellis JM, Zhang Q, Farber CR, Aja S, et al. Wnt-Lrp5 signaling regulates fatty acid metabolism in the osteoblast. *Mol Cell Biol.* (2015) 35:1979–91. doi: 10.1128/MCB.01343-14
3. Kim SP, Li Z, Zoch ML, Frey JL, Bowman CE, Kushwaha P, et al. Fatty acid oxidation by the osteoblast is required for normal bone acquisition in a sex- and diet-dependent manner. *JCI Insight*. (2017) 2:e92704. doi: 10.1172/jci.insight.92704
4. Corsi A, Palmisano B, Tratwal J, Riminucci M, Naveiras O. Brief report from the 3rd international meeting on bone marrow adiposity. (BMA 2017). *Front Endocrinol.* (2019) 10:336. doi: 10.3389/fendo.2019.00336
5. Dempster DW, Compston JE, Drezner MK, Glorieux FH, Kanis JA, Malluche H, et al. Standardized nomenclature, symbols, and units for bone histomorphometry:a 2012 update of the report of the ASBMR Histomorphometry Nomenclature Committee. *J Bone Miner Res.* (2013) 28:2–17. doi: 10.1002/jbmr.1805
6. Bizzozero G. Sulla funzione ematopoetica del midollo delle ossa. Comunicazione preventiva. *Gazz Med Ital Lombardia.* (1868) 28:381–2.
7. Neumann E. Ueber die Bedeutung des Knochenmarks fur die Blutbildung. *Zentralbl Fur Die Medicinischen Wiss.* (1868) 6:689.
8. Ranvier L. *Traité Technique D'Histologie.* Paris: Librairie Savy F (1875).
9. Neumann E. Das Gesetz der Verbreitung des gelben und roten Knochenmarkes. *Zentralbl Fur Die Medicinischen Wiss.* (1882) 20:321–3.
10. Coats J. *A Manual of Pathology.* Philadelphia, PA: H. C. Lea's Son and Co. (1883).
11. Muir R, Drummond WB. On the structure of the bone-marrow in relation to blood-formation. *J Anat Physiol.* (1893) 28:125–41.
12. Piney A. The anatomy of the bone marrow: with special reference to the distribution of the red marrow. *Br Med J.* (1922) 1922:792–5.
13. Custer RP. Studies on the structure and function of bone marrow:I. Variability of the hemopoietic pattern and consideration of method for examination. *J Lab Clin Med.* (1932) 17:951–60.
14. Custer RP, Ahlfeldt FE. Studies on the structure and function of bone marrow:II. Variations in cellularity in various bones with advancing years of life and their relative response to stimuli. *J Lab Clin Med.* (1932) 17:960–2.
15. Steele BF. The effects of blood loss and blood destruction upon the erythroid cells in the bone marrow of rabbits. *J Exp Med.* (1933) 57:881–96. doi: 10.1084/jem.57.6.881
16. Rhoads CP, Castle WB. The pathology of the bone marrow in sprue anemia. *Am J Pathol.* (1933) 9:813–26.

17. Andersen DH. Benzol poisoning with hyperplasia of the bone marrow. *Am J Pathol*. (1934) 10:101–12.
18. Custer RP. Studies on the structure and function of bone marrow: IV. Bone Marrow in Agranulocytosis. *Am J Med Sci*. (1935) 189:507–15. doi: 10.1097/00000441-193504000-00005
19. Huggins C, Blocksom BH. Changes in outlying bone marrow accompanying a local increase of temperature within physiological limits. *J Exp Med*. (1936) 64:253–74. doi: 10.1084/jem.64.2.253
20. Shouse SS, Warren SL, Whipple GH. II. Aplasia of marrow and fatal intoxication in dogs produced by roentgen radiation of all bones. *J Exp Med*. (1931) 53:421–35. doi: 10.1084/jem.53.3.421
21. Sabin FR, Miller FR, Smithburn KC, Thomas RM, Hummel LE. Changes in the bone marrow and blood cells of developing rabbits. *J Exp Med*. (1936) 64:97–120. doi: 10.1084/jem.64.1.97
22. Miller DK, Rhoads CP. The effect of hemoglobin injections on erythropoiesis and erythrocyte size in rabbits rendered anemic by bleeding. *J Exp Med*. (1934) 59:333–46. doi: 10.1084/jem.59.3.333
23. Hilditch TP, Murti KS. The component acids of an ox bone marrow fat. *Biochem J*. (1940) 34:1299–300. doi: 10.1042/bj0341299
24. Evans JD, Baker JM, Oppenheimer MJ. Alteration of rabbit marrow fat in anemia from acetylphenylhydrazine. *Am J Physiol Legacy Content*. (1955) 181:504–8. doi: 10.1152/ajplegacy.1955.181.3.504
25. Berman L, Axelrod AR. Fat, total cell and megakaryocyte content of sections of aspirated marrow of normal persons. *Am J Clin. Pathol.* (1950) 20:686–7. doi: 10.1093/ajcp/20.7_ts.686
26. Berman L, Axelrod AR, Horan TN, Jacobson SD, Sharp EA, Vonderheide EC. The blood and bone marrow in patients with cirrhosis of the liver. *Blood*. (1949) 4:511–33. doi: 10.1182/blood.V4.5.511.511
27. Evans JD, Riemenschneider RW, Herb SF. Fat composition and in vitro oxygen consumption of marrow from fed and fasted rabbits. *Arch Biochem Biophys.* (1954) 53:157–66. doi: 10.1016/0003-9861(54)90242-8
28. Cohen P, Gardner FH. Effect of massive triamcinolone administration in blunting the erythropoietic response to phenylhydrazine hemolysis. *J Lab Clin Med*. (1965) 65:88–101.
29. Gong JK, Arnold JS. Skeletal marrow volume in dog. *Am J Physiol Legacy Content*. (1965) 209:340–6. doi: 10.1152/ajplegacy.1965.209.2.340
30. Miyoshi I, Irino S, Hiraki K. Fibroblast-like transformation of human bone marrow fat cells *in vitro*. *Exp Cell Res.* (1966) 41:220–3. doi: 10.1016/0014-4827(66)90564-7
31. Zakaria E, Shafrir E. Yellow bone marrow as adipose tissue. *Proc Soc Exp Biol Med*. (1967) 124:1265–8. doi: 10.3181/00379727-124-31983
32. Gengozian N, Batson JS, Nelson BM. Bone-marrow grafting attempts in marmosets after whole-body irradiation. *Int J Radiat Biol Relat Stud Phys Chem Med*. (1967) 11:553–61. doi: 10.1080/09553006714550221
33. Zach E, Shafrir E. Composition of bone marrow adipose tissue in relation to body fat depots in various species. *Isr J Med Sci*. (1974) 10:1541–50.
34. Tavassoli M. Ultrastructural development of bone marrow adipose cell. *Acta Anat.* (1976) 94:65–77. doi: 10.1159/000144545
35. Meunier P, Aaron J, Edouard C, Vignon G. Osteoporosis and the replacement of cell populations of the marrow by adipose tissue. A quantitative study of 84 iliac bone biopsies. *Clin Orthop Relat Res.* (1971) 80:147–54. doi: 10.1097/00003086-197110000-00021
36. Oberling F, Cazenave JP, Waitz R. Ultrastructure of adipose tissue in the normal hematopoietic marrow of the rabbit. *Pathol Biol.* (1972) 20:337–47.
37. Tavassoli M. Marrow adipose cells. Ultrastructural and histochemical characterization. *Arch Pathol.* (1974) 98:189–92.
38. Tavassoli M. Differential response of bone marrow and extramedullary adipose cells to starvation. *Experientia*. (1974) 30:424–5. doi: 10.1007/BF01921701
39. Tavassoli M. Marrow adipose cells. Histochemical identification of labile and stable components. *Arch Pathol Lab Med*. (1976) 100:16–8.
40. Tavassoli M, Houchin DN, Jacobs P. Fatty acid composition of adipose cells in red and yellow marrow: a possible determinant of haematopoietic potential. *Scand J Haematol*. (1977) 18:47–53. doi: 10.1111/j.1600-0609.1977.tb01476.x
41. Bathija A, Davis S, Trubowitz S. Marrow adipose tissue:response to erythropoiesis. *Am J Hematol.* (1978) 5:315–21. doi: 10.1002/ajh.2830050406
42. Wood C. Membranous lipodystrophy of bone. *Arch Pathol Lab Med*. (1978) 102:22–7.
43. Tavassoli M. Cytochemistry of marrow and extramedullary adipocytes in monolayer cultures. *Scand J Haematol.* (1978) 20:330–4. doi: 10.1111/j.1600-0609.1978.tb02464.x
44. Bathija A, Davis S, Trubowitz S. Bone marrow adipose tissue:response to acute starvation. *Am J Hematol.* (1979) 6:191–8. doi: 10.1002/ajh.2830060303
45. Bryon PA, Gentilhomme O, Fiere D. [Histomorphometric analysis of bone-marrow adipose density and heterogeneity in myeloid aplasia and dysplasia. (author's transl)]. *Pathol Biol.* (1979) 27:209–13.
46. Tavassoli M, Crosby WH. Bone marrow histogenesis:a comparison of fatty and red marrow. *Science*. (1970) 169:291–3. doi: 10.1126/science.169.3942.291
47. Maniatis A, Tavassoli M, Crosby WH. Factors affecting the conversion of yellow to red marrow. *Blood*. (1971) 37:581–6. doi: 10.1182/blood.V37.5.581.581
48. Tavassoli M, Maniatis A, Crosby WH. Induction of sustained hemopoiesis in fatty marrow. *Blood*. (1974) 43:33–8. doi: 10.1182/blood.V43.1.33.33
49. Trubowitz S, Bathija A. Cell size and plamitate-1–14c turnover of rabbit marrow fat. *Blood*. (1977) 49:599–605. doi: 10.1182/blood.V49.4.599.bloodjournal494599
50. Cornbleet PJ, Moir RC, Wolf PL. A histochemical study of bone marrow hypoplasia in anorexia nervosa. *Virchows Arch A Pathol Anat Histol.* (1977) 374:239–47. doi: 10.1007/BF00427118
51. Bathija A, Ohanian M, Davis S, Trubowitz S. The marrow fat cell: response to X-ray induced aplasia. *Life Sci*. (1979) 25:921–7. doi: 10.1016/0024-3205(79)90497-1
52. Tavassoli M, Watson LR, Khademi R. Retention of hemopoiesis in tail vertebrae of newborn rats. *Cell Tissue Res.* (1979) 200:215–22. doi: 10.1007/BF00236414
53. Totty WG, Murphy WA, Ganz WI, Kumar B, Daum WJ, Siegel BA. Magnetic resonance imaging of the normal and ischemic femoral head. AJR. *Am J Roentgenol*. (1984) 143:1273–80. doi: 10.2214/ajr.143.6.1273
54. Littrup PJ, Aisen AM, Braunstein EM, Martel W. Magnetic resonance imaging of femoral head development in roentgenographically normal patients. *Skeletal Radiol.* (1985) 14:159–63. doi: 10.1007/BF00355555
55. Yoshida H, Asai S, Yashiro N, Iio M. MRI of bone marrow. *Radiat Med*. (1985) 3:47–55.
56. Wismer GL, Rosen BR, Buxton R, Stark DD, Brady TJ. Chemical shift imaging of bone marrow:preliminary experience. *Am J Roentgenol*. (1985) 145:1031–7. doi: 10.2214/ajr.145.5.1031
57. McKinstry CS, Steiner RE, Young AT, Jones L, Swirsky D, Aber V. Bone marrow in leukemia and aplastic anemia: MR imaging before, during, and after treatment. *Radiology*. (1987) 162:701–7. doi: 10.1148/radiology.162.3.3544034
58. Laval-Jeantet AM, Roger B, Bouysee S, Bergot C, Mazess RB. Influence of vertebral fat content on quantitative CT density. *Radiology*. (1986) 159:463–6. doi: 10.1148/radiology.159.2.3961178
59. Goodsitt MM, Rosenthal DI. Quantitative computed tomography scanning for measurement of bone and bone marrow fat content. A comparison of single- and dual-energy techniques using a solid synthetic phantom. *Invest Radiol*. (1987) 22:799–810. doi: 10.1097/00004424-198710000-00006
60. Rosenthal DI, Hayes CW, Rosen B, Mayo-Smith W, Goodsitt MM. Fatty replacement of spinal bone marrow due to radiation:demonstration by dual energy quantitative CT and MR imaging. *J Comput Assist Tomogr*. (1989) 13:463–5. doi: 10.1097/00004728-198905000-00018
61. Gluer CC, Genant HK. Impact of marrow fat on accuracy of quantitative CT. *J Comput Assist Tomogr*. (1989) 13:1023–35. doi: 10.1097/00004728-198911000-00015
62. Arashi K. Quantitative analysis of biopsied bone marrow tissue embedded in resin from hemopathic patients. I. Distribution of marrow adipose volume. (MAV) and hematopoietic cells. (HC) in certain part of the bone marrow biopsied specimen. *Nihon Ketsueki Gakkai Zasshi*. (1983) 46:65–80.
63. Rozman C, Feliu E, Berga L, Reverter JC, Climent C, Ferran MJ. Age-related variations of fat tissue fraction in normal human bone marrow depend both on size and number of adipocytes: a stereological study. *Exp Hematol.* (1989) 17:34–7.

64. Wright JA. A comparison of rat femoral, sternebral and lumbar vertebral bone marrow fat content by subjective assessment and image analysis of histological sections. *J Comp Pathol*. (1989) 100:419–26. doi: 10.1016/0021-9975(89)90007-8
65. Rosenthal DI, Mayo-Smith W, Goodsitt MM, Doppelt S, Mankin HJ. Bone and bone marrow changes in Gaucher disease: evaluation with quantitative. *Radiology*. (1989) 170:143–6. doi: 10.1148/radiology.170.1.2909087
66. Shen W, Chen J, Punyanitya M, Shapses S, Heshka S, Heymsfield SB. MRI-measured bone marrow adipose tissue is inversely related to DXA-measured bone mineral in Caucasian women. *Osteoporos Int*. (2007) 18:641–7. doi: 10.1007/s00198-006-0285-9
67. Fazeli PK, Bredella MA, Freedman L, Thomas BJ, Breggia A, Meenaghan E, et al. Marrow fat and preadipocyte factor-1 levels decrease with recovery in women with anorexia nervosa. *J Bone Miner Res*. (2012) 27:1864–71. doi: 10.1002/jbmr.1640
68. Chan GK, Duque G. Age-related bone loss:old bone, new facts. *Gerontology*. (2002) 48:62–71. doi: 10.1159/000048929
69. Fournier C, Perrier A, Thomas M, Laroche N, Dumas V, Rattner A, et al. Reduction by strontium of the bone marrow adiposity in mice and repression of the adipogenic commitment of multipotent C3H10T1/2 cells. *Bone*. (2012) 50:499–509. doi: 10.1016/j.bone.2011.07.038
70. Scheller EL, Troiano N, Vanhoutan JN, Bouxsein MA, Fretz JA, Xi Y, et al. Use of osmium tetroxide staining with microcomputerized tomography to visualize and quantify bone marrow adipose tissue *in vivo*. *Methods Enzymol*. (2014) 537:123–39. doi: 10.1016/B978-0-12-411619-1.00007-0
71. Karampinos DC, Ruschke S, Dieckmeyer M, Diefenbach M, Franz D, Gersing AS, et al. Quantitative MRI and spectroscopy of bone marrow. *J Magn Reson Imaging*. (2018) 47:332–53. doi: 10.1002/jmri.25769
72. Bianco P, Robey PG. Skeletal stem cells. In: Lanza R, Gearhart J, Hogan B, Melton D, Pedersen R, Thomson J, West M, editors. *Handbook of Adult and Fetal Stem Cells*. Burlington, NJ: Academic Press (2004). 415–24. doi: 10.1016/B978-012436643-5/50129-2
73. Scheller EL, Doucette CR, Learman BS, Cawthorn WP, Khandaker S, Schell B, et al. Region-specific variation in the properties of skeletal adipocytes reveals regulated and constitutive marrow adipose tissues. *Nat Commun*. (2015) 6:7808. doi: 10.1038/ncomms8808
74. Attané C, Estève D, Chaoui K, Iacovoni J, Corre J, Moutahir M, et al. Yellow adipocytes comprise a new adipocyte sub-type present in human bone marrow. *bioRxiv*. (2019) 2019:641886. doi: 10.1101/641886
75. Hardouin P, Marie PJ, Rosen CJ. New insights into bone marrow adipocytes: report from the First European Meeting on Bone Marrow Adiposity. (BMA 2015). *Bone*. (2016) 93:212–5. doi: 10.1016/j.bone.2015.11.013
76. van der Eerden B, van Wijnen A. Meeting report of the 2016 bone marrow adiposity meeting. *Adipocyte*. (2017) 6:304–13. doi: 10.1080/21623945.2017.1313374
77. Friedlis MF, Centeno CJ. Performing a better bone marrow aspiration. *Phys Med Rehabil Clin N Am*. (2016) 27:919–39. doi: 10.1016/j.pmr.2016.06.009
78. Holton J, Imam MA, Snow M. Bone marrow aspirate in the treatment of chondral injuries. *Front Surg*. (2016) 3:33. doi: 10.3389/fsurg.2016.00033
79. Rosen ED, Spiegelman BM. What we talk about when we talk about fat. *Cell*. (2014) 156:20–44. doi: 10.1016/j.cell.2013.12.012
80. Sulston RJ, Cawthorn WP. Bone marrow adipose tissue as an endocrine organ:close to the bone? *Horm Mol Biol Clin Investig*. (2016) 28:21–38. doi: 10.1515/hmbci-2016-0012
81. Laharrague P, Larrouy D, Fontanilles AM, Truel N, Campfield A, Tenenbaum R, et al. High expression of leptin by human bone marrow adipocytes in primary culture. *FASEB J*. (1998) 12:747–52. doi: 10.1096/fasebj.12.9.747
82. Laharrague P, Truel N, Fontanilles AM, Corberand JX, Penicaud L, Casteilla L. Regulation by cytokines of leptin expression in human bone marrow adipocytes. *Horm Metab Res*. (2000) 32:381–5. doi: 10.1055/s-2007-978658
83. Ryden M, Dicker A, Gotherstrom C, Astrom G, Tammik C, Arner P, Le Blanc K. Functional characterization of human mesenchymal stem cell-derived adipocytes. *Biochem Biophys Res Commun*. (2003) 311:391–7. doi: 10.1016/j.bbrc.2003.10.010
84. Cawthorn WP, Scheller EL, Learman BS, Parlee SD, Simon BR, Mori H, et al. Bone marrow adipose tissue is an endocrine organ that contributes to increased circulating adiponectin during caloric restriction. *Cell Metab*. (2014) 20:368–75. doi: 10.1016/j.cmet.2014.06.003
85. Scheller EL, Burr AA, MacDougald OA, Cawthorn WP. Inside out:Bone marrow adipose tissue as a source of circulating adiponectin. *Adipocyte*. (2016) 5:251–69. doi: 10.1080/21623945.2016.1149269
86. Holt V, Caplan AI, Haynesworth SE. Identification of a subpopulation of marrow MSC-derived medullary adipocytes that express osteoclast-regulating molecules:marrow adipocytes express osteoclast mediators. *PLoS ONE*. (2014) 9:e108920. doi: 10.1371/journal.pone.0108920
87. Fan Y, Hanai JI, Le PT, Bi R, Maridas D, DeMambro V, et al. Parathyroid hormone directs bone marrow mesenchymal cell fate. *Cell Metab*. (2017) 25:661–72. doi: 10.1016/j.cmet.2017.01.001
88. Takeshita S, Fumoto T, Naoe Y, Ikeda K. Age-related marrow adipogenesis is linked to increased expression of RANKL. *J Biol Chem*. (2014) 289:16699–710. doi: 10.1074/jbc.M114.547919
89. Ambrosi TH, Scialdone A, Graja A, Gohlke S, Jank AM, Bocian C, et al. Adipocyte accumulation in the bone marrow during obesity and aging impairs stem cell-based hematopoietic and bone regeneration. *Cell Stem Cell*. (2017) 20:771–84.e6. doi: 10.1016/j.stem.2017.02.009
90. Zhou BO, Yu H, Yue R, Zhao Z, Rios JJ, Naveiras O, et al. Bone marrow adipocytes promote the regeneration of stem cells and haematopoiesis by secreting SCF. *Nat Cell Biol*. (2017) 19:891–903. doi: 10.1038/ncb3570
91. Laharrague P, Fontanilles AM, Tkaczuk J, Corberand JX, Penicaud L, Casteilla L. Inflammatory/haematopoietic cytokine production by human bone marrow adipocytes. *Eur Cytokine Netw*. (2000) 11:634–9.
92. Gasparrini M, Rivas D, Elbaz A, Duque G. Differential expression of cytokines in subcutaneous and marrow fat of aging C57BL/6J mice. *Exp Gerontol*. (2009) 44:613–8. doi: 10.1016/j.exger.2009.05.009
93. Ferland-McCollough D, Maselli D, Spinetti G, Sambataro M, Sullivan N, Blom A, Madeddu P. MCP-1 feedback loop between adipocytes and mesenchymal stromal cells causes fat accumulation and contributes to hematopoietic stem cell rarefaction in the bone marrow of patients with diabetes. *Diabetes*. (2018) 67:1380–94. doi: 10.2337/db18-0044
94. Mattiucci D, Maurizi G, Izzi V, Cenci L, Ciarlantini M, Mancini S, et al. Bone marrow adipocytes support hematopoietic stem cell survival. *J Cell Physiol*. (2018) 233:1500–11. doi: 10.1002/jcp.26037
95. Miggitsch C, Meryk A, Naismith E, Pangrazzi L, Ejaz A, Jenewein B, et al. Human bone marrow adipocytes display distinct immune regulatory properties. *EBioMed*. (2019) 46:387–98. doi: 10.1016/j.ebiom.2019.07.023
96. Tran MA, Dang TL, Berlan M. Effects of catecholamines on free fatty acid release from bone marrow adipose tissue. *J Lipid Res*. (1981) 22:1271–6.
97. Tran MA, Lac DT, Berlan M, Lafontan M. Interplay of alpha-2 and beta adrenoceptors in the control of free fatty acid release from bone marrow adipose tissue. *J Pharmacol Exp Ther*. (1984) 230:228–31.
98. Scheller EL, Khandaker S, Learman BS, Cawthorn WP, Anderson LM, Pham HA, et al. Bone marrow adipocytes resist lipolysis and remodeling in response to β-adrenergic stimulation. *Bone*. (2018) 118:32–41. doi: 10.1016/j.bone.2018.01.016
99. Veldhuis-Vlug AG, Rosen CJ. Clinical implications of bone marrow adiposity. *J Intern Med*. (2018) 283:121–39. doi: 10.1111/joim.12718
100. Sebo ZL, Rendina-Ruedy E, Ables GP, Lindskog DM, Rodeheffer MS, Fazeli PK, et al. Bone marrow adiposity:basic and clinical implications. *Endocr Rev*. (2019) 40:1187–206. doi: 10.1210/er.2018-00138
101. Cannon B, Nedergaard J. Brown adipose tissue:function and physiological significance. *Physiol Rev*. (2004) 84:277–359. doi: 10.1152/physrev.00015.2003
102. Krings A, Rahman S, Huang S, Lu Y, Czernik PJ, Lecka-Czernik B. Bone marrow fat has brown adipose tissue characteristics, which are attenuated with aging and diabetes. *Bone*. (2012) 50:546–52. doi: 10.1016/j.bone.2011.06.016
103. Rahman S, Lu Y, Czernik PJ, Rosen CJ, Enerback S, Lecka-Czernik B. Inducible brown adipose tissue, or beige fat, is anabolic for the skeleton. *Endocrinology*. (2013) 154:2687–701. doi: 10.1210/en.2012-2162
104. Dezso Z, Nikolsky Y, Sviridov E, Shi W, Serebriyskaya T, Dosymbekov D, et al. A comprehensive functional analysis of tissue specificity of human gene expression. *BMC Biol*. (2008) 6:49. doi: 10.1186/1741-7007-6-49

105. Thorrez L, Van Deun K, Tranchevent LC, Van Lommel L, Engelen K, Marchal K, et al. Using ribosomal protein genes as reference:a tale of caution. *PLoS ONE*. (2008) 3:e1854. doi: 10.1371/journal.pone.0001854
106. Liu LF, Shen WJ, Ueno M, Patel S, Kraemer FB. Characterization of age-related gene expression profiling in bone marrow and epididymal adipocytes. *BMC Genom*. (2011) 12:212. doi: 10.1186/1471-2164-12-212
107. Craft CS, Robles H, Lorenz MR, Hilker ED, Magee KL, Andersen TL, et al. Bone marrow adipose tissue does not express UCP1 during development or adrenergic-induced remodeling. *Sci Rep*. (2019) 9:17427. doi: 10.1038/s41598-019-54036-x
108. Suchacki KJ, Tavares AS, Mattiucci D, Scheller EL, Papanastasiou G, Gray C, Sinton MC, et al. Bone marrow adipose tissue is a unique adipose subtype with distinct roles in systemic glucose homeostasis. *bioRxiv*. (2019) 2019:673129. doi: 10.1101/673129
109. Scheller EL, Cawthorn WP, Burr AA, Horowitz MC, MacDougald OA. Marrow adipose tissue:trimming the fat. *Trends Endocrinol Metab*. (2016) 27:392–403. doi: 10.1016/j.tem.2016.03.016
110. Vernon RG, Flint DJ. ADIPOSE TISSUE|Structure and function of white adipose tissue. In: Caballero B, editor. *Encyclopedia of Food Sciences and Nutrition*, *2nd Edn*. Oxford: Academic Press (2003). p. 23–9. doi: 10.1016/B0-12-227055-X/00007-9
111. Yap ES, Koh PL, Ng CH, de Mel S, Chee YL. A bone marrow aspirate and trephine simulator. *Simulation Healthcare*. (2015) 10:245–8. doi: 10.1097/SIH.0000000000000092
112. Cawthorn WP, Scheller EL. Editorial: bone marrow adipose tissue:formation, function, and impact on health and disease. *Front Endocrinol*. (2017) 8:112. doi: 10.3389/fendo.2017.00112
113. Craft CS, Li Z, MacDougald OA, Scheller EL. Molecular differences between subtypes of bone marrow adipocytes. *Curr Mol Biol Rep*. (2018) 4:16–23. doi: 10.1007/s40610-018-0087-9
114. Scheller EL, Rosen CJ. What's the matter with MAT? Marrow adipose tissue, metabolism, and skeletal health. *Ann N Y Acad Sci*. (2014) 1311:14–30. doi: 10.1111/nyas.12327
115. Cawthorn WP, Scheller EL, Parlee SD, Pham HA, Learman BS, Redshaw CM, et al. Expansion of bone marrow adipose tissue during caloric restriction is associated with increased circulating glucocorticoids and not with hypoleptinemia. *Endocrinology*. (2016) 157:508–21. doi: 10.1210/en.2015-1477
116. Sulston RJ, Learman BS, Zhang B, Scheller EL, Parlee SD, Simon BR, et al. Increased circulating adiponectin in response to thiazolidinediones: investigating the role of bone marrow adipose tissue. *Front Endocrinol*. (2016) 7:128. doi: 10.3389/fendo.2016.00128
117. McIlroy GD, Suchacki K, Roelofs AJ, Yang W, Fu Y, Bai B, et al. Adipose specific disruption of seipin causes early-onset generalised lipodystrophy and altered fuel utilisation without severe metabolic disease. *Mol Metabol*. (2018) 10:55–65. doi: 10.1016/j.molmet.2018.01.019
118. Bianco P, Robey PG. Skeletal stem cells. *Development*. (2015) 142:1023–7. doi: 10.1242/dev.102210
119. Owen M, Friedenstein AJ. Stromal stem cells:marrow-derived osteogenic precursors. *Ciba Found Symp*. (1988) 136:42–60. doi: 10.1002/9780470513637.ch4
120. Kuznetsov SA, Krebsbach PH, Satomura K, Kerr J, Riminucci M, Benayahu D, Robey PG. Single-colony derived strains of human marrow stromal fibroblasts form bone after transplantation *in vivo*. *J Bone Miner Res*. (1997) 12:1335–47. doi: 10.1359/jbmr.1997.12.9.1335
121. Friedenstein AJ, Chailakhyan RK, Latsinik NV, Panasyuk AF, Keiliss-Borok IV. Stromal cells responsible for transferring the microenvironment of the hemopoietic tissues. Cloning in vitro and retransplantation *in vivo*. *Transplantation*. (1974) 17:331–40. doi: 10.1097/00007890-197404000-00001
122. Sacchetti B, Funari A, Michienzi S, Di Cesare S, Piersanti S, Saggio I, et al. Self-renewing osteoprogenitors in bone marrow sinusoids can organize a hematopoietic microenvironment. *Cell*. (2007) 131:324–36. doi: 10.1016/j.cell.2007.08.025
123. Ambrosi TH, Longaker MT, Chan CK. A revised perspective of skeletal stem cell biology. *Front Cell Dev Biol*. (2019) 7:189. doi: 10.3389/fcell.2019.00189
124. Caplan AI. Mesenchymal stem cells. *J Orthop Res*. (1991) 9:641–50. doi: 10.1002/jor.1100090504
125. Caplan AI. All MSCs are pericytes? *Cell Stem Cell*. (2008) 3:229–30. doi: 10.1016/j.stem.2008.08.008
126. Sacchetti B, Funari A, Remoli C, Giannicola G, Kogler G, Liedtke S, et al. No identical "Mesenchymal Stem Cells" at different times and sites: human committed progenitors of distinct origin and differentiation potential are incorporated as adventitial cells in microvessels. *Stem Cell Rep*. (2016) 6:897–913. doi: 10.1016/j.stemcr.2016.05.011
127. Jacobs FA, Sadie-Van Gijsen H, van de Vyver M, Ferris WF. Vanadate impedes adipogenesis in mesenchymal stem cells derived from different depots within bone. *Front Endocrinol*. (2016) 7:108. doi: 10.3389/fendo.2016.00108
128. Jacobs FA, van de Vyver M, Ferris WF. Isolation and characterization of different mesenchymal stem cell populations from rat femur. *Methods Mol Biol*. (2019) 1916:133–47. doi: 10.1007/978-1-4939-8994-2_13
129. MacCord K. Mesenchyme. In: University AS, editor. *Embryo Project Encyclopedia*. (2012). Available online at: https://embryo.asu.edu/pages/mesenchyme
130. da Silva Meirelles L, Chagastelles PC, Nardi NB. Mesenchymal stem cells reside in virtually all post-natal organs and tissues. *J Cell Sci*. (2006) 119:2204–13. doi: 10.1242/jcs.02932
131. Parfitt AM, Drezner MK, Glorieux FH, Kanis JA, Malluche H, Meunier PJ, et al. Bone histomorphometry:standardization of nomenclature, symbols, and units. Report of the ASBMR Histomorphometry Nomenclature Committee. *J Bone Miner Res*. (1987) 2:595–610. doi: 10.1002/jbmr.5650020617
132. Horowitz MC, Berry R, Holtrup B, Sebo Z, Nelson T, Fretz JA, et al. Bone marrow adipocytes. *Adipocyte*. (2017) 6:193–204. doi: 10.1080/21623945.2017.1367881
133. Roche B, David V, Vanden-Bossche A, Peyrin F, Malaval L, Vico L, et al. Structure and quantification of microvascularisation within mouse long bones:what and how should we measure? *Bone*. (2012) 50:390–9. doi: 10.1016/j.bone.2011.09.051
134. Lundberg LG, Lerner R, Sundelin P, Rogers R, Folkman J, Palmblad J. Bone marrow in polycythemia vera, chronic myelocytic leukemia, and myelofibrosis has an increased vascularity. *Am J Pathol*. (2000) 157:15–9. doi: 10.1016/S0002-9440(10)64511-7
135. Kerckhofs G, Stegen S, van Gastel N, Sap A, Falgayrac G, Penel G, et al. Simultaneous three-dimensional visualization of mineralized and soft skeletal tissues by a novel microCT contrast agent with polyoxometalate structure. *Biomaterials*. (2018) 159:1–12. doi: 10.1016/j.biomaterials.2017.12.016
136. Gomariz A, Helbling PM, Isringhausen S, Suessbier U, Becker A, Boss A, et al. Quantitative spatial analysis of haematopoiesis-regulating stromal cells in the bone marrow microenvironment by 3D microscopy. *Nat Commun*. (2018) 9:2532. doi: 10.1038/s41467-018-04770-z
137. Yeung DK, Griffith JF, Antonio GE, Lee FK, Woo J, Leung PC. Osteoporosis is associated with increased marrow fat content and decreased marrow fat unsaturation:a proton MR spectroscopy study. *J Magn Reson Imaging*. (2005) 22:279–85. doi: 10.1002/jmri.20367
138. Baum T, Yap SP, Karampinos DC, Nardo L, Kuo D, Burghardt AJ, et al. Does vertebral bone marrow fat content correlate with abdominal adipose tissue, lumbar spine bone mineral density, and blood biomarkers in women with type 2 diabetes mellitus? *J Magn Reson Imaging*. (2012) 35:117–24. doi: 10.1002/jmri.22757
139. Patsch JM, Li X, Baum T, Yap SP, Karampinos DC, Schwartz AV, et al. Bone marrow fat composition as a novel imaging biomarker in postmenopausal women with prevalent fragility fractures. *J Bone Miner Res*. (2013) 28:1721–8. doi: 10.1002/jbmr.1950
140. Bredella MA, Fazeli PK, Daley SM, Miller KK, Rosen CJ, Klibanski A, et al. Marrow fat composition in anorexia nervosa. *Bone*. (2014) 66:199–204. doi: 10.1016/j.bone.2014.06.014
141. Huovinen V, Viljakainen H, Hakkarainen A, Saukkonen T, Toiviainen-Salo S, Lundbom N, et al. Bone marrow fat unsaturation in young adults is not affected by present or childhood obesity, but increases with age: a pilot study. *Metabolism*. (2015) 64:1574–81. doi: 10.1016/j.metabol.2015.08.014
142. Singhal V, Bredella MA. Marrow adipose tissue imaging in humans. *Bone*. (2019) 118:69–76. doi: 10.1016/j.bone.2018.01.009

143. Zebaze R, Osima M, Bui M, Lukic M, Wang X, Ghasem-Zadeh A, et al. Adding marrow adiposity and cortical porosity to femoral neck areal bone mineral density improves the discrimination of women with nonvertebral fractures from controls. *J Bone Miner Res*. (2019) 34:1451–60. doi: 10.1002/jbmr.3721
144. Bredella MA, Daley SM, Kalra MK, Brown JK, Miller KK, et al. Marrow adipose tissue quantification of the lumbar spine by using dual-energy CT and single-Voxel. (1)H MR spectroscopy:a feasibility study. *Radiology*. (2015) 277:230–5. doi: 10.1148/radiol.2015142876
145. Arentsen L, Hansen KE, Yagi M, Takahashi Y, Shanley R, McArthur A, et al. Use of dual-energy computed tomography to measure skeletal-wide marrow composition and cancellous bone mineral density. *J Bone Miner Metab*. (2017) 35:428–36. doi: 10.1007/s00774-016-0796-1
146. Xiao Z, Cao L, Liang Y, Huang J, Stern AR, Dallas M, et al. Osteoblast-specific deletion of Pkd2 leads to low-turnover osteopenia and reduced bone marrow adiposity. *PLoS ONE*. (2014) 9:e114198. doi: 10.1371/journal.pone.0114198
147. Khoury BM, Bigelow EM, Smith LM, Schlecht SH, Scheller EL, Andarawis-Puri N, et al. The use of nano-computed tomography to enhance musculoskeletal research. Connect. *Tissue Res*. (2015) 56:106–19. doi: 10.3109/03008207.2015.1005211

Conflict of Interest: The authors declare that the research was conducted in the absence of any commercial or financial relationships that could be construed as a potential conflict of interest.

frontiers in Endocrinology

REVIEW
published: 28 February 2020
doi: 10.3389/fendo.2020.00065

Reporting Guidelines, Review of Methodological Standards, and Challenges Toward Harmonization in Bone Marrow Adiposity Research. Report of the Methodologies Working Group of the International Bone Marrow Adiposity Society

Josefine Tratwal[1], Rossella Labella[2], Nathalie Bravenboer[3,4], Greet Kerckhofs[5,6], Eleni Douni[7,8], Erica L. Scheller[9], Sammy Badr[10,11], Dimitrios C. Karampinos[12], Sarah Beck-Cormier[13,14], Biagio Palmisano[15], Antonella Poloni[16], Maria J. Moreno-Aliaga[17,18,19], Jackie Fretz[20], Matthew S. Rodeheffer[21], Parastoo Boroumand[22], Clifford J. Rosen[23], Mark C. Horowitz[24], Bram C. J. van der Eerden[25], Annegreet G. Veldhuis-Vlug[4,23,26†] and Olaia Naveiras[1,27*†] on behalf of the Methodologies Working Group for the International Bone Marrow Adiposity Society (BMAS)*

[1] Laboratory of Regenerative Hematopoiesis, Institute of Bioengineering and Swiss Institute for Experimental Cancer Research, Polytechnique Fédérale de Lausanne, Lausanne, Switzerland, [2] Tissue and Tumour Microenvironments Lab, The Kennedy Institute of Rheumatology, University of Oxford, Oxford, United Kingdom, [3] Department of Clinical Chemistry, Amsterdam University Medical Centers, Vrije Universiteit, Amsterdam Movement Sciences, Amsterdam, Netherlands, [4] Section of Endocrinology, Department of Internal Medicine, Center for Bone Quality, Leiden University Medical Center, Leiden, Netherlands, [5] Biomechanics Lab, Institute of Mechanics, Materials and Civil Engineering, UCLouvain, Louvain-la-Neuve, Belgium, [6] Department Materials Engineering, KU Leuven, Leuven, Belgium, [7] Laboratory of Genetics, Department of Biotechnology, Agricultural University of Athens, Athens, Greece, [8] Institute for Bioinnovation, Biomedical Sciences Research Center Alexander Fleming, Athens, Greece, [9] Division of Bone and Mineral Diseases, Department of Medicine, Washington University, St. Louis, MO, United States, [10] Univ. Lille, EA 4490 - PMOI - Physiopathologie des Maladies Osseuses Inflammatoires, Lille, France, [11] CHU Lille, Service de Radiologie et Imagerie Musculosquelettique, Lille, France, [12] Department of Diagnostic and Interventional Radiology, Technical University of Munich, Munich, Germany, [13] Inserm, UMR 1229, RMeS, Regenerative Medicine and Skeleton, Université de Nantes, ONIRIS, Nantes, France, [14] Université de Nantes, UFR Odontologie, Nantes, France, [15] Department of Genetics and Development, Columbia University Irving Medical Center, New York, NY, United States, [16] Hematology, Department of Clinic and Molecular Science, Università Politecnica Marche-AOU Ospedali Riuniti, Ancona, Italy, [17] Centre for Nutrition Research and Department of Nutrition, Food Science and Physiology, School of Pharmacy and Nutrition, University of Navarra, Pamplona, Spain, [18] IdiSNA, Navarra's Health Research Institute, Pamplona, Spain, [19] CIBERobn Physiopathology of Obesity and Nutrition, Centre of Biomedical Research Network, ISCIII, Madrid, Spain, [20] Department of Orthopaedics and Rehabilitation, Cellular and Developmental Biology, Yale University School of Medicine, New Haven, CT, United States, [21] Department of Comparative Medicine and Molecular, Cellular and Developmental Biology, Yale University School of Medicine, New Haven, CT, United States, [22] Cell Biology Program, The Hospital for Sick Children, Toronto, ON, Canada, [23] Maine Medical Center Research Institute, Center for Clinical and Translational Research, Scarborough, ME, United States, [24] Department of Orthopaedics and Rehabilitation, Yale University School of Medicine, New Haven, CT, United States, [25] Laboratory for Calcium and Bone Metabolism, Department of Internal Medicine, Erasmus University Medical Center, Rotterdam, Netherlands, [26] Jan van Goyen Medical Center/OLVG Hospital, Department of Internal Medicine, Amsterdam, Netherlands, [27] Hematology Service, Departments of Oncology and Laboratory Medicine, Centre Hospitalier Universitaire Vaudois, Lausanne, Switzerland

OPEN ACCESS

Edited by:
Basem M. Abdallah, University of Southern Denmark, Denmark

Reviewed by:
Urszula T. Iwaniec, Oregon State University, United States
Graziana Colaianni, University of Bari Aldo Moro, Italy

***Correspondence:**
Annegreet G. Veldhuis-Vlug
annegreetveldhuis@live.nl
Olaia Naveiras
olaia.naveiras@epfl.ch;
olaia.naveiras@chuv.ch

[†] These authors have contributed equally to this work

Specialty section:
This article was submitted to Bone Research, a section of the journal Frontiers in Endocrinology

Received: *30 August 2019*
Accepted: *31 January 2020*
Published: *28 February 2020*

Citation:
Tratwal J, Labella R, Bravenboer N, Kerckhofs G, Douni E, Scheller EL, Badr S, Karampinos DC, Beck-Cormier S, Palmisano B, Poloni A, Moreno-Aliaga MJ, Fretz J, Rodeheffer MS, Boroumand P, Rosen CJ, Horowitz MC, van der Eerden BCJ, Veldhuis-Vlug AG and Naveiras O (2020) Reporting Guidelines, Review of Methodological Standards, and Challenges Toward Harmonization in Bone Marrow Adiposity Research. Report of the Methodologies Working Group of the International Bone Marrow Adiposity Society. Front. Endocrinol. 11:65. doi: 10.3389/fendo.2020.00065

The interest in bone marrow adiposity (BMA) has increased over the last decade due to its association with, and potential role, in a range of diseases (osteoporosis, diabetes, anorexia, cancer) as well as treatments (corticosteroid, radiation, chemotherapy, thiazolidinediones). However, to advance the field of BMA research, standardization

of methods is desirable to increase comparability of study outcomes and foster collaboration. Therefore, at the 2017 annual BMA meeting, the International Bone Marrow Adiposity Society (BMAS) founded a working group to evaluate methodologies in BMA research. All BMAS members could volunteer to participate. The working group members, who are all active preclinical or clinical BMA researchers, searched the literature for articles investigating BMA and discussed the results during personal and telephone conferences. According to the consensus opinion, both based on the review of the literature and on expert opinion, we describe existing methodologies and discuss the challenges and future directions for (1) histomorphometry of bone marrow adipocytes, (2) *ex vivo* BMA imaging, (3) *in vivo* BMA imaging, (4) cell isolation, culture, differentiation and *in vitro* modulation of primary bone marrow adipocytes and bone marrow stromal cell precursors, (5) lineage tracing and *in vivo* BMA modulation, and (6) BMA biobanking. We identify as accepted standards in BMA research: manual histomorphometry and osmium tetroxide 3D contrast-enhanced μCT for *ex vivo* quantification, specific MRI sequences (WFI and H-MRS) for *in vivo* studies, and RT-qPCR with a minimal four gene panel or lipid-based assays for *in vitro* quantification of bone marrow adipogenesis. Emerging techniques are described which may soon come to complement or substitute these gold standards. Known confounding factors and minimal reporting standards are presented, and their use is encouraged to facilitate comparison across studies. In conclusion, specific BMA methodologies have been developed. However, important challenges remain. In particular, we advocate for the harmonization of methodologies, the precise reporting of known confounding factors, and the identification of methods to modulate BMA independently from other tissues. Wider use of existing animal models with impaired BMA production (e.g., *Pfrt*$^{-/-}$, Kit$^{W/W-v}$) and development of specific BMA deletion models would be highly desirable for this purpose.

Keywords: bone marrow adiposity, bone marrow adipose tissue, bone marrow fat, marrow, adipocyte, standards, methods, Bone Marrow Adiposity Society

INTRODUCTION

Bone marrow adipocytes (BMAds) reside in the bone marrow (BM) in close contact with bone, hematopoietic cells, marrow stromal cells, nerves, and blood vessels. Bone marrow adipose tissue (BMAT) thus refers to BM areas where BMAds are the predominant cell type, and BMA refers more broadly to BMAT across all skeletal locations and metabolic states. Over the last decades, interest in the functional role of BMAds has gradually increased and it is now evident that BMAds are actively involved in bone metabolism, hematopoiesis, and energy metabolism (1, 2). In addition, a possible role for BMAds in many diseases has emerged (3), and research groups all over the world are investigating the origin, function, and interaction of BMAds. However, different methods, models, and techniques are being used, which creates a challenge to compare or combine the results. Therefore, the International BMAS initiated a Methodologies Working Group to describe the existing methodologies, to identify associated challenges, and to establish standards in reporting as guidance for future studies in the field.

BMAT encompasses a heterogeneous population of mature adipocytes and preadipocytes, with distinct morphologies, lipid content, gene expression and function. Committed preadipocytes have a fibroblast-like morphology when observed *in vitro*, and are therefore morphologically indistinguishable from the progenitor populations encompassed within the term bone marrow stromal cells (BMSCs). However, preadipocytes are phenotypically very different from mature adipocytes. Preadipocytes are defined as cells committed through adipogenesis and characterized by the expression of early adipogenic genes (PPARγ and CEBPa) (4, 5). Mature BMAds express late adipogenic genes (AdipoQ, Glut4, FABP4, LPL, PLIN1, ZFP423) and contain a single large lipid droplet, therefore resembling white adipocytes in appearance. In particular, adiponectin (AdipoQ) expression is already present in BM preadipocytes and stromal precursors, then increases with differentiation (6). Additionally, Krings et al. (7) have revealed that BMAT from whole tibiae in C57BL/6 mice possibly have a distinctive phenotype, expressing genes characteristic of both white and brown adipose tissue (WAT and BAT, respectively), congruent

with the expression pattern of purified, primary human BMAds (7–9).

Indeed, Tavassoli et al. identified in 1976 two distinct populations of BMAds: after treatment with hemolytic anemia-inducing agent phenylhydrazine (10) one population remained stable while another population disappeared, and was described as labile BMAds. These two different "stable" and "labile" BMAd populations could be distinguished using performic acid Schiff (PFAS) staining (11). The presence of two different populations of BMAds localized to different regions of the skeleton was also more recently shown by Scheller et al. In mice, smaller BMAds (31–33 μm cell diameter) are interspersed between hematopoietic cells in the femur, the proximal portion of the tibia, and almost all skeletal segments that contain hematopoietic BM, while larger BMAds (38–39 um) are localized in the distal portion of the tibiae and phalanx [(12); **Figure 1**]. When challenged with cold exposure, BMAds interspersed in the red/hematopoietic marrow decreased in size and number, while the adipocytes localized in the yellow/adipocytic marrow did not change. The terms "regulated" and "constitutive" BMAT, respectively, have thus been proposed.

BMSCs and committed BM pre-adipocytes are more easily isolated and have seen a larger number of *in vitro* assays developed than mature BMAds, which are more difficult to handle in culture or to process in whole bone samples. *In vivo* lineage tracing models have started to pave the way, while specific markers for BMAd maturation remain to be identified. If successful, identification of specific biomarkers at the different stages of BM adipogenesis in both mouse and human will provide tools to dissect the impact of BMA in physiology and disease. *In vivo* imaging technologies are being adapted from studies of different tissues (e.g., peripheral adipose tissue) and species (e.g., human to mouse), while novel *ex vivo* imaging techniques are being adapted and developed specifically for BMAds and BM stromal imaging. All such techniques and their limitations and challenges are reviewed in the six sections that constitute this review, and guidelines for reporting of BMA-related results to maximize comparability are proposed in the concluding remarks (**Table 1**). For clarity, an abbreviation table is provided the manuscript (**Table 2**).

Of note, even with such significant technological advances over the last decade, histological analysis has been a historical contributor in the understanding of BM composition and architecture, and is rapidly evolving through automatization via Digital Pathology. Histomorphometry therefore remains an important aspect of standard methodological practices in basic or translational research as well as clinical laboratories.

In addition, although rats and non-rodent animal models are recommended by the food and drug administration (FDA) or European Union as a model for osteoporosis, the field of BMA extends beyond bone health itself to the study of energy metabolism, hematopoiesis and metastatic bone disease, amongst other subfields. Mice constitute very important models for these other aspects of BMA research, especially in their quality of premier animal for genetic studies, and are thus recognized as preclinical model in this context. Nonetheless, we would like to encourage the study of BMA in larger animals and other rodents, especially when bone health and biomechanical properties of bone are being assessed.

HISTOMORPHOMETRY

The field of bone histomorphometry was accelerated in 1976 when Dr. Parfitt published "Terminology and symbols in bone morphometry" which lay the foundation for the first Guideline on Bone histomorphometry (13). We can now build on this important consensus to establish additional guidelines on histomorphometry of BMAT. In 1987 Parfitt et al. listed three different meanings for bone; mineralized bone matrix, bone matrix, and bone tissue (14). Bone tissue encompasses bone and a soft tissue within it, the BM. The BM includes hematopoietic cells and its precursors, physically and functionally supported by diverse BM stromal cell populations [reviewed in (15)]. The latter is a three-dimensional network of cells in contact with developing blood cells in the extravascular space. The known main cell types that constitute this network are: osteogenic cells near bone surfaces, perivascular cells associated to sinusoids, and adipocytes. As discussed in this first section, methods to quantify marrow components via histomorphometry are based on different sample preparation, embedding and staining techniques, most requiring an intermediate step of decalcification and some allowing for epitope conservation for immunostaining. Paraffin-embedded samples have the advantage of access to large retrospective collections and potential comparability across sites, especially for the clinical setting where paraffin-embedding is standard. Other conservation procedures allow for more precise histomorphometric quantification, and some do not require decalcification [methyl methacrylate (MMA), or resin embedding, including technovit 900].

Sample Preparation

Histomorphometric analysis relies predominantly on the quality of the sample. Therefore, careful consideration of the sample preparation is important. To prepare a BM sample, either calcified or decalcified bone samples can be embedded in paraffin or plastic, depending on the desired staining procedure (16, 17). For both procedures, the BM sample is regularly fixed in 4% Paraformaldehyde. Afterwards, the sample can be sectioned in conventionally 4–5 μm sections.

Decalcification

Several options of decalcifying agents are available, though Ethylenediaminetetraacetic acid (EDTA) is advised as compared to acid-based decalcification to enable most enzymatic and immunohistochemical stainings (18). Different factors can control the rate of the decalcification process: concentration of decalcifying agent, temperature, density of the sample, agitation and thickness of the tissue. In general, a large volume (e.g., 20x that of the sample), a high concentration of decalcifying agent and a high temperature (e.g., 20–37°C) during decalcification can speed up the reaction process. In contrast, increase of the size, density, and thickness of the sample may require longer decalcification time (17, 18). For an optimal immunostaining,

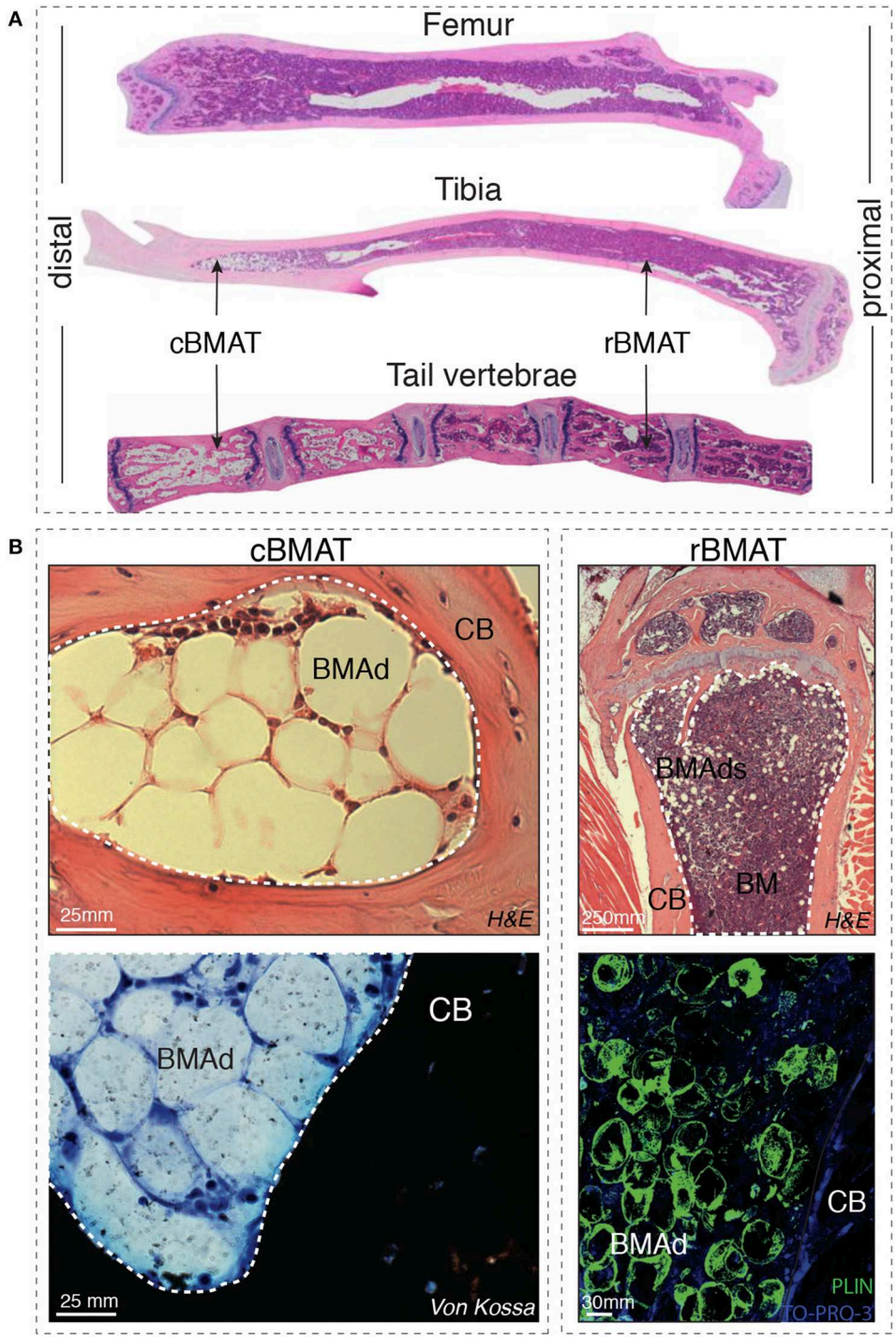

FIGURE 1 | (A) Distal-proximal representative images in Hematoxylin & Eosin (H&E) stain of 4 μm paraffin sections of femur, tibia and tail of 8-week-old mice. Note that the artefactually empty region in the center of tibia and femur corresponds to the expansion of the central vein lumen due to fixation-mediated retraction. **(B)** Left panels: Murine bone marrow adipocytes in the tail vertebrae of 24-week-old mice (cBMAT) of 3μm paraffin sections stained with H&E (top) and 6μm sections stained with von Kossa/Methylene Blue (bottom). Right panels: murine bone marrow adipocytes in the proximal tibia of 24 weeks-old mice (rBMAT) of 3μm paraffin sections stained with H&E (top) and 100μm sections stained with perilipin immunofluorescence (bottom, Perilipin in green and TO-PRO-3 nuclear counterstain) of 50-week-old mice. All images correspond to C57BL/6 female mice housed at room temperature fed *ad libitum* standard diet. BM, bone marrow; BMAd, bone marrow adipocyte; CB, cortical bone; cBMAT, constitutive bone marrow adipose tissue; H&E, hematoxylin and eosin; rBMAT, regulated bone marrow adipose tissue.

TABLE 1 | Challenges and goals ahead for the BMA field and the BMAS WG in methodologies.

	Challenges	Goals
Main challenge	Standardize	Increase comparability by: • Homogenous definitions (c.f. BMAS consensus in nomenclature) • Homogenous reporting (c.f. BMAS Reporting Guidelines below) Increase reproducibility by: • Establishing consensus on standardized bone sites for analysis (e.g., rBMAT/cBMAT transition zones: tibia, caudal vertebrae) • Establishing consensus on reference groups • Establishing recommended standardized protocols: ○ For *in vivo* modulation ○ For *in vivo* extraction of primary BMAd and BMSCs ○ For method-specific thresholds for BMA detection • Minimize effects of known confounding factors, to increase inter-study and multi-site comparison • Increase availability and accessibility of imaging techniques to implement use in routine clinical practice
Technical aspects	Adhere to minimal reporting guidelines	Implement the following **"BMAS Reporting Guidelines"**: • Specify precise BMA skeletal location in all figure legends • Report known confounding factors for all experiments: ○ Skeletal location, gender, age, strain ○ Ambient temperature (e.g., average housing temperature) ○ Nutritional status (e.g., average food intake, antibiotics) ○ Metabolic state (e.g., fasting, time of collection) ○ Exercise (e.g., type of enrichment material in cages) • Report isolation technique with sufficient precision to reproduce; consider depositing protocol (e.g., protocol sharing platforms as recommended in the BMAS working group site at www.bma-society.org) • Report BMAd purity (e.g., hematopoietic/CD45$^+$ cells, endothelial contamination, and CFU-F/BMSC) and viability/intactness • Report detailed imaging parameters, post-processing tools and algorithms
	Innovate	Development of: • Models for specific BMAd deletion • Specific BMA biomarkers • Recommended reference gene-set for adipogenic differentiation • Move from descriptive to mechanistic studies
Clinical perspectives	Define standards	Define the normal physiological values and increase functional understanding: • In humans by age, gender, skeletal location and lipid composition • In animal models by establishing a consensus reference group to be included as comparison in all animal studies (i.e., C57BL/6J 8-week-old female mouse as homeostatic control group)
	Disseminate	Facilitate access and use of unbiased BMA methodologies to non-experts (e.g., automated imaging, reference gene sets, reference cell trajectory maps)

BMA, bone marrow adiposity; BMAd, bone marrow adipocyte; BMAS, Bone Marrow Adiposity Society; BMSC, bone marrow stromal cell; cBMAT, constitutive bone marrow adipose tissue; CFU-F, Colony Forming Unit-Fibroblast; rBMAT, regulated bone marrow adipose tissue.

an uniform decalcification of the sample is important, and we recommend decalcification at room temperature or 4°C on constant shaking, a large volume of EDTA to sample (at least 10:1 v/v) and several refreshments of the solution (every 3–4 days) to prevent calcium saturation (19).

Decalcification can also be performed using acidic agents to dissolve the calcium salts from the bone. This group of agents includes strong and weak acids. However, strong acid agents (nitric and hydrochloric acid) should be avoided in order to preserve the integrity of the cells and the enzymatic activity if subsequent immunostainings are desired (20). Among the group of weak acids (picric, acetic, and formic acid), decalcification performed with Morse's solution (50% formic acid and 20% sodium citrate) can also preserve the integrity of the sample for immunohistochemistry while allowing for high quality architectural evaluation with Hematoxylin and Eosin (H&E) staining (21). Dehydration is required prior to embedding. Ethanol dehydration in graded increases of ethanol and xylene, can allow for long-term storage of bones in 70% ethanol prior to embedding (22).

Embedding

To embed the samples after dehydration, several options exist. Most common and available is paraffin embedding. Decalcification is, however, necessary. This protocol is very useful to perform immunostaining, but the integrity of BM content, due to the juxtaposition of hard (decalcified bone) vs. soft (marrow) tissue is not guaranteed. Alternatives to paraffin are MMA or technovit 900 embedding. These do not require decalcification and allow for better preservation of the adipocyte morphology. However MMA and technovit 900 are less available in most laboratories and immunohistochemical staining becomes a challenge due to the destruction of the antigen presentation with the conventional MMA embedding protocols (23). With all embedding methods the histological procedure dissolves all the lipids in the vacuole, therefore the adipocytes are referred to as

TABLE 2 | List of abbreviations.

Abbreviation	Definition
2D/3D	Two/Three Dimensional
β3-AR	Beta-3 Adrenergic Receptor
Σ	Summation
μCT	Microfocus Computed Tomography
ACTH	Adrenocorticotropic Hormone
Ad.Ar	Adipocyte Area
Ad.Dm	Adipocyte Diameter
Ad.Pm	Adipocyte Perimeter
AdipoQ	Adiponectin
BADGE	Bisphenol A Diglycidyl Ether
BAT	Brown Adipose Tissue
BM	Bone Marrow
BMA	Bone Marrow Adiposity
BMAS	Bone Marrow Adiposity Society
BMAd	Bone Marrow Adipocyte
BMAT	Bone Marrow Adipose Tissue
BMD	Bone Mineral Density
BMFF	Bone Marrow Fat Fraction
BMSC	Bone Marrow Stromal Cell
BODIPY	Boron-Dipyrromethene
BV	Bone Volume
cBMAds	Constitutive Bone Marrow Adipocytes
CD	Cluster of Differentiation
COX	Cyclooxygenase-2
CR	Caloric Restriction
cAMP	Cyclic Adenosine Monophosphate
CEBPα	CCAAT Enhancer Binding Protein Alpha
CE-CT	Contrast-Enhanced Computed Tomography
CESA	Contrast-Enhancing Staining Agents
CFU-F	Colony-Forming Unit-Fibroblast
DAPI	4′,6-Diamidino-2-Phenylindole
DECT	Dual-Energy Computed Tomography
DIO	Diet Induced Obesity
DMI	Cocktail for Dexamethasone, IBMX And Insulin
EDTA	Ethylenediaminetetraacetic Acid
EGFP	Enhanced Green Fluorescent Protein
EM	Electron Microscopy
EU	European Union
FABP4	Fatty Acid Binding Protein 4
FACS	Fluorescence-Activated Cell Sorting
FBS	Fetal Bovine Serum
FDA	Food and Drug Administration
FSH	Follicle Stimulating Hormone
GDPR	General Data Protection Regulation
GFP	Green Fluorescent Protein
GH	Growth Hormone
Glut4	Glucose Transporter Type 4
H&E	Hematoxylin and Eosin
^{1}H-MRS	Proton Magnetic Resonance Spectroscopy
Hf-WD-POM	Hafnium Wells-Dawson Polyoxometalate
HFD	High Fat Diet
HIV	Human Immunodeficiency Virus
Hm.Ar	Hematopoietic Area
HSL	Hormone-Sensitive Lipase
IBMX	Isobutylmethylxanthin
IGF-1	Insulin Growth Factor 1
IHC	Immunohistochemistry
ISCT	International Society for Cellular Therapy
Lepr	Leptin Receptor
LPL	Lipoprotein Lipase
Ma.Ar	Marrow Area
Ma.V	Marrow Volume
MAGP1	Microfibril-Associated Glycoprotein-1
MMA	Methyl Methacrylate
MR	Methionine Restriction
MRI	Magnetic Resonance Imaging
N.Ad	Adipocyte Number
NCD	Normal Chow Diet
ORO	Oil Red O
OsO_4	Osmium Tetroxide
OVX	Ovariectomized
PLIN1	Perilipin 1
PCR	Polymerase Chain Reaction
PDGFRα	Platelet Derived Growth Factor Alpha
PDFF	Proton-Density Fat Fraction
PFAS	Performic Acid Schiff
Ppm	Parts Per Million
PPARγ	Peroxisome Proliferator-Activated Receptor Gamma
PRESS	Point-Resolved Spectroscopy
P/S	Penicillin/Streptomycin
PTH	Parathyroid Hormone
PTRF	Polymerase I and Transcript-Release Factor
rAAV	Recombinant Adeno-Associated Virus
rBMAd	Regulated Bone Marrow Adipocyte
RBC	Red Blood Cell Lysis
RFP	Red Fluorescent Protein
RNA	Ribonucleic Acid
RT-qPCR	Real-Time Quantitative Polymerase Chain Reaction
SFF	Signal Fat Fraction
SSC	Skeletal Stem Cell
STEAM	Stimulated Echo Acquisition Mode
SVF	Stromal Vascular Fraction
T.Ar	Tissue Area
TRAP	Tartrate-Resistant Acid Phosphatase
TV	Tissue Volume
TZD	Thiazolidinediones
UCP1	Uncoupling Protein 1
v/v	Volume/Volume
VMH	Ventromedial Hypothalamus
WAT	White Adipose Tissue
WFI	Water–Fat MR Imaging
WT	Wild Type
ZFP423	Zinc Finger Protein 423

"ghosts," which makes it impossible to investigate lipid content and composition in combination with histology.

To resolve this issue, Erben et al. developed an alternative protocol for plastic embedding, that avoids the complete loss of enzymatic activity in the tissue by adding methylbenzoate during the infiltration process and polymerization of the plastic (24). Here, cold embedding seems to be crucial for antigen presentation in the immunohistochemical procedure. Enzymatic activity is also preserved by using another resin embedding system (e.g., Technovit 9100) that contains methyl methacrylate and catalysators that allow the polymerization at low temperature (4°C) (25).

Staining

Although the adipocyte lipid vacuole is empty due to the ethanol-based dehydration necessary for histological procedures, these mature adipocyte ghosts are easily identifiable with several standardized staining procedures. The most frequently used in paraffin embedded bone is the H&E stain. Standardized staining procedures for plastic embedded bone, such as Goldner's trichrome, toluidine blue and Von Kossa staining can also be used to identify mature adipocyte ghost cells (24).

The discrimination between BMAds and blood vessels in a cross section can be difficult since the BM microenvironment is densely populated by blood vessels of different types and diameter and the endothelial wall is not always identifiable (26). Immunohistochemistry for Perilipin (27), a marker of mature adipocytes, is therefore useful for identification of BMAds in both human and murine tissues (**Figure 1**). Alternatively, immunostaining for Endomucin and/or CD31, markers for endothelial cells can be used to discriminate between blood vessels and adipocytes (28).

Quantification

Two types of dimensional quantification are possible: two dimensional in terms of perimeter, diameter and area, and three dimensional in terms of volume and surface (29). Moreover, as described in the consensus on bone histomorphometry (30) and extensively discussed in the accompanying BMAS nomenclature position paper, BMA parameters should be presented in relation to a reference region (31). By using a common referent, it is possible to assess changes in the number or percentage of adipocytes following an intervention or comparing physiological and pathological states. For histological measures of BMAT, two-dimensional measurements of BMAT are applicable and two reference areas should be used: Marrow area (Ma.Ar) and total tissue area (T.Ar). It is important to distinguish between these two areas since the interpretation is notably different. When bone mass is lost and replaced by other marrow tissue, the Ma.Ar is increased while T.Ar remains similar. Marrow adiposity increases only when the area of BMAds increases relative to the marrow space. For three-dimensional *ex vivo* or *in vivo* measurement, Marrow volume (Ma.V) and Total tissue Volume (TV) should be used. A priori, two-dimensional measures should be used in standard bone histomorphometry and three-dimensional measures should be reserved for techniques which rely on 3D measurements, as discussed in the *ex vivo* or *in vivo* sections. Three-dimensional measurements may be used in histomorphometry when analysis of serial sections is performed to approximate volumes.

Additionally, measurement of the size of individual adipocytes is important in the analysis of BMAT, since the changes in total adipose tissue can be due to either an increase in the number of adipocytes or an increase in the size of the adipocytes. This distinction is important since the mechanism behind these changes can reveal both differences in adipogenic differentiation (affecting the number) or in lipolysis (affecting the size). In consensus with the Nomenclature working group of the BMAS, we suggest to use the terms Perimeter (Ad.Pm), Diameter (Ad.Dm), and mean Adipocyte Area (Ad.Ar) to address adipocyte size. Adipocyte areas can be reported for individual BMAds, giving rise to the frequency distribution of BMAd areas and corresponding measurement of mean or median Ad.Ar. In addition, adipocyte area can be reported at the tissue level as % of total adipocyte area relative to hematopoietic area (ΣAd.Ar/Hm.Ar), tissue area (ΣAd.Ar/T.Ar) or, most commonly, to marrow area (ΣAd.Ar/Ma.Ar) also commonly reported as "marrow adipose area" or less precisely as "marrow adiposity." Hematopoietic area is defined either by CD45 positivity in immunohistochemistry or, morphologically, by the areas defined by the high density of hematopoietic cell nuclei within the marrow space. Exhaustive recommendations on BMA nomenclature are available in the accompanying white paper authored by the BMAS Working Group in Nomenclature (31).

Another important histological measure for adipocytes is the density of adipocytes. This is also used to differentiate between adipogenesis or enlargement of the adipocyte due to lipid storage. Adipocyte density can be measured as number of adipocytes per marrow area (N.Ad/Ma.Ar), number of adipocytes per hematopoietic area (N.Ad/Hm.Ar) or as number of adipocytes per tissue area (N.Ad/T.Ar). Adipocyte density varies greatly in the endocortical vs. trabecular regions of the bone, and thus detailed annotation and standardization of the quantified region is paramount, as detailed in the BMAS reporting guidelines (**Table 1**).

Software

To quantify these parameters, a selection of software packages are available. Some have been developed for extramedullary adipose tissue and require manual adipocyte measurements, while others are designed for assessment of BM sections and are semi-automated, with a few entirely automated (listed in **Table 3**). Automated or semi-automated detection programs use shape (roundness, circularity) and the absence of color within the lipid vacuole for detection of BMAds. While such software packages are not yet routine, most laboratories have developed them in-house in order to perform adipocyte histomorphometry. Some of these software packages are freely available online (peerJ, fathisto, and MarrowQuant, see **Table 3**).

Challenges and Limitations

Histomorphometric analysis is a very useful tool to determine the quality of bone and assess changes in the number and size of

TABLE 3 | Description of the most used software for bone marrow histomorphometry.

Software	Species, sample	Automatic or manual	Other methods	Reported parameters	Proposed parameters	Other measures	Stains (embedding)	References
OsteoMeasure	Monkey, proximal femur	Manual	–	–	Ad.Ar/T.Ar	–	–	(32)
OsteoMeasure	Human, biopsy	Manual	Blinded count	N.Ad, % Ad.V /TV (AV/TV); total Ad.Pm	ΣAd.Ar/T.Ar; N.Ad/T.Ar; total Ad.Pm	–	Goldner, 20x	(33)
OsteoMeasure	Mouse, femur	Manual	–	AV/TV; Ad.Pm; N.Ad/T.Ar.	ΣAd.Ar/T.Ar; Ad.Pm; N.Ad/T.Ar	Bone standard histomorphometry	Goldner's Trichrome/Von Kossa	(34)
OsteoMeasure	Mouse, distal femur	Manual	–	N.Ad/T.Ar	N.Ad/T.Ar	Bone standard histomorphometry	–	(35)
OsteoMeasure	Proximal tibia metaphysis	Manual	–	–	N.Ad/T.Ar	Bone standard histomorphometry	unstained (paraffin)	(36)
OsteoMeasure	Mouse, femur	Semi-automatic	–	Marrow fat content % (AV/TV)	ΣAd.Ar/T.Ar	Bone standard histomorphometry	H&E	(37)
OsteoMeasure	Mouse, tibia	manual	–	N.Ad/T.Ar; Ad.Dm	N.Ad/T.Ar; Ad.Dm	Bone standard histomorphometry	TRAP/toluidine blue	(38)
OsteoMeasure	Mouse, distal femur	Manual	–	Ad.Ar/T.Ar; N.Ad/T.Ar	Ad.Ar/T.Ar; N.Ad/T.Ar	Bone standard histomorphometry	TRAP/toluidine blue	(39)
OsteoMeasure	Mouse, distal femur metaphysis	Manual	Fat extraction and analysis	Ma. adiposity; Ad. Density	ΣAd.Ar/T.Ar; ΣAd.Ar/Ma.Ar; N.Ad/Ma.Ar	Bone standard histomorphometry	Methyl-methacrylate	(40)
OsteoMeasure	Human, bone biopsy	Manual	–	Ad.Ar/Ma.Ar	Ad.Ar/Ma.Ar	Bone standard histomorphometry	unstained, (plastic) 10x	(41)
OsteoMeasure	Mouse, tibia	Manual	–	N.Ad/T.Ar Ad.Ar/T.Ar	N.Ad/T.Ar; Ad.Ar/T.Ar	Bone standard histomorphometry	H&E	(42)
OsteoMeasure	Mouse, distal femur	Manual	–	Ad.V/TV	ΣAd.Ar/T.Ar	Bone standard histomorphometry	–	(43)
Image Pro	Mouse, distal femur	Manual	–	N.Ad; Ad.Ar	Ad.Ar/T.Ar; N.Ad/Ma.Ar	–	H&E	(44)
Image Pro Plus	Mouse, tibia	Manual	–	–	ΣAd.Ar/T.Ar; Ad.Ar/Ma.Ar; N.Ad/Ma.Ar	–	H&E	(45)
Image Pro Plus	Mouse, tibia	Manual	–	Ad.Ar	Ad.Ar/Ma.Ar	Bone standard histomorphometry	H&E	(46)
Image Pro Plus v6	Rat, femur	Manual	Manual count	N.Ad; Ad.Ar; Ad.Dm, Ad. density	ΣAd.Ar/T.Ar; ΣAd.Ar/Ma.Ar; N.Ad/Ma.Ar; Ad.Dm	Bone standard histomorphometry	H&E	(47)
Image Pro Plus v6	Rat, femur	Manual	–	Ad.Dm, N.Ad/Ma.Ar %Ad.Ar	Ad.Dm; ΣAd.Ar/T.Ar ΣAd.Ar/Ma.Ar; N.Ad/Ma.Ar	Bone standard histomorphometry	H&E	(48)
Image Pro Plus v6	Rabbit, distal femur	Manual	–	Ad.Dm; N.Ad/Ma.Ar; Ad.Ar/Ma.Ar	Ad.Dm; N.Ad/Ma.Ar; ΣAd.Ar/Ma.Ar	–	H&E	(49)
ImageJ	Rat, proximal tibia	Manual	–	Ad. content (Ad.Ar, T.Ar)	Ad.Ar; ΣAd.Ar/T.Ar	–	H&E	(50)
ImageJ	Mouse, femur or tibia	Manual	–	Ad.V/Ma.V	ΣAd.Ar/Ma.Ar	Bone standard histomorphometry	H&E (plastic or paraffin) 20x	(51)
ImageJ	Rat, proximal tibia	Manual	–	N.Ad/T.Ar; Ad.Ar/T.Ar	N.Ad/T.Ar; Ad.Ar/T.Ar	–	H&E	(52)
ImageJ	Mouse, distal femoral metaphysis	Automatic/ manual	OsteoMeasure	T.Ar adiposity, N.Ad/T.Ar, adiposity (%)	ΣAd.Ar/T.Ar; ΣAd.Ar/Ma.Ar; N.Ad/T.Ar; N.Ad/Ma.Ar	–	Von Kossa tetrachrome	(53)

(Continued)

TABLE 3 | Continued

Software	Species, sample	Automatic or manual	Other methods	Reported parameters	Proposed parameters	Other measures	Stains (embedding)	References
OsteoidHisto	Human, biopsy	Semi-automatic	–	Ad.V/TV; Ad.V/Ma.V Ad.Dm N.Ad/Ma.Ar	ΣAd.Ar/T.Ar; ΣAd.Ar/Ma.Ar; Ad.Dm; N.Ad/Ma.Ar	Bone standard histomorphometry	Goldner's Trichrome	(54)
OsteoidHisto	Mouse, tibia	Semi-automatic	–	Ad.V/TV Ad.V/Ma.V Ad.Dm Ad.Dm	ΣAd.Ar/T.Ar; ΣAd.Ar/Ma.Ar; Ad.Dm; N.Ad/T.Ar	Bone standard histomorphometry	Calcein blue/TRAP	(55)
Bioquant Osteo	Human, biopsy	Semi-automatic	Blinded count	N.Ad, Ad. size,	N.Ad/Ma.V; ΣAd.Ar/Ma.Ar	Bone standard histomorphometry	–	(56)
Bioquant Osteo	Rat, tibia	Manual	–	N.Ad/TV	N.Ad/T.Ar	Bone standard histomorphometry	Goldner's trichrome	(57)
Bioquant Osteo II	Mouse, femur	No information	–	AV/TV	ΣAd.Ar/T.Ar	Bone standard histomorphometry	Goldner's Trichrome or TRAP	(58)
Leica Q-win Plus	Rabbit, vertebrae	No information	–	Ad.Dm; N.Ad/Ma.Ar	Ad.Dm; N.Ad/Ma.Ar	–	Oil-Red-O	(59)
MarrowQuant	Mouse, skeleton	Semi-automatic	Osmium tetroxide stain with μCT	T.Ar; Ma.Ar; N.Ad; Ad.Ar; ΣAd.Ar/Ma.Ar; Ad.V (μCT)	T.Ar; Ma.Ar; N.Ad; Ad.Ar; ΣAd.Ar/Ma.Ar; N.Ad/Ma.Ar	Bone Ar, hematopoietic Ar, vascular Ar	H&E (paraffin) 20x	(60, 61)
MarrowQuant	Mouse, tibia	Semi-automatic	–	T.Ar; Ma.Ar; Ad.Ar; ΣAd.Ar/Ma.Ar	T.Ar; Ma.Ar; N.Ad; Ad.Ar; ΣAd.Ar/Ma.Ar; N.Ad/Ma.Ar	hematopoietic Ar, vascular Ar	H&E (paraffin)	[Rojas-Sutterlin et al. as reviewed in (61, 62)]
Metamorph	Mouse, femur	Semi-automatic	–	Ad.Ar; N.Ad	ΣAd.Ar/T.Ar; N.Ad/Ma.Ar; Ad.Dm	–	H&E	(63)

Ad., adipocyte; Ad.Ar, adipocyte area; Ad.Dm, adipocyte diameter; N.Ad, adipocyte number; Ar, Area; Ma., marrow; Ma.Ar, marrow area; AV, total adipocyte volume; H&E, hematoxylin and eosin; TRAP, tartrate-resistant acid phosphatase; TV, total tissue volume; Σ, summation; μCT, micro-computerized tomography.

cells. One of the limitations is that histomorphometry is a time-consuming technique requiring microscopy, software and/or manual quantification. In addition, it is a technique that until now has relied on the interpretation of the single investigator, and therefore demands a solid quality control system. The detection of BMAds can be hampered by the close connection of adipocytes in yellow/adipocytic areas, making the separation and adequate counting of clustered adipocytes a big challenge, in particular if membranes are not intact. In mice, the number of adipocytes in long bones tends to be lower in sites of regulated BMAT, and thus separate adipocytes can be more easily discerned and counted in the red/hematopoietic marrow.

However, the distinction of adipocytes from small blood vessels can be a challenge, whether for manual quantification or automated algorithms, especially in the younger animals or in the context of marrow regeneration. Additional immunostains to discern microvasculature from adipocyte ghosts are thus highly recommended as a validation step. Moreover, one must keep in mind that histological sections are a cross-section of the bone/marrow organ and thus of the BMAd itself. In general, validation of automatic detection of adipocytes is not described, neither by presenting data on quality control measurements nor by comparison with a manual method. We therefore consider manual detection of adipocytes the gold standard for histomorphometry until automated software packages have been validated. Annotation and standardization of the quantified region, as well as reporting of the experimental parameters as detailed in the BMAS reporting guidelines (**Table 1**) cannot be emphasized enough. Additionally, correlation of histomorphometry findings with *ex vivo* or *in vivo* bone measurements of lipid content to calcified tissue constitutes a much-valued biological validation of findings. Finally, a recommendation on which bone may be considered as standard for reporting is premature, but we agree that choosing areas of transition between regulated and constitutive BMAT is most informative (e.g., tibia and/or caudal tail for mice).

EX VIVO WHOLE-BONE IMAGING

Histological slicing and histomorphometry remain the gold standard for the *ex vivo* evaluation and characterization of biological tissues in general, and BMAT in particular, by measuring adipocyte cell size and cell number. However, histological assessment (sectioning, staining, imaging, and analysis) remains a challenging, time-consuming, and often costly technique (29). Moreover, spatial patterns as well as the spatial inter-relationship between different tissues within one sample (for example BMAT in relation to bone and vasculature)

can be inaccurate or impossible. To overcome some of the limitations of 2D analyses, several 3D imaging techniques have emerged to quantify the morphometry, spatial distribution of BMAT and its inter-relationship with other tissues in the marrow. In addition, mass spectrometry and high-profile liquid chromatography remain complementary standard methods to dissect lipid composition upon extraction (64, 65).

Contrast-Enhanced Microfocus Computed Tomography

X-ray microfocus computed tomography (μCT) is a very powerful tool for 3D imaging of mineralized tissues (66). High-resolution μCT (<2 μm voxel size) and nanoCT [down to 150 nm (67)] scans are achievable and a high field of view to voxel size ratio can be obtained (68). While one of the biggest advantages of μCT is its non-destructive character, a considerable limitation of this technology is its lack of specificity for soft tissues. Phase contrast μCT is a possible solution, as it can be used to, for example, enhance edges, which allows a better visualization of soft tissues (69). Indeed, it provides information concerning changes in the phase of an X-ray beam that passes through an object. Moreover, it uses monochromatic X-rays, resulting in accurate measures of the attenuation coefficient, and thus enabling quantitative μCT imaging. This technique requires, however, highly dedicated hard- and software, and is not readily available. In addition, to the best of our knowledge, phase contrast imaging has so far not been used to visualize BMAT. Therefore, the focus of this review is rather on desktop single energy, polychromatic absorption contrast-enhanced μCT (CE-CT) imaging. Although having its limitations in the cone-beam shape of the X-ray bundle and the lower X-ray flux compared to synchrotron μCT, scanning times down to 15 min for high-resolution imaging can be achieved nowadays. For this kind of CE-CT, typically, there are two kinds of contrast agents used for the visualization of soft tissues: perfusion contrast agents, mostly used for *in vivo* or *ex vivo* indirect imaging of vasculature, and contrast agents that bind to the tissues for *ex vivo* imaging, further referred to as contrast-enhancing staining agents (CESAs). Here, we will focus on CESAs, which have proven to allow CE-CT imaging of BMAT.

The introduction of CESAs has enabled contrast-enhanced CE-CT to become a very important tool in biomedical imaging. CESAs bind to tissues of interest, increasing the X-ray attenuation coefficient (70). The very first reports on the use of CESAs for CE-CT imaging of soft tissues go back to only about a decade ago. Indeed, several groups (71–73) used osmium tetroxide (OsO_4) on mouse embryos, pig lungs, and honeybees, respectively, to enable virtual 3D anatomical analyses using CE-CT. Although in these studies OsO_4 was used for general tissue staining, it is well-known for its specific binding to unsaturated lipids (74, 75). Consequently, several years later, Scheller et al. reported the use of OsO_4 for 3D CE-CT visualization of BMAT and quantification of its amount and distribution in long bones of mice using standard μCT (12, 76) and subsequently, ultrahigh-resolution μCT (77).

OsO_4-based BMAT characterization requires a two-step scanning protocol: first, bones are detached and thoroughly cleaned from soft tissues, fixed, and scanned to enable characterization of 3D calcified bone parameters. The fixed bones are subsequently decalcified and then stained with OsO_4 for 48 h (76) or longer if the mouse models develop severe BMAT accumulation. Subsequently, OsO_4-stained bones are rescanned. These images provide 3D quantification of BMAT structural properties, such as adipocyte volume/total volume (Ad.V/TV), adipocyte volume/marrow volume (Ad.V/Ma.V), and adipocyte volume/bone volume (Ad.V/BV), which are quantified based on the amount of osmium-bound lipid. When combining OsO_4 staining with high-resolution μCT imaging, individual adipocytes can be distinguished (**Figures 2A,C,E**) and a distribution of diameter can be calculated. When combined with image coordinate registration, this technique allows alignment of both the BMAT distribution and bone micro-architecture, as well as calculation of the distance of the BMAds from the bone surface (80). Some studies have also used this approach to measure BMAd density (cells/mm^2 Ma.V) (81). The use of OsO_4 for CE-CT-based BMAT visualization in mouse bones has quickly become widespread due to its compatibility with existing μCT infrastructure, ease of use, and reasonable cost (63, 82–84). As with most techniques, a high level of standardization is needed for each step in the procedure (fixation, decalcification, OsO_4 staining, imaging, and analysis). For example, insufficient decalcification can lead to problematic osmium penetration and staining (85). Indeed, the limited tissue penetration capability makes staining of dense regions of adipocytes or larger bones problematic, restricting this technique primarily to whole bones in mice. Moreover, OsO_4 staining is highly toxic, needing careful handling within a fume hood and appropriate disposal (86, 87).

To overcome these limitations, a recent study by Kerckhofs et al. reported the simultaneous visualization of mineralized and soft tissue structures within bones (**Figure 2F**) utilizing Hafnium Wells-Dawson polyoxometalate (Hf-WD-POM) as CESA (78). For this technique, murine long bones are incubated in POM powder dissolved in phosphate buffered saline while shaking gently for 48-h to 5-days. Samples are then scanned in the staining solution, or wrapped in parafilm and put in a sample holder for scanning. Thanks to the combination of the hydrophobic behavior of adipocytes and the binding of Hf-WD-POM to the BM tissue, visualization of the adipocytes is possible. When combining this CESA with high-resolution scanning (about 2 μm voxel size, maximum total image volume about $6 \times 4.8 \times 6$ mm^3), BMAds can be imaged at the single cell level (**Figures 2B,D,F**). This not only facilitates measurement of the volume fraction of BMAT within the bone (Ad.V), but also enables the quantification of the BMAd Number (N.Ad), density (N.Ad/TV), and Diameter (Ad.Dm). Additionally, with sufficient contrast, the vascular network can be discriminated from the other marrow tissues. This allows for full 3D blood vessel network assessment (i.e., branching and spatial distribution). Hence, Hf-WD POM-based CE-CT provides complementary data to standard histomorphometry, with enhanced 3D spatial information and inter-relation between different tissues in the

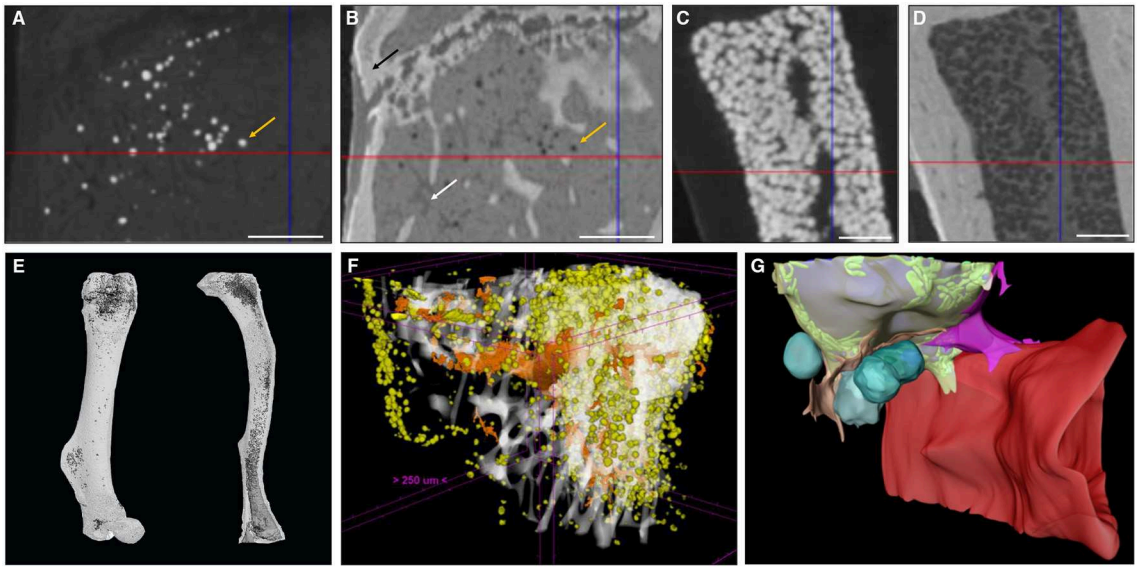

FIGURE 2 | Zoom of a longitudinal CE-CT cross-section of the metaphysis of a murine tibia from a 16-week-old C57BL/6Rj male mouse fed *ad libitum* standard diet, using **(A)** osmium tetroxide and **(B)** Hf-WD POM staining, on the same sample. The orange arrows indicate the same adipocyte. The black arrow in **(B)** indicates the bone and the white arrow indicates a blood vessel. Zoom of a longitudinal CE-CT cross-section of the diaphysis of a murine long bone using **(C)** osmium tetroxide and **(D)** Hf-WD POM staining on the same sample. Scale bars = 250 μm. 3D rendering of **(E)** an osmium tetroxide stained murine femur (left) and tibia (right) from an 11-week-old C57BL/6J male fed *ad libitum* standard diet at room temperature, where adipocytes are presented in dark gray and bone in light gray. **(F)** Hf-WD POM stained murine tibia from a 30-week-old C57BL/6Rj male mouse fed high fat diet for 22 weeks [reprinted with permission from (78)], where white represents the bone, orange the blood vessels and yellow the marrow adipocytes. **(G)** 3D EM image of an adipocyte [reprinted with permission from (79)]. Lipid is shown in gray, mitochondria in green, cytoplasm in semi-transparent yellow, vascular sinusoid in red, perivascular cells in pink and orange, and blood cells in turquoise.

BM compartment (**Figure 2F**). This was recently used to show that BMAT increased after menopause, and that increased BMAT was associated with osteoporosis and prevalent vertebral fractures (55). It should be highlighted that Hf-WD POM is non-invasive and non-toxic, and does not interfere with subsequent histological processing and immunostaining. A limitation of Hf-WD POM, however, is that it is not yet commercially available, although it can be requested in the frame of a collaboration.

When making a direct comparison between Hf-WD POM and OsO_4 using high-resolution CE-CT, it was observed that both CESAs performed equally well for detecting BMAds (**Figure 2**). For locations with a low to medium BMAT amount, however, OsO_4 staining was more sensitive in visualizing the sparsely distributed adipocytes (**Figures 2A,B**). For medium to high BMAT content, OsO_4 tended to overestimate the adipocyte size due to high contrast difference between stained adipocytes and background, and thus contributed to the partial volume effect (**Figures 2C,D**). For this condition, Hf-WD POM allowed more accurate separation of individual adipocytes. Advantages and disadvantages of these *ex vivo* techniques are summarized in **Table 4**.

Future Challenges: 3D Microscopy

In recent years, standard microscopy techniques have also been optimized to gain 3D information about whole-bone cellular networks and nanoscale insight into the microenvironment of single cells. For example, tissue clearing strategies in skeletal tissues allow mapping of vascular networks and cell distributions in whole bones using light-sheet or two-photon microscopy (88, 89). Similarly, >50 μm-thick section immunohistochemistry can provide *ex vivo* insight into cell localization in 3D via conventional confocal microscopy (90). Though not yet published, we anticipate that clearing techniques described for marrow tissue will be used to provide novel information about BMAT localization and function. A key advantage relative to CT-based analyses is the ability to interrogate local cells and pathways that are defined based on expression of specific proteins and biomolecules using antibodies or genetically modified rodents.

At the nanoscale, focused ion beam scanning electron microscopy (EM), a form of serial EM that allows for 3D reconstructions at subcellular resolution, was recently applied to the BMAT adipocyte niche (79). This work builds upon previous 2D EM analyses of BMAT (11) and has helped to define interactions of BMAT with surrounding cells at the endothelial interface, within the hematopoietic milieu, and at the bone surface (**Figure 2G**). The major limitation of all of these techniques is the need for specialized imaging equipment. In many instances, data handling and analysis paradigms, which require very sophisticated statistical analysis to correct for the boundaries imposed by the confined bone architecture (91), are also just beginning to emerge. In any case, the development of regularly revised common standards and the commitment to BMAS reporting guidelines, as specified in **Table 1**, will increase comparability and pave the way for the comparative studies necessary to determine future gold standards in this rapidly evolving field.

TABLE 4 | Main quantitative parameters assessed when using *ex vivo* imaging techniques to explore bone marrow adipose tissue.

	Parameters	Method	Advantages	Limitations
2D techniques	**Histomorphometry**			
	• Adipocyte number (N.Ad) • Adipocyte size (Ad.V) • Adipocyte density (N.Ad/Ma.Ar) • Spatial localization (2D)	Resin, paraffin, or frozen sections (<5–10 μm)	• General availability • Can be used in all species • Pairs well with histological stains	• Slice/region bias • Limited field of view • Time consuming • High cost
3D techniques	**μCT—Osmium**			
	• BMAT volume (mm^3) • BMAT density (%) • Adipocyte number* (N.Ad) • Adipocyte size* (Ad.V) • Spatial localization (3D)	• Whole bones or tissue samples, decalcified, and stained in osmium tetroxide solution. • Samples imaged and analyzed with μ- or high-resolution CT	• Adapts existing CT infrastructure and analysis techniques • Simple protocol • Low cost • Commercially available reagents • Highly sensitive for sparse BMAds	• Poor penetration in large, or high adiposity samples • Two-step scanning protocol for bone and BMAT analyses • Overestimates Ad.Dm • Highly toxic
	μCT—POM			
	• BMAT volume (mm^3) • BMAT density (%) • Adipocyte number* (N.Ad) • Adipocyte size* (Ad.V) • Spatial localization (3D)	• Whole bones or tissue samples are immersed in POM solution. • Samples imaged and analyzed with μ- or nanoCT.	• Simultaneous visualization of bone, BMAT, and vessels in a single dataset* • Adapts existing CT infrastructure and analysis techniques • Simple staining protocol • Non-invasive • Accurate measure of Ad.Dm	• High spatial and contrast resolution needed to discriminate blood vessel network • Not yet commercially available • Not very sensitive for sparsely BMAds • Diffusion can take several days, depending on the sample size
	FIB-SEM			
	• Ultrastructure • Cell-cell interactions	3D electron microscopy	• Cellular and sub-cellular resolution of BMAd within niche	• Requires highly specialized equipment • Time-consuming • Limited field of view • High cost

**High-resolution μCT only (<2 μm resolution). Ad.Dm, Adipocyte diameter; N.Ad, Adipocyte number; Ad.V, Adipocyte volume; BMAd, bone marrow adipocyte; BMAT, bone marrow adipose tissue; FIB-SEM, Focused Ion Beam Scanning Electron Microscopy; POM, polyoxometalate; Ma.Ar, Marrow Area; μCT, micro-computed tomography.*

IN VIVO IMAGING

While *ex-vivo* techniques provide ample information of structures and allow for specific quantification of tissues, non-invasive imaging tools are essential when it comes to clinical studies so as to better understand the pathological processes that affect the BM *in situ*. To date, magnetic resonance imaging (MRI) is considered as the reference imaging modality to appraise *in vivo* BMA (92, 93). This powerful imaging tool has been used in animals, for example to follow the effects of zoledronic acid treatment on marrow adipogenesis in ovariectomized rats (47), to quantify the decrease in BMAT volume in obese exercising mice (63), and to follow the progression of BMA in murine hematopoietic recovery [(60, 61); **Figures 3C,D**]. Due to their small size, such measurements are not straightforward in rodents, as they require very strong magnetic fields for meaningful BMA signal detection, and dual-energy μCT is a valid alternative. MRI techniques are primarily applied *in vivo* in humans (**Figures 3A,B**). Indeed, the growing interest in BMA in relation with post-menopausal osteoporosis, fractures, metabolic perturbations, as well as over- or undernutrition states, opens up potential exciting perspectives for clinicians (94). However, the multiple interfaces between trabecular bone and bone marrow foster local magnetic inhomogeneities and challenge the accuracy and precision of BMAT quantification.

What Can We Measure?

Main MR Imaging Biomarkers

The most relevant imaging biomarker used to quantitatively assess BMAT using MRI is the proton-density fat fraction (PDFF), which is the ratio of *unconfounded* fat signal to the sum of the *unconfounded* fat and water signals [(92, 92, 95, 96); **Table 5**]. As a result, the main challenge and limitation with quantitative BMAT assessment using MRI is to minimize the confounding factors to measure only signals coming from lipid protons. Interestingly, PDFF assessment of BMAT has benefited from technical developments in abdominal imaging. These technological improvements have been crucial for the emergence of reliable and non-invasive approaches to quantify adipose tissue in a standardized manner, especially through single-voxel proton spectroscopy (^{1}H-MRS) and chemical shift encoding-based water-fat imaging (WFI) techniques (95).

The second most common quantitative parameter reported in the literature reflects BMAT fatty acid composition. This

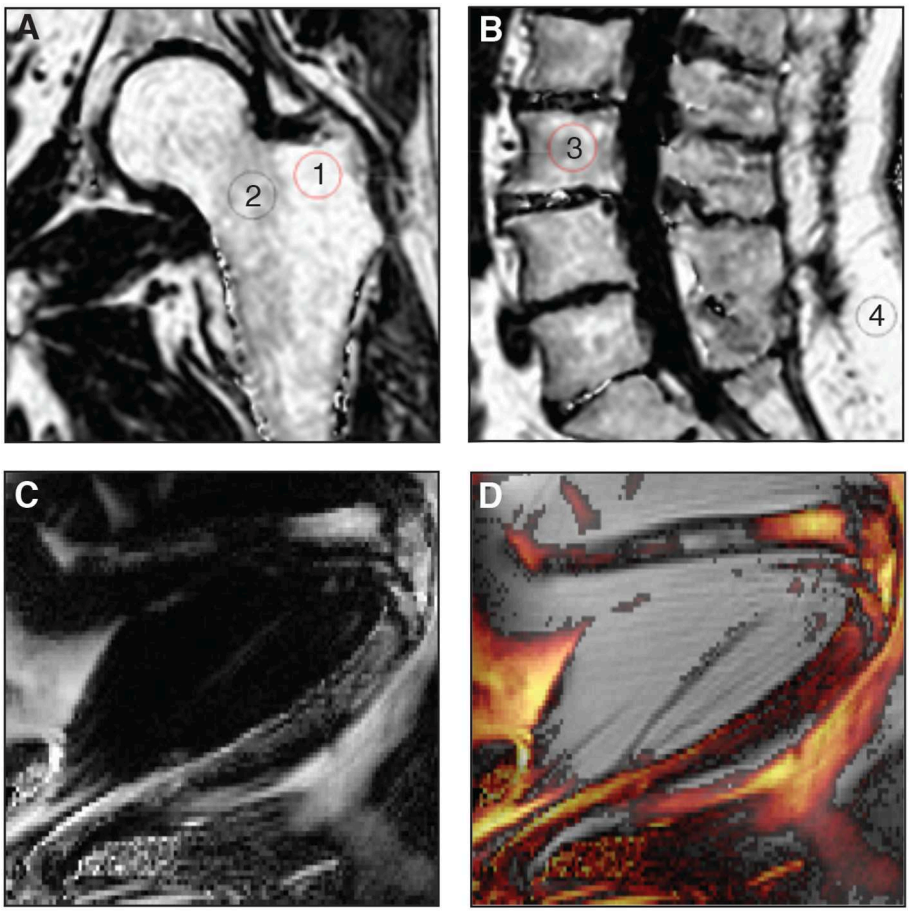

FIGURE 3 | (A,B) Proton-density fat fraction (PDFF) maps generated using chemical shift encoding-based water-fat imaging from a commercially available sequence on a 3 Tesla magnetic resonance scanner. Coronal oblique acquisition of the left hip **(A)** and sagittal acquisition of the lumbar spine **(B)** of a 69-year-old woman with chronic lumbar and inguinal pain. Regions of interest can be drawn to assess bone marrow adiposity [(1) 94%, (2) 77%, (3) 71%, (4) 96%] at different anatomical sites through the PDFF parameter. **(C,D)** A three-point Dixon acquisition using a spin-echo based sequence and chemical shift encoding-based water-fat separation was conducted on a 9.4 Tesla horizontal magnet, to assess BMAT *in vivo* at the peak of aplasia after irradiation and bone marrow transplant in an 8-week-old C57BL6 female mice housed at room temperature fed *ad libitum* standard diet with antibiotics supplemented in the drinking water. The lower limb is shown as imaged in maximal flexion (61). Normalized fat content map **(C)** and fat content overlaid a magnitude image, red 10% - yellow 100% **(D)** show high BMAT content in the distal femur and also some BMAT in the proximal femur (horizontal, top of image) and throughout the tibia (diagonally across the image), in comparison to fat signal of surrounding extramedullary adipose tissue.

specific evaluation is a topic of growing interest, as saturated fatty acids may have deleterious effects on the osteoblast lineage and may play a role in multiple inflammatory processes along with certain polyunsaturated fatty acids, affecting bone health (97). Fat composition assessment can be performed through an expression of its degree of unsaturation or polyunsaturation, calculated, respectively as the ratio of signal coming from the olefinic protons at 5.31 ppm or diallylic protons at 2.8 ppm on ^{1}H-MRS acquisitions, to the sum of all lipid signals (**Table 5**), as discussed in detail in section Single-Voxel Proton Spectroscopy (93).

Robustness of ^{1}H-MRS and WFI Methodologies

When the main biases are taken into account, WFI sequences appear to be robust in quantifying PDFF against changes in experimental parameters, in good agreement with ^{1}H-MRS [$r = 0.979$ reported by (98), and $R^2 = 0.92$ by (99)], using calibration constructs [BM phantoms: $R^2 = 0.97$; (100)], and in agreement with histology using excised lumbar vertebrae [$r = 0.72$; (101)]. The intraclass correlation coefficients for repeatability and reproducibility of WFI were, respectively 0.997 and 0.984 (102), and the coefficient of variation in the quantification of PDFF varied from 0.69 to 1.70% (103). Moreover, a negative correlation ($r = -0.77$; 77) was demonstrated between ^{1}H-MRS-based PDFF and *ex vivo* biomechanical vertebral properties (failure load), highlighting the relevancy of this parameter in bone strength (104). The reproducibility of ^{1}H-MRS is known to be excellent, especially when assessing the lumbar spine *in vivo*, with an average coefficient of variation of vertebral bone marrow content of 1.7% (93, 105). Although ^{1}H-MRS has long been considered the gold standard (105), WFI seems therefore to be a relevant and efficient alternative due to its ability to derive spatially resolved PDFF maps, with an absolute precision error

TABLE 5 | Main quantitative parameters assessed when using *in vivo* imaging techniques to explore bone marrow adipose tissue.

	Parameter	Definition	Properties	Main imaging techniques	Outcome
MRI- or CT-based techniques	Bone marrow fat fraction (BMFF)	Estimate of relative bone marrow fat content	• Generic term • Sensitive to experimental parameters when measured with MRI	• Single-voxel proton spectroscopy • Water-fat imaging • Dual-energy CT	Marrow fat content
MRI-based techniques	Signal fat fraction (SFF)	Ratio of fat signal to the sum of the fat and water signals	• Generic term • Specific to MRI techniques • Can be sensitive to MRI parameters	• Single-voxel proton spectroscopy • Water-fat imaging	
	Proton-density fat fraction (PDFF)	Ratio of *unconfounded* fat signal to the sum of the *unconfounded* fat and water signals	• Unconfounded imaging biomarker • Insensitive to MRI parameters	• Single-voxel proton spectroscopy • Water-fat imaging	
	Degree of lipid unsaturation	Ratio of signal coming from unsaturated lipids to the sum of all lipid signals	• Olefinic protons (5.31 ppm) are often used as an estimate of unsaturated lipids	• Single-voxel proton spectroscopy	Marrow fatty acid composition

BMFF, bone marrow fat fraction; CT, computed tomography; MRI, magnetic resonance imaging; PDFF, proton density fat fraction; SFF, signal fat fraction.

of 1.7% between C3 and L5 vertebrae (106), and no significant differences with spectroscopic assessment in children (99) or in adults (98).

With regard to BMAT composition, although similar values have been reported between measurements from high-resolution proton spectroscopy acquisitions on *ex vivo* specimen and *in vivo* imaging ($R = 0.61$; 71), the true BMAT unsaturation level is consistently underestimated in *in vivo* acquisitions because of the fewer visible peaks. As a result, Li et al. preferred the use of *pseudo*-unsaturation level to better discriminate the apparent BMAT composition assessment in *in vivo* studies from *ex vivo* measurements. This differentiation in terminology reflects well the need to bear in mind the technical limitations encountered when evaluating fat composition *in vivo*.

Toward a Better Standardization of MRI Techniques

Because ^{1}H-MRS and WFI can be performed in most clinical facilities, their main technical limitations must be taken into account when assessing *in vivo* BMAT. A better standardization of the methodologies used to quantitatively assess BMAT would increase the accuracy of the reported PDFF in the literature, as well as the relevancy of inter-study comparisons.

Single-Voxel Proton Spectroscopy

Based on the frequency shift which exists between molecular groups, signals from water and lipid protons can be discriminated in a defined voxel of interest through 1H-MRS. However, although the area under each peak of the acquired spectrum is related to the number of protons of a specific chemical moiety, the MRS acquisition and post-processing analysis to calculate PDFF needs to consider the following confounding effects.

First, the water and fat components of BMAT have different T_2 relaxation times. Therefore, in the absence of any T_2-correction, the calculated signal fat fraction from ^{1}H-MRS acquisitions is T_2-weighted, depends on sequence parameters and overestimates the true PDFF. An ^{1}H-MRS acquisition at different echo times combined with a T_2 correction can removed T_2-weighting effects (107, 108).

Second, even though initial ^{1}H-MRS studies mainly considered the methylene group peak at 1.3 ppm to calculate bone marrow fat fraction or lipid/water ratio, adipose tissue has a complex spectrum made of multiple peaks. An oversimplification of the model used may reduce the accuracy of the qualitative and quantitative fat assessment. However, the trabecular microarchitecture promotes broad spectral peaks which make peak fitting challenging (93). Nevertheless, constrained peak fitting methodologies have been depicted and performed successfully at the hip and lumbar spine (107, 108).

Third, the short T_1 value of bone marrow fat compared to water induces a relative amplification of the measured signal. PDFF calculations might be subsequently biased if T_1 effects are not minimized. This effect can be minimized by using long repetition times for ^{1}H-MRS acquisitions (93, 95, 109, 110).

Finally, the choice of the sequence mode is also of importance and depends on the employed echo times. By lowering J-coupling effects and being able to acquire spectra using shorter echo times, stimulated echo acquisition mode (STEAM) might offer a more accurate precise BMAT quantification compared to point-resolved spectroscopy (PRESS) sequences, despite its relatively noisier sensitivity (93).

The consideration of the above confounding effects is critical for assuring the robustness of MRS-based PDFF measurements across imaging protocols and imaging platforms, and essential toward the standardization of MRS-based PDFF measurements.

Water-Fat Imaging

Dedicated WFI techniques for BMAT assessment

WFI techniques share comparable confounding factors with ^{1}H-MRS: there is a need for T_2^* decay correction and T_1 bias minimization, as well as a consideration of the multi-peak spectral characteristics of fat.

Indeed, due to the complex bone microarchitecture, the multiple interfaces between trabeculae and bone marrow induce an important but differential T_2^*-shortening effect affecting both water and fat. T_2^* decay effects have therefore to be considered

in the estimation of PDFF based on WFI. Despite its theoretical justification, a dual-T_2^* decay correction adjusting both water and fat relaxation times provides accurate bone marrow fat fractions at a nominal fat fraction close to 50% but noisy PDFF maps were reported in the spine in regions with lower values (104). Therefore, a single T2* decay model should be at least adopted in BMAT WFI (93).

Regarding the T_1-effect, the relative signal amplification can be easily lessened by using low flip angles or predetermined calibration values on WFI acquisitions (93, 95, 109, 110).

Finally, concerning the multi-peak spectral characteristics of fat, one direct consequence in WFI that illustrates an oversimplification of the model used is the "grayish" appearance of adipose tissues on water-only images generated from WFI reconstructions considering a single fat peak. This residual fatty signal may come from an incomplete discrimination of fat and water signals, especially between olefinic fat protons and water (111). Although this simplification is acceptable for most clinical applications, a more advanced modeling of the fat spectrum is necessary for a quantitative purpose.

Commercially available WFI solutions

As mentioned above, the methodological improvements of fat quantification using MRI emerged mainly from abdominal imaging. Most MRI vendors have played an active role in the development of these sequences. Although these commercial quantitative WFI solutions aim to quantify liver PDFF, these techniques may be an easier and interesting alternative to ^{1}H-MRS in quantifying BMAT. An approximation with the multi-peak liver fat spectrum can indeed be considered, as only a negligible difference between the total signal fat from the 3 main peaks was reported when comparing the proximal femoral bone marrow and the liver (87 vs. 90%, respectively) (93, 107, 112). In addition, these sequences implement de facto a T_2^* decay correction, and because the T_1-effect can be simply lowered through a low flip angle, these solutions might be performed for BMAT PDFF assessment.

Other Technical Considerations

Other confounding factors may also be taken into account, such as noise-related bias (especially when using complex-based methods), eddy currents effects, gradient timing mis-registrations, phase errors in WFI and correction of J-coupling effects and chemical shift displacement effects in ^{1}H-MRS (99, 107, 110). Their description goes beyond the purpose of this review, but they are fundamental for the development of future techniques.

Current Challenges When Imaging *In Vivo* BMAT

A More Accurate Description of BMAT Fatty Acid Composition

Reporting of BMAT fatty acid composition through an expression of its degree of unsaturation constitutes the second most common quantitative parameter provided in the literature after PDFF-based quantification of total BMAT. Currently, only ^{1}H-MRS can reliably assess BMAT composition.

However, contrary to PDFF assessment, there is not sufficient literature on the methodological considerations that should be followed in imaging studies. The importance of STEAM acquisitions over PRESS when assessing BMAT composition has been nevertheless highlighted, as a low reproducibility of unsaturation level measurements has been reported using the latter, with a reported coefficient of variation of 10.7% (105).

Moreover, the proximity and partial overlap of the olefinic peak with the water peak (present at 4.7 ppm) reduce the robustness of the peak fitting process. As a result, in addition to the previously described technical considerations, post-processing the spectra for this specific purpose is challenging, especially in young adults. Areas with low fat content, more frequently encountered in red bone marrow, limits the accuracy and precision of the reported measurements (93). The extraction of BMAT unsaturation levels is subsequently less prone to variations in yellow bone marrow or red marrow with elevated fat content.

Consequently, there is an urge to standardize and improve the reliability of this potential biomarker, as the degree of unsaturation of BMAT might have clinical implications, such as its potential role in the occurrence of fragility fractures (113, 114).

A Better Depiction of Physiological Values

To date, studies performed in healthy subjects have allowed for the description of physiological variations, especially in the spine. In children, WFI showed a decrease in PDFF measurements from the lumbar to the cervical spine, with a natural logarithmic increase with age but without sex difference (99). However, in adults, sex-related variations in addition to age-dependence of PDFF have been reported in the spine (106, 108). Regarding BMAT composition, differences in the degree of saturation have also been observed between adult males and females, with unsaturated lipids being higher in women (115).

Nonetheless, even though these physiological variations are critical for a better understanding of BMAT physiology, data is still insufficient in the literature to determine the exact normal values by age and gender, primarily due to the lack of standardization in methods used to assess BMAT.

Alternatives to ^{1}H-MRS and WFI

Diffusion weighted-imaging, relaxometry, texture analysis, direct signal intensity, and dynamic contrast-enhanced imaging are alternative tools that have been performed to assess bone marrow adiposity. Although they provide interesting information, such as functional parameters related to bone marrow vascularization (116), these MRI techniques have not yet reached a consensus due to the insufficient number of relevant publications.

On the contrary, dual-energy computed tomography (DECT) is an emergent technique which may become a powerful alternative to MRI techniques as it can provide quantitative parameters representing both mineral and organic bone components (117). Consequently, whereas conventional single-energy quantitative computed tomography methods underestimate volumetric BMD measurements, DECT can correct for BMAT, resulting in more accurate densitometric

measurements (118–120). Furthermore, BMAT content can be explored reliably, as good correlations have been reported with WFI and histology on cadavers (121, 122), and 1H-MRS *in vivo* (123). Potential interesting applications exist in oncology, to follow marrow fat expansion and BMD involution in patients after chemotherapy or radiotherapy (124). The main limitations of this modality are the radiation exposure, the need for prior phantom calibration, and the lack of standardization and data regarding reproducibility between different scanners and manufacturers.

In summary, MRI constitutes the current gold standard for *in vivo* imaging of BMAT in a clinical research setting, with current acquisition methods allowing for inter-center comparability. The field would however benefit from increased standardization, both in terms of reporting of confounding factors of the measured subjects as recommended in **Table 1** and in terms of definition of standard sites of measurements, in order to increase comparability and to establish physiological reference ranges in humans and possibly larger mammals. The use of MRI for mouse models is only starting, due to the need for very strong magnetic fields for meaningful BMA signal detection; dual-energy μCT is a valid alternative for murine *in vivo* imaging.

FROM CELL ISOLATION TO *IN VITRO* MODULATION

BMAds exist in a complex microenvironment within the bone, embedded within the marrow tissue where access to live cells for functional analysis is not trivial. Complementary to the above discussed challenges associated to BMAd imaging within their native environment, *in vitro* systems and *ex vivo* assays are crucial for understanding of the BMAd and its subtypes at the cellular level. The difficulty in isolating and handling primary mature adipocytes from the BM has led to the use of *in vitro* adipogenic differentiation assays from BM stromal cells as a surrogate method to study BMAd, an approach widely used in the field of peripheral adipocyte biology. This approach relies on the isolation of a stromal vascular fraction (SVF) from adipose tissue which is then plated and expanded in tissue culture plastic. The resulting adherent monolayer of stromal cells isolated from the BM, the so-called BMSC fraction, acquires the phenotype of multilocular and sometimes fully mature unilocular adipocytes in the presence of specific differentiation cocktails in standard 2D cultures. Mature BMAds, which *in vivo* develop only after birth (125), most likely originate from a specific subset of progenitor cells present within the BMSC fraction. This biological sequence thus supports, in part, the use of differentiated BMSCs to model BM adipogenesis. *In vitro* differentiation assays, however, reveal a cellular response to chemical stimuli resulting in a sum of specific phenotypes which describe *in vitro* plasticity, but do not necessarily reflect their native *in vivo* differentiation potential. The *in vitro* plasticity of BMSCs is in fact often larger than the plasticity revealed by *in vivo* readouts in native or injury-repair conditions, highlighting the importance of complementary *in vitro* assays and *in vivo* readouts to establish cell fate mapping within the BM, as described below and extensively reviewed elsewhere (126, 127). The sections below summarize key challenges and practical considerations to minimize variability and increase comparability in future BMAT cell-based studies, whether based on the isolation of primary BMAds or *in vitro* adipogenesis from BMSCs.

BMAT: Location and Isolation

The BM is a soft tissue within the medullary cavity of compact bone. A mixture of hematopoietic precursors and differentiated cells, adipocytic cells, stromal cells, blood vessels, and nerve fibers occupy the marrow space within a complex network of extracellular matrix. Several techniques to isolate BMAT have been developed, all of which require invasive procedures to extract different populations from the encompassing bone.

In juvenile (age 8 to 12-week-old) mice, yellow/adipocytic marrow is present essentially in the distal tibia (filling up about one third of the total shaft length), the tail vertebrae and phalanx. Of the mouse strains systematically compared, BMAT is maximal in these locations in C3H/HeJ mice, and minimal in C57BL6/J mice (12). Older mice show a progressive increase in BMAT from distal to proximal, gradually gaining mature adipocytes in most skeletal sites of red/hematopoietic marrow. BMAT development and progression varies with strain and gender (128). Sites of murine BMAT for isolation in steady-state are thus small, and obtaining sufficient number of cells for cell sorting or cell culture purposes requires in most cases pooling samples from several animals.

It is important to note, as discussed in the *in vivo* modulation and *in vivo* tracing sections, that there may be differences in developmental origin according to the site of BMAT isolation. Due to the high degree of yellow/adipocytic marrow in the distal tibia, which also contains less trabecular bone than the caudal vertebrae, isolation of intact BMAT is relatively straightforward from the tibia after section at the epiphyses followed by gentle flushing or centrifugation. Contrarily, enzymatic digestion or mechanical disruption provides a higher yield of primary adipocytes from the tail due to the high number of caudal vertebrae and the predictable yellow/adipocytic marrow transition in the murine tail from the non-weight bearing segments. It is particularly important to note, however, that the fibrous tissue surrounding tail vertebrae is very rich in subcutaneous and periosteal adipocytes which require extensive mechanical removal or enzymatic digestion prior to isolation of BMAds to avoid contamination from subcutaneous adipocytes. One should also be aware that crushing bones can result in high cell death of BMAds and BMSCs, and it is thus to be avoided. Extraction of the intact BM plug or gentle mechanical disruption of the bone by fragmentation with a scalpel or scissors is thus preferred. Alternatively, a disrupted marrow plug can be obtained from smaller bones by removing the epiphysis and placing the open shaft in a PCR tube with a pierced bottom inside an Eppendorf tube containing a small amount of media (e.g., 200 μl), then gently centrifuging (e.g., 1 s at 500 g). BMAd markers are present in the top buoyant layer, while hematopoietic markers are only present in the pellet fraction upon RNA transcription analysis.

The long bones of mice are of similar size than human iliac crest biopsies, also called trephine biopsies, which involve the spongy bone and are performed for diagnostic purposes in hematology (1–2 cm long and 0.2–0.4 cm in diameter). Isolation and mounting approaches are thus often appropriate for both murine and human samples. Bone marrow aspirates are in most instances performed in parallel to trephine biopsies. In pediatric practice, BM aspirates are often performed from the sternum. Either are excellent sources of BMAT for research purposes after appropriate ethical approval. Debris from hip- or knee-replacement surgeries, including limb amputations, as well as spine neurosurgery also provide material rich in BMAds, as these are skeletal sites of abundant yellow/adipocytic marrow in the human adult.

Due to physiological BMAT specific variations according to species, strain, age, gender and skeletal site, as well as variations imposed by the isolation technique (flushing, spin-down, direct collagenase digestion, other enzymatic digestion), it is extremely important that researchers detail these parameters and indicate yield of primary BMAds or BMSC populations to favor comparisons across groups. Future efforts of the field should include evidence-based recommendations on extraction protocols that best preserve the heterogeneity of BMAd and their precursors. Other factors that may influence BMAT quality, and therefore yield, are related to body weight, bone weight or length and presence of metabolic perturbations or disease. BMAT obtained from human samples may be normalized to weight (μg) of tissue. Weight-based normalization remains however challenging for the small murine samples, where normalization per bone or "per leg" (e.g., tibia and femur) is standard (129).

Mature BMAds: Isolation and Culture

Isolation of primary mature BMAds has been done to high purity by multiple gentle centrifugation steps (9, 56, 130, 131) and may include enzymatic digestion to aid dissociation of BMAds from their surrounding connective tissue. BMAds, just like visceral adipocytes, are fragile cells that are very sensitive to the strains of handling and temperature gradients. Samples must be manipulated gently and typically at 17–37°C to avoid lipid droplets from bursting. Generally, BMAd numbers obtained from murine bones are low due to the small volumes and their affinity to plastic and proneness to floatation or bursting, which encumbers handling. Cell counting of mature adipocytes by hemocytometer or flow cytometry is not representative of the sample at hand, and quality controls for purity and viability need to be devised through other methods including, for example, immunofluorescence for adipocyte yield and quantification of hematopoietic cell contamination (e.g., DAPI, phalloidin, LipidTox-DR and anti-CD45) or nuclei counting coupled to ceiling culture for quantification of yield of viable mature adipocytes. For claims on purified BMAds, especially those that refer to population based transcriptional analysis or proteomics/lipidomics, it is paramount that researchers specify the degree of hematopoietic and undifferentiated BMA cell contamination in both mouse and human BMAT. Single cell RNA sequencing techniques will facilitate BMAT studies, albeit at a high cost.

The possibility of fluorescence activated cell sorting (FACS)-based purification of mature adipocytes for downstream studies has been recently described for extramedullary adipocytes, based on forward/side scatter light signal and viability ensured by manual adjustments to the sorting pressure (132). It is to be demonstrated whether this approach may be compatible with primary BMAd isolation.

Regardless of the isolation approach, a large number of primary BMAds must be initially isolated for most downstream assays (see section on BMAd assessment *in vitro*). On successful isolation of mature BMAds, their culture is delicate and short-lived. Ceiling culture in 2D allows for maintenance of BMAds for about 1 week (**Figure 4E**), after which de-lipidation is often observed. To avoid de-lipidation, irradiation of the cells has proven to be technically beneficial prior to culture (9). The recent description of protective 3D BMAd cultures in engineered devices or silk scaffolds holds great promise to recapitulate important clues for their behavior *in vivo* (133–135), but raises new challenges to develop efficient cell extraction protocols for endpoint analysis and 3D imaging techniques compatible with these set-ups.

BMAd Progenitors: Isolation, Culture, and Modulation *in vitro*

Mature BMAds coexist hand-in-hand with their immature progenitors, which constitute a subset of the total BMSC fraction. The BMSC fraction has been defined by either (i) exclusion of endothelial and hematopoietic markers [typically CD31 to exclude endothelial components, CD45 to exclude hematopoietic components, and either murine Ter119 or human Glycophorine A to exclude nucleated erythroid lineage cells which lost CD45 expression, as discussed in Boulais et al. (136)], or (ii) by adherence and expansion in tissue culture plastic. Specific subpopulations with functionally validated *in vivo* stem cell or progenitor function, the so-called skeletal stem cells (SSCs) and their downstream committed or partially committed stromal, bone and cartilage progenitors have been recently described in mouse and human BM (137, 138). They present *in vitro* adipogenic potential and different degrees of *in vivo* adipogenesis, with human CD146 constituting the best functionally characterized marker for prospective isolation of SSCs (139, 140). Other skeletal multi-potent populations have been identified within the BM, including PαS ($CD45^{-}Ter119^{-}PDGFR\alpha^{+}Sca1^{+}$) (141, 142), although care must be taken when defining clonal multi-potency (125, 140). Specific markers to prospectively isolate intermediate steps within the stromal to adipocyte commitment axis have also recently been identified in mice by Ambrosi et al. Namely, a tri-potent bone/cartilage/adipocytic perivascular $CD45^{-}CD31^{-}Sca1^{+}CD24^{+}$ stem-cell like population, a $CD45^{-}CD31^{-}Sca1^{+}CD24^{-}$ adipocytic progenitor population and a more mature $CD45^{-}CD31^{-}Sca1^{-}Zfp423^{+}$ BMAd precursor population were identified in the

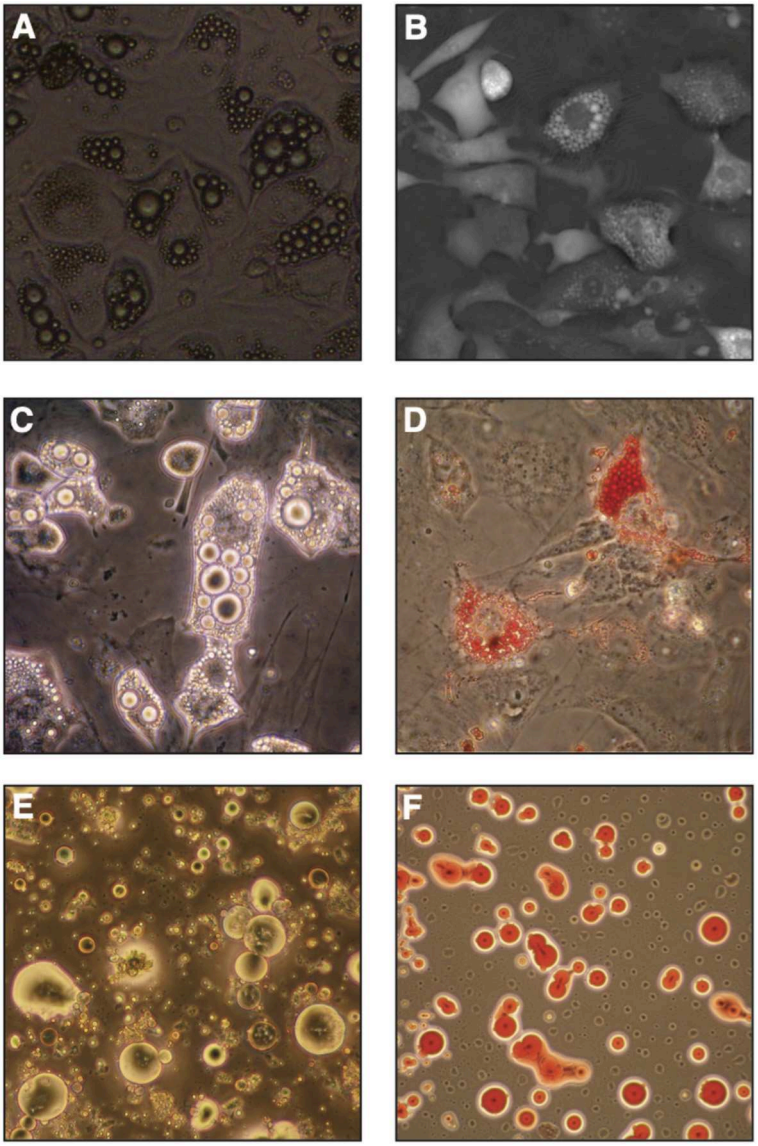

FIGURE 4 | *In vitro* bone marrow adipocyte differentiation. **(A)** Bright field image (objective 10x) of OP9 cells differentiated in presence of serum, dexamethasone, insulin and IBMX (DMI cocktail) for 6 days, **(B)** Digital Holographic Microscopy (DHM) image of OP9 cells differentiated in DMI for 7 days. **(C,D)** Primary murine bone marrow stromal cells after *in vitro* differentiation in similar conditions imaged by light-transmission microscopy, where lipid droplets show a high refractive index **(C)** or stained with neutral lipid oil-soluble colorant Oil Red O **(D)**. **(E,F)** Primary murine BMAds from 2-month-old FVB female mice as seen by light-transmission microscopy **(E)** or stained with Oil Red O **(F)**.

context of aging, high-fat diet (HFD) induced obesity and bone regeneration (5). No equivalent adipocytic differentiation hierarchy has yet been described in the human BM.

Due to the difficulty in isolating and expanding highly purified BMAd progenitors in mice, and to the lack of specific prospective BMAd progenitor markers in human BM, most studies to date have used unfractionated murine BMSCs, or *in vitro* expanded human BMSCs complying with International Society for Cellular Therapy (ISCT) standards (143) to produce *in vitro* differentiated BMAds for functional studies. ISCT standards provide a minimal set of surface markers and functional assays to validate human BMSC homogeneity. Standardized downstream functional assays have been proposed by the FDA (144–146). BMSC cultures rely on the rapid adherence of the cells to the culture dish, which allows exclusion of most hematopoietic cells from the culture. Nonetheless, passaging and sometimes sorting is necessary to eliminate macrophage contamination. As for primary isolated BMAds and to maximize comparability across studies, it is paramount to detail the source of BMSCs (gender, age, strain if applicable, metabolic diseases, skeletal location) and the method of isolation, such as specific enzymatic (e.g., collagenase-1,-2,-4, a combination thereof, trypsin) or mechanical dissociation as well as the specific expansion protocol, whose heterogeneity may explain some disparities in the field (summarized in **Table 6**, BMAS reporting guidelines as summarized in **Table 1**) (162). It

TABLE 6 | Variability in murine bone marrow stromal cell isolation protocols.

Samples	Isolation medium	RBC lysis	Enzymatic digestion	Depletion/ enrichment	Application	References
Flushed BM	DMEM/F12, 20% FBS, P/S, 2 mM L-glutamine, 0.1 mM NEAA, 3 mM sodium pyruvate	–	–	–	Cell culture	(147)
	PBS, 2%FBS, 2 mM EDTA	–	3 mg/ml col. I + 4 mg/ml Dispase (15 min 37°C)	–	Cell culture	(148)
	Leibovitz's L-15 medium, 1 mg/ml BSA, 10 mM HEPES, 1% P/S	0.8% NH_4Cl	0.005% trypsin + 0.002% EDTA + 0.25 mg/ml col. IV (4 min 37°C)	Anti-CD45, Nestin-GFP+ FACS	Flow cytometry	(149)
	HBSS, 2%FBS	–	DNase I + col. IV *or* + liberase^{DL} (15 *or* 20 min 37°C)	–	Flow cytometry	(27, 150)
	DMEM, 15% FBS, 2 mM L-Glutamine, 1% P/S, 3.7 g/l $NaHCO_3$	–	–	–	Cell culture	(151)
	α-MEM, 10% FBS, 1% P/S	–	–	–	Cell culture	(152)
	α-MEM, 15% FBS, 1% P/S, 2.2/l $NaHCO_3$	–	–	–	Cell culture	(153)
	α-MEM	–	–	–	Cell culture	(154, 155)
	RPMI-1640, 10% FBS, 1% P/S	–	–	–	Cell culture	(156)
	-	-	Trypsin (2 min 37°C)	–	Cell culture	(84)
	Long term medium	–	–	–	Cell culture	(157)
	RPMI-1640, 20% FBS, 2 mM glutamine, 1% P/S	–	–	–	Cell culture	(158)
Centrifuged BM	N/A	RBC lysis buffer	–	–	BMAd isolation	(56)
	N/A	–	–	–	Cell culture	(135, 159)
Crushed long bones	PBS	–	col. (20 min 37°C)	–	Flow cytometry	(28)
Flushed and cut long bones	α-MEM, 10% FBS	–	1 mg/ml col. II (1–2 h 37°C)	–	Cell culture	(160)
Cut and washed long bones	DMEM	H_2O 6 s	0.2% col. (1 h 37°C)	–	Flow cytometry	(141)
	N/A	–	5% col.	Anti-CD45, anti-Ter119, anti-CD31	Cell Culture	(161)
Cut long bones	PBS, 20% FBS	ACK	0.5% col. II (1 h 37°C)	–	Flow cytometry	(5)

BSA, bovine serum albumin; Col., collagenase; DMEM, dulbeco's modified eagle medium; FBS, fetal bovine serum; RBC, red blood cell; RPMI, L-glutamine, phenol red, reduced serum; P/S, penicillin/streptomycin; NEAA, non-essential amino acids.

is equally important to include quantification of contamination with hematopoietic or endothelial cells, and, specifically for BMSC populations, and to quantify the overall progenitor function of the primary isolate through fibroblastic colony forming unit assays (CFU-F) prior to adipocytic differentiation.

Induction of adipogenesis from BMSCs *in vitro* has included a variety of inducers in standard 2D culture conditions, as summarized for primary murine samples in **Table 7**. Most differentiation techniques are based on methods developed for murine extramedullary pre/adipocytes (e.g., 3T3L1) or BMSCs primed for adipogenic differentiation (such as C3H10T1/2, 3T3-L1, or OP9). The common denominator includes a combination of the corticosteroid dexamethasone, which ultimately induces master transcriptional regulator of adipogenesis C/EBP-α, and phosphodiesterase inhibitor isobutylmethylxanthine (IBMX), which leads to cAMP accumulation, protein kinase A activation and thus PPAR-γ expression. The cocktail is classically accompanied by insulin exposure, whether from the serum or exogenously administered. Thus the acronym "DMI" cocktail for Dexamethasone, IBMX and insulin (163).

TABLE 7 | Variability of *in vitro* murine bone marrow stromal cell adipogenic differentiation protocols.

References	(147)	(84)	(156)	(160)	(56) (135)			(5)	
Maintenance									
Medium	DMEM:F12	α-MEM	RPMI	α-MEM	α-MEM or DMEM			60% DMEM low Glc: 40%MCDB	
Serum	20% FBS	10% FBS	10% FBS	10% FBS	20% or 10% FBS			2% FBS	
Other	0.1 mM NEAA	200 μM NEAA						ITS, linoleic acid, dexa, AA, EGF, LIF, PDGFBB, bFGF	
Adipogenic									
Medium	DMEM:F12	α-MEM	DMEM	α-MEM	α-MEM or DMEM			60% DMEM low Glc: 40%MCDB	
Serum	20% FBS	10% FBS	9% horse serum	10% FBS	20% or 10% FBS			2% FBS	
Other		200 μM NEAA							
IBMX (μM)	500	500	450	0.5	500			0.5	
Dexa or Hydrocortisone (μM)	1	0.5	0.25	1	1			1	
Indomethacin (μM)	100	60						50	
Insulin (μg/ml)	5		5	0.01	10	10	10	5	5
Rosiglitazone (μM)			1		1	1			
T3 (nM)								1	1
Differentiation time	2 weeks	3 weeks	12 days	2 weeks	2–4 days	3–4 days	4 days	48 h	5 days

NEAA, non-essential amino acids; dexa, dexamethasone; ITS, insulin-transferrin-selenium mix; AA, L-ascorbic acid 2-phosphate; EGF, epidermal growth factor; LIF, leukemia inhibitory factor; PDGFBB, platelet-derived growth factor BB; bFGF, basic fibroblast growth factor; FBS, fetal bovine serum.

In addition, adipogenesis can be further boosted through the use of cyclooxygenase-2 (COX) inhibitor indomethacin or PPAR-γ agonist rosiglitazone. Of note, the mechanical properties of the substrate are also determinant for BMSC differentiation, and even dominant to exogenous biochemical signaling (164), with softer matrixes favoring adipogenesis. The role of extracellular matrix components in this context, and its rate of degradation, has been however largely understudied in this context.

BMAd Differentiation Assessment: *In Vitro* Assays and Applications

Multiple different cell types have the ability to accumulate lipid droplets, and thus we must evaluate the criteria with which we distinguish BMAds from other cells of the BM. In the context of extramedullary stromal differentiation, some groups have adopted the criteria of presence of at least four lipid droplets to define an adipocyte (165). This is especially useful as a threshold in imaging techniques where lipid droplets are visible (**Figures 4A,C,E**). As such, each investigator should critically evaluate what threshold is used as a definition.

Adipocytic differentiation is not completely efficient from primary BMSCs obtained on isolation, and the heterogeneity in cultures is well-known (166). This may be due to undetected heterogeneity of the initial BMSC population and adipocyte progenitors therein, to paracrine signaling cues in the culture, or, possibly, to presence of stromal cells that actively inhibit adipogenesis as recently described for $CD142^+$ SVF cells in murine extramedullary adipogenesis (167). Moreover, as discussed above, *in vitro* differentiation potential may not faithfully reflect *in vivo* potential. Stringent *in vivo* assays in the form of heterotopic marrow formation by *in vivo* transplant in permissive conditions should thus be the norm to reveal the true lineage potential (140, 168, 169). Researchers must therefore rely on genetically modified mouse models with differential donor/recipient marker expression, or, in the case of human samples, in xenotransplants into immune-deficient mice with species-specific surface marker, Alu sequence or mitochondrial DNA detection to determine donor vs. host BMAds.

Upon isolation and culture or differentiation *in vitro*, assessment of BMAd maturation relies on the definition of the BMSC-to-BMAd axis and on established or forthcoming readouts. Classical biochemical techniques (including western blot, real-time qPCR, flow cytometry, RNA sequencing, lipidomics) require relatively large cell numbers, thereby limiting assay performance for BMAds. Importantly, the cells on each extreme of the maturation spectrum vary greatly, as simply illustrated by the morphological changes when comparing the spindle-shaped BMSCs with large lipid-filled BMAds (**Figure 4**). This must be accounted for in the selection of suitable references, such as reference genes for RT-qPCR that do not change upon adipocytic differentiation. Thus, cytoskeletal or metabolic genes must strictly be avoided as reference genes, while at least two early/mid- (PPARγ, CEBPα) and two late- (AdipoQ, Glut4, FABP4, LPL, PLIN1) stage markers should be quantified as genes of interest to cover the adipocytic maturation spectrum. The stability of reference genes needs to be demonstrated upon differentiation in every experimental setting, but others have identified good reference gene in the context of adipocytic differentiation from peripheral stromal cultures human and rodent studies (170, 171).

In vitro microscopy-based readouts classically detect lipid droplet formation with fluorescent dyes (e.g., Nile Red, ORO, BODIPY) (**Figure 4F**), or use of cells from fluorescently-tagged reporter mice (e.g., tdTomato, RFP, GFP as extensively reviewed in section *in vivo* Lineage Tracing). Whether for microscopy or flow cytometric applications, careful interpretation of results is required, as most mature BMAds will be lost on liquid handling, and care must be taken not to count lipid vacuoles from broken cells as BMAds. More recently, label-free techniques such as digital holographic microscopy (**Figure 4B**) or Raman-based microspectroscopy have been developed for *in vitro* BMAd cultures with high resolution and potentially improved performance over classical techniques (172, 173). By preventing staining and liquid-handling biases, these methods provide additional information on lipid content along with quantification of morphological parameters. Additionally, microspectroscopy holds the promise to reveal information on chemical composition at the single cell level, which may reveal physiologically relevant heterogeneity.

Challenges in Cell-Based Assays

Isolation of primary BMAds remains challenging in both mouse and human. *In vitro* BMSC or BMAd precursor differentiation provides a valid alternative for studying the role of BMAds in cell-based assays, although potential differences with *in vivo* differentiated BMAds should always be acknowledged. This presents a challenge for normalization with age-matched control groups where the BMAds do not undergo similar changes. For appropriate normalization, it is thus important to account for both cell number and tissue weight, with pooling of control group mice to reach similar levels of BMAd isolation from the experimental and control groups for appropriate comparisons. For both primary BMAds and BMSCs, the cell mixtures obtained are highly dependent on the source and handling, and thus gender, age, skeletal location, metabolic perturbations, as well-extraction and culture methods should be thoroughly described as detailed in the recommended BMAS reporting guidelines (**Table 1**). With the application of *in vivo* BMA induction protocols (reviewed in **Tables 8**, **9**), BMAds are modulated in cell size, number, and phenotypic/functional properties. Additionally, measures of BMAd purity and BMSC CFU-F progenitor function should be reported to increase comparability of results across different researchers. It is imperative that as the BMA field matures, so must the publication of consensus protocols as well as definitions for both BMAd and BMSC isolation and differentiation.

TABLE 8 | *In vivo* modulation of bone marrow adipose tissue by dietary and environmental factors.

***In vivo* environmental intervention**	**Animal model**	**Outcomes (assay)**	**References**
High fat diet (45–60%)	C57BL/6J mice	↑BMAT ↔or ↓ Bone mass (O, μCT)	(174) (175) (161)
Physical exercise (voluntary exercise wheel in NCD and HFD mice)	C57BL/6 mice	↓BMAT volume in NCD and HDF-fed mice. ↑Bone mass (O, μCT)	(176) (63)
Caloric restriction (CR)	C57BL/6J mice (CR: 30% of NCD)	↑ BMA volume (H, MR)	(35)
	New Zealand White rabbits [CR: Moderate (30%) or extensive (50–70%)]	↑BMAT volume (O, μCT, H)	(177)
Acute fasting (48 h)	Sprague-Dawley rats	BMAd size: ↓proximal tibia ↔tail vertebrae (O, μCT)	(178)
Cold exposure (4°C)	C57BL/6J C3H/He	↓rBMAT ↔ cBMAT (O, μCT)	(12)
CLA +FO supplementation	C57BL/6 mice	↓BMAT (H)	(179)
Dietary methionine restriction	C57BL/6J mice	↑BMAT (O, μCT)	(180)

↓, Decrease; ↑, Increase; ↔, No change; BW, body weight; CLA, conjugated linoleic acid; FO, fish oil; HFD, high fat diet; O, osmium tetroxide staining; BMAT, bone marrow adipose tissue; NCD, normal chow diet; rBMAT, regulated BMAT; cBMAT, constitutive BMAT; BMAd, bone marrow adipocyte.

IN VIVO BMAT MODULATION

In Vivo Lineage Tracing

It is now well-accepted that BMAds differentiate from a small number of radioresistant mesenchymal progenitor cells that reside in the bone marrow. The ability to identify these early progenitor cells, more mature precursor cells, mature marrow adipocytes, and other mesenchymal lineage derived cells (e.g., osteoblasts), has been accomplished by the advent of modern lineage tracing using relatively specific Cre-drivers and fluorescent reporters (5, 84, 137, 199–202). This approach has the added benefit of being able to compare marrow adipocytes to white, brown, and beige adipocytes, and adipocytes in different anatomical locations *in vivo*.

Today's lineage tracing consistently depends on the Cre/Lox system (203). In the standard Cre/Lox system, Cre recombinase is expressed under the control of a tissue-specific promoter to permanently activate a reporter gene that functions to mark the original Cre-expressing cell population and all daughter cells that develop. Therefore, it is paramount that one has a detailed understanding of the Cre driver's spatiotemporal expression. Lack of this understanding can result in false interpretations of the origin of the cells. As an example, *PdgfRα-cre* traces all the adipocytes in white adipose tissue, but within the bone marrow, it traces about 50% of the adipocytes (202). By contrast, *Prx-1-cre* traces all marrow adipocytes (202). It also traces posterior subcutaneous white adipose tissue, including beige adipocyte precursors, as the mesenchymal origin of this

TABLE 9 | *In vivo* modulation of bone marrow adipose tissue by hormonal and pharmacological treatments in animal models.

***In vivo* intervention**	**Animal model (route of administration)**	**Outcomes (assays)**	**References**
Leptin	*ob/ob* mice (s.c. osmotic pumps)	↓ BMAT volume, ↑ bone formation (H-t)	(181)
	Type 1 Diabetic mice (s.c. osmotic pumps)	↓ Adipocyte number, ↔ bone mass loss (H, μCT)	(182)
	C57BL/6J mice (s.c.)	↓ BMAT formation induced by CR, ↔ BMD (O, μCT, H)	(183)
	Sprague-Dawley rats (VMH injection)	↓ number of BMAT adipocytes (H-t)	(184)
	ob/ob mice (rAAV-Lep, i.c.v.)	↓ BMAT, ↑ bone formation (H-f)	(185)
Orchidectomy	C57BL/6J mice	↑ BMAT (H-f)	(152)
PPARγ Agonists *Rosiglitazone* *Ovariectomy (OVX)* *OVX + Rosiglitazone*	Wistar rats (gavage)	↔ Ad.A./M.A., ↑ Ad.A./M.A., ↑ Ad.A./M.A. (H-t)	(186)
Troglitazone	ApoE$^{-/-}$ mice (mixed with diet)	↑ BMAT (Ad.A./M.A.) (H-t)	(187)
Rosiglitazone	C57BL/6J mice C57BL/6J mice + Exercise	*C57BL/6J:* ↑ BMAT (adipocyte number) (H-t) *Exercise:* ↓ BMAT-induced by rosiglitazone (O, μCT)	(188) (189)
	C57BL/6J mice C3H/HeJ mice DBA/2J mice A/J mice	*C57BL/6J:* ↑↑ BMAT (H-f) *C3H/HeJ:* ↑ BMAT (H-f) *DBA/2J:* ↔ BMAT (H-f) *A/J:* ↔ BMAT (H-f)	(190)
	Diabetic yellow agouti Avy/a	↑ BAT/WAT gene expression in marrow of C57BL/6 mice, not increase BAT genes in diabetic mice (H-t, RT-PCR)	(7)
	Ocn-Wnt10b mice (mixed with diet)	↓ BMAT *vs*. WT (O, μCT)	(191)
PPARγ Antagonists *Bisphenol A Diglycidil Ether, BADGE (partial antagonist properties)*	BALB/c (streptozotocin-induced diabetes) male C57BL/6J mice C57BL/6J mice + lethal irradiation C57BL/6J mice + cytarabine C57BL/6J mice + high fat diet (35%) (i.p)	↓ BMAT, ↔ BMD ↓ BMAT, ↑ BMD ↓ BMAT, ↑ hematopoietic recovery ↔ BMAT, rescue BMD (H-t, μCT, IF, RT-PCR)	(192) (37) (193) (194) (195)
GW9662 (pure antagonist)	C57BL/6 into C.B10-immune BM aplasia (i.p.)	↓ BMAT, ↑ hematopoietic recovery (IF, RT-PCR)	(196)
B-3 Adrenergic agonists *Isoproterenol or CL316,243*	Sprague-Dawley rats (i.p.) C3H/HeJ mice (i.p.)	BMAT from distal tibia and tail vertebrae resists β-adrenergic-induced lipolysis Moderate lipid droplet remodeling of BMAT adipocytes (proximal tibia); (O, μCT, IHC)	(178)
Dexamethasone	C57BL/6J mice (i.p.)	↑ BMAT, ↓BMD (H-f, μCT)	(197)
Lethal irradiation + BM Transplantation	FVB	↑ BMAT ↔ BMAT, ↑ BMD in "fatless" FVB.A-ZIP/F (H-f, μCT)	(193)
	C57BL/6J mice	↑ M.Ad./M.A. ↑ Ad. number and size (MQ-t, f,st,sp & MRI-f)	(61)
	Beagle dogs	↑ BMAT (H-t, hu, r)	(198)
Cytarabine (ARAC) Ablative chemotherapy	C57BL/6J mice	↑ BMAT; (H-t)	(194)

↓, Decrease; ↑, Increase; ↔, No change; BAT, brown adipose tissue; BMAT, bone marrow adipose tissue; BMD, bone mineral density; f, femur; H, histomorphometry; hu, humerus; IF, immunofluorescence; IHC, immunohistochemistry; i.p., intraperitoneal; O, Osmium tetroxide staining; r, radius; st, sternum; sp, spine; t, tibia; WAT, white adipose tissue; rAAV-Lep, recombinant adeno-associated virus (rAAV)-Leptin; BADGE, Bisphenol A Diglycidyl Ether; BM, bone marrow; CR, calorie restriction; Ad.A., adipocyte area; M.A., marrow area; PPARγ, μCT, micro-computed tomography; RTPCR, real-time quantitative polymerase chain reaction; OVX, ovariectomy; VMH, Ventromedial Hypothalamus; WT, wild-type; s.c., subcutaneous; VMH, ventromedial hypothalamus; i.c.v., intracerebroventricular.

depot gets recombined during limb development. In contrast, *Prx1* does not trace the majority of brown adipocytes or any visceral adipocytes (204). Thus, it is useful because of its relative specificity, especially compared to *adiponectin-cre*, which traces all adipocytes including marrow adipocytes (**Figure 5A**), and a range of BMSC precursors (6). Another advantage to this system are inducible Cres. As an example, *Prx1-ER-cre*, where Cre expression is activated in Prx1 positive cells by tamoxifen injection. These types of constructs allow for the timed induction of the reporter. A caveat to be considered when using tamoxifen and ER-inducible cre-drivers, however, is that the dose of tamoxifen required to efficiently activate Cre expression can be 100–1,000 times greater than required to activate estrogen receptors. A single dose of tamoxifen is reported to have irreversible effects on the uterus. Furthermore, tamoxifen crosses the blood brain barrier to regulate energy metabolism, is a potent immune modulator in mice, and can induce bone marrow failure (205–207). Investigators who choose to use tamoxifen in spite of its potent estrogen receptor-mediated actions, should be advised to include a no treatment control as well as a tamoxifen-treated/no Cre control. Equally important is the nature of the reporter gene used. For example, adipocytes possess little cytoplasm relative to other cell types, therefore cytoplasmic reporters such as LacZ are not optimal for tracing adipocytes. Instead, membrane-targeted reporters such as mT/mG (membrane Tomato/membrane GFP) provide superior results (208, 209). For extensive discussions on this topic see Jeffery et al. (210) and Sanchez-Gurmaches et al. (211).

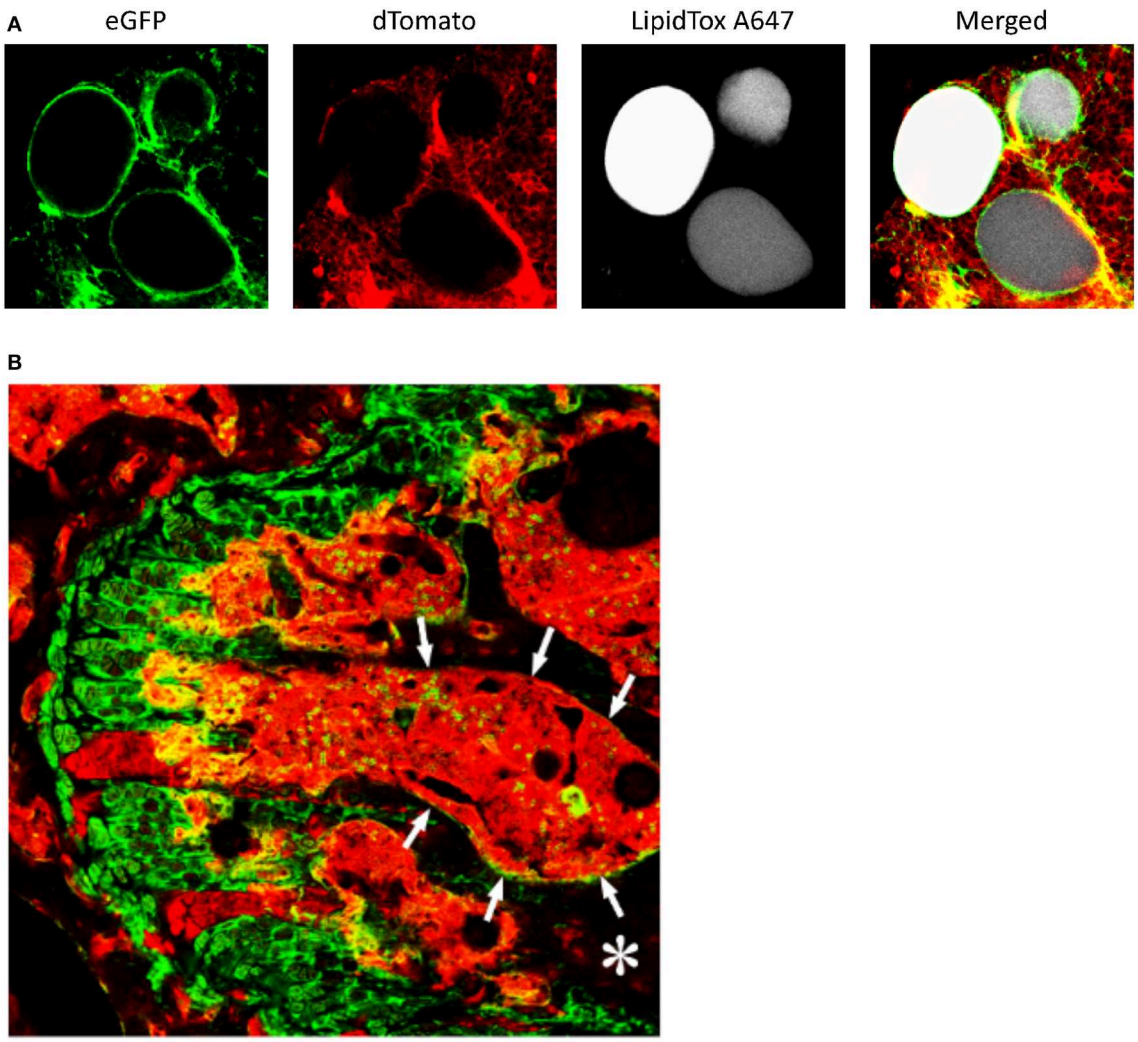

FIGURE 5 | Lineage tracing of bone marrow adipocytes and bone marrow stromal cells. **(A)** Adiponectin-cre:mT/mG mice received a single dose of x-irradiation (1,000 rads) to induce bone marrow adipogenesis. Following irradiation, the mice were reconstituted by an intravenous. injection of 106 syngeneic bone marrow cells to prevent radiation induced bone marrow damage. Bone marrow was collected from the femur as an intact plug, stained with LipidTox (fluorescent lipophilic dye), and marrow adipocytes visualized by confocal microscopy. Greater than 95% of the cells were eGFP$^+$ indicating they were traced by expression of Adiponectin. **(B)** The femur from *Twist-2-cre:mT/mG* mice was isolated, the femoral head removed and the bone fixed in 4% paraformaldehyde overnight. The bones were then immersed in 30% sucrose for 3–4 days, then placed in optimal cutting temperature compound, and frozen. Five to 10 μm thick-sections were imaged by confocal microscopy. Columns of growth plate cartilage cells were eGFP$^+$. In the bone marrow (outlined by arrows and appearing red), a small number of eGFP$^+$ cells can be seen. In addition, approximately 50% of osteocytes (*bone, appearing black) were also eGFP$^+$. Cells that were eGFP$^+$ were traced by the expression of *Twist-2*.

Once the Cre-reporter has been selected, which will be dictated by the demands of the experiment, either an *ex-vivo* or *in situ* approach can be taken.

The *ex-vivo* approach involves dissecting out the femur, cutting off the femoral head and removing the distal epiphysis above the growth plate. A 20-gauge needle can then be inserted down the medullary canal (from proximal to distal), and punching out the needle through the distal growth plate. Because the distal growth plate is intact this causes the bone marrow to fill the needle. The needle is then attached to a syringe and the marrow plug can then be deposited on a microscope slide by depressing the barrel of the syringe. The adipocytes in the marrow plug can then be prepared for imaging by confocal microscopy. Femora are preferred for this technique because they are fairly uniformly cylindrical along the length of the bone making them amenable to boring.

Advantages: (1) This is a straight forward simple method that requires no specialized equipment, with the exception of the confocal microscope; (2) The method is rapid. It avoids the requirement of decalcification or sectioning; (3) Using *mT/mG* reporter mice, in addition to tracing mature marrow adipocytes, will show whether marrow adipocyte precursors (GFP^+) expressed the gene of interest; (4) The marrow adipocytes, in the marrow plug, can be stained with a fluorescent lipophilic dye (i.e., LipidTOX) allowing for easy identification of the mature adipocytes. This also allows for better determination of cell counts and size. This approach can be combined with immunofluorescence to co-stain for other cell markers if desired.

Challenges: (1) Because adult mice (C57BL/6 background) have few marrow adipocytes in the femur, induction of marrow adipogenesis is recommended. However, the choice of which induction protocol to be used (x-irradiation, high fat diet feeding, feeding with a methionine restricted diet or a rosiglitazone containing diet, see **Tables 8**, **9**) will depend on the experimental design; (2) The femoral medullary canal in adult mice is the only site sufficiently large to collect a workable bone marrow plug; (3) Because the cells are removed from the marrow their anatomical location, especially as it relates to trabecular bone and the endosteum is lost.

The second, *in situ*, approach maintains anatomical location with respect to the growth plate and endosteum, but by maintaining the calcified bone matrix, introduces its own complications. Although the *in situ* approach involves collecting fresh femurs, from that point, the method varies significantly from investigator to investigator. The bones can be fixed in paraformaldehyde overnight and then given a partial decalcification in EDTA, sucrose incubation follows, and then embedding in either a cryomedia or carboxymethyl cellulose, followed by frozen sectioning (**Figure 5B**). Some of the best images have been acquired using a tape-transfer system and cutting 10–30 μm sections (137, 199–201). Other investigators have even used paraffin embedding instead of frozen sections, although this necessitates the use of antibodies, even in fluorescence reporter mice (5). After sectioning, the tissue can then be stained with the desired antibody-conjugate (direct i.e., GFP, or indirect using a secondary fluorescent antibody or biotin-avidin conjugate), and imaged by fluorescence or confocal microscopy. However, the fixation and decalcification can vary greatly form investigator to investigator, including some who use no fixation and rapid freezing (200). In addition, to immunofluorescent staining, transient fluorescent reporter mice (e.g., *Zfp423-EGFP*) or Cre/Lox lineage tracing fluorescent reporter mice can be used.

Advantages: (1) The major advantage to this method is that it allows for direct visualization of the cells within intact bone. Thus, the spatial relationship between marrow adipocytes, other cells, and bone is maintained; (2) Using *mT/mG* reporter mice can be a significant advantage; (3) Mature marrow adipocytes can be imaged.

Challenges: (1) This method requires expertise and experience in bone histology and specialized histologic equipment (e.g., tungsten-carbide knifes to section bone); (2) Sectioning small bones (e.g., distal tibia and caudal vertebrae) can be difficult; (3) Difficulties using the tape-transfer systems have been reported; (4) The embedding techniques and section preparation often exclude the combined use of lipid-tracing dyes.

It is clear that great progress in lineage tracing of marrow adipocytes has been made during the last few years, due to advances such as the Cre/Lox system. Our ability to delineate cells in the bone marrow adipocyte lineage will only get better with the advent of more specific Cre-drivers and more robust reporters. Refinements in our ability to process bone to make it more accessible to these methods will result in an even better understanding of the lineage, how it relates to other mesenchymal lineage cells, and the myriad of other cells in bone marrow.

In vivo Modulation of BMA

BMAT is a complex and dynamic depot that is highly regulated and can affect the function of other tissues/organs. Whether presence of BMAT is necessary for normal physiological responses is still controversial. While some studies have shown that BMAT negatively influences bone mass, a study in BMAT-deficient $Kit^{W/W-v}$ ($BMAT^-$) mice suggested that the absence of BMAT did not have any relevant effect on ovariectomy-induced bone loss (22). However, a recent study in $BMAT^-$ male mice has shown that absence of BMAT exacerbated bone loss during hindlimb unloading (212).

The expandability of BMAT is regulated by nutritional and environmental factors, aging, endocrine signals, and pharmacological agents. Here, we critically summarize experimental models used to study *in vivo* regulation of BMAT development and function.

Nutritional and Environmental Interventions

In C57BL/6J mice, a strain susceptible to obesity and diabetes, HFD feeding induces also BMAT expansion (174, 175). When diet-induced obesity (DIO) is reversed by switching to normal chow diet (NCD) to mimic weight loss, the HFD-induced BMAT recedes (175). Some of these alterations are microbiota-dependent (195). The alterations induced by the HFD on BMAT gene expression differ from that observed

in peripheral adipose tissues. In contrast to visceral WAT, pro-inflammatory gene expression was decreased while the expression of genes of the insulin signaling pathway increased in BMAT of HFD-fed mice, suggesting a differential metabolic regulation of BMAT adipocytes (161). Walji et al. (213) used microfibril-associated glycoprotein-1 (MAGP1) deficient (*Mfap2*$^{-/-}$) mice that develop adult-onset obesity that precedes insulin resistance. In these mice, BMAT increased relative to WT mice coincident with the development of insulin resistance, and not with excess peripheral adiposity, hyperglycemia, change in trabecular bone volume or hematopoiesis.

Exercise is a life-style intervention proposed to prevent/counteract obesity-associated BMAT expansion (**Table 8**). Voluntary wheel running in C57BL/6 fed NCD or HFD demonstrated that exercise prevented the increase in BMAT acquisition (176). Styner et al. (189) found that exercise (alone or in combination with rosiglitazone) reduced BMAT volume and upregulated UCP1 expression in whole tibia (**Table 9**). Exercise can also reverse the increase of BMAT observed in previously obese animals (HFD-fed for 3 months) by decreasing both adipocyte number and size (63). Exercise was associated with higher trabecular and cortical bone quantity in lean and obese mice, but HFD itself did not influence bone quantity. Importantly, a recent study, also provided evidence that physical exercise modulates vertebral BMAT in humans (214).

The differential *in vivo* regulation of BMAT by nutritional status also occurs in animal models of caloric restriction (CR). In contrast to what is observed in visceral or subcutaneous WAT, BMAT is preserved or even increased in states of CR [(35, 177, 178, 183); **Tables 8**, **9**]. Indeed, CR (30%) in young growing mice alters bone formation, but despite having a lower body weight and body fat percentage, they exhibit a dramatic increase in BMAT (35). In patients with anorexia nervosa, CR is also associated with increased BMAT (215, 216). However, in New Zealand rabbits moderate or extensive CR did not cause BMAT expansion (177). It has been suggested that the increase in BMAT is especially prominent when nutrient deprivation occurs during periods of skeletal growth, such as childhood or adolescence (178). This period of rapid skeletal growth may already be poised for BMAT development as this is also a time of rapid baseline BMAT accumulation (217).

The expansion of BMAT during CR has also been associated with changes in several neuroendocrine factors that are modulated in response to energy deprivation. The decrease in leptin that occurs during CR-induced weight loss may account for the increased BMAT. Indeed, BMAT is increased in leptin-deficient *ob/ob* mice (218), and subcutaneous leptin treatment induces loss of BMAT adipocytes and increases bone formation in these mice (181). Moreover, peripheral leptin therapy is effective in reversing the increased BMAT observed in type 1 diabetic mice and CR models, but does not stop the bone loss that occurs concomitantly [(182, 183); **Table 9**]. Furthermore, central injections of leptin into the ventromedial hypothalamus (VMH) of Sprague-Dawley rats, as well as leptin gene therapy (intraventricular administration of recombinant adeno-associated virus (rAAV)-leptin gene) to *ob/ob* mice also reduced BMAT (184, 185). Interestingly, mice with selective deletion of the leptin receptor (Lepr) in limb bone marrow stromal cells (Prx1-Cre;Lepr$^{fl/fl}$ mice) exhibited normal body mass and hematopoiesis, but have decreased BMAT, and increased osteogenesis (219). Moreover, Prx1-Cre;Lepr$^{fl/fl}$ mice were protected from the HFD-increases in BMAT and reductions in osteogenesis. It therefore appears that hypothalamic and peripheral leptin signaling may have different or multiple effects on adipogenesis within bone marrow.

Aging

Increased BMAT is also observed during aging, and has been negatively correlated with bone health, and sometimes precipitates impaired hematopoiesis in animals (5, 220) and humans (221–223). Dietary strategies have also been proposed to counteract the increased BMAT associated with aging, and combination of conjugated linoleic acid with fish oil can decrease age-associated BMAT in C57BL/6J mice (179). Dietary methionine restriction (MR) increases longevity in rodent models, however MR promotes BMAT accumulation in contrast to WAT reduction (180).

Endocrine Regulation

From an endocrine perspective, bone and BMAT metabolism are tightly linked and therefore BMAT is under extensive hormonal regulation. First of all, already a long time ago it has been observed that ovariectomy increases BMAT in animals (224) and ovariectomy is now commonly used to induce BMAT in animal models. These observations have been extended to humans, as BMAT increases during aging and this increase is accelerated in women around the time of menopause (225). Post-menopausal hormonal replacement therapy with estradiol, both long term (1 year) and short term (2 weeks) decreases BMAT in women (33, 226), showing that indeed estradiol is an important regulator of BMAT. At the same time that estradiol secretion by the ovaries ceases, compensatory follicle stimulating hormone (FSH) secretion by the pituitary gland increases. In addition to the effect of hormonal replacement therapy, also FSH blocking therapy has been shown to decrease BMA in mice (83). In addition to gonadal hormones, glucocorticoids have a profound effect on adipose metabolism and this also holds true for bone marrow adiposity. Cushing's disease, defined by increased adrenocorticotropic hormone (ACTH) production by a pituitary adenoma and therefore hypercortisolemia, increases BMAT and this reverses again following surgical cure by removal of the pituitary adenoma (227). Also, long-term glucocorticoid treatment leads to increased BMAT (228) and can be used to induce BMAT in animal models. Finally, parathyroid hormone, an important regulator of bone metabolism and potent osteoanabolic drug, also has an effect on BMA. Teriparatide treatment in osteopenic women reduces BMAT (229) and animal studies showed that this effect can be recapitulated by genetic deletion of the parathyroid hormone receptor in skeletal stromal cells (56). Interestingly, additional studies from the Rosen lab showed that the effect of PTH is not only on the differentiation of the SSC into the adipocytic lineage, but that Parathyroid Hormone (PTH) can also induce lipolysis in BM adipocytes (230). In

addition, growth hormone (GH) is an important regulator of skeletal growth and growth hormone deficiency or resistance has been associated with changes in BMAT. In growing rats, hypophysectomy dramatically increases BMAT and this could not be reversed by treatment with either estradiol, thyroid hormone, cortisol or Insulin Growth Factor-1 (IGF-1), but was completely reversed by treatment with GH (231). In healthy, premenopausal women, vertebral BMAT measured with 1H-MRS was inversely associated with IGF-1 concentrations, but not stimulated GH concentrations (232). However, treatment with recombinant GH for 6 months in premenopausal obese women, did not change BMAT, although there was a significant difference between the GH treated and placebo treated groups due to the decrease in BMAT in the placebo group (233). Therefore, the role of GH in the regulation of BMAT in adult humans remains uncertain and studies in children during growth have not been performed.

BMAT is not only regulated by hormones, but also acts as an important endocrine organ itself. Cawthorn et al. (234) found that increased BMAT significantly contributes to the higher circulating adiponectin levels during CR. Moreover, studies in Ocn-Wnt10b mice, which resist BMAT expansion during CR, demonstrated that increased BMAT is required for the elevated circulating adiponectin in this condition. Furthermore, BMAT and adiponectin levels increase in patients undergoing therapy for ovarian or endometrial cancer, despite no change in total fat mass (234). Increased adiponectin levels and BMAT volume were also observed in DIO WT (C57BL/6J) mice treated with Rosiglitazone. However, female Ocn-Wnt10b mice treated with Rosiglitazone had mildly blunted hyperadiponectinemia (191) while males did not, suggesting a sex-specific response.

Pharmacological Modulation

Several drugs also regulate BMAT. PPARγ is a master transcription factor for adipocyte differentiation, and treatment with the insulin-sensitizing drugs thiazolidinediones (TZDs), which are PPARγ agonists, affects marrow adiposity. As shown in **Table 9**, treatment with several PPARγ agonists such as Rosiglitazone and Troglitazone enhanced BMAT in different animal models (187, 188). However, the effects of TZDs on BMAT seem to be strain-specific (190) and age-dependent, favoring BMAT accumulation in older mice rather than in young-growing animals (188). In ovariectomized (OVX) rats, treatment with rosiglitazone (BRL49653) exacerbated bone loss and increased BMAT (186). On the other hand, several studies have shown that treatment with PPARγ agonists increased BMAT without affecting trabecular bone volume, suggesting that adipogenesis and osteogenesis can be regulated independently *in vivo* (187). Similarly, netoglitazone administered to 6-month-old C57BL/6 mice had a strong adipogenic induction with no change in the trabecular architecture and modest decreases in cortical bone mineralization (235). In contrast, a reduction in BMAT has been observed in all studies administering PPARγ antagonists after chemo/radiotherapy, which are potent inductors of BMAT [(37, 192–194, 196, 236); **Table 8**]. Moreover, genetic models of PPARγ loss show a pronounced increase in bone mass with extramedullary hematopoiesis (237, 238). The effects of BMAT in the recovering of hematopoietic compartment seem apparently contradictory, possibly due to the differential effects of distinct BMAd subtypes and differentiation stages in hematopoietic progenitor support [reviewed in (239, 240)]. Methodologically, it is to be noted that although effective in reducing BMAT, the most commonly used PPARγ "antagonist" for *in vivo* experimentation, Bisphenol A Diglycidyl Ether (BADGE), has partial PPARγ agonist effects and is a potential endocrine disruptor receptor anti-androgenic and pro-estrogenic properties (241–243). It is therefore recommended that future *in vivo* studies use a more specific PPARγ antagonist such as GW9662 (196).

BMAT thus accumulates following hematopoietic marrow ablation. A wave of BMAT precedes hematopoietic repopulation and peaks from 2 to 3 weeks after whole-body radiation depending on dose and recipient characteristics (700–1,000 Gy) (193, 202). BMAT is then lost and the timing of recovery depends on the radiation dose and on the number of hematopoietic cells used for the rescue. Sublethal models which do not require hematopoietic rescue have also been developed with 5-fluorouracil or cytarabine treatments (194, 236). Both radiation and chemotherapeutic treatments induce dramatic increases in BMAT also in patients (234, 244), whereas certain disorders of inefficient hematopoiesis (e.g., W/Wv mice) are associated with greatly reduced BMAT and a modified lipid composition of the stroma (245, 246). The biological implications of BMAT in neoplastic progression within the BM microenvironment are only beginning to unravel (247–251).

Sympathetic Regulation

A very important issue when studying the *in vivo* modulation of BMAT is to consider the region-specific variation in the properties of the skeletal adipocytes, as already discussed in the BMAT isolation section. The studies of Scheller et al. (12) in mice strongly support the existence of a constitutive (cBMAT) and a regulated (rBMAT) depot. cBMAT is in the distal long bones fills the medullary canal from the tibia-fibular junction into the malleolus and caudal vertebrae, histologically resembles WAT, appears rapidly in the early postnatal period, does not usually respond to stimuli or pathophysiological changes (202), though it can reduced over several months with thermoneutrality (252). In contrast, rBMAT is situated in the proximal regions of long bones and in spinal vertebrae, develops after cBMAT, and is interspersed with hematopoietic cells. rBMAT increases or decreases in various conditions (DIO, aging, CR, etc.) (253).

The study of Scheller et al. (12) also revealed that knockout of PTRF ($Ptrf^{-/-}$ mice, a model of congenital generalized lipodystrophy 4) selectively inhibits formation of rBMAT adipocytes without affecting cBMAT, which could be one step toward generation of a genetic model of rBMAT ablation (12).

The lack of response of BMAT adipocytes to lipolysis during energy deprivation has been attributed to resistance to β-adrenergic stimulation, but this effect also shows region-specific differences. Acute fasting (48 h) decreases cell size of BMAT adipocytes within the proximal tibia but not within the tail vertebrae in Sprague-Dawley rats (178). Moreover, BMAT from distal tibia and tail vertebrae of these rats resists β-adrenergic-induced phosphorylation of Hormone-Sensitive Lipase (HSL)

and/or perilipin, which are required for stimulation of lipolysis. Furthermore, treatment of C3H/HeJ mice with CL316,243, a β3-AR agonist, caused remodeling/beigeing of WAT, but only moderate remodeling of lipid droplets in BMAT of proximal tibia without affecting mid or distal tibia (**Table 9**). Furthermore, β-adrenergic stimulation through cold exposure shows lipolytic response by rBMAT (decreased rBMAT in the tibial epiphysis and in the proximal tibia) while cBMAT remained unchanged (12). Therefore, these data suggest that the lipolytic response to β-adrenergic stimulation is more pronounced in rBMAT than in cBMAT (178).

Another important factor to take into account when designing and interpreting studies about *in vivo* BMAT regulation is the effect of housing temperature. Most of the studies in mouse models are performed at room temperature (RT, around 22°C), which is below the thermoneutral temperature for mice (around 32°C). Therefore, RT housing can increase non-shivering thermogenesis by the sympathetic outflow and the activation of UCP1 in BAT (254, 255) showed that thermoneutral housing not only reduces UCP1 expression in BAT, but also increase BMAT and the percentage of body fat as compared with RT-housed mice. Therefore, the mild cold stress induced by RT-housing could be a non-considered confounding factor in mice studies.

In vivo Modulation Challenges

All these studies have demonstrated that BMAT expansion accompanies metabolic dysfunction. However, many physiopathological changes take place in these processes, and dissecting the role of BMAT expansion from the role of peripheral adipocytes and other metabolic perturbations make mechanistic studies a challenge. Furthermore, the divergent BMAT responses to different strains/species suggest the existence of a strong genetic background effect, which should be considered when designing studies, highlighting once more the importance of adhering to the BMAS minimal reporting guidelines when communicating results (see **Table 1**). Possibly, standard *in vivo* experimental conditions need to be defined for inter-laboratory comparisons. As we continue to identify the physiological processes that underlie the formation of BMAT and the environmental and genetic cues that control its accumulation, it is becoming increasingly evident that BMAT may be heterogenous.

Finally, in spite of their limitations, wider use of available genetic models of non-selective BMAT depletion (e.g., Ptrf$^{-/-}$, W/Wv), which have lesser metabolic phenotypes than severely lipodystrophic mice (e.g., A-ZIP/F), should advance the field until models of highly-specific BMAT depletion can be developed. Furthermore, it is paramount to consider that the BMA, bone, vascular and hematopoietic compartments are tightly interlinked within the BM, such that *in vivo* analysis requires functional measurements of all four compartments to reach mechanistic conclusions.

BIOBANKING

The BMAS Working Group on Biobanking has the ambition to generate standardized approaches toward isolation, characterization and long-term storage of tissues/cells related to BMA and their associated data and annotations. Although difficult to achieve due to several challenges (see below), creating minimal standards to isolate and characterize BMAds as well as freezing protocols for long-term storage should significantly reduce variability in outcomes between studies and laboratories. This is especially important to ensure viability and conservation of heterogeneity in cell-based assays, and to ensure sample stability for chemical analysis including mass spectrometry. Most importantly, unified biobanking standards along with the protection of associated data will enable responsible use and exchange of samples for comparative and larger-scale studies. Ultimately, the field will benefit from improved applicability of animal and human BMA-related samples, which may better facilitate the discovery of novel therapeutics to target BMA.

In a complementary fashion to the BMAS Working Group in Methodologies, one of the foci of the BMAS Biobanking Working Group will be to congregate methodologies related to the collection, freezing/thawing and long-term storage of BMAds. Additional aspects of biobanking that the working group will scrutinize are privacy regulations regarding participants/patients, data protection and ethical guidelines to facilitate collaborative efforts. Main challenges toward this objective are briefly introduced below.

Isolation of BMAds

Different types of materials have been and will be employed to study BMA, including BM aspirates, biopsies, specific cell types, BM plasma fraction, etc. After having defined these, recommended standard procedures are required regarding BMA isolation, processing and characterization. For example, isolation protocols vary substantially between laboratories (digestion with collagenase or other enzymes, incubation times, etc.). In addition, it is important to distinguish protocols for animal studies vs. human materials as BMA is different in composition, location, metabolism and regulation. For human bone marrow–related samples, recommended patient screening should be additionally established (HIV, Hepatitis B and C virus). Finally, minimal standards should also be established for sample annotation, which should include description of the site of collection, method of collection and isolation, including time and type of digestion, time from collection to freezing, etc.

Characterization of BMAds

One of the biggest challenges is to define a healthy control set, especially for human samples (see **Table 1**). What is regarded as normal population and a standard site of collection and how do we define this? What is the minimal set of parameters required to define such a set? One solution is to propose a minimal set of specific surface molecules, gene expression markers and/or other biomarkers (e.g., lipid profiles) to facilitate comparisons and thus also multicenter studies. Some specific markers have been proposed (adipokine markers, absence of hematopoietic, endothelial, and hematopoietic markers) but additional species-specific markers are needed to be able to characterize BMAds in a uniform and reliable fashion.

Long-Term Storage of BMA-Related Samples

To date it has proven impossible to freeze BMAds, and the only access point to retrospective samples relies on the identification of adipocyte ghosts in paraffin blocks. Tissue samples containing adipocytes are being collected but these require purification and/or digestion steps before freezing. On the other hand, storage of precursor cells (SSCs) may poorly reflect the BMA situation at the time of isolation, most often due to cellular expansion (and deviation) *in vitro* before or after freezing. In order to create as much homogeneity as possibly, it is vital to define freezing and thawing procedures employed with a minimum of interfering steps as well as viability and cell growth/differentiation characteristics of previously stored BMA samples. Non-frozen samples, including paraffin blocks, may pose less issues, but still homogeneity in tissue processing and database management are required to optimize storage and exchange of samples.

Ethical Issues and Data Protection

With the installment of the General Data Protection Regulation (GDPR) in 2018 (EU GDPR Portal (website), accessed August 27, 2019, http://eugdpr.org) the protection of people and data has become more stringent. Trying to come up with a standardized procedure toward biobanking will face challenges, including different national regulations, institutionalized rules, etc. Ethical guidelines varying between countries should be dealt with to assess the possibility to generalize ethical topics into one document for samples to be collected in the future. Related to this, a general template for informed consent and awareness of mutual use of obtained samples by all involved may improve standardization and the possibility to share samples, which is especially relevant in the context of rare diseases. A BMAS consortium-wide material transfer agreement may be instrumental for this.

Issues related to data protection include the assurance that participant/patient data remains anonymous at all costs. Although the consciousness around this subject is increasing, the working group will assess these issues in detail and will aim to propose a comprehensive recommended protocol to safeguard anonymity and data protection that originates from any of the laboratories. Data obtained in the European union (EU) often cannot be stored on servers outside the EU and similar regulations may apply to different continents as well. Therefore, a robust data management plan needs to be installed that can explore and potentially overcome challenges such as decentralized storage of samples and associated files.

In conclusion, biobanking, and methodological challenges are tightly linked. Minimal standards and international overarching ethical guidelines for BMA sample collection and data protection will be critical to increase the quality of fundamental and multicenter clinical studies, and interpret with greater confidence the outcome and impact of BMA research within the next few years.

CONCLUDING REMARKS

Specific methodologies for the study of BMA have been developed in the last decade, paralleling the increasing interest in the field. Gold standard methodologies currently exist for the assessment of BMA *ex vivo*, *in vivo* and *in vitro* (e.g., histomorphometry and OsO_4– 3D contrast-enhanced μCT for *ex vivo*, WFI and 1H-MRS MRI sequences for *in vivo* studies, lipid-dye-based and RT-qPCR-based assessment for assessment of *in vitro* BM adipogenesis) and emerging techniques may soon come to complement or substitute these gold standards (i.e., digital pathology algorithms for histomorphometry, POM-based contrast-enhanced CT for *ex vivo* imaging, dual energy CT for *in vivo* imaging as well as more reproducible parameters for *in vivo* MRI spectroscopy, label-free or 3D microscopy and microspectroscopy for *in vitro* imaging, or 3D adipose organoids for *in vitro* cultures).

However, great challenges still remain. First, given the inherent fragility of BMAds and their difficult access within the bone, protocols for extraction, *ex vivo* handling, and *in vitro* culture/differentiation of BMAds or BMSC progenitors vary greatly. Thus, recommended standardized protocols for *in vivo* modulation and extraction, minimal standards for BMAd purity assessment, and standardization of method-specific thresholds for BMA detection would greatly increase inter-study comparison and multi-site collaborations. Second, given the number of factors that affect BMA mass, and possibly type (e.g., skeletal location, gender, age, strain, nutritional status, metabolic state, exercise, ambient temperature, isolation technique), great attention needs to be paid in careful annotation and reporting of these confounding factors for all BMA scientific output. Third, in order to move forward the functional understanding of BMA, tools for the specific ablation of BMAds are urgently needed to uncouple the local BMA-effects from the metabolic effects of systemic lipodystrophy.

The BMAS Working Group in Methodologies and the collaborative BMAS community at large present the opportunity to reach methodological consensus guidelines and propose minimal standards that would strengthen the quality of our scientific output, increase comparability and prepare the field for multi-site preclinical and clinical studies which can pave the way to sound clinical translation. As a first step, incorporation of the BMAS nomenclature guidelines presented in the accompanying piece of this issue (31) and adherence to the methodology reporting guidelines presented here (**Table 1**) will ensure a common language for our community. In addition, we would like to invite readers to contribute by commenting on this review in the comments section of the "Frontiers in Endocrinology" website.

AUTHOR CONTRIBUTIONS

JT, AV-V, and ON conceptualized the manuscript, coordinated the writing, and edited the sections. JT, BP, RL, and PB mounted the manuscript and tables. RL, NB, JT, and AV-V wrote the histomorphometry section. GK, ED, and ES wrote

the *ex vivo* imaging section. SB and DK wrote the *in vivo* imaging section. JT, SB-C, BP, AP, PB, and ON wrote the *in vitro* section. MM-A, JF, AV-V, and ON wrote the *in vivo* modulation section. JF, MR, CR, and MH wrote the *in vivo* reporter section. ON and BE wrote the biobanking section. All authors edited and approved the final version of the manuscript.

FUNDING

The BMA2017 annual meeting to constitute BMAS and its Working Groups was funded by Swiss National Science Foundation (SNSF) grant 31CO30_173949. ON and JT were founded by SNSF grants PP00P3_183725 and PP00P3_176990 and the Anna Fuller Fund. MM-A was founded by grant BFU2015-65937-R (MINECO/FEDER, Government of Spain). SB-C was founded by Université de Nantes, Regional's Pays de Loire and Société Française de Rhumatologie.

ACKNOWLEDGMENTS

A special thank you to William Cawthorn, University of Edinburgh, for help on aligning this manuscript with the accompanying BMAS nomenclature position paper. We thank Giulia Frangi, Université de Nantes for contributing to compilation of data for **Tables 6**, **7**, Vasco Campos, EPFL, for the Digital Holographic Microscopy image on **Figure 4**, and Mara Riminucci, Sapienza University of Rome, for kindly providing the histological images for **Figures 1**, **4**. We acknowledge the Medical Research Council (CDA: MR/P02209X/1) grant to Anjali Kusumbe, University of Oxford for providing the immunofluorescent staining in **Figure 1**.

REFERENCES

1. Cawthorn WP, Scheller EL. Editorial: bone marrow adipose tissue: formation, function, and impact on health and disease. *Front Endocrinol. (*2017) 8:112. doi: 10.3389/fendo.2017.00112
2. Li Q, Wu Y, Kang N. Marrow adipose tissue: its origin, function, and regulation in bone remodeling and regeneration. *Stem Cells International*. (2018) 2018:7098456. doi: 10.1155/2018/7098456
3. Veldhuis-Vlug AG, Rosen CJ. Clinical implications of bone marrow adiposity. *J Int Med*. (2018) 283:121–39. doi: 10.1111/joim.12718
4. Raajendiran A, Tsiloulis T, Watt MJ. Adipose tissue development and the molecular regulation of lipid metabolism. *Essays Biochem*. (2016) 60:437–50. doi: 10.1042/EBC20160042
5. Ambrosi TH, Scialdone A, Graja A, Gohlke S, Jank AM, Bocian C, et al. Adipocyte accumulation in the bone marrow during obesity and aging impairs stem cell-based hematopoietic and bone regeneration. *Cell Stem Cell*. (2017) 20:771–84.6. doi: 10.1016/j.stem.2017.02.009
6. Mukohira H, Hara T, Abe S, Tani-Ichi S, Sehara-Fujisawa A, Nagasawa T, et al. Mesenchymal stromal cells in bone marrow express adiponectin and are efficiently targeted by an adiponectin promoter-driven cre transgene. *Int Immunol*. (2019). doi: 10.1093/intimm/dxz042
7. Krings A, Rahman S, Huang S, Lu Y, Czernik PJ, Lecka-Czernik B. *Bone* marrow fat has brown adipose tissue characteristics, which are attenuated with aging and diabetes. *Bone*. (2012) 50:546–52. doi: 10.1016/j.bone.2011.06.016
8. Lecka-Czernik B, Stechschulte LA, Czernik PJ, Sherman SB, Huang S, Krings A. Marrow adipose tissue: skeletal location, sexual dimorphism, and response to sex steroid deficiency. *Front Endocrinol.* (2017) 8:188. doi: 10.3389/fendo.2017.00188
9. Mattiucci D, Maurizi G, Izzi V, Cenci L, Ciarlantini M, Mancini S, et al. Bone marrow adipocytes support hematopoietic stem cell survival. *J Cell Physiol*. (2018) 233:1500–11. doi: 10.1002/jcp.26037
10. Jain SK, Subrahmanyam D. On the mechanism of phenylhydrazine-induced hemolytic anemia. *Biochem Biophys Res Commun.* (1978) 82:1320–4. doi: 10.1016/0006-291X(78)90332-7
11. Tavassoli M. Marrow adipose cells. Histochemical identification of labile and stable components. *Arch Pathol Lab Med*. (1976) 100:16–8.
12. Scheller EL, Doucette CR, Learman BS, Cawthorn WP, Khandaker S, Schell B, et al. Region-specific variation in the properties of skeletal adipocytes reveals regulated and constitutive marrow adipose tissues. *Nat Commun*. (2015) 6:7808. doi: 10.1038/ncomms8808
13. Parfitt AM. Terminology and symbols in bone morphometry. In: Zfg J, editor. *Proceedings of the First International Workshop on Bone Morphometry*. Ottawa, ON: Ottawa University Press. p. 331–5 (1976).
14. Parfitt AM, Drezner MK, Glorieux FH, Kanis JA, Malluche H, Meunier PJ, et al. Bone histomorphometry: standardization of nomenclature, symbols, and units. *J Bone Min Metab*. (1987) 2:595–610. doi: 10.1002/jbmr.5650020617
15. Mendelson A, Frenette PS. Hematopoietic stem cell niche maintenance during homeostasis and regeneration. *Nat Med*. (2014) 20:833–46. doi: 10.1038/nm.3647
16. Erben RG, Glosmann M. Histomorphometry in rodents. *Methods Mol Biol*. (2012) 816:279–303. doi: 10.1007/978-1-61779-415-5_19
17. Malhan D, Muelke M, Rosch S, Schaefer AB, Merboth F, Weisweiler D, et al. An optimized approach to perform bone histomorphometry. *Front. Endocrinol*. (2018) 9:666. doi: 10.3389/fendo.2018.00666
18. Prasad P, Donoghue M. A comparative study of various decalcification techniques. *Indian J Dent Res*. (2013) 24:302–8. doi: 10.4103/0970-9290.117991
19. Kusumbe AP, Ramasamy SK, Starsichova A, Adams RH. Sample preparation for high-resolution 3D confocal imaging of mouse skeletal tissue. *Nature Protocols*. (2015) 10:1904–14. doi: 10.1038/nprot.2015.125
20. Savi FM, Brierly GI, Baldwin J, Theodoropoulos C, Woodruff MA. Comparison of different decalcification methods using rat mandibles as a model. *J Histochem Cytochem*. (2017) 65:705–22. doi: 10.1369/0022155417733708
21. González-Chávez SA, Pacheco-Tena C, Macías-Vázquez CE, Luévano-Flores E. Assessment of different decalcifying protocols on osteopontin and osteocalcin immunostaining in whole bone specimens of arthritis rat model by confocal immunofluorescence. *Int J Clin Exp Pathol*. (2013) 6:1972–83.
22. Iwaniec UT, Turner RT. Failure to generate bone marrow adipocytes does not protect mice from ovariectomy-induced osteopenia. *Bone*. (2013) 53:145–53. doi: 10.1016/j.bone.2012.11.034
23. Yang R, Davies CM, Archer CW, Richards RG. Immunohistochemistry of matrix markers in Technovit 9100 New-embedded undecalcified bone sections. *Eur Cells Mater*. (2003) 6:57–71; discussion: 71. doi: 10.22203/eCM.v006a06
24. Erben RG. Embedding of bone samples in methylmethacrylate: an improved method suitable for bone histomorphometry, histochemistry, and immunohistochemistry. *J Histochem Cytochem*. (1997) 45:307–13. doi: 10.1177/002215549704500215
25. Beck-Cormier S, Lelliott CJ, Logan JG, Lafont DT, Merametdjian L, Leitch VD, et al. Slc20a2, encoding the phosphate transporter PiT2, is an important genetic determinant of bone quality and strength. *J Bone Miner Res*. (2019) 34:1101–14. doi: 10.1002/jbmr.3691
26. Bixel MG, Kusumbe AP, Ramasamy SK, Sivaraj KK, Butz S, Vestweber D, et al. Flow dynamics and HSPC homing in bone marrow microvessels. *Cell Reports*. (2017) 18:1804–16. doi: 10.1016/j.celrep.2017.01.042
27. Zhou BO, Yu H, Yue R, Zhao Z, Rios JJ, Naveiras O, et al. Bone marrow adipocytes promote the regeneration of stem cells and haematopoiesis

by secreting SCF. *Nat Cell Biol*. (2017) 19:891–903. doi: 10.1038/ncb3570
28. Kusumbe AP, Ramasamy SK, Itkin T, Mäe MA, Langen UH, Betsholtz C, et al. Age-dependent modulation of vascular niches for haematopoietic stem cells. *Nature*. (2016) 532:380–4. doi: 10.1038/nature17638
29. Silva J, Zanette I, Noël PB, Cardoso MB, Kimm MA, Pfeiffer F. Three-dimensional non-destructive soft-tissue visualization with X-ray staining micro-tomography. *Sci Rep*. (2015) 5:14088. doi: 10.1038/srep14088
30. Dempster DW, Compston JE, Drezner MK, Glorieux FH, Kanis JA, Malluche H, et al. Standardized nomenclature, symbols, and units for bone histomorphometry: a 2012 update of the report of the ASBMR Histomorphometry Nomenclature Committee. *J Bone Miner Res*. (2013) 28:2–17. doi: 10.1002/jbmr.1805
31. Bravenboer N, Bredella MA, Chauveau C, Corsi A, Douni E, Ferris WF, et al. Standardized nomenclature, abbreviations, and units for the study of bone marrow adiposity: report of the nomenclature working group of the international bone marrow adiposity society. *Front Endocrinol.* (2019) 10:923. doi: 10.3389/fendo.2019.00923
32. Sato M, Westmore M, Ma YL, Schmidt A, Zeng QQ, Glass EV, et al. Teriparatide [PTH(1-34)] strengthens the proximal femur of ovariectomized nonhuman primates despite increasing porosity. *J Bone Miner Res*. (2004) 19:623–9. doi: 10.1359/JBMR.040112
33. Syed FA, Oursler MJ, Hefferanm TE, Peterson JM, Riggs BL, Khosla S. Effects of estrogen therapy on bone marrow adipocytes in postmenopausal osteoporotic women. *Osteoporos Int*. (2008) 19:1323–30. doi: 10.1007/s00198-008-0574-6
34. Razidlo DF, Whitney TJ, Casper ME, Mcgee-Lawrence ME, Stensgard BA, Li X, et al. Histone deacetylase 3 depletion in osteo/chondroprogenitor cells decreases bone density and increases marrow fat. *PLoS ONE*. (2010) 5:e11492. doi: 10.1371/journal.pone.0011492
35. Devlin MJ, Cloutier AM, Thomas NA, Panus DA, Lotinun S, Pinz I, et al. Caloric restriction leads to high marrow adiposity and low bone mass in growing mice. *J Bone Miner Res*. (2010) 25:2078–88. doi: 10.1002/jbmr.82
36. Motyl KJ, Dick-De-Paula I, Maloney AE, Lotinun S, Bornstein S, De Paula FJ, et al. Trabecular bone loss after administration of the second-generation antipsychotic risperidone is independent of weight gain. *Bone*. (2012) 50:490–8. doi: 10.1016/j.bone.2011.08.005
37. Duque G, Li W, Vidal C, Bermeo S, Rivas D, Henderson J. Pharmacological inhibition of PPARgamma increases osteoblastogenesis and bone mass in male C57BL/6 mice. *J Bone Miner Res*. (2013) 28:639–48. doi: 10.1002/jbmr.1782
38. Nallamshetty S, Wang H, Rhee EJ, Kiefer FW, Brown JD, Lotinun S, et al. Deficiency of retinaldehyde dehydrogenase 1 induces BMP2 and increases bone mass *in vivo*. *PLoS ONE*. (2013) 8:e71307. doi: 10.1371/journal.pone.0071307
39. Turner RT, Philbrick KA, Wong CP, Olson DA, Branscum AJ, Iwaniec UT. Morbid obesity attenuates the skeletal abnormalities associated with leptin deficiency in mice. *J Endocrinol*. (2014) 223:M1–15. doi: 10.1530/JOE-14-0224
40. Philbrick KA, Turner RT, Branscum AJ, Wong CP, Iwaniec UT. Paradoxical effects of partial leptin deficiency on bone in growing female mice. *Anat Rec*. (2015) 298:2018–29. doi: 10.1002/ar.23267
41. Wesseling-Perry K, Makitie RE, Valimaki VV, Laine T, Laine CM, Valimaki MJ, et al. Osteocyte protein expression is altered in low-turnover osteoporosis caused by mutations in WNT1 and PLS3. *J Clin Endocrinol Metab*. (2017) 102:2340–8. doi: 10.1210/jc.2017-00099
42. Le PT, Bishop KA, Maridas DE, Motyl KJ, Brooks DJ, Nagano K, et al. Spontaneous mutation of Dock7 results in lower trabecular bone mass and impaired periosteal expansion in aged female Misty mice. *Bone*. (2017) 105:103–14. doi: 10.1016/j.bone.2017.08.006
43. Devlin MJ, Robbins A, Cosman MN, Moursi CA, Cloutier AM, Louis L, et al. Differential effects of high fat diet and diet-induced obesity on skeletal acquisition in female C57BL/6J vs. *FVB/NJ Mice Bone Rep*. (2018) 8:204–14. doi: 10.1016/j.bonr.2018.04.003
44. Liu SH, Chen C, Yang RS, Yen YP, Yang YT, Tsai C. Caffeine enhances osteoclast differentiation from bone marrow hematopoietic cells and reduces bone mineral density in growing rats. *J Orthop Res*. (2011) 29:954–60. doi: 10.1002/jor.21326
45. Wang FS, Lian WS, Weng WT, Sun YC, Ke HJ, Chen YS, et al. Neuropeptide Y mediates glucocorticoid-induced osteoporosis and marrow adiposity in mice. *Osteoporos Int*. (2016) 27:2777–89. doi: 10.1007/s00198-016-3598-3
46. Zou Q, Hong W, Zhou Y, Ding Q, Wang J, Jin W, et al. Bone marrow stem cell dysfunction in radiation-induced abscopal bone loss. *J Orthop Surg Res*. (2016) 11:3. doi: 10.1186/s13018-015-0339-9
47. Li GW, Xu Z, Chang SX, Zhou L, Wang XY, Nian H, et al. Influence of early zoledronic acid administration on bone marrow fat in ovariectomized rats. *Endocrinology*. (2014) 155:4731–8. doi: 10.1210/en.2014-1359
48. Li G, Xu Z, Hou L, Li X, Li X, Yuan W, et al. Differential effects of bisphenol A diglicydyl ether on bone quality and marrow adiposity in ovary-intact and ovariectomized rats. *Am J Physiol Endocrinol Metab*. (2016) 311:E922–7. doi: 10.1152/ajpendo.00267.2016
49. Li G, Xu Z, Chen Y, Chang S, Calimente H, Hu J, et al. Longitudinal assessment of marrow fat content using three-point Dixon technique in osteoporotic rabbits. *Menopause*. (2016) 23, 1339–1344. doi: 10.1097/GME.0000000000000721
50. Kim HJ, Bae YC, Park RW, Choi SW, Cho SH, Choi YS, et al. Bone-protecting effect of safflower seeds in ovariectomized rats. *Calcif Tissue Int*. (2002) 71:88–94. doi: 10.1007/s00223-001-1080-4
51. Bornstein S, Moschetta M, Kawano Y, Sacco A, Huynh D, Brooks D, et al. Metformin affects cortical bone mass and marrow adiposity in diet-induced obesity in male mice. *Endocrinology*. (2017) 158:3369–85. doi: 10.1210/en.2017-00299
52. Yang YJ, Zhu Z, Wang DT, Zhang XL, Liu YY, Lai WX, et al. Tanshinol alleviates impaired bone formation by inhibiting adipogenesis via KLF15/PPARgamma2 signaling in GIO rats. *Acta Pharmacol Sin*. (2018) 39:633–41. doi: 10.1038/aps.2017.134
53. Costa S, Fairfield H, Reagan MR. Inverse correlation between trabecular bone volume and bone marrow adipose tissue in rats treated with osteoanabolic agents. *Bone*. (2019) 123:211–23. doi: 10.1016/j.bone.2019.03.038
54. Beekman KM, Veldhuis-Vlug AG, Den Heijer M, Maas M, Oleksik AM, Tanck MW, et al. The effect of raloxifene on bone marrow adipose tissue and bone turnover in postmenopausal women with osteoporosis. *Bone*. (2019) 118:62–8. doi: 10.1016/j.bone.2017.10.011
55. Beekman KM, Veldhuis-Vlug AG, Van Der Veen A, Den Heijer M, Maas M, Kerckhofs G, et al. The effect of PPARγ inhibition on bone marrow adipose tissue and bone in C3H/HeJ mice. *Am J Physiol Endocrinol Metab*. (2019) 316:E96–105. doi: 10.1152/ajpendo.00265.2018
56. Fan Y, Hanai JI, Le PT, Bi R, Maridas D, Demambro V, et al. Parathyroid hormone directs bone marrow mesenchymal cell fate. *Cell Metab*. (2017) 25:661–72. doi: 10.1016/j.cmet.2017.01.001
57. Chandra A, Lin T, Tribble MB, Zhu J, Altman AR, Tseng WJ, et al. PTH1-34 alleviates radiotherapy-induced local bone loss by improving osteoblast and osteocyte survival. *Bone*. (2014) 67:33–40. doi: 10.1016/j.bone.2014.06.030
58. Brennan TA, Egan KP, Lindborg CM, Chen Q, Sweetwyne MT, Hankenson KD, et al. Mouse models of telomere dysfunction phenocopy skeletal changes found in human age-related osteoporosis. *Dis Model Mech*. (2014) 7:583–92. doi: 10.1242/dmm.014928
59. Li GW, Chang SX, Fan JZ, Tian YN, Xu Z, He YM. Marrow adiposity recovery after early zoledronic acid treatment of glucocorticoid-induced bone loss in rabbits assessed by magnetic resonance spectroscopy. *Bone*. (2013) 52:668–75. doi: 10.1016/j.bone.2012.11.002
60. Tratwal J, Boussema C, Burri O, Koliqi T, Campos V, Nardi V, et al. A standardized quantification tool for bone marrow components in histological sections. *Exp Hematol*. (2017) 53:S62–3. doi: 10.1016/j.exphem.2017.06.112
61. Tratwal J. *Quantitative approaches to unravel bone marrow adipocyte site-specificity and its implication in hematopoiesis* (dissertation). Ecole Polytechnique Fédérale de Lausanne, Lausanne, Switzerland (2020).
62. Rodrigues AC, Leal TF, Costa A, Silva FJ, Soares LL, Brum PC, et al. Effects of aerobic exercise on the inflammatory cytokine profile and expression of lipolytic and thermogenic genes in beta1-AR(-/-) mice adipose tissue. *Life Sci*. (2019) 221:224–32. doi: 10.1016/j.lfs.2019.02.031
63. Styner M, Pagnotti GM, Mcgrath C, Wu X, Sen B, Uzer G, et al. Exercise decreases marrow adipose tissue through β-oxidation in obese running mice. *J Bone Miner Res*. (2017) 32:1692–702. doi: 10.1002/jbmr.3159

64. Poulsen RC, Gotlinger KH, Serhan CN, Kruger MC. Identification of inflammatory and proresolving lipid mediators in bone marrow and their lipidomic profiles with ovariectomy and omega-3 intake. *Am J Hematol.* (2008) 83:437–45. doi: 10.1002/ajh.21170
65. During A. Lipid determination in bone marrow and mineralized bone tissue: from sample preparation to improved high-performance thin-layer and liquid chromatographic approaches. *J Chromatogr A*. (2017) 1515:232–44. doi: 10.1016/j.chroma.2017.08.004
66. Neues F, Epple M. X-ray microcomputer tomography for the study of biomineralized endo- and exoskeletons of animals. *Chem Rev*. (2008) 108:4734–41. doi: 10.1021/cr078250m
67. Salmon LPS, Alexander Y. Application of Nano-CT and high-resolution micro-CT to study bone quality and ultrastructure, scaffold biomaterials and vascular networks. In: Qin L, Genant HK, Griffith JF, Leung KS, editors. *Advanced Bioimaging Technologies in Assessment of the Quality of Bone and Scaffold Materials*. Berlin;Heidelberg: Springer (2007). p. 323–31. doi: 10.1007/978-3-540-45456-4_19
68. Kerckhofs G, Durand M, Vangoitsenhoven R, Marin C, Van Der Schueren B, Carmeliet G, et al. Changes in bone macro-and microstructure in diabetic obese mice revealed by high resolution microfocus X-ray computed tomography. *Sci Rep*. (2016) 6:35517. doi: 10.1038/srep35517
69. Ritman EL. Current status of developments and applications of micro-CT. *Ann Rev Biomed Eng.* (2011) 13:531–52. doi: 10.1146/annurev-bioeng-071910-124717
70. De Bournonville S, Vangrunderbeeck S, Kerckhofs G. Contrast-enhanced microCT for virtual 3D anatomical pathology of biological tissues: a literature review. *Contrast Media Mol Imaging*. (2019) 2019:8617406. doi: 10.1155/2019/8617406
71. Johnson JT, Hansen MS, Wu I, Healy LJ, Johnson CR, Jones GM, et al. Virtual histology of transgenic mouse embryos for high-throughput phenotyping. *PLoS Genet*. (2006) 2:471–7. doi: 10.1371/journal.pgen.0020061
72. Litzlbauer HD, Neuhaeuser C, Moell A, Greschus S, Breithecker A, Franke FE, et al. Three-dimensional imaging and morphometric analysis of alveolar tissue from microfocal X-ray-computed tomography. *Am J Physiol Lung Cell Mol Physiol*. (2006) 291:L535–45. doi: 10.1152/ajplung.00088.2005
73. Ribi W, Senden TJ, Sakellariou A, Limaye A, Zhang S. Imaging honey bee brain anatomy with micro-X-ray-computed tomography. *J Neurosci Methods*. (2008) 171:93–7. doi: 10.1016/j.jneumeth.2008.02.010
74. Palade BYGE. A study of fixation for electron microscopy. *J Exp Med*. (1951) 95:285–307. doi: 10.1084/jem.95.3.285
75. Turello R, Snyder D, Hartman HA. A modification the osmium tetroxide post-fixation technique for the demonstration of extracellular lipid in paraffin-embedded tissue sections. *J Histotechnol*. (1984) 7:75–7. doi: 10.1179/his.1984.7.2.75
76. Scheller EL, Troiano N, Vanhoutan JN, Bouxsein MA, Fretz JA, Xi Y, et al. Use of osmium tetroxide staining with microcomputerized tomography to visualize and quantify bone marrow adipose tissue *in vivo*. *Methods Enzymol*. (2014) 537:123–39. doi: 10.1016/B978-0-12-411619-1.00007-0
77. Khoury BM, Bigelow EMR, Smith LM, Schlecht SH, Scheller EL, Andarawis-Puri N, et al. The use of nano-computed tomography to enhance musculoskeletal research. *Connect Tissue Res.* (2015) 56:106–19. doi: 10.3109/03008207.2015.1005211
78. Kerckhofs G, Stegen S, Van Gastel N, Sap A, Falgayrac G, Penel G, et al. Simultaneous three-dimensional visualization of mineralized and soft skeletal tissues by a novel microCT contrast agent with polyoxometalate structure. *Biomaterials*. (2018) 159:1–12. doi: 10.1016/j.biomaterials.2017.12.016
79. Robles H, Park SJ, Joens MS, Fitzpatrick JA J, Craft CS, Scheller EL. Characterization of the bone marrow adipocyte niche with three-dimensional electron microscopy. *Bone*. (2019) 118:89–98. doi: 10.1016/j.bone.2018.01.020
80. Coutel X, Olejnik C, Marchandise P, Delattre J, Behal H, Kerckhofs G, et al. A novel microCT method for bone and marrow adipose tissue alignment identifies key differences between mandible and tibia in rats. *Calcified Tissue Int*. (2018) 103:189–97. doi: 10.1007/s00223-018-0397-1
81. Xiao Z, Cao L, Liang Y, Huang J, Stern AR, Dallas M, et al. Osteoblast-specific deletion of Pkd2 leads to low-turnover osteopenia and reduced bone marrow adiposity. *PLoS ONE*. (2014) 9:e114198. doi: 10.1371/journal.pone.0114198
82. Balani DH, Ono N, Kronenberg HM. Parathyroid hormone regulates fates of murine osteoblast precursors *in vivo*. *J Clin Investig*. (2017) 127:3327–38. doi: 10.1172/JCI91699
83. Liu P, Ji Y, Yuen T, Rendina-Ruedy E, Demambro VE, Dhawan S, et al. Blocking FSH induces thermogenic adipose tissue and reduces body fat. *Nature*. (2017) 546:107–12. doi: 10.1038/nature22342
84. Yu B, Huo L, Liu Y, Deng P, Szymanski J, Li J, et al. PGC-1α controls skeletal stem cell fate and bone-fat balance in osteoporosis and skeletal aging by inducing TAZ. *Cell Stem Cell*. (2018) 23:193–209.e5. doi: 10.1016/j.stem.2018.09.001
85. Metscher BD. MicroCT for developmental biology: a versatile tool for high-contrast 3D imaging at histological resolutions. *Dev Dyn*. (2009) 238:632–40. doi: 10.1002/dvdy.21857
86. Makarovsky I, Markel G, Hoffman A, Schein O, Finkelstien A, Brosh-Nissimov T, et al. Osmium tetroxide: a new kind of weapon. *Israel Med Assoc J*. (2007) 9:750–2.
87. Nakakoshi M, Nishioka H, Katayama E. New versatile staining reagents for biological transmission electron microscopy that substitute for uranyl acetate. *J Electr Microscopy*. (2011) 60:401–7. doi: 10.1093/jmicro/dfr084
88. Greenbaum A, Chan KY, Dobreva T, Brown D, Balani DH, Boyce R, et al. Bone CLARITY: clearing, imaging, and computational analysis of osteoprogenitors within intact bone marrow. *Sci Transl Med*. (2017) 9:eaah6518. doi: 10.1126/scitranslmed.aah6518
89. Jing D, Zhang S, Luo W, Gao X, Men Y, Ma C, et al. Tissue clearing of both hard and soft tissue organs with the pegasos method. *Cell Res*. (2018) 28:803–18. doi: 10.1038/s41422-018-0049-z
90. Coutu DL, Kokkaliaris KD, Kunz L, Schroeder T. Three-dimensional map of nonhematopoietic bone and bone-marrow cells and molecules. *Nat Biotechnol*. (2017) 35:1202–10. doi: 10.1038/nbt.4006
91. Gomariz A, Helbling PM, Isringhausen S, Suessbier U, Becker A, Boss A, et al. Quantitative spatial analysis of haematopoiesis-regulating stromal cells in the bone marrow microenvironment by 3D microscopy. *Nature Communications*. (2018) 9:2532. doi: 10.1038/s41467-018-04770-z
92. Hu HH, Kan HE. Quantitative proton MR techniques for measuring fat. *NMR Biomed*. (2013) 26:1609–29. doi: 10.1002/nbm.3025
93. Karampinos DC, Ruschke S, Dieckmeyer M, Diefenbach M, Franz D, Gersing AS, et al. Quantitative MRI and spectroscopy of bone marrow. *J Magn Reson Imaging*. (2018) 47:332–53. doi: 10.1002/jmri.25769
94. Paccou J, Hardouin P, Cotten A, Penel G, Cortet B. The role of bone marrow fat in skeletal health: usefulness and perspectives for clinicians. *J Clin Endocrinol Metab*. (2015) 100:3613–21. doi: 10.1210/jc.2015-2338
95. Reeder SB, Cruite I, Hamilton G, Sirlin CB. Quantitative assessment of liver fat with magnetic resonance imaging and spectroscopy. *J Magn Reson Imaging*. (2011) 34:729–49. doi: 10.1002/jmri.22580
96. Reeder SB, Hu HH, Sirlin CB. Proton density fat-fraction: a standardized MR-based biomarker of tissue fat concentration. *J Magn Reson Imaging*. (2012) 36:1011–4. doi: 10.1002/jmri.23741
97. Pino AM, Rodríguez JP. Is fatty acid composition of human bone marrow significant to bone health? *Bone*. (2019) 118:53–61. doi: 10.1016/j.bone.2017.12.014
98. Li G, Xu Z, Gu H, Li X, Yuan W, Chang S, et al. Comparison of chemical shift-encoded water-fat MRI and MR spectroscopy in quantification of marrow fat in postmenopausal females. *J Magn Reson Imaging*. (2017) 45:66–73. doi: 10.1002/jmri.25351
99. Ruschke S, Pokorney A, Baum T, Eggers H, Miller JH, Hu HH, et al. Measurement of vertebral bone marrow proton density fat fraction in children using quantitative water-fat MRI. *MAGMA*. (2017) 30:449–60. doi: 10.1007/s10334-017-0617-0
100. Gee CS, Nguyen JT, Marquez CJ, Heunis J, Lai A, Wyatt C, et al. Validation of bone marrow fat quantification in the presence of trabecular bone using MRI. *J Magn Reson Imaging*. (2015) 42:539–44. doi: 10.1002/jmri.24795
101. Macewan IJ, Glembotski NE, D'lima D, Bae W, Masuda K, Rashidi HH, et al. Proton density water fraction as a biomarker of bone marrow cellularity:

validation in *ex vivo* spine specimens. *Magn Reson Imaging.* (2014) 32:1097–101. doi: 10.1016/j.mri.2014.03.005
102. Zhang T, Duan Y, Ye J, Xu W, Shu N, Wang C, et al. Brain MRI characteristics of patients with anti-N-methyl-D-aspartate receptor encephalitis and their associations with 2-year clinical outcome. *AJNR Am J Neuroradiol.* (2018) 39:824–9. doi: 10.3174/ajnr.A5593
103. Aoki T, Yamaguchi S, Kinoshita S, Hayashida Y, Korogi Y. Quantification of bone marrow fat content using iterative decomposition of water and fat with echo asymmetry and least-squares estimation (IDEAL): reproducibility, site variation and correlation with age and menopause. *Br J Radiol.* (2016) 89:20150538. doi: 10.1259/bjr.20150538
104. Karampinos DC, Ruschke S, Gordijenko O, Grande Garcia E, Kooijman H, Burgkart R, et al. Association of MRS-based vertebral bone marrow fat fraction with bone strength in a human *in vitro* model. *J Osteoporos.* (2015) 2015:152349. doi: 10.1155/2015/152349
105. Li X, Kuo D, Schafer AL, Porzig A, Link TM, Black D, et al. Quantification of vertebral bone marrow fat content using 3 Tesla MR spectroscopy: reproducibility, vertebral variation, and applications in osteoporosis. *J Magn Reson Imaging.* (2011) 33:974–9. doi: 10.1002/jmri.22489
106. Baum T, Yap SP, Dieckmeyer M, Ruschke S, Eggers H, Kooijman H, et al. Assessment of whole spine vertebral bone marrow fat using chemical shift-encoding based water-fat MRI. *J Magn Reson Imaging.* (2015) 42:1018–23. doi: 10.1002/jmri.24854
107. Karampinos DC, Melkus G, Baum T, Bauer JS, Rummeny EJ, Krug R. Bone marrow fat quantification in the presence of trabecular bone: initial comparison between water-fat imaging and single-voxel MRS. *Magn Reson Med.* (2014) 71:1158–65. doi: 10.1002/mrm.24775
108. Dieckmeyer M, Ruschke S, Cordes C, Yap SP, Kooijman H, Hauner H, et al. The need for T(2) correction on MRS-based vertebral bone marrow fat quantification: implications for bone marrow fat fraction age dependence. *NMR Biomed.* (2015) 28:432–9. doi: 10.1002/nbm.3267
109. Liu CY, Mckenzie CA, Yu H, Brittain JH, Reeder SB. Fat quantification with IDEAL gradient echo imaging: correction of bias from T(1) and noise. *Magn Reson Med.* (2007) 58:354–64. doi: 10.1002/mrm.21301
110. Hu HH, Bornert P, Hernando D, Kellman P, Ma J, Reeder S, et al. ISMRM workshop on fat-water separation: insights, applications and progress in MRI. *Magn Reson Med.* (2012) 68:378–88. doi: 10.1002/mrm.24369
111. Yu H, Shimakawa A, Mckenzie CA, Brodsky E, Brittain JH, Reeder SB. Multiecho water-fat separation and simultaneous R2* estimation with multifrequency fat spectrum modeling. *Magn Reson Med.* (2008) 60:1122–34. doi: 10.1002/mrm.21737
112. Le Ster C, Gambarota G, Lasbleiz J, Guillin R, Decaux O, Saint-Jalmes H. Breath-hold MR measurements of fat fraction, T1, and T2 * of water and fat in vertebral bone marrow. *J Magn Reson Imaging.* (2016) 44:549–55. doi: 10.1002/jmri.25205
113. Yeung DK, Griffith JF, Antonio GE, Lee FK, Woo J, Leung PC. Osteoporosis is associated with increased marrow fat content and decreased marrow fat unsaturation: a proton MR spectroscopy study. *J Magn Reson Imaging.* (2005) 22:279–85. doi: 10.1002/jmri.20367
114. Patsch JM, Li X, Baum T, Yap SP, Karampinos DC, Schwartz AV, et al. Bone marrow fat composition as a novel imaging biomarker in postmenopausal women with prevalent fragility fractures. *J Bone Miner Res.* (2013) 28:1721–8. doi: 10.1002/jbmr.1950
115. Maciel JG, De Araujo IM, Carvalho AL, Simao MN, Bastos CM, Troncon LE, et al. Marrow fat quality differences by sex in healthy adults. *J Clin Densitom.* (2017) 20:106–13. doi: 10.1016/j.jocd.2016.08.002
116. Budzik JF, Lefebvre G, Forzy G, El Rafei M, Chechin D, Cotten A. Study of proximal femoral bone perfusion with 3D T1 dynamic contrast-enhanced MRI: a feasibility study. *Eur Radiol.* (2014) 24:3217–23. doi: 10.1007/s00330-014-3340-5
117. Goodsitt MM, Rosenthal DI. Quantitative computed tomography scanning for measurement of bone and bone marrow fat content. A comparison of single- and dual-energy techniques using a solid synthetic phantom. *Invest Radiol.* (1987) 22:799–810. doi: 10.1097/00004424-198710000-00006
118. Laval-Jeantet AM, Roger B, Bouysee S, Bergot C, Mazess RB. Influence of vertebral fat content on quantitative CT density. *Radiology.* (1986) 159:463–6. doi: 10.1148/radiology.159.2.3961178
119. Arentsen L, Hansen KE, Yagi M, Takahashi Y, Shanley R, Mcarthur A, et al. Use of dual-energy computed tomography to measure skeletal-wide marrow composition and cancellous bone mineral density. *J Bone Miner Metab.* (2017) 35:428–36. doi: 10.1007/s00774-016-0796-1
120. Rosenthal DI, Hayes CW, Rosen B, Mayo-Smith W, Goodsitt MM. Fatty replacement of spinal bone marrow due to radiation: demonstration by dual energy quantitative CT and MR imaging. *J Comput Assist Tomogr.* (1989) 13:463–5. doi: 10.1097/00004728-198905000-00018
121. Arentsen T, Raith H, Qian Y, Forssberg H, Diaz Heijtz R. Host microbiota modulates development of social preference in mice. *Microb Ecol Health Dis.* (2015) 26:29719. doi: 10.3402/mehd.v26.29719
122. Magome T, Froelich J, Takahashi Y, Arentsen L, Holtan S, Verneris MR, et al. Evaluation of functional marrow irradiation based on skeletal marrow composition obtained using dual-energy computed tomography. *Int J Radiat Oncol Biol Phys.* (2016) 96:679–87. doi: 10.1016/j.ijrobp.2016.06.2459
123. Bredella MA, Daley SM, Kalra MK, Brown JK, Miller KK, Torriani M. Marrow adipose tissue quantification of the lumbar spine by using dual-energy CT and single-voxel (1)H MR spectroscopy: a feasibility study. *Radiology.* (2015) 277:230–5. doi: 10.1148/radiol.2015142876
124. Hui SK, Arentsen L, Sueblinvong T, Brown K, Bolan P, Ghebre RG, et al. A phase I feasibility study of multi-modality imaging assessing rapid expansion of marrow fat and decreased bone mineral density in cancer patients. *Bone.* (2015) 73:90–7. doi: 10.1016/j.bone.2014.12.014
125. Bianco P, Robey PG. Skeletal stem cells. *Development.* (2015) 142:1023–7. doi: 10.1242/dev.102210
126. Bianco P, Gehron Robey P. Marrow stromal stem cells. *J Clin Invest.* (2000) 105:1663–8. doi: 10.1172/JCI10413
127. Kassem M, Bianco P. Skeletal stem cells in space and time. *Cell.* (2015) 160:17–9. doi: 10.1016/j.cell.2014.12.034
128. Hardouin P, Rharass T, Lucas S. Bone marrow adipose tissue: to be or not to be a typical adipose tissue? *Front Endocrinol.* (2016) 7:85. doi: 10.3389/fendo.2016.00085
129. Colvin GA, Lambert JF, Abedi M, Hsieh CC, Carlson JE, Stewart FM, et al. Murine marrow cellularity and the concept of stem cell competition: geographic and quantitative determinants in stem cell biology. *Leukemia.* (2004) 18:575–83. doi: 10.1038/sj.leu.2403268
130. Poloni A, Maurizi G, Serrani F, Mancini S, Zingaretti MC, Frontini A, et al. Molecular and functional characterization of human bone marrow adipocytes. *Exp Hematol.* (2013) 41:558–66.e2. doi: 10.1016/j.exphem.2013.02.005
131. Hozumi A, Osaki M, Sakamoto K, Goto H, Fukushima T, Baba H, et al. Dexamethasone-induced plasminogen activator inhibitor-1 expression in human primary bone marrow adipocytes. *Biomed Res.* (2010) 31:281–6. doi: 10.2220/biomedres.31.281
132. Hagberg CE, Li Q, Kutschke M, Bhowmick D, Kiss E, Shabalina IG, et al. Flow cytometry of mouse and human adipocytes for the analysis of browning and cellular heterogeneity. *Cell Rep.* (2018) 24:2746–56.e5. doi: 10.1016/j.celrep.2018.08.006
133. Torisawa YS, Spina CS, Mammoto T, Mammoto A, Weaver JC, Tat T, et al. Bone marrow-on-a-chip replicates hematopoietic niche physiology *in vitro*. *Nat Methods.* (2014) 11:663–9. doi: 10.1038/nmeth.2938
134. Bourgine PE, Klein T, Paczulla AM, Shimizu T, Kunz L, Kokkaliaris KD, et al. In vitro biomimetic engineering of a human hematopoietic niche with functional properties. *Proc Natl Acad Sci USA.* (2018) 115:E5688–95. doi: 10.1073/pnas.1805440115
135. Fairfield H, Falank C, Farrell M, Vary C, Boucher JM, Driscoll H, et al. Development of a 3D bone marrow adipose tissue model. *Bone.* (2019) 118:77–88. doi: 10.1016/j.bone.2018.01.023
136. Boulais PE, Mizoguchi T, Zimmerman S, Nakahara F, Vivie J, Mar JC, et al. The majority of CD45(-) Ter119(-) CD31(-) bone marrow cell fraction is of hematopoietic origin and contains erythroid and lymphoid progenitors. *Immunity.* (2018) 49:627–39.e6. doi: 10.1016/j.immuni.2018.08.019
137. Worthley DL, Churchill M, Compton JT, Tailor Y, Rao M, Si Y, et al. Gremlin 1 identifies a skeletal stem cell with bone, cartilage, and reticular stromal potential. *Cell.* (2015) 160:269–84. doi: 10.1016/j.cell.2014.11.042

138. Chan CKF, Gulati GS, Sinha R, Tompkins JV, Lopez M, Carter AC, et al. Identification of the human skeletal stem cell. *Cell*. (2018) 175:43–56.e21. doi: 10.1016/j.cell.2018.07.029
139. Tormin A, Li O, Brune JC, Walsh S, Schutz B, Ehinger M, et al. CD146 expression on primary nonhematopoietic bone marrow stem cells is correlated with in situ localization. *Blood*. (2011) 117:5067–77. doi: 10.1182/blood-2010-08-304287
140. Serafini M, Sacchetti B, Pievani A, Redaelli D, Remoli C, Biondi A, et al. Establishment of bone marrow and hematopoietic niches *in vivo* by reversion of chondrocyte differentiation of human bone marrow stromal cells. *Stem Cell Res*. (2014) 12:659–72. doi: 10.1016/j.scr.2014.01.006
141. Houlihan DD, Mabuchi Y, Morikawa S, Niibe K, Araki D, Suzuki S, et al. Isolation of mouse mesenchymal stem cells on the basis of expression of Sca-1 and PDGFR-alpha. *Nat Protoc*. (2012) 7:2103–11. doi: 10.1038/nprot.2012.125
142. Li H, Ghazanfari R, Zacharaki D, Ditzel N, Isern J, Ekblom M, et al. Low/negative expression of PDGFR-alpha identifies the candidate primary mesenchymal stromal cells in adult human bone marrow. *Stem Cell Rep*. (2014) 3:965–74. doi: 10.1016/j.stemcr.2014.09.018
143. Dominici M, Le Blanc K, Mueller I, Slaper-Cortenbach I, Marini F, Krause D, et al. Minimal criteria for defining multipotent mesenchymal stromal cells. The international society for cellular therapy position statement. *Cytotherapy*. (2006) 8:315–7. doi: 10.1080/14653240600855905
144. Robey PG, Kuznetsov SA, Ren J, Klein HG, Sabatino M, Stroncek DF. Generation of clinical grade human bone marrow stromal cells for use in bone regeneration. *Bone*. (2015) 70:87–92. doi: 10.1016/j.bone.2014.07.020
145. Tanavde V, Vaz C, Rao MS, Vemuri MC, Pochampally RR. Research using mesenchymal stem/stromal cells: quality metric towards developing a reference material. *Cytotherapy*. (2015) 17:1169–77. doi: 10.1016/j.jcyt.2015.07.008
146. Arcidiacono JA, Bauer SR, Kaplan DS, Allocca CM, Sarkar S, Lin-Gibson S. FDA and NIST collaboration on standards development activities supporting innovation and translation of regenerative medicine products. *Cytotherapy*. (2018) 20:779–84. doi: 10.1016/j.jcyt.2018.03.039
147. Sreejit P, Dilip KB, Verma RS. Generation of mesenchymal stem cell lines from murine bone marrow. *Cell Tissue Res*. (2012) 350:55–68. doi: 10.1007/s00441-012-1458-9
148. Suire C, Brouard N, Hirschi K, Simmons PJ. Isolation of the stromal-vascular fraction of mouse bone marrow markedly enhances the yield of clonogenic stromal progenitors. *Blood*. (2012) 119:e86–95. doi: 10.1182/blood-2011-08-372334
149. Mendez-Ferrer S, Michurina TV, Ferraro F, Mazloom AR, Macarthur BD, Lira SA, et al. Mesenchymal and haematopoietic stem cells form a unique bone marrow niche. *Nature*. (2010) 466:829–34. doi: 10.1038/nature09262
150. Ding L, Saunders TL, Enikolopov G, Morrison SJ. Endothelial and perivascular cells maintain haematopoietic stem cells. *Nature*. (2012) 481:457–62. doi: 10.1038/nature10783
151. Soleimani M, Nadri S. A protocol for isolation and culture of mesenchymal stem cells from mouse bone marrow. *Nat Protoc*. (2009) 4:102–6. doi: 10.1038/nprot.2008.221
152. Sui B, Hu C, Liao L, Chen Y, Zhang X, Fu X, et al. Mesenchymal progenitors in osteopenias of diverse pathologies: differential characteristics in the common shift from osteoblastogenesis to adipogenesis. *Sci Rep*. (2016) 6:30186. doi: 10.1038/srep30186
153. Huang S, Xu L, Sun Y, Wu T, Wang K, Li G. An improved protocol for isolation and culture of mesenchymal stem cells from mouse bone marrow. *J Orthop Translat*. (2015) 3:26–33. doi: 10.1016/j.jot.2014.07.005
154. Robey PG, Kuznetsov SA, Riminucci M, Bianco P. Bone marrow stromal cell assays: *in vitro* and *in vivo*. *Methods Mol Biol*. (2014) 1130:279–93. doi: 10.1007/978-1-62703-989-5_21
155. Ko FC, Martins JS, Reddy P, Bragdon B, Hussein AI, Gerstenfeld LC, et al. Acute phosphate restriction impairs bone formation and increases marrow adipose tissue in growing mice. *J Bone Miner Res*. (2016) 31:2204–14. doi: 10.1002/jbmr.2891
156. Abdallah BM, Alzahrani AM, Kassem M. Secreted clusterin protein inhibits osteoblast differentiation of bone marrow mesenchymal stem cells by suppressing ERK1/2 signaling pathway. *Bone*. (2018) 110:221–9. doi: 10.1016/j.bone.2018.02.018
157. Calvi LM, Adams GB, Weibrecht KW, Weber JM, Olson DP, Knight MC, et al. Osteoblastic cells regulate the haematopoietic stem cell niche. *Nature*. (2003) 425:841–6. doi: 10.1038/nature02040
158. Caroti CM, Ahn H, Salazar HF, Joseph G, Sankar SB, Willett NJ, et al. A novel technique for accelerated culture of murine mesenchymal stem cells that allows for sustained multipotency. *Sci Rep*. (2017) 7:13334. doi: 10.1038/s41598-017-13477-y
159. Peister A, Mellad JA, Larson BL, Hall BM, Gibson LF, Prockop DJ. Adult stem cells from bone marrow (MSCs) isolated from different strains of inbred mice vary in surface epitopes, rates of proliferation, and differentiation potential. *Blood*. (2004) 103:1662–8. doi: 10.1182/blood-2003-09-3070
160. Zhu H, Guo ZK, Jiang XX, Li H, Wang XY, Yao HY, et al. A protocol for isolation and culture of mesenchymal stem cells from mouse compact bone. *Nat Protoc*. (2010) 5:550–60. doi: 10.1038/nprot.2009.238
161. Tencerova M, Figeac F, Ditzel N, Taipaleenmaki H, Nielsen TK, Kassem M. High-fat diet-induced obesity promotes expansion of bone marrow adipose tissue and impairs skeletal stem cell functions in mice. *J Bone Miner Res*. (2018) 33:1154–65. doi: 10.1002/jbmr.3408
162. Nagasawa T, Omatsu Y, Sugiyama T. Control of hematopoietic stem cells by the bone marrow stromal niche: the role of reticular cells. *Trends Immunol*. (2011) 32:315–20. doi: 10.1016/j.it.2011.03.009
163. Scott MA, Nguyen VT, Levi B, James AW. Current methods of adipogenic differentiation of mesenchymal stem cells. *Stem Cells Dev*. (2011) 20:1793–804. doi: 10.1089/scd.2011.0040
164. Gobaa S, Hoehnel S, Lutolf MP. Substrate elasticity modulates the responsiveness of mesenchymal stem cells to commitment cues. *Integr Biol*. (2015) 7:1135–42. doi: 10.1039/c4ib00176a
165. Gubelmann C, Schwalie PC, Raghav SK, Roder E, Delessa T, Kiehlmann E, et al. Identification of the transcription factor ZEB1 as a central component of the adipogenic gene regulatory network. *Elife*. (2014) 3:e03346. doi: 10.7554/eLife.03346.020
166. Whitfield MJ, Cheng W, Lee J, Vliet KJV. Onset of heterogeneity in culture-expanded bone marrow stromal cells. *Stem Cell Res*. (2013) 11:1365–77. doi: 10.1016/j.scr.2013.09.004
167. Schwalie PC, Dong H, Zachara M, Russeil J, Alpern D, Akchiche N, et al. A stromal cell population that inhibits adipogenesis in mammalian fat depots. *Nature*. (2018) 559:103–8. doi: 10.1038/s41586-018-0226-8
168. Friedenstein AJ, Petrakova KV, Kurolesova AI, Frolova GP. Heterotopic of bone marrow. Analysis of precursor cells for osteogenic and hematopoietic tissues. *Transplantation*. (1968) 6:230–47. doi: 10.1097/00007890-196803000-00009
169. Sacchetti B, Funari A, Michienzi S, Di Cesare S, Piersanti S, Saggio I, et al. Self-renewing osteoprogenitors in bone marrow sinusoids can organize a hematopoietic microenvironment. *Cell*. (2007) 131:324–36. doi: 10.1016/j.cell.2007.08.025
170. Krautgasser C, Mandl M, Hatzmann FM, Waldegger P, Mattesich M, Zwerschke W. Reliable reference genes for expression analysis of proliferating and adipogenically differentiating human adipose stromal cells. Cell *Mol Biol Lett*. (2019) 24:14. doi: 10.1186/s11658-019-0140-6
171. Santos BP, da Costa Diesel LF, da Silva Meirelles L, Nardi NB, Camassola M. Identification of suitable reference genes for quantitative gene expression analysis in rat adipose stromal cells induced to trilineage differentiation. *Gene*. (2016) 594:211–9. doi: 10.1016/j.gene.2016.09.002
172. Smus JP, Moura CC, Mcmorrow E, Tare RS, Oreffo ROC, Mahajan S. Tracking adipogenic differentiation of skeletal stem cells by label-free chemically selective imaging. *Chem Sci*. (2015) 6:7089–96. doi: 10.1039/C5SC02168E
173. Campos V, Rappaz B, Kuttler F, Turcatti G, Naveiras O. High-throughput, nonperturbing quantification of lipid droplets with digital holographic microscopy. *J Lipid Res*. (2018) 59:1301–10. doi: 10.1194/jlr.D085217
174. Doucette CR, Horowitz MC, Berry R, Macdougald OA, Anunciado-Koza R, Koza RA, et al. A high fat diet increases bone marrow adipose tissue (MAT) but does not alter trabecular or cortical bone mass in C57BL/6J mice. *J Cell Physiol*. (2015) 230:2032–7. doi: 10.1002/jcp.24954
175. Scheller EL, Khoury B, Moller KL, Wee NK, Khandaker S, Kozloff KM, et al. Changes in skeletal integrity and marrow adiposity during

high-fat diet and after weight loss. *Front Endocrinol.* (2016) 7:102. doi: 10.3389/fendo.2016.00102
176. Styner M, Thompson WR, Galior K, Uzer G, Wu X, Kadari S, et al. *Bone* marrow fat accumulation accelerated by high fat diet is suppressed by exercise. *Bone*. (2014) 64:39–46. doi: 10.1016/j.bone.2014.03.044
177. Cawthorn WP, Scheller EL, Parlee SD, Pham HA, Learman BS, Redshaw CM, et al. Expansion of bone marrow adipose tissue during caloric restriction is associated with increased circulating glucocorticoids and not with hypoleptinemia. *Endocrinology*. (2016) 157:508–21. doi: 10.1210/en.2015-1477
178. Scheller EL, Khandaker S, Learman BS, Cawthorn WP, Anderson LM, Pham HA, et al. *Bone* marrow adipocytes resist lipolysis and remodeling in response to beta-adrenergic stimulation. *Bone*. (2019) 118:32–41. doi: 10.1016/j.bone.2018.01.016
179. Halade GV, Rahman MM, Williams PJ, Fernandes G. Combination of conjugated linoleic acid with fish oil prevents age-associated bone marrow adiposity in C57Bl/6J mice. *J Nutr Biochem*. (2011) 22:459–69. doi: 10.1016/j.jnutbio.2010.03.015
180. Plummer J, Park M, Perodin F, Horowitz MC, Hens JR. Methionine-restricted diet increases miRNAs that can target RUNX2 expression and alters bone structure in young mice. *J Cell Biochem*. (2017) 118:31–42. doi: 10.1002/jcb.25604
181. Hamrick MW, Della-Fera MA, Choi YH, Pennington C, Hartzell D, Baile CA. Leptin treatment induces loss of bone marrow adipocytes and increases bone formation in leptin-deficient ob/ob mice. *J Bone Miner Res*. (2005) 20:994–1001. doi: 10.1359/JBMR.050103
182. Motyl KJ, Mccabe LR. Leptin treatment prevents type I diabetic marrow adiposity but not bone loss in mice. *J Cell Physiol*. (2009) 218:376–84. doi: 10.1002/jcp.21608
183. Devlin MJ, Brooks DJ, Conlon C, Vliet M, Louis L, Rosen CJ, et al. Daily leptin blunts marrow fat but does not impact bone mass in calorie-restricted mice. *J Endocrinol*. (2016) 229:295–306. doi: 10.1530/JOE-15-0473
184. Hamrick MW, Della Fera MA, Choi YH, Hartzell D, Pennington C, Baile CA. Injections of leptin into rat ventromedial hypothalamus increase adipocyte apoptosis in peripheral fat and in bone marrow. *Cell Tissue Res*. (2007) 327:133–41. doi: 10.1007/s00441-006-0312-3
185. Lindenmaier LB, Philbrick KA, Branscum AJ, Kalra SP, Turner RT, Iwaniec UT. Hypothalamic leptin gene therapy reduces bone marrow adiposity in ob/ob mice fed regular and high-fat diets. *Front Endocrinol.* (2016) 7:110. doi: 10.3389/fendo.2016.00110
186. Sottile V, Seuwen K, Kneissel M. Enhanced marrow adipogenesis and bone resorption in estrogen-deprived rats treated with the PPARgamma agonist BRL49653 (rosiglitazone). *Calcif Tissue Int*. (2004) 75:329–37. doi: 10.1007/s00223-004-0224-8
187. Tornvig L, Mosekilde LI, Justesen J, Falk E, Kassem M. Troglitazone treatment increases bone marrow adipose tissue volume but does not affect trabecular bone volume in mice. *Calcif Tissue Int*. (2001) 69:46–50. doi: 10.1007/s002230020018
188. Lazarenko OP, Rzonca SO, Hogue WR, Swain FL, Suva LJ, Lecka-Czernik B. Rosiglitazone induces decreases in bone mass and strength that are reminiscent of aged bone. *Endocrinology*. (2007) 148:2669–80. doi: 10.1210/en.2006-1587
189. Styner M, Pagnotti GM, Galior K, Wu X, Thompson WR, Uzer G, et al. Exercise regulation of marrow fat in the setting of PPARγ agonist treatment in female C57BL/6 mice. *Endocrinology.* (2015) 156:2753–61. doi: 10.1210/en.2015-1213
190. Ackert-Bicknell CL, Shockley KR, Horton LG, Lecka-Czernik B, Churchill GA, Rosen CJ. Strain-specific effects of rosiglitazone on bone mass, body composition, and serum insulin-like growth factor-I. *Endocrinology*. (2009) 150:1330–40. doi: 10.1210/en.2008-0936
191. Sulston RJ, Learman BS, Zhang B, Scheller EL, Parlee SD, Simon BR, et al. Increased circulating adiponectin in response to thiazolidinediones: investigating the role of bone marrow adipose tissue. *Front Endocrinol.* (2016) 7:128. doi: 10.3389/fendo.2016.00128
192. Botolin S, Mccabe LR. Inhibition of PPARgamma prevents type I diabetic bone marrow adiposity but not bone loss. *J Cell Physiol*. (2006) 209:967–76. doi: 10.1002/jcp.20804
193. Naveiras O, Nardi V, Wenzel PL, Hauschka PV, Fahey F, Daley GQ. Bone-marrow adipocytes as negative regulators of the haematopoietic microenvironment. *Nature*. (2009) 460:259–63. doi: 10.1038/nature 08099
194. Zhu RJ, Wu MQ, Li ZJ, Zhang Y, Liu KY. Hematopoietic recovery following chemotherapy is improved by BADGE-induced inhibition of adipogenesis. *Int J Hematol*. (2013) 97:58–72. doi: 10.1007/s12185-012-1233-4
195. Luo Y, Chen GL, Hannemann N, Ipseiz N, Kronke G, Bauerle T, et al. Microbiota from obese mice regulate hematopoietic stem cell differentiation by altering the bone niche. *Cell Metab*. (2015) 22:886–94. doi: 10.1016/j.cmet.2015.08.020
196. Sato K, Feng X, Chen J, Li J, Muranski P, Desierto MJ, et al. PPARgamma antagonist attenuates mouse immune-mediated bone marrow failure by inhibition of T cell function. *Haematologica*. (2016) 101:57–67. doi: 10.3324/haematol.2014.121632
197. Li J, Zhang N, Huang X, Xu J, Fernandes JC, Dai K, et al. Dexamethasone shifts bone marrow stromal cells from osteoblasts to adipocytes by C/EBPalpha promoter methylation. *Cell Death Dis.* (2013) 4:e832. doi: 10.1038/cddis.2013.348.
198. Calvo W, Fliedner TM, Herbst E, Hugl E, Bruch C. Regeneration of blood-forming organs after autologous leukocyte transfusion in lethally irradiated dogs. II Distribution and cellularity of the marrow in irradiated and transfused animals. *Blood*. (1976) 47:593–601. doi: 10.1182/blood.V47.4.593.593
199. Kalajzic Z, Li H, Wang L-P, Jiang X, Lamothe K, Adams DJ, et al. Use of an alpha-smooth muscle actin GFP reporter to identify an osteoprogenitor population. *Bone*. (2008) 43:501–10. doi: 10.1016/j.bone.2008.04.023
200. Mizoguchi T, Pinho S, Ahmed J, Kunisaki Y, Hanoun M, Mendelson A, et al. Osterix marks distinct waves of primitive and definitive stromal progenitors during bone marrow development. *Dev Cell*. (2014) 29:340–9. doi: 10.1016/j.devcel.2014.03.013
201. Zhou BO, Yue R, Murphy MM, Peyer JG, Morrison SJ. Leptin-receptor-expressing mesenchymal stromal cells represent the main source of bone formed by adult bone marrow. *Cell Stem Cell*. (2014) 15:154–68. doi: 10.1016/j.stem.2014.06.008
202. Horowitz MC, Berry R, Holtrup B, Sebo Z, Nelson T, Fretz JA, et al. Bone marrow adipocytes. *Adipocyte*. (2017) 6:193–204. doi: 10.1080/21623945.2017.1367881
203. Kretzschmar K, Watt FM. Lineage tracing. *Cell*. (2012) 148:33–45. doi: 10.1016/j.cell.2012.01.002
204. Sanchez-Gurmaches J, Hsiao WY, Guertin DA. Highly selective *in vivo* labeling of subcutaneous white adipocyte precursors with Prx1-Cre. *Stem Cell Rep*. (2015) 4:541–50. doi: 10.1016/j.stemcr.2015.02.008
205. Hammad S, Othman A, Meyer C, Telfah A, Lambert J, Dewidar B, et al. Confounding influence of tamoxifen in mouse models of Cre recombinase-induced gene activity or modulation. *Arch Toxicol.* (2018) 92:2549–61. doi: 10.1007/s00204-018-2254-4
206. Perry MJ, Gujra S, Whitworth T, Tobias JH. Tamoxifen stimulates cancellous bone formation in long bones of female mice. *Endocrinology.* (2005) 146:1060–5. doi: 10.1210/en.2004-1114
207. Ye R, Wang QA, Tao C, Vishvanath L, Shao M, McDonald JG, et al. Impact of tamoxifen on adipocyte lineage tracing: Inducer of adipogenesis and prolonged nuclear translocation of Cre recombinase. *Mol Metab.* (2015) 4:771–8. doi: 10.1016/j.molmet.2015.08.004
208. Soriano P. Generalized lacZ expression with the ROSA26 Cre reporter strain. *Nat Genet*. (1999) 21:70–1. doi: 10.1038/5007
209. Muzumdar MD, Tasic B, Miyamichi K, Li L, Luo L. A global double-fluorescent cre reporter mouse. *Genesis.* (2007) 605:593–605. doi: 10.1002/dvg.20335
210. Jeffery E, Berry R, Church CD, Yu S, Shook BA, Horsley V, et al. Characterization of Cre recombinase models for the study of adipose tissue. *Adipocyte*. (2014) 3:206–11. doi: 10.4161/adip.29674
211. Sanchez-Gurmaches J, Hung CM, Guertin DA. Emerging complexities in adipocyte origins and identity. *Trends Cell Biol*. (2016) 26:313–26. doi: 10.1016/j.tcb.2016.01.004
212. Keune JA, Wong CP, Branscum AJ, Iwaniec UT, Turner RT. Bone marrow adipose tissue deficiency increases disuse-induced bone loss in male mice. *Sci Rep.* (2017) 7:46325. doi: 10.1038/srep46325

213. Walji TA, Turecamo SE, Sanchez AC, Anthony BA, Abou-Ezzi G, Scheller EL, et al. Marrow adipose tissue expansion coincides with insulin resistance in MAGP1-deficient mice. *Front Endocrinol (Lausanne)*. (2016) 7:87. doi: 10.3389/fendo.2016.00087
214. Belavy DL, Quittner MJ, Ridgers ND, Shiekh A, Rantalainen T, Trudel G. Specific modulation of vertebral marrow adipose tissue by physical activity. *J Bone Miner Res*. (2018) 33:651–7. doi: 10.1002/jbmr.3357
215. Mayo-Smith W, Rosenthal DI, Goodsitt MM, Klibanski A. Intravertebral fat measurement with quantitative CT in patients with Cushing disease and anorexia nervosa. *Radiology*. (1989) 170:835–8. doi: 10.1148/radiology.170.3.2916039
216. Bredella MA, Fazeli PK, Miller KK, Misra M, Torriani M, Thomas BJ, et al. Increased bone marrow fat in anorexia nervosa. *J Clin Endocrinol Metab*. (2009) 94:2129–36. doi: 10.1210/jc.2008-2532
217. Moore SG, Dawson KL. Red and yellow marrow in the femur: age-related changes in appearance at MR imaging. *Radiology*. (1990) 175:219–23. doi: 10.1148/radiology.175.1.2315484
218. Hamrick MW, Pennington C, Newton D, Xie D, Isales C. Leptin deficiency produces contrasting phenotypes in bones of the limb and spine. *Bone*. (2004) 34:376–83. doi: 10.1016/j.bone.2003.11.020
219. Yue R, Zhou BO, Shimada IS, Zhao Z, Morrison SJ. Leptin receptor promotes adipogenesis and reduces osteogenesis by regulating mesenchymal stromal cells in adult bone marrow. *Cell Stem Cell*. (2016) 18:782–96. doi: 10.1016/j.stem.2016.02.015
220. Takeshita S, Fumoto T, Naoe Y, Ikeda K. Age-related marrow adipogenesis is linked to increased expression of RANKL. *J Biol Chem*. (2014) 289:16699–710. doi: 10.1074/jbc.M114.547919
221. Justesen J, Stenderup K, Ebbesen EN, Mosekilde L, Steiniche T, Kassem M. Adipocyte tissue volume in bone marrow is increased with aging and in patients with osteoporosis. *Biogerontology*. (2001) 2:165–71. doi: 10.1023/A:1011513223894
222. Tuljapurkar SR, Mcguire TR, Brusnahan SK, Jackson JD, Garvin KL, Kessinger MA, et al. Changes in human bone marrow fat content associated with changes in hematopoietic stem cell numbers and cytokine levels with aging. *J Anat*. (2011) 219:574–81. doi: 10.1111/j.1469-7580.2011.01423.x
223. Bani Hassan E, Demontiero O, Vogrin S, Ng A, Duque G. Marrow adipose tissue in older men: association with visceral and subcutaneous fat, bone volume, metabolism, and inflammation. *Calcif Tissue Int*. (2018) 103:164–74. doi: 10.1007/s00223-018-0412-6
224. Martin RB, Zissimos SL. Relationships between marrow fat and bone turnover in ovariectomized and intact rats. *Bone*. (1991) 12:123–31. doi: 10.1016/8756-3282(91)90011-7
225. Baum T, Rohrmeier A, Syvari J, Diefenbach MN, Franz D, Dieckmeyer M, et al. Anatomical variation of age-related changes in vertebral bone marrow composition using chemical shift encoding-based water-fat magnetic resonance imaging. *Front Endocrinol.* (2018) 9:141. doi: 10.3389/fendo.2018.00141
226. Limonard EJ, Veldhuis-Vlug AG, Van Dussen L, Runge JH, Tanck MW, Endert E, et al. Short-term effect of estrogen on human bone marrow fat. *J Bone Miner Res*. (2015) 30:2058–66. doi: 10.1002/jbmr.2557
227. Maurice F, Dutour A, Vincentelli C, Abdesselam I, Bernard M, Dufour H, et al. Active cushing syndrome patients have increased ectopic fat deposition and bone marrow fat content compared to cured patients and healthy subjects: a pilot 1H-MRS study. *Eur J Endocrinol*. (2018) 179:307–17. doi: 10.1530/EJE-18-0318
228. Li H, Li H, Guo H, Liu F. Cholesterol suppresses adipocytic differentiation of mouse adipose-derived stromal cells via PPARgamma2 signaling. *Steroids*. (2013) 78:454–61. doi: 10.1016/j.steroids.2013.02.009
229. Yang Y, Luo X, Xie X, Yan F, Chen G, Zhao W, et al. Influences of teriparatide administration on marrow fat content in postmenopausal osteopenic women using MR spectroscopy. *Climacteric*. (2016) 19:285–91. doi: 10.3109/13697137.2015.1126576
230. Maridas DE, Rendina-Ruedy E, Helderman RC, Demambro VE, Brooks D, Guntur AR, et al. Progenitor recruitment and adipogenic lipolysis contribute to the anabolic actions of parathyroid hormone on the skeleton. *FASEB J*. (2019) 33:2885–98. doi: 10.1096/fj.201800948RR
231. Menagh PJ, Turner RT, Jump DB, Wong CP, Lowry MB, Yakar S, et al. Growth hormone regulates the balance between bone formation and bone marrow adiposity. *J Bone Min Res*. (2010) 25:757–68. doi: 10.1359/jbmr.091015
232. Bredella MA, Torriani M, Ghomi RH, Thomas BJ, Brick DJ, Gerweck AV, et al. Vertebral bone marrow fat is positively associated with visceral fat and inversely associated with IGF-1 in obese women. *Obesity*. (2011) 19:49–53. doi: 10.1038/oby.2010.106
233. Bredella MA, Gerweck AV, Barber LA, Breggia A, Rosen CJ, Torriani M, et al. Effects of growth hormone administration for 6 months on bone turnover and bone marrow fat in obese premenopausal women. *Bone*. (2014) 62:29–35. doi: 10.1016/j.bone.2014.01.022
234. Cawthorn WP, Scheller EL, Learman BS, Parlee SD, Simon BR, Mori H, et al. Bone marrow adipose tissue is an endocrine organ that contributes to increased circulating adiponectin during caloric restriction. *Cell Metab*. (2014) 20:368–75. doi: 10.1016/j.cmet.2014.06.003
235. Lazarenko OP, Rzonca SO, Suva LJ, Lecka-Czernik B. Netoglitazone is a PPAR-gamma ligand with selective effects on bone and fat. *Bone*. (2006) 38:74–84. doi: 10.1016/j.bone.2005.07.008
236. Lu W, Wang W, Wang S, Feng Y, Liu K. Rosiglitazone promotes bone marrow adipogenesis to impair myelopoiesis under stress. *PLoS ONE*. (2016) 11:e0149543. doi: 10.1371/journal.pone.0149543
237. Cock TA, Back J, Elefteriou F, Karsenty G, Kastner P, Chan S, et al. Enhanced bone formation in lipodystrophic PPARgamma(hyp/hyp) mice relocates haematopoiesis to the spleen. *EMBO Rep*. (2004) 5:1007–12. doi: 10.1038/sj.embor.7400254
238. Wilson A, Fu H, Schiffrin M, Winkler C, Koufany M, Jouzeau JY, et al. Lack of adipocytes alters hematopoiesis in lipodystrophic mice. *Front Immunol*. (2018) 9:2573. doi: 10.3389/fimmu.2018.02573
239. Mattiucci D, Naveiras O, Poloni A. Bone marrow "yellow" and "red" adipocytes: good or bad cells? *Curr Mol Biol Rep*. (2018) 4:117–22. doi: 10.1007/s40610-018-0098-6
240. Cuminetti V, Arranz L. Bone marrow adipocytes: the enigmatic components of the hematopoietic stem cell niche. *J Clin Med*. (2019) 8:707. doi: 10.3390/jcm8050707
241. Seimandi M, Lemaire G, Pillon A, Perrin A, Carlavan I, Voegel JJ, et al. Differential responses of PPARalpha, PPARdelta, and PPARgamma reporter cell lines to selective PPAR synthetic ligands. *Analyt Biochem*. (2005) 344:8–15. doi: 10.1016/j.ab.2005.06.010
242. Desdoits-Lethimonier C, Lesne L, Gaudriault P, Zalko D, Antignac JP, Deceuninck Y, et al. Parallel assessment of the effects of bisphenol A and several of its analogs on the adult human testis. *Hum Reprod*. (2017) 32:1465–73. doi: 10.1093/humrep/dex093
243. Van Leeuwen SP, Bovee TF, Awchi M, Klijnstra MD, Hamers AR, Hoogenboom RL, et al. BPA, BADGE and analogues: a new multi-analyte LC-ESI-MS/MS method for their determination and their *in vitro* (anti)estrogenic and (anti)androgenic properties. *Chemosphere*. (2019) 221:246–53. doi: 10.1016/j.chemosphere.2018.12.189
244. Bolan PJ, Arentsen L, Sueblinvong T, Zhang Y, Moeller S, Carter JS, et al. Water-fat MRI for assessing changes in bone marrow composition due to radiation and chemotherapy in gynecologic cancer patients. *J Magn Reson Imaging*. (2013) 38:1578–84. doi: 10.1002/jmri.24071
245. Geissler EN, Russell ES. Analysis of the hematopoietic effects of new dominant spotting (W) mutations of the mouse. I. Influence upon hematopoietic stem cells. *Exp Hematol*. (1983) 11:452–60.
246. Potter JE, Wright EG. Bone marrow lipids in normal and anemic mice. *Am J Hematol*. (1980) 8:361–7. doi: 10.1002/ajh.2830080404
247. Chen JR, Lazarenko OP, Wu X, Tong Y, Blackburn ML, Shankar K, et al. Obesity reduces bone density associated with activation of PPARgamma and suppression of Wnt/beta-catenin in rapidly growing male rats. *PLoS ONE*. (2010) 5:e13704. doi: 10.1371/journal.pone.0013704
248. Wang J, Chen GL, Cao S, Zhao MC, Liu YQ, Chen XX, et al. Adipogenic niches for melanoma cell colonization and growth in bone marrow. *Lab Invest*. (2017) 97:737–45. doi: 10.1038/labinvest.2017.14

249. Boyd AL, Reid JC, Salci KR, Aslostovar L, Benoit YD, Shapovalova Z, et al. Acute myeloid leukaemia disrupts endogenous myelo-erythropoiesis by compromising the adipocyte bone marrow niche. *Nat Cell Biol*. (2017) 19:1336–47. doi: 10.1038/ncb3625
250. Cahu X, Carre M, Recher C, Pigneux A, Hunault-Berger M, Vey N, et al. Impact of body-surface area on patients' outcome in younger adults with acute myeloid leukemia. *Eur J Haematol*. (2017) 98:443–9. doi: 10.1111/ejh.12850
251. Lu W, Weng W, Zhu Q, Zhai Y, Wan Y, Liu H, et al. Small bone marrow adipocytes predict poor prognosis in acute myeloid leukemia. *Haematologica*. (2018) 103:e21–4. doi: 10.3324/haematol.2017.173492
252. Huggins C, Blocksom BH. Changes in outlying bone marrow accompanying a local increase of temperature within physiological limits. *J Exp Med*. (1936) 64:253–74. doi: 10.1084/jem.64.2.253
253. Suchacki KJ, Cawthorn WP. Molecular interaction of bone marrow adipose tissue with energy metabolism. *Curr Mol Biol Rep*. (2018) 4:41–9. doi: 10.1007/s40610-018-0096-8
254. Cannon B, Nedergaard J. Nonshivering thermogenesis and its adequate measurement in metabolic studies. *J Exp Biol*. (2011) 214:242–53. doi: 10.1242/jeb.050989
255. Iwaniec UT, Philbrick KA, Wong CP, Gordon JL, Kahler-Quesada AM, Olson DA, et al. Room temperature housing results in premature cancellous bone loss in growing female mice: implications for the mouse as a preclinical model for age-related bone loss. *Osteoporosis Int*. (2016) 27:3091–101. doi: 10.1007/s00198-016-3634-3

Conflict of Interest: AV-V and ON are co-chairs and JT is coordinator of the BMAS Working Group in methodologies. BP, BE, CR, ED, and ON are members of the BMAS Executive Board. AV-V, DK, ES, GK, and MH are members of the BMAS Scientific Board.

The remaining authors declare that the research was conducted in the absence of any commercial or financial relationships that could be construed as a potential conflict of interest.

frontiers in Endocrinology

ORIGINAL RESEARCH
published: 17 March 2020
doi: 10.3389/fendo.2020.00117

Effects of Propranolol on Bone, White Adipose Tissue, and Bone Marrow Adipose Tissue in Mice Housed at Room Temperature or Thermoneutral Temperature

Russell T. Turner[1,2], *Kenneth A. Philbrick*[1], *Carmen P. Wong*[1], *Amanda R. Gamboa*[1], *Adam J. Branscum*[3] *and Urszula T. Iwaniec*[1,2]*

[1] *Skeletal Biology Laboratory, School of Biological and Population Health Sciences, Oregon State University, Corvallis, OR, United States,* [2] *Center for Healthy Aging Research, Oregon State University, Corvallis, OR, United States,* [3] *Biostatistics Program, School of Biological and Population Health Sciences, Oregon State University, Corvallis, OR, United States*

Growing female mice housed at room temperature (22°C) weigh the same but differ in body composition compared to mice housed at thermoneutrality (32°C). Specifically, mice housed at room temperature have lower levels of white adipose tissue (WAT). Additionally, bone marrow adipose tissue (bMAT) and cancellous bone volume fraction in distal femur metaphysis are lower in room temperature-housed mice. The metabolic changes induced by sub-thermoneutral housing are associated with lower leptin levels in serum and higher levels of *Ucp1* gene expression in brown adipose tissue. Although the precise mechanisms mediating adaptation to sub-thermoneutral temperature stress remain to be elucidated, there is evidence that increased sympathetic nervous system activity acting via β-adrenergic receptors plays an important role. We therefore evaluated the effect of the non-specific β-blocker propranolol (primarily β_1 and β_2 antagonist) on body composition, femur microarchitecture, and bMAT in growing female C57BL/6 mice housed at either room temperature or thermoneutral temperature. As anticipated, cancellous bone volume fraction, WAT and bMAT were lower in mice housed at room temperature. Propranolol had small but significant effects on bone microarchitecture (increased trabecular number and decreased trabecular spacing), but did not attenuate premature bone loss induced by room temperature housing. In contrast, propranolol treatment prevented housing temperature-associated differences in WAT and bMAT. To gain additional insight, we evaluated a panel of genes in tibia, using an adipogenesis PCR array. Housing temperature and treatment with propranolol had exclusive as well as shared effects on gene expression. Of particular interest was the finding that room temperature housing reduced, whereas propranolol increased, expression of the gene for acetyl-CoA carboxylase (*Acacb*), the rate-limiting step for fatty acid synthesis and a key regulator of β-oxidation. Taken together, these findings provide evidence that increased activation of β_1 and/or β_2 receptors contributes to reduced bMAT by regulating adipocyte metabolism, but that this pathway is unlikely to be responsible for premature cancellous bone loss in room temperature-housed mice.

Keywords: β-adrenergic, non-shivering thermogenesis, thermoneutral, cancellous bone, premature bone loss

OPEN ACCESS

Edited by:
Nathalie Bravenboer, VU University Medical Center, Netherlands

Reviewed by:
Erica L. Scheller, Washington University in St. Louis, United States
Ormond A. MacDougald, University of Michigan, United States

***Correspondence:**
Urszula T. Iwaniec
urszula.iwaniec@oregonstate.edu

Specialty section:
This article was submitted to Bone Research, a section of the journal Frontiers in Endocrinology

Received: *11 June 2019*
Accepted: *21 February 2020*
Published: *17 March 2020*

Citation:
Turner RT, Philbrick KA, Wong CP, Gamboa AR, Branscum AJ and Iwaniec UT (2020) Effects of Propranolol on Bone, White Adipose Tissue, and Bone Marrow Adipose Tissue in Mice Housed at Room Temperature or Thermoneutral Temperature. Front. Endocrinol. 11:117. doi: 10.3389/fendo.2020.00117

INTRODUCTION

The thermoneutral zone, also called the zone of thermal comfort, is the temperature range where the resting rate of heat production is in equilibrium with the rate of heat loss to the environment. The thermoneutral range varies among species and is ∼10°C higher for mice than for humans (1). Environmental temperatures outside the thermoneutral zone induce adaptive responses in homeothermic animals to preserve core body temperature (e.g., shivering to increase body temperature and sweating/panting to decrease body temperature). In contrast to humans and larger rodents such as rats, mice are not strict homeotherms, but instead function as daily facultative heterotherms. This fundamental difference in energy homeostasis contributes to important differences in physiology between mice and humans. Daily torpor, where decreases in body temperature result in energy savings, is a common strategy utilized by mice and other small mammals to cope with low environmental temperatures and fluctuations in food availability (2). Cold stress induced by housing mice at standard room temperature results in physiological changes that can influence experimental outcomes. Tumor growth, for example, is significantly greater in mice housed at room temperature than in mice housed at thermoneutrality, and anti-tumor immune response is suppressed at room temperature (3). Furthermore, chronic stress induced by housing mice at room temperature increases the resistance of hematopoietic stem and progenitor cells to total body radiation-induced apoptosis (4). The impact of cold stress on response to tumor growth and radiation in the aforementioned studies depends on β-adrenergic signaling and is antagonized by treatment with propranolol, a non-specific antagonist of β-adrenergic receptors (3, 4).

When housed at room temperature, C57BL/6 mice of both sexes exhibit rapid loss of cancellous bone prior to cessation of linear bone growth (5–7). Importantly, housing mice at thermoneutrality prevents the premature bone loss (6, 7). The lower cancellous bone volume fraction in distal femur of mice housed at room temperature compared to mice housed at thermoneutrality is due, in part, to decreased bone formation; osteoblast-lined bone perimeter, bone formation rate measured using fluorochrome labels, mRNA levels for bone matrix proteins, and serum osteocalcin are lower in mice housed at room temperature. In contrast, osteoclast-lined bone perimeter is higher, suggesting locally increased bone resorption (7). Bone formation and cancellous bone volume fraction are often inversely associated with bone marrow adiposity (8–15). However, an inverse relationship was not observed with housing temperature; female mice housed at room temperature had lower bone formation as well as lower bMAT compared to mice housed at thermoneutrality, whereas male mice had lower bone formation but did not exhibit differences in bMAT (6, 7).

Bone is innervated and bone growth and turnover balance is regulated, in part, via sensory and sympathetic signaling (16). β-adrenergic receptors are located in skeletal tissue (17) and treatment with propranolol is reported to influence bone mass in some animal models (17–21) and increase fat accrual in humans (22, 23). Thermogenesis induced by cold stress is mediated, at least in part, by increased sympathetic outflow from the hypothalamus to peripheral tissues, including brown adipose tissue (BAT) (24). The purpose of this study was to assess the role of β-adrenergic signaling (by blocking β-adrenergic receptors with propranolol) in mediating the differential effects of housing temperature on body composition, bone, and bMAT levels in female mice.

MATERIALS AND METHODS

Experimental Design

The Institutional Animal Care and Use Committee approved the experimental protocol used in this study and animals were maintained in accordance with the NIH Guide for the Care and the Use of Laboratory Animals. A total of 40, 4-week-old, female C57BL/6 (B6) mice were obtained from Jackson Laboratory (Bar Harbor, ME, USA) and housed individually in a room on a 12 h light:12 h dark cycle. Food (Teklad 8604, Harlen Laboratories, Indianapolis, IN) and water were provided *ad libitum* to all animals. Body weight and food consumption were measured weekly for the 14-week duration of study.

Mice were randomized by weight into one of four groups, 22°C ± propranolol or 32°C ± propranolol ($n = 10$/group), and maintained at their respective temperatures and treatments until 18 weeks of age. Propranolol (Sigma, St. Louis) was administered in drinking water (0.5 g/l, pH 3.0) using aluminum foil-covered drinking tubes. Control mice received acidified water (vehicle). Water was changed twice/week. Water consumption was calculated as ml/d and the dose rate of propranolol calculated as mg/g/d. This method of delivery and dose of propranolol was chosen because it has been shown to be effective in blocking β_1 and β_2 but not β_3 adrenergic receptors (25–27).

Mice were anesthetized with 2–3% isoflurane delivered in oxygen and body composition determined immediately prior to sacrifice. The mice were bled by cardiac puncture. Serum was collected and stored at −80°C for measurement of leptin and global markers of bone turnover. Abdominal white adipose tissue (WAT) and uteri were excised and weighed. Femora were removed, fixed overnight in 10% formalin, and stored in 70% ethanol for microcomputed tomography (μCT) and histomorphometric analyses. Tibiae and brown adipose tissue (BAT) were removed, frozen in liquid nitrogen, and stored at −80°C for mRNA analysis.

Serum Chemistry

Serum leptin was measured using Mouse Leptin Quantikine ELISA Kit (R&D Systems, Minneapolis, MN), serum osteocalcin was measured using Mouse Gla-Osteocalcin High Sensitive EIA Kit (Clontech, Mountain View, CA), and serum CTX-1 was measured using Mouse CTX-1 ELISA kit (Life Sciences Advanced Technologies, Petersburg, FL) according to the respective manufacturer's protocol.

Dual Energy X-Ray Absorptiometry

Percent body fat was determined using dual energy x-ray absorptiometry (DXA) (Piximus, Lunar Corp., Madison, WI, USA).

Microcomputed Tomography

Bone volume and architecture were assessed using μCT. We scanned right femora in 70% ethanol using a Scanco μCT40 scanner (Scanco Medical AG, Basserdorf, Switzerland) at a voxel size of 12 μm on a side (55 kVp x-ray voltage, 145 μA intensity, and 200 ms integration time). We set filtering parameters sigma and support to 0.8 and 1, respectively. Bone segmentation was conducted at a threshold of 245 (scale, 0–1,000) determined empirically. Total femur mineralized tissue volume (cancellous + cortical bone) was evaluated first. This was followed by evaluation of cancellous bone in the distal femur metaphysis. For the femoral metaphysis, 42 consecutive slices (504 μm) of cancellous bone, 45 slices (540 μm) proximal to the growth plate/metaphysis boundary, were evaluated. We used irregular manual contouring a few pixels interior to the endocortical surface to delineate cancellous from cortical bone. Direct cancellous bone measurements included cancellous bone volume fraction (bone volume/tissue volume, %), connectivity density (mm^{-3}), trabecular thickness (μm), trabecular number (mm^{-1}), and trabecular separation (μm).

Histomorphometry

Methods used for measuring bone histomorphometry have been described (28) with modifications for mice (29). Briefly, distal right femora were dehydrated in a graded series of ethanol and xylene, and embedded undecalcified in modified methyl methacrylate. A vertical bed microtome (Leica 2065) was used to cut coronal sections (4 μm thick), which were then affixed to slides precoated with 1% gelatin solution. One section/animal was stained for tartrate resistant acid phosphatase, counterstained with toluidine blue (Sigma, St. Louis), and used for cell-based measurements. All data were collected with a 20x objective using the OsteoMeasure System (OsteoMetrics, Inc., Atlanta, GA). The sampling site for the distal femoral metaphysis was located 0.25–1.25 mm proximal to the growth plate and 0.1 mm from cortical bone.

Cell-based measurements included osteoblast perimeter (osteoblast perimeter/bone perimeter, %), osteoclast perimeter (osteoclast perimeter/bone perimeter, %), marrow adipocyte area fraction (adipocyte area/tissue area, %), adipocyte density (number of adipocytes/tissue area, #/mm^2) and adipocyte size (μm^2). Osteoblasts were identified morphologically as plump cuboidal cells immediately adjacent to a thin layer of osteoid in direct contact with the bone perimeter. Osteoclasts were identified as multinucleated (two or more nuclei) cells with acid phosphatase positive (red-stained) cytoplasm in contact with the bone perimeter. Adipocytes were identified as large circular or oval-shaped cells bordered by a prominent cell membrane and lacking cytoplasmic staining due to alcohol extraction of intracellular lipids during processing. This method has been previously validated by fat extraction and analysis (30). All bone histomorphometric data are reported using standard 2-dimensional nomenclature (31).

Gene Expression

Tibiae ($n = 8$/group) were pulverized with a mortar and pestle in liquid nitrogen and homogenized in Trizol (Life Technologies, Grand Island, NY). Total RNA was isolated according to the manufacturer's protocol, and mRNA was reverse transcribed into cDNA using SuperScript III First-Strand Synthesis SuperMix for qRT-PCR (Life Technologies). Gene expression for a panel of genes related to adipocyte differentiation and function (Mouse Adipogenesis RT2 Profiler PCR Array, PAMM-049ZE-4) was determined according to the manufacturer's protocol (Qiagen, Valencia, CA). Gene expression was normalized to GAPDH. Relative quantification was determined (ΔΔCt method) using RT2 Profiler PCR Array Data Analysis software version 3.5 (Qiagen). Fold-change was calculated relative to mice housed at 32°C as the reference control. Specifically, we compared changes in tibia gene expression in (1) mice housed at 22°C relative to mice housed at 32°C and (2) mice housed at 22°C and treated with propranolol relative to mice housed at 32°C to identify overlap between genes differentially expressed in response to sub-thermoneutral housing or propranolol. Furthermore, the expression of additional genes (*Adrb1, Adrb3, Alpl*, and *Bglap*) was determined using gene-specific primers (*Adrb1* - for: CTCATCGTGGTGGGTAACGTG, rev: ACACACAGCACA TCTACCGAA; *Adrb3* – for: GGCCCTCTCTAGTTCCCAG, rev: TAGCCATCAAACCTGTTGAGC; *Alpl* – Qiagen RT² qPCR Primer Assay PPM03155A; *Bglap*– Qiagen RT² qPCR Primer Assay PPM04465F), and changes in gene expression between treatment groups were analyzed using the ΔΔCt method as described above.

Statistical Analysis

A 2×2 factorial experimental design was used with mice randomized to a temperature group (22 or 32°C) and treatment group (vehicle control or propranolol). Mean comparisons were made using a two-factor linear model with an interaction between temperature and treatment. Residual analysis, Levene's test for homogeneity of variance, and Anderson-Darling tests of normality were used to assess the conditions for use of a linear model. A general linear model with unequal variances for the temperature groups, treatment groups, or both temperature and treatment groups (i.e., four distinct variance parameters) was used when the assumption of homogeneity of variance was violated. When interaction was present, inference focused on comparing temperature groups separately for vehicle and propranolol treated mice (i.e., focusing on how treatment modified the effect of temperature). The Benjamini and Hochberg (32) method for maintaining the false discovery rate at 5% was used to adjust for multiple comparisons. Differences were considered significant at $p \leq 0.05$. All data are presented as mean ± SE. Data analysis was performed using R version 3.4.3.

RESULTS

The daily dose of propranolol—administered in drinking water—in mice housed at room temperature (22°C) or thermoneutral temperature (32°C) is shown in **Figure 1**. When averaged over the 14 weeks of study, mice housed at 22 and 32°C consumed 0.13 ± 0.01 mg/g/d and 0.14 ± 0.01mg/g/d of propranolol, respectively.

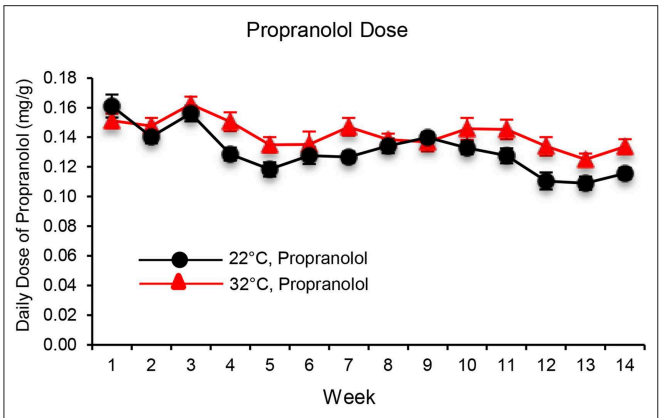

FIGURE 1 | The daily dose of propranolol—administered in drinking water—in mice housed at room temperature (22°C) and thermoneutral temperature (32°C) over the 14-week duration of study. Data are mean ± SE. $N = 10$/group.

The respective effects of housing temperature and propranolol treatment on food and body weight, body composition, serum chemistry, and *Ucp1* gene expression in BAT are shown in **Figure 2**. Mice housed at room temperature consumed more food per day than mice housed at thermoneutrality (panel A), resulting in 91% increase in cumulative food intake (panel B). However, housing temperature had no effect on body weight (panels C and D). Treatment with propranolol had no effect on daily or cumulative food intake or on body weight and no housing temperature x treatment interactions were noted for the aforementioned endpoints. Interactions between housing temperature and treatment were detected for percent body fat (panel E), abdominal WAT weight (panel F), and serum leptin levels (panel H); treatment with propranolol prevented the differential effects of housing temperature on these endpoints. Room temperature-housed mice had higher uterine weight (panel G). Finally, room temperature-housed mice had higher blood glucose (panel I) and higher BAT *Ucp1* gene expression (panel J), endpoints not influenced by propranolol treatment.

The respective effects of housing temperature and treatment with propranolol on bone microarchitecture in the distal femur metaphysis are shown in **Figure 3**. Mice housed at room temperature had lower bone volume fraction (panel A), connectivity density (panel B), trabecular thickness (panel C), and trabecular number (panel D), and higher trabecular separation (panel E). Treatment with propranolol resulted in higher trabecular number and lower trabecular separation. No housing temperature × treatment interactions were detected for any of the measured indices of bone microarchitecture.

The respective effects of housing temperature and treatment with propranolol on osteoblast perimeter, osteoclast perimeter and indices of bone marrow adiposity in distal femur metaphysis are shown in **Figure 4**. Mice housed at room temperature had lower osteoblast perimeter (panel A) and higher osteoclast perimeter (panel B). Interactions between housing temperature and treatment were detected for adipocyte area fraction (panel C) and adipocyte density (panel D); specifically, treatment with propranolol prevented the differential effects of housing temperature on both indices of marrow adiposity. However, neither housing temperature nor treatment altered adipocyte size. The differences in histomorphometry can be appreciated in the representative micrographs shown in panels F–I.

The respective effects of housing temperature and treatment with propranolol on serum osteocalcin and CTX-1 are shown in **Figure 5**. An interaction between housing temperature and treatment was noted for osteocalcin; the differential effects of housing temperature were attenuated by treatment with propranolol. Neither temperature nor treatment with propranolol had an effect on serum CTX-1.

The respective effects of housing temperature and treatment on expression of a panel of 84 genes (adipogenesis PCR array), including *Adrb2* (β-adrenergic receptor 2), in tibia of mice housed at 22°C ± propranolol relative to mice housed at 32°C are shown in **Figure 6**. Housing temperature resulted in differential expression of 27 genes (22°C Veh vs. 32°C Veh); 12 of these genes were not differentially expressed in mice housed at 22°C and treated with propranolol and included genes for hormones (*Adipoq, Lep*), transcription factors and enhancer proteins (*Cebpb, Dkk1, Klf2, Klf15, Jun, Src*), regulators of cell cycle progression (*Cdk4, Cdkn1b, Foxc2*), and extracellular signaling factors (*Sfrp1*). Compared to mice housed at 32°C, *Acacb* was higher in mice housed at 22°C but lower in mice housed at 22°C and treated with propranolol. Finally, 31 differentially expressed genes were unique to propranolol treatment (22°C propranolol vs. 32°C vehicle). Expression levels for *Adrb2* did not differ between mice housed at 22 and 32°C. However, expression levels were higher in propranolol-treated mice housed at 22°C compared to vehicle-treated mice housed at 32°C.

In addition to the panel of 84 genes described above, we determined the effect of housing temperature and propranolol treatment on expression of two additional β-adrenergic receptor subtypes (*Adrb1* and *Adrb3*) and two genes coding for proteins related to bone formation, osteocalcin (*Bglap*) and alkaline phosphatase (*Alpl*). Mice housed at 22°C had lower levels of *Adrb3* (−1.8; $p < 0.002$), *Bglap* (−1.3; $p < 0.03$) and *Alpl* (−1.4; $p < 0.003$) compared to mice housed at 32°C but no difference in expression of *Adrb1*. Propranolol treatment of mice housed at 22°C did not influence expression of *Bglap*, *Alpl,* or *Adrb1*. Expression levels of *Adrb3* did not differ between propranolol-treated mice housed at 22°C and vehicle-treated mice housed at 32°C.

DISCUSSION

Compared to thermoneutral temperature (32°C), mice housed at room temperature (22°C) had lower percent body fat, lower abdominal WAT, lower cancellous bone volume fraction, connectivity density, trabecular thickness, trabecular number, osteoblast-lined bone perimeter, and bMAT (adipocyte area fraction and adipocyte density) in distal femur metaphysis, lower leptin and osteocalcin in serum, and lower mRNA levels for osteocalcin and alkaline phosphatase in tibia. In contrast, osteoclast-lined bone perimeter and trabecular separation

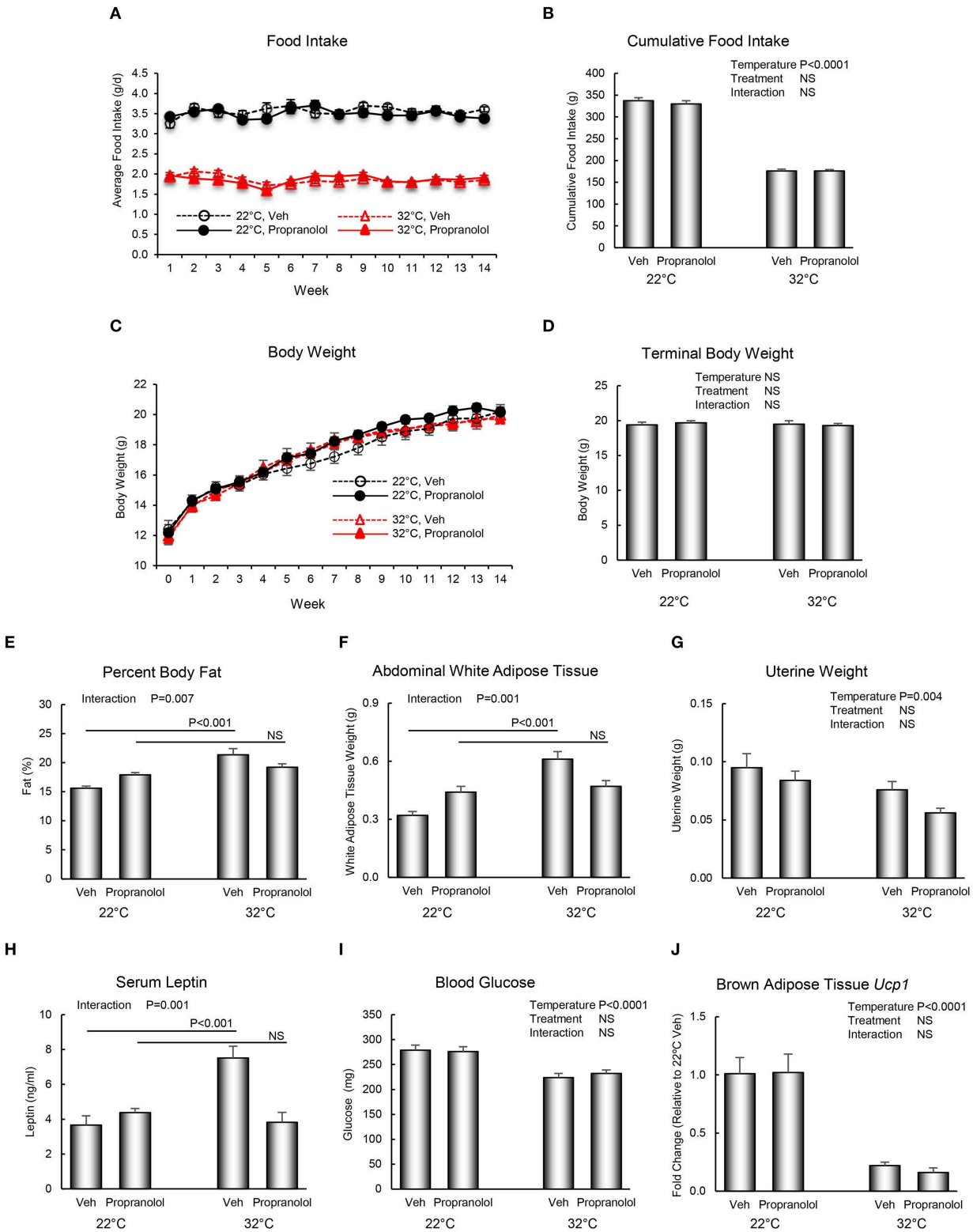

FIGURE 2 | Effect of housing temperature (temperature) and treatment with propranolol (treatment) on **(A,B)** food intake, **(C,D)** body weight, **(E)** percent body fat, **(F)** abdominal white adipose tissue weight, **(G)** uterine weight, **(H)** serum leptin, **(I)** blood glucose, and **(J)** brown adipose tissue *Ucp1* gene expression. Data are mean ± SE. $N = 10$/group for **(A–I)** and $n = 8$/group for **(J)**. *Post–hoc* analysis was performed when there was a significant interaction term.

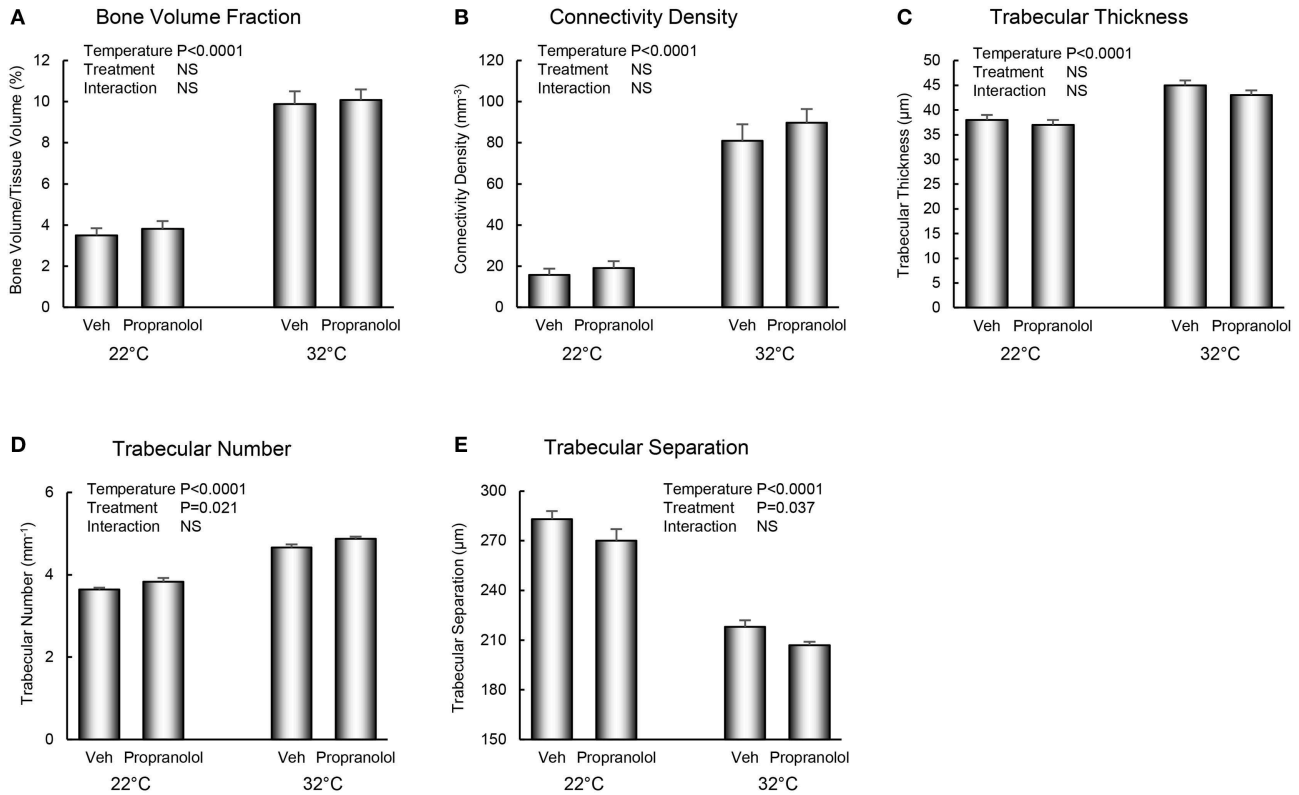

FIGURE 3 | Effect of housing temperature (temperature) and treatment with propranolol (treatment) on cancellous bone architecture in distal femur metaphysic: **(A)** cancellous bone volume fraction, **(B)** connectivity density, **(C)** trabecular thickness, **(D)** trabecular number, and **(E)** trabecular separation. Data are mean ± SE. $N = 10$/group.

were higher in room temperature-housed mice. Treatment with propranolol prevented housing temperature-associated differences in percent body fat, abdominal WAT, serum leptin, and distal femur metaphysis bMAT, but had no effect on bone response to housing temperature. Finally, there were shared as well as unique genes differentially regulated in response to room temperature housing and treatment with propranolol.

Housing of growing female and male mice at room temperature results in dramatic cancellous bone loss prior to skeletal maturity (5–7). The bone loss is not uniform, with more loss occurring in long bones than in lumbar vertebrae (7, 33) and in the distal femur, more loss occurring in metaphysis than in epiphysis (34). Importantly, housing mice at thermoneutrality prevents premature bone loss (6, 7). In female mice, changes in bMAT levels in response to differences in housing temperature follow a similar pattern in that the bMAT levels are lower in distal femur metaphysis of mice housed at room temperature (7). We did not measure bone marrow adiposity in lumbar vertebra or distal femur epiphysis because adipocytes are very uncommon at these sites in mice housed at either room or thermoneutral temperature. The lower levels of bMAT and lower levels of cancellous bone observed in female mice housed at room temperature appear consistent with a shared mechanism. However, a different response occurred in male mice; whereas premature cancellous bone loss was evident in males housed at room temperature, differences in bMAT were not observed (6). The divergent response of bMAT to room temperature-induced cold stress in female and male mice does not support a shared mechanism.

The quantity of bMAT in distal femur metaphysis is context-dependent and, as recently reviewed (35), influenced by numerous factors, including skeletal site, age, food availability, and housing temperature. Increased bMAT occurs with extremes in energy availability; obesity and rapid weight loss each result in increased bMAT. Treatment of rats with β-adrenergic agonists, such as isoproterenol, increased lipolysis in bMAT but to a lesser extent than inguinal WAT (36). Baek et al. (37) found that β-blockade using propranolol had no effect on bMAT in mice fed a normal diet but partially reduced increases in bMAT induced by both calorie restriction and calorie excess. Blocking β-adrenergic signaling in growing female rats fed a calorie-restricted diet attenuated reductions in circulating leptin, cancellous bone mass and increases in marrow adiposity. However, as was the case for mice fed a normal diet, propranolol treatment had no effect on bMAT in *ad libitum*-fed rats (19). Propranolol was shown to reduce dietary fat absorption and fat mass in mice fed high fat diet by suppressing expression of pancreatic lipase (26). In the present study, propranolol treatment prevented the differences in bMAT

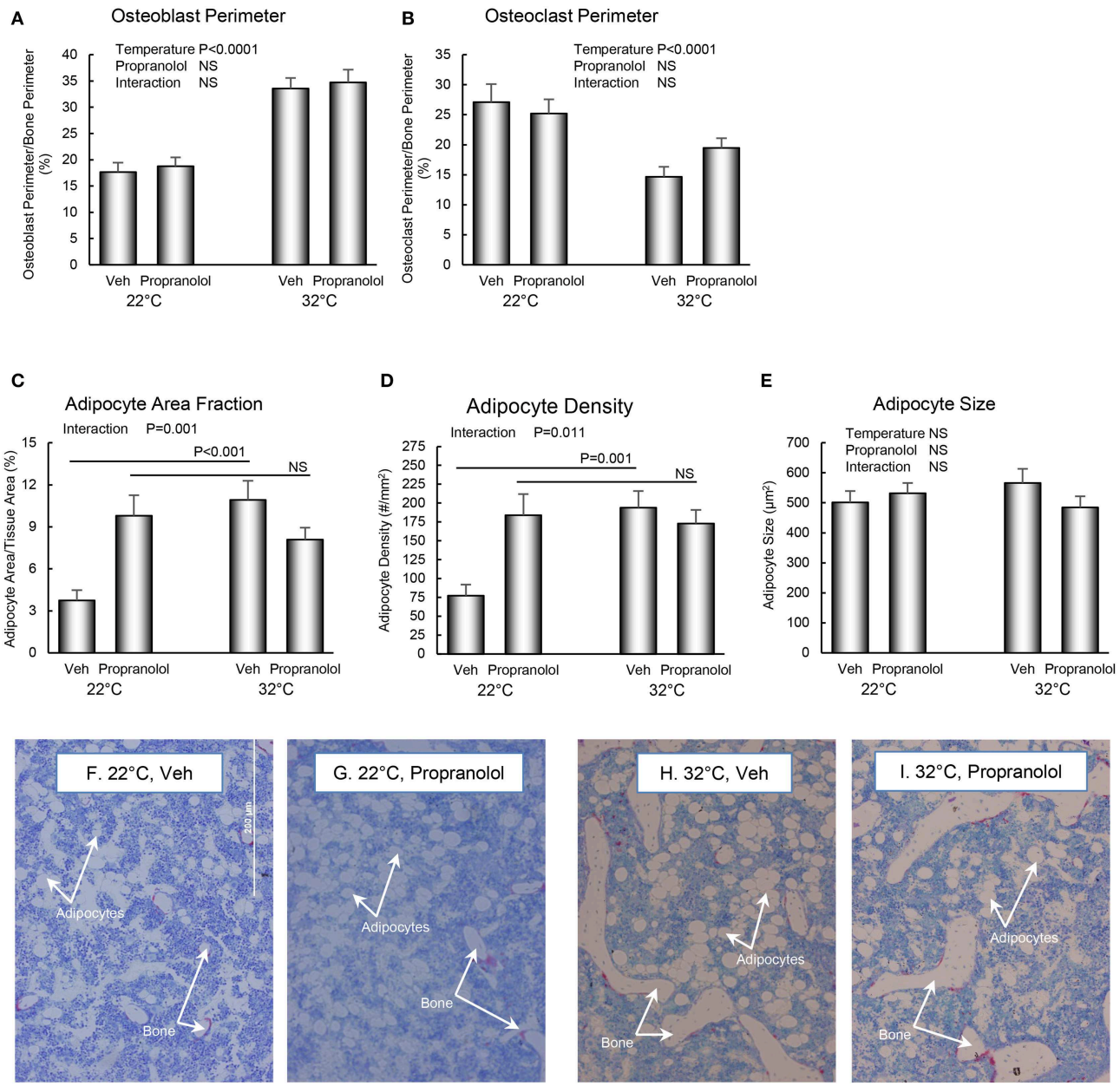

FIGURE 4 | Effect of housing temperature (temperature) and treatment with propranolol (treatment) on indices of bone formation, bone resorption, and marrow adiposity in distal femur metaphysis: **(A)** osteoblast perimeter, **(B)** osteoclast perimeter, **(C)** adipocyte area fraction, **(D)** adipocyte density, and **(E)** adipocyte size. Representative images of the bone marrow compartment showing bMAT and cancellous bone in each treatment group in the distal femur metaphysis are shown in **(F–I)**. Data are mean ± SE. $N = 10$/group. *Post-hoc* analysis was performed when there was a significant interaction term.

in distal femur metaphysis between female mice housed at room temperature and thermoneutral temperature.

We housed mice individually in the present study to facilitate measurement of food intake and to prevent huddling. Additionally, the mice were not offered material for nest building. These measures were important because mice employ huddling and nesting as strategies to decrease reliance on non-shivering thermogenesis when housed at sub-thermoneutral temperature (38). The 10°C higher housing temperature resulted in an impressive ∼280% difference in cancellous bone volume fraction in distal femur metaphysis, a commonly evaluated skeletal site. While a detailed temperature response curve has yet to be established, the magnitude of observed change suggest even small differences in housing temperature, within or among vivariums, could influence results. Thus, factors with potential for altering thermoregulation (e.g., housing conditions or treatment)

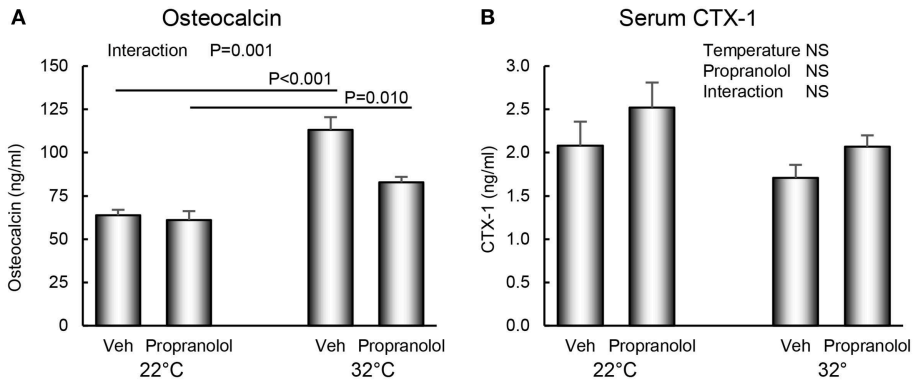

FIGURE 5 | Effect of housing temperature (temperature) and treatment with propranolol (treatment) on **(A)** serum osteocalcin, a marker of global bone formation and **(B)** serum CTX-1, a marker of global bone resorption. Data are mean ± SE. *N* = 10/group. *Post-hoc* analysis was performed when there was a significant interaction term.

should be evaluated for their effect on bone mass, architecture, growth, and turnover.

The mechanisms mediating the impact of adaptive thermogenesis on bone metabolism during room temperature housing have received little attention. As anticipated, housing temperature strongly influenced gene expression levels for *Ucp1* in BAT but the adaptive response to changes in housing temperature was not altered by treatment with propranolol. This finding is consistent with evidence that activation of *Ucp1*gene expression by increased sympathetic outflow induced by cold stress is primarily mediated through β_3 receptor signaling (39). Commonly referred to as a non-specific β-blocker, propranolol inhibits β_1, β_2 and β_3 receptors. However, it is reported to be only a weak inhibitor of β_3 at the dose used in the present study (40). This conclusion is supported by the lack of an effect of propranolol in the present study on *Ucp1* expression in BAT of mice housed at either room temperature or at thermoneutral. Notably, while propranolol treatment resulted in higher trabecular number in distal femur metaphysis, this effect was not influenced by temperature. Thus, it is unlikely that room temperature-induced bone loss requires β_1 and β_2 receptor signaling. It is interesting to note that room temperature housing resulted in lower mRNA levels for β_3 receptor in tibia and that this response was blocked by treatment with propranolol. Further studies will be required to determine whether β_3 receptor signaling contributes to bone loss in room temperature-housed mice.

Studies performed in *Ucp1* knockout mice suggest that *Ucp1* expression has a protective effect on bone during cold stress induced by sub-thermoneutral temperature housing (41). However, deletion of *Ucp1* increases activation of alternative forms of thermogenesis to maintain energy homeostasis, including increased shivering, in mice housed at room temperature. Because of the increased energy cost to activate alternative forms of adaptive thermogenesis, *Ucp1* knockout mice are resistant to diet-induced obesity when housed at room temperature. In contrast, when housed at thermoneutrality, *Ucp1* knockout mice have increased sensitivity to diet-induced obesity (42, 43). The fundamental difference in thermoregulation between mice and humans and the growing number of examples that housing temperature influences experimental outcomes (3, 44–59) argue strongly that thermoneutral housing of mice more accurately reflects the thermal environment in humans and preclinical studies performed in mice should be conducted at housing temperatures that minimize cold stress.

Propranolol treatment is associated with increased body weight in some individuals (22, 23, 60) and deletion of β_1, β_2, and β_3 receptors in mice increases sensitivity to diet-induced weight gain (61). Adaptive thermogenesis in response to cold stress is energy demanding; in the present study, mice housed at room temperature required ∼90%more energy to match the growth rate of mice housed at thermoneutrality. Although body weight did not differ, there were differences in body composition and serum leptin levels. Specifically, mice housed at room temperature had lower percent body mass as adipose tissue, lower abdominal WAT, and not surprisingly, lower serum leptin levels. Treatment with propranolol had no effect on weight but prevented the temperature-associated changes in body composition, potentially by inhibiting expression of pancreatic lipase as well as suppressing β-adrenergic signaling in bone.

Some, but not all, studies report that propranolol influences bone growth, mass and turnover in mice and rats. Factors such as gonadal status, mechanical loading and energy balance appear to influence the skeletal response to treatment with propranolol (18, 19, 21). In the present study, propranolol-treated mice exhibited small but significant changes in bone microarchitecture; trabecular number was increased and trabecular separation decreased. In contrast to adipose tissues, propranolol did not blunt the dramatic differences in bone mass, osteoblast-lined and osteoclast-lined bone perimeters, or expression levels for osteocalcin and alkaline phosphatase in long bones between mice housed at room temperature and thermoneutral temperature. These findings provide additional strong evidence that the mechanisms responsible for adipose and skeletal adaptations to cold stress differ. Elevated glucocorticoid and thyroid hormone levels, and

A

Differentially Expressed Genes Compared to 32°C Veh (Control)

22°C Veh *versus* 32°C Veh			22°C Propranolol *versus* 32°C Veh		
Symbol	Fold Change	p-values	Symbol	Fold Change	p-values
Acacb	**1.4**	**0.009**	***Acacb***	**-1.4**	**0.009**
Adipoq	-1.3	0.007	*Adrb2*	1.2	0.024
Agt	**-1.5**	**0.000**	***Agt***	**-1.3**	**<0.001**
Axin1	**-1.2**	**0.011**	***Axin1***	**-1.3**	**<0.001**
Ccnd1	**-1.2**	**0.036**	***Ccnd1***	**-1.3**	**<0.001**
Cdk4	-1.2	0.012	***Cdkn1a***	**-1.6**	**<0.001**
Cdkn1a	**-1.4**	**0.001**	*Cebpa*	2.3	<0.001
Cdkn1b	-1.4	0.004	*Cebpd*	1.7	<0.001
Cebpb	-1.3	0.003	*Creb1*	1.2	0.014
Dkk1	-1.6	0.002	*Dio2*	1.4	0.003
Fgf1	**-1.2**	**0.001**	*E2f1*	1.2	0.032
Foxc2	-1.3	0.043	*Egr2*	7.3	<0.001
Foxo1	**-1.2**	**0.011**	*Fasn*	1.2	0.036
Irs2	**-1.3**	**0.022**	***Fgf1***	**-1.2**	**0.012**
Jun	-1.2	0.012	*Fgf10*	2.8	0.003
Klf15	1.3	0.030	*Fgf2*	1.6	0.002
Klf2	-1.3	0.012	***Foxo1***	**-1.3**	**0.001**
Lep	-1.3	0.045	*Gata3*	2.2	<0.001
Lrp5	**-1.3**	**<0.001**	*Insr*	1.3	0.009
Ncor2	**-1.1**	**0.018**	***Irs2***	**-1.4**	**0.008**
Ppard	**1.2**	**0.020**	*Klf3*	1.2	0.023
Sfrp1	-1.4	0.015	*Klf4*	-1.3	0.000
Sfrp5	**-1.4**	**0.002**	*Lipe*	-1.1	0.036
Src	-1.3	0.002	*Lmna*	-1.3	<0.001
Tcf7l2	**-1.3**	**0.003**	***Lrp5***	**-1.3**	**<0.001**
Vdr	**-2.0**	**<0.001**	***Ncor2***	**-1.2**	**0.001**
Wnt5b	**-1.3**	**0.012**	*Nr0b2*	1.9	0.002
			Nrf1	1.2	0.015
			Ppara	1.5	0.044
			Ppard	**1.3**	**0.045**
			Pparg	1.2	0.043
			Ppargc1b	-1.3	0.000
			Prdm16	1.3	0.004
			Rb1	1.6	0.004
			Retn	4.1	0.003
			Runx1t1	1.5	<0.001
			Sfrp5	**-1.5**	**0.003**
			Sirt1	1.4	<0.001
			Sirt2	-1.2	0.004
			Slc2a4	-1.1	<0.001
			Srebf1	-1.3	<0.001
			Taz	-1.1	0.026
			Tcf7l2	**-1.3**	**0.000**
			Tsc22d3	-1.4	0.016
			Vdr	**-2.2**	**<0.001**
			Wnt5b	**-1.5**	**0.001**

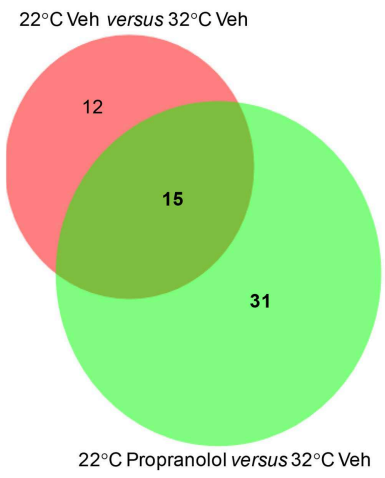

FIGURE 6 | Effect of housing temperature and treatment with propranolol on expression of adipogenesis-associated genes (adipogenesis PCR array) in whole tibia. The Venn diagram shows the number of differentially expressed genes unique to temperature (22°C Veh vs. 32°C Veh, $n = 12$), number of differentially expressed genes unique to propranolol (22°C Propranolol vs. 32°C Veh, $n = 31$) and number shared by temperature and propranolol ($n = 15$). The gene list for differentially expressed genes is shown in the accompanying Table. Shared genes are bolded.

decreased leptin levels may contribute to the rapid cancellous bone loss observed in male and female mice housed at room temperature. Glucocorticoids, thyroid hormone and leptin are important regulators of bone metabolism and their levels are altered by housing temperature (62–69). Further research is required to establish the role of changes in these hormones in premature cancellous bone loss in mice housed at sub-thermoneutral temperatures.

As previously indicated, sensory and sympathetic nerve fibers innervate bone (70, 71) and adrenoceptors, and receptors for vasointestinal peptide, substance P and calcitonin gene-related peptide are expressed on cells located within bone

marrow, including osteoblasts, osteoclasts, chondrocytes, and their precursors (72–74). Cells within skeletal tissue also synthesize neuropeptides. Thus, cells in bone marrow are well positioned to respond to circulating as well as locally-produced neuropeptides whose levels are influenced by temperature. However, no change was observed in *Ucp1* gene expression in bone marrow (data not shown), a finding that contrasts with the increase in *Ucp1* gene expression in brown fat in room temperature-housed mice. Additionally, the decreases in cancellous bone mass and bone formation rate in room temperature-housed mice were associated with lower leptin, an adipokine known to increase sympathetic tone in mice (75–77). These findings do not preclude a role for sympathetic outflow in mediating the osteopenic effects of cold stress induced by room temperature housing but rather suggest they are unlikely to be mediated through β_1 and β_2 receptor signaling (78).

We evaluated expression levels for genes associated with adipogenesis and adipocyte function (using a PCR microarray), β-adrenergic receptors, and bone formation. These analyses identified genes in tibia of mice housed at room temperature in the presence or absence of propranolol that were differentially expressed compared to mice housed at thermoneutrality. These data reflect the product of number of cells within the tissue expressing a gene and expression level/cell and provide a broad-based index of the magnitude of change resulting from differences in housing temperature and treatment. In addition to genes exclusive to housing temperature ($n = 12$) and propranolol ($n = 31$), there were genes differentially expressed and changed in the same direction by both interventions ($n = 14$). One shared gene changed in opposite direction. Taken together, these findings further support the conclusion that β_1 and/or β_2 signaling contribute(s) to the changes in bMAT associated with adaptation to cold temperature stress. Based on our initial screen, it is notable that propranolol altered the effect of room temperature housing on expression levels of *Adipoq*, *Lep, Klf2,* and *Klf15*, genes whose protein products play important roles in adipogenesis (79–81). Specifically, these genes were no longer differentially expressed in response to room temperature housing. The expression level of the gene for acetyl-CoA carboxylase (*Acacb*), the rate-limiting step for fatty acid synthesis and key regulator of β-oxidation (82), was higher in mice housed at room temperature and lower in propranolol-treated mice, findings consistent with propranolol attenuating the lower bMAT in room temperature-housed mice. It is also of interest that propranolol treatment resulted in differential expression of a large number of genes not influenced by housing temperature. Bone marrow is a complex organ system and β-adrenergic receptors are not limited to mesenchymal cell lineages (83). Thus, the antagonistic effects of propranolol on the adaptive response of bMAT to changes in housing temperature could be due a combination of direct effects on β-adrenergic signaling by adipocyte progenitors and/or adipocytes and indirect effects mediated through β-adrenergic signaling by cells not related to adipocytes (e.g., hematopoietic lineage cells). Additional research is required to decipher the precise contribution of target cells and individual signaling pathways.

In summary, the lower percent body fat and abdominal WAT weight and higher *Ucp1* gene expression in BAT in room temperature-housed mice, compared to mice housed at thermoneutrality, is consistent with increased β-oxidation and increased non-shivering thermogenesis, respectively. Both mechanisms likely contribute to the temperature-associated differences in body composition. Our findings evaluating the effects of propranolol on mice housed at room temperature or thermoneutral suggest that β_1/β_2 receptor signaling contributes to lower WAT and bMAT levels in room temperature-housed mice. Osteoblasts and adipocytes share a common mesenchymal stem cell progenitor (84). However, failure of propranolol to attenuate the reduction in osteoblast-lined bone perimeter associated with room temperature cold stress does not support β_1/β_2 receptor signaling as a mechanism for premature bone loss associated with standard room temperature housing.

DATA AVAILABILITY STATEMENT

All data for this study are included in the article. The datasets will also be deposited with NASA and made available to anyone upon request.

AUTHOR CONTRIBUTIONS

RT, KP, AB, and UI: Conceptualization. KP, CW, AG, and RT: Data collection. AB: Data analysis. RT: Drafting manuscript. RT, KP, CW, AB, AG, and UI: Revising manuscript content. RT, KP, CW, AB, AG, and UI: Approving final version. UI: Takes responsibility for the integrity of the data.

FUNDING

This work was supported by NIH (AR 054609), USDA (38420-17804), and NASA (80NSSC19K0430).

REFERENCES

1. Gordon CJ. Thermal physiology of laboratory mice: defining thermoneutrality. *J Therm Biol*. (2012) 37:654–85. doi: 10.1016/j.jtherbio.2012.08.004
2. Schubert KA, Boerema AS, Vaanholt LM, de Boer SF, Strijkstra AM, Daan S. Daily torpor in mice: high foraging costs trigger energy saving hypothermia. *Biol Lett*. (2010) 6:132–5. doi: 10.1098/rsbl.2009.0569
3. Hylander BL, Eng JW, Repasky EA. The impact of housing temperature-induced chronic stress on preclinical mouse tumor models and therapeutic responses: an important role for the nervous system. *Adv Exp Med Biol*. (2017) 1036:173–89. doi: 10.1007/978-3-319-67577-0_12
4. Povinelli BJ, Kokolus KM, Eng JW, Dougher CW, Curtin L, Capitano ML, et al. Standard sub-thermoneutral caging temperature influences radiosensitivity of hematopoietic stem and progenitor cells. *PLoS ONE*. (2015) 10:e0120078. doi: 10.1371/journal.pone.0120078

5. Glatt V, Canalis E, Stadmeyer L, Bouxsein ML. Age-related changes in trabecular architecture differ in female and male C57BL/6J mice. *J Bone Miner Res*. (2007) 22:1197–207. doi: 10.1359/jbmr.070507
6. Martin SA, Philbrick KA, Wong CP, Olson DA, Branscum AJ, Jump DB, et al. Thermoneutral housing attenuates premature cancellous bone loss in male C57BL/6J mice. *Endocr Connect*. (2019) 8:1455–67. doi: 10.1530/EC-19-0359
7. Iwaniec UT, Philbrick KA, Wong CP, Gordon JL, Kahler-Quesada AM, Olson DA, et al. Room temperature housing results in premature cancellous bone loss in growing female mice: implications for the mouse as a preclinical model for age-related bone loss. *Osteoporos Int*. (2016) 27:3091–101. doi: 10.1007/s00198-016-3634-3
8. Burkhardt R, Kettner G, Bohm W, Schmidmeier M, Schlag R, Frisch B, et al. Changes in trabecular bone, hematopoiesis and bone marrow vessels in aplastic anemia, primary osteoporosis, and old age: a comparative histomorphometric study. *Bone*. (1987) 8:157–64. doi: 10.1016/8756-3282(87)90015-9
9. Gimble JM, Robinson CE, Wu X, Kelly KA, Rodriguez BR, Kliewer SA, et al. Peroxisome proliferator-activated receptor-gamma activation by thiazolidinediones induces adipogenesis in bone marrow stromal cells. *Mol Pharmacol*. (1996) 50:1087–94.
10. Justesen J, Stenderup K, Ebbesen EN, Mosekilde L, Steiniche T, Kassem M. Adipocyte tissue volume in bone marrow is increased with aging and in patients with osteoporosis. *Biogerontology*. (2001) 2:165–71. doi: 10.1023/A:1011513223894
11. Meunier P, Aaron J, Edouard C, Vignon G. Osteoporosis and the replacement of cell populations of the marrow by adipose tissue. A quantitative study of 84 iliac bone biopsies. *Clin Orthop Relat Res*. (1971) 80:147–54. doi: 10.1097/00003086-197110000-00021
12. Moerman EJ, Teng K, Lipschitz DA, Lecka-Czernik B. Aging activates adipogenic and suppresses osteogenic programs in mesenchymal marrow stroma/stem cells: the role of PPAR-gamma2 transcription factor and TGF-beta/BMP signaling pathways. *Aging Cell*. (2004) 3:379–89. doi: 10.1111/j.1474-9728.2004.00127.x
13. Nuttall ME, Patton AJ, Olivera DL, Nadeau DP, Gowen M. Human trabecular bone cells are able to express both osteoblastic and adipocytic phenotype: implications for osteopenic disorders. *J Bone Miner Res*. (1998) 13:371–82. doi: 10.1359/jbmr.1998.13.3.371
14. Rodriguez JP, Garat S, Gajardo H, Pino AM, Seitz G. Abnormal osteogenesis in osteoporotic patients is reflected by altered mesenchymal stem cells dynamics. *J Cell Biochem*. (1999) 75:414–23.
15. Rosen CJ, Ackert-Bicknell C, Rodriguez JP, Pino AM. Marrow fat and the bone microenvironment: developmental, functional, and pathological implications. *Crit Rev Eukaryot Gene Expr*. (2009) 19:109–24. doi: 10.1615/CritRevEukarGeneExpr.v19.i2.20
16. Hill EL, Turner R, Elde R. Effects of neonatal sympathectomy and capsaicin treatment on bone remodeling in rats. *Neuroscience*. (1991) 44:747–55. doi: 10.1016/0306-4522(91)90094-5
17. Bonnet N, Beaupied H, Vico L, Dolleans E, Laroche N, Courteix D, et al. Combined effects of exercise and propranolol on bone tissue in ovariectomized rats. *J Bone Miner Res*. (2007) 22:578–88. doi: 10.1359/jbmr.070117
18. Baek K, Bloomfield SA. Beta-adrenergic blockade and leptin replacement effectively mitigate disuse bone loss. *J Bone Miner Res*. (2009) 24:792–9. doi: 10.1359/jbmr.081241
19. Baek K, Bloomfield SA. Blocking beta-adrenergic signaling attenuates reductions in circulating leptin, cancellous bone mass, and marrow adiposity seen with dietary energy restriction. *J Appl Physiol*. (2012) 113:1792–801. doi: 10.1152/japplphysiol.00187.2012
20. Narkiewicz K, Kjeldsen SE, Oparil S, Hedner T. Beta-blockers as sub-optimal treatment for hypertension: time for first-line therapy revision? *Blood Press*. (2006) 15:323–4. doi: 10.1080/08037050601164986
21. Sliwinski L, Folwarczna J, Pytlik M, Cegiela U, Nowinska B, Trzeciak H, et al. Do effects of propranolol on the skeletal system depend on the estrogen status? *Pharmacol Rep*. (2013) 65:1345–56. doi: 10.1016/S1734-1140(13)71493-2
22. Martinez-Mir I, Navarro-Badenes J, Palop V, Morales-Olivas FJ, Rubio E. Weight gain induced by long-term propranolol treatment. *Ann Pharmacother*. (1993) 27:512. doi: 10.1177/106002809302700423
23. Sharma AM, Pischon T, Hardt S, Kunz I, Luft FC. Hypothesis: beta-adrenergic receptor blockers and weight gain: a systematic analysis. *Hypertension*. (2001) 37:250–4. doi: 10.1161/01.HYP.37.2.250
24. Morrison SF. Efferent neural pathways for the control of brown adipose tissue thermogenesis and shivering. *Handb Clin Neurol*. (2018) 156:281–303. doi: 10.1016/B978-0-444-63912-7.00017-5
25. Asai K, Yang GP, Geng YJ, Takagi G, Bishop S, Ishikawa Y, et al. Beta-adrenergic receptor blockade arrests myocyte damage and preserves cardiac function in the transgenic G(salpha) mouse. *J Clin Invest*. (1999) 104:551–8. doi: 10.1172/JCI7418
26. Baek K, Park D, Hwang HR, Kim SG, Lee H, Baek JH. Blocking beta(1)/beta(2)-adrenergic signaling reduces dietary fat absorption by suppressing expression of pancreatic lipase in high fat-fed mice. *Int J Mol Sci*. (2018) 19:E857. doi: 10.3390/ijms19030857
27. Kroeger RJ, Groszmann RJ. Effect of selective blockade of beta 2-adrenergic receptors on portal and systemic hemodynamics in a portal hypertensive rat model. *Gastroenterology*. (1985) 88:896–900. doi: 10.1016/S0016-5085(85)80005-6
28. Iwaniec UT, Wronski TJ, Turner RT. Histological analysis of bone. *Methods Mol Biol*. (2008) 447:325–41. doi: 10.1007/978-1-59745-242-7_21
29. Turner RT, Kalra SP, Wong CP, Philbrick KA, Lindenmaier LB, Boghossian S, et al. Peripheral leptin regulates bone formation. *J Bone Miner Res*. (2013) 28:22–34. doi: 10.1002/jbmr.1734
30. Menagh PJ, Turner RT, Jump DB, Wong CP, Lowry MB, Yakar S, et al. Growth hormone regulates the balance between bone formation and bone marrow adiposity. *J Bone Miner Res*. (2010) 25:757–68. doi: 10.1359/jbmr.091015
31. Dempster DW, Compston JE, Drezner MK, Glorieux FH, Kanis JA, Malluche H, et al. Standardized nomenclature, symbols, and units for bone histomorphometry: a 2012 update of the report of the ASBMR Histomorphometry Nomenclature Committee. *J Bone Miner Res*. (2013) 28:2–17. doi: 10.1002/jbmr.1805
32. Benjamini Y, Hochberg Y. Controlling the false discovery rate: a practical and powerful approach to multiple testing. *J R Stat Soc Ser B*. (1995) 57:289–300. doi: 10.1111/j.2517-6161.1995.tb02031.x
33. Rickard DJ, Iwaniec UT, Evans G, Hefferan TE, Hunter JC, Waters KM, et al. Bone growth and turnover in progesterone receptor knockout mice. *Endocrinology*. (2008) 149:2383–90. doi: 10.1210/en.2007-1247
34. Philbrick KA, Martin SA, Colagiovanni AR, Branscum AJ, Turner RT, Iwaniec UT. Effects of hypothalamic leptin gene therapy on osteopetrosis in leptin-deficient mice. *J Endocrinol*. (2018) 236:57–68. doi: 10.1530/JOE-17-0524
35. Turner RT, Martin SA, Iwaniec UT. Metabolic coupling between bone marrow adipose tissue and hematopoiesis. *Curr Osteoporos Rep*. (2018) 16:95–104. doi: 10.1007/s11914-018-0422-3
36. Scheller EL, Khandaker S, Learman BS, Cawthorn WP, Anderson LM, Pham HA, et al. Bone marrow adipocytes resist lipolysis and remodeling in response to beta-adrenergic stimulation. *Bone*. (2019) 118:32–41. doi: 10.1016/j.bone.2018.01.016
37. Baek K, Park HJ, Hwang HR, Baek JH. Propranolol attenuates calorie restriction- and high calorie diet-induced bone marrow adiposity. *BMB Rep*. (2014) 47:587–92. doi: 10.5483/BMBRep.2014.47.10.176
38. Gordon CJ, Aydin C, Repasky EA, Kokolus KM, Dheyongera G, Johnstone AF. Behaviorally mediated, warm adaptation: a physiological strategy when mice behaviorally thermoregulate. *J Therm Biol*. (2014) 44:41–6. doi: 10.1016/j.jtherbio.2014.06.006
39. Klaus S, Muzzin P, Revelli JP, Cawthorne MA, Giacobino JP, Ricquier D. Control of beta 3-adrenergic receptor gene expression in brown adipocytes in culture. *Mol Cell Endocrinol*. (1995) 109:189–95. doi: 10.1016/0303-7207(95)03502-X
40. Cannon B, Nedergaard J. Brown adipose tissue: function and physiological significance. *Physiol Rev*. (2004) 84:277–359. doi: 10.1152/physrev.00015.2003
41. Nguyen AD, Lee NJ, Wee NKY, Zhang L, Enriquez RF, Khor EC, et al. Uncoupling protein-1 is protective of bone mass under mild

cold stress conditions. *Bone*. (2018) 106:167–78. doi: 10.1016/j.bone.2015.05.037
42. Enerback S, Jacobsson A, Simpson EM, Guerra C, Yamashita H, Harper ME, et al. Mice lacking mitochondrial uncoupling protein are cold-sensitive but not obese. *Nature*. (1997) 387:90–4. doi: 10.1038/387090a0
43. Liu X, Rossmeisl M, McClaine J, Riachi M, Harper ME, Kozak LP. Paradoxical resistance to diet-induced obesity in UCP1-deficient mice. *J Clin Invest*. (2003) 111:399–407. doi: 10.1172/JCI200315737
44. Clayton ZS, McCurdy CE. Short-term thermoneutral housing alters glucose metabolism and markers of adipose tissue browning in response to a high-fat diet in lean mice. *Am J Physiol Regul Integr Comp Physiol*. (2018) 315:R627–37. doi: 10.1152/ajpregu.00364.2017
45. Dickson I. NAFLD: thermoneutral housing of mice improves modelling of NAFLD. *Nat Rev Gastroenterol Hepatol*. (2017) 14:451. doi: 10.1038/nrgastro.2017.90
46. do Carmo JM, da Silva AA, Romero DG, Hall JE. Changes in ambient temperature elicit divergent control of metabolic and cardiovascular actions by leptin. *FASEB J*. (2017) 31:2418–28. doi: 10.1096/fj.201601224R
47. Fischer AW, Cannon B, Nedergaard J. Optimal housing temperatures for mice to mimic the thermal environment of humans: an experimental study. *Mol Metab*. (2018) 7:161–70. doi: 10.1016/j.molmet.2017.10.009
48. Ganeshan K, Chawla A. Warming the mouse to model human diseases. *Nat Rev Endocrinol*. (2017) 13:458–65. doi: 10.1038/nrendo.2017.48
49. Giles DA, Moreno-Fernandez ME, Stankiewicz TE, Graspeuntner S, Cappelletti M, Wu D, et al. Thermoneutral housing exacerbates nonalcoholic fatty liver disease in mice and allows for sex-independent disease modeling. *Nat Med*. (2017) 23:829–38. doi: 10.1038/nm.4346
50. Giles DA, Ramkhelawon B, Donelan EM, Stankiewicz TE, Hutchison SB, Mukherjee R, et al. Modulation of ambient temperature promotes inflammation and initiates atherosclerosis in wild type C57BL/6 mice. *Mol Metab*. (2016) 5:1121–30. doi: 10.1016/j.molmet.2016.09.008
51. Keijer J, Li M, Speakman JR. What is the best housing temperature to translate mouse experiments to humans? *Mol Metab*. (2019) 25:16–76. doi: 10.1016/j.molmet.2019.04.001
52. Lee B, Kim G, Jo Y, Lee B, Shin YI, Hong C. Aquatic exercise at thermoneutral water temperature enhances antitumor immune responses. *Immune Netw*. (2019) 19:e10. doi: 10.4110/in.2019.19.e10
53. Ndongson-Dongmo B, Lang GP, Mece O, Hechaichi N, Lajqi T, Hoyer D, et al. Reduced ambient temperature exacerbates SIRS-induced cardiac autonomic dysregulation and myocardial dysfunction in mice. *Basic Res Cardiol*. (2019) 114:26. doi: 10.1007/s00395-019-0734-1
54. Neff EP. Thermoneutral mice heat up research. *Lab Anim*. (2017) 46:331. doi: 10.1038/laban.1340
55. Qi Y, Purtell L, Fu M, Sengmany K, Loh K, Zhang L, et al. Ambient temperature modulates the effects of the Prader-Willi syndrome candidate gene Snord116 on energy homeostasis. *Neuropeptides*. (2017) 61:87–93. doi: 10.1016/j.npep.2016.10.006
56. Rubin RL. Mice housed at elevated vivarium temperatures display enhanced T-cell response and survival to *Francisella tularensis*. *Comp Med*. (2017) 67:491–7.
57. Small L, Gong H, Yassmin C, Cooney GJ, Brandon AE. Thermoneutral housing does not influence fat mass or glucose homeostasis in C57BL/6 mice. *J Endocrinol*. (2018) 239:313–24. doi: 10.1530/JOE-18-0279
58. Stemmer K, Kotzbeck P, Zani F, Bauer M, Neff C, Muller TD, et al. Thermoneutral housing is a critical factor for immune function and diet-induced obesity in C57BL/6 nude mice. *Int J Obes*. (2015) 39:791–7. doi: 10.1038/ijo.2014.187
59. Uhlig S, Kuebler WM. Difficulties in modelling ARDS (2017 Grover Conference Series). *Pulm Circ*. (2018) 8:2045894018766737. doi: 10.1177/2045894018766737
60. Rossner S, Taylor CL, Byington RP, Furberg CD. Long term propranolol treatment and changes in body weight after myocardial infarction. *BMJ*. (1990) 300:902–3. doi: 10.1136/bmj.300.6729.902
61. Ueta CB, Fernandes GW, Capelo LP, Fonseca TL, Maculan FD, Gouveia CH, et al. beta(1) adrenergic receptor is key to cold- and diet-induced thermogenesis in mice. *J Endocrinol*. (2012) 214:359–65. doi: 10.1530/JOE-12-0155
62. Bassett JH, Williams GR. Role of thyroid hormones in skeletal development and bone maintenance. *Endocr Rev*. (2016) 37:135–87. doi: 10.1210/er.2015-1106
63. Canalis E, Delany AM. Mechanisms of glucocorticoid action in bone. *Ann N Y Acad Sci*. (2002) 966:73–81. doi: 10.1111/j.1749-6632.2002.tb04204.x
64. Coghlan MJ, Jacobson PB, Lane B, Nakane M, Lin CW, Elmore SW, et al. A novel antiinflammatory maintains glucocorticoid efficacy with reduced side effects. *Mol Endocrinol*. (2003) 17:860–9. doi: 10.1210/me.2002-0355
65. Gogakos AI, Duncan Bassett JH, Williams GR. Thyroid and bone. *Arch Biochem Biophys*. (2010) 503:129–36. doi: 10.1016/j.abb.2010.06.021
66. Iwen KA, Oelkrug R, Brabant G. Effects of thyroid hormones on thermogenesis and energy partitioning. *J Mol Endocrinol*. (2018) 60:R157–70. doi: 10.1530/JME-17-0319
67. Li L, Li B, Li M, Speakman JR. Switching on the furnace: regulation of heat production in brown adipose tissue. *Mol Aspects Med*. (2019) 68:60–73. doi: 10.1016/j.mam.2019.07.005
68. Philbrick KA, Wong CP, Branscum AJ, Turner RT, Iwaniec UT. Leptin stimulates bone formation in ob/ob mice at doses having minimal impact on energy metabolism. *J Endocrinol*. (2017) 232:461–74. doi: 10.1530/JOE-16-0484
69. Uchida K, Shiuchi T, Inada H, Minokoshi Y, Tominaga M. Metabolic adaptation of mice in a cool environment. *Pflugers Arch*. (2010) 459:765–74. doi: 10.1007/s00424-010-0795-3
70. Hill EL, Elde R. Distribution of CGRP-, VIP-, D beta H-, SP-, and NPY-immunoreactive nerves in the periosteum of the rat. *Cell Tissue Res*. (1991) 264:469–80. doi: 10.1007/BF00319037
71. Hohmann EL, Elde RP, Rysavy JA, Einzig S, Gebhard RL. Innervation of periosteum and bone by sympathetic vasoactive intestinal peptide-containing nerve fibers. *Science*. (1986) 232:868–71. doi: 10.1126/science.3518059
72. Aitken SJ, Landao-Bassonga E, Ralston SH, Idris AI. Beta2-adrenoreceptor ligands regulate osteoclast differentiation in vitro by direct and indirect mechanisms. *Arch Biochem Biophys*. (2009) 482:96–103. doi: 10.1016/j.abb.2008.11.012
73. Bliziotes M, Murtagh J, Wiren K. Beta-adrenergic receptor kinase-like activity and beta-arrestin are expressed in osteoblastic cells. *J Bone Miner Res*. (1996) 11:820–6. doi: 10.1002/jbmr.5650110613
74. Lai LP, Mitchell J. Beta2-adrenergic receptors expressed on murine chondrocytes stimulate cellular growth and inhibit the expression of Indian hedgehog and collagen type X. *J Cell Biochem*. (2008) 104:545–53. doi: 10.1002/jcb.21646
75. Belin de Chantemele EJ, Mintz JD, Rainey WE, Stepp DW. Impact of leptin-mediated sympatho-activation on cardiovascular function in obese mice. *Hypertension*. (2011) 58:271–9. doi: 10.1161/HYPERTENSIONAHA.110.168427
76. Enriori PJ, Sinnayah P, Simonds SE, Garcia Rudaz C, Cowley MA. Leptin action in the dorsomedial hypothalamus increases sympathetic tone to brown adipose tissue in spite of systemic leptin resistance. *J Neurosci*. (2011) 31:12189–97. doi: 10.1523/JNEUROSCI.2336-11.2011
77. Rahmouni K. Leptin-induced sympathetic nerve activation: signaling mechanisms and cardiovascular consequences in obesity. *Curr Hypertens Rev*. (2010) 6:104–209. doi: 10.2174/157340210791170994
78. Razzoli M, Emmett MJ, Lazar MA, Bartolomucci A. Beta-adrenergic receptors control brown adipose UCP-1 tone and cold response without affecting its circadian rhythmicity. *FASEB J*. (2018) 32:5640–6. doi: 10.1096/fj.201800452R
79. Lindenmaier LB, Philbrick KA, Branscum AJ, Kalra SP, Turner RT, Iwaniec UT. Hypothalamic leptin gene therapy reduces bone marrow adiposity in ob/ob mice fed regular and high-fat diets. *Front Endocrinol*. (2016) 7:110. doi: 10.3389/fendo.2016.00110
80. Pearson R, Fleetwood J, Eaton S, Crossley M, Bao S. Kruppel-like transcription factors: a functional family. *Int J Biochem Cell Biol*. (2008) 40:1996–2001. doi: 10.1016/j.biocel.2007.07.018
81. Yokota T, Meka CS, Medina KL, Igarashi H, Comp PC, Takahashi M, et al. Paracrine regulation of fat cell formation in bone marrow cultures via adiponectin and prostaglandins. *J Clin Invest*. (2002) 109:1303–10. doi: 10.1172/JCI0214506

82. Munday MR, Hemingway CJ. The regulation of acetyl-CoA carboxylase–a potential target for the action of hypolipidemic agents. *Adv Enzyme Regul*. (1999) 39:205–34. doi: 10.1016/S0065-2571(98)00016-8
83. Maestroni GJM. Adrenergic modulation of hematopoiesis. *J Neuroimmune Pharmacol*. (2019). doi: 10.1007/s11481-019-09840-7
84. Jaiswal RK, Jaiswal N, Bruder SP, Mbalaviele G, Marshak DR, Pittenger MF. Adult human mesenchymal stem cell differentiation to the osteogenic or adipogenic lineage is regulated by mitogen-activated protein kinase. *J Biol Chem*. (2000) 275:9645–52. doi: 10.1074/jbc.275.13.9645

Conflict of Interest: The authors declare that the research was conducted in the absence of any commercial or financial relationships that could be construed as a potential conflict of interest.

frontiers in Endocrinology

ORIGINAL RESEARCH
published: 24 September 2020
doi: 10.3389/fendo.2020.00480

MarrowQuant Across Aging and Aplasia: A Digital Pathology Workflow for Quantification of Bone Marrow Compartments in Histological Sections

*Josefine Tratwal[1], David Bekri[1‡], Chiheb Boussema[1†‡], Rita Sarkis[1‡], Nicolas Kunz[2], Tereza Koliqi[1], Shanti Rojas-Sutterlin[1], Frédérica Schyrr[1], Daniel Naveed Tavakol[1], Vasco Campos[1], Erica L. Scheller[3], Rossella Sarro[4], Carmen Bárcena[5], Bettina Bisig[4], Valentina Nardi[6], Laurence de Leval[4], Olivier Burri[7] and Olaia Naveiras[1,8]**

[1] Laboratory of Regenerative Hematopoiesis, Institute of Bioengineering and Institute for Experimental Cancer Research, Ecole Polytechnique Fédérale de Lausanne (EPFL), Lausanne, Switzerland, [2] Animal Imaging and Technology Core, Center for Biomedical Imaging, Ecole Polytechnique Fédérale de Lausanne (EPFL), Lausanne, Switzerland, [3] Division of Bone and Mineral Diseases, Department of Internal Medicine, Washington University, Saint Louis, MO, United States, [4] Institute of Pathology, Lausanne University Hospital (CHUV), Lausanne University (UNIL), Lausanne, Switzerland, [5] Department of Pathology, University Hospital 12 de Octubre, Madrid, Spain, [6] Department of Pathology, Massachusetts General Hospital, Harvard Medical School, Boston, MA, United States, [7] Bioimaging and Optics Core Facility, Ecole Polytechnique Fédérale de Lausanne (EPFL), Lausanne, Switzerland, [8] Department of Oncology, Hematology Service, Lausanne University Hospital (CHUV), Lausanne, Switzerland

The bone marrow (BM) exists heterogeneously as hematopoietic/red or adipocytic/yellow marrow depending on skeletal location, age, and physiological condition. Mouse models and patients undergoing radio/chemotherapy or suffering acute BM failure endure rapid adipocytic conversion of the marrow microenvironment, the so-called "red-to-yellow" transition. Following hematopoietic recovery, such as upon BM transplantation, a "yellow-to-red" transition occurs and functional hematopoiesis is restored. Gold Standards to estimate BM cellular composition are pathologists' assessment of hematopoietic cellularity in hematoxylin and eosin (H&E) stained histological sections as well as volumetric measurements of marrow adiposity with contrast-enhanced micro-computerized tomography (CE-μCT) upon osmium-tetroxide lipid staining. Due to user-dependent variables, reproducibility in longitudinal studies is a challenge for both methods. Here we report the development of a semi-automated image analysis plug-in, *MarrowQuant,* which employs the open-source software QuPath, to systematically quantify multiple bone components in H&E sections in an unbiased manner. *MarrowQuant* discerns and quantifies the areas occupied by bone, adipocyte ghosts, hematopoietic cells, and the interstitial/microvascular compartment. A separate feature, *AdipoQuant,* fragments adipocyte ghosts in H&E-stained sections of extramedullary adipose tissue to render adipocyte area and size distribution. Quantification of BM hematopoietic cellularity with *MarrowQuant* lies within the range of scoring by four independent pathologists, while quantification of the total adipocyte area in whole bone sections compares with volumetric measurements. Employing our tool, we were able to develop a standardized map of BM hematopoietic cellularity and adiposity

OPEN ACCESS

Edited by:
Gudrun Stenbeck,
Brunel University London,
United Kingdom

Reviewed by:
Claire Edwards,
University of Oxford, United Kingdom
Ormond A. MacDougald,
University of Michigan, United States

***Correspondence:**
Olaia Naveiras
olaia.naveiras@epfl.ch;
olaia.naveiras@chuv.ch

†Present address:
Chiheb Boussema,
Robotics Institute, Carnegie Mellon University, Pittsburgh, PA,
United States

‡These authors shared second authorship

Specialty section:
This article was submitted to Bone Research, a section of the journal Frontiers in Endocrinology

Received: 07 April 2020
Accepted: 17 June 2020
Published: 24 September 2020

Citation:
Tratwal J, Bekri D, Boussema C, Sarkis R, Kunz N, Koliqi T, Rojas-Sutterlin S, Schyrr F, Tavakol DN, Campos V, Scheller EL, Sarro R, Bárcena C, Bisig B, Nardi V, de Leval L, Burri O and Naveiras O (2020) MarrowQuant Across Aging and Aplasia: A Digital Pathology Workflow for Quantification of Bone Marrow Compartments in Histological Sections. Front. Endocrinol. 11:480. doi: 10.3389/fendo.2020.00480

in mid-sections of murine C57BL/6 bones in homeostatic conditions, including quantification of the highly predictable red-to-yellow transitions in the proximal section of the caudal tail and in the proximal-to-distal tibia. Additionally, we present a comparative skeletal map induced by lethal irradiation, with longitudinal quantification of the "red-to-yellow-to-red" transition over 2 months in C57BL/6 femurs and tibiae. We find that, following BM transplantation, BM adiposity inversely correlates with kinetics of hematopoietic recovery and that a proximal to distal gradient is conserved. Analysis of *in vivo* recovery through magnetic resonance imaging (MRI) reveals comparable kinetics. On human trephine biopsies *MarrowQuant* successfully recognizes the BM compartments, opening avenues for its application in experimental, or clinical contexts that require standardized human BM evaluation.

Keywords: bone marrow, hematoxylin and eosin, histology, adipocyte, pathology, skeleton, cellularity, hematopoietic

INTRODUCTION

Bone marrow adipocytes (BMAds) were long considered as passive fillers of the marrow cavity. In recent years, they have become accepted as occupying an important role within the bone marrow (BM) microenvironment in health and disease, while also contributing to whole-body energy homeostasis (1, 2).

At birth, the murine and human skeleton is entirely hematopoietic. BMAds appear shortly thereafter and increase throughout juvenile development in a centripetal fashion as the skeleton matures (3). This reciprocal relationship between adipocytic and hematopoietic content has been known since the enunciation of the "Neumann" law in 1902, describing the age-driven adipocytic conversion of the marrow in distal bones. Indeed, due to the macroscopic coloration of the predominant cell types, the marrow has been broadly categorized as hematopoietic/red or adipocytic/yellow marrow (4). In humans, adipocytes become the most abundant cellular component in the adult BM. In mice, age-dependent adipocytic conversion of the marrow is highly strain-dependent (5). Notably, the C57BL/6 murine strain, which constitutes the most widely used model for experimental hematopoiesis, presents the lowest degree of BM adipocyte content upon homeostatic skeletal maturation. However, upon hematopoietic ablation (e.g., after chemo- or radiotherapy) a massive adipocytic conversion has been consistently described in humans and across different mouse strains. The BM is thus heterogeneous depending on specific skeletal location, age, and physiological condition [reviewed in (6)].

At the single-cell level, however, BMAd heterogeneity was first described by the terms "labile" and "stable" (7). These terms were coined upon the discovery that performic acid Schiff (PFAS) positive and negative stains respectively differentiate "labile" BMAds interspersed within the hematopoietic red BM, which respond to hematopoietic demand (PFAS positive) from "stable" BMAds comprising the non-hematopoietic yellow BM of the distal long bones (PFAS negative) (4, 5, 7). The integration of macroscopic characteristics and single-cell response at the tissue level resulted in the terms "regulated" BM adipose tissue (rBMAT) and "constitutive" BMAT (cBMAT), and prompted further investigation on their differential skeletal distribution, cell size, and relative lipid composition. Mechanistically, specific loss of rBMAT with conservation of cBMAT has been described in the long bones upon cold exposure, and in lipodystrophic *Ptrf* knock-out mice, while an overall loss of BMAds is characteristic of *c-kit* mutant *W/Wv* mice (5, 8, 9).

The association between increased vertebral fracture risk and BM adiposity (BMA) in humans, as well as hematopoietic stem cell (HSC) quiescence and BMA has prompted increased interest in marrow adiposity. Adipocytic conversion of the marrow has been associated to increased vertebral fracture risk in humans, although a cause-effect relationship is not clearly established (10). While mature BMAds generally induce HSC quiescence in humans and mice, BMAd precursors, and their adiponectin-expressing immature counterparts support hematopoietic expansion *in vitro* and *in vivo* (11–18). In mouse models and patients suffering acute BM failure or receiving chemo- or radiotherapy, a rapid and massive adipocytic infiltration of the BM takes place ("red-to-yellow" transition). Following treatment with intensive chemotherapy, and sometimes HSC transplantation, hematopoietic recovery ensues when BMAds recede and functional hematopoiesis is restored ("yellow-to-red" transition). In the clinic, hematopoietic activity is assessed by pathologists' scoring of hematopoietic cellularity in trephine bone biopsies of the iliac crest, and is functionally correlated with circulating blood cell counts (19). Hematopoietic cellularity assessment at low power examination is performed systematically for all diagnostic trephine biopsies, and complementary to immunohistochemistry molecular and cytogenetic techniques for establishing the diagnosis of certain hematological disorders characterized by either hypercellularity (e.g., myeloproliferative neoplasias) or hypocellularity (e.g., hypoplastic bone marrow failure syndromes), or to follow disease progression and response to treatment (e.g., myeloablation for acute leukemias).

In vivo, Gold Standard quantifications of BMA in the research setting are contrast-enhanced (CE) osmium tetroxide (OsO_4) lipid staining coupled to micro-computerized tomography

(μCT) for rodents, and magnetic resonance imaging (MRI) fat-to-water ratio for human. Although highly informative, especially on higher resolution such as nano-CT, this method is costly and sample preparation requires handling of highly toxic products. Thus, accessibility to CE μ/nanoCT and/or MRI expertise can be limited outside of clinical laboratories or specific research settings.

Given the context-dependent heterogeneity of BM compartments and the challenges associated to the accessibility and longitudinal reproducibility of Gold Standards, we set out to develop a tool that could provide quantitative information on both BMA and hematopoietic cellularity with means accessible to most laboratories. Histological information obtained from hematoxylin-and-eosin (H&E) stained sections has long been the standard method to provide information on the architecture of biological samples. While the BM is a particularly difficult organ for histological analysis, in part due to the soft and hard tissue that are juxtaposed, the overall analysis of its multiple components (bone, blood progenitors, adipocytes) provides important information to understand its physiopathology. Available histomorphometric analysis programs usually specialize in detecting individual components, and either require targeted staining protocols to detect specific components within the bone fraction, or use less adapted tools from the extramedullary adipose field to quantify the BMAd fraction [(8, 9, 20–27); and also reviewed in (6)]. In order to reduce inter-observer variability and to quantify sections of entire murine bones rather than representative fields of view, automation and standardization of methods are key. We have developed a semi-automated digital pathology plugin compatible with QuPath (28), named *MarrowQuant*, which subdivides and quantifies the total marrow area (Ma.Ar) in H&E stained mid-sections of mouse bones. The plugin subclassifies an user-defined area ("Tissue Boundaries," see definitions under Image Processing Logic) into four compartments: the mineralized bone, the hematopoietic, adipocytic, and interstitial/microvascular compartments, as well as an unattributed area if present. Upon segmentation, *MarrowQuant* then provides a BMAd area (Ad.Ar) and size distribution for individual adipocytes, both in the context of BMAds and of extramedullary adipocytes. *MarrowQuant* thus provides absolute and relative areas for discrete BM compartments, calculating the hematopoietic cellularity and adiposity on H&E stained sections from murine whole-bone sections. Specifically, the results presented here validate the use of *MarrowQuant* in murine bone marrow in the context of aging as well as in longitudinal studies upon radiation-induced aplasia, and show compatibility with the analysis of human bone trephine biopsies. Additionally, the stand-alone *AdipoQuant* plugin quantifies relative number and performs adipocyte ghost size fragmentation on H&E-stained extramedullary adipose tissue. Adipocyte ghosts are the delipidated derivatives of adipocytes resulting from sample processing and resembling void areas on H&E.

Our software is thus complementary to other available plugins for BMA quantification [comparative review provided in (6)] in that, together with more classically reported values for individual adipocytes or bone components, it provides quantification of hematopoietic cellularity within the range of pathologists' evaluations, while providing overall architectural segmentation of the BM space. We expect *MarrowQuant* will be a valuable addition to the rapidly evolving Digital Pathology field for use in a fundamental research setting or as a tool for the "digitally-enhanced" pathologist in the clinical setting.

RESULTS

Development of the Digital Plugin

Based on a combination of color and texture of whole-bone H&E stained sections as compared to background, we found *MarrowQuant* to most reliably perform marrow quantification when set to segment bone sections into four mutually exclusive detected compartments (**Figure 1**): (i) cortical and trabecular bone, (ii) nucleated/hematopoietic cells, (iii) BMA, based on adipocyte ghost detection, and (iv) interstitium/microvasculature, which recognizes both red blood cells (RBCs) and the eosinophilic protein or serous infiltrate that fills the remaining marrow space. If present, areas within the marrow space that are not recognized as any of the above will be categorized and shown as "Undetected area." The Ma.Ar is used as denominator (see "Image processing logic" for definitions) to calculate the percentage of each of the detected areas apart from percentage bone which the user may calculate themselves. Percentage of trabecular bone can be calculated if the tissue boundaries encompass only the marrow cavity, whereas percentage of cortical plus trabecular bone can be calculated if the tissue boundaries also include the cortical bone. From the adipocyte ghost segmentation, *MarrowQuant* additionally approximates the adipocyte count and size distribution. This function can also be applied to extramedullary adipose tissue sections with the stand-alone *AdipoQuant* function (**Figure 2**). The *MarrowQuant* plugin for bone sections operates through QuPath using Fiji as an extension, thus allowing the user to work with a more intuitive interface.

Summary of the Image Processing Logic

The workflow underlying the *MarrowQuant* processing is shown in **Figure 3**. Image files from total slide scans acquired at 20x magnification (VSI format or extracted TIFF files) are directly loaded into QuPath for processing (**Figure 3A**). Firstly, and prior to image processing, the user must manually identify the region of interest (ROI) to be analyzed, denoted as "Tissue Boundaries" (**Figure 3B**). The wand tool in QuPath greatly simplifies this step. The user may also classify at this step regions that should be excluded from processing as "Artifacts." In our dataset, we excluded significant fixation artifacts at this step, which are common upon retraction of the marrow tissue from the endosteum. For our dataset, we also systematically excluded the retraction artifact that creates a central vein lumen. Secondly, a representative small area within the Tissue Boundaries must be defined as "Background" and will serve as a reference background correction factor for the whole ROI. These regions are selected manually by the user with built-in drawing tools in QuPath and

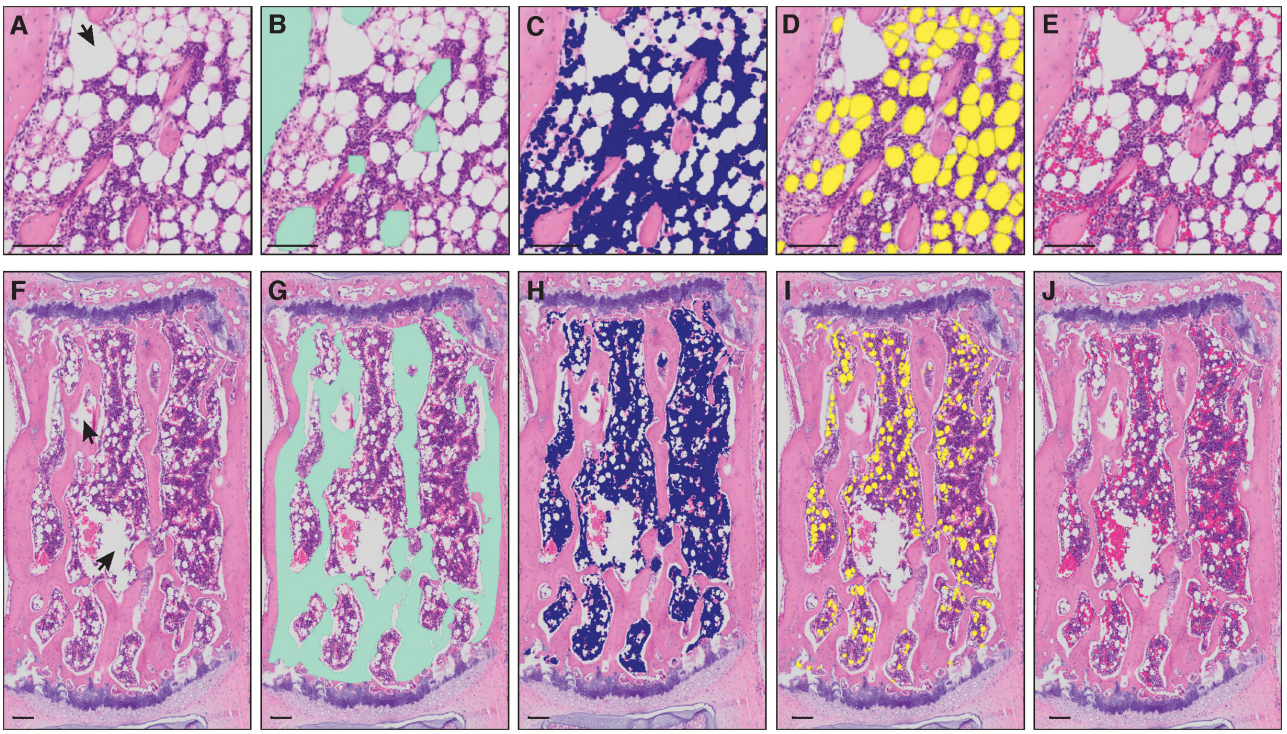

FIGURE 1 | Masks of bone marrow compartment areas detected by *MarrowQuant*. **(A–E)** Proximal tibia and **(F–J)** caudal vertebra (Cd2). Arrowheads in **(A,F)** represent manually excluded *artefacts*. **(A,F)** Unprocessed H&E image, **(B,G)** bone detection (green), **(C,H)** nucleated cell detection (violet), **(D,I)** adipocyte ghost detection (yellow), **(E,J)** interstitium and microvasculature (pink). Image from the proximal tibia at day 15 post lethal irradiation and total bone marrow transplant **(A)** and caudal vertebra 2 **(F)** of a C57BL/6 2-months-old female mouse housed at room temperature fed a standard ad libitum chow diet. Scale bars are 50 μm **(A–E)** and 100 μm **(F–J)**. *MarrowQuant* user-defined parameters set at recommended values for bone marrow analysis (minimum adipocyte size: 120 μm^2, maximum adipocyte size: 5,000 μm^2, minimum circularity: 0.3, exclude edges: false).

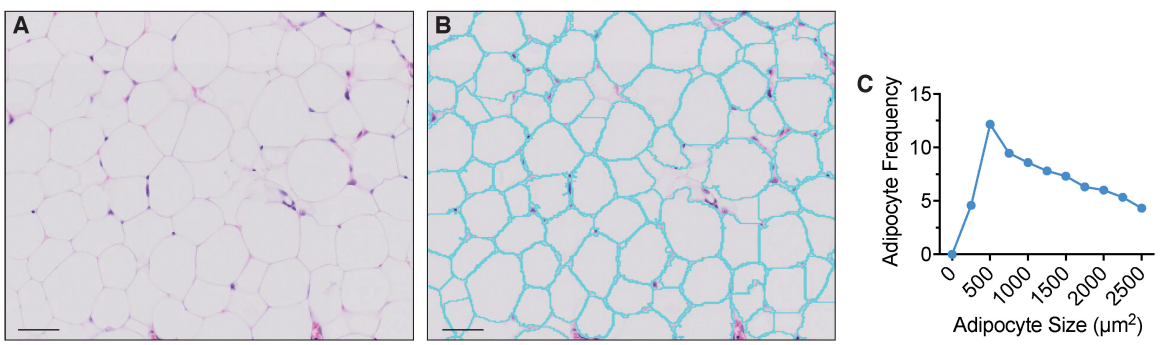

FIGURE 2 | Extramedullary adipocyte fragmentation by *AdipoQuant*. **(A)** unprocessed image, **(B)** adipocyte ghost membrane detection and fragmentation (cyan), **(C)** adipocyte size fragmentation distribution. Omental adipose tissue from a C57BL/6 10-weeks-old female mice housed at room temperature fed a standard *ad libitum* chow diet. Scale bars are 50 μm. *AdipoQuant* user-defined parameters set at recommended values for extramedullary adipocytes (minimum adipocyte size: 300 μm^2, maximwn adipocyte size: 2,500 μm^2, minimum circularity: 0, exclude edges: true). Binning has been set to 250 μm^2.

assigned the corresponding annotation class (see *MarrowQuant* Demo in **Supplementary Video 1**, **Supplementary Datasheets 1** and **2**). Preset parameters for adipocyte ghost circularity, roundness, and size are defined, but may be changed by the user depending on their application (e.g., tissues of different origin). For our dataset, we kept these parameters conservative to include all possible adipocytes and thereby test the robustness of *MarrowQuant* (see Methods and **Figures 1**, **2** legends for details). More restrictive values can be set and should be determined by the user on their particular dataset.

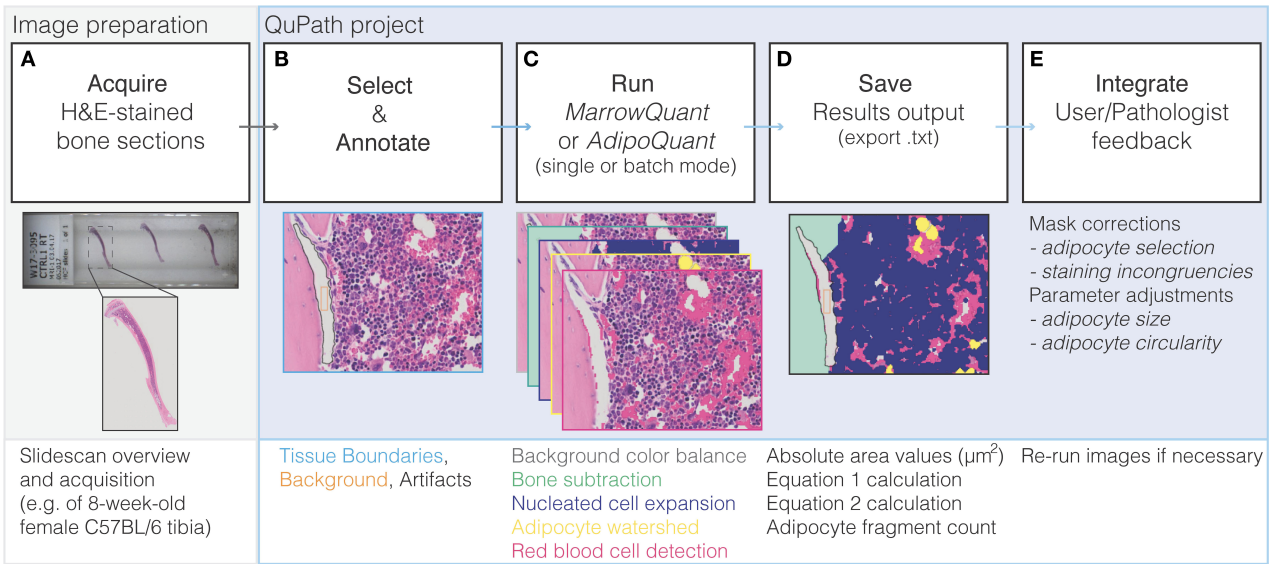

FIGURE 3 | Flow diagram of *MarrowQuant* logic. **(A)** A slidescan is acquired of an H&E stained bone section and loaded into QuPath. **(B)** User defines Tissue Boundaries, Background, and Artifacts with the help of the magic wand tool. **(C)** *MarrowQuant* is run on the created qProject in single or batch mode with preset or user-adjusted parameters. **(D)** Results can be saved as bone marrow mask images and a.txt file of area and calculated outputs. **(E)** User and/or pathologists' feedback is integrated by removing false-positive adipocyte selection and if necessary, processing images with adjusted adipocyte parameters.

Extramedullary Adipocyte Quantification With *AdipoQuant*

As suggested by the opposing effects of extramedullary adipocyte hyperplasia and adipocyte hypertrophy, the measurement of adipocyte size and number has become relevant in the context of multiple patho/physiological conditions (29, 30). We thus developed *AdipoQuant* to provide the adipocyte detection function as a stand-alone plugin which detects the total area covered by adipocyte ghosts and identifies individual adipocyte ghosts through recognition of the remaining membranes, providing a fragmentation size distribution count which can be applied to extramedullary white adipose tissues (**Figure 2**). Of note, adipocytes can only be identified as lipid ghosts in H&E images, as the lipid content in the vacuoles is dissolved on the alcohols used for the processing. Changes in relative adipocyte size of a whole adipose tissue may be thus quantified with the *AdipoQuant* script directly. The user must manually outline "Tissue Boundaries," unwanted "Artifacts," and the "Background" as described above. Not drawing any "Tissue Boundaries" will result in the entire image being analyzed. A.txt file is generated upon processing which lists the adipocyte ghost fragmentation count and size. The tool relies on identification of intact, clearly-stained H&E membranes for the most reliable generation of a watershed algorithm that fragments the mask. A mask is a pixel annotation of a specific region of the original image resulting from image processing (31). Therefore, a reliable size distribution is highly dependent on the quality of sample preparation (including staining, sectioning, and image acquisition).

Bone Marrow Quantification With *MarrowQuant*

Following the initial manual steps performed by the user in setting "Tissue Boundaries," excluding "Artifacts," and defining the "Background" within the QuPath environment as described above (**Figure 3B**), the *MarrowQuant* plugin first identifies the bone compartment within the given "Tissue Boundaries." The bone mask is then subtracted to generate the total area of interest that we define as the "Total Marrow Area" (Ma.Ar) ascribing to the nomenclature recommendations for BMA (32). Within the "Total Marrow Area," nucleated cells are detected to generate the "Hematopoietic Cellularity" mask. A watershed mask then detects and defines adipocyte ghosts by their intact cell membranes in the remaining area to generate the "Adiposity" mask. Finally, both the serous infiltrate and the RBCs, located either within the microvasculature or dispersed across the marrow space, are detected based on their eosinophilic properties to define the "Interstitium/microvasculature" mask. The remaining area within the "Total Marrow Area," if any, is then quantified as unattributed "Undetected Area." The five masks are mutually exclusive in the priority order specified above (**Figure 3C**). Therefore, "Total Marrow Area" (Ma.Ar) constitutes the sum of "Hematopoietic Cellularity" plus "Adiposity" plus "Interstitium/microvasculature" plus the unattributed "Undetected Area." Derived parameters are the adipocyte size fragmentation distribution, and the ratio of hematopoietic area over the hematopoietic and adipocytic areas combined (see Equations 1 and 2 below). A mask output for the four defined compartments overlaid on the original image lets the user confirm the results (**Figures 3D,E**).

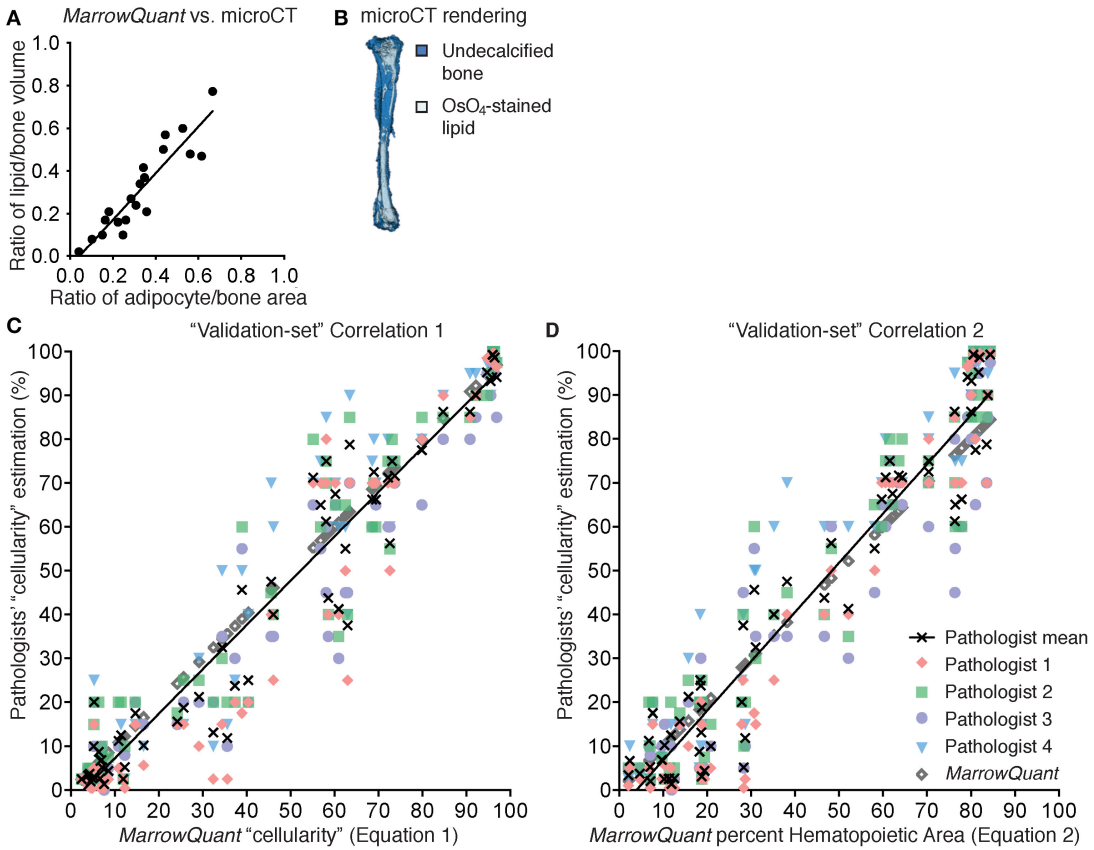

FIGURE 4 | Correlation to gold standards for *MarrowQuant* bone marrow adiposity and hematopoietic cellularity measurements. **(A)** *MarrowQuant* adipose area vs. osmium-tetroxide contrast-enhanced CT measurements of lipid ($n = 23$ bones, $R^2 = 0.84$). Quantifications performed on femurs and tibiae of 18-months-old male mice, 8-weeks, 9-months, or 18-months-old female mice and of a select ion from **(C)**. **(B)** μCT rendering (white: osmium-tetroxide stained lipids; blue: undecalcified bone) of a tibia from an 18-months-old C57BL/6 female mouse. **(C)** *MarrowQuant* "cellularity" (Equation 1) vs. Pathologists' "cellularity" assessment on the "validation-set" of images of full-length bones (Pathologists $n = 4$, images $n = 59$, $R^2 = 0.93$). **(D)** *MarrowQuant* percent Hematopoietic Area (Equation 2) vs. Pathologists' "cellularity" assessment of the "validation-set" (Pathologists $n = 4$, images $n = 59$, $R^2 = 0.93$). Evaluations done for femurs and tibiae of 2-months-old female mice at 0–42 days post lethal irradiation and transplant of 125,000 total bone marrow cells. All mice were C57BL/6 housed at room temperature and fed a standard ad libitum chow diet. OsO4, osmium tetroxide; μCT, micro-computerized tomography.

Validation of *MarrowQuant* With Gold Standards

μCT is an established technique used to quantify changes in bone mineral density and bone architecture. It is now widely used in the field of BMA for lipid detection. *Ex vivo* CT imaging of the native bone is combined with a second CT acquisition after bones have been decalcified and stained with the highly lipophilic dye OsO_4. This procedure is usually referred to as OsO_4-contrast-enhanced μCT or OsO_4-CE-μCT. The ground truth assessment of hematopoiesis constitutes pathologists' assessment of H&E stained paraffin- or plastic-embedded bone sections. We therefore compared these Gold Standard evaluations of murine marrow, first for BM adiposity then for hematopoietic cellularity, to *MarrowQuant* detection. Importantly, mid-bone sections were defined by a complete bone silhouette plus the presence of the distal marrow space in the mid-sagittal tibial sections, and the femoral head marrow space in mid-longitudinal sections of the femur.

BM Adipose Quantification

We first compared the volumetric assessment of lipid content via OsO_4-CE-μCT in C57BL/6 murine long bones to the *MarrowQuant* two-dimensional assessment of BM adipose area in mid-bone sections. Quantification of contralateral bones (right vs. left) with the two techniques over a range of percentage adiposity spanning from 0 to 64% indicates a high correlation (**Figure 4A**, $n = 23$, $R^2 = 0.84$) despite the comparison of a volumetric (**Figure 4B**) with a two-dimensional assessment. In our dataset, 2D quantification of mid-sagittal sections are thus a robust estimate of volumetric renderings of bone and adiposity in the contralateral bone.

BM Hematopoietic Quantification

In spite of the species-specific differences discussed later, we decided to compare the performance of *MarrowQuant* with pathologists' assessment of hematopoietic cellularity in murine bones. To set up the *MarrowQuant* code and optimize the

model parameters we curated a "training-set" of 89 images from murine bones at homeostasis or post-irradiation aplasia, spanning pathologist evaluated hematopoietic cellularity from 0 to 100%.

In human pathology, hematopoietic "cellularity" is defined as "the proportion of cellular elements relative to marrow adipose tissue" (33, 34), and therefore uses the sum of the hematopoietic and adipocytic areas as denominator for the calculation of "cellularity" (Equation 1, % hematopoietic cellularity). The pathologist definition of hematopoietic "cellularity" underscores the reciprocal relationship between the hematopoietic and adipose tissue in the BM.

$$"Cellularity" = \frac{hematopoietic\ area}{(hematopoietic + adipocytic)\ area} \quad (1)$$

We found a strong linear correlation between the *MarrowQuant* calculation of hematopoietic cellularity and the mean of the pathologist's scoring of "cellularity" (Equation 1, **Figure S1A**, $n = 89$, $R^2 = 0.98$). *MarrowQuant* "cellularity" values thus fell within the inter-observer variability of four independent pathologists' assessments, with a higher correlation to the mean at high "cellularity" values. *MarrowQuant* performance at estimating "cellularity" was subsequently confirmed on an independent "validation-set" from 59 images of murine long bones (**Figure 4C**, $n = 59$, $R^2 = 0.93$).

In accordance with the *MarrowQuant* logic to subclassify the marrow space into three different compartments (hematopoietic, adipocytic, and interstitium/microvasculature) and an unattributed "undetected area" when present, we then calculated the hematopoietic cellularity as defined by hematopoietic area over total Ma.Ar (Equation 2, % Hematopoietic Area).

$$\%\ Hematopoietic\ Area = \frac{hematopoietic\ area}{total\ marorw\ area} \quad (2)$$

We found that *MarrowQuant* measurement of percent Hematopoietic Area (Equation 2) progressed linearly when compared to the mean of the pathologists' "cellularity" scoring (Equation 1). Equation 2, however, better correlates to the mean of the pathologists' "cellularity" scoring at low hematopoietic content (**Figure S1B**, $n = 79$, $R^2 = 0.96$). The *MarrowQuant* measurement of percentage Hematopoietic Area was also validated on an independent "validation-set" (**Figure 4D**, $n = 59$, $R^2 = 0.93$). Note that *MarrowQuant* evaluation of percent Hematopoietic Area does not reach 100%, as opposed to pathologist-rated "cellularity," precisely because it uses a different denominator that takes into account the entirety of the marrow space including the interstitium/microvasculature compartment.

In conclusion, in C57BL/6 mice, *MarrowQuant* 2D evaluation of BM adiposity (% Adipocytic Area/ Total Ma.Ar) in mid-bone sections highly correlated with gold standard OsO_4-CE-μCT detection of marrow lipids in 3D measurements. Evaluation of hematopoietic content with *MarrowQuant* also highly correlated with gold standard "cellularity" scoring by pathologists. For evaluation of the hematopoietic compartment, *MarrowQuant* generates results according to two different equations that differ on the denominator. Equation 1 better correlates to the mean of the pathologist scoring in samples of high cellularity, while Equation 1 better correlates at low cellularities. For *MarrowQuant* evaluation of the percentage Hematopoietic Area as compared to other BM compartments, only Equation 2 is applicable as *MarrowQuant* uses Total Marrow Area as a denominator for all compartments.

Application of *MarrowQuant*

We hypothesized that quantification of BM components as a first architectural assessment of BM regeneration may provide valuable information on homeostatic states and disease progression. The C57BL/6 mouse constitutes the most widely used animal model in experimental hematopoiesis. Its skeleton is often assumed to be homogeneously hematopoietic, whereas it has now been well-described that BMAds are interspersed within specific regions of the marrow (5, 17).

Skeleton of the Homeostatic C57BL/6 Female Mouse

Here we provide for the first time a quantitative BMA skeletal map of the homeostatic C57BL/6 8-weeks-old female mouse, which reveals a transition of low adiposity, red BM (high cellularity) to high adiposity, yellow BM (low cellularity) in the proximal to distal regions of the skeleton (**Figure 5**). This transition is most notable in the proximal-to-distal tibia (**Figure 6C**), and highly predictable in the caudal vertebrae of the tail at the level of the Cd3–Cd4 transition (**Figures 5G,H**). The extremities of the skeleton such as the metatarsals or caudal tail vertebrae (e.g., Cd5, 76 ± 4% adiposity) are highly adipocytic whereas the axial skeleton such as the sternum (2.0 ± 0.1% adiposity) and thoracic/lumbar vertebrae (e.g., L4, 6 ± 1% adiposity) are almost entirely hematopoietic. These gradients of red and yellow marrow have also been reported in human, where the adult distal skeleton is nearly completely adipocytic (3, 35). Location-specific BMA may be explained from the perspective of skeletal development, musculoskeletal forces, and temperature gradients (36).

Long Bones of the 18-Months-Old C57BL76 Female Mouse

BMA has been described to increase with age, which may in part be attributed to the terminal differentiation and depletion of BMAd precursors, and in part to the potential protective function assigned to mature BMAds of surrounding cells such as low-proliferating HSCs. In the clinical diagnostic setting, values for normal cellularity of standard trephine biopsies from the pelvic bone in humans are interpreted according to age such that normal, age-adjusted cellularity is described by the formula: normal cellularity = 100% – age (years) ± 20% (33).

In C57BL/6 mice, significant differences in BMA are seen between 8 weeks and 18 months of age (**Figure 6**). The femurs of juvenile mice at 8 weeks of age contain relatively few BMAds (2 ± 1%) that are mostly located at the distal site. With age, BMA in the femur of female C57BL/6 mice increases slightly to 4 ± 2% adiposity ($P = 0.03$) and also appears in the proximal femur (**Figures 6A,B**). While the distal tibia already contains BMAds at an early age with 4 ± 1% adiposity at 8 weeks old, BMA expands further up the BM cavity, especially

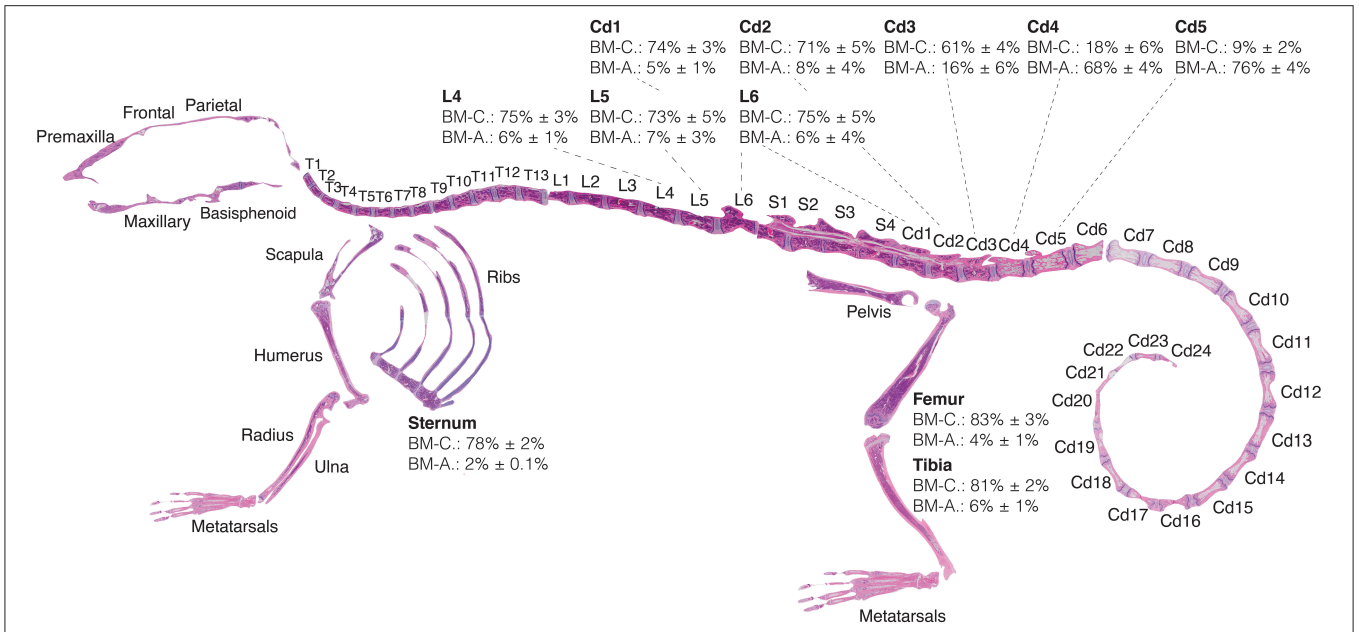

FIGURE 5 | Red-to-yellow marrow transition in homeostasis. Eight-weeks old C57BL/6 reconstructed skeletal map locates the proximal-to-distal red-to-yellow marrow transition in the first caudal vertebrae and proximal-to-distal tibia approximately at the site of the fibular insertion. Skeletal map and quantifications performed for bones of female mice housed at room temperature and fed a standard *ad libitum* chow diet. Percentages of MarrowQuant cellularity (BM-C) and adiposity (BM-A) from Equation 2 are shown for select bones (femur, $n = 6$; tibia, $n = 6$; sternum, $n = 10$; lumbar, $n = 7$; tail, $n = 6$; all are mean ± s.d.). Cd, caudal (vertebrae); L, lumbar; S, sacral; T, thoracic.

at the epiphysis of the proximal tibia to 31 ± 14% ($P = 0.01$) at 18 months old (**Figures 6C,D**). BMAd size fragmentation distributions tibia in homeostasis (8-weeks-old C57BL/6 females) shows the distribution shifted toward larger adipocyte size in the distal tibia as compared to the proximal tibia (**Figure 6E**) as has been previously reported (5). Adipocyte size fragmentation in the tibiae of aged mice (18-months-old C57BL/6 females) show comparatively larger adipocytes as compared to the young animals (**Figure 6F**). Interestingly, older mice present no difference in the size distribution of distal vs. proximal adipocytes across the tibia, suggesting reduced remodeling as compared to young mice (**Figures 6E,F**, compare orange lines). BMA is also increased in the proximal tail of aged mice while maintaining the red-to-yellow marrow transition in the first caudal vertebrae (**Figures 6G,H**). Other strains such as the C3H, with high bone mass, or NSG, that are prone to obesity, have higher BMA than the C57BL/6 strain (not shown).

Irradiation-Induced BM Aplasia in the Skeleton of the C57BL/6 Female Mouse

In certain pathophysiological circumstances such as in osteoporosis, anorexia, or obesity, the marrow becomes more adipocytic. In stress hematopoiesis, such as after chemo/radiotherapy to overcome malignant hematopoiesis, the plasticity of the marrow becomes very apparent. In the timespan of several weeks, the marrow undergoes a rapid "red-to-yellow" conversion, and then recovers thanks to residual or transplanted HSCs. We set up a murine stress hematopoiesis model by applying lethal irradiation immediately followed (day 1) by transplantation of a limited number of healthy BM cells. In this model, the marrow initially becomes necrotic and highly hemorrhagic due to the breakage of the marrow-blood barrier (day 4–10 post-transplant), such that the marrow space is characterized by a high content of RBCs and serous infiltrate. During this time, circulating white blood cells and platelets are reduced 10-fold (**Figure S2**). Shortly thereafter BMAds begin to occupy the marrow space such that the BM reaches peak adiposity at days 13–17 post-transplant in the femur and tibia (**Figures 7, 8A,B**). At this time, and in parallel to revascularization, the new hematopoietic system starts to recover. Around day 25 post-transplant, circulating blood levels show exit from severe thrombo- and neutropenia (<200 and <0.5 cells/mm^3, respectively) (**Figure S2**). Over the next several weeks, blood counts increase and eventually return to normal levels of functional hematopoiesis. Importantly, the overall peak of aplasia and time of recovery in this model closely resembles that observed in patients undergoing HSC transplantation (37, 38).

Examination of the C57BL/6 skeleton at murine peak of aplasia shows that myeloablation renders the entire skeleton of the C57BL/6 8-weeks-old female mouse highly adipocytic and aplastic (**Figure 7**). Specifically, we find at day 17 post-irradiation a low hematopoietic cellularity (average BM-C 15–37%) in skeletal sites that are highly hematopoietic at homeostasis (average BM-C >50% hematopoietic cellularity, e.g., axial skeleton including sternum and vertebrae Cd1-3)

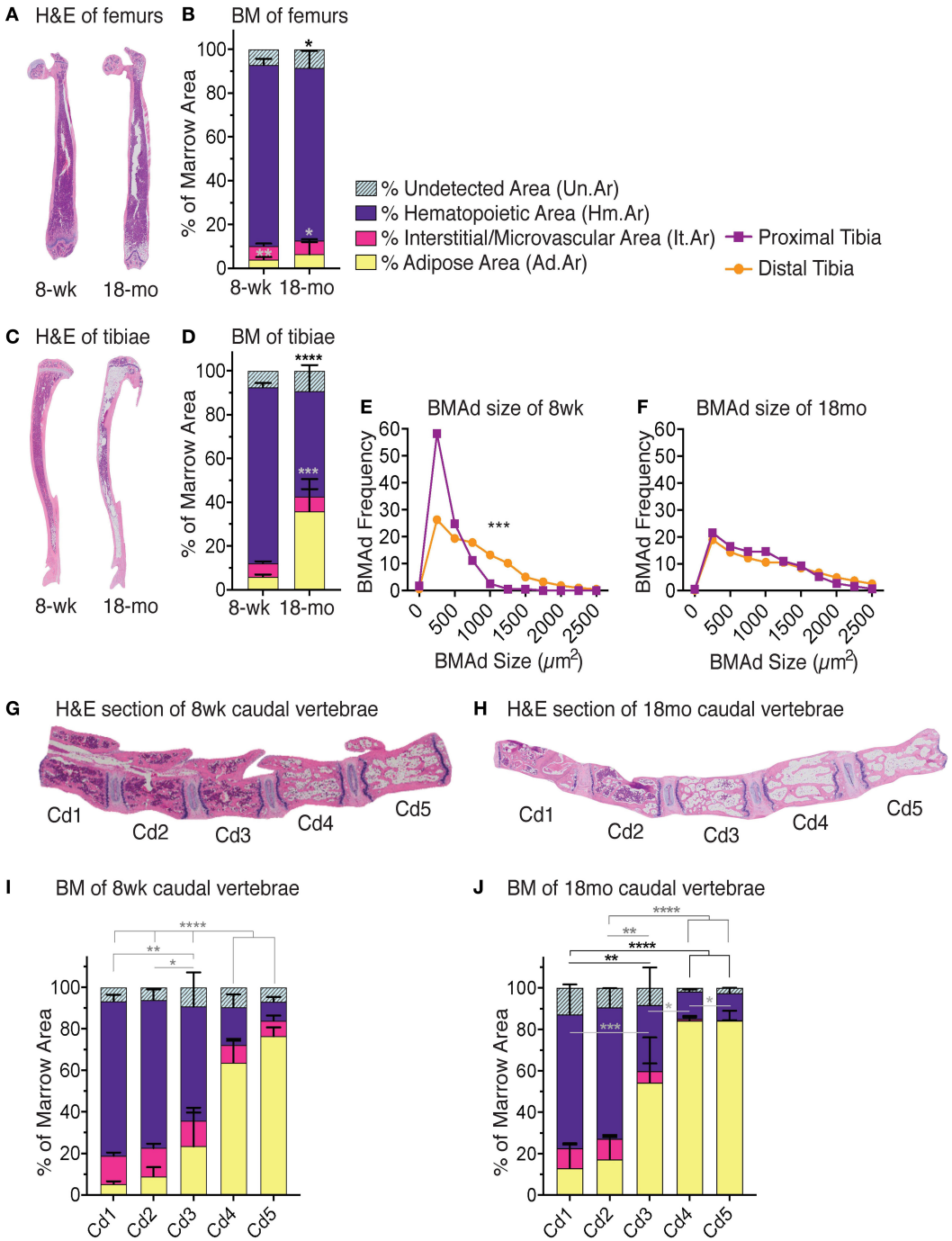

FIGURE 6 | Red-to-yellow transition with aging. Representative H&E images of femurs **(A)** tibiae **(C)**. Note high adiposity on proximal and distal but not mid-shaft of 18-months-old female tibia. *MarrowQuant* analysis for **(B)** femurs ($n = 3$) and **(D)** tibiae ($n = 3$) from 8-weeks-old and 18-months-old C57BL/6 females. BM adiposity is significantly higher in 8-weeks-old tibias vs. femurs ($P = 0.0045$) and in 18-months-old tibias vs. femurs ($P = 0.0316$). Hematopoiesis is greater in 18-months-old femurs than tibias ($P = 0.0993$). Error bars represent mean ± s.d. *P*-values are indicated for hematopoietic compartment (purple) and adipocytic compartment (yellow) are $^{*}P < 0.05$, $^{**}P < 0.01$, $^{***}P < 0.001$, $^{****}P < 0.0001$ by Student's *t*-test for cellularity (black) and adiposity (gray). **(E)** BMAd fragmentation distribution of the proximal (purple) and distal (orange) 8-weeks-old tibia ($n = 10$) vs. **(F)** the 18-months-old tibia ($n = 3$). $^{***}P < 0.001$ by multiple comparisons test. Representative mid-longitudinal H&E section of bone marrow compartments in the proximal-to-distal caudal vertebrae of **(G)** 8-weeks-old and **(H)** 18-months-old mice. *MarrowQuant* analysis of caudal vertebrae in **(I)** 8-weeks-old ($n = 6$) and **(J)** 18-months-old ($n = 4$) female mice. $^{****}P < 0.0001$, $^{**}P < 0.01$ for cellularity and adiposity and $^{*}P < 0.05$ for cellularity by two-way ANOVA. Mice were C57BL/6 females housed at room temperature and fed a standard ad libitum chow diet. BM, bone marrow; BMAd, bone marrow adipocyte; H&E, hematoxylin and eosin; mo, month; wk, week.

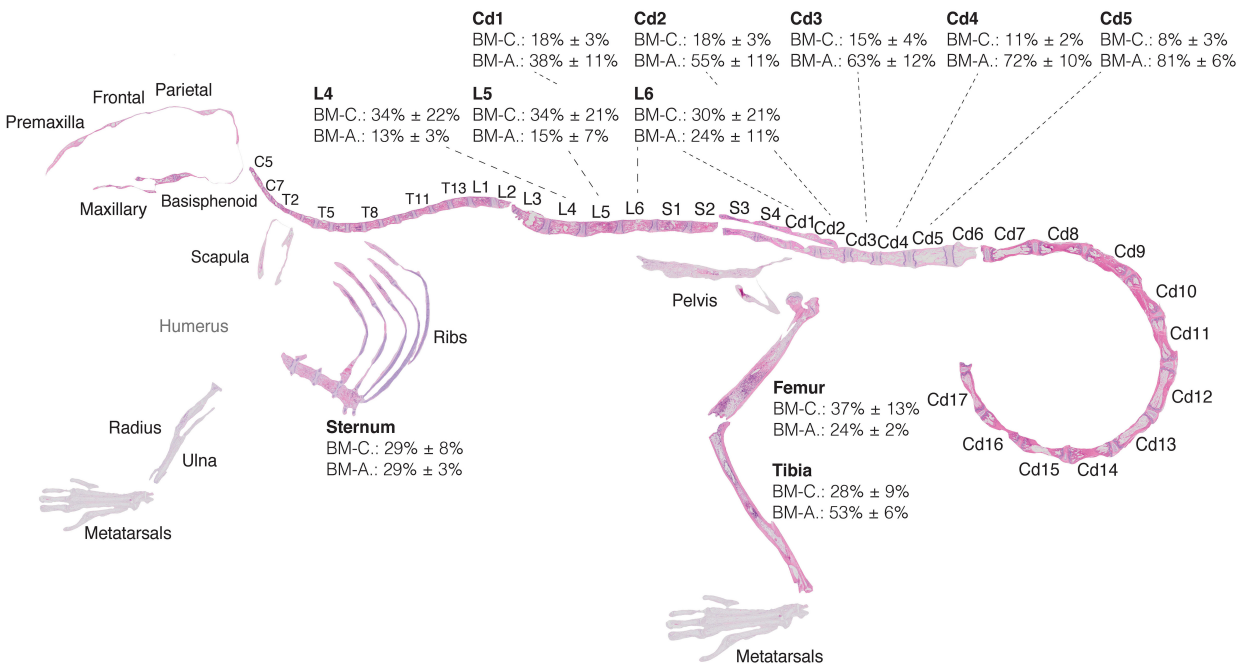

FIGURE 7 | Red-to-yellow-to-red transition in bone marrow aplasia and hematopoietic recovery. Skeletal map of an 8-weeks-old C57Bl/6 female mouse 17 days post-lethal irradiation and transplant of 125,000 total bone marrow cells. Results for *MarrowQuant* quantification of hematopietic cellularity and adiposity are shown for select bones (femur, $n = 3$; tibia, $n = 10$; sternum, $n = 3$; lumbar, $n = 4$; tail, $n = 4$, all error bars represent mean ± s.d). Note that average adiposity (BM-A) and hematopoietic cellularity (BM-C) are homogenous across the axial skeleton (lumbar vertebrae and sternum) and femur, while the tibia and caudal vertebrae present higher adiposity and lower cellularity. BM-C is higher in sternum than Cd5 ($P = 0.0001$) and Cd4 ($P = 0.0002$), while BM-A is higher in Cd-5 ($P < 0.0001$) and Cd4 ($P = 0.0002$) than sternum by Student's *t*-test. Cd, caudal (vertebrae); L, lumbar; S, sacral; T, thoracic.

(**Figures 5**, **7**). Site-specificity variations including a proximal to distal hematopoietic gradient are conserved, and can be reliably measured in the lumbar to caudal transition (**Figure 8F**). Moreover, longitudinal analysis of the "red-to-yellow-to-red" transition in femurs (**Figure 8A**) and tibiae (**Figure 8B**) also indicated a peak of adiposity at days 14–17 post-irradiation, and a higher peak of adiposity in the tibiae than in the femurs.

The first 2 weeks post-irradiation entail important vascular remodeling. Quantitatively, the interstitium/microvasculature even constitute the most important compartment in some of the proximal sites (e.g., femur D4-10, Cd1 on day 17). Interestingly, when samples of varying cellularities post-irradiation are compounded (all images from **Figure 4D**), the measure of hematopoietic cellularity presents preferential reciprocity with the adiposity and interstitium/microvasculature compartments (**Figure S3**), suggesting that hematopoietic expansion or retraction might be the driver of marrow remodeling. Changes in BMAd size fragmentation of lethally irradiated mice as compared to homeostatic C57BL/6 8-weeks-old females, indicate a shift toward more and larger BMAds in the proximal tibia (**Figures 6E**, **8C**, compare purple lines). The increase in number and size signifies hyperplasia and hypertrophy of the labile BMAds in the proximal tibia at the peak of aplasia putatively originating from a differentiation of skeletal stromal/stem cells or pre-BMAds. However, a small change in size fragmentation in the distal tibia, which is predominantly composed of stable adipocytes, indicates that constitutive BMA could also be undergoing some degree of remodeling. A similar "red-to-yellow-to-red" conversion occurs in the femur during the time of aplasia.

Just as with CE-μCT in homeostasis, we set to validate our findings with MRI as an available tool for Gold Standard measurements of BMA. BMA quantification performed in murine limb bones was possible through access to a 9.4 Tesla magnet for small animal imaging. We chose MRI *in vivo* imaging as an alternative to *ex vivo* imaging because repetitive imaging allows for a very significant reduction on the number of animals required to study the kinetics of marrow recovery, as compared to the *ex vivo* terminal experiments. MRI analysis validated the time course of marrow recovery in the femurs of mice undergoing lethal irradiation followed by BM transplantation, as compared to *MarrowQuant* analysis of full bone mid-longitudinal sections (**Figure 8D**). Additionally, MRI measurements also revealed that the proximal femur appears to recover more rapidly (max at D10 and decreases, **Figure 8D**) than the distal portion (max D15–D30, **Figure 8D**), which already contains some BMAds during homeostasis (stable/constitutive BMAds). In conclusion, volumetric measurements by MRI show a progression of fat signal that corresponds to the bidimensional quantification of adipocyte ghosts observed on histology with one of the most commonly used techniques to estimate fat content of a tissue *in vivo* (39).

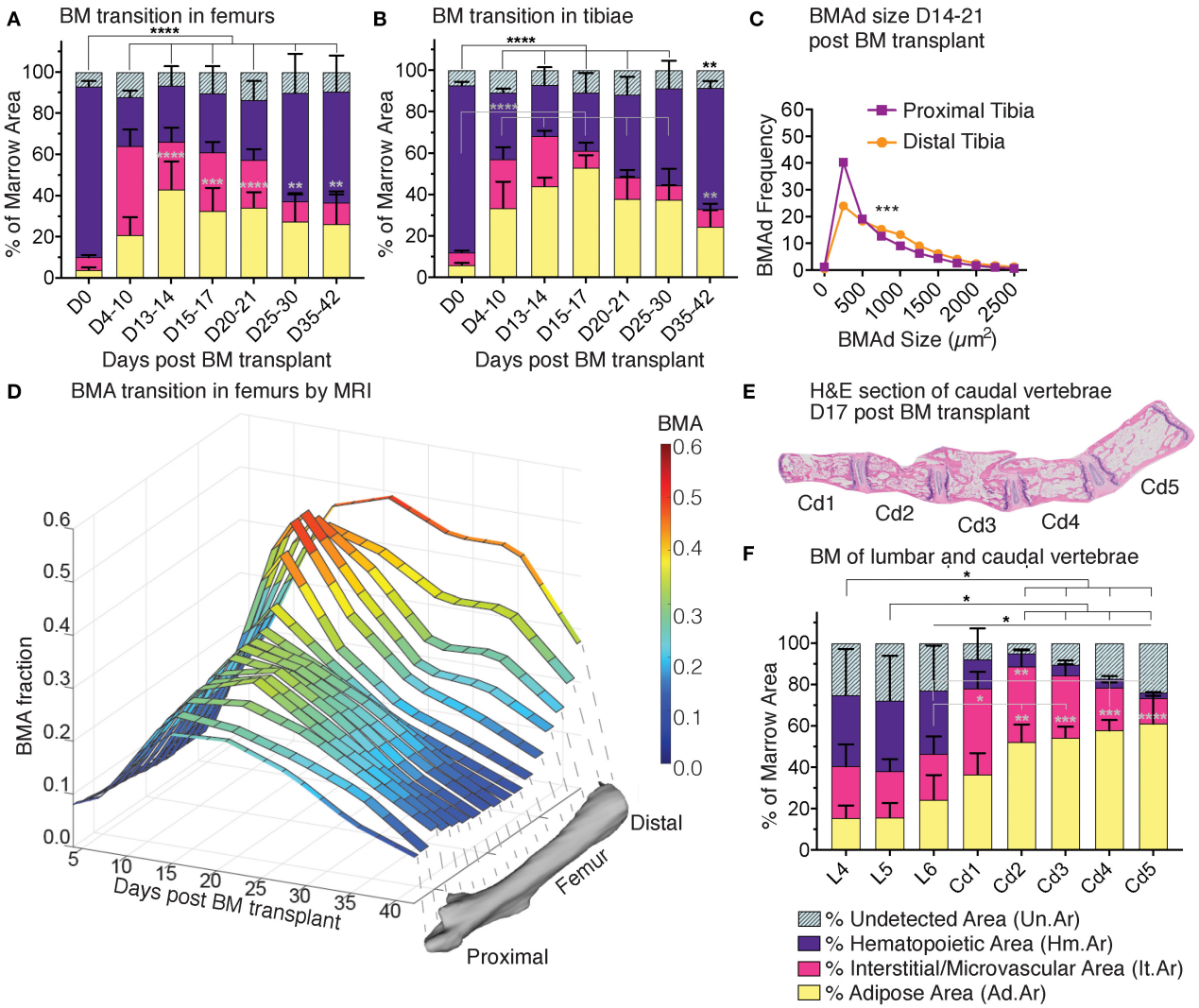

FIGURE 8 | Red-to-yellow-to-red transit ion in bone marrow aplasia and hematopoietic recovery. *MarrowQuant* results for quantifications of **(A)** femurs and **(B)** tibiae in hematopoietic recovery at 0–42 days post lethal irradiation and transplant of 125,000 total bone marrow cells in 2-months-old C57BL/6 female mice. ****$P <$ 0.0001, ***$P < 0.001$, **$P < 0.01$, *$P < 0.05$ by two-way ANOVA for cellularity (black) and adiposity (gray). **(C)** BMAd size fragmentation distribution in the proximal and distal tibia at peak of aplasia on days 17–21 ($n = 10$ tibiae) from *MarrowQuant* measurements extracted from **(B)**. **(D)** Changes in BMA fraction measured by MRI after lethal irradiation and total BM transplant as a time-course of recovery in the whole femur *in vivo* under the same conditions as **(A)**, $n = 3$–5 bones per time point. ***$P < 0.001$ by multiple comparisons test. **(E)** Mid-longitudinal H&E section and **(F)** quantification of bone marrow compartments in the proximal-to-distal caudal vertebrae at day 17 post lethal irradiation and transplant of 125,000 total bone marrow cells in 2-months-old C57BL/6 female mice. ****$P < 0.0001$, **$P < 0.01$, and *$P < 0.05$ for BM adiposity by two-way ANOVA. All error bars represent mean ± s.d. Mice were housed at room temperature and fed a standard *ad libitum* chow diet. BM, bone marrow; BMA, bone marrow adiposity; BMAd, bone marrow adipocyte; Cd, caudal (vertebrae); D, day; L, lumbar; MRI, magnetic resonance imaging; S, sacral; T, thoracic.

Human Trephine Biopsies

MarrowQuant has been developed for quantification of mouse bone H&E stained paraffin sections and is also able to detect BM compartments in human trephine biopsies (**Figure S4**). While samples analyzed from mice have the entire bone encompassing the marrow still intact, trephine biopsies although similar in size (roughly 2 cm long and 2 mm in diameter) also have trabecular bone but not the cortical bone encompassing the marrow. Cells are larger in general (40) thus presenting a different texture to stained mouse sections and may also present with a larger degree of serous infiltrate that is not detectable with the current version of *MarrowQuant*. Additionally, due to their surgical nature, trephine biopsies are by definition hemorrhagic with RBCs detected throughout the majority of the interstitium. Note that currently *MarrowQuant* cannot separate the interstitial and the microvascular components. Despite these differences, initial correlations, indicate promising results (pathologists $n = 2$, images $n = 32$, $R^2 = 0.85$, **Figure S4F**).

DISCUSSION

MarrowQuant provides a means to quantitatively evaluate overall BM architecture in H&E-stained sections in single- or batch-mode by subclassification into the bone, adipose, hematopoietic, and interstitial/microvascular compartments. Systematic comparison of training and validation sets with gold standards for adiposity and hematopoietic cellularity showed robust correlations. To our knowledge, this is the first semi-automated digital pathology tool to quantitatively evaluate murine marrow composition and in particular the hematopoietic and interstitial/microvascular compartment. Other approaches in murine and human tissues have been described which focus mainly on bone morphometry and use stains non-compatible with concurrent hematopoietic evaluation such as Goldner's Trichrome or Von Kossa or TRAcP (6, 41).

While standard practices for evaluating bone morphometry and hematopoietic cellularity have existed for many years, the field of BMA is newly emerging and thus methods of quantification are currently being defined. Automatization of sample preparation and quantification is required to increase accuracy, comparability, and reproducibility of results (6). This is rapidly developing in clinical and experimental pathophysiology with image-analysis programs emerging for quantification and detection of specific cell types related to disease progression (42, 43). Indeed, the high-quality image collection of over 192 murine H&E-stained bone sections that composes our dataset may become useful in training deep-learning algorithms for full automatization and finer detection of BM compartments. Histomorphometry reveals abundant architectural information about a specimen that may be missed by the gating inherent to immunofluorescence. In the future, highly multiplexed immunofluorescence staining has the possibility to reveal as much information of cellular composition as conventional flow cytometry analysis while conserving information on tissue structure (44). *MarrowQuant* constitutes an example of a histomorphometry digital pathology tool that can provide quantitative data complementary to visual analysis of architectural features.

BM Compartment Detection

MarrowQuant relies on the user's definition of a region of interest and the exclusion of artifacts that may arise from sample processing (such as fixation retractions). High-quality stained sections provide best results as the tool relies on intact adipocyte membranes and an even staining coloration for quantification. Image acquisition is also an important initial aspect of preparation as the tool relies on background identification, and therefore stitched images should not show a gradient that would produce an uneven shade of the background and influence subsequent processing steps. Despite these measures that must be accounted for during setup, the automation of image quantification with *MarrowQuant* means that numerous samples can be batch processed. While the automated quantification is up to four times longer than a pathologists' assessment of hematopoietic cellularity (2 min on a standard laptop computer vs. less than a minute per image for pathologists), it has the advantage of providing quantitative information on several BM compartments at once in a highly reproducible manner.

The quantitative output for the bone, adiposity and interstitium/microvasculature mask in the *MarrowQuant* results is straight-forward. Two results are provided for the quantification of the hematopoietic compartment due to discrepancies in the most appropriate denominator to be used. For users interested in subdividing the BM compartment (e.g., **Figures 5–8**) the only relevant output for the hematopoietic compartment is the result of Equation 2. For users who would like to use *MarrowQuant* exclusively for quantification of the hematopoietic compartment, similarly to pathologist evaluation of "cellularity," we propose using Equation 1. Note that datasets with a prominent number of low cellularity samples (<30% cellularity) may benefit from choosing Equation 2 (**Figure 7**).

The user should be aware of some limitations of MarrowQuant regarding BM segmentation. Firstly, the current version of *MarrowQuant* provides area values which compound the full area of interest. Thus, *MarrowQuant* calculations do not provide a regional gradient of cellularity or adiposity within each bone unless the user manually fragments the bone into separate images. A measure of dispersion across a single bone may be of interest when the marrow compartment is expected to be highly heterogenous. This is the case, for example, in early hematopoietic recovery post-aplasia, where loci of hematopoiesis appear heterogeneously across the marrow space.

Secondly, osteoblasts or bone lining cells with prominent nuclei that have a similar color and texture to the nucleated cells that make up the hematopoietic mask, may be included in the hematopoietic area if detached from the endosteal surface (**Figures S5A,E**). *MarrowQuant* contains a bone mask dilation feature that will prevent cells in direct endosteal position from being counted in the hematopoietic area. However, if detached, depending on the extent of the artifact and the overall hematopoietic cellularity of the sample, such cells may be misclassified as a significant portion of the hematopoietic mask. In this case, the user should manually exclude them as artifacts. Other non-hematopoietic cells with prominent nuclei, likely including both bone lining cells (45, 46) and stromal cells are expected to be recognized within the hematopoietic mask or fall within the undetected area.

Thirdly, since hematopoietic detection is based on identification of nuclei, the area occupied by adipocytic nuclei may contribute to the hematopoietic compartment (**Figures S5B,F**). In our dataset, this phenomenon constitutes a systematic bias of <5% (see crossing of *MarrowQuant* values on x-axis, **Figure 4D**), which is an insignificant contribution to the hematopoietic area in samples of medium to high cellularity, but may add variability in samples of low hematopoietic cellularity and high adiposity.

Fourthly, while the nuclei of megakaryocytes are correctly assigned to the hematopoietic mask, their cytoplasm is often included within the microvascular/interstitial compartment, and sometimes identified as bone area due to their similar texture and color (**Figures S5C,G**). These mis-assigned bone areas are easily detected as squares within the marrow space, and will be automatically subtracted from the total Ma.Ar. In our

dataset, the area of mis-assigned megakaryocytes is minimal, but this may become relevant in other biological contexts where megakaryocytes are significantly enlarged and/or increased in number (e.g., myeloproliferative neoplasms). Finally, the interstitium/microvasculature is well-detected by *MarrowQuant* but may be problematic when the RBCs and/or serous infiltrate are lost upon tissue fixation in specific areas, such as on hemorrhage with leakage of vessels, or in perfused samples. The empty spaces must then be taken as artifacts to avoid them being counted as adipocytes, although the total area of interest is thus reduced to quantify the conserved tissue only. A related inherent bias is the fact that the mid region of the bone (e.g., mid-sagittal sections for the tibiae and mid-longitudinal sections for femurs) often contains the central vein, whose lumen is enlarged due to the fixation-related retraction artifact. In the interest of consistency across the dataset, we have opted to classify the enlarged central lumen as an artifact. Sections across the lumen therefore contain a reduced "total area of interest" for analysis. These are examples of issues that the user should be familiar with, and aware of when interpreting results.

Adipocyte Fragmentation

Adipocyte quantification on BM sections will be largely dependent on the quality of the sample and absolute values must be interpreted with caution. One caveat is that adipocyte size fragmentation is a comparative measure and *MarrowQuant* may hyper- or hypo-fragment adipocytes where membranes are not clear (**Figures S5D,H**). In our dataset hypo/hyper-fragmentation does not contribute to the overall adipocytic area as compared to manual classification. However, when membranes are intact, as is more often the case with extramedullary adipose tissue due to the nature of the samples, hypo/hyper-fragmentation is a negligible factor.

In our hands, the adipocyte-only detection function of *AdipoQuant* is somewhat more convenient to apply on extramedullary tissue than other current open-source softwares developed specifically for white adipose tissue. Although the number of adipocytes obtained are similar, the area identified by *AdipoQuant* (or *MarrowQuant* at large) seems truer to size. The fragmentation of the adipocytes lies clearly on the membranes and not within the adipocyte itself when compared to, for example, Adiposoft (**Figure S6**) (47). Identifying an area of interest before quantification also allows the user to quantify whole tissue sections and to eliminate regions that may be irrelevant for a particular analysis (such as vasculature). Thus, while Adiposoft may give a more accurate total adipocyte count in samples of lower quality, *MarrowQuant* will be truer to the total adipocytic area and distribution. Moreover, the *MarrowQuant* adipocyte fragmentation and separate annotation per adipocyte linked to the flexibility of QuPath, allows the user to easily correct for false positives during the post-analysis validation and eliminate them from the analysis.

Human Application

We have found that the most important difference affecting *MarrowQuant* results between human and mouse lies in the fact that hematopoietic nuclei are less densely packed in human as compared to mouse marrow. Indeed, in our experience, the cytosolic space of mouse hematopoietic cells is relatively small in histological sections as compared to human samples. Additionally, while mouse marrow samples are encased by cortical bone, human trephine biopsies of a similar size comprise only a small part of the entire bone and thus the marrow space as seen in these histological samples are not fully surrounded by cortical bone. Other processing issues come from visible color differences between mouse and human samples. The potentially duller stain of the human samples has consequences on the efficiency for the thresholding methods used in the code and can sometimes result in mis-segmentation. The observed color difference may be due to the nature of the samples, the preparation and staining protocols, and/or subsequent storage of slides before image acquisition. The method for decalcification of the bone may be different which may influence bone staining. Additionally, human slides were imaged weeks after staining whereas mouse image were usually scanned days after staining. These points could explain the observed color alteration in human samples. Technical adaptations are ongoing for an improved quantification of human BM in a later *MarrowQuant* release. In conclusion, due to the different nature of human biopsies compared to mouse samples, several parameters of the plugin must still be optimized to obtain accurate and reliable measurements, which will be the subject of a separate study and a new software release.

CONCLUSION

H&E is the most common and routinely performed stain in histopathology. *MarrowQuant* is a semi-automated digital pathology tool and workflow for QuPath, that quantifies four detectable BM compartments (adipocytic, hematopoietic, osseous, interstitial/microvascular, interstitium/microvasculature) and the remaining undetected area, if any, on H&E stained sections of whole intact murine bones. *MarrowQuant* was optimized for paraffin-stained sections but could potentially be applicable to plastic-embedded samples that are also widely used for histomorphometry. Despite some discordances in mid-cellularity samples which also present a high inter-observer variability, *MarrowQuant* cellularity calculation falls within the range of pathologists' estimations.

While the paraffin sections present only one slice of the whole organ, in our experimental setup with mid-sections of entire bones from C57BL/6 mice, the quantification correlates highly with volumetric quantifications of the contralateral whole bone by μCT combined with osmium-tetroxide staining. We were also able to apply the non-invasive technique of MRI *in vivo* to follow changes in fat signal on murine hematopoietic recovery. The results correspond to *MarrowQuant* histological assessment and correlate with blood recovery curves at peak of aplasia. Moreover, *MarrowQuant* provides a size fragmentation distribution of adipocytes and thus may additionally be applied to H&E sections of extramedullary white (omental or inguinal)

adipose tissue. This feature has been extracted to offer the possibility of independent use from *MarrowQuant*, and has been named "AdipoQuant."

Future iterations of the tool applied to human samples could incorporate machine learning methods to overcome the hurdles of the distinct morphology of human tissue and detection of specific cells (e.g., macrophages and megakaryocytes with large cytoplasms, bone-lining cells). Close collaboration with hematopathologists will help to further develop this tool for human tissues and potential clinical research and/or computer-aided diagnostic applications.

METHODS

Mice

In vivo procedures were carried out in accordance with the Swiss law after approval from the local authorities (Service Vétérinaire de l'Etat de Vaud) and experiments were designed according to the ARRIVE guidelines. Eight-weeks old C57BL/6J were purchased from Charles River Laboratories International and maintained at the Center for Studying Living System (CAV) at the EPFL in microisolator cages. Mice were provided continuously with sterile food and water *ad libitum*, and bedding. Mice were housed at room temperature in 12 h light/dark cycles and fed a standard *ad libitum* chow diet.

Human Samples

This work was performed under the approval of the local ethical authorities (CER-VD). Images of human bone marrow H&E stained paraffin sections from diagnostic samples of patients undergoing treatment for acute myeloid leukemia were received for analysis as blinded, anonymous images form the Institute of Pathology at Lausanne University Hospital (CHUV). The trephine biopsies were processed for standard pathology diagnosis and H&E stained paraffin sections were scanned using a 40x objective.

Bone Marrow Transplantation

Eight-weeks-old female C57BL/6 mice were lethally irradiated with a total 850 rad dose in an X-ray radiator (RS-2000, RAD SOURCE) 24 h before transplant. The dose was split in two doses of 425 rads separated by a 4-h interval. Total bone marrow cells were isolated from crushed bone marrow of 8-weeks-old female C57BL/6J donor mice in phosphate buffered saline (PBS, Life Technologies 10010056) solution with 1 mM EDTA (Thermo Fisher Scientific 15575020). Total BM cells for transplantations by SR-S were obtained by flushing instead of crushing. RBCs were removed by incubation with ice-cold lysis buffer (BioLegend) for 30 s. Samples were filtered through a 70 μm cell strainer (Sigma Aldrich CLS431751) and centrifuged at 300 g for 10 min at 4°C. Recipient mice were injected with 125,000 donor cells via tail-vein injection. For at least 2 weeks after lethal irradiation mice were treated with paracetamol and antibiotics in the form of 30 mg of Enrofloxacin (300 μl of Baytril 10% solution, 100 mg/ml, Bayer) and 125 mg of Amoxicillin (2.5 ml of Amoxi-Mepha 200 mg/4 ml, Mepha Pharma AG) as well as 500 mg of Paracetamol (Dafalgan®) to 250 ml of drinking water protected from light. Peripheral blood was collected to assess blood recovery (blood volume 50 μl) and analyzed by standard veterinarian blood cell counter (ABC™). Mice were sacrificed by CO_2 inhalation.

Magnetic Resonance Imaging

All experiments were conducted on a 9.4T/26 cm horizontal magnet (Agilent/Varian) using a home-built quadrature transceiver of 20 mm diameter loops (**Figure S7**). Animals were anesthetized with 1.5% of isoflurane, respiration, and temperature were monitored during the whole study. Animals were placed on their side and the leg was immobilized in a contracted position. A triple point Dixon acquisition (39) was performed using a spin-echo based sequence (te = 9 ms, tr = 1.5 s) with 10 coronal slices of 0.8 mm on a FOV 25 × 20 mm^2 (acq. Matrix 192 × 128). Dixon's technique in combination with a spin-echo based sequence minimized signal loss of the marrow due to bone magnetic susceptibility. Three acquisitions were performed with the echo acquisition shifted 0, 0.4, and 0.8 ms corresponding to the fat-water chemical shift of 1,250 Hz at 9.4 T. Images were reconstructed using a homebuilt Matlab script to extract water and fat maps. Phase unwrapping was performed using a toolbox from Matlab file exchange (48). At the end of the MR acquisitions, animals were sacrificed, tibia and femur were dissected to conduct histology and validate MR Dixon acquisitions.

Histology

Bones were extracted and cleaned of soft tissue. Long bones and cranium were placed loosely in histology cassettes while spine (including tail) and paws were placed in histology cassettes (Simport M505-11) with sponges (Simport M476-1) to flatten the samples for facilitated sectioning. Bones were fixed for 24 h at room temperature in 10% neutral buffered formalin (VWR 11699404), then rinsed three times with phosphate buffered saline (1x PBS) solution. Bones were decalcified in 20% sodium-citrate (Sigma Aldrich 71405) and formic acid (ROTH 4724.3) solution (v/v) for 30–36 h or in 0.4 M EDTA pH 7.4 (Sigma Aldrich 607-429-00-8) for 2 weeks (solution changed every 3 days) at room temperature. The two different decalcification protocols resulted in similar quality of H&E-stained paraffin sections. Bones were washed three times in PBS or under running tap water for 2 h before transferring to 70% ethanol (Reactolab 96170). The tissues were submitted for stepwise dehydration and embedded in paraffin blocks for sectioning at 3–4 μm thickness with a rotary microtome (RM, Leica microsystems). All cuts were mid-bone sections (i.e., mid-longitudinal for femurs and mid-sagittal for tibiae). Bone silhouettes that do not correspond to those presented in **Figures 5**, **6** for mid-bone sections were discarded. For mid-longitudinal sections of the femur, at the proximal end, both the head and the neck should be visible, while at the distal end, the two condyli (medial and lateral) should be visible. For mid-sagittal sections of the tibia, at the proximal end, the tibial plate should be intact with conservation of the tuberosity and crest of the tibia; at the distal end, insertion of the fibula as well as the lateral and medial malleolous at the ankle joint should be visible. Femoral and tibial silhouettes

that preserve these features should then preserve a contiguous marrow cavity. After floating on a water bath to flatten, sections were mounted on glass slides (Superfrost+ slides, Menzel gläser). Paraffin sections were stained with Hematoxylin and eosine (H&E) using the Tissue-Tek Prisma automate (Sakura) and permanently mounted using the Tissue-Tek glass G2-coverslipper (Sakura) to assess morphology.

Image Acquisition and Processing

Whole-slide images were acquired with an automated slide scanner (Olympus VS120-SL) at 20x magnification with focus points along the total area of interest or using the *in-situ* focus mode using the accompanying software (Olympus VS-ASW L100 2.9). VSI files obtained from scanning were directly loaded into QuPath for analysis on Windows or Mac operating systems. Extracted TIFF files were also used for analysis. The "training-set" consisted of 79 images of full or partial bones. The "validation-set" consisted of 59 images of full bones. Parameters are pre-set but adjustable by the user if deemed necessary (e.g., adipocyte circularity or size, see tutorial for details). The software workflow follows basic morphological operations, color deconvolutions, thresholding, smoothing operations, and watershed as annotated in the code provided as open source and described in the technical guidelines. When accounting for pre-processing steps such as the drawing of the regions of interests as well the as the segmentation process, it typically takes 1–2 min in order to obtain *MarrowQuant* outputs for an image with a sample of a mouse bone. Technical details are annotated in the code and details on download, installation and use of the plugin with the QuPath software are given in the tutorial (*MarrowQuant* Tutorial, **Supplementary Material**).

MicroCT

Fixed bones were scanned for reconstruction of undecalcified bone. Samples were placed in an Eppendorf tube with PBS and scanned using a Quantum X-Ray Micro-CT Scanner (Perkin Elmer Quantum) at 90 kV, 160 μA, CT 160, live 80, and field of view (voxel size) 20 μm^2 at setting "Fine" for 2 min per sample. A hydroxyapatite phantom was included as control. The software suite provided by the manufacturer was used for image acquisition and reconstruction. Bones were then processed further with formic acid decalcification and osmium tetroxide staining.

Osmium Tetroxide Staining

Decalcified bones were rinsed in distilled water. Osmium tetroxide solution was prepared fresh (1% osmium tetroxide [Electron Microscopy Sciences 19110), 2.5% dichromate potassium solution (VWR 1.04864.0500)] with appropriate chemical safety protection and samples stained in 20 ml glass scintillation vials (Electron Microscopy Sciences 7632) in 2 ml of solution at room temperature for 48 h. Bones were washed with distilled water three times and transferred to Eppendorf tubes with distilled water for μCT acquisition as done previously. Quantifications were done on the Analyzer 10.0 software (Analyze Direct, Inc.).

Statistical Analysis

Values are shown as mean plus or minus the standard deviation. Statistical analysis was performed using GraphPad Prism (version 8.0.0, GraphPad Software) or R Statistical Analysis Software (2013, R Core Team). Mean values were compared by Student's *t*-test or two-way analysis of variance (ANOVA). Statistical significance was accepted for $P < 0.05$, and reported.

DATA AVAILABILITY STATEMENT

A full package of MarrowQuant and AdipoQuant codes is available on GitHub (https://github.com/Naveiras-Lab/MarrowQuant/tree/qupath-0.1.4), along with a detailed tutorial to download QuPath 0.1.4 and install MarrowQuant and AdipoQuant plugins, as well as the Image Data Resource link and accession number to the full dataset and image bank [IDR, (49)].

ETHICS STATEMENT

The studies involving human participants were reviewed and approved by Comission cantonale d'étique de la recherche sur l'être humain du Canton de Vaud (CER-VD). Written informed consent for participation was not required for this study in accordance with the national legislation and the institutional requirements. The animal study was reviewed and approved by Service de la consommation et des affaires vétérinaires du Canton de Vaud (SCAV).

AUTHOR CONTRIBUTIONS

ON and JT conceived ideas, designed experiments, analyzed results, and wrote the manuscript. JT performed all experiments and analyses unless otherwise stated. CB, OB, and RSark conceptualized, designed, and implemented the code. DB, TK, RSark, and OB edited and migrated the code to the final version. DB, RSark, and FS performed histological quantifications. Pathologists BB, RSarr, VN, LL, and CB evaluated histological sections for hematopoietic cellularity, provided valuable feedback, and discussions. NK customized a coil and protocols for imaging, and performed MR imaging and analyses. DT contributed to microCT analysis and blood recovery curves. SR-S, FS, DT, and VC contributed to specific transplants and histological mounting/analysis. ES provided slides and discussions on histology. ON initiated the project. All authors edited and reviewed the final manuscript.

FUNDING

ON and lab members were supported by the Machaon Foundation, the Dr. Henri Dubois-Ferrière Dinu Lipatti Leukemia Foundation, the Fondation Pierre Mercier pour la science, the Anna Fuller fund, and Swiss National Science Foundation (SNF/SNSF) Professorship grants PP00P3_144857, PP00P3_176990, and PP00P3_183725, as well as discretionary EPFL SV funds. NK was funded by the Leenards and Jeantet

foundation. SR-S was funded by the EPFL Fellows-Marie Sklodowska-Curie scheme. ES was funded by a grant from the National Institutes of Health, U01-DK116317.

ACKNOWLEDGMENTS

This work could not have been possible without the expertise and investment of the EPFL Bioimaging and Optics Platform, especially OB, Romain Guiet, and Arne Seitz. We thank members of the Center for the Study of Living Systems at EPFL for animal care, the EPFL Electron Microscopy Facility, namely Graham Knott and Stephanie Rosset for providing osmium and solution preparation, and the EPFL Phenogenomics Unit and E. Meylan for flexibility and assistance on microCT imaging. We thank the Center for Biomedical Imaging Animal veterinarians for their kind help during experiments. The histology data was performed at or with the help of the EPFL Histology Core Facility, notably Dr. Jessica Sordet-Dessimoz. We are grateful to Frédéric Schütz from the Swiss Institute of Bioinformatics for valuable statistical guidance, to Teresa Didonna and Bart Deplancke for feedback on the beta version of *AdipoQuant,* and to Andrew Janowczyk for critical reading of the manuscript. ON would like to thank Prof. Paolo Bianco (Sapienza University, Rome, Italy) as well as Prof. George Q. Daley and Dr. Roderick Bronson (Harvard Medical School, Boston, USA) for the inspiration and encouragement to pursue this work.

SUPPLEMENTARY MATERIAL

The Supplementary Material for this article can be found online at: https://www.frontiersin.org/articles/10.3389/fendo.2020.00480/full#supplementary-material

REFERENCES

1. Scheller EL, Rosen CJ. What's the matter with MAT? Marrow adipose tissue, metabolism, and skeletal health: marrow adipose tissue and skeletal health. *Ann N Y Acad Sci.* (2014) 1311:14–30. doi: 10.1111/nyas.12327
2. Scheller EL, Khoury B, Moller KL, Wee NK, Khandaker S, Kozloff KM, et al. Changes in skeletal integrity and marrow adiposity during high-fat diet and after weight loss. *Front Endocrinol.* (2016) 7:102. doi: 10.3389/fendo.2016.00102
3. Kricun ME. Red-yellow marrow conversion: its effect on the location of some solitary bone lesions. *Skeletal Radiol.* (1985) 14:10–9. doi: 10.1007/BF00361188
4. Neumann E. The law of distribution of yellow and red marrow in the bones of the extremities. *Cent J Med Sci.* (1882) 20:321–3.
5. Scheller EL, Doucette CR, Learman BS, Cawthorn WP, Khandaker S, Schell B, et al. Region-specific variation in the properties of skeletal adipocytes reveals regulated and constitutive marrow adipose tissues. *Nat Commun.* (2015) 6:7808. doi: 10.1038/ncomms8808
6. Tratwal J, Labella R, Bravenboer N, Kerckhofs G, Douni E, Scheller EL, et al. Reporting guidelines, review of methodological standards, and challenges toward harmonization in bone marrow adiposity research. Report of the Methodologies Working Group of the International Bone Marrow Adiposity Society. *Front Endocrinol.* (2020) 11:65. doi: 10.3389/fendo.2020.00065
7. Tavassoli M. Marrow adipose cells. Histochemical identification of labile and stable components. *Arch Pathol Lab Med.* (1976) 100:16–8.
8. Iwaniec UT, Turner RT. Failure to generate bone marrow adipocytes does not protect mice from ovariectomy-induced osteopenia. *Bone.* (2013) 53:145–53. doi: 10.1016/j.bone.2012.11.034
9. Keune JA, Wong CP, Branscum AJ, Iwaniec UT, Turner RT. Bone marrow adipose tissue deficiency increases disuse-induced bone loss in male mice. *Sci Rep.* (2017) 7:46325. doi: 10.1038/srep46325
10. Schwartz AV. Marrow fat and bone: review of clinical findings. *Front Endocrinol.* (2015) 6:40. doi: 10.3389/fendo.2015.00040
11. Ambrosi TH, Scialdone A, Graja A, Gohlke S, Jank A-M, Bocian C, et al. Adipocyte accumulation in the bone marrow during obesity and aging impairs stem cell-based hematopoietic and bone regeneration. *Cell Stem Cell.* (2017) 20:771–84.e6. doi: 10.1016/j.stem.2017.02.009
12. Ding L, Morrison SJ. Haematopoietic stem cells and early lymphoid progenitors occupy distinct bone marrow niches. *Nature.* (2013) 495:231–5. doi: 10.1038/nature11885
13. Ding L, Saunders TL, Enikolopov G, Morrison SJ. Endothelial and perivascular cells maintain haematopoietic stem cells. *Nature.* (2012) 481:457–62. doi: 10.1038/nature10783
14. Mattiucci D, Maurizi G, Izzi V, Cenci L, Ciarlantini M, Mancini S, et al. Bone marrow adipocytes support hematopoietic stem cell survival. *J Cell Physiol.* (2018) 233:1500–11. doi: 10.1002/jcp.26037
15. Méndez-Ferrer S, Michurina TV, Ferraro F, Mazloom AR, MacArthur BD, Lira SA, et al. Mesenchymal and haematopoietic stem cells form a unique bone marrow niche. *Nature.* (2010) 466:829–34. doi: 10.1038/nature09262
16. Nakamura Y, Arai F, Iwasaki H, Hosokawa K, Kobayashi I, Gomei Y, et al. Isolation and characterization of endosteal niche cell populations that regulate hematopoietic stem cells. *Blood.* (2010) 116:1422–32. doi: 10.1182/blood-2009-08-239194
17. Naveiras O, Nardi V, Wenzel PL, Hauschka PV, Fahey F, Daley GQ. Bone-marrow adipocytes as negative regulators of the haematopoietic microenvironment. *Nature.* (2009) 460:259–63. doi: 10.1038/nature08099
18. Zhou BO, Yu H, Yue R, Zhao Z, Rios JJ, Naveiras O, et al. Bone marrow adipocytes promote the regeneration of stem cells and haematopoiesis by secreting SCF. *Nat Cell Biol.* (2017) 19:891–903. doi: 10.1038/ncb3570
19. Wilke C, Holtan SG, Sharkey L, DeFor T, Arora M, Premakanthan P, et al. Marrow damage and hematopoietic recovery following allogeneic bone marrow transplantation for acute leukemias: effect of radiation dose and conditioning regimen. *Radiother Oncol.* (2016) 118:65–71. doi: 10.1016/j.radonc.2015.11.012
20. Beekman KM, Veldhuis-Vlug AG, van der Veen A, den Heijer M, Maas M, Kerckhofs G, et al. The effect of PPARγ inhibition on bone marrow adipose tissue and bone in C3H/HeJ mice. *Am J Physiol Endocrinol Metab.* (2019) 316:E96–105. doi: 10.1152/ajpendo.00265.2018
21. Bornstein S, Moschetta M, Kawano Y, Sacco A, Huynh D, Brooks D, et al. Metformin affects cortical bone mass and marrow adiposity in diet-induced obesity in male mice. *Endocrinology.* (2017) 158:3369–85. doi: 10.1210/en.2017-00299
22. Costa S, Fairfield H, Reagan MR. Inverse correlation between trabecular bone volume and bone marrow adipose tissue in rats treated with osteoanabolic agents. *Bone.* (2019) 123:211–23. doi: 10.1016/j.bone.2019.03.038
23. Devlin MJ, Cloutier AM, Thomas NA, Panus DA, Lotinun S, Pinz I, et al. Caloric restriction leads to high marrow adiposity and low bone mass in growing mice. *J Bone Miner Res.* (2010) 25:2078–88. doi: 10.1002/jbmr.82
24. Le PT, Bishop KA, Maridas DE, Motyl KJ, Brooks DJ, Nagano K, et al. Spontaneous mutation of Dock7 results in lower trabecular bone mass and impaired periosteal expansion in aged female Misty mice. *Bone.* (2017) 105:103–14. doi: 10.1016/j.bone.2017.08.006
25. Styner M, Pagnotti GM, McGrath C, Wu X, Sen B, Uzer G, et al. Exercise decreases marrow adipose tissue through ss-oxidation in obese running mice. *J Bone Miner Res.* (2017) 32:1692–702. doi: 10.1002/jbmr.3159
26. Syed FA, Oursler MJ, Hefferan TE, Peterson JM, Riggs BL, Khosla S. Effects of estrogen therapy on bone marrow adipocytes in postmenopausal osteoporotic

women. *Osteoporos Int.* (2008) 19:1323–30. doi: 10.1007/s00198-008-0574-6
27. Wesseling-Perry K, Mäkitie RE, Välimäki V-V, Laine T, Laine CM, Välimäki MJ, et al. Osteocyte protein expression is altered in low-turnover osteoporosis caused by mutations in WNT1 and PLS3. *J Clin Endocrinol Metab*. (2017) 102:2340–8. doi: 10.1210/jc.2017-00099
28. Bankhead P, Loughrey MB, Fernández JA, Dombrowski Y, McArt DG, Dunne PD, et al. QuPath: open source software for digital pathology image analysis. *Sci Rep*. (2017) 7:5. doi: 10.1038/s41598-017-17204-5
29. Lu W, Wan Y, Li Z, Zhu B, Yin C, Liu H, et al. Growth differentiation factor 15 contributes to marrow adipocyte remodeling in response to the growth of leukemic cells. *J Exp Clin Cancer Res.* (2018) 37:66. doi: 10.1186/s13046-018-0738-y
30. Lu W, Weng W, Zhu Q, Zhai Y, Wan Y, Liu H, et al. Small bone marrow adipocytes predict poor prognosis in acute myeloid leukemia. *Haematologica.* (2018) 103:e21–4. doi: 10.3324/haematol.2017.173492
31. Aeffner F, Zarella M, Buchbinder N, Bui M, Goodman M, Hartman D, et al. Introduction to digital image analysis in whole-slide imaging: a white paper from the digital pathology association. *J Pathol Inform.* (2019) 10:9. doi: 10.4103/jpi.jpi_82_18
32. Bravenboer N, Bredella MA, Chauveau C, Corsi A, Douni E, Ferris WF, et al. Standardised nomenclature, abbreviations, and units for the study of bone marrow adiposity: report of the Nomenclature Working Group of the International Bone Marrow Adiposity Society. *Front Endocrinol.* (2020) 10:923. doi: 10.3389/fendo.2019.00923
33. Pfeifer JD, Dehner LP, Humphrey PA. *The Washington Manual of Surgical Pathology*. Wolters Kluwer Health (2019).
34. Riley RS, Williams D, Ross M, Zhao S, Chesney A, Clark BD, et al. Bone marrow aspirate and biopsy: a pathologist's perspective. II interpretation of the bone marrow aspirate and biopsy. *J Clin Lab Anal.* (2009) 23:259–307. doi: 10.1002/jcla.20305
35. Cawthorn WP, Scheller EL, Learman BS, Parlee SD, Simon BR, Mori H, et al. Bone marrow adipose tissue is an endocrine organ that contributes to increased circulating adiponectin during caloric restriction. *Cell Metabol.* (2014) 20:368–75. doi: 10.1016/j.cmet.2014.06.003
36. Tavassoli M, Yoffey JM. *Bone Marrow, Structure and Function*. New York, NY: AR Liss. (1983).
37. Dominietto A, Lamparelli T, Raiola AM, Van Lint MT, Gualandi F, Berisso G, et al. Transplant-related mortality and long-term graft function are significantly influenced by cell dose in patients undergoing allogeneic marrow transplantation. *Blood.* (2002) 100:3930–4. doi: 10.1182/blood-2002-01-0339
38. Schmitz N, Pfistner B, Sextro M, Sieber M, Carella AM, Haenel M, et al. Aggressive conventional chemotherapy compared with high-dose chemotherapy with autologous haemopoietic stem-cell transplantation for relapsed chemosensitive Hodgkin's disease: a randomised trial. *Lancet.* (2002) 359:2065–71. doi: 10.1016/S0140-6736020 8938-9
39. Glover GH. Multipoint Dixon technique for water and fat proton and susceptibility imaging. *J Magn Reson Imaging.* (1991) 1:521–30. doi: 10.1002/jmri.1880010504
40. Fukuda T, Asou E, Nogi K, Goto K. Evaluation of mouse red blood cell and platelet counting with an automated hematology analyzer. *J Vet Med Sci.* (2017) 79:1707–11. doi: 10.1292/jvms.17-0387
41. van't Hof RJ, Rose L, Bassonga E, Daroszewska A. Open source software for semi-automated histomorphometry of bone resorption and formation parameters. *Bone.* (2017) 99:69–79. doi: 10.1016/j.bone.2017.03.051
42. Tjin G, Flores-Figueroa E, Duarte D, Straszkowski L, Scott M, Khorshed RA, et al. Imaging methods used to study mouse and human HSC niches: current and emerging technologies. *Bone.* (2019) 119:19–35. doi: 10.1016/j.bone.2018.04.022
43. Kozlowski C, Fullerton A, Cain G, Katavolos P, Bravo J, Tarrant JM. Proof of concept for an automated image analysis method to quantify rat bone marrow hematopoietic lineages on H&E sections. *Toxicol Pathol.* (2018) 46:336–47. doi: 10.1177/0192623318766458
44. Coutu DL, Kokkaliaris KD, Kunz L, Schroeder T. Multicolor quantitative confocal imaging cytometry. *Nat Methods.* (2018) 15:39–46. doi: 10.1038/nmeth.4503
45. Matic I, Matthews BG, Wang X, Dyment NA, Worthley DL, Rowe DW, et al. Quiescent bone lining cells are a major source of osteoblasts during adulthood. *Stem Cells.* (2016) 34:2930–42. doi: 10.1002/stem.2474
46. Tormin A, Li O, Brune JC, Walsh S, Schutz B, Ehinger M, et al. CD146 expression on primary non-hematopoietic bone marrow stem cells is correlated with *in situ* localization. *Blood.* (2011) 117:5067–77. doi: 10.1182/blood-2010-08-304287
47. Galarraga M, Campión J, Muñoz-Barrutia A, Boqué N, Moreno H, Martínez JA, et al. Adiposoft: automated software for the analysis of white adipose tissue cellularity in histological sections. *J Lipid Res.* (2012) 53:2791–6. doi: 10.1194/jlr.D023788
48. Ghiglia DC, Pritt MD. *Two-Dimensional Phase Unwrapping: Theory, Algorithms, and Software (Vol. 4)*. New York, NY: Wiley. (1998).
49. Williams E, Moore J, Li SW, Rustici G, Tarkowska A, Chessel A, et al. Image data resource: a bioimage data integration and publication platform. *Nat Methods.* (2017) 14:775–81. doi: 10.1038/nmeth.4326

Conflict of Interest: The authors declare that the research was conducted in the absence of any commercial or financial relationships that could be construed as a potential conflict of interest.

Advantages of publishing in Frontiers

OPEN ACCESS
Articles are free to read for greatest visibility and readership

FAST PUBLICATION
Around 90 days from submission to decision

HIGH QUALITY PEER-REVIEW
Rigorous, collaborative, and constructive peer-review

TRANSPARENT PEER-REVIEW
Editors and reviewers acknowledged by name on published articles

Frontiers
Avenue du Tribunal-Fédéral 34
1005 Lausanne | Switzerland

Visit us: www.frontiersin.org
Contact us: info@frontiersin.org | +41 21 510 17 00

REPRODUCIBILITY OF RESEARCH
Support open data and methods to enhance research reproducibility

DIGITAL PUBLISHING
Articles designed for optimal readership across devices

FOLLOW US
@frontiersin

IMPACT METRICS
Advanced article metrics track visibility across digital media

EXTENSIVE PROMOTION
Marketing and promotion of impactful research

LOOP RESEARCH NETWORK
Our network increases your article's readership